

# Geodätisch-geophysikalische Arbeiten in der Schweiz

(Fortsetzung der Publikationsreihe  
«Astronomisch-geodätische Arbeiten in der Schweiz»)

herausgegeben von der

Schweizerischen Geodätischen Kommission  
(Organ der Akademie der Naturwissenschaften Schweiz)

**Vierundneunzigster Band  
Volume 94**

**Determination of a Precise Gravity Field  
for the CLIC Feasibility Studies**

Sébastien Guillaume

2015

Adresse der Schweizerischen Geodätischen Kommission:

Institut für Geodäsie und Photogrammetrie  
Eidg. Technische Hochschule Zürich  
ETH Zürich  
8093 Zürich  
Switzerland

Internet: <http://www.sgc.ethz.ch>

ISBN 978-3-908440-40-6

Redaktion des 94. Bandes:  
Dr. S. Guillaume, J. Müller-Gantenbein, Prof. A. Geiger  
Druck: Print-Atelier ADAG, Zürich



## VORWORT

Das Schwerfeld ist allgegenwärtig. Weder bei hochtechnologisierten Forschungen und Anwendungen noch im Alltag kann man sich den gravitativen Effekten entziehen. Und trotzdem existieren unter Umständen zu gewissen schwerfeldbezogenen Fragen kaum oder keine Untersuchungen. Herr Guillaume nimmt sich den speziellen Umständen an und beantwortet entsprechende Fragen in nahezu abschliessender Tiefe. Die Umstände betreffen den möglichen Bau eines Linearbeschleunigers beim CERN. Dazu müsste ein gerader Tunnel von ca. 40 km Länge ausgebrochen werden, was von geodätischer Seite her kein unlösbares Problem darstellt. Dazu kommen allerdings die Genauigkeitsanforderungen an Tunnelinstallationen, die die Vorgaben bisher erstellter Bauten deutlich übertreffen. Mit 10 Mikrometern Genauigkeit pro 200m Länge liegt die Anforderung an der Grenze des Machbaren in einer Nicht-Laborumgebung. Das Institut für Geodäsie und Photogrammetrie (IGP) der ETH Zürich blickt auf etliche Jahre Erfahrung im Bereich der Geoidbestimmung zurück. Insbesondere wurde die astrogeodätische Methode vorangetrieben, die durch die Arbeiten Herrn Guillaumes nochmals verbessert und operationalisiert wurde. Im Speziellen ist das neue Zenit Kamera System CODIAC zu erwähnen, das von Herrn Dr. Bürki und Herrn Guillaume entwickelt wurde.

Bereits in den 80-Jahren hatte das IGP Kontakte zum CERN. Damals im Zusammenhang mit GPS Messungen und ebenfalls lokaler Geoidbestimmung. Das CERN fasste die Planung des Baus eines Linearbeschleunigers ins Auge und trug den Wunsch an uns heran, die Machbarkeit einer hochgenauen geodätischen Referenz zu prüfen und Lösungsvorschläge zu deren Realisierung auszuarbeiten. Eine spezielle Herausforderung stellt dabei die Höhenreferenz dar, weil das Schwerfeld mit den diversen Störeffekten sich direkt in der Lösung abbildet. Die möglichst gute Kenntnis aller beeinflussenden Grössen ist wichtig.

In diesem Bericht sind nun die Ergebnisse zusammengefasst und mit entsprechender Theorie hinterlegt dargestellt. Das erarbeitete konsistente näherungsfreie Theorie-Gerüst ist ausserordentlich wichtig, da die zu beschreibenden Einflüsse sehr klein sind und viele Ansätze oder Rechenprogramme zum Teil stillschweigend Approximationen und Vereinfachungen machen, die ohne Weiteres zu Fehlinterpretationen führen können.

Diese Arbeit reiht sich in die Schwerfeld bezogenen Arbeiten des Institutes für Geodäsie und Photogrammetrie der ETH Zürich und der Schweizerischen Geodätischen Kommission (SGK) ein. Wir danken dem Verfasser, Herrn Guillaume, für den wertvollen Beitrag zur Geodäsie. Dem CERN gebührt Dank für die Teilfinanzierung und Unterstützung.

Der SCNAT danken wir für die Übernahme der Druckkosten.

**Prof. Dr. M. Rothacher**  
Institut für Geodäsie und Photogrammetrie  
ETH Zürich

**Prof. Dr. Alain Geiger**  
ETH Zürich  
Präsident der SGK

## PREFACE

Le champ de gravité est une chose omniprésente dans notre vie. Ni dans la recherche et ses applications de haute technologie ni dans les travaux journaliers de chacun, personnes n'échappe des effets de la pesanteur. Malgré cela il n'existe dans certains domaines relatifs au champ gravifique que de la littérature et des recherches éparses.

Monsieur Guillaume a profité de ce manque d'information pour donner des réponses approfondies tout au long de ce travail. Le sujet concerne la possible construction d'un accélérateur linéaire de particules au CERN (Centre Européen de Recherche Nucléaire). L'excavation d'environ 40 km de longueur pour un tunnel rectiligne est faisable avec les moyens géodésiques modernes. Cependant une très haute précision, jamais requise précédemment, est requise pour le pré-alignement du tube et des aimants de l'accélérateur. L'exigence d'une précision de 10 microns sur une distance de 200 mètres est réellement à la limite du faisable. L'institut de géodésie et photogrammétrie (IGP) de ETH Zurich a une expérience de nombreuses années dans la détermination du géoïde. Particulièrement la méthode astro-géodésique a été continuellement poursuivie et développée et opérationnellement mise en œuvre durant le travail du Monsieur Guillaume. Il doit aussi être mentionné qu'il a, avec le Dr. B. Bürki, développé le nouveau système de la camera zénithale CODIAC.

Dès le début des années 80 l'IGP a établi des contacts avec le CERN pour la détermination du géoïde et pour des mesures GPS. Plus tard lorsque le CERN a envisagé la construction d'un accélérateur linéaire il a offert à l'IGP une collaboration pour une recherche sur la faisabilité de l'établissement d'une référence géodésique de haute précision et pour des suggestions pour sa mise en œuvre. L'établissement d'une référence d'altitude est un défi particulier car le champ de pesanteur, avec ses divers effets perturbateurs, influence la solution finale. C'est pourquoi la connaissance de tous les effets agissants sur  $g$  est de la plus haute importance.

Ce rapport concentre et met ensemble tous les résultats des diverses recherches et présente une théorie de base correspondante. L'élaboration d'une théorie consistante et libre d'approximations est importante pour la compréhension de tous les effets. Beaucoup de programmes d'ordinateurs disponibles utilisent, tacitement, des approximations et des simplifications qui peuvent conduire à des conclusions erronées.

Le présent travail représente une pièce maitresse dans la série des recherches sur le champ de pesanteur de l'IGP et de la commission géodésique suisse (CGS). Nous remercions Monsieur Guillaume pour cette contribution de grande valeur à la géodésie. Nos remerciements vont aussi au CERN pour leur support actif et leur financement partiel de ces recherches.

La Commission Géodésique Suisse (CGS) est reconnaissante envers l'Académie Suisse des Sciences Naturelles (SCNAT) pour avoir pris à sa charge les coûts d'impression du présent manuscrit.

**Prof. Dr. M. Rothacher**  
Institut de Géodésie et Photogrammétrie  
ETH Zürich

**Prof. Dr. Alain Geiger**  
ETH Zürich  
Président de la CGS

## FOREWORD

The gravity field is omnipresent. Nor in high technology research and applications nor in every day's work one can escape the effects of gravity. Despite this there exist only sparse literature and investigation on certain gravity field related topics. Sébastien Guillaume takes up this lack of information and gives in-depth answers along his work. The topic concerns the possible construction of a linear accelerator at CERN. The excavation of the about 40 km long, straight tunnel is feasible with modern geodetic means, however the unprecedented high demand on precision is required by the pre-alignment of the accelerator magnets and tube. The required 10 microns over 200 meters precision is really at the cutting-edge. The Institute of Geodesy and Photogrammetry (IGP) of ETH Zurich looks back on a number of years of experience in the area of geoid determination. Notably, the astrogeodetic method has been pursued and further developed and operationalized by the work of Sébastien Guillaume. It has to be mentioned that he and Dr. Beat Bürki have also devised the new Zenith Camera System CODIAC.

As early as in the 80'ies IGP established contacts to CERN for geoid determination and GPS measurements. CERN, later on was envisaging building a linear accelerator and offered the cooperation to investigate the feasibility of the establishment of a high precision geodetic reference and to provide suggestions for its realization. A special endeavor is given by the establishment of the height reference, because the gravity field with its divers disturbing effects directly influences the final solution. Therefore, the knowledge of all the acting effects is of utmost importance.

This report concatenates and concentrates all the results of the investigations and presents the corresponding background-theory. The elaborated consistent theory, free of approximations, is important to understand all the effects. Many available software does tacitly use approximations and simplifications which easily could lead to faulty interpretations.

This investigation represents a further master piece in the series of gravity field research of the Institute of Geodesy and Photogrammetry and the Swiss Geodetic Commission (SGC).

Thanks go to the author, Sébastien Guillaume, for his valuable contribution to geodesy. Thanks are given to CERN for their active support and for partially funding the investigation and to the Swiss Academy of Sciences for covering the printing costs of this volume.

**Prof. Dr. M. Rothacher**  
Institute of Geodesy and Photogrammetry  
ETH Zurich

**Prof. Dr. A. Geiger**  
ETH Zurich  
President of SGC



# Summary

This work is part of the studies conducted by CERN as part of a project for a future electron-positron linear collider (CLIC) of 50 kilometers. In particular, it addresses a specific aspect related to its pre-alignment in the vertical dimension. In fact, in order to ensure a high collision probability of incident particles (called luminosity), it is necessary that the diameter of the beams, at the collision point after 25 kilometers of continuous acceleration, do not exceed a few nanometers. This is only possible if some technical constraints are fulfilled. One of them concerns the accuracy for the pre-alignment of quadrupoles along the whole machine. This alignment must be related to a straight line in Euclidean space with a precision of 10 microns over 200 meters sliding window. In practice, this can only be envisaged if a positioning system is capable to determine positions at this level of accuracy. In vertical, hydrostatic levelling systems (HLS) benefit of several advantages and represent serious candidates. In addition to their sub-micrometric resolution, HLS are robust and appear to be particularly reliable with respect to radiations. However, they are unable to realize a Euclidean straight line. Indeed, they are related to the surface of the fluid in hydrostatic equilibrium, connecting the different sensors, whose geometry is an equipotential of the Earth's gravity field.

The principal aim of this work is the study of the feasibility of the determination of underground gravity equipotential in a tunnel located at approximately 150 meters in depth. Moreover, a practical strategy which may be implemented is proposed. In a first step, after the rigorous definition of an operator which measures the misalignment, it is demonstrated that the Newtonian mechanic framework is precise enough in the frame of this project. Then, thanks to a rigorous formulation of forces contributing to the variations of the fluid-gas interface in a 200 meters HLS system, it is shown that this interface can be approximated by equipotentials of the gravity field with a precision better than 1 micron.

The theoretical framework being fixed, the precision of astrogravimetric underground equipotential determinations is analyzed, on the one hand, by numerical Monte-Carlo simulations which model different kind of noise sources, and on the other hand, by several gravity field simulations generated by topography, near-field realistic geological anomalies and by surface variations of the Lake of Geneva. It appears that the principal source of uncertainty comes from the orthometric correction. In particular from the determination of the mean gravity acceleration along the plumbline. For the determination of the profile of CLIC, despite the fact that gravimetric measurements can be carried out on the surface of topography and in the tunnel, it is necessary to know the density of the

masses between the surface and the tunnel with a precision between 100 and 200  $\frac{\text{kg}}{\text{m}^3}$  for wavelengths between 200 to 3'000 meters. Concerning the pure astrogeodetic part, it is shown that the accuracy constraints can be reached within a reasonable time, less than one year, when five modern zenith cameras are deployed in parallel. In this regard, a new zenith camera system, called CODIAC (Compact Digital Astrometric Camera), entirely developed and manufactured at the Institute of Geodesy and Photogrammetry of ETH Zurich, is presented.

In order to validate the astrogravimetric method, the results of a campaign at CERN, along the tunnel TZ32, 850 meters in length, are presented. The comparisons of the astrogravimetric determination with the predictions from a precise mass model integrating the topography, the near-field geology and the existing TZ32 and LHC tunnels, are in the order of 20 microns with respect to alignments over 200 meters, in agreement with predictions.

Finally, a direct and non-ambiguous method for the determination of underground equipotential is proposed. It is based on observations of underground deflections of the vertical variations. These observations are supposed to be carried out with a new instrument, called differential geodetic interferometric deflectometer, whose principle is simple and consists in measuring the tilt of a movable chariot, along a profile, by an interferometer and a tiltmeter. Because of atmospheric perturbations, the whole device is placed in an appropriate vacuum tube. For a practical application, it is necessary to have a deflectometer length of minimum 50 meters. In order to validate the feasibility of this new kind of instrument, a first prototype of 12 meters was entirely designed and developed in the frame of this thesis, in collaboration with CERN. The first measurements showed that there are systematic effects remaining which must be reduced at least by one order of magnitude before considering the construction of a longer range instrument.

# Résumé

Ce travail fait partie des études menées par le CERN dans le cadre d'un projet de futur collisionneur linéaire électron-positon (CLIC) de 50 kilomètres. En particulier, il traite d'un aspect spécifique lié à son pré-alignement dans la dimension verticale. En effet, afin de garantir une grande probabilité de collisions entre les particules incidentes (appelé luminosité), il est nécessaire que les diamètres des faisceaux, au point de collision, après 25 kilomètres d'accélération ininterrompues, ne soient que de quelques nanomètres. Ceci n'est envisageable que si plusieurs contraintes techniques sont assurées. L'une d'elle est la contrainte de précision extrême que nécessite l'alignement des quadripôles tout au long de la future machine. Cet alignement doit se faire par rapport à une ligne droite dans l'espace Euclidien avec une précision de 10 microns sur une fenêtre glissante de 200 mètres. En pratique, cela ne peut être réalisé que si un système de positionnement est capable de déterminer des positions avec cette précision. En vertical, un système basé sur des techniques de nivellement hydrostatique (HLS) bénéficie de nombreux avantages et se profile comme un sérieux candidat. En plus de leur résolution sub-micrométrique, les HLS permettent de déterminer facilement des différences d'altitudes de points très éloignés les uns des autres. De plus, de part la simplicité de leur principe, ils s'avèrent être très robustes et particulièrement fiables en milieu radioactif. Malgré cela, les systèmes HLS sont incapables de réaliser une ligne droite Euclidienne. De fait, ils se réfèrent à la surface du fluide en équilibre hydrostatique qui les relie, dont la géométrie est une équipotentielle du champ gravifique de la terre.

Ce travail a donc pour objet principal l'étude de faisabilité de la détermination d'équipotentiels du champ gravifique en sous-terrain dans un tunnel situé à environ 150 mètres de profondeur, et tenter de proposer une méthode pratique qui pourrait être mise en œuvre. Dans un premier temps, après avoir défini rigoureusement un opérateur mesurant le désalignement, il est démontré que la précision du cadre de la mécanique newtonienne est suffisante pour le traitement du champ de gravité dans ce projet. Ensuite, grâce à une formulation rigoureuse des forces contribuant aux variations de la surface de l'interface fluide-gaz d'un système HLS de 200 mètres, il est démontré que cette dernière peut être approximée de façon satisfaisante, à moins de 1 micron, par la surface équipotentielle du champ gravifique.

Le cadre théorique étant fixé, la précision de détermination de la géométrie des équipotentiels en sous-sol par la méthode astro-gravimétrique est analysée d'une part par des méthodes numériques de Monte-Carlo en modélisant différents types de bruits de mesures, ainsi que sur la base de nombreuses simulations de champs de gravité générés par diverses anoma-

lies topographiques, sous-terraines, géologiquement réalistes, ainsi que celles provoquées par les variations de la surface du Lac Léman. Il en ressort que la principale source d'incertitude provient de la correction orthométrique, et en particulier de la détermination de la valeur de l'accélération de la pesanteur moyenne le long de la ligne d'aplomb en chaque point du profil à déterminer. Le long du profil du futur CLIC, malgré le fait d'avoir la possibilité de faire des mesures gravimétriques en surface ainsi que dans le tunnel, il sera nécessaire de connaître la densité de la roche en sous-sol, entre la topographie et le tunnel, avec une incertitude d'environ 100 à 200  $\frac{\text{kg}}{\text{m}^3}$  pour des longueurs d'ondes de 200 à 3'000 mètres. Concernant la partie proprement astrogéodésique, il est démontré qu'une précision suffisante peut être obtenue dans un temps raisonnable, moins d'une année, avec la mise en oeuvre parallèle de cinq caméras zénithales de dernière génération. De ce fait, une nouvelle caméra zénithale, appelée CODIAC (Compact Astrometric Digital Camera) entièrement développée et manufacturée à l'Institut de géodésie et de photogrammétrie de l'ETH Zurich est également présentée dans cette thèse.

Afin de valider la méthode astrogravimétrique, les résultats d'une campagne de mesure au CERN, le long d'un tunnel (TZ32) de 850 mètres, sont également présentés. La comparaison de la détermination astrogravimétrique avec les prédictions d'un modèle de masses précis intégrant la topographie, les anomalies géologiques de champs proche ainsi que les tunnels TZ32 et LHC, sont de l'ordre de 20 microns pour un alignement sur 200 mètres, en accord avec les prédictions d'incertitudes.

Finalement, une méthode plus directe et non-ambigue de détermination d'équipotentielles sous-terraines, basée sur des observations de variations de déviations de la verticale est présentée. Ces variations seraient mesurées par un nouvel instrument, appelé défléctomètre interférométrique différentiel géodésique, dont le principe est très simple et consiste à déterminer l'inclinaison d'un chariot le long d'un profil par interférométrie et par inclinométrie. En raison des perturbations atmosphériques, tout le dispositif doit être placé dans un tube à vide prévu à cet effet. Pour une application pratique, il serait nécessaire de disposer d'un défléctomètre d'au minimum 50 mètres. Avant cela, un premier prototype de 12 mètres, été entièrement développé dans le cadre de cette thèse en collaboration avec le CERN, a été construit dans le but de valider sa faisabilité. Des premiers tests ont pu être réalisés et indiquent que les systématismes résiduels de ce nouvel instrument doivent être réduits d'au moins un ordre de grandeur avant de pouvoir envisager le développement d'un instrument de plus longue portée.



# Contents

<b>1</b>	<b>Introduction</b>	<b>1</b>
<b>2</b>	<b>Basic Tools for Misalignment Analyses</b>	<b>7</b>
2.1	Misalignment Operator $\mathcal{M}$ . . . . .	7
2.2	Representations of Misalignment . . . . .	8
<b>3</b>	<b>Fundamentals of Earth's Gravity Field</b>	<b>11</b>
3.1	Introduction . . . . .	11
3.2	Gravity in Modern Physics and Geodesy . . . . .	11
3.2.1	Order of Magnitude of Relativistic Effects in Terrestrial Geodesy . .	12
3.2.2	Relativistic Geoid . . . . .	13
3.2.3	Concluding Remarks . . . . .	18
3.3	Classical Mechanics and Newtonian Theory of Gravitation . . . . .	19
3.3.1	Introduction . . . . .	19
3.3.2	Newton's Laws of Motion in Inertial Systems . . . . .	19
3.3.3	Newton's Law of Universal Gravitation . . . . .	23
3.4	Apparent Acceleration in Earth's Fixed Reference System . . . . .	25
3.4.1	General Formulation . . . . .	25
3.4.2	Gravitational Forces . . . . .	25
3.4.3	Acceleration of the Origin of the Earth's Rotating System . . . . .	26
3.4.4	Centripetal Acceleration . . . . .	27
3.4.5	Euler Acceleration . . . . .	28
3.4.6	Coriolis Acceleration . . . . .	28
3.4.7	Observed Acceleration . . . . .	28
3.4.8	Apparent Gravity . . . . .	30
3.4.9	Equation of Motion . . . . .	31
3.4.10	Apparent Gravity for a Deformable Earth . . . . .	31
3.5	Potential Theory . . . . .	32
3.5.1	Introduction . . . . .	32
3.5.2	Work . . . . .	34
3.5.3	Conservative Force Field . . . . .	34
3.5.4	Potential Function . . . . .	35
3.6	Shape of Fluid-Air Interface . . . . .	35
3.6.1	General Solution . . . . .	35
3.6.2	Vertically Integrated Solution . . . . .	36

3.6.3	Forced Harmonic Oscillator Solution . . . . .	38
3.6.4	Hydrostatic Solution . . . . .	48
3.7	Apparent Gravity Potential in the Earth Fixed Reference System . . . . .	49
3.7.1	Numerical Computation of the Eulerian Acceleration . . . . .	50
3.7.2	Earth's Gravitational Potential . . . . .	56
3.7.3	Centrifugal Potential . . . . .	56
3.7.4	Tidal Potential . . . . .	56
3.8	Geometry of Equipotential Surfaces . . . . .	61
3.8.1	Normal Potential and Equipotential Ellipsoid . . . . .	62
3.8.2	Disturbing Potential . . . . .	69
3.8.3	Link between Potential Field and Geometry of Equipotential Surfaces . . . . .	72
<b>4</b>	<b>Determination of Equipotential Surfaces . . . . .</b>	<b>81</b>
4.1	Introduction . . . . .	81
4.1.1	Direct Observation of the Geometry of Equipotentials . . . . .	81
4.1.2	Determination of Equipotential Surfaces from Gravity Observables . . . . .	82
4.2	Gravity Observables . . . . .	84
4.2.1	First order observables . . . . .	84
4.2.2	Second order observables . . . . .	84
4.3	Solutions for the Geometrical Determination . . . . .	86
4.3.1	Oriented Normal System . . . . .	86
4.3.2	Oriented Topocentric System . . . . .	87
4.3.3	Gravity Vectors and Gradiometric Tensors in the Oriented Normal System . . . . .	88
4.3.4	Astrogeodetic Levelling . . . . .	88
4.3.5	Gradiometric Levelling . . . . .	91
4.4	Reductions of the Gravity Field and Observations . . . . .	92
4.4.1	Reductions in Astronomical Levelling Determinations . . . . .	93
4.4.2	Orthometric Correction . . . . .	95
4.4.3	Mean Gravity along the Plumbline from Mass Models . . . . .	97
4.4.4	Mean Gravity along the Plumbline from Mass Models and Observations . . . . .	98
4.4.5	Mean Gravity along the Plumbline using Remove and Restore Technique . . . . .	101
4.4.6	Non-Modeled Mean Gravity along the Plumbline using Least-Squares Collocation . . . . .	101
4.4.7	Comparisons of the Various Methods . . . . .	107
4.5	Alignment Accuracy of Geometric Determinations . . . . .	115
4.5.1	Definition of the Misalignment Accuracy . . . . .	115
4.5.2	Monte-Carlo Simulation . . . . .	115
4.5.3	Generation of Noisy Observables . . . . .	117
4.5.4	Alignment Accuracy of Astrogeodetic Levelling . . . . .	119
4.5.5	Alignment Accuracy of the Orthometric Corrections . . . . .	121
4.5.6	Alignment Accuracy of Gradiometric Levelling . . . . .	125
4.6	Alignment Accuracy with Several Zenith Camera Systems . . . . .	127
4.6.1	Observation Setup and Noise Model . . . . .	127

4.6.2	Mathematical Models . . . . .	127
4.6.3	Monte-Carlo Simulation Scheme . . . . .	130
4.6.4	Results of the Simulations . . . . .	131
4.7	Cloud Cover in Geneva . . . . .	135
4.8	Concluding Remarks . . . . .	135
<b>5</b>	<b>Computation of Gravitational Fields</b>	<b>139</b>
5.1	Numerical Computation of the Gravitational Field . . . . .	141
5.1.1	Point Mass . . . . .	141
5.1.2	Homogeneous Sphere . . . . .	142
5.1.3	Homogeneous Polyhedron . . . . .	142
5.2	Development of QGravity . . . . .	152
5.2.1	Software Overview . . . . .	152
5.2.2	Coordinate Transformation Pipeline . . . . .	153
5.2.3	Mass Models . . . . .	155
5.2.4	Geometric Computations . . . . .	163
5.2.5	Gravity Fields . . . . .	165
5.2.6	Batch Processing . . . . .	166
5.2.7	3D Visualization . . . . .	167
5.2.8	Validation of the Polyhedron Algorithm . . . . .	168
<b>6</b>	<b>Expected Gravity Field Signals and Observability at Short Wavelengths</b>	<b>171</b>
6.1	Introduction . . . . .	171
6.1.1	Shape of Fluid-Air Interface . . . . .	172
6.1.2	Determination of Equipotential Surfaces . . . . .	173
6.1.3	Gravity Field Modeling for the Simulation of Stationary Mass Anomalies . . . . .	174
6.1.4	Outputs of the Simulations . . . . .	175
6.2	Normal Equipotential . . . . .	176
6.3	Systematic Analysis of Lateral Varying Anomalies . . . . .	178
6.3.1	Connected Slab Anomalies SLAB . . . . .	179
6.3.2	Sinusoidal Prism Anomalies SIN . . . . .	180
6.3.3	Misalignment Analyses due to SLAB Anomalies . . . . .	181
6.3.4	Misalignment Analyses due to SIN Anomalies . . . . .	190
6.4	Topography . . . . .	206
6.4.1	Topography Anomalies TOPO . . . . .	206
6.4.2	Misalignment Analyses due to TOPO(2670) Anomaly . . . . .	208
6.4.3	Misalignment Analyses due to TOPO(50) $\rightarrow$ TOPO(500) Anomalies . . . . .	213
6.5	Time-Varying Centrifugal Effects . . . . .	215
6.5.1	Global Variations . . . . .	216
6.5.2	Misalignment Analyses for CLIC . . . . .	216
6.6	Earth Tides . . . . .	219
6.7	Lake of Geneva . . . . .	222
6.7.1	Overall Lake Level Variation . . . . .	223
6.7.2	Seiches . . . . .	227
6.8	Concluding Remarks . . . . .	233

<b>7</b>	<b>Astrogeodetic Determination of Deflections of the Vertical</b>	<b>235</b>
7.1	Astrogeodetic Determination of the Local Gravity Unit Vector . . . . .	235
7.1.1	Topocentric Apparent Places of Celestial Bodies (Stars) . . . . .	236
7.1.2	Atmospheric Refraction . . . . .	238
7.2	The Digital Astronomical Deflection System DIADEM . . . . .	245
7.2.1	Instrumental Design . . . . .	245
7.3	The Compact Digital Astrometric Camera CODIAC . . . . .	248
7.3.1	Instrumental Design . . . . .	248
7.3.2	First CODIAC Validation in Corbin USA . . . . .	250
<b>8</b>	<b>Astro-Gravimetric Campaign at CERN (TZ32)</b>	<b>253</b>
8.1	Gravimetric Observations . . . . .	255
8.1.1	Absolute Gravimetric Reference Network . . . . .	255
8.1.2	Gravimetric Measurements along the TZ32 Profile . . . . .	256
8.2	Astrogeodetic Observations . . . . .	257
8.3	Mass Models . . . . .	260
8.3.1	Topography . . . . .	260
8.3.2	Lake of Geneva . . . . .	260
8.3.3	Near-Field Geology . . . . .	261
8.3.4	Underground Infrastructure . . . . .	262
8.4	Expected Gravity Fields and Observability . . . . .	264
8.4.1	Expected Gravity Field and Error-Free Observations . . . . .	264
8.4.2	Expected Misalignments Generated by known Masses . . . . .	264
8.4.3	Observability by Astrogravimetric Levelling . . . . .	265
8.5	Predicted versus Observed Measurements . . . . .	268
8.6	Computation of the Equipotential Profile in the Tunnel . . . . .	270
<b>9</b>	<b>Development of a Differential Geodetic Interferometric Deflectometer</b>	<b>273</b>
9.1	Introduction . . . . .	273
9.2	Basic Principle . . . . .	274
9.3	Analysis of the Precision by Simulations . . . . .	275
9.3.1	Mathematical Model . . . . .	275
9.3.2	Monte-Carlo Simulations . . . . .	278
9.4	Development of the first Prototype . . . . .	279
9.4.1	Main Components . . . . .	280
9.4.2	Calibration Process . . . . .	280
9.4.3	Measurement of a Profile . . . . .	282
9.5	Conclusion . . . . .	285
<b>10</b>	<b>Conclusions and Outlooks</b>	<b>287</b>
	<b>Bibliography</b>	<b>293</b>
	<b>Appendices</b>	<b>301</b>

<b>A</b>	<b>Transformation between Celestial and Terrestrial Reference Systems</b>	<b>301</b>
A.1	Transformation according to the IAU 1980 resolutions . . . . .	301
A.1.1	Polar Motion including Diurnal and Sub-Diurnal Periods . . . . .	302
A.1.2	Earth Rotation Angle including Diurnal and Sub-Diurnal Periods . .	302
A.2	Transformation using Axis Vectors . . . . .	303
<b>B</b>	<b>Numerical Computation of the Earth's Rotation Vector</b>	<b>305</b>
B.1	Earth's rotation vector in ITRS . . . . .	305
B.1.1	Time Series and Spectral Analysis . . . . .	306
B.2	Earth's rotation vector in GCRS . . . . .	306
B.3	Time derivative of the Earth's rotation vector in GCRS . . . . .	307
B.3.1	Time Series and Spectral Analysis . . . . .	307
B.4	Time derivative of the Earth's rotation vector in ITRS . . . . .	308
B.4.1	Time Series and Spectral Analysis . . . . .	308
<b>C</b>	<b>Conversion between Geodetic and Ellipsoidal Coordinates</b>	<b>313</b>
C.1	Geodetic to Ellipsoidal Coordinates $(\lambda, \varphi, h) \rightarrow (\lambda, \beta, u)$ . . . . .	313
C.2	Ellipsoidal to Geodetic Coordinates $(\lambda, \beta, u) \rightarrow (\lambda, \varphi, h)$ . . . . .	314
<b>D</b>	<b>Very Short Introduction to Stochastic Processes</b>	<b>317</b>
D.1	Stochastic Processes . . . . .	317
D.2	Gaussian Random Bias Process . . . . .	318
D.3	Gaussian Random Drift Process . . . . .	318
D.4	White Noise Process . . . . .	319
D.5	First-Order Gauss-Markov Processes . . . . .	319
D.6	Gaussian Random Walk Process . . . . .	319
<b>E</b>	<b>Very Short Introduction to Monte-Carlo Simulations</b>	<b>321</b>
E.1	Uniform Random Generator . . . . .	321
E.1.1	Physical Methods . . . . .	321
E.1.2	Computational Methods . . . . .	321
E.2	Generation of Uncorrelated Random Variables . . . . .	322
E.2.1	The Inverse-Transform Method . . . . .	323
E.3	Generation of Correlated Random Variables . . . . .	324
E.3.1	Example . . . . .	326
E.4	Monte Carlo Simulations . . . . .	326
<b>F</b>	<b>Results of the Simulations: Alignment Accuracy of Geometric Determinations</b>	<b>329</b>
F.1	Astrogeodetic Levelling . . . . .	329
F.1.1	Misalignment due to Drift Noise . . . . .	329
F.1.2	Misalignment due to Random Drift Noise . . . . .	329
F.1.3	Misalignment due to White Noise . . . . .	329
F.1.4	Misalignment due to Correlated Noise . . . . .	331
F.2	Alignment Accuracy of the Orthometric Corrections . . . . .	334
F.2.1	Misalignment due to Drift Noise ( $E1$ ) . . . . .	334
F.2.2	Misalignment due to Random Drift Noise ( $E1$ ) . . . . .	334

F.2.3	Misalignment due to White Noise ( $E1$ ) . . . . .	334
F.2.4	Misalignment due to Correlated Noise ( $E1$ ) . . . . .	335
F.2.5	Misalignment due to White Noise ( $E2$ ) . . . . .	336
F.2.6	Misalignment due to Correlated Noise ( $E2$ ) . . . . .	336
F.3	Alignment Accuracy of Gradiometric Levelling . . . . .	338
F.3.1	Misalignment due to Bias Noise . . . . .	338
F.3.2	Misalignment due to Random Bias Noise . . . . .	338
F.3.3	Misalignment due to Deterministic Drift Noise . . . . .	338
F.3.4	Misalignment due to Random Drift Noise . . . . .	339
F.3.5	Misalignment due to White Noise . . . . .	339
F.3.6	Misalignment due to Correlated Noise . . . . .	340
<b>G</b>	<b>Batch Functionalities in QGravity</b>	<b>343</b>
<b>H</b>	<b>Validation of the Polyhedron Algorithm in QGravity</b>	<b>345</b>
<b>I</b>	<b>Summary of the Observations of the TZ32 Campaign</b>	<b>351</b>

# Chapter 1

## Introduction

The Compact Linear Collider (CLIC) is a project proposed by CERN for a future electron-positron linear collider with a length of 50 km, which would be an essential complement to the existing Large Hadron Collider (LHC) in order to establish beyond doubt the validity of the Standard Model (*Braun et al.*, 2008). In order to reach the nominal energy for the particle collisions, and the expected luminosity (number of collisions per second), an active pre-alignment system must aim at ensuring the alignment of the components with a precision of  $10\text{ }\mu\text{m}$  ( $1\sigma$ ) over 200 m with respect to a straight line in Euclidean space (*Schulte*, 2009).

Various alignment systems are under investigation at CERN and at other particle physics laboratories. Among them, alignment systems based on an optical laser beam ( $\lambda = 632\text{ nm}$ ) (*Griffith*, 1989) or an x-ray laser beam ( $\lambda = 0.063\text{ nm}$ ) (*Yang and Friedsam*, 2006) are in principle very promising from their concepts, however, they still suffer from some technical difficulties. First, the beam must propagate in a vacuum tube in order to ensure a straight line reference. Second, the reliable and precise geometrical external tie with the reference beam is a difficult task. Finally, the alignment system must be designed to operate in real-time in a radioactive environment. The latest alignment strategy published at CERN, including the horizontal reference network, can be found in *Touzé* (2011).

Due to the implicit design constraints, a hydrostatic levelling system (HLS) is a suitable candidate for the vertical reference network. However, the physical reference of an HLS is the instantaneous water surface rather than a perfect straight line (see Figure 1.1), which then requires the determination of micrometric instantaneous equipotential profiles at the location of the future accelerator, in a Euclidean reference system (*Becker et al.*, 2002). This implies that some special investigations have to be done in order to determine on the one hand, if a determination at this level of precision can be reached, and on the other hand what the optimal strategy is that could be practically applied.

Without going into much into details of the CLIC project, two variants are nowadays considered. They are located and centered at the same place but differ in length, see Figure 1.2. The high-energy variant, CLIC 3.0 TeV, as a length of about 49.3 km in total, whilst the low-energy variant, CLIC 0.5 TeV, extends only over 12.5 km approximately. In the frame of this thesis, only the CLIC 3 TeV version is considered while the latter can

just be considered as its central part. The collider consists of two main linear accelerators (both 24.65 km long) which are straight, but not collinear in the vertical plane. They have a crossing angle of 20 (mrad), see Figure 1.3.

The Chapter 2 concerns the definition of the precision indicators for alignments over 200 meters with respect to a straight line. A simple misalignment operator is defined in order to quantify the quality of alignment in an unambiguous and consistent manner.

The Chapter 3 has the objective to introduce all theoretical aspects needed for the mathematical formulation of the geometry of the reference surface of a HLS system, whether the geometry of the interface between the water and the air. The starting point consists of estimating the order of magnitude of general relativistic effects in geoid modeling in order to validate the use of the Newtonian framework, without restrictions, for the rest of the thesis. Afterwards, the basic concepts of Newtonian mechanics and classical gravitation are exposed in inertial and non-inertial frames in order to formulate precisely, in the Earth fixed reference system, the real acceleration felt by particles in fluids or by geodetic instruments. From this point onward, the geometry of the fluid-air interface is analyzed regarding different approximations of the equations of fluid dynamics. It is demonstrated that the hydrostatic solution is acceptable regarding the accuracy constraints of CLIC, and implies that the complex problem of determining the geometry of the fluid-air interface in a HLS system can be reduced to the determination of the equipotential surface of the gravity field.

The Chapter 4 is also destined to non-geodesists who would like to become more familiar with the geodetic approach of gravity field determination. It consists of reviewing some fundamental basic aspects of the determination of equipotential profiles, with a special emphasis on the quasi-geometric method provided by astrogravimetric levelling. In this context, the accuracy of astrogravimetric levelling affected by different sources of errors is analyzed in terms of misalignment over 200 meters.

The Chapter 5 describes the software **QGravity** developed in the context of this thesis for the simulation and the representation of complex gravitational fields. The software is intensively used in the next chapters.

In the Chapter 6, expected gravity signals at very short wavelengths  $< 1$  km are analyzed in a systematic manner. In addition, in order to increase the realness of the estimation of the real capability of a given methodology to determine equipotential profiles, the concept of observability is introduced. In this context, preliminary observability analyses are performed for the astrogravimetric levelling for the determination of the equipotential profile along the projected emplacement of CLIC.

The Chapter 7 deals with the astrogeodetic determination of deflections of the vertical (DoV). It presents some theoretical fundamental aspects with particular emphasis on the modelization of the anomalous refraction which is presently the limiting factor of practical astrogeodetic DoV determination. To that point, the new zenith camera system CODIAC, designed and developed in the frame of this thesis is exposed.



In Chapter 8 the different aspects exposed in the previous chapters are applied to an astrogravimetric campaign which took place at CERN, along a straight tunnel of 850 meters in length, called TZ32, linked to the LHC, at a depth of 80 meters. The equipotential profile determined from surface astrogeodetic deflections of the vertical and surface and underground gravimetric measurements is then compared to predictions based on known mass models which include topography, near-field geological density fields, the lake of Geneva and the underground infrastructure formed by the LHC and TZ32 tunnels.

Finally, the Chapter 9 presents the first developments of a differential geodetic interferometric deflectometer which has potentially many benefits compared to astrogravimetric levelling. It is designed to measure variations in the deflection of the vertical variations directly in the tunnel and would permit a direct determination of the geometry of underground equipotential profiles without making any assumptions about the actual density field.

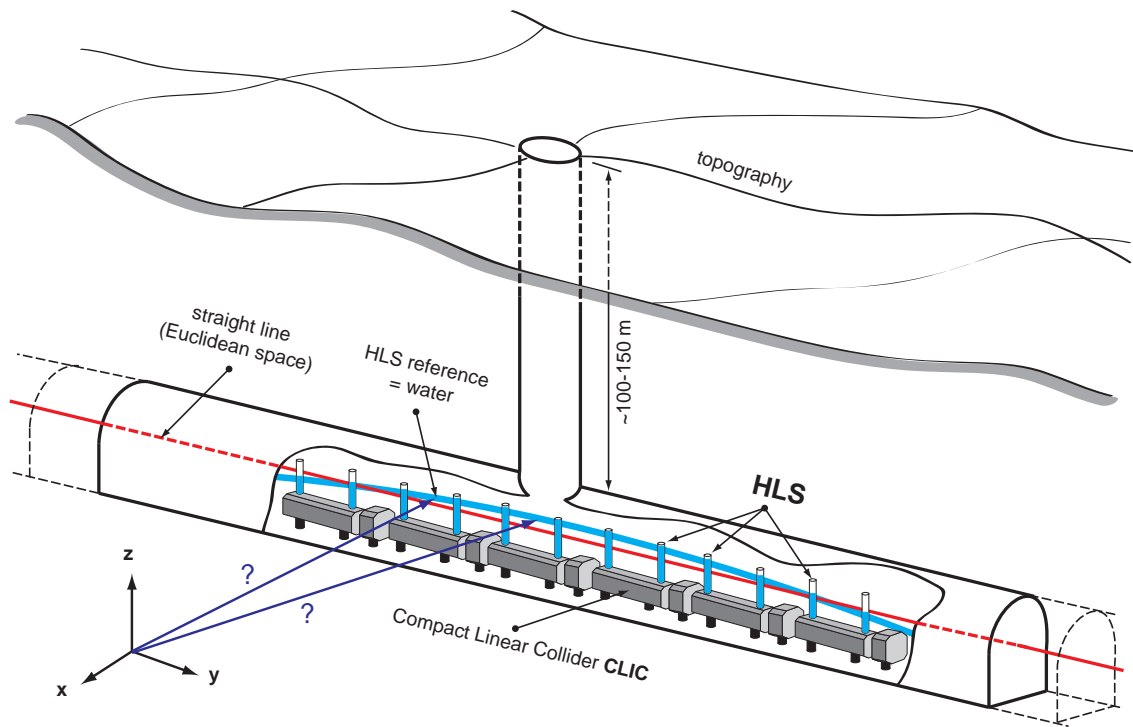


**Figure 1.1:** Schematic drawing of the Compact Linear Collider (CLIC).

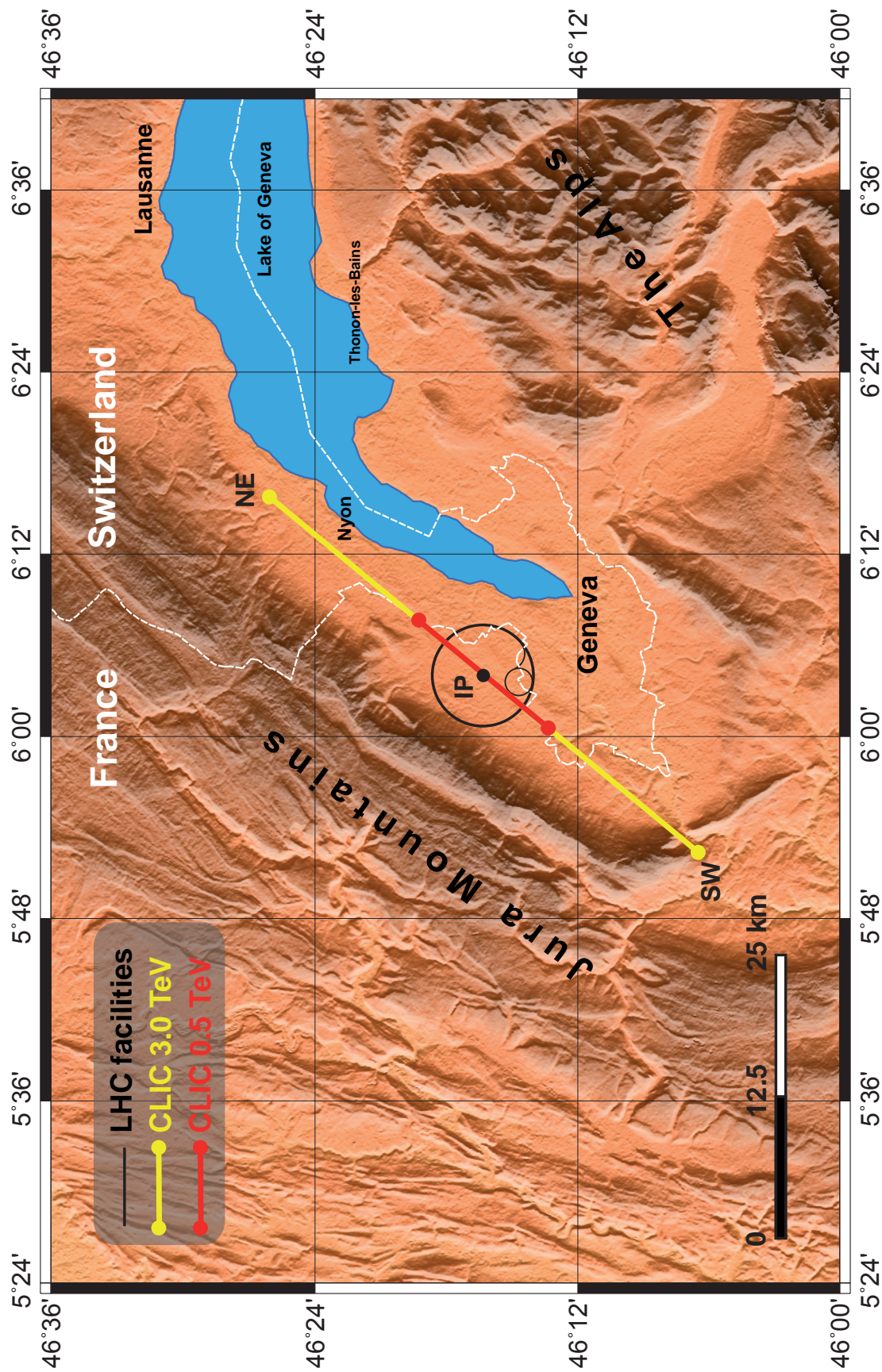


**Figure 1.2:** Overview map of the region of Geneva with the existing CERN-LHC facilities and the projected location of CLIC. The first extremity of CLIC is noted **SW** (South-West), the second extremity **NE** (North-East), and the interaction point **IP**. Source of DTM data: ASTER GDEM is a product of METI and NASA.

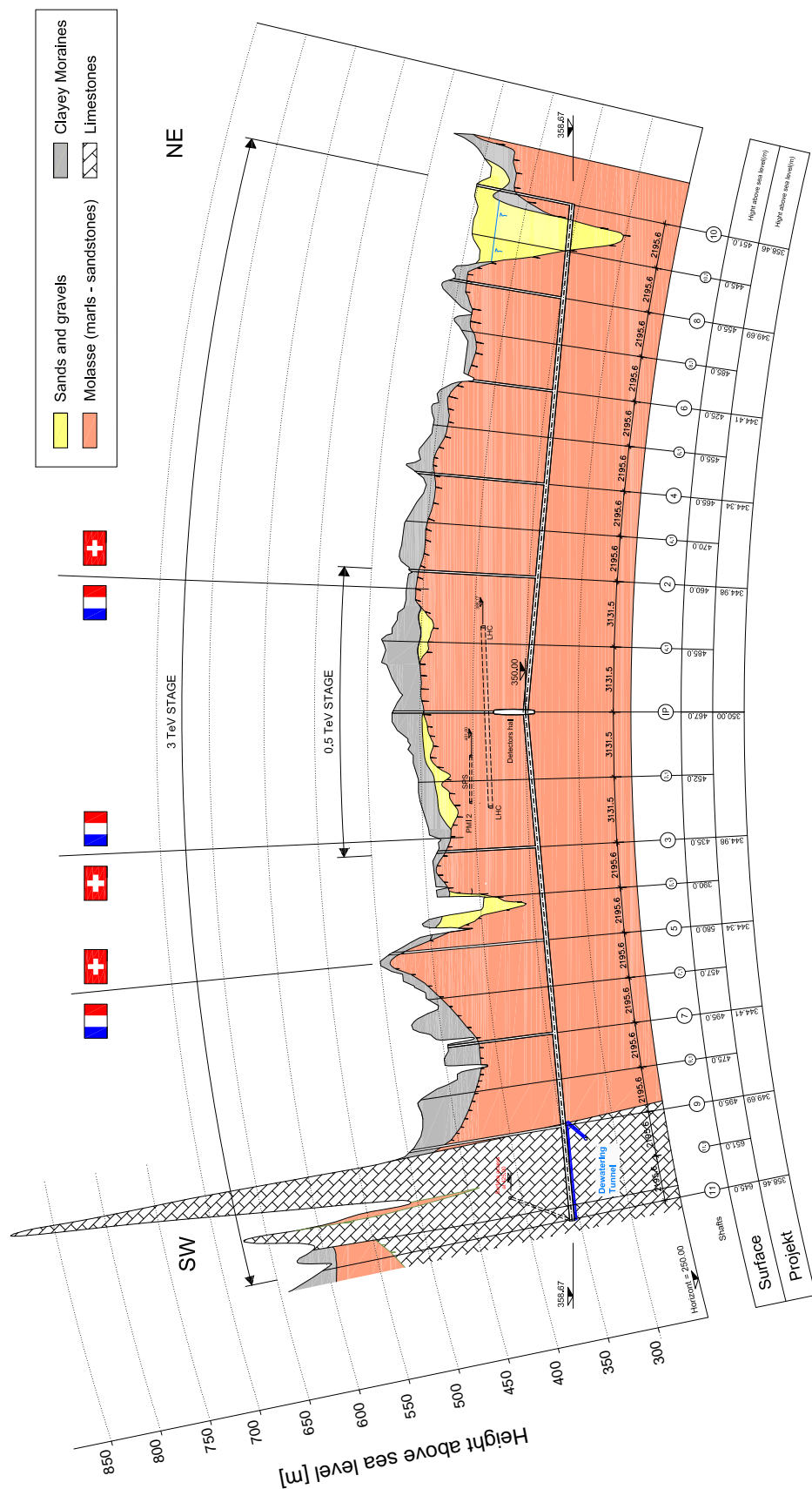


Figure 1.3: Geological longitudinal profile along the projected location of CLIC. Source: Aicheler et al. (2012), by Amberg Engineering.



## Chapter 2

# Basic Tools for Misalignment Analyses

### 2.1 Misalignment Operator $\mathcal{M}$

The ultimate objective is to be able to align accelerator components with respect to a straight line in Euclidian space, at the required precision of  $10 \mu\text{m}$ , over a wavelength of 200 m. From this point of view, it is necessary to define a mathematical tool which can be applied to a trajectory (which can represent the positions of accelerator components or the shape of an equipotential of the gravity field) to generate objective alignment – or misalignment – criteria. The principle is very basic, it was introduced by *Becker* (2003) and used by *Touzé* (2011) in the context of accelerator alignment. However, the first rigorous definition of the following operator was introduced by *Guillaume et al.* (2014a). The operator  $\mathcal{M}$ , which is briefly described, gives the maximal alignment error at a certain position, for a certain wavelength, by analysing the residuals of best-fit straight lines.

Assuming that we have an arbitrary spatial trajectory  $\mathcal{P}$  which is discretized by a series of  $N$  position vectors  $\mathbf{p}_i$ , where  $i = 1, \dots, N$ , can be interpreted as a curvilinear index in  $\mathcal{P}$ . The least-squares best-fit line  $\mathcal{L}_{k \rightarrow l}$  passing through the sub-path  $\mathcal{P}_{k \rightarrow l}$  can be computed as follows:

$$\mathcal{L}_{k \rightarrow l} \equiv \mathbf{p}_m + \alpha \cdot \mathbf{d} \quad (2.1)$$

$$\mathbf{p}_m = \frac{1}{l - k + 1} \sum_{i=k}^l \mathbf{p}_i \quad \mathbf{d} = \max \text{eig} [\mathbf{P} \cdot \mathbf{P}^T] \quad (2.2)$$

$$\mathbf{P} = [\mathbf{p}_k - \mathbf{p}_m \quad \cdots \quad \mathbf{p}_l - \mathbf{p}_m]$$

where  $\alpha$  is an arbitrary scalar and  $\max \text{eig}[\dots]$  represents the normalized eigenvector associated with the largest eigenvalue. Now, if  $\mathbf{p}_m$  and  $\mathbf{d}$  are known, the misalignment vectors  $\mathbf{m}_i$  can be computed as the differences between the position vectors  $\mathbf{p}_i$  and their orthogonal projections on  $\mathcal{L}_{k \rightarrow l}$ :

$$\mathbf{m}_i = (\mathbf{p}_i - \mathbf{p}_m) - [(\mathbf{p}_i - \mathbf{p}_m)^T \cdot \mathbf{d}] \cdot \mathbf{d} \quad (2.3)$$



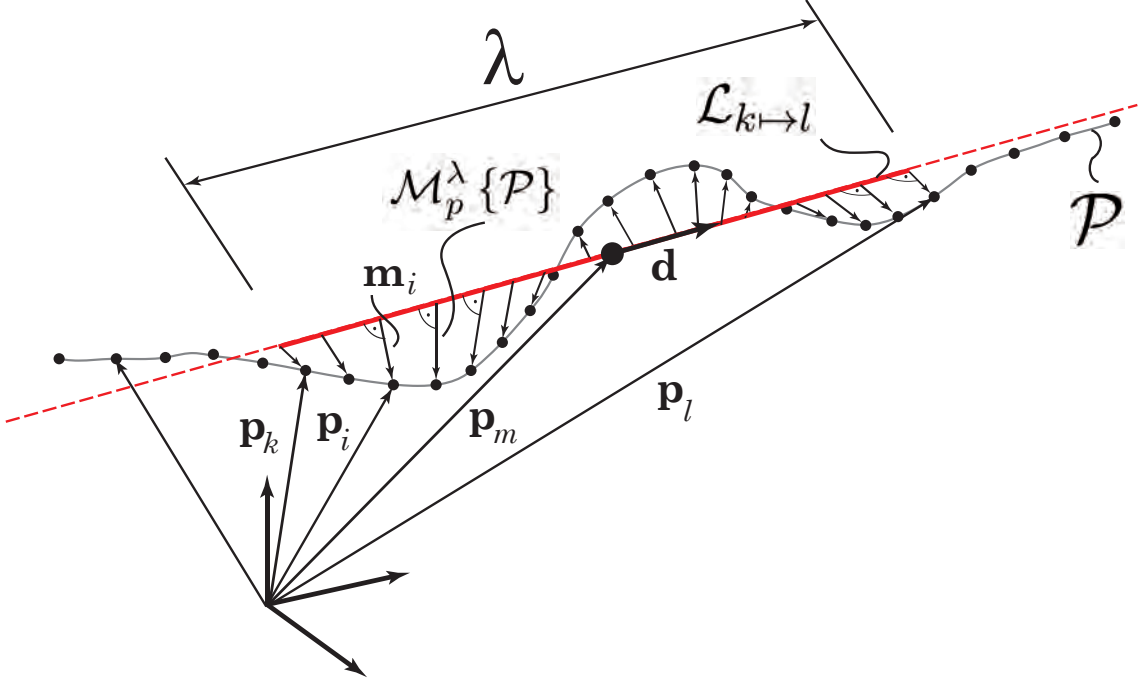


Figure 2.1: Misalignment Operators.

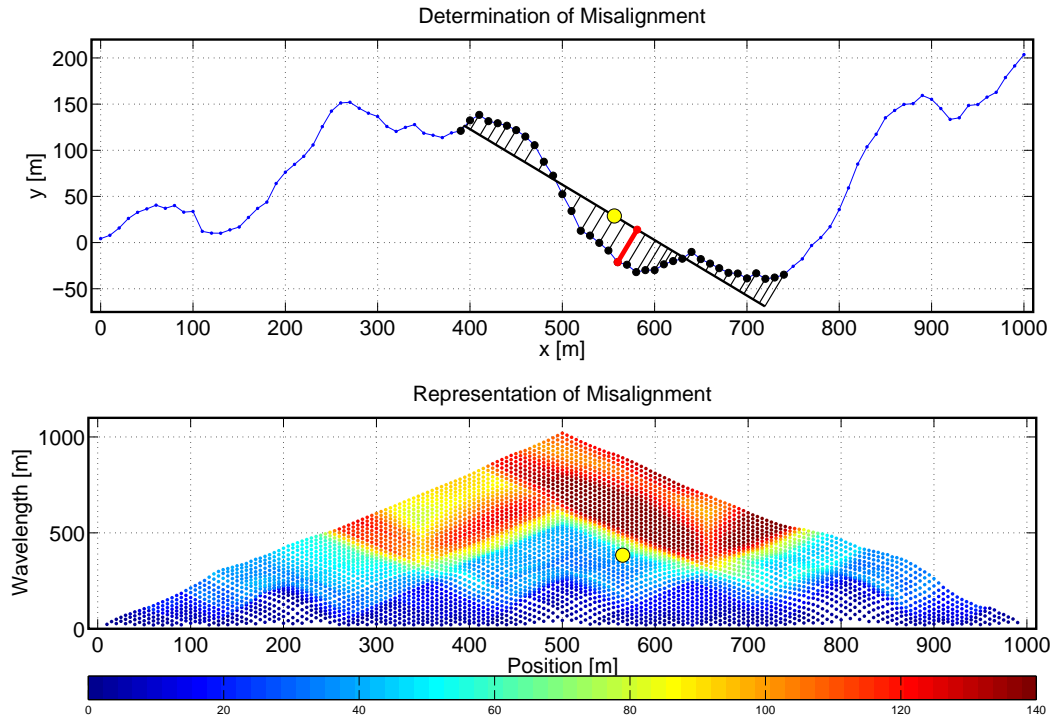
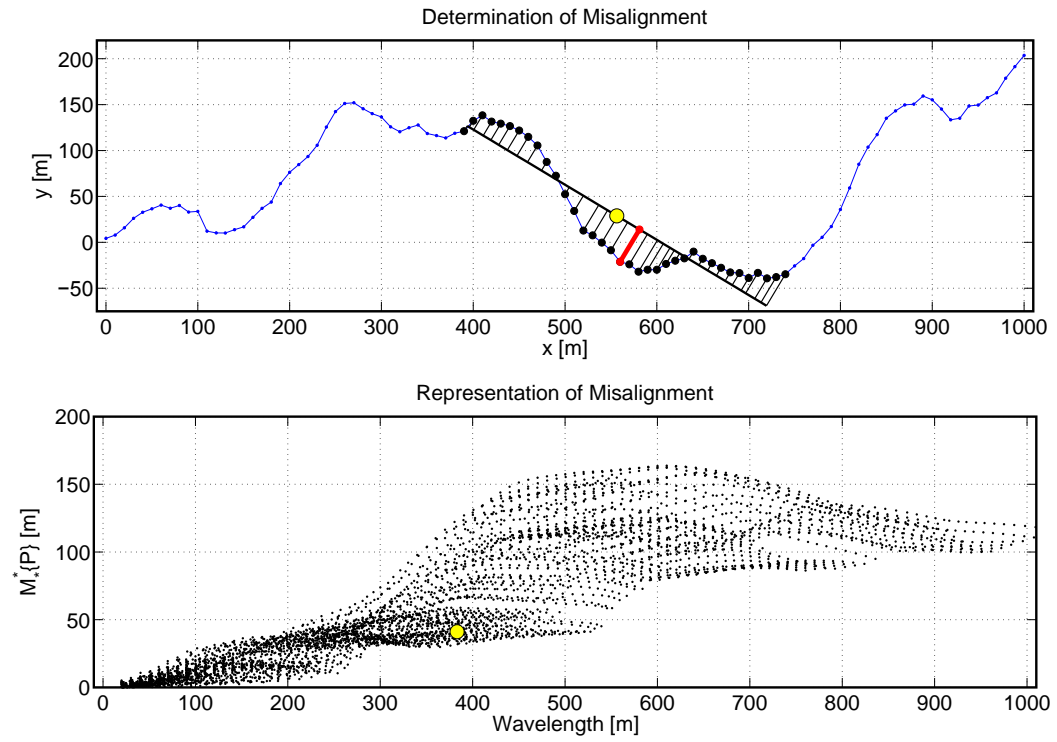
Finally, the misalignment error  $\mathcal{M}_p^\lambda\{\mathcal{P}\}$  of the trajectory  $\mathcal{P}$  at the position  $p = \mathbf{p}_m$  for the wavelength  $\lambda = |\mathbf{p}_l - \mathbf{p}_k|$  is computed as follows:

$$\mathcal{M}_p^\lambda\{\mathcal{P}\} = \max |\mathbf{m}_i| \quad (2.4)$$

which is a scalar value. For the misalignment error at every position of  $\mathcal{P}$ , and for a particular wavelength  $\lambda$ , the operator is noted  $\mathcal{M}_\star^\lambda\{\mathcal{P}\}$ . In a similar way, for the misalignment errors at a particular position  $p$  and for all possible wavelengths, the operator is noted as  $\mathcal{M}_p^\star\{\mathcal{P}\}$ . Finally for all misalignment errors, at every position and every possible wavelength, the operator may be written as  $\mathcal{M}_\star^\star\{\mathcal{P}\}$ .

## 2.2 Representations of Misalignment

In order to illustrate the behavior of the misalignment operator  $\mathcal{M}$ , some representations are presented. They are based on a 2D discrete trajectory  $\mathcal{P}$  shown in the upper plots of all upcoming figures of this section. If all misalignments over of  $\mathcal{M}_\star^\star\{\mathcal{P}\}$  have to be represented, two possibilities are available. The first is shown in figure 2.2, where a colored dot represents a particular  $\mathcal{M}_p^\lambda\{\mathcal{P}\}$ . The second is given in figure 2.3, where the particular  $\mathcal{M}_p^\lambda\{\mathcal{P}\}$  are plotted in function of the wavelength  $\lambda$  only, but the information about the position  $p$  is no longer available. If only misalignments  $\mathcal{M}_\star^{\lambda=100,200,300}\{\mathcal{P}\}$  at specific wavelengths  $\lambda$  in function of positions  $p$  are of interest, a possible representation is given in figure 2.4. Finally, the figure 2.5 shows a representation of the misalignments  $\mathcal{M}_{p=500}^\star\{\mathcal{P}\}$ , if the position  $p$  is fixed and all possible wavelengths are explored.

Figure 2.2: Representation of  $\mathcal{M}_{\star}^{\star}\{\mathcal{P}\}$ Figure 2.3: Representation of  $\mathcal{M}_{\star}^{\star}\{\mathcal{P}\}$

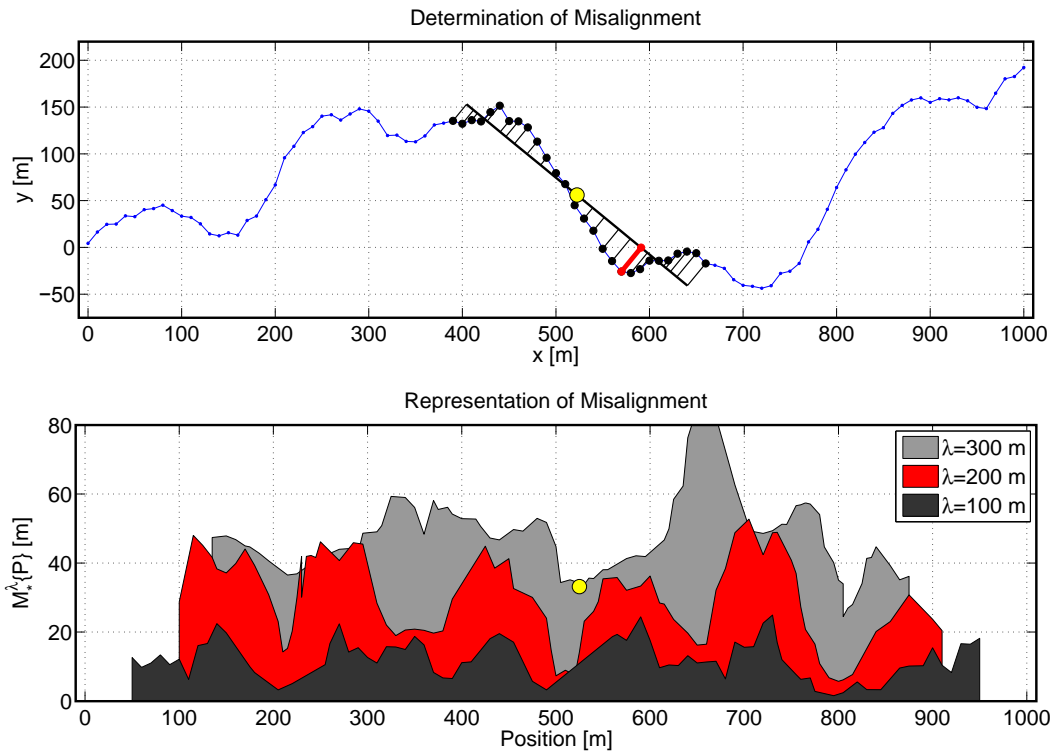


Figure 2.4: Representation of  $\mathcal{M}_{\star}^{\lambda=100,200,300} \{P\}$

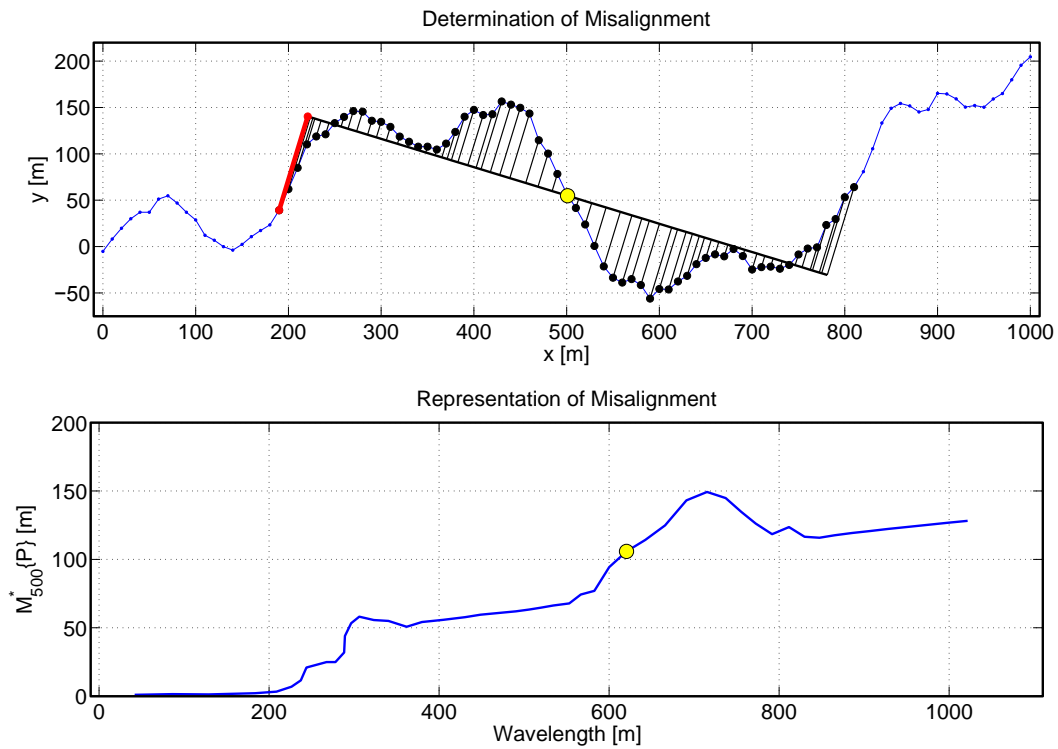


Figure 2.5: Representation of  $\mathcal{M}_{p=500}^* \{P\}$



## Chapter 3

# Fundamentals of Earth's Gravity Field

### 3.1 Introduction

In this chapter, the fundamental physical concepts related to the gravity field are reviewed. It begins with determining the approximation level of Newtonian mechanics with respect to Einstein's general theory of relativity (GRT) concerning the gravity field of the Earth. Some orders of magnitude of the GRT effects are provided for various geodetic observables and also for the geoid. This confirms that the Newtonian framework is precise enough with respect to the level of precision we are trying to approach in this thesis.

Secondly, the main concepts of Newtonian mechanics and gravitation in inertial and accelerated systems are explained in order to derive the forces which are felt by observers, and enter the equation of motion for particles on the Earth. On this basis, the determination of the shape of the fluid-air-interface is discussed from the general case of fluid dynamics to the special case of hydrostatic equilibrium which is fundamental to this thesis. In this context, it is shown that the consequences of the hydrostatic solution are linked to the fact that the forces acting on the particles of a fluid must be curl-free. Unfortunately, this is not the case for the Eulerian acceleration usually neglected in geodesy. Therefore, in order to quantify the consequences of the Eulerian acceleration in hydrostatic levelling systems, a simple HLS model is numerically investigated.

### 3.2 Gravity in Modern Physics and Geodesy

In modern physics, the current theory of gravitation<sup>1</sup> is given by the general theory of relativity formulated by *Einstein* (1916). Since 1916, the theory of general relativity has never been falsified by any observations and made it possible, for the first time, to handle the whole universe as a single mathematical object. It led to the emergence of modern cosmology.

---

<sup>1</sup>the general relativity theory is not only a theory of gravitation but unifies, in a consistent formalism, the concepts of dynamics, classical electromagnetism, gravitation and special relativity.

When Einstein succeeded to integrate the postulates of special relativity and the principle of equivalence in a formalism independent to any reference system, the new concepts behind GRT revolutionized the classical Newtonian mechanics in all of these components:

- The spatio-temporal framework of Newtonian mechanics, which assumes a radical separation of the three dimensions of space and the dimension of time, is replaced by an interlaced four-dimensional space-time.
- The belief that a preferred general inertial system exists wherein all events can be identified with respect to an absolute time is destroyed by GRT. The concept of an inertial system exists only locally and varies at each point of space-time. It is defined in such a way that the effect of gravitation can be completely canceled by the free-fall of the system itself. Furthermore, the physics in the local inertial system is governed by the laws of special relativity.
- Gravitation is no longer formulated as an instantaneous force field generated by masses, but as a consequence of the intrinsic geometrical curvature of space-time, generated by the content in mass and energy. Moreover, in opposition to Newton's law of gravitation, because the principles of special relativity are completely integrated in the GRT, the gravitational effects have a finite propagation velocity.
- In accordance with the principle of least action, the trajectories of objects not subjected to external forces are given by the geodesics in the curved four-dimensional space-time.

Despite the fact that the concepts of GRT and Newtonian gravitation are completely different, it can be proven that the Newtonian theory is the correct limit of GRT for a weak gravitational field and for velocities of matter and observers that are small compared to the speed of light (*Kopeikin et al.*, 2011).

### 3.2.1 Order of Magnitude of Relativistic Effects in Terrestrial Geodesy

In the vicinity of the Earth, the order of magnitude of the differences between the predictions of general relativity and the predictions of Newtonian physics depends on the reference system which is considered. In *Müller et al.* (2008) and *Soffel et al.* (2003), we find that the magnitude of the main GRT effects are of order:

- $\eta^{\text{BCRS}} \sim 10^{-8}$  for the Barycentric Celestial Reference System (BCRS)<sup>2</sup>.
- $\eta^{\text{GCRS}} \sim 10^{-9}$  for the Geocentric Celestial Reference System (GCRS)<sup>3</sup>.

with

$$\eta^{\text{BCRS}} = \frac{\Phi_{\odot}}{c^2} = \frac{1}{c^2} \cdot \frac{GM_{\odot}}{|\mathbf{r}_{\odot} - \mathbf{r}_s|} \cong 9.87 \cdot 10^{-9} \quad (3.1)$$

<sup>2</sup>the BCRS is the reference system defined in the GRT framework which is used to model the light propagation of distant celestial objects and for the computation of orbits of celestial bodies of the solar system (*Soffel et al.*, 2003).

<sup>3</sup>the GCRS is the reference system defined in the GRT framework which is used to model the phenomena in the vicinity of the Earth (*Soffel et al.*, 2003).

and

$$\eta^{\text{GCRS}} = \frac{\Phi_{\delta}}{c^2} = \frac{1}{c^2} \cdot \frac{GM_{\delta}}{R_{\delta}} \cong 6.96 \cdot 10^{-10} \quad (3.2)$$

where:

$G$	$\cong 6.674 \cdot 10^{-11}$	$\left[ \frac{\text{m}^3}{\text{kg} \cdot \text{s}^2} \right]$	$=$	gravitational constant.
$c$	$\cong 2.998 \cdot 10^8$	$\left[ \frac{\text{m}}{\text{s}} \right]$	$=$	speed of light in vacuum.
$\Phi_{\odot}$	$\cong 8.876 \cdot 10^8$	$\left[ \frac{\text{m}^2}{\text{s}^2} \right]$	$=$	gravitational potential of the Sun in the vicinity of the Earth's surface.
$\Phi_{\delta}$	$\cong 6.250 \cdot 10^7$	$\left[ \frac{\text{m}^2}{\text{s}^2} \right]$	$=$	gravitational potential of the Earth in the vicinity of the Earth's surface.
$GM_{\odot}$	$\cong 1.327 \cdot 10^{20}$	$\left[ \frac{\text{m}^3}{\text{s}^2} \right]$	$=$	heliocentric gravitational constant.
$GM_{\delta}$	$\cong 3.986 \cdot 10^{14}$	$\left[ \frac{\text{m}^3}{\text{s}^2} \right]$	$=$	geocentric gravitational constant.
$ \mathbf{r}_{\odot} - \mathbf{r}_{\delta} $	$\cong 1.495 \cdot 10^{11}$	$[\text{m}]$	$=$	distance between the Earth and the Sun.
$R_{\delta}$	$\cong 6.378 \cdot 10^6$	$[\text{m}]$	$=$	Earth's radius.

The parameters  $\eta^{\text{BCRS}}$  and  $\eta^{\text{GCRS}}$  are derived from the post-Newtonian approximation<sup>4</sup> (PNA) of the GRT. They are dimensionless and represent the order of magnitude of the main sources of gravitation not modeled in the Newtonian framework. In addition, they can be seen as the approximate frequency shifts<sup>5</sup> which could be observed between a perfect clock attached to the surface of the Earth and a perfect clock situated at the origin of the BCRS (the center of mass of the solar system) or at the origin of the GCRS (the Earth's center of mass), respectively.

The magnitude of relativistic effects on various terrestrial geodetic observables is given in *Soffel* (1989). Furthermore, in *Kopeikin* (1991), we can find a proper formulation of PNA of Einstein's equations in geocentric and topocentric coordinate systems including some orders of magnitude of relativistic effects expected for gravity and gradiometry observables. In Table 3.1 some relativistic effects not modeled by the Newtonian framework are listed. They are mainly obtained from *Soffel* (1989). As we can see, the relativistic effects are usually very small compared to the accuracy which can be achieved by current terrestrial geodetic measurement techniques. Only time series from highly precise superconducting gravimeters and recent optical clocks might be able to observe relativistic phenomena.

### 3.2.2 Relativistic Geoid

*Soffel et al.* (1988) proposes two different definitions for a relativistic geoid:

<sup>4</sup>Post-Newtonian approximations are methods used for solving Einstein's equation of general relativity up to a certain level of approximation. They are used when bodies are moving slowly compared to the speed of light and when the gravitational field is weak. They consist in developing the metric tensor  $g_{\mu\nu}$  into inverse powers of the speed of light.

<sup>5</sup>also called gravitational redshift.

**Table 3.1:** Terrestrial geodetic measurements and relativistic effects.  $d$  = distance [m] to target,  $\Delta h$  = height difference [m] between two clocks.

observable	method	accuracy		relativistic effect	
distance	EDM	$10^{-6} \cdot d$	[m]	$10^{-9} \cdot d$	[m]
	interferometer	$10^{-8} \cdot d$	[m]	$10^{-9} \cdot d$	[m]
horizontal direction	theodolite	$10^{-6}$	[rad]	—	—
zenith angle	theodolite	$10^{-6}$	[rad]	$10^{-16} \cdot d$	[rad]
gravity potential	atomic clock	$10^{-13}$	$\left[\frac{\text{s}}{\text{day}}\right]$	$10^{-11} \cdot \Delta h$	$\left[\frac{\text{s}}{\text{day}}\right]$
gravity acceleration	free-fall gravimeter	$10^{-8}$	$\left[\frac{\text{m}}{\text{s}^2}\right]$	$10^{-8}$	$\left[\frac{\text{m}}{\text{s}^2}\right]$
	super-conducting gravimeter	$10^{-10}$	$\left[\frac{\text{m}}{\text{s}^2}\right]$	$10^{-8}$	$\left[\frac{\text{m}}{\text{s}^2}\right]$
	astro-geodetic zenith camera	$10^{-1}$	[arcsec]	$10^{-4}$	[arcsec]
gravity gradient	torsion balance	$10^{-9}$	$\left[\frac{1}{\text{s}^2}\right]$	$10^{-16}$	$\left[\frac{1}{\text{s}^2}\right]$

1. the  $u$ -geoid is defined to be the surface, close to mean sea level where, the rate of the proper time of an ideal clock is constant with respect to the geocentric coordinate time. The prefix  $u$  refers to the relativistic four-velocity vector  $\mathbf{u}$  of a co-moving atomic clock.
2. the  $a$ -geoid is defined to be the surface, close to mean sea level, of constant geocentric rates and orthogonal everywhere to the topocentric direction of the Earth's gravity. The prefix  $a$  refers to the relativistic four-acceleration vector  $\mathbf{a}$  which is related to the direction of the plumbline.

In addition, *Soffel et al.* (1988) demonstrate that the  $u$ -geoid and the  $a$ -geoid are equivalent for any stationary metric.

Subsequently, *Kopeikin* (1991) demonstrates that the  $u$ -geoid and the  $a$ -geoid are also equivalent for constant rigid-body rotation of the Earth. Moreover, he shows that the level surface of a self-gravitating fluid in the post-Newtonian approximation of GRT coincides exactly with the equipotential surface represented by the geoid. This important result makes it possible to directly transpose the physical interpretation of the Newtonian geoid as level surface to that of the relativistic geoid (*Kopeikin et al.*, 2011).

To get some numerical estimates of relativistic effects for the geoid, we have to refer to *Müller et al.* (2008), who provide the equation of the  $u$ -geoid. They approximate the gravitational potential of the Earth as a post-Newtonian multipole series formed by a scalar PN potential  $\Phi_{\text{PN}}$  and a PN vector potential  $\mathbf{\Pi}_{\text{PN}}$ <sup>6</sup>. They found that surfaces of constant clock rates for observers at rest in an Earth fixed coordinate system (e.g. ITRS)

<sup>6</sup>also called gravito-magnetic vector potential of the Earth which is usually related to the Lense-Thirring effect (*Soffel et al.*, 2003).

are given by:

$$\begin{aligned}
 \Phi_{\text{PN},\delta} &= \Phi_{\text{PN},0} = \text{cst} \\
 &= \Phi_{\text{PN}} + \frac{1}{2} \cdot |\mathbf{v}^{\text{GCRS}}|^2 \\
 &\quad - \frac{\Phi_{\text{PN}}^2}{2c^2} - \frac{4 \cdot \mathbf{\Pi}_{\text{PN}} \cdot \mathbf{v}^{\text{GCRS}}}{c^2} + \frac{3 \cdot \Phi_{\text{PN}} \cdot |\mathbf{v}^{\text{GCRS}}|^2}{2c^2} + \frac{|\mathbf{v}^{\text{GCRS}}|^4}{8c^2}
 \end{aligned} \tag{3.3}$$

with:

$$\mathbf{\Pi}_{\text{PN}} = -\frac{G}{2} \cdot \frac{\mathbf{r}^{\text{GCRS}} \times \mathbf{S}_{\delta}^{\text{GCRS}}}{|\mathbf{r}^{\text{GCRS}}|^3} \quad \text{and} \quad \mathbf{S}_{\delta}^{\text{GCRS}} = \mathbf{I}_{\delta}^{\text{GCRS}} \cdot \boldsymbol{\omega}_{\delta}^{\text{GCRS}} \tag{3.4}$$

where:

$G$	$\left[ \frac{\text{m}^3}{\text{kg} \cdot \text{s}^2} \right]$	=	gravitational constant.
$c$	$\left[ \frac{\text{m}}{\text{s}} \right]$	=	speed of light in vacuum.
$\Phi_{\text{PN},\delta}$	$\left[ \frac{\text{m}^2}{\text{s}^2} \right]$	=	post-Newtonian gravity potential of the Earth.
$\Phi_{\text{PN},0}$	$\left[ \frac{\text{m}^2}{\text{s}^2} \right]$	=	post-Newtonian gravity potential constant of the Earth, at mean sea level.
$\Phi_{\text{PN}}$	$\left[ \frac{\text{m}^2}{\text{s}^2} \right]$	=	post-Newtonian gravitational scalar potential of the Earth.
$\mathbf{\Pi}_{\text{PN}}$	$\left[ \frac{\text{m}^3}{\text{s}^3} \right]$	=	post-Newtonian gravitational vector potential of the Earth.
$\mathbf{r}^{\text{GCRS}}$	$[\text{m}]$	=	position of an observer in GCRS.
$\mathbf{v}^{\text{GCRS}}$	$\left[ \frac{\text{m}}{\text{s}} \right]$	=	velocity of an observer in GCRS.
$\mathbf{S}_{\delta}^{\text{GCRS}}$	$\left[ \frac{\text{kg} \cdot \text{m}^2}{\text{s}} \right]$	=	total angular momentum of the Earth.
$\mathbf{I}_{\delta}^{\text{GCRS}}$	$[\text{kg} \cdot \text{m}^2]$	=	inertial tensor of the Earth.
$\boldsymbol{\omega}_{\delta}^{\text{GCRS}}$	$\left[ \frac{\text{rad}}{\text{s}} \right]$	=	spin vector of the Earth.

In Equation 3.3, the post-Newtonian scalar potential  $\Phi_{\text{PN}}$  can be related to the standard Newtonian potential, the second term to the standard centrifugal potential, and the last four terms, which are proportional to  $c^{-2}$ , can be identified as purely relativistic corrections. These corrections can be analyzed in terms of geoid undulations  $\delta N_i$ , if *Brun's* formula (see Equation 3.196) is applied. This can be done, if we assume that the

relativistic corrections are considered as disturbing potentials:

$$\begin{aligned}
\delta N_1 &= -\frac{1}{\gamma_0} \cdot \frac{\Phi_{\text{PN}}^2}{2c^2} \\
\delta N_2 &= -\frac{1}{\gamma_0} \cdot \frac{4 \cdot \mathbf{\Pi}_{\text{PN}} \cdot \mathbf{v}^{\text{GCRS}}}{c^2} \\
\delta N_3 &= +\frac{1}{\gamma_0} \cdot \frac{3 \cdot \Phi_{\text{PN}} \cdot |\mathbf{v}^{\text{GCRS}}|^2}{2c^2} \\
\delta N_4 &= +\frac{1}{\gamma_0} \cdot \frac{|\mathbf{v}^{\text{GCRS}}|^4}{8c^2}
\end{aligned} \tag{3.5}$$

The order of magnitude of these effects can be computed assuming the following values:

$$\gamma_0 = 9.81 \quad \left[ \frac{\text{m}}{\text{s}^2} \right] \quad , \quad \Phi_{\text{PN}} = 6.250 \cdot 10^7 \quad \left[ \frac{\text{m}^2}{\text{s}^2} \right] \tag{3.6}$$

$$\mathbf{I}_{\delta}^{\text{GCRS}} = \begin{pmatrix} 8.008 & 0.000 & 0.000 \\ 0.000 & 8.008 & 0.000 \\ 0.000 & 0.000 & 8.036 \end{pmatrix} \cdot 10^{37} \quad \left[ \text{kg} \cdot \text{m}^2 \right] \quad , \quad \boldsymbol{\omega}_{\delta}^{\text{GCRS}} = \begin{pmatrix} 0.000 \\ 0.000 \\ 7.292 \end{pmatrix} \cdot 10^{-5} \quad \left[ \frac{\text{rad}}{\text{s}} \right] \tag{3.7}$$

$$\mathbf{S}_{\delta}^{\text{GCRS}} = \mathbf{I}_{\delta}^{\text{GCRS}} \cdot \boldsymbol{\omega}_{\delta}^{\text{GCRS}} = \begin{pmatrix} 0.000 \\ 0.000 \\ 5.860 \end{pmatrix} \cdot 10^{33} \quad \left[ \frac{\text{kg} \cdot \text{m}^2}{\text{s}} \right] \tag{3.8}$$

and if we assume that:

$$\mathbf{v}^{\text{GCRS}} = \boldsymbol{\omega}_{\delta}^{\text{GCRS}} \times \mathbf{r}^{\text{GCRS}} \tag{3.9}$$

With these approximations, it is easy to see that all  $\delta N_i$  are stationary, i.e., they do not vary with time. In addition,  $\delta N_1$  is also independent of the position  $\mathbf{r}^{\text{GCRS}}$  and can be reduced to a constant value of approximately  $\delta N_1 = 2.2$  mm. Concerning the three others terms, we can prove that they vary only with the latitude and have their maximal amplitudes at the equator as we can see from Figures 3.1 and 3.2. Figure 3.2 shows the total relativistic correction  $\delta N_{\text{rel}}$ , which is simply the sum of all  $\delta N_i$ :

$$\delta N_{\text{rel}} = \delta N_1 + \delta N_2 + \delta N_3 + \delta N_4 \tag{3.10}$$

### Misalignment due to the relativistic effects

Relativistic effects can produced systematic effects up to 2 mm over the whole Earth. According to *Müller et al.* (2008), the magnitude seems to be very small at global scale

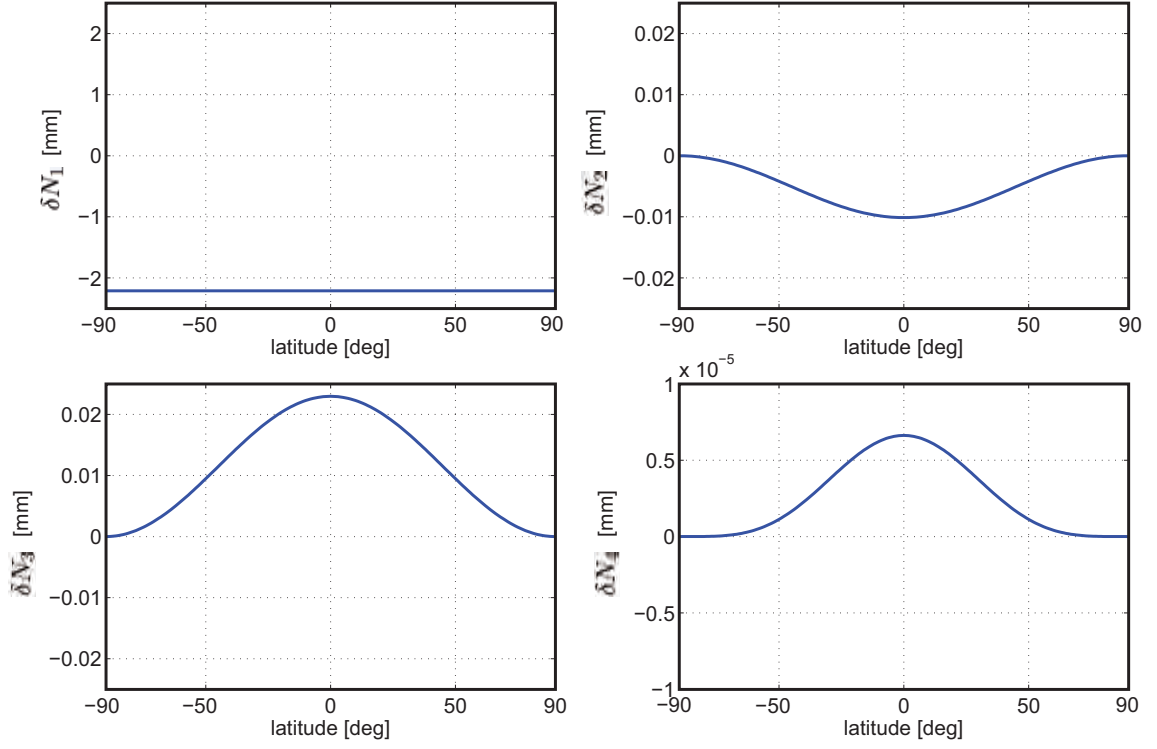


**Figure 3.1:** Post-Newtonian geoid undulation corrections  $\delta N_1, \delta N_2, \delta N_3$  and  $\delta N_4$  as a function of the latitude according to Equation 3.5.

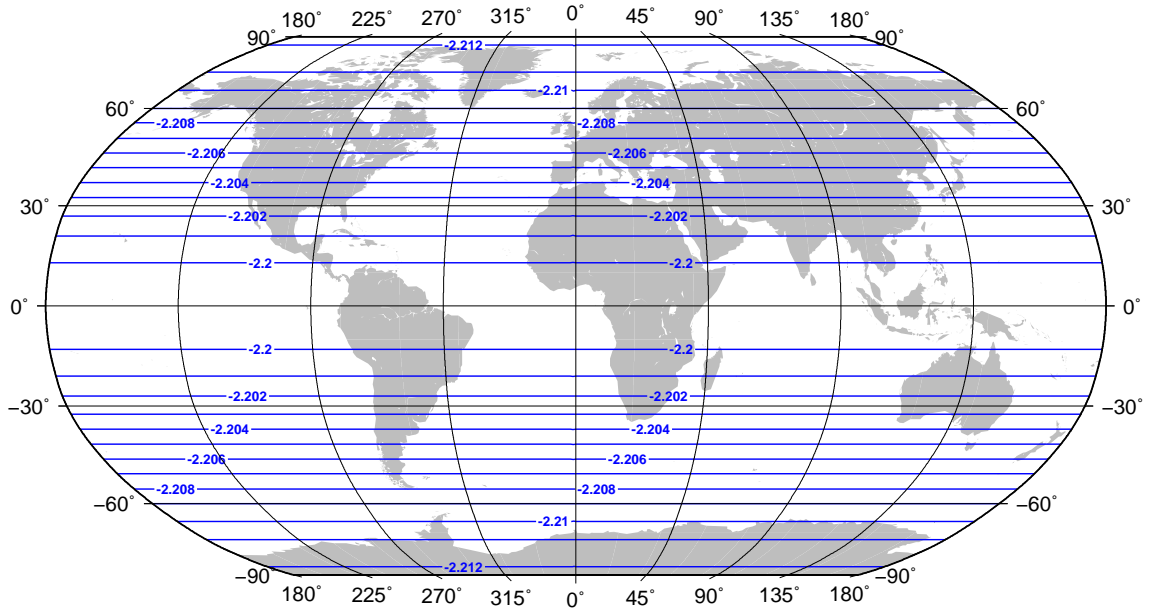


**Figure 3.2:** Post-Newtonian geoid undulation corrections over the Earth. The contour lines represent the sum of all corrections exposed in Equation 3.5.

but could become significant in the next years with the increasing accuracy of global geoid solutions obtained with space techniques. It follows that *Müller et al.* (2008) advise to formulate the next generation of global geoid realizations according to a proper post-Newtonian framework.

Concerning the issue of regional relative geoid determination and, especially, the alignment of linear colliders with respect to current alignment specifications, it is not surprising that relativistic effects are largely negligible. In fact, if we compute the misalignment along an arbitrary meridian we get maximal misalignments of approximately  $8.0 \mu\text{m}$  for wavelengths of  $\lambda \approx 20'000 \text{ km}$ , and  $1.0 \mu\text{m}$  for  $\lambda \approx 4'000 \text{ km}$  (see Figure 3.3). In other words, the misalignment signal due to GRT has an order of magnitude of  $10^{-13}$ .

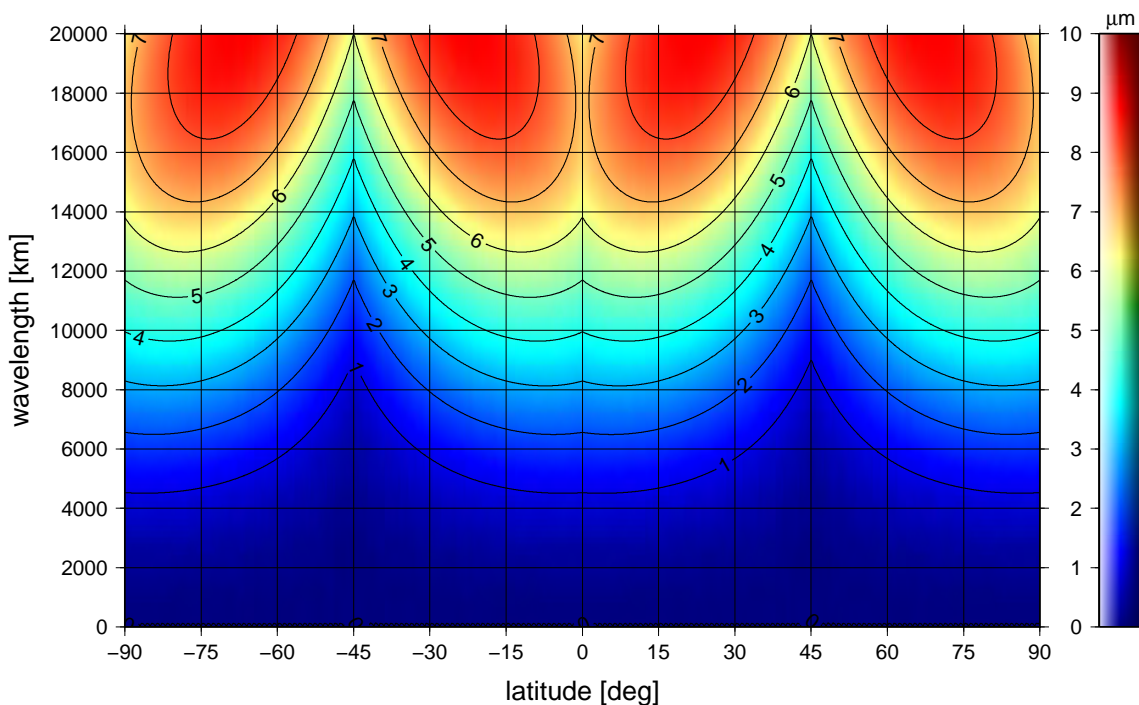


**Figure 3.3:** Misalignment generated by the effects of general relativity on the geoid, along an arbitrary meridian. The  $x$ -axis represents the position (given by the latitude) along the meridian, the  $y$ -axis the wavelength  $\lambda$  and the misalignment  $\mathcal{M}_*^* \{\delta N_{\text{rel}}\}$  is color-coded.

### 3.2.3 Concluding Remarks

In this very short introduction, it was the goal to give a very brief overview of the current theory of space-time and gravitation and some consequences for geodetic observables, in particular concerning the Earth's equipotential surfaces. As expected, in regional geodetic applications, the purely relativistic effects are negligible.



### 3.3 Classical Mechanics and Newtonian Theory of Gravitation

#### 3.3.1 Introduction

In this work, only the classical mechanics framework is considered. Its foundation comes from one of the most important books in the history of sciences: *Philosophiæ Naturalis Principia Mathematica*, written by *Newton* (1687). This book contains the formulation of the famous *Newton's laws of motion* and the *Newton's law of universal gravitation* which is of particular importance in this thesis.

A very important aspect of the Newtonian theories is that the laws are based on a simple space-time framework, which postulate a complete independence of space and time. They are considered to be absolute and independent of the happening of any physical events. The space is defined as a three-dimensional Euclidean space and the time as a one-dimensional variable which behaves identically at every position in space. Moreover, the mathematical formulation of the laws are only valid in a specific class of reference systems, dynamically equivalent, called inertial systems.

#### 3.3.2 Newton's Laws of Motion in Inertial Systems

##### Newton's First Law

The first law says that if the resultant of the external forces  $\mathbf{F}_i$  acting on a particle is equal to  $\mathbf{0}$ , the velocity  $\mathbf{v}$  of this particle remains unchanged.

$$\sum_{\forall i} \mathbf{F}_i = \mathbf{0} \rightarrow \frac{d\mathbf{v}}{dt} = \mathbf{0} \quad (3.11)$$

In other words, if the net forces are equal to zero, a particle at rest stay at rest, and for a particle in motion, the motion corresponds to a rectilinear motion of constant velocity. This first law seems to be only a special case of the second law, but this is not the case. It defines the class of reference systems for which the laws are valid. These reference systems are called inertial systems.

##### Newton's Second Law

The modern version of the second law says that the rate of change of the linear momentum  $\mathbf{p}$  of a particle is equal to the resultant of the external forces  $\mathbf{F}_i$  acting on this particle.

$$\frac{d\mathbf{p}}{dt} = \sum_{\forall i} \mathbf{F}_i \quad (3.12)$$

where the linear momentum  $\mathbf{p} = m \cdot \mathbf{v}$  is equal to the product of the inertial mass  $m$  and the velocity  $\mathbf{v}$  of the particle. In the case when the mass does not vary with time, the second law can be written as:

$$m \cdot \frac{d\mathbf{v}}{dt} = m \cdot \mathbf{a} = m \cdot \frac{d^2\mathbf{r}}{dt^2} = m \cdot \ddot{\mathbf{r}} = \sum_{\forall i} \mathbf{F}_i \quad (3.13)$$

where  $\mathbf{a}$  represents the acceleration and  $\mathbf{r}$  the position of the particle in an inertial system.

### Newton's Third Law

The third law says that, if an object  $\mathcal{A}$  exerts a force  $\mathbf{F}_{\mathcal{A} \rightarrow \mathcal{B}}$  on an object  $\mathcal{B}$ , the object  $\mathcal{B}$  exerts simultaneously a force

$$\mathbf{F}_{\mathcal{B} \rightarrow \mathcal{A}} = -\mathbf{F}_{\mathcal{A} \rightarrow \mathcal{B}} \quad (3.14)$$

or in terms of linear momentum

$$d\mathbf{p}_{\mathcal{B} \rightarrow \mathcal{A}} = -d\mathbf{p}_{\mathcal{A} \rightarrow \mathcal{B}} \quad (3.15)$$

which has the same amplitude but the opposite direction. This means also that only pairs of forces exist that act simultaneously.

### Transformation between Inertial Systems

Two inertial reference systems  $i_1$  and  $i_2$  are related by the fact that they differ only by a rectilinear constant velocity  $\mathbf{v}_{i_1}^{i_2}$ . At time  $t$ , if we know the coordinates  $\mathbf{r}^{i_1}(t)$  of a particle in  $i_1$ , we can find the coordinates of this particle  $\mathbf{r}^{i_2}(t)$  in  $i_2$  by:

$$\mathbf{r}^{i_2}(t) = \mathbf{r}^{i_1}(t) - \mathbf{v}_{i_1}^{i_2} \cdot t \quad (3.16)$$

if at  $t = 0$  the origins of  $i_1$  and  $i_2$  coincide. In this case, it is easy to see that Newton's second law is invariant with respect to a Galilean transformation because:

$$m \cdot \frac{d^2 \mathbf{r}^{i_1}}{dt^2} = m \cdot \ddot{\mathbf{r}}^{i_1} = m \cdot \frac{d^2 \mathbf{r}^{i_2}}{dt^2} = m \cdot \ddot{\mathbf{r}}^{i_2} \quad (3.17)$$

### Newton's Second Law in Non-Inertial Systems

Ideally, it would be preferable to work always in inertial systems and apply Newton's laws as described before. Unfortunately, this is not always possible. First, when a reference system is defined, how can we be sure that it is really inertial? Nowadays, since the development of GRT, we know that a global inertial system does not exist. However, it is possible to find an operational quasi-inertial system which appears as inertial up to the level of accuracy which is needed. Actually, we can check if a system is inertial enough by observing motions and forces of objects in this system, and check if Newton's second law is respected. In geodesy, the most fundamental reference system considered to be quasi-inertial is given by the *International Celestial Reference System* ICRS which is realized by observations of distant emitting galaxies, so-called quasars<sup>7</sup>.

Nonetheless, in most cases, we observe motions of objects and forces in non-inertial systems. Therefore it is necessary to reformulate Newton's second law for non-inertial systems. This can be done if we look at the position, velocity and acceleration of a particle  $\mathcal{P}$  given in the inertial system  $i$  and in the accelerated system  $a$ . The vector  $\mathbf{r}$  represents the position of  $\mathcal{P}$  in the inertial system  $i$ , and the vector  $\boldsymbol{\rho}$  the position in the accelerated system  $a$ . In the general case, as can be seen in Figure 3.4, the position vectors are related by:

$$\mathbf{r}^i(t) = \mathbf{O}^i(t) + \mathbf{R}_a^i(t) \cdot \boldsymbol{\rho}^a(t) \quad (3.18)$$

---

<sup>7</sup>quasars : quasi-stellar radio source.

where  $\mathbf{O}^i$  represents the motion of the origin of  $a$  in the  $i$ -system, and  $\mathbf{R}_a^i$  is a time-dependent rotation matrix which transforms the components of a vector given in the  $a$ -system into components which are parallel to the  $i$ -system. If we write all components of Equation 3.18 we have:

$$\begin{pmatrix} r_x^i(t) \\ r_y^i(t) \\ r_z^i(t) \end{pmatrix} = \begin{pmatrix} O_x^i(t) \\ O_y^i(t) \\ O_z^i(t) \end{pmatrix} + \begin{pmatrix} \mathbf{e}_{ax}^i(t) & \mathbf{e}_{ay}^i(t) & \mathbf{e}_{az}^i(t) \end{pmatrix} \cdot \begin{pmatrix} \rho_x^a(t) \\ \rho_y^a(t) \\ \rho_z^a(t) \end{pmatrix} \quad (3.19)$$

where  $\mathbf{e}_{ax}^i$ ,  $\mathbf{e}_{ay}^i$ ,  $\mathbf{e}_{az}^i$  represent the unit axis vectors of system  $a$  in system  $i$ .

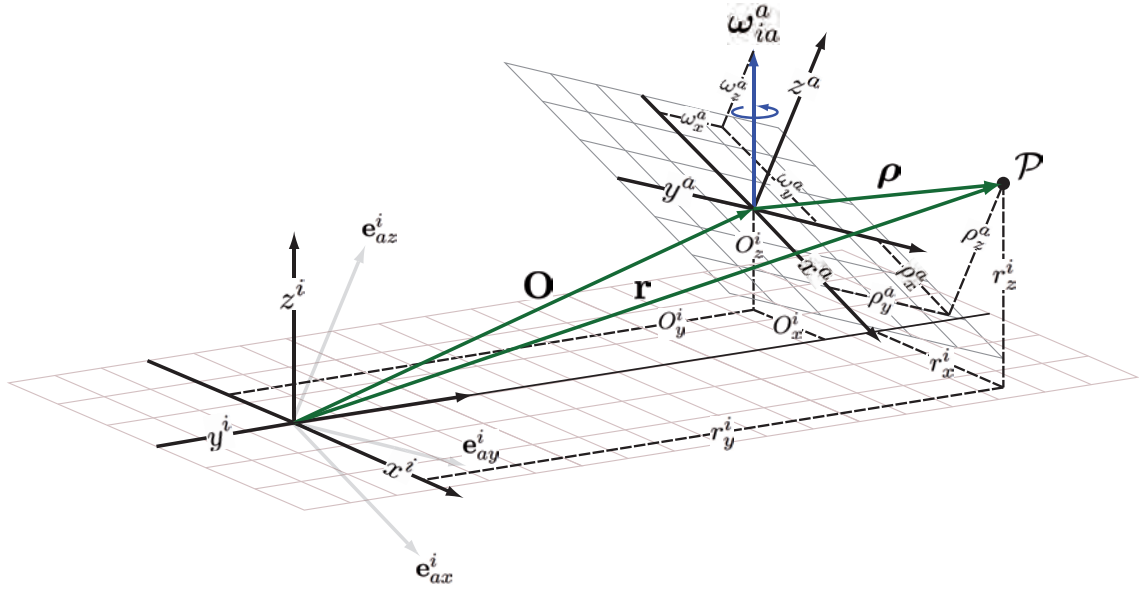


**Figure 3.4:** Representation of an inertial system  $i$  and an accelerated system  $a$ .

The velocity  $\mathbf{v}^i(t)$  can be found, when Equation 3.18 is differentiated with respect to time:

$$\begin{aligned} \mathbf{v}^i &= \dot{\mathbf{r}}^i \\ &= \dot{\mathbf{O}}^i + \dot{\mathbf{R}}_a^i \cdot \boldsymbol{\rho}^a + \mathbf{R}_a^i \cdot \dot{\boldsymbol{\rho}}^a \end{aligned} \quad (3.20)$$

and the acceleration is found, when Equation 3.20 is differentiated with respect to time:

$$\begin{aligned} \mathbf{a}^i &= \ddot{\mathbf{r}}^i \\ &= \ddot{\mathbf{O}}^i + \ddot{\mathbf{R}}_a^i \cdot \boldsymbol{\rho}^a + \dot{\mathbf{R}}_a^i \cdot \dot{\boldsymbol{\rho}}^a + \dot{\mathbf{R}}_a^i \cdot \dot{\boldsymbol{\rho}}^a + \mathbf{R}_a^i \cdot \ddot{\boldsymbol{\rho}}^a \\ &= \ddot{\mathbf{O}}^i + \ddot{\mathbf{R}}_a^i \cdot \boldsymbol{\rho}^a + 2 \cdot \dot{\mathbf{R}}_a^i \cdot \dot{\boldsymbol{\rho}}^a + \mathbf{R}_a^i \cdot \ddot{\boldsymbol{\rho}}^a \end{aligned} \quad (3.21)$$

and introducing the relations:

$$\begin{aligned} \dot{\mathbf{R}}_a^i &= \mathbf{R}_a^i \cdot \boldsymbol{\Omega}_{ia}^a \\ \ddot{\mathbf{R}}_a^i &= \mathbf{R}_a^i \cdot \boldsymbol{\Omega}_{ia}^a \cdot \boldsymbol{\Omega}_{ia}^a + \mathbf{R}_a^i \cdot \dot{\boldsymbol{\Omega}}_{ia}^a \end{aligned} \quad (3.22)$$

in Equation 3.21 leads to

$$\ddot{\mathbf{r}}^i = \ddot{\mathbf{O}}^i + \mathbf{R}_a^i \cdot \boldsymbol{\Omega}_{ia}^a \cdot \boldsymbol{\Omega}_{ia}^a \cdot \boldsymbol{\rho}^a + \mathbf{R}_a^i \cdot \dot{\boldsymbol{\Omega}}_{ia}^a \cdot \boldsymbol{\rho}^a + 2 \cdot \mathbf{R}_a^i \cdot \boldsymbol{\Omega}_{ia}^a \cdot \dot{\boldsymbol{\rho}}^a + \mathbf{R}_a^i \cdot \ddot{\boldsymbol{\rho}}^a \quad (3.23)$$

where the skew-symmetric matrix

$$\boldsymbol{\Omega}_{ia}^a = \begin{pmatrix} 0 & -\omega_z^a & +\omega_y^a \\ +\omega_z^a & 0 & -\omega_x^a \\ -\omega_y^a & +\omega_x^a & 0 \end{pmatrix} \quad (3.24)$$

contains the components of the instantaneous spin vector  $\boldsymbol{\omega}_{ia}^a$ :

$$\boldsymbol{\omega}_{ia}^a = \begin{pmatrix} \omega_x^a \\ \omega_y^a \\ \omega_z^a \end{pmatrix} \quad (3.25)$$

Finally, Newton's second law becomes:

$$\begin{aligned} m \cdot \ddot{\mathbf{r}}^i &= \sum \mathbf{F}^i \\ &= m \cdot \ddot{\mathbf{O}}^i + m \cdot \mathbf{R}_a^i \cdot \boldsymbol{\Omega}_{ia}^a \cdot \boldsymbol{\Omega}_{ia}^a \cdot \boldsymbol{\rho}^a + m \cdot \dot{\boldsymbol{\Omega}}_{ia}^a \cdot \boldsymbol{\rho}^a + 2m \cdot \mathbf{R}_a^i \cdot \boldsymbol{\Omega}_{ia}^a \cdot \dot{\boldsymbol{\rho}}^a + m \cdot \mathbf{R}_a^i \cdot \ddot{\boldsymbol{\rho}}^a \end{aligned} \quad (3.26)$$

If we apply the inverse rotation  $\mathbf{R}_i^a = (\mathbf{R}_a^i)^T$  and multiply by  $\frac{1}{m}$ , we have:

$$\begin{aligned} \mathbf{R}_i^a \cdot \ddot{\mathbf{r}}^i &= \frac{1}{m} \mathbf{R}_i^a \cdot \sum \mathbf{F}^i = \frac{1}{m} \sum \mathbf{F}^a \\ &= \mathbf{R}_i^a \cdot \ddot{\mathbf{O}}^i + \boldsymbol{\Omega}_{ia}^a \cdot \boldsymbol{\Omega}_{ia}^a \cdot \boldsymbol{\rho}^a + \dot{\boldsymbol{\Omega}}_{ia}^a \cdot \boldsymbol{\rho}^a + 2 \cdot \boldsymbol{\Omega}_{ia}^a \cdot \dot{\boldsymbol{\rho}}^a + \ddot{\boldsymbol{\rho}}^a \end{aligned} \quad (3.27)$$

which can be rearranged in order to get  $\ddot{\boldsymbol{\rho}}^a$  explicitly:

$$\ddot{\boldsymbol{\rho}}^a = \frac{1}{m} \sum \mathbf{F}^a - \mathbf{R}_i^a \cdot \ddot{\mathbf{O}}^i - \boldsymbol{\Omega}_{ia}^a \cdot \boldsymbol{\Omega}_{ia}^a \cdot \boldsymbol{\rho}^a - \dot{\boldsymbol{\Omega}}_{ia}^a \cdot \boldsymbol{\rho}^a - 2 \cdot \boldsymbol{\Omega}_{ia}^a \cdot \dot{\boldsymbol{\rho}}^a \quad (3.28)$$

According to *Britting* (1971) and *Rothacher and Rummel* (2012), this general equation contains six terms:

1.  $\ddot{\boldsymbol{\rho}}^a$  is the acceleration of the particle  $\mathcal{P}$  measured by an observer situated at the origin of the accelerated  $a$ -system. It is important to understand that this acceleration is **not** the acceleration which is sensed — or measured — by an observer attached to  $\mathcal{P}$ . It is simply the acceleration obtained when the position of  $\mathcal{P}$  observed with respect to the  $a$ -system,  $\boldsymbol{\rho}^a(t)$ , is differentiated two times with respect to time  $t$ .
2.  $\frac{1}{m} \sum \mathbf{F}^a$  is the sum of all real forces  $\mathbf{F}^a$ , expressed in the  $a$ -system, acting on the particle  $\mathcal{P}$  divided by the mass  $m$  of  $\mathcal{P}$ . The real forces are the sum of the gravitational, electromagnetic, nuclear forces and forces induced by the exchange of a part of the linear momentum with other particles — or objects — which collide with  $\mathcal{P}$ .

Again, this term is **not** the acceleration which is sensed — or measured — by an observer attached to  $\mathcal{P}$ . The acceleration  $\mathbf{a}_{\text{obs}}^a$  which is felt — or observed — at  $\mathcal{P}$  is called *specific force* — or *proper acceleration*. Actually, the proper acceleration  $\mathbf{a}_{\text{obs}}^a$  is the sum of all non-gravitational forces divided by the mass  $m$ . It can also be interpreted as the acceleration relative to free-fall. Formally it is related to the total real accelerations by:

$$\mathbf{a}_{\text{obs}}^a = \frac{1}{m} \sum \mathbf{F}^a - \frac{1}{m} \sum \mathbf{F}_{\text{grav}}^a \quad (3.29)$$

and in combination with Equation 3.28 we have:

$$\mathbf{a}_{\text{obs}}^a = \ddot{\boldsymbol{\rho}}^a - \frac{1}{m} \sum \mathbf{F}_{\text{grav}}^a + \mathbf{R}_i^a \cdot \ddot{\mathbf{O}}^i + \boldsymbol{\Omega}_{ia}^a \cdot \boldsymbol{\Omega}_{ia}^a \cdot \boldsymbol{\rho}^a + \dot{\boldsymbol{\Omega}}_{ia}^a \cdot \boldsymbol{\rho}^a + 2 \cdot \boldsymbol{\Omega}_{ia}^a \cdot \dot{\boldsymbol{\rho}}^a \quad (3.30)$$

3.  $-\mathbf{R}_i^a \cdot \ddot{\mathbf{O}}^i$  is the acceleration of the origin of the  $a$ -system with respect to the  $i$ -system, and where the components are rotated into the  $a$ -system. This acceleration is independent of the position or the velocity of  $\mathcal{P}$ .
4.  $-\boldsymbol{\Omega}_{ia}^a \cdot \boldsymbol{\Omega}_{ia}^a \cdot \boldsymbol{\rho}^a$  is the centrifugal acceleration. This term exists if the  $a$ -system rotates with respect to the  $i$ -system and if  $\mathcal{P}$  is not located on the axis defined by the spin vector  $\boldsymbol{\omega}$ .
5.  $-\dot{\boldsymbol{\Omega}}_{ia}^a \cdot \boldsymbol{\rho}^a$  is the Euler acceleration. This term only exists if there is a change in the rotation rate of the  $a$ -system with respect to the  $i$ -system.
6.  $-2 \cdot \boldsymbol{\Omega}_{ia}^a \cdot \dot{\boldsymbol{\rho}}^a$  is the Coriolis acceleration. This term exists if the  $a$ -system rotates with respect to the  $i$ -system and if  $\mathcal{P}$  moves with respect to the  $a$ -system.

### 3.3.3 Newton's Law of Universal Gravitation

The discovery of the law of universal gravitation stated in *Newton* (1687) is one of the most important events in the history of science and humanity. This allowed, for the first time, the unification of the description of phenomena observed on the Earth and in the universe. In fact, the genius Newton was able to realize that the fundamental cause which is responsible for falling objects on Earth is identical to that which makes the Earth revolve around the Sun — or which makes the Moon revolve around the Earth. This fundamental cause is the gravitational force which is acting on all massive particles and which is generated by the same massive particles.

In other words, considering two particles  $\mathcal{P}_1$  and  $\mathcal{P}_2$ , of mass  $m_1$  and  $m_2$ , respectively; the gravitational force  $\mathbf{F}_{12}$ , the force acting on  $\mathcal{P}_1$  generated by  $\mathcal{P}_2$ , is proportional to the masses  $m_1$  and  $m_2$  and inversely proportional to the square of the distance between  $\mathcal{P}_1$  and  $\mathcal{P}_2$ . The proportionality factor is called the *gravitational constant*  $G$ . Formally, the law can be written as:

$$\mathbf{F}_{12} = G \cdot \frac{m_1 \cdot m_2}{|\mathbf{r}_2 - \mathbf{r}_1|^2} \cdot \frac{\mathbf{r}_2 - \mathbf{r}_1}{|\mathbf{r}_2 - \mathbf{r}_1|} \quad (3.31)$$

where  $\mathbf{r}_1$  and  $\mathbf{r}_2$  represent the position vectors of  $\mathcal{P}_1$  and  $\mathcal{P}_2$ . Equivalently, if we are interested in the force acting on  $\mathcal{P}_2$  generated by  $\mathcal{P}_1$ , we have:

$$\mathbf{F}_{21} = G \cdot \frac{m_1 \cdot m_2}{|\mathbf{r}_1 - \mathbf{r}_2|^2} \cdot \frac{\mathbf{r}_1 - \mathbf{r}_2}{|\mathbf{r}_1 - \mathbf{r}_2|} \quad (3.32)$$

which implies:

$$\mathbf{F}_{12} = -\mathbf{F}_{21} \quad (3.33)$$

This law is universal and is effective in this form in all reference systems, inertial and non-inertial. In other words, all observers agree about the gravitational force.

### Principle of Superposition

A key property of the gravitational force is that it generate a field which is superposable. This means that the gravitational effect  $\mathbf{F}_{1S}$  caused by a set  $\mathcal{S} = \{\mathcal{P}_2, \dots, \mathcal{P}_i, \dots, \mathcal{P}_{N+1}\}$ , of  $N$  individual particles, on a test particle  $\mathcal{P}_1$ , is equal to the sum of the effect of each particles  $\mathcal{P}_i$  on  $\mathcal{P}_1$ :

$$\begin{aligned} \mathbf{F}_{1S} &= \sum_{i=2}^{N+1} \mathbf{F}_{1i} \\ &= \sum_{i=2}^{N+1} G \cdot \frac{m_1 \cdot m_i}{|\mathbf{r}_i - \mathbf{r}_1|^2} \cdot \frac{\mathbf{r}_i - \mathbf{r}_1}{|\mathbf{r}_i - \mathbf{r}_1|} \\ &= G \cdot m_1 \cdot \sum_{i=2}^{N+1} \frac{m_i}{|\mathbf{r}_i - \mathbf{r}_1|^2} \cdot \frac{\mathbf{r}_i - \mathbf{r}_1}{|\mathbf{r}_i - \mathbf{r}_1|} \end{aligned} \quad (3.34)$$

This can be generalized for a continuous object — or body —  $\mathcal{B}$ , of boundary  $\partial\mathcal{B}$ , which contains a number of particles which tend to infinity,  $N \rightarrow \infty$ , and where the masses tends to zero  $m_i \rightarrow 0$ . At limit we get:

$$\begin{aligned} \mathbf{F}_{1B} &= G \cdot m_1 \cdot \lim_{\substack{N \rightarrow \infty \\ m_i \rightarrow 0}} \left\{ \sum_{i=2}^{N+1} \frac{m_i}{|\mathbf{r}_i - \mathbf{r}_1|^2} \cdot \frac{\mathbf{r}_i - \mathbf{r}_1}{|\mathbf{r}_i - \mathbf{r}_1|} \right\} \\ &= G \cdot m_1 \cdot \iiint_{\mathcal{B}} \frac{1}{|\mathbf{r}' - \mathbf{r}_1|^2} \cdot \frac{\mathbf{r}' - \mathbf{r}_1}{|\mathbf{r}' - \mathbf{r}_1|} \cdot dm(\mathbf{r}') \\ &= G \cdot m_1 \cdot \iiint_{\mathcal{B}} \frac{\mathbf{r}' - \mathbf{r}_1}{|\mathbf{r}' - \mathbf{r}_1|^3} \cdot dm(\mathbf{r}') \end{aligned} \quad (3.35)$$

and if we introduce the mass density field  $\rho(\mathbf{r}')$  which is related to the differential mass element  $dm$  by:

$$dm(\mathbf{r}') = \rho(\mathbf{r}') \cdot dV \quad (3.36)$$

where  $dV$  is the differential volume element, we finally obtain:

$$\mathbf{F}_{1B} = G \cdot m_1 \cdot \iiint_{\mathcal{B}} \frac{\mathbf{r}' - \mathbf{r}_1}{|\mathbf{r}' - \mathbf{r}_1|^3} \cdot \rho(\mathbf{r}') \cdot dV \quad (3.37)$$

where:

$\mathbf{F}_{1\mathcal{B}}$	$\left[\frac{\text{kg}\cdot\text{m}}{\text{s}^2}\right]$	=	force vector induced by $\mathcal{B}$ acting on $\mathcal{P}_1$ .
$G$	$\left[\frac{\text{m}^3}{\text{kg}\cdot\text{s}^2}\right]$	=	gravitational constant.
$m_1$	$[\text{kg}]$	=	mass of particle $\mathcal{P}_1$ .
$\rho(\mathbf{r}')$	$\left[\frac{\text{kg}}{\text{m}^3}\right]$	=	mass density at location $\mathbf{r}_i$ .
$dV$	$[\text{m}^3]$	=	differential volume element.
$\mathbf{r}_1$	$[\text{m}]$	=	position vector of $\mathcal{P}_1$ .
$\mathbf{r}'$	$[\text{m}]$	=	position vector of $\mathcal{P}'$ .

### 3.4 Apparent Acceleration in Earth's Fixed Reference System

#### 3.4.1 General Formulation

Here, we are interested in the acceleration — or proper acceleration — felt by a particle  $\mathcal{P}$  attached to the Earth. Before going into the details of the equations, we have to fix some assumptions:

1. The inertial system  $i$  is given by a barycentric system comparable to ICRS.
2. The accelerated system  $a$  — Earth's rotating system — is comparable to ITRS. It is geocentric, at a certain time  $t = T_0$ , the axis  $\mathbf{e}_{az}$  is parallel to the Earth's rotation vector  $\boldsymbol{\omega}_\delta$ .
3. Only the Sun  $\odot$  and the Moon  $\lrcorner$  are the celestial bodies which are considered. They are assumed to be perfect homogeneous spheres.

Using Equation 3.30 we have:

$$\mathbf{a}_{\text{obs}}^a = -\frac{1}{m} \sum \mathbf{F}_{\text{grav}}^a + \mathbf{R}_i^a \cdot \ddot{\mathbf{O}}^i + \boldsymbol{\Omega}_{ia}^a \cdot \boldsymbol{\Omega}_{ia}^a \cdot \boldsymbol{\rho}^a + \dot{\boldsymbol{\Omega}}_{ia}^a \cdot \boldsymbol{\rho}^a + 2 \cdot \boldsymbol{\Omega}_{ia}^a \cdot \dot{\boldsymbol{\rho}}^a + \ddot{\boldsymbol{\rho}}^a \quad (3.38)$$

#### 3.4.2 Gravitational Forces

The gravitational forces acting on  $\mathcal{P}$  can be computed with Equations 3.31 and 3.37 as follows:

$$\begin{aligned} -\frac{1}{m} \sum \mathbf{F}_{\text{grav}}^a &= -G \cdot \iiint_{\delta} \frac{\boldsymbol{\rho}'^a - \boldsymbol{\rho}^a}{|\boldsymbol{\rho}'^a - \boldsymbol{\rho}^a|^3} \cdot \rho(\boldsymbol{\rho}'^a) \cdot dV \\ &\quad - G \cdot \iiint_{\odot} \frac{\boldsymbol{\rho}'^a - \boldsymbol{\rho}^a}{|\boldsymbol{\rho}'^a - \boldsymbol{\rho}^a|^3} \cdot \rho(\boldsymbol{\rho}'^a) \cdot dV \\ &\quad - G \cdot \iiint_{\lrcorner} \frac{\boldsymbol{\rho}'^a - \boldsymbol{\rho}^a}{|\boldsymbol{\rho}'^a - \boldsymbol{\rho}^a|^3} \cdot \rho(\boldsymbol{\rho}'^a) \cdot dV \end{aligned} \quad (3.39)$$

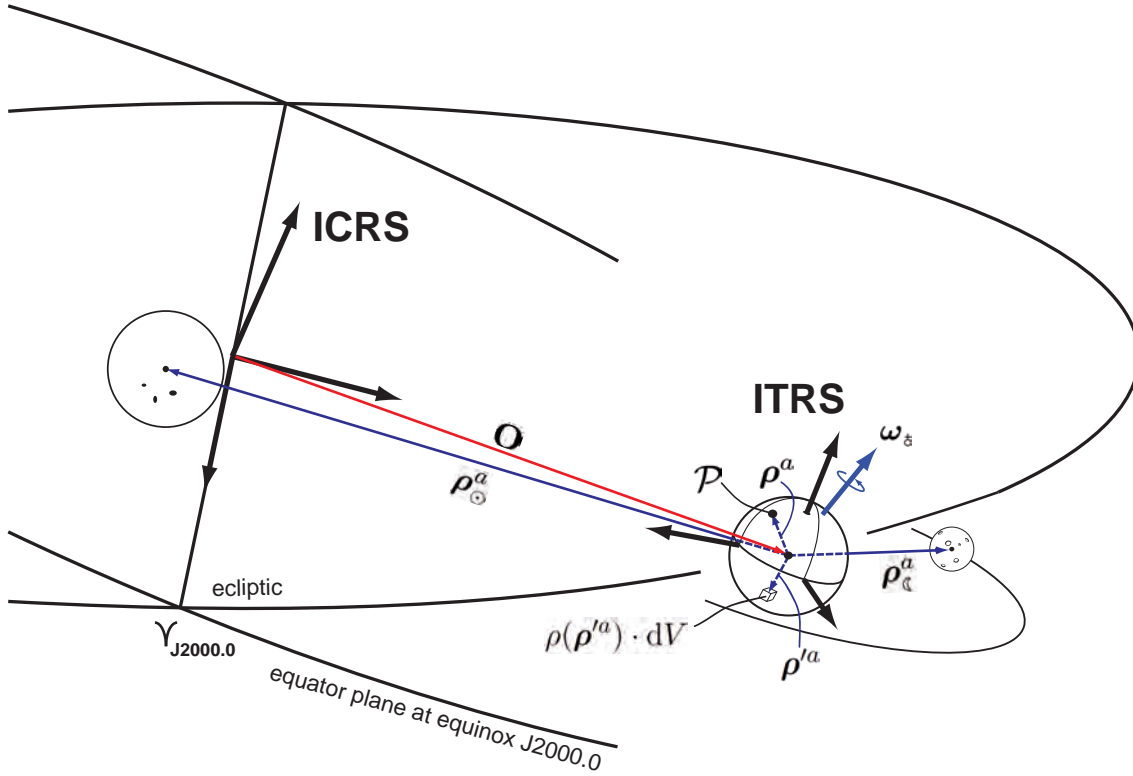


**Figure 3.5:** Representation of the (quasi-) inertial system ICRS and the accelerated system ITRS.

which can be simplified considering the Sun and the Moon as homogeneous spheres:

$$\begin{aligned}
 -\frac{1}{m} \sum \mathbf{F}_{\text{grav}}^a &= -G \cdot \iiint_{\delta} \frac{\boldsymbol{\rho}'^a - \boldsymbol{\rho}^a}{|\boldsymbol{\rho}'^a - \boldsymbol{\rho}^a|^3} \cdot \rho(\boldsymbol{\rho}'^a) \cdot dV \\
 &\quad - GM_{\odot} \cdot \frac{\boldsymbol{\rho}_{\odot}^a - \boldsymbol{\rho}^a}{|\boldsymbol{\rho}_{\odot}^a - \boldsymbol{\rho}^a|^3} \\
 &\quad - GM_{\zeta} \cdot \frac{\boldsymbol{\rho}_{\zeta}^a - \boldsymbol{\rho}^a}{|\boldsymbol{\rho}_{\zeta}^a - \boldsymbol{\rho}^a|^3}
 \end{aligned} \tag{3.40}$$

where  $M_{\odot}$  and  $M_{\zeta}$  represents the mass of the Sun and the Moon, and  $\boldsymbol{\rho}_{\odot}^a$  and  $\boldsymbol{\rho}_{\zeta}^a$  the position vectors, in the Earth's rotating system  $a$ , of the center of mass of the Sun and the Moon, respectively.

### 3.4.3 Acceleration of the Origin of the Earth's Rotating System

In our case, the origin  $\mathbf{O}^i$  of the Earth's rotating system  $a$  is defined as the center of mass of the Earth, the geocenter  $\mathcal{G}$ . In this case, the acceleration of  $\mathcal{G}$ , in the inertial system  $i$ , is equal to the sum of all accelerations induced by all gravitational forces acting on the



center of mass of the Earth:

$$\begin{aligned}
 +\mathbf{R}_i^a \cdot \ddot{\mathbf{O}}^i &= +G \cdot \iiint_{\delta} \frac{\rho'^a}{|\rho'^a|^3} \cdot \rho(\rho'^a) \cdot dV \\
 &+ GM_{\odot} \cdot \frac{\rho_{\odot}^a}{|\rho_{\odot}^a|^3} \\
 &+ GM_{\zeta} \cdot \frac{\rho_{\zeta}^a}{|\rho_{\zeta}^a|^3}
 \end{aligned} \tag{3.41}$$

where the first term is, by definition, equal to zero when  $\mathcal{O} \equiv \mathcal{G}$ , and it follows that:

$$+\mathbf{R}_i^a \cdot \ddot{\mathbf{O}}^i = +GM_{\odot} \cdot \frac{\rho_{\odot}^a}{|\rho_{\odot}^a|^3} + GM_{\zeta} \cdot \frac{\rho_{\zeta}^a}{|\rho_{\zeta}^a|^3} \tag{3.42}$$

### 3.4.4 Centripetal Acceleration

The centripetal acceleration is given by

$$+\boldsymbol{\Omega}_{ia}^a \cdot \boldsymbol{\Omega}_{ia}^a \cdot \rho^a \tag{3.43}$$

where the skew-symmetric matrix  $\boldsymbol{\Omega}_{ia}^a$  contains the elements of the instantaneous angular velocity vector of the Earth  $\boldsymbol{\omega}_{\delta}$ , given in the Earth's fixed system  $a$ .

The Earth's rotation vector  $\boldsymbol{\omega}_{\delta}$  is almost parallel to the axis  $\mathbf{e}_{az}$ . The small difference in direction, called *polar motion* comes from the fact that the axis  $\mathbf{e}_{az}$  is not defined to be parallel to  $\boldsymbol{\omega}_{\delta}$  over time. Indeed, the axis  $\mathbf{e}_{ax}, \mathbf{e}_{ay}, \mathbf{e}_{az}$  are defined to keep minimal variations of the components of the position's vectors  $\rho^a$  of benchmarks fixed on the Earth's crust<sup>8</sup>. The polar motion is defined by two small angles  $(x_p, y_p)$ , where  $x_p$  is the angle between  $\boldsymbol{\omega}_{\delta}$  and  $\mathbf{e}_{az}$  projected on the plane containing the meridian of Greenwich, and  $y_p$  the angle projected on the plane containing the 90°W meridian.

For many non-geodetic applications, polar motion can be neglected since it represents an angle which does not exceed a few 0.1 arcsec. In contrary, for geodetic applications, polar motion is crucial. Assuming that  $x_p$  and  $y_p$  are small and given in radian, the components of the Earth's rotation vector  $\boldsymbol{\omega}_{\delta}^a$  are given by:

$$\boldsymbol{\omega}_{\delta}^a = \omega_{\delta} \cdot \begin{pmatrix} +x_p \\ -y_p \\ \sqrt{1 - x_p^2 - y_p^2} \end{pmatrix} \tag{3.44}$$

where  $\omega_{\delta}$  is the Earth's rotation angular velocity. Further details concerning the numerical computation of  $\boldsymbol{\omega}_{\delta}$  in the inertial and in the Earth's fixed system can be found in Appendix B.

<sup>8</sup>This is realized with the concept of no-net rotation.

It follows that the matrix  $\mathbf{\Omega}_{ia}^a$  beomes:

$$\mathbf{\Omega}_{ia}^a = \omega_{\delta} \cdot \begin{pmatrix} 0 & -\gamma & -y_p \\ \gamma & 0 & -x_p \\ +y_p & +x_p & 0 \end{pmatrix} \quad (3.45)$$

if we define  $\gamma = \sqrt{1 - x_p^2 - y_p^2}$ . Finally, the centripetal acceleration is given by:

$$+\mathbf{\Omega}_{ia}^a \cdot \mathbf{\Omega}_{ia}^a \cdot \boldsymbol{\rho}^a = \omega_{\delta}^2 \cdot \begin{pmatrix} -1 + x_p^2 & -y_p \cdot x_p & x_p \cdot \gamma \\ -y_p \cdot x_p & -1 + y_p^2 & -y_p \cdot \gamma \\ x_p \cdot \gamma & -y_p \cdot \gamma & -y_p^2 - x_p^2 \end{pmatrix} \cdot \begin{pmatrix} \rho_x \\ \rho_y \\ \rho_z \end{pmatrix} \quad (3.46)$$

### 3.4.5 Euler Acceleration

The Euler acceleration is given by

$$+\dot{\mathbf{\Omega}}_{ia}^a \cdot \boldsymbol{\rho}^a \quad (3.47)$$

where  $\dot{\mathbf{\Omega}}_{ia}^a$  contains the components, given in the  $a$ -system, of the time derivative of the Earth's rotation vector  $\boldsymbol{\omega}_{\delta}^a$ .

### 3.4.6 Coriolis Acceleration

The Coriolis acceleration is given by

$$+2 \cdot \mathbf{\Omega}_{ia}^a \cdot \dot{\boldsymbol{\rho}}^a \quad (3.48)$$

which depends on the velocity  $\dot{\boldsymbol{\rho}}^a$  on the particle  $\mathcal{P}$  with respect to the Earth's fixed  $a$ -system and the Earth's rotation vector  $\boldsymbol{\omega}_{\delta}^a$ .

### 3.4.7 Observed Acceleration

Using Equation 3.38, if we write explicitly the gravitational acceleration given in Equation 3.40 and the acceleration of the origin of the Earth's fixed system  $a$  given in Equation 3.42

we have:

$$\begin{aligned}
\mathbf{a}_{\text{obs}}^a = & -G \cdot \iiint_{\delta} \frac{\boldsymbol{\rho}'^a - \boldsymbol{\rho}^a}{|\boldsymbol{\rho}'^a - \boldsymbol{\rho}^a|^3} \cdot \rho(\boldsymbol{\rho}'^a) \cdot dV - GM_{\odot} \cdot \frac{\boldsymbol{\rho}_{\odot}^a - \boldsymbol{\rho}^a}{|\boldsymbol{\rho}_{\odot}^a - \boldsymbol{\rho}^a|^3} - GM_{\zeta} \cdot \frac{\boldsymbol{\rho}_{\zeta}^a - \boldsymbol{\rho}^a}{|\boldsymbol{\rho}_{\zeta}^a - \boldsymbol{\rho}^a|^3} \\
& + GM_{\odot} \cdot \frac{\boldsymbol{\rho}_{\odot}^a}{|\boldsymbol{\rho}_{\odot}^a|^3} + GM_{\zeta} \cdot \frac{\boldsymbol{\rho}_{\zeta}^a}{|\boldsymbol{\rho}_{\zeta}^a|^3} \\
& + \boldsymbol{\Omega}_{ia}^a \cdot \boldsymbol{\Omega}_{ia}^a \cdot \boldsymbol{\rho}^a \\
& + \dot{\boldsymbol{\Omega}}_{ia}^a \cdot \boldsymbol{\rho}^a \\
& + 2 \cdot \boldsymbol{\Omega}_{ia}^a \cdot \dot{\boldsymbol{\rho}}^a \\
& + \ddot{\boldsymbol{\rho}}^a
\end{aligned} \tag{3.49}$$

and by rearranging some terms we obtain:

$$\begin{aligned}
\mathbf{a}_{\text{obs}}^a = & -G \cdot \iiint_{\delta} \frac{\boldsymbol{\rho}'^a - \boldsymbol{\rho}^a}{|\boldsymbol{\rho}'^a - \boldsymbol{\rho}^a|^3} \cdot \rho(\boldsymbol{\rho}'^a) \cdot dV \\
& + \boldsymbol{\Omega}_{ia}^a \cdot \boldsymbol{\Omega}_{ia}^a \cdot \boldsymbol{\rho}^a \\
& - GM_{\odot} \cdot \left\{ \frac{\boldsymbol{\rho}_{\odot}^a - \boldsymbol{\rho}^a}{|\boldsymbol{\rho}_{\odot}^a - \boldsymbol{\rho}^a|^3} - \frac{\boldsymbol{\rho}_{\odot}^a}{|\boldsymbol{\rho}_{\odot}^a|^3} \right\} - GM_{\zeta} \cdot \left\{ \frac{\boldsymbol{\rho}_{\zeta}^a - \boldsymbol{\rho}^a}{|\boldsymbol{\rho}_{\zeta}^a - \boldsymbol{\rho}^a|^3} - \frac{\boldsymbol{\rho}_{\zeta}^a}{|\boldsymbol{\rho}_{\zeta}^a|^3} \right\} \\
& + \dot{\boldsymbol{\Omega}}_{ia}^a \cdot \boldsymbol{\rho}^a \\
& + 2 \cdot \boldsymbol{\Omega}_{ia}^a \cdot \dot{\boldsymbol{\rho}}^a \\
& + \ddot{\boldsymbol{\rho}}^a
\end{aligned} \tag{3.50}$$

and if we define:

$$\begin{aligned}
\mathbf{a}_{\text{grav},\delta}^a = & -G \cdot \iiint_{\delta} \frac{\boldsymbol{\rho}'^a - \boldsymbol{\rho}^a}{|\boldsymbol{\rho}'^a - \boldsymbol{\rho}^a|^3} \cdot \rho(\boldsymbol{\rho}'^a) \cdot dV \\
\mathbf{a}_{\text{centrp}}^a = & + \boldsymbol{\Omega}_{ia}^a \cdot \boldsymbol{\Omega}_{ia}^a \cdot \boldsymbol{\rho}^a \\
\mathbf{a}_{\text{tidal}}^a = & -GM_{\odot} \cdot \left\{ \frac{\boldsymbol{\rho}_{\odot}^a - \boldsymbol{\rho}^a}{|\boldsymbol{\rho}_{\odot}^a - \boldsymbol{\rho}^a|^3} - \frac{\boldsymbol{\rho}_{\odot}^a}{|\boldsymbol{\rho}_{\odot}^a|^3} \right\} - GM_{\zeta} \cdot \left\{ \frac{\boldsymbol{\rho}_{\zeta}^a - \boldsymbol{\rho}^a}{|\boldsymbol{\rho}_{\zeta}^a - \boldsymbol{\rho}^a|^3} - \frac{\boldsymbol{\rho}_{\zeta}^a}{|\boldsymbol{\rho}_{\zeta}^a|^3} \right\} \\
\mathbf{a}_{\text{Eulerian}}^a = & + \dot{\boldsymbol{\Omega}}_{ia}^a \cdot \boldsymbol{\rho}^a \\
\mathbf{a}_{\text{Coriolis}}^a = & + 2 \cdot \boldsymbol{\Omega}_{ia}^a \cdot \dot{\boldsymbol{\rho}}^a
\end{aligned} \tag{3.51}$$

we can write Equation 3.50 as follows :

$$\mathbf{a}_{\text{obs}}^a = \mathbf{a}_{\text{grav},\delta}^a + \mathbf{a}_{\text{centrp}}^a + \mathbf{a}_{\text{tidal}}^a + \mathbf{a}_{\text{Eulerian}}^a + \mathbf{a}_{\text{Coriolis}}^a + \ddot{\boldsymbol{\rho}}^a \tag{3.52}$$

### 3.4.8 Apparent Gravity

If we look at the directions of the individual terms in Equation 3.52, it can be surprising that they are pointing exactly to the opposite direction as what we intuitively expect! For example, the gravitational part  $\mathbf{a}_{\text{grav},\delta}^a$  is not pointing to the center of the Earth, as we would expect, but to the opposite direction. The same is true concerning the centripetal acceleration  $\mathbf{a}_{\text{centrp}}^a$ : the vector is pointing into the direction of the Earth's rotation axis and not into the opposite direction — we would expect a centrifugal acceleration instead — as we intuitively expect, etc.

This ambiguous feeling comes from the fact that the particle  $\mathcal{P}$  does not feel what we call *observed* here. What does the particle really observe? It observes the acceleration which is needed to maintain  $\mathcal{P}$  on the trajectory given by  $\boldsymbol{\rho}(t)$  even if  $\mathcal{P}$  is subjected to the attracting gravitational forces. This becomes more evident when we look at the special case, when  $\mathcal{P}$  is assumed to be fixed to the surface of a non-rotating solid Earth and when the tides are neglected. Mathematically this corresponds to:

$$\begin{aligned}\dot{\boldsymbol{\rho}}^a &= \mathbf{0}; \quad \ddot{\boldsymbol{\rho}}^a = \mathbf{0} \\ \boldsymbol{\Omega}_{ia}^a &= \mathbf{0}; \quad \dot{\boldsymbol{\Omega}}_{ia}^a = \mathbf{0}\end{aligned}\tag{3.53}$$

which simplifies Equation 3.52 to:

$$\mathbf{a}_{\text{obs}}^a = \mathbf{a}_{\text{grav},\delta}^a \cong -\mathbf{g}^a\tag{3.54}$$

What does the particle  $\mathcal{P}$  really feel? It feels that it is pushed to the ground and this corresponds to the *reaction* of  $\mathcal{P}$  with respect to the observed acceleration  $\mathbf{a}_{\text{obs}}^a$ .

For this reason, we define the apparent gravity  $\mathbf{g}_{\text{obs}}^a$  as the opposite of the observed acceleration  $\mathbf{a}_{\text{obs}}^a$ :

$$\begin{aligned}\mathbf{g}_{\text{obs}}^a &= -\mathbf{a}_{\text{obs}}^a = -\mathbf{a}_{\text{grav},\delta}^a - \mathbf{a}_{\text{centrp}}^a - \mathbf{a}_{\text{tidal}}^a - \mathbf{a}_{\text{Eulerian}}^a - \mathbf{a}_{\text{Coriolis}}^a - \ddot{\boldsymbol{\rho}}^a \\ &= +\mathbf{g}_{\text{grav},\delta}^a + \mathbf{g}_{\text{centr}}^a + \mathbf{g}_{\text{tidal}}^a + \mathbf{g}_{\text{Eulerian}}^a + \mathbf{g}_{\text{Coriolis}}^a - \ddot{\boldsymbol{\rho}}^a\end{aligned}\tag{3.55}$$

with:

$$\begin{aligned}\mathbf{g}_{\text{grav},\delta}^a &= G \cdot \iiint_{\delta} \frac{\boldsymbol{\rho}'^a - \boldsymbol{\rho}^a}{|\boldsymbol{\rho}'^a - \boldsymbol{\rho}^a|^3} \cdot \rho(\boldsymbol{\rho}'^a) \cdot dV \\ \mathbf{g}_{\text{centr}}^a &= -\boldsymbol{\Omega}_{ia}^a \cdot \boldsymbol{\Omega}_{ia}^a \cdot \boldsymbol{\rho}^a \\ \mathbf{g}_{\text{tidal}}^a &= +GM_{\odot} \cdot \left\{ \frac{\boldsymbol{\rho}_{\odot}^a - \boldsymbol{\rho}^a}{|\boldsymbol{\rho}_{\odot}^a - \boldsymbol{\rho}^a|^3} - \frac{\boldsymbol{\rho}_{\odot}^a}{|\boldsymbol{\rho}_{\odot}^a|^3} \right\} + GM_{\mathfrak{C}} \cdot \left\{ \frac{\boldsymbol{\rho}_{\mathfrak{C}}^a - \boldsymbol{\rho}^a}{|\boldsymbol{\rho}_{\mathfrak{C}}^a - \boldsymbol{\rho}^a|^3} - \frac{\boldsymbol{\rho}_{\mathfrak{C}}^a}{|\boldsymbol{\rho}_{\mathfrak{C}}^a|^3} \right\} \\ \mathbf{g}_{\text{Eulerian}}^a &= -\dot{\boldsymbol{\Omega}}_{ia}^a \cdot \boldsymbol{\rho}^a \\ \mathbf{g}_{\text{Coriolis}}^a &= -2 \cdot \boldsymbol{\Omega}_{ia}^a \cdot \dot{\boldsymbol{\rho}}^a\end{aligned}\tag{3.56}$$

where the sum of the gravitational acceleration — only integrated over the Earth — and the centrifugal acceleration is defined as the gravity acceleration vector  $\mathbf{g}^a$ , see *Torge and Müller (2012)*:

$$\mathbf{g}^a = \mathbf{g}_{\text{grav},\delta}^a + \mathbf{g}_{\text{centr}}^a\tag{3.57}$$

The main reason for this definition comes from the wish to distinguish between the time quasi-invariant part —  $\mathbf{g}^a$  — and the time varying part mainly represented by the tidal acceleration  $\mathbf{g}_{\text{tidal}}^a$ . Concerning the Eulerian acceleration vector  $\mathbf{g}_{\text{Eulerian}}^a$ , this term is usually neglected because of its small order of magnitude  $\sim 10^{-9} \left[ \frac{\text{m}}{\text{s}^2} \right]$  and by the fact that the vertical component — in the local topocentric system — is always equal to zero<sup>9</sup>, see 3.7.1.

### 3.4.9 Equation of Motion

From Equations 3.55 and 3.57 it is possible to write the equation of motion of a particle  $\mathcal{P}$  in a Earth's fixed reference system:

$$\begin{aligned}\ddot{\boldsymbol{\rho}}^a &= \mathbf{g}_{\text{grav},\delta}^a + \mathbf{g}_{\text{centr}}^a + \mathbf{g}_{\text{tidal}}^a + \mathbf{g}_{\text{Eulerian}}^a + \mathbf{g}_{\text{Coriolis}}^a - \mathbf{g}_{\text{obs}}^a \\ &= \mathbf{g}^a + \mathbf{g}_{\text{tidal}}^a + \mathbf{g}_{\text{Eulerian}}^a + \mathbf{g}_{\text{Coriolis}}^a - \mathbf{g}_{\text{obs}}^a \\ &= \mathbf{g}_{\text{dyn}}^a - \mathbf{g}_{\text{obs}}^a\end{aligned}\tag{3.58}$$

where  $\mathbf{g}_{\text{dyn}}^a = \mathbf{g}^a + \mathbf{g}_{\text{tidal}}^a + \mathbf{g}_{\text{Eulerian}}^a + \mathbf{g}_{\text{Coriolis}}^a$  is defined here as the dynamical gravity vector.

### 3.4.10 Apparent Gravity for a Deformable Earth

In the previous development, we made the assumption that the Earth is perfectly rigid. It is obvious that this is not the case in reality and the solid part of the Earth is deformed in reaction to all apparent forces acting on it. Moreover, the effects on the gravity and the deformations due to the movement of all fluid masses (like oceans) must be taken into account. In this case, the mathematical formulation of the global Earth-Moon-Sun deformable system can be a very difficult task.

The most fundamental way would be to consider the field of deformations  $\mathbf{u}(\boldsymbol{\rho}, t) \equiv \mathbf{u}$  as unknown, associated with a rheological model and a fluid model in order to be able to couple the deformations to the apparent forces. In geodesy, this approach is usually applied for regional applications limited to the studying of surface deformations and not for the prediction of the apparent gravity observed on the Earth.

An other possibility, if we consider that the field of deformations  $\mathbf{u}$  is known or can be determined by a simple geophysical model, is to integrate the deformations into Equations 3.55 and 3.56. This can be done, when Equation 3.56 is modified in the following way:

1. For an observer  $\mathcal{P}$  attached to the surface of the Earth, the position  $\boldsymbol{\rho}$  is now given by the sum of a reference position  $\boldsymbol{\rho}_0$ , supposed to be fix in the Earth's fixed system, and the displacement vector  $\mathbf{u}(\boldsymbol{\rho}, t) \equiv \mathbf{u}$ :

$$\boldsymbol{\rho}^a = \boldsymbol{\rho}_0^a + \mathbf{u}^a\tag{3.59}$$

which now depends always on time. This implies that the Coriolis acceleration  $\mathbf{g}_{\text{Coriolis}}$  and the term  $\ddot{\boldsymbol{\rho}}$  are not equal to  $\mathbf{0}$  anymore.

---

<sup>9</sup>only in the spherical approximation.

2. The gravitational acceleration  $\mathbf{g}_{\text{grav},\delta}$  must be integrated over the deformed Earth as follows:

$$\mathbf{g}_{\text{grav},\delta}^a = G \cdot \iiint_{\delta} \frac{(\boldsymbol{\rho}'^a + \mathbf{u}'^a) - \boldsymbol{\rho}^a}{|(\boldsymbol{\rho}'^a + \mathbf{u}'^a) - \boldsymbol{\rho}^a|^3} \cdot \rho(\boldsymbol{\rho}'^a + \mathbf{u}'^a) \cdot dV \quad (3.60)$$

We see that all components of the apparent gravity are affected by the time-dependent deformation field. This signifies that all components of the apparent gravity  $\mathbf{g}_{\text{obs}}$  must be re-computed each time we want to predict the apparent gravity for an observer attached to the surface of the Earth. This rigorous approach is simple and elegant but still difficult to apply in practice due to the huge amount of computations which are needed.

Nowadays, in geodesy, another solution is usually applied in order to predict the apparent gravity. Due to the fact that the largest time-variable signal in the apparent gravity is caused by Earth tides, all effects concerning the deformation of the Earth and all variations in gravity (direct and indirect effects) are modeled by linear functionals of the tidal forces  $\mathbf{g}_{\text{tidal}}$  only. The other parts of the apparent gravity are computed with position vectors,  $\boldsymbol{\rho}$  and  $\boldsymbol{\rho}'$ , reduced to a *conventional tide free*<sup>10</sup> crust model, see (*Petit and Luzum, 2010*). More details about the treatment and the order of magnitude of the tides are given in section 3.7.4.

**Remark** For the rest of this thesis, if the reference system is not explicitly specified it is supposed to be the Earth fixed system  $a$ .

## 3.5 Potential Theory

### 3.5.1 Introduction

To mathematics and physics, the concept of *potential* and *potential energy* is central. These discoveries are closely related to the introduction of the general theory of energy associated with its *law of conservation of energy*. Since the formulation of Newton's laws in 1687, it took a long time with many confusions before the creation of an unambiguous general modern formulation of potential energy. In *Roche (2003)*, we can find that various famous scientists (D. Bernoulli<sup>11</sup>, L. Euler<sup>12</sup>, J.-L. Lagrange<sup>13</sup>, L. Carnot<sup>14</sup>, G. Green<sup>15</sup>, W. Thomson<sup>16</sup>) anticipated the concept of potential energy but without reaching the generality and the conceptual power used today in modern physics.

According to *Roche (2003)*, the first proper introduction of the modern definition of energy is attributed to W.J.M. Rankine<sup>17</sup> in *Rankine (1853)* who defines energy as follows:

<sup>10</sup>as the positions in ITRF.

<sup>11</sup>Daniel Bernoulli (1700-1782), Swiss mathematician and physicist.

<sup>12</sup>Leonhard Euler (1707-1783), Swiss mathematician and physicist

<sup>13</sup>Joseph-Louis Lagrange (1736-1813), French and Italian mathematician and astronomer.

<sup>14</sup>Lazare Carnot (1753-1823), French politician, engineer, and mathematician

<sup>15</sup>George Green (1793-1841), British mathematical physicist.

<sup>16</sup>William Thomson, 1st Baron Kelvin (1824-1907), British mathematical physicist and engineer.

<sup>17</sup>William John Macquorn Rankine (1820-1872), Scottish civil engineer, physicist and mathematician.

*"The term energy comprehends every state of a substance which constitutes the capacity for performing work. Quantities of energy are measured by the quantities of work which they constitute the means of performing."*

and postulates that all conceivable forms of energy may be divided into two kinds:

1. the **actual** or sensible energy:

*"Actual energy is a measurable, transferable, and transformable affection of substance, the presence of which causes the substance to tend to change its state in one or more respect; by the occurrence of which changes actual energy disappears, and is replaced by potential energy, which is measurable by the amount of a change in the condition of a substance, and that of the tendency or force whereby that change is produced (or, what is the same thing, of the resistance overcome in producing it), taken jointly."*

which is called, today, *kinetic energy*.

2. the **potential** or latent energy:

*"Potential energy, which is measured by the amount of a change in the condition of a substance, and that of the tendency or force whereby that change is produced (or, what is the same thing, of the resistance overcome in producing it), taken jointly. If the change whereby potential energy has been developed be exactly reversed, then as the potential energy disappears, the actual energy which had previously disappeared is reproduced."*

Today, according to *Feynman et al.* (1999), the potential energy of an object is defined as the energy due to the **interactions** of this objects with other objects related to the **positions** of these objects. This implies that the interactions which can be associated to a potential energy must arise from a **conservative** force field. For example:

- the work done by the gravitational force field is called *gravitational potential energy*.
- the work done by the Coulomb force field is called *electrostatic potential energy*.
- the work done by the nuclear forces field is called *nuclear potential energy*.
- etc.

in contrary, frictional and viscous forces are **non-conservative**. From all these definitions, we can see that they are all defined with respect to the concept of **work done by a force**, introduced by G.-G. Coriolis<sup>18</sup> in 1829 together with the correct expression of kinetic energy.

<sup>18</sup>Gaspard-Gustave de Coriolis (1792-1843), French mathematician, mechanical engineer and scientist.

### 3.5.2 Work

According to *Blakely* (1996), the work  $W(\mathbf{F}, \mathbf{r}_1, \mathbf{r}_2, \mathcal{S})$  done by the force field  $\mathbf{F}(\mathbf{r})$  on a particle of mass  $m$  is defined as the kinetic energy  $K(t_1, t_2)$  expended by  $\mathbf{F}$  in moving the particle from  $\mathbf{r}_1(t_1)$  to  $\mathbf{r}_2(t_2)$  along the path  $\mathcal{S}$ . Between  $t_1$  and  $t_2$ , the variation of kinetic energy can be written as follows:

$$\begin{aligned} K(t_1, t_2) &= \int_{t_1}^{t_2} \frac{d}{dt} \left[ \frac{1}{2} m \cdot \dot{\mathbf{r}}(t) \cdot \dot{\mathbf{r}}(t) \right] \cdot dt \\ &= \int_{t_1}^{t_2} \frac{1}{2} m \cdot [\ddot{\mathbf{r}}(t) \cdot \dot{\mathbf{r}}(t) + \dot{\mathbf{r}}(t) \cdot \ddot{\mathbf{r}}(t)] \cdot dt \\ &= \int_{t_1}^{t_2} m \cdot \ddot{\mathbf{r}}(t) \cdot \dot{\mathbf{r}}(t) \cdot dt \end{aligned} \quad (3.61)$$

From Newton's second law we know that  $\mathbf{F}(t) = m \cdot \ddot{\mathbf{r}}(t)$  which implies that:

$$\begin{aligned} K(t_1, t_2) &= \int_{t_1}^{t_2} \mathbf{F}(t) \cdot \dot{\mathbf{r}}(t) \cdot dt \\ &= \int_{t_1}^{t_2} \mathbf{F}(t) \cdot \frac{d\mathbf{r}(t)}{dt} \cdot dt \\ &= \int_{\mathbf{r}_1, \mathcal{S}}^{\mathbf{r}_2} \mathbf{F}(\mathbf{r}) \cdot d\mathbf{r} = W(\mathbf{F}, \mathbf{r}_1, \mathbf{r}_2, \mathcal{S}) \end{aligned} \quad (3.62)$$

This shows that the work done by a force  $\mathbf{F}(\mathbf{r})$  is also equal to the path integral along  $\mathcal{S}$  of the scalar product of the force  $\mathbf{F}(\mathbf{r})$  and the differential displacement element  $d\mathbf{r}$  of the particle. In this general case, the work  $W(\mathbf{F}, \mathbf{r}_1, \mathbf{r}_2, \mathcal{S})$  depends on the path  $\mathcal{S}$  taken by the particle. However, if we can prove that the work done by a force field is always independent of the path taken by the particle, the force field is called *conservative* and benefits from very interesting properties.

### 3.5.3 Conservative Force Field

A force field  $\mathbf{F}(\mathbf{r})$  is called conservative if the work  $W(\mathbf{F}, \mathbf{r}_1, \mathbf{r}_2, \mathcal{S})$  done by this field is independent of the path  $\mathcal{S}$ . Then, we can write:

$$W(\mathbf{F}, \mathbf{r}_1, \mathbf{r}_2, \forall \mathcal{S}) = W(\mathbf{F}, \mathbf{r}_1, \mathbf{r}_2) = \int_{\mathbf{r}_1, \forall \mathcal{S}}^{\mathbf{r}_2} \mathbf{F}(\mathbf{r}) \cdot d\mathbf{r} \quad (3.63)$$

This gives the possibility to define a *scalar work field*  $W(\mathbf{r})$ , assuming an origin  $\mathbf{r}_0$  is fixed for  $\mathbf{r}_1$ , and we compute the work for all points  $\mathbf{r}$  of the space:

$$W(\mathbf{r}) = W(\mathbf{F}, \mathbf{r}_0, \mathbf{r}) = \int_{\mathbf{r}_0}^{\mathbf{r}} \mathbf{F}(\mathbf{r}') \cdot d\mathbf{r}' \quad (3.64)$$

In addition, because the function  $W(\mathbf{r})$  is independent of the integration path, we can see that the work between two arbitrary positions  $\mathbf{r}_1$  and  $\mathbf{r}_2$  is simply given by:

$$W(\mathbf{F}, \mathbf{r}_1, \mathbf{r}_2) = W(\mathbf{r}_2) - W(\mathbf{r}_1) \quad (3.65)$$



But the most important property of  $W(\mathbf{r})$  is that it can directly be linked to the vectorial force field  $\mathbf{F}$  with the gradient operator:

$$\nabla W(\mathbf{r}) = \mathbf{F}(\mathbf{r}) \quad (3.66)$$

which implies that  $\mathbf{F}$  is mandatory an irrotational field. This comes from the general identity of vector analysis which say that the curl of the gradient of any scalar field is always the zero vector:

$$\nabla \times [\nabla W(\mathbf{r})] = \nabla \times \mathbf{F}(\mathbf{r}) = \mathbf{0} \quad (3.67)$$

The inverse statement is not true. If the curl of a force field is irrotational, a scalar potential exists but the field is not necessarily conservative (e.g. a time-varying gravitational field).

### 3.5.4 Potential Function

According to *Blakely* (1996), the *potential function*  $\Phi(\mathbf{r})$  is a special case of the work scalar field where  $\mathbf{r}_0$  is chosen at infinity and the force is scaled by the mass of the particle. From Equation 3.64 we get:

$$\Phi(\mathbf{r}) = \frac{1}{m} \int_{\mathbf{r}_0 \rightarrow \infty}^{\mathbf{r}} \mathbf{F}(\mathbf{r}') \cdot d\mathbf{r}' \quad (3.68)$$

## 3.6 Shape of Fluid-Air Interface

### 3.6.1 General Solution

In the general case of hydrodynamics, the determination of the shape of a fluid-gaz interface  $\rho_{\sim}(t)$  — or two-phase free surface flows — is a difficult task for many reasons. First, it comes from the fact that the governing partial differential equations for fluids, the *Navier-Stokes equations*, are highly non-linear. Secondly, the shape — or the geometry — of the interface is not directly a field — like pressure or the velocity fields (which are explicit fields of the Navier-Stokes equations). Actually, based on the two possible specifications of the flow field (*Lagrangian* and *Eulerian*), there exist two classes of approaches in order to determine the shape of the interface.

When the Lagrangian specification is used for the integration of the Navier-Stokes equations, the domain of integration follows the fluid. It must always match, at any time, the space occupied by the fluid. It follows that the free surface is considered as a free deformable boundary condition which has to be tracked in time.

When the Eulerian specification is used, however the domain of integration is fixed and the fluid is propagated in this fixed space. If we want to know if a certain point of the space is occupied by the fluid or not, it is necessary to introduce a new "matter" field, computed after the advection step. Then, from this field, the geometry of the interface is defined as the set of the paths which separate the space occupied by matter and no matter. In *Caboussat* (2005) we can find a summary of the methods used in computational fluid dynamics simulations.

### Navier-Stokes Equations for Incompressible Newtonian Fluids

The governing equations of a fluid described by a velocity vector field  $\mathbf{v}(\boldsymbol{\rho}, t)$ , a pressure scalar field  $p(\boldsymbol{\rho}, t)$ , a density  $\rho$  and a kinematic viscosity  $\nu$  are called the Navier-Stokes equations. In the special case when the density of the fluid is assumed to be constant<sup>19</sup>, the temperature field is neglected<sup>20</sup> and the fluid is assumed to be Newtonian<sup>21</sup>, we get a system of four partial differential equations. Three equations<sup>22</sup> express the conservation of momentum<sup>23</sup> and one equation<sup>24</sup> expresses the conservation of mass. In the non-inertial system  $a$  we have:

$$\begin{cases} \frac{\partial \mathbf{v}}{\partial t} + \mathbf{v} \cdot \nabla \mathbf{v} = -\frac{1}{\rho} \cdot \nabla p + \nu \cdot \Delta \mathbf{v} + \mathbf{g}_{\text{dyn}} \\ \nabla \cdot \mathbf{v} = 0 \end{cases} \quad (3.69)$$

where:

$$\begin{aligned} \mathbf{v}(\boldsymbol{\rho}, t) \quad \left[ \frac{\text{m}}{\text{s}} \right] &= \text{velocity field.} \\ p(\boldsymbol{\rho}, t) \quad \left[ \frac{\text{N}}{\text{m}^2} \right] &= \text{pressure field.} \\ \rho \quad \left[ \frac{\text{kg}}{\text{m}^3} \right] &= \text{density of the fluid.} \\ \nu \quad \left[ \frac{\text{m}^2}{\text{s}} \right] &= \text{kinematic viscosity of the fluid.} \\ \mathbf{g}_{\text{dyn}}(\boldsymbol{\rho}, t) \quad \left[ \frac{\text{m}}{\text{s}^2} \right] &= \text{dynamical gravity.} \end{aligned}$$

### 3.6.2 Vertically Integrated Solution

For a specific class of problems, it is possible to integrate partially the Navier-Stokes equations. If the vertical dimension of the problem is significantly smaller than the horizontal dimensions, the Navier-Stokes equations can be integrated in the vertical dimension. This, unlike in the case of Navier-Stokes equations, allows to get a set of partial differential equations which contains directly the geometry of the free surface interface as field. In the literature, we can find two basic types of vertical integrated equations. The *Boussinesq equations* and the *shallow water equations* — or *St-Venant equations*. The main differences concern the hypotheses assumed for the vertically velocity profile: the Boussinesq equations can take into account variations in the vertical velocity profile, while the shallow water equations consider that the velocity is constant over a water column, see Figure 3.6. The main consequence is that only the Boussinesq equation modelizes dispersion phenomena in the wave propagation. However, because only very small water velocities are considered in this work, only the shallow water equations are considered.

<sup>19</sup>incompressibility.

<sup>20</sup>no thermal convection and conduction.

<sup>21</sup>the shear stress of the fluid is proportional to the derivative of the velocity component that is parallel to the direction of shear.

<sup>22</sup>regrouped in the first line of the system of Equations 3.69.

<sup>23</sup>Newton's second law.

<sup>24</sup>the second line of the system of Equations 3.69.

### Shallow Water Equations

From the Navier-Stokes equations 3.69 we can derive the shallow water equations considering the following assumptions (Figure 3.6):

- the thickness of the water is described by a new scalar field  $h(x, y, t)$  depending on the horizontal coordinates<sup>25</sup> and time only. The locus of the fluid-gaz interface  $\boldsymbol{\rho}_\sim(t)$  is described as follows:

$$\boldsymbol{\rho}_\sim(t) = \begin{pmatrix} x \\ y \\ h(x, y, t) + h_{\text{floor}}(x, y) \end{pmatrix} \quad (3.70)$$

where  $h_{\text{floor}}(x, y)$  represents the time-invariant surface of the floor.

- the slope of the water surface is small:

$$|\nabla h(x, y, t)| \ll 1 \quad (3.71)$$

- the velocity field is assumed to be constant along the vertical axis:

$$\mathbf{v}(\boldsymbol{\rho}, t) = \mathbf{v}(x, y, t) \quad (3.72)$$

- the pressure field  $p(\boldsymbol{\rho}, t)$  is assumed to be known and hydrostatic. In addition, we assume a constant vertical component of the gravity acceleration  $g_z \cong -9.81 \frac{\text{m}}{\text{s}^2}$ . Moreover, the pressure on the free surface  $\boldsymbol{\rho}_\sim$  is assumed to be constant and equal to  $p(\boldsymbol{\rho}_\sim, t) = p_0$ :

$$p(\boldsymbol{\rho}, t) = -\rho \cdot g_z \cdot [h(x, y, t) - z + h_{\text{floor}}(x, y)] + p_0 \quad (3.73)$$

- the viscosity of the fluid is neglected:

$$\nu = 0 \quad (3.74)$$

with these assumptions we can find the two-dimensional shallow water equations:

$$\begin{cases} \frac{\partial \mathbf{v}}{\partial t} + \mathbf{v} \cdot \nabla \mathbf{v} = g_z \cdot \nabla h + \mathbf{g}_{\text{dyn}} \\ \frac{\partial h}{\partial t} = -\nabla \cdot (h \cdot \mathbf{v}) \end{cases} \quad (3.75)$$

where:

---

<sup>25</sup>here the components  $x, y$  represent the horizontal coordinates and  $z$  the vertical component in a topocentric system.

$h(x, y, t)$	$[m]$	= free surface elevation with respect to the fixed bottom boundary limit (e.g. oceanic floor).
$\mathbf{v}(x, y, t)$	$[\frac{m}{s}]$	= velocity field.
$\mathbf{g}_{\text{dyn}}(x, y, t)$	$[\frac{m}{s^2}]$	= dynamical gravity.
$\rho$	$[\frac{kg}{m^3}]$	= density of the fluid.
$g_z$	$[\frac{m}{s^2}]$	= vertical gravity acceleration.

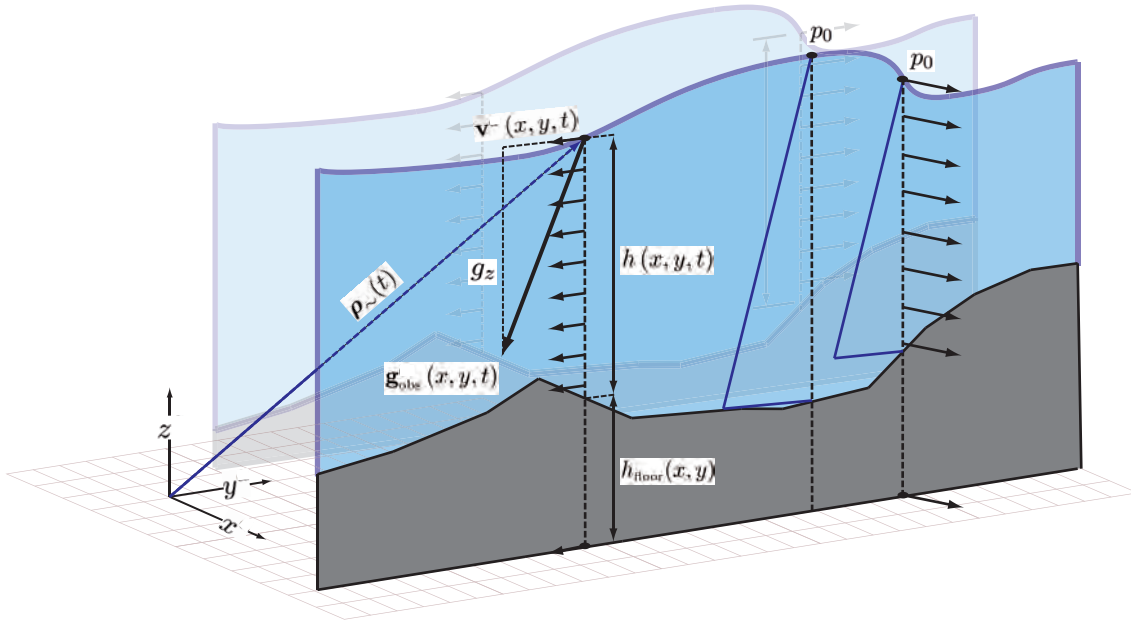


**Figure 3.6:** Schematic representation of the simplified model used for the shallow water equations. The parallel continuous blue lines represent the assumed hydrostatic pressure as a function of the depth at two different positions. This shows clearly that the resulting horizontal force due to the pressure gradient depends directly on the height of the water  $h(x, y, t)$ .

### 3.6.3 Forced Harmonic Oscillator Solution

If we go further in the restriction of systems involving fluids, it is sometimes possible to solve analytically free-surface fluid dynamic problems. This can be the case if the governing equation takes the form of a time-invariant second order linear differential equation of which solutions are analytic. Furthermore, because such systems are linear and time-invariant<sup>26</sup>, they can be completely characterized by *transfer functions* which can be used to compute the response of any input excitation and to analyze easily both, frequency and phase responses.

<sup>26</sup>also called LTI systems.

For example, in *d'Oreye de Lantremange* (2003) or *Boudin* (2004), simple models of hydrostatic levelling systems (HLS), which result from LTI equations, can be found. In *Boudin* (2004) the governing linear differential equation is derived from the Navier-Stokes equations while *d'Oreye de Lantremange* (2003) derives it from the *Lagrangian* of the system in a very elegant manner.

### Dynamic Model of a Basic Hydrostatic Levelling System

Here, a simplified version of the HLS model, presented by *d'Oreye de Lantremange* (2003), is developed. The HLS, see Figure 3.7, is formed by two cylindrical pots at the extremities which are connected by a circular tube which is assumed to be always filled by fluid. Because of the configuration of the system, the dimension of the problem can be reduced from three to two, one horizontal component  $x$  which is represented by the axis passing through the centers of the pots, and the vertical component  $z$ . The model assumes the following hypotheses:

- the origin of the system  $a$  is defined at the center of the first pot at the level equilibrium of the fluid.
- the shape of the free surface  $\rho_{\sim}$  is reduced to a set of two position vectors  $\rho_{\sim_1}$  and  $\rho_{\sim_2}$  which represent the levels of the fluid in the pots.
- the HLS is assumed to be perfectly fixed to a solid Earth and the pots are separated by a distance  $L$ . This implies:

$$\rho_{\sim_1}(t) = \begin{pmatrix} 0 \\ 0 \\ z_1(t) \end{pmatrix} \quad \text{and} \quad \rho_{\sim_2}(t) = \begin{pmatrix} L \\ 0 \\ z_2(t) \end{pmatrix} \quad (3.76)$$

where  $z_1(t)$  and  $z_2(t)$  represents the vertical component of the free surface in the pots.

- the cross sections  $S_{\text{pot}}$  of the pots are identical and the velocity of the fluid inside a single pot  $\dot{\rho}_i(t)$  is assumed to be vertical and constant:

$$\dot{\rho}_i(t) = \begin{pmatrix} 0 \\ 0 \\ \dot{z}_i(t) \end{pmatrix} \quad (3.77)$$

- the cross section of the tube is represented by  $S_{\text{tube}}$  and the velocity of the fluid inside the tube  $\dot{\rho}_{\text{tube}}(t)$  is assumed to be constant and horizontal:

$$\dot{\rho}_{\text{tube}}(t) = \begin{pmatrix} \dot{x}_{\text{tube}}(t) \\ 0 \\ 0 \end{pmatrix} \quad (3.78)$$



forces and if we add the contribution of the non-conservative forces in the generalized *Euler-Lagrange differential equation*, see Equation 3.94. Considering that  $\approx$  represents the total region of the HLS occupied by the fluid and  $\simeq$  the region occupied by the fluid in hydrostatic equilibrium, the total kinetic energy is defined as:

$$\begin{aligned}
 E_{\text{kin}}(\dot{\rho}) &= \frac{1}{2} \rho \cdot \iiint_{\approx} \dot{\rho} \cdot \dot{\rho} \cdot dV \\
 &= \underbrace{\frac{1}{2} \rho \cdot S_{\text{pot}} \cdot [H + z_1(t)] \cdot \dot{z}_1(t)^2}_{\text{pot 1}} + \underbrace{\frac{1}{2} \rho \cdot S_{\text{pot}} \cdot [H + z_2(t)] \cdot \dot{z}_2(t)^2}_{\text{pot 2}} \\
 &\quad + \underbrace{\frac{1}{2} \rho \cdot S_{\text{tube}} \cdot L \cdot \dot{x}_{\text{tube}}(t)^2}_{\text{tube}}
 \end{aligned} \tag{3.83}$$

where  $H$  corresponds to the vertical distance between the floor of the pots and the free surface at equilibrium. Considering Equation 3.79 we can write Equation 3.83, as a function of  $\dot{z}(t)$ :

$$E_{\text{kin}}(\dot{z}) = \dot{z}(t)^2 \cdot \left( \rho \cdot S_{\text{pot}} \cdot H + \frac{1}{2} \rho \cdot \frac{S_{\text{pot}}^2}{S_{\text{tube}}} \cdot L \right) \tag{3.84}$$

The total potential energy of the fluid which differs from equilibrium is given by:

$$E_{\text{pot}}(\rho) = \rho \cdot \iiint_{\approx} [-\Phi(\rho)] \cdot dV - \rho \cdot \iiint_{\simeq} [-\Phi(\rho)] \cdot dV \tag{3.85}$$

Assuming that the conservative acceleration  $\mathbf{g}_{\text{cons}}$  is generated by the simplified potential linearized in the vicinity of the Earth's surface, we have:

$$\Phi(\rho^a) = \Phi(z) = g_z \cdot |z(t)| \tag{3.86}$$

and we can write Equation 3.85 as the sum of the contributions of the fluid which differs from equilibrium:

$$\begin{aligned}
 E_{\text{pot}}(z) &= \underbrace{\rho \cdot \int_{z'=0}^{z'=z_1(t)=z(t)} -g_z \cdot |z'| \cdot S_{\text{pot}} \cdot dz'}_{\text{pot 1}} + \underbrace{\rho \cdot \int_{z'=0}^{z'=z_2(t)=-z(t)} -g_z \cdot |z'| \cdot S_{\text{pot}} \cdot dz'}_{\text{pot 2}} \\
 &= -\frac{1}{2} \rho \cdot g_z \cdot S_{\text{pot}} \cdot z(t)^2 - \frac{1}{2} \rho \cdot g_z \cdot S_{\text{pot}} \cdot z(t)^2 \\
 &= -z(t)^2 \cdot \rho \cdot g_z \cdot S_{\text{pot}}
 \end{aligned} \tag{3.87}$$

Finally, introducing Equation 3.83 and 3.85 in Equation 3.82 gives the Lagrangian of the system:

$$\mathcal{L}(z, \dot{z}, t) = \dot{z}(t)^2 \cdot \left( \rho \cdot S_{\text{pot}} \cdot H + \frac{1}{2} \rho \cdot \frac{S_{\text{pot}}^2}{S_{\text{tube}}} \cdot L \right) + z(t)^2 \cdot \rho \cdot g_z \cdot S_{\text{pot}} \tag{3.88}$$

### Equation of Motion

From the Lagrangian function  $\mathcal{L}$ , it is possible to find directly the equation of motion using the *Euler-Lagrange* differential equation. This comes from the fundamental principle that a physical system, during a given time interval  $[t_0, t_1]$ , evolves always in order to produce an extremal *action*  $S(t_0, t_1)$ . The action is given by:

$$S(t_0, t_1) = \int_{t_0}^{t_1} \mathcal{L}(z, \dot{z}, t) \cdot dt \quad (3.89)$$

and the equation of motion is given when the action is extremal:

$$S(t_0, t_1) = \int_{t_0}^{t_1} \mathcal{L}(z, \dot{z}, t) \cdot dt \rightarrow \text{extremal} \quad (3.90)$$

or when:

$$\delta S(t_0, t_1) = \delta \int_{t_0}^{t_1} \mathcal{L}(z, \dot{z}, t) \cdot dt = 0 \quad (3.91)$$

where the solution is given by the Euler-Lagrange differential equation. In our case, we have:

$$\frac{d}{dt} \left[ \frac{\partial \mathcal{L}(z, \dot{z}, t)}{\partial \dot{z}} \right] - \frac{\partial \mathcal{L}(z, \dot{z}, t)}{\partial z} = 0 \quad (3.92)$$

Applied to Equation 3.88 this gives:

$$2 \left( \rho \cdot S_{\text{pot}} \cdot H + \frac{1}{2} \rho \cdot \frac{S_{\text{pot}}^2}{S_{\text{tube}}} \cdot L \right) \cdot \ddot{z}(t) - 2\rho \cdot g_z \cdot S_{\text{pot}} \cdot z(t) = 0 \quad (3.93)$$

which is the solution if the non-conservative forces are neglected. In the case that we have non-conservative forces  $f_z$  acting on the system, it can be proven that the equation of motion can be written as follows:

$$\frac{d}{dt} \left[ \frac{\partial \mathcal{L}(z, \dot{z}, t)}{\partial \dot{z}} \right] - \frac{\partial \mathcal{L}(z, \dot{z}, t)}{\partial z} = f_z \quad (3.94)$$

In our case, the force generated by the non-conservative acceleration  $\mathbf{a}_{\text{non-cons}}$  has only one horizontal component  $a_x(t)$ , which is acting on the fluid inside the tube of mass  $m_{\text{tube}}$ . This corresponds to an additional horizontal non-conservative force:

$$f_x = m_{\text{tube}} \cdot a_x(t) = \rho \cdot S_{\text{tube}} \cdot L \cdot a_x(t) \quad (3.95)$$

which can be transposed to a vertical force  $f_z$  if we again consider Equation 3.79 which implies the conservation of mass. The horizontal acceleration  $a_x(t) = \ddot{x}_{\text{tube}}$  inside the tube corresponds to a vertical acceleration  $-\frac{S_{\text{pot}}}{S_{\text{tube}}} \cdot \ddot{z}$  of the fluid inside pot 1 so that:

$$f_x \longrightarrow f_z = -\rho \cdot S_{\text{tube}} \cdot L \cdot \frac{S_{\text{tube}}}{S_{\text{pot}}} \cdot a_x(t) \quad (3.96)$$

and from Equations 3.88, 3.94 and 3.96 we have the final equation of motion:

$$2 \left( \rho \cdot S_{\text{pot}} \cdot H + \frac{1}{2} \rho \cdot \frac{S_{\text{pot}}^2}{S_{\text{tube}}} \cdot L \right) \cdot \ddot{z}(t) - 2\rho \cdot g_z \cdot S_{\text{pot}} \cdot z(t) = -\rho \cdot S_{\text{tube}} \cdot L \cdot \frac{S_{\text{tube}}}{S_{\text{pot}}} \cdot a_x(t) \quad (3.97)$$



which can be written in the form of a forced undamped harmonic oscillator:

$$\ddot{z}(t) + \omega_0^2 \cdot z(t) = k \cdot a_x(t) \quad (3.98)$$

with

$$\omega_0^2 = -\frac{2g_z}{2H + \frac{S_{\text{pot}}}{S_{\text{tube}}} \cdot L} \quad (3.99)$$

and

$$k = -\frac{S_{\text{tube}}^2 \cdot L}{S_{\text{pot}}^2 \cdot \left(2H + \frac{S_{\text{pot}}}{S_{\text{tube}}} \cdot L\right)} \quad (3.100)$$

where  $\omega_0$  is the resonance angular frequency and  $k \cdot a_x(t)$  the non-homogeneous forcing term.

### Transfer Function

From the ordinary linear differential Equation 3.98 and a set of initial conditions<sup>27</sup>, it is possible to predict the function  $z(t)$  and analyze the behavior of the system using different methods.

The classical way is to solve the differential equation analytically in the time domain in order to get an explicit function for  $z(t)$ . The direct time-domain resolution implies that the time-dependent forcing term  $a_x(t)$  is given explicitly. In the case where we do not want to analyze the response of the system to a specific forcing function but the response to an arbitrary function, it is more convenient to solve the system using the LTI system theory.

The LTI system theory is based on the properties of the *Laplace-transform*  $\mathcal{L}\{\}$  which gives the possibility to transform the linear differential equation into an algebraic equation. This transformed algebraic equation can be solved very easily and automatically produces a simple transfer function, which completely links the transformed input of the system to the transformed output of the system by a simple multiplication. This signifies that the behavior of the system can be completely characterized by the transfer function only. In addition, the transfer function gives the possibility to directly find the frequency and the phase response of the system.

The formal definition of the Laplace transform of a function  $f(t)$  is given by:

$$\mathcal{L}\{f(t)\} = F(s) = \int_0^\infty e^{-s \cdot t} \cdot f(t) \cdot dt \quad \text{with} \quad s = \sigma + i\omega \quad (3.101)$$

which has the following useful properties:

$$\begin{aligned} \mathcal{L}\{a \cdot f(t) + b \cdot g(t)\} &= a \cdot \mathcal{L}\{f(t)\} + b \cdot \mathcal{L}\{g(t)\} \\ \mathcal{L}\{\dot{f}(t)\} &= s \cdot \mathcal{L}\{f(t)\} - f(0) \end{aligned} \quad (3.102)$$

<sup>27</sup>in this case it is the initial water level  $z(t_0) = z_0$  and the initial velocity  $\dot{z}(t_0) = v_0$  at time  $t_0$

In our case, if we consider the non-conservative acceleration function  $a_x(t)$  as the input function of the system and the level of the fluid function  $z(t)$  as the output of the system, and if we assume in addition, that the initial conditions are  $z(t=0) = 0$  and  $\dot{z}(t=0) = 0$ , the Laplace transform of Equation 3.98 is:

$$\begin{aligned}\mathcal{L}\{\ddot{z}(t) + \omega_0^2 \cdot z(t)\} &= \mathcal{L}\{k \cdot a_x(t)\} \\ \mathcal{L}\{\ddot{z}(t)\} + \mathcal{L}\{\omega_0^2 \cdot z(t)\} &= \mathcal{L}\{k \cdot a_x(t)\} \\ s^2 \cdot \mathcal{L}\{z(t)\} + \omega_0^2 \cdot \mathcal{L}\{z(t)\} &= k \cdot \mathcal{L}\{a_x(t)\}\end{aligned}\tag{3.103}$$

which can be rewritten as:

$$\mathcal{L}\{z(t)\} = \frac{k}{s^2 + \omega_0^2} \cdot \mathcal{L}\{a_x(t)\}\tag{3.104}$$

or:

$$Z(s) = H(s) \cdot A_x(s)\tag{3.105}$$

where

$$H(s) = \frac{k}{s^2 + \omega_0^2}\tag{3.106}$$

is the transfer function of the system which links the Laplace-transform of the input  $A_x(s)$  to the Laplace transform of the output  $Z(s)$ . Moreover,  $H(s)$  is also equal to the Laplace transform of the impulse response function  $h(t)$  which represents the output of the system excited by a Dirac delta distribution  $\delta(t)$ .

### Amplitude and Phase Responses

From the transfer function  $H(s)$  given by Equation 3.106 it is easy to find the amplitude and the phase responses. When we set  $s = i\omega$ , the amplitude response  $A(\omega)$  is given by the module and the phase response  $\phi(\omega)$  by the argument of  $H(i\omega)$ . In our case we get:

$$H(i\omega) = \frac{k}{(i\omega)^2 + \omega_0^2} = \frac{k}{\omega_0^2 - \omega^2}\tag{3.107}$$

where the amplitude response is:

$$A(\omega) = |H(i\omega)| = \left| \frac{k}{\omega_0^2 - \omega^2} \right|\tag{3.108}$$

and the phase response is

$$\phi(\omega) = \arg\{H(i\omega)\} = \begin{cases} 0 & \text{if } 0 < \omega < \omega_0 \\ -\pi & \text{if } \omega_0 < \omega < +\infty \end{cases}\tag{3.109}$$

In Figure 3.8, the amplitude and phase responses of HLS of various length  $L = 1 \dots 100'000$  m can be seen. In this case, the equilibrium height is fixed to  $H = 0.05$  and the ratio between the section of the pot and the section of the tube is fixed to  $\frac{S_{\text{pot}}}{S_{\text{tube}}} = 4.0$ . The horizontal axis represents the period  $T$  of the horizontal acceleration forcing term  $a_x(t)$ . The period  $T$  [s] is related to the angular frequency  $\omega$   $\left[\frac{\text{rad}}{\text{s}}\right]$  by:

$$T = \frac{2\pi}{\omega} \quad (3.110)$$

If we look at the behavior of the amplitude response, we can see that the amplitude

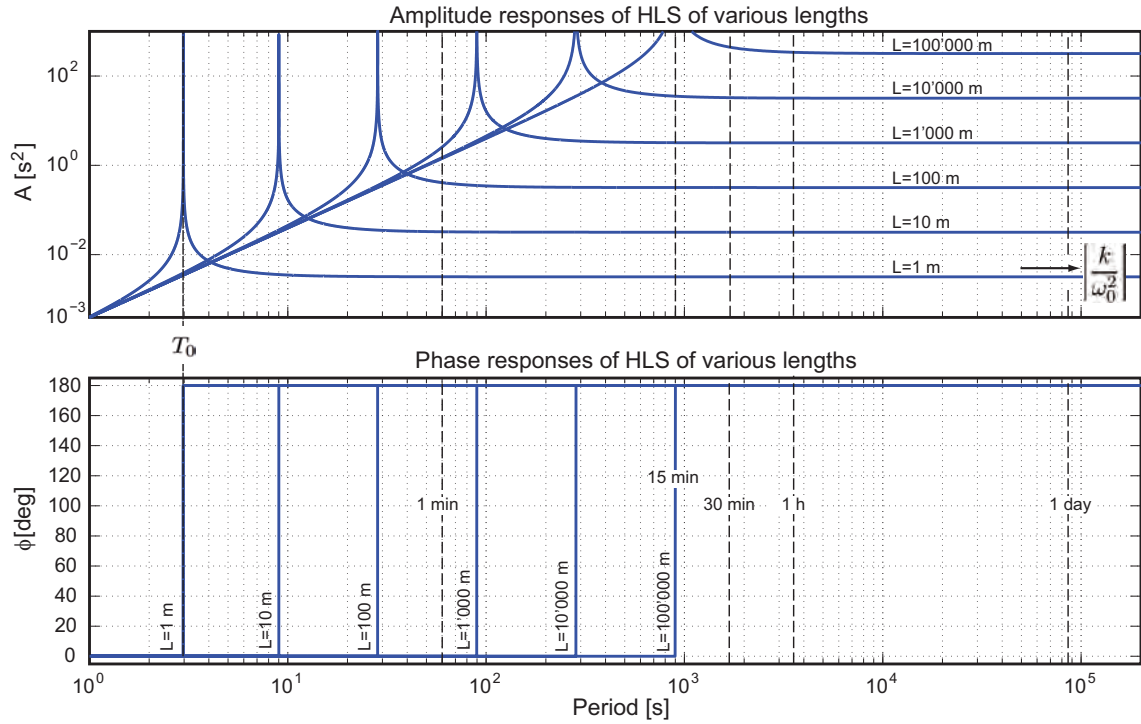


**Figure 3.8:** Amplitude (upper) and phase response (lower), in function of the period, for HLS of various length  $L$  according to Equations 3.108 and 3.109. The equilibrium height is fixed at  $H = 0.05$  m and the ratio between the section of the pot and the section of the tube is fixed at  $\frac{S_{\text{pot}}}{S_{\text{tube}}} = 4.0$ .

response converges to a well defined value when the angular frequency approaches zero ( $\omega \rightarrow 0$ ) — or when the period approaches infinity ( $T \rightarrow \infty$ ). According to Equation 3.108 this amplitude is given by:

$$A_{\text{lim}} = \lim_{\omega \rightarrow 0} A(\omega) = \left| \frac{k}{\omega_0^2} \right| = \lim_{T \rightarrow \infty} A(T) = \left| \frac{k \cdot T_0^2}{4\pi^2} \right| \quad (3.111)$$

On the opposite side, when the angular frequency approaches infinity ( $\omega \rightarrow \infty$ ) — or when the period approaches zero ( $T \rightarrow 0$ ) — we see that the amplitude response decreases rapidly toward 0. In between, the amplitude response increases to infinity when the angular frequency  $\omega$  approaches the resonance frequency  $\omega_0$  — or when the period  $T$

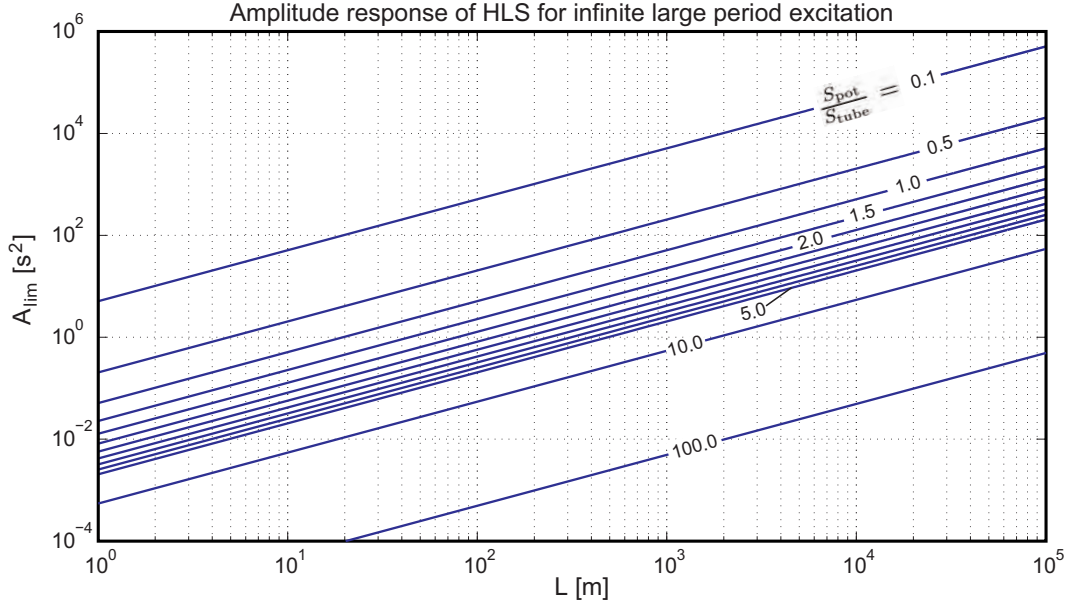


**Figure 3.9:** Long period amplitude response  $A_{\text{lim}}$ , according to Equations 3.111, of HLS of various lengths  $L$  and various ratios between the section of the pot and the section of the tube  $\frac{S_{\text{pot}}}{S_{\text{tube}}}$ .

approaches the resonance period  $T_0$ . From these observations, it is possible to define three main regions which summarize the response of the HLS, see table 3.2.

1. The region  $\mathcal{R}_1 = [0; T_1]$ , where the input signal  $a_x(t)$  can be considered to be filtered out.
2. The region  $\mathcal{R}_2 = [T_1; T_2]$ , where the input signal  $a_x(t)$  is amplified due to resonance phenomena.
3. The region  $\mathcal{R}_3 = [T_2; \infty[$ , where the input signal  $a_x(t)$  is transmitted without amplification due to resonance.

The periods  $T_1$  and  $T_2$  are defined as follows:

- $T_1$  is the period, for which the amplitude response is equal to one percent of the amplitude response at very large periods. From Equations 3.111 and 3.108, we can compute the corresponding angular frequency  $\omega_1$  as follows:

$$\omega_1 = \sqrt{101} \cdot \omega_0 \quad (3.112)$$

and using Equation 3.110:

$$T_1 = \frac{T_0}{\sqrt{101}} \quad (3.113)$$

- $T_2$  is the period, for which the amplitude response is equal to hundred-one percent of the amplitude response at very large period. From Equations 3.111 and 3.108, we can compute the corresponding angular frequency  $\omega_2$  as follows:

$$\omega_2 = \sqrt{0.01} \cdot \omega_0 \quad (3.114)$$

and using Equation 3.110:

$$T_2 = \frac{T_0}{\sqrt{0.01}} \quad (3.115)$$

**Table 3.2:** Long period amplitude response  $A_{\text{lim}}$ , resonance period  $T_0$ , largest period  $T_1$  which is assumed to be absorbed by the HLS and smallest period  $T_2$  which is assumed to be transmitted without resonance amplification for various HLS of length  $L$  and cross-section ratio  $\frac{S_{\text{pot}}}{S_{\text{tube}}}$ .

L	$\frac{S_{\text{pot}}}{S_{\text{tube}}}$	$A_{\text{lim}}$	$T_0$	$T_1$	$T_2$
[m]	[-]	[s <sup>2</sup> ]	[hh:mm:ss.s]	[hh:mm:ss.s]	[hh:mm:ss.s]
1	0.1	$5.1 \cdot 10^{+0}$	00:00:01.0	00:00:00.1	00:00:10.0
	1.0	$5.1 \cdot 10^{-2}$	00:00:01.7	00:00:00.2	00:00:16.8
	4.0	$3.2 \cdot 10^{-3}$	00:00:03.0	00:00:00.3	00:00:29.8
	10.0	$5.1 \cdot 10^{-4}$	00:00:04.6	00:00:00.4	00:00:45.7
	100.0	$5.1 \cdot 10^{-6}$	00:00:14.2	00:00:01.4	00:02:22.1
	1000.0	$5.1 \cdot 10^{-8}$	00:00:44.9	00:00:04.4	00:07:28.7
10	0.1	$5.1 \cdot 10^{+1}$	00:00:01.7	00:00:00.2	00:00:16.8
	1.0	$5.1 \cdot 10^{-1}$	00:00:04.6	00:00:00.5	00:00:45.7
	4.0	$3.2 \cdot 10^{-2}$	00:00:09.0	00:00:00.9	00:01:30.1
	10.0	$5.1 \cdot 10^{-3}$	00:00:14.2	00:00:01.4	00:02:22.1
	100.0	$5.1 \cdot 10^{-5}$	00:00:44.9	00:00:04.5	00:07:28.7
	1000.0	$5.1 \cdot 10^{-7}$	00:02:21.9	00:00:14.1	00:23:38.5
100	0.1	$5.1 \cdot 10^{+2}$	00:00:04.6	00:00:00.5	00:00:45.7
	1.0	$5.1 \cdot 10^{+0}$	00:00:14.2	00:00:01.4	00:02:22.1
	4.0	$3.2 \cdot 10^{-1}$	00:00:28.4	00:00:02.8	00:04:43.8
	10.0	$5.1 \cdot 10^{-2}$	00:00:44.9	00:00:04.5	00:07:28.7
	100.0	$5.1 \cdot 10^{-4}$	00:02:21.9	00:00:14.1	00:23:38.5
	1000.0	$5.1 \cdot 10^{-6}$	00:07:28.6	00:00:44.6	01:14:45.7
1000	0.1	$5.1 \cdot 10^{+3}$	00:00:14.2	00:00:01.4	00:02:22.1
	1.0	$5.1 \cdot 10^{+1}$	00:00:44.9	00:00:04.5	00:07:28.7
	4.0	$3.2 \cdot 10^{+0}$	00:01:29.7	00:00:08.9	00:14:57.2
	10.0	$5.1 \cdot 10^{-1}$	00:02:21.9	00:00:14.1	00:23:38.5
	100.0	$5.1 \cdot 10^{-3}$	00:07:28.6	00:00:44.6	01:14:45.7
	1000.0	$5.1 \cdot 10^{-5}$	00:23:38.5	00:02:21.1	03:56:25.0
10000	0.1	$5.1 \cdot 10^{+4}$	00:00:44.9	00:00:04.5	00:07:28.7
	1.0	$5.1 \cdot 10^{+2}$	00:02:21.9	00:00:14.1	00:23:38.5
	4.0	$3.2 \cdot 10^{+1}$	00:04:43.7	00:00:28.2	00:47:17.0
	10.0	$5.1 \cdot 10^{+0}$	00:07:28.6	00:00:44.6	01:14:45.7
	100.0	$5.1 \cdot 10^{-2}$	00:23:38.5	00:02:21.1	03:56:25.0
	1000.0	$5.1 \cdot 10^{-4}$	01:14:45.7	00:07:26.3	12:27:37.0
100000	0.1	$5.1 \cdot 10^{+5}$	00:02:21.9	00:00:14.1	00:23:38.5
	1.0	$5.1 \cdot 10^{+3}$	00:07:28.6	00:00:44.6	01:14:45.7
	4.0	$3.2 \cdot 10^{+2}$	00:14:57.1	00:01:29.3	02:29:31.4
	10.0	$5.1 \cdot 10^{+1}$	00:23:38.5	00:02:21.1	03:56:25.0
	100.0	$5.1 \cdot 10^{-1}$	01:14:45.7	00:07:26.3	12:27:37.0
	1000.0	$5.1 \cdot 10^{-3}$	03:56:25.0	00:23:31.5	39:24:10.3

### 3.6.4 Hydrostatic Solution

In the case where we assume that the the velocity of all particles in the fluid are at rest  $\mathbf{v} = \dot{\boldsymbol{\rho}} = \mathbf{0}$ , we can prove that the locus of the fluid-gaz interface  $\boldsymbol{\rho}_{\sim}$  can be found in a very elegant and powerful way. From the first Navier-Stokes equation 3.69 we get:

$$\mathbf{0} = -\frac{1}{\rho} \cdot \nabla p + \mathbf{g}_{\text{stat}} \quad (3.116)$$

or

$$\frac{1}{\rho} \cdot \nabla p = \mathbf{g}_{\text{stat}} \quad (3.117)$$

with

$$\begin{aligned} \mathbf{g}_{\text{stat}} &= \mathbf{g}_{\text{dyn}} - \mathbf{g}_{\text{Coriolis}} \\ &= \mathbf{g} + \mathbf{g}_{\text{tidal}} + \mathbf{g}_{\text{Eulerian}} \end{aligned} \quad (3.118)$$

which represents the gravity acceleration vector for a particle at rest in the Earth fixed system,  $\dot{\boldsymbol{\rho}} = \mathbf{0} \rightarrow \mathbf{g}_{\text{Coriolis}} = \mathbf{0}$ .

Moreover, if we look at Equation 3.117, we can see that it can only be valid if the gravity acceleration field  $\mathbf{g}_{\text{stat}}$  is the gradient of a scalar potential function  $\Phi_{\text{stat}}$ :

$$\mathbf{g}_{\text{stat}} = \nabla \Phi_{\text{stat}} \quad (3.119)$$

If this is the case, combining Equations 3.117 and 3.119 gives the usual form of hydrostatic equilibrium:

$$\frac{1}{\rho} \cdot \nabla p = \nabla \Phi_{\text{stat}} \quad (3.120)$$

in addition, if we assume that the density of the fluid  $\rho$  is not homogeneous, we get the general form of the hydrostatic equation:

$$\nabla p(\boldsymbol{\rho}) = \rho(\boldsymbol{\rho}) \cdot \nabla \Phi_{\text{stat}}(\boldsymbol{\rho}) \quad (3.121)$$

#### Consequences of Hydrostatic Equilibrium

From Equation 3.121 it is possible to see very interesting properties of fluids in hydrostatic equilibrium.

The first consequence comes from a property of potential fields which tells that the gradient of a potential field is irrotational, see Equation 3.67. This means that the gravity field  $\mathbf{g}_{\text{stat}}$  must be irrotational (*Gallavotti, 2002*):

$$\nabla \times \mathbf{g}_{\text{stat}} = \mathbf{0} \quad (3.122)$$

The second consequence is that the surfaces of equal pressure, *isobars*,  $\mathcal{S}_p \equiv p(\boldsymbol{\rho}) = \text{const}$  are parallel to the surfaces of identical potential, *equipotential*,  $\mathcal{S}_{\Phi} \equiv \Phi_{\text{stat}}(\boldsymbol{\rho}) = \text{const}$ :

$$\mathcal{S}_p \parallel \mathcal{S}_{\Phi} \quad (3.123)$$

This can be proved when we first observe that the gradient of the pressure  $\nabla p(\boldsymbol{\rho})$  and the gradient of the potential  $\nabla \Phi_{\text{stat}}(\boldsymbol{\rho})$  are always parallel because they differ only by a scaling factor represented by the density field  $\rho(\boldsymbol{\rho})$  and, secondly, from the property of gradient fields which tells that the level set of a differentiable scalar function is always orthogonal to its gradient field.

The third consequence is that surfaces of constant density, *isopycnics*,  $\mathcal{S}_\rho \equiv \rho(\boldsymbol{\rho}) = \text{const}$  are parallel to equipotentials  $\mathcal{S}_\Phi$  and isobars  $\mathcal{S}_p$ :

$$\mathcal{S}_\rho \parallel \mathcal{S}_\Phi \parallel \mathcal{S}_p \quad (3.124)$$

This can be proved if we take the curl of Equation 3.121 (*Lautrup, 2005*):

$$\begin{aligned} \nabla \times \nabla p(\boldsymbol{\rho}) &= \nabla \times [\rho(\boldsymbol{\rho}) \cdot \nabla \Phi_{\text{stat}}(\boldsymbol{\rho})] \\ \mathbf{0} &= \rho(\boldsymbol{\rho}) \cdot \underbrace{\nabla \times \Phi_{\text{stat}}(\boldsymbol{\rho})}_{=0} + \nabla \rho(\boldsymbol{\rho}) \times \nabla \Phi_{\text{stat}}(\boldsymbol{\rho}) \\ \mathbf{0} &= \nabla \rho(\boldsymbol{\rho}) \times \nabla \Phi_{\text{stat}}(\boldsymbol{\rho}) \end{aligned} \quad (3.125)$$

which shows that the vector product between the gradient of the density field  $\nabla \rho(\boldsymbol{\rho})$  and the gradient of the potential field  $\nabla \Phi_{\text{stat}}(\boldsymbol{\rho})$  is equal to  $\mathbf{0}$ , if both fields are parallel, or equivalently, if their level sets coincide.

### Geometry of Hydrostatic Liquid-Gas Interface

If we look at physical systems formed by liquids and gazes, the hydrostatic equilibrium is only achieved when both, the liquids and the gazes fulfill the hydrostatic Equation 3.121. In this case, the geometry of the liquid-gas interface  $\boldsymbol{\rho}_\sim$  is equivalently given by the geometry of the isopycnic surface  $\mathcal{S}_{\rho_\sim}$ , the isobar surface  $\mathcal{S}_{p_\sim}$  or the equipotential surface  $\mathcal{S}_{\Phi_\sim}$  passing through a limit point where the density is jumping from the density of the liquid to the density of the gas.

In this very special case, we see that the geometry of the interface can be completely determined by the knowledge of the potential  $\Phi_{\text{stat}}$ . In addition, the hydrostatic case benefits from another very nice property: the solution does not depend on the geometry of the boundaries.

## 3.7 Apparent Gravity Potential in the Earth Fixed Reference System

In Section 3.6.4 we saw that the hydrostatic equilibrium solution is very attractive for the determination of the shape of liquid-air interfaces. However, the equilibrium can only be achieved when the gravity field  $\mathbf{g}_{\text{stat}}$  can be derived from a potential function  $\Phi_{\text{stat}}$ . Using Equation 3.67, it is possible to check if a vector field can be derived from a scalar potential just by looking whether it is irrotational or not. In our case, if we do that by

applying the curl operator on each element of Equation 3.118, we can prove that all terms are irrotational except the Eulerian acceleration  $\mathbf{g}_{\text{Eulerian}}$ . Formally, we have:

$$\begin{aligned}\nabla \times \mathbf{g}_{\text{grav},\delta} &= 0 \\ \nabla \times \mathbf{g}_{\text{centr}} &= 0 \\ \nabla \times \mathbf{g}_{\text{tidal}} &= 0 \\ \nabla \times \mathbf{g}_{\text{Eulerian}} &= -2 \cdot \dot{\boldsymbol{\omega}}_{ia}^a\end{aligned}\tag{3.126}$$

This has several theoretical consequences. If the rotation vector  $\boldsymbol{\omega}_{ia}^a$  is subject to time variation, the Eulerian acceleration  $\mathbf{g}_{\text{Eulerian}}$  is non-zero which implies that:

- We can find a potential function neither for the Eulerian acceleration  $\mathbf{g}_{\text{Eulerian}}$  nor, by consequences, for the apparent gravity field  $\mathbf{g}_{\text{stat}}$ .
- The hydrostatic equilibrium can never be achieved — no hydrostatic solution exists — the liquid is forced to be in motion (*Gallavotti, 2002*).
- The geometry of the liquid-air interface must be computed using the Navier-Stokes equations or a partially integrated version. This implies that the solution depends also on the geometry of the boundary conditions. The behavior is not the same for an ocean, a lake or hydrostatic measurement systems connected with pipes of various dimensions.
- The geometry of the liquid-air interface cannot be derived directly and easily from an equipotential surface of the apparent gravity potential field.

In our model, the rotation vector  $\boldsymbol{\omega}_{ia}^a$  is equal to the Earth's rotation vector  $\boldsymbol{\omega}_\delta$  which is subject to very complicated variations in time, like precession, nutation and polar motion, see Appendix B. Thus, it is important to see what is the order of magnitude and the behavior of the Eulerian acceleration in order to be able to anticipate its effects on the geometry of a liquid-air interface, on a HLS in our case.

### 3.7.1 Numerical Computation of the Eulerian Acceleration

In order to have a better idea of the real effect of the Eulerian acceleration on the Earth, a time series of the time derivative  $\dot{\boldsymbol{\omega}}_{ia}^a \equiv \dot{\boldsymbol{\omega}}_\delta^{\text{ITRS}}$  of the Earth's rotation vector, for 1-hour intervals between 1980 and 2013 is computed, see Figure 3.10. The computations are based on the libraries *NOVAS-C* (*Kaplan et al., 2009*) and on the Earth orientation parameter (EOP) time series EOP 08 C04 (IAU1980) provided by the International Earth Rotation and Reference Systems Service (IERS) data center. Moreover, in order to take into account the diurnal and sub-diurnal terms which model the effects of ocean tides and libration on the Earth's rotation vector, the routine *INTERP.f* of the IERS data center is used.

The time derivative  $\dot{\boldsymbol{\omega}}_\delta^{\text{ITRS}}$  of the Earth's rotation vector is computed in two steps, see Appendix B for the details.



1. The time-derivative  $\dot{\omega}_{ia}^i \equiv \dot{\omega}_{\delta}^{\text{ICRS}} \equiv \dot{\omega}_{\delta}^{\text{GCRS}}$  of the Earth's rotation vector in the inertial system is computed numerically from the time series of  $\omega_{\delta}^{\text{GCRS}}$ .

$$\dot{\omega}_{\delta}^{\text{GCRS}}(t_i) \cong \frac{\omega_{\delta}^{\text{GCRS}}(t_{i+1}) - \omega_{\delta}^{\text{GCRS}}(t_i)}{t_{i+1} - t_i} \quad (3.127)$$

where:

$$\begin{aligned} \dot{\omega}_{\delta}^{\text{GCRS}} \left[ \frac{\text{rad}}{\text{s}^2} \right] &= \text{time derivative of the Earth's rotation vector in the geocentric celestial reference system.} \\ \omega_{\delta}^{\text{GCRS}} \left[ \frac{\text{rad}}{\text{s}} \right] &= \text{Earth's rotation vector in the geocentric celestial reference system.} \end{aligned}$$

2.  $\dot{\omega}_{\delta}^{\text{ITRS}}$  is finally computed by transforming  $\dot{\omega}_{\delta}^{\text{GCRS}}$  into the ITRS system with the rotation matrix  $\mathbf{S}_{\text{GCRS}}^{\text{ITRS}}$ .

$$\dot{\omega}_{\delta}^{\text{ITRS}}(t_i) \cong \mathbf{S}_{\text{GCRS}}^{\text{ITRS}}(t_i) \cdot \dot{\omega}_{\delta}^{\text{GCRS}}(t_i) \quad (3.128)$$

where:

$$\begin{aligned} \dot{\omega}_{\delta}^{\text{ITRS}} \left[ \frac{\text{rad}}{\text{s}^2} \right] &= \text{time derivative of the Earth's rotation vector in the terrestrial reference system.} \\ \dot{\omega}_{\delta}^{\text{GCRS}} \left[ \frac{\text{rad}}{\text{s}^2} \right] &= \text{time derivative of the Earth's rotation vector in the geocentric celestial reference system.} \\ \mathbf{S}_{\text{GCRS}}^{\text{ITRS}} &= \text{Transformation matrix from GCRS to ITRS.} \end{aligned}$$

As we can see in Figure 3.10, the vector  $\dot{\omega}_{\delta}^{\text{ITRS}}$  is practically parallel to the equatorial plane and the order of magnitude of the  $x$ - and  $y$ -component is five times larger than the  $z$ -component. According to Equation 3.56, the Eulerian acceleration  $\mathbf{g}_{\text{Eulerian}}^{\text{ITRS}}$  can be computed by:

$$\begin{aligned} \mathbf{g}_{\text{Eulerian}}^{\text{ITRS}} &= -\dot{\boldsymbol{\Omega}}_{\delta}^{\text{ITRS}} \cdot \boldsymbol{\rho}^{\text{ITRS}} \\ &= - \begin{pmatrix} 0 & -\dot{\omega}_{\delta z}^{\text{ITRS}} & +\dot{\omega}_{\delta y}^{\text{ITRS}} \\ +\dot{\omega}_{\delta z}^{\text{ITRS}} & 0 & -\dot{\omega}_{\delta x}^{\text{ITRS}} \\ -\dot{\omega}_{\delta y}^{\text{ITRS}} & +\dot{\omega}_{\delta x}^{\text{ITRS}} & 0 \end{pmatrix} \cdot \begin{pmatrix} \rho_x^{\text{ITRS}} \\ \rho_y^{\text{ITRS}} \\ \rho_z^{\text{ITRS}} \end{pmatrix} \end{aligned} \quad (3.129)$$

where:

$$\begin{aligned} \mathbf{g}_{\text{Eulerian}}^{\text{ITRS}} \left[ \frac{\text{m}}{\text{s}^2} \right] &= \text{Euler acceleration vector in the terrestrial reference system.} \\ \dot{\boldsymbol{\Omega}}_{\delta}^{\text{ITRS}} \left[ \frac{\text{rad}}{\text{s}^2} \right] &= \text{time derivative of the Earth's rotation skew-symmetric matrix in the terrestrial reference system.} \\ \boldsymbol{\rho}^{\text{ITRS}} [\text{m}] &= \text{Position vector in the terrestrial reference system.} \end{aligned}$$

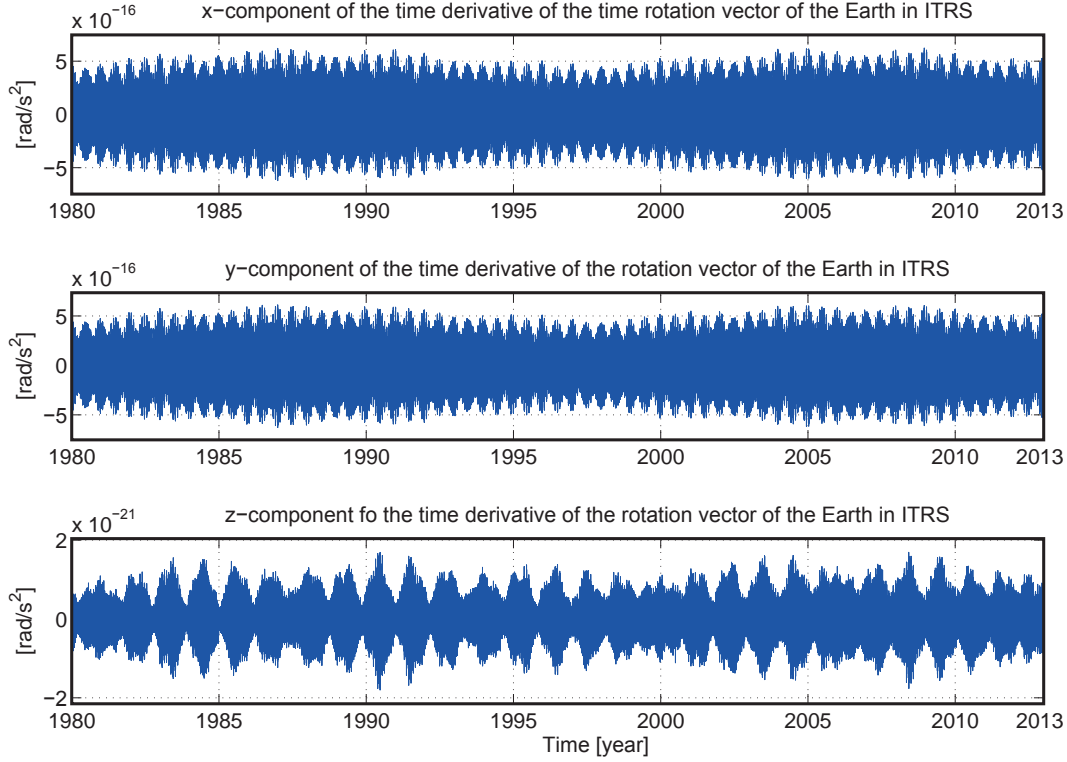


**Figure 3.10:** Time series of the x-y and z-component of  $\dot{\omega}_{\delta}^{\text{ITRS}}$  the time derivative Earth's rotation vector based on the libraries NOVAS-C (*Kaplan et al.*, 2009), the routine INTERP.f of the IERS data center and on the Earth orientation parameter time series EOP 08 C04 (IAU1980).

which can be transformed into the topocentric system by:

$$\mathbf{g}_{\text{Eulerian}}^{\text{Topo}} = \mathbf{T}_{\text{ITRS}}^{\text{Topo}}(\boldsymbol{\rho}^{\text{ITRS}}) \cdot \mathbf{g}_{\text{Eulerian}}^{\text{ITRS}} \quad (3.130)$$

where:

$\mathbf{g}_{\text{Eulerian}}^{\text{Topo}} \quad \left[ \frac{\text{m}}{\text{s}^2} \right] =$  Euler acceleration vector in the topocentric reference system.

$\mathbf{g}_{\text{Eulerian}}^{\text{ITRS}} \quad \left[ \frac{\text{m}}{\text{s}^2} \right] =$  Euler acceleration vector in the terrestrial reference system.

$\mathbf{T}_{\text{ITRS}}^{\text{Topo}} =$  Transformation matrix from ITRS to the topocentric system.

$\boldsymbol{\rho}^{\text{ITRS}} \quad [\text{m}] =$  Position vector in the terrestrial reference system.

A trivial property<sup>28</sup> of the vector field resulting from Equations 3.129 and 3.130 is that the Eulerian acceleration is always perpendicular to  $\boldsymbol{\rho}^{\text{ITRS}}$  or equivalently, is always contained in the local topocentric horizontal plane<sup>29</sup>. This means that the Eulerian acceleration

<sup>28</sup>property of the vector product.

<sup>29</sup>if we consider that the deflection of the vertical can be neglected in this case.

cannot be observed by a gravimeter. Theoretically, only instruments which are sensitive to lateral accelerations allows the observation of this acceleration.

The numerical values of the norm of the Eulerian acceleration for position vectors all over the world between 1980 and 2003 are very small and never exceed  $5 \cdot 10^{-9} \frac{\text{m}}{\text{s}^2}$ , see Figure 3.11, and show that the dominant periods are given around one day. They are identical to the dominant periods of  $\dot{\omega}_{\delta}^{\text{ITRS}}$ , see Figure B.7.

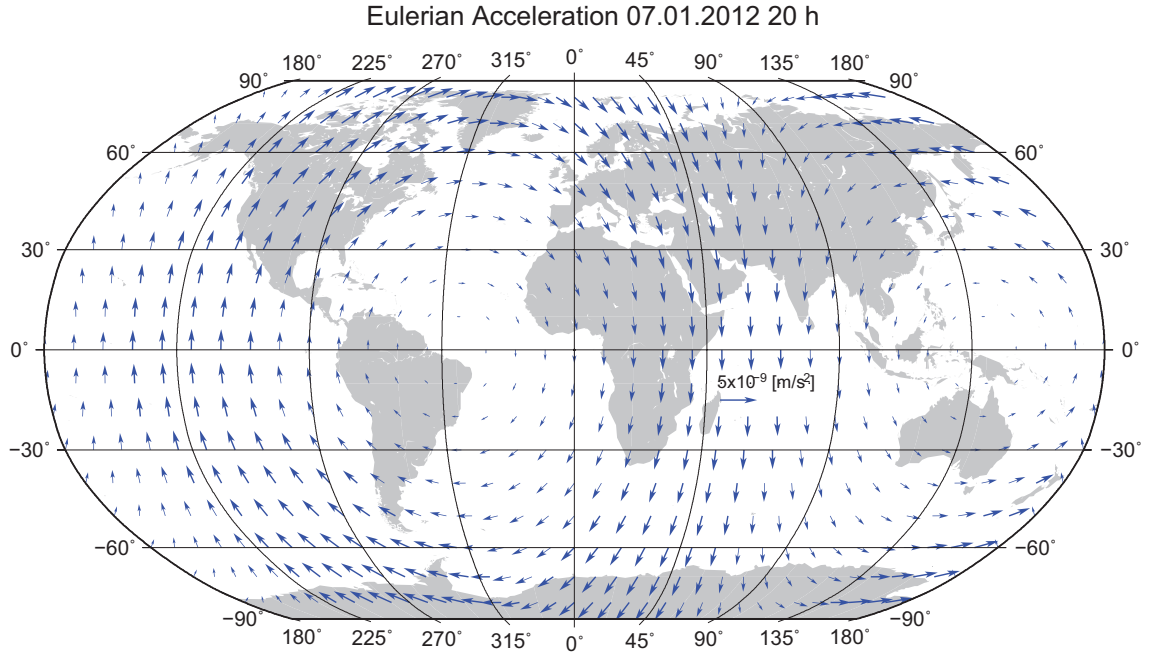


**Figure 3.11:** Eulerian acceleration on the Earth's surface due to the time variation of the Earth's rotation vector on 07.01.2012 at 20:00 UTC.

### Eulerian Acceleration and Response of HLS along the CLIC Profile

When we look at the Eulerian acceleration in the region of Geneva and especially the horizontal component projected onto the profile of CLIC, it is possible to estimate the response of a HLS according to the Eulerian acceleration.

The time series of the Eulerian acceleration projected onto the profile of CLIC from 1980 to 2013 together with its amplitude spectrum are shown in Figure 3.12 and confirm the order of magnitude of the effect and the dominant periods, see Table 3.3. We can see three remarkable groups of periods. Around one day, we have the Oppolzer periods which have an order of magnitude of  $10^{-9} \frac{\text{m}}{\text{s}^2}$ . The second dominant group has periods larger than one year, which are related to polar motion, have order of magnitude of  $10^{-11} \frac{\text{m}}{\text{s}^2}$ . The last group contains sub-daily polar motion effects around 0.5 days with an order of magnitude of  $10^{-12} \frac{\text{m}}{\text{s}^2}$ .

We now want to look at the variation of the water level in a HLS due to the Eulerian

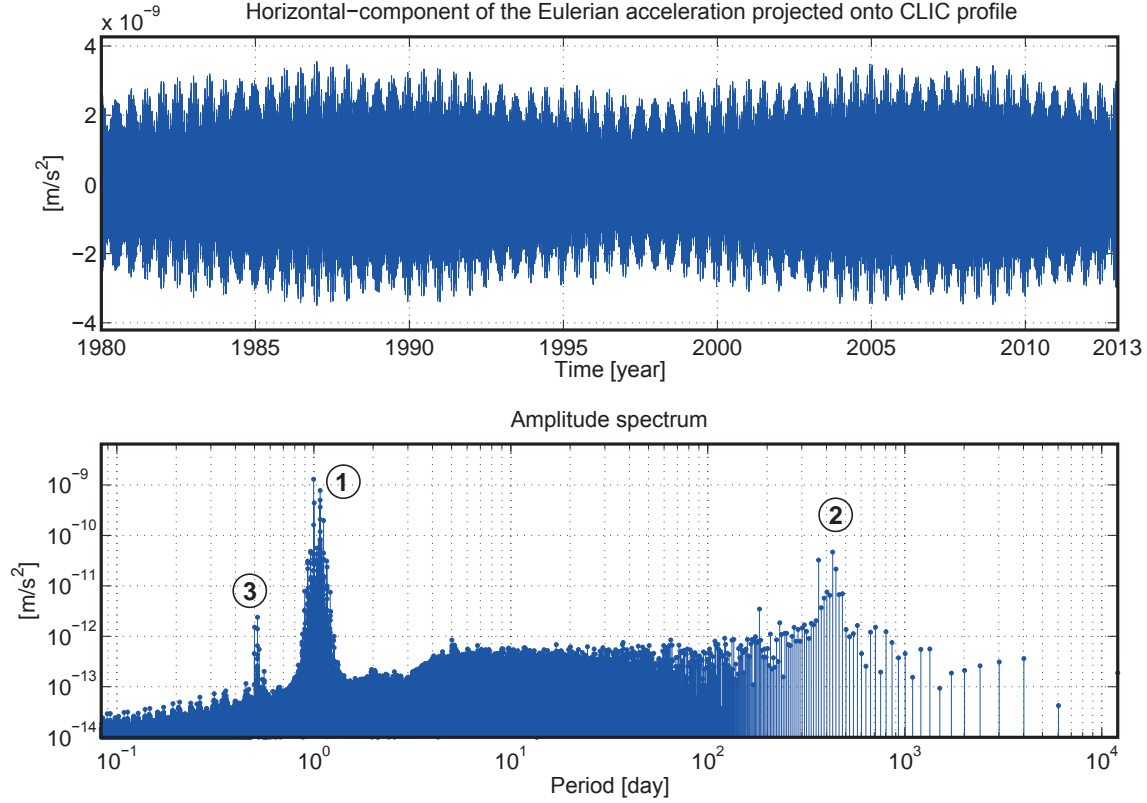


**Figure 3.12:** Time series (upper) and amplitude spectrum (lower) of the Eulerian acceleration from 1980 to 2013 based on the libraries NOVAS-C (*Kaplan et al.*, 2009), the routine INTERP.f of the IERS data center and on the Earth orientation parameter time series EOP 08 C04 (IAU1980).

**Table 3.3:** List of the main periods of the components of the Eulerian acceleration projected on the profile of CLIC.

Rank	Period	Amplitude
[-]	[day]	$\left[\frac{\text{m}}{\text{s}^2}\right]$
1	0.99726	$1.292 \cdot 10^{-9}$
2	1.07576	$7.755 \cdot 10^{-10}$
3	1.07585	$4.993 \cdot 10^{-10}$
4	1.00274	$4.390 \cdot 10^{-10}$
18	430.497	$4.678 \cdot 10^{-11}$
32	365.270	$3.229 \cdot 10^{-11}$
51	446.441	$2.162 \cdot 10^{-11}$
384	0.51751	$2.382 \cdot 10^{-12}$

acceleration. To do this, we use the simplified HLS model, exposed in Section 3.6.3, leading a forced harmonic oscillator. The general solution of the response of the system excited by an arbitrary time series requires the computation of the convolution between the transfer function, Equation 3.106, and the time series of the Eulerian acceleration. In our case, it is not necessary to do this complicated computation. In fact, when we look at

the spectrum of the transfer function and the spectrum of the Eulerian acceleration, we can see that all significant signals have periods which are contained in the region  $\mathcal{R}_3$ , see Table 3.2, where no resonance effects can be seen. In this case, the response can simply be computed by the multiplication of the times series of the Eulerian acceleration with the amplitude response limit  $A_{\text{lim}}$  given in Equation 3.111:

$$z(t) = A_{\text{lim}} \cdot g_{\text{Eulerian}}^{\text{CLIC}} \quad (3.131)$$

where  $g_{\text{Eulerian}}^{\text{CLIC}}$  represents the horizontal component of the Eulerian acceleration projected onto the profile of CLIC. In Figure 3.13 we can see a version of Figure 3.9 which is complemented by the amplitude of the water level change due to an Eulerian acceleration of  $5 \cdot 10^{-9} \frac{\text{m}}{\text{s}^2}$ .

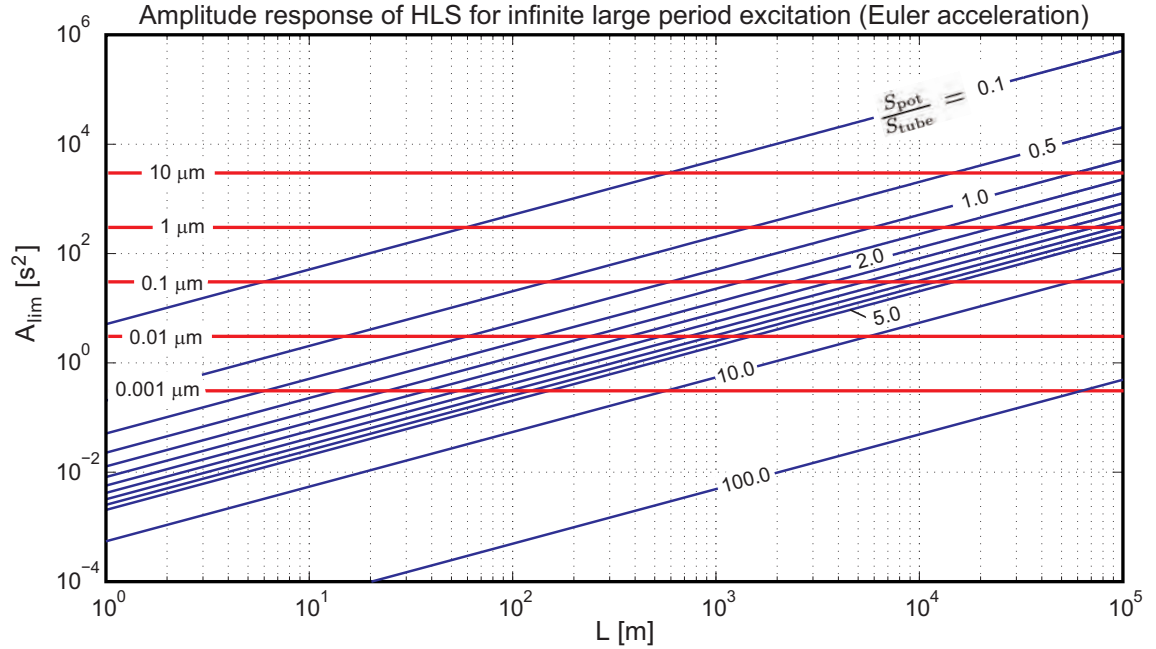


**Figure 3.13:** Long period amplitude response  $A_{\text{lim}}$ , according to Equations 3.111, of a HLS systems of various lengths  $L$  and various ratios between the section of the pot and the section of the tube  $\frac{S_{\text{pot}}}{S_{\text{tube}}}$ . In red, the amplitude produced by the Eulerian acceleration due to the time variation of the Earth's rotation vector is shown.

### Concluding Remarks

Despite the fact that the order of magnitude of the Eulerian acceleration is known to be very small with respect to the other components contributing to gravity, it was interesting to compute a realistic time series applied to a simple physical model of the HLS in order to predict quantitatively up to which order of approximation we can consider the hydrostatic modelization as acceptable. In the case of an alignment system for the CLIC based on overlapping HLS systems of approximately 200 meters in length, we can definitively assume that the Eulerian acceleration is a negligible term. As we can see in Figure 3.13, the effects

are significantly below 1 micron for all  $\frac{S_{\text{pot}}}{S_{\text{tube}}}$  ratios, except for the rather unrealistic ratio of  $\frac{S_{\text{pot}}}{S_{\text{tube}}} = 0.1$ .

### 3.7.2 Earth's Gravitational Potential

The Earth's gravitational potential function  $\Phi_{\text{grav},\delta}$  is defined so that:

$$\nabla \Phi_{\text{grav},\delta} = \mathbf{g}_{\text{grav},\delta} \quad (3.132)$$

and is given by:

$$\Phi_{\text{grav},\delta}(\boldsymbol{\rho}, t) = +G \cdot \iiint_{\delta} \frac{1}{|\boldsymbol{\rho} - \boldsymbol{\rho}'|} \cdot \rho(\boldsymbol{\rho}', t) \cdot dV \quad (3.133)$$

where the potential vanishes when the position  $\boldsymbol{\rho}$  tends to infinity:

$$\Phi_{\text{grav},\delta}(\boldsymbol{\rho} \rightarrow \infty, t) = 0 \quad (3.134)$$

### 3.7.3 Centrifugal Potential

The centrifugal potential function  $\Phi_{\text{centr}}$  is defined so that:

$$\nabla \Phi_{\text{centr}} = \mathbf{g}_{\text{centr}} \quad (3.135)$$

and is given by:

$$\Phi_{\text{centr}}(\boldsymbol{\rho}, t) = +\frac{1}{2} \cdot \left\{ |\boldsymbol{\omega}_{ia}^a(t)|^2 \cdot |\boldsymbol{\rho}|^2 - (\boldsymbol{\rho} \cdot \boldsymbol{\omega}_{ia}^a(t))^2 \right\} \quad (3.136)$$

where the potential vanishes when the position  $\boldsymbol{\rho}$  is on the rotation axis  $\boldsymbol{\omega}(t)$ .

### 3.7.4 Tidal Potential

The tidal potential function  $\Phi_{\text{tidal}}$  is defined so that:

$$\nabla \Phi_{\text{tidal}} = \mathbf{g}_{\text{tidal}} \quad (3.137)$$

and is given by:

$$\begin{aligned} \Phi_{\text{tidal}}(\boldsymbol{\rho}, t) = & +GM_{\odot} \cdot \left\{ \frac{1}{|\boldsymbol{\rho}_{\odot}(t) - \boldsymbol{\rho}|} - \frac{\boldsymbol{\rho}_{\odot}(t) \cdot \boldsymbol{\rho}}{|\boldsymbol{\rho}_{\odot}(t)|^3} - \frac{1}{|\boldsymbol{\rho}_{\odot}(t)|} \right\} \\ & + GM_{\zeta} \cdot \left\{ \frac{1}{|\boldsymbol{\rho}_{\zeta}(t) - \boldsymbol{\rho}|} - \frac{\boldsymbol{\rho}_{\zeta}(t) \cdot \boldsymbol{\rho}}{|\boldsymbol{\rho}_{\zeta}(t)|^3} - \frac{1}{|\boldsymbol{\rho}_{\zeta}(t)|} \right\} \end{aligned} \quad (3.138)$$

where the terms in Equation 3.138

$$-\frac{1}{|\boldsymbol{\rho}_{\odot}(t)|} \quad \text{and} \quad -\frac{1}{|\boldsymbol{\rho}_{\zeta}(t)|} \quad (3.139)$$

are just integrating constants which make the potential vanish when the position  $\boldsymbol{\rho}$  is at the geocenter  $\mathcal{G}$  (Wenzel, 1997):

$$\Phi_{\text{tidal}}(\boldsymbol{\rho} \equiv \mathcal{G} \equiv \mathbf{0}, t) = 0 \quad (3.140)$$

### Spherical Harmonic Expansion of the Tidal Potential for a Rigid Earth

In geodesy, the tidal potential formulated in Equation 3.138 is usually reformulated in terms of spherical harmonics instead of the vector formulation. Assuming that the positions of the celestial bodies are provided, the vector formulation gives a simple straightforward way to compute solid Earth tides for an ocean-less rigid Earth model. However, if we want to predict the Earth tides of a non-rigid Earth model, it is necessary to make a spectral decomposition of the tidal potential in terms of spherical harmonics functions (Wenzel, 1997).

Firstly, we have to reformulate Equation 3.138 with scalar variables. If only the Moon<sup>30</sup> is considered we have:

$$\Phi_{\text{tidal}}(\boldsymbol{\rho}, t) = + GM_{\mathcal{C}} \cdot \left\{ \frac{1}{s_{\mathcal{C}}(t)} - \frac{r \cos \psi_{\mathcal{C}}(t)}{r_{\mathcal{C}}^2(t)} - \frac{1}{r_{\mathcal{C}}(t)} \right\} \quad (3.141)$$

where:

$$s_{\mathcal{C}}(t) \quad [\text{m}] \quad = \quad |\boldsymbol{\rho}_{\mathcal{C}}(t) - \boldsymbol{\rho}|, \text{ distance between the point } \mathcal{P} \text{ on the Earth and the Moon.}$$

$$r_{\mathcal{C}}(t) \quad [\text{m}] \quad = \quad |\boldsymbol{\rho}_{\mathcal{C}}(t)|, \text{ distance between the geocenter } \mathcal{G} \text{ and the Moon.}$$

$$r \quad [\text{m}] \quad = \quad |\boldsymbol{\rho}|, \text{ distance between the geocenter } \mathcal{G} \text{ and the point } \mathcal{P} \text{ on the Earth.}$$

$$\psi_{\mathcal{C}}(t) \quad [\text{rad}] \quad = \quad \arccos \left( \frac{\boldsymbol{\rho}_{\mathcal{C}}(t) \cdot \boldsymbol{\rho}}{|\boldsymbol{\rho}_{\mathcal{C}}(t)| \cdot |\boldsymbol{\rho}|} \right), \text{ spatial angle between } \boldsymbol{\rho}_{\mathcal{C}}(t) \text{ and } \boldsymbol{\rho}.$$

Secondly, if the reciprocal distance  $\frac{1}{s_{\mathcal{C}}}$  is given as a function of  $r_{\mathcal{C}}$ ,  $r$  and  $\psi_{\mathcal{C}}$

$$\frac{1}{s_{\mathcal{C}}} = \frac{1}{\sqrt{r_{\mathcal{C}}^2 + r^2 + 2r_{\mathcal{C}} r \cos \psi_{\mathcal{C}}}} \quad (3.142)$$

and expanded in terms of Legendre polynomials

$$\begin{aligned} \frac{1}{s_{\mathcal{C}}} &= \frac{1}{r_{\mathcal{C}}} \cdot \sum_{n=0}^{\infty} \left( \frac{r}{r_{\mathcal{C}}} \right)^n P_n(\cos \psi_{\mathcal{C}}) \\ &= \underbrace{\frac{1}{r_{\mathcal{C}}}}_{n=0} + \underbrace{\frac{1}{r_{\mathcal{C}}} \cdot \frac{r}{r_{\mathcal{C}}} \cdot \cos(\psi_{\mathcal{C}})}_{n=1} + \frac{1}{r_{\mathcal{C}}} \cdot \sum_{n=2}^{\infty} \left( \frac{r}{r_{\mathcal{C}}} \right)^n P_n(\cos \psi_{\mathcal{C}}) \end{aligned} \quad (3.143)$$

the Equation 3.143 can be inserted into Equation 3.141 and we obtain:

$$\Phi_{\text{tidal}}(\boldsymbol{\rho}, t) = + \frac{GM_{\mathcal{C}}}{r_{\mathcal{C}}} \cdot \sum_{n=2}^{\infty} \left( \frac{r}{r_{\mathcal{C}}} \right)^n P_n(\cos \psi_{\mathcal{C}}) \quad (3.144)$$

where we can see that the terms for the degrees  $l = 0$  and  $l = 1$  are simplified and disappear. The Equation 3.144 is given in terms of Legendre polynomials where the argument

<sup>30</sup>the treatment of the other celestial bodies is identical.

is the spatial angle  $\psi_{\mathcal{C}}$ . It means that the spectral decomposition (in space) of the tides is related to  $\psi_{\mathcal{C}}$ .

If we want to go a step further and decompose the tides (in space) as a function of the geocentric spherical coordinates of  $\mathcal{P}$ ,  $\boldsymbol{\rho} \equiv (\lambda, \vartheta, r)^{31}$ , and the position of the Moon,  $\boldsymbol{\rho}_{\mathcal{C}} \equiv (\lambda_{\mathcal{C}}, \vartheta_{\mathcal{C}}, r_{\mathcal{C}})$ , we can formulate the Legendre polynomials of degree  $n$ ,  $P_n$ , in terms of fully normalized spherical harmonics of degree  $n$  and order  $m$ ,  $\bar{P}_{nm}$  by:

$$P_n(\cos \psi_{\mathcal{C}}) = \frac{1}{2n+1} \cdot \sum_{m=0}^n \bar{P}_{nm}(\cos \vartheta) \cdot \bar{P}_{nm}(\cos \vartheta_{\mathcal{C}}) \cdot \cos(m\lambda - m\lambda_{\mathcal{C}}) \quad (3.145)$$

as we can find in *Wenzel* (1997). Finally, the spherical harmonic expansion of the tidal potential of a rigid Earth is given by inserting Equation 3.145 into Equation 3.144:

$$\begin{aligned} \Phi_{\text{tidal}}(\boldsymbol{\rho}, t) &= + \frac{GM_{\mathcal{C}}}{r_{\mathcal{C}}} \cdot \sum_{n=2}^{\infty} \left( \frac{r}{r_{\mathcal{C}}} \right)^n \frac{1}{2n+1} \cdot \sum_{m=0}^n \bar{P}_{nm}(\cos \vartheta) \cdot \bar{P}_{nm}(\cos \vartheta_{\mathcal{C}}) \cdot \cos(m\lambda - m\lambda_{\mathcal{C}}) \\ &= + \sum_{n=2}^{\infty} \sum_{m=0}^n \frac{GM_{\mathcal{C}}}{r_{\mathcal{C}}} \cdot \left( \frac{r}{r_{\mathcal{C}}} \right)^n \frac{1}{2n+1} \cdot \bar{P}_{nm}(\cos \vartheta) \cdot \bar{P}_{nm}(\cos \vartheta_{\mathcal{C}}) \cdot \cos(m\lambda - m\lambda_{\mathcal{C}}) \\ &= + \sum_{n=2}^{\infty} \sum_{m=0}^n \Phi_{\text{tidal},nm} \end{aligned} \quad (3.146)$$

**Remarks** For practical computations, it is not necessary to consider the terms larger than degree four ( $n = 4$ ). In fact, the spherical harmonics series converges rapidly  $\left(\frac{r}{r_{\mathcal{C}}}\right)^n \approx \left(\frac{1}{60}\right)^n$ , for the Moon, and  $\left(\frac{r}{r_{\odot}}\right)^n \approx \left(\frac{1}{23600}\right)^n$  for the Sun. Moreover it can be proven that 98% of the total tidal potential is modeled by the first term (which is the second degree  $n = 2$ ), see *Wenzel* (1997) and *Torge and Müller* (2012).

From the last remarks it is possible to get a very good order of magnitude of the tidal potential by looking at the first term ( $n=2$ ). This can be done using Equation 3.144:

$$\Phi_{\text{tidal}}(\boldsymbol{\rho}, t) \approx + \frac{GM_{\mathcal{C}}}{r_{\mathcal{C}}} \cdot \left( \frac{r}{r_{\mathcal{C}}} \right)^2 \cdot \left( \frac{3}{2} \cos^2 \psi_{\mathcal{C}} - \frac{1}{2} \right) \quad (3.147)$$

which attains its maximum when  $\psi_{\mathcal{C}} = k \cdot \pi$ , with ( $k = 0, 1, 2, \dots$ ). In this case (for the Moon only) we have:

$$\max \{ \Phi_{\text{tidal}}(\boldsymbol{\rho}, t) \} \approx + \frac{GM_{\mathcal{C}} \cdot r^2}{r_{\mathcal{C}}^3} \approx 3.5 \left[ \frac{\text{m}^2}{\text{s}^2} \right] \quad (3.148)$$

for the Sun, we get:

$$\max \{ \Phi_{\text{tidal}}(\boldsymbol{\rho}, t) \} \approx + \frac{GM_{\odot} \cdot r^2}{r_{\odot}^3} \approx 1.6 \left[ \frac{\text{m}^2}{\text{s}^2} \right] \quad (3.149)$$

---

<sup>31</sup>the geocentric spherical coordinates are given by the longitude  $\lambda$ , the co-latitude  $\vartheta$  and the radius  $r$ .



and for Venus, we get:

$$\max \{ \Phi_{\text{tidal}}(\boldsymbol{\rho}, t) \} \approx 2.3 \cdot 10^{-4} \left[ \frac{\text{m}^2}{\text{s}^2} \right] \quad (3.150)$$

### Spherical Harmonics Expansion of the Tidal Potential for a Deformable Earth

As mentioned in Section 3.4.10, the modelization of the consequences of the non-rigid Earth for the positions attached to the Earth's body and the apparent gravity are formulated directly within the Earth's tides model. In the following developments the Earth is assumed to be free from moving waters like oceans and seas, incompressible, homogeneous, non-rotating and spherically symmetric, see *Agnew* (2007) and *Torge and Müller* (2012).

From the seminal work of *Love* (1911), the problem can be decomposed into two main aspects. Firstly, the computation of the impact of the tidal potential on the geometry — or the shape — of the Earth and, secondly, the computation of the consequences of the new deformed Earth on the potential or on some observable quantities (which are functions of the potential and the new position of the observer) like geoid undulation, gravity, tilt, deflection of the vertical, strain, levelling observation, etc.

Concerning the deformation of the surface of the Earth in response to the tides, we assume that the deformations  $\mathbf{u}_{nm}$  of degree  $n$  and order  $m$  are proportional to the rigid Earth's tidal potential  $\Phi_{\text{tidal},nm}$  given in Equation 3.146. To be more precise, they are proportional to the displacements  $\tilde{\mathbf{u}}$  of the equilibrium surface of a hypothetical liquid Earth, given by  $\tilde{\mathbf{u}} = \frac{\Phi_{\text{tidal}}}{g}$ , where  $g$  represents the acceleration of gravity.

The proportionality factors for the vertical component,  $h_{nm}$ , are called *first Love numbers*. For the horizontal components they are given by the factors  $l_{nm}$  called *Shida numbers*. In other words, in the case where the Earth would be completely liquid, we would have  $h_{nm} = l_{nm} = 1$ , and in the case where the Earth would be perfectly rigid, we would have  $h_{nm} = l_{nm} = 0$  (*Vaníček and Krakiwsky*, 1982). In a local topocentric system ( $x$  = North,  $y$  = East,  $z$  = height) we have:

$$\begin{aligned} u_z &= \sum_{n=2}^{\infty} \sum_{m=0}^n h_{nm} \cdot u_{z,nm} = \frac{1}{g} \sum_{n=2}^{\infty} \sum_{m=0}^n h_{nm} \cdot \Phi_{\text{tidal},nm} \\ u_x &= \sum_{n=2}^{\infty} \sum_{m=0}^n l_{nm} \cdot u_{x,nm} = -\frac{1}{g} \sum_{n=2}^{\infty} \sum_{m=0}^n l_{nm} \cdot \frac{\partial \Phi_{\text{tidal},nm}}{\partial \vartheta} \\ u_y &= \sum_{n=2}^{\infty} \sum_{m=0}^n l_{nm} \cdot u_{y,nm} = \frac{1}{g} \sum_{n=2}^{\infty} \sum_{m=0}^n l_{nm} \cdot \frac{1}{\sin \vartheta} \cdot \frac{\partial \Phi_{\text{tidal},nm}}{\partial \lambda} \end{aligned} \quad (3.151)$$

The second step is to compute the changes in the potential due to the deformations given by the relations in Equation 3.151. This additional indirect potential is also called the *deformation potential*, noted  $\Phi_{\text{tidal},\text{deform}}$ , which is also proportional to the rigid Earth's tidal potential. The proportionality factors  $k_{nm}$  associated with the degree  $n$  and order  $m$  of the spherical harmonics expansion are called second Love numbers. Similarly to the

factors  $h_{nm}$  and  $l_{nm}$ , for a perfectly rigid Earth, we would find  $k_{nm} = 0$ . Formally we can write:

$$\Phi_{\text{tidal,deform}}(\boldsymbol{\rho}, t) = \sum_{n=2}^{\infty} \sum_{m=0}^n k_{nm} \cdot \Phi_{\text{tidal},nm} \quad (3.152)$$

As it is well explained in *Vaníček and Krakiwsky* (1982) we could imagine to compute a further deformation field based on the deformation potential which would generate again an additional deformation potential and so on, up to infinity. Actually, we do not need to process in this way because we assume that the *Love* and *Shida* numbers are given for final deformations when the equilibrium is reached. In Table 3.4, we can see the values of  $h_{nm}$ ,  $l_{nm}$  and  $k_{nm}$  up to the degree and order 4 as they are given in the software ETERNA (*Wenzel, 1993*) provided by the *International Center for Earth Tides* (ICET).

**Table 3.4:** *Love* and *Shida* numbers up to the degree and order 4 as they are given in the software ETERNA.

$n$	$m$	$h_{nm}$	$k_{nm}$	$l_{nm}$
[–]	[–]	[–]	[–]	[–]
2	0	0.6180	0.3035	0.0875
2	1	0.6072	0.3015	0.0832
2	2	0.6144	0.3055	0.0828
3	0	0.2946	0.0942	0.0149
3	1	0.2946	0.0942	0.0149
3	2	0.2946	0.0942	0.0149
3	3	0.2955	0.0963	0.0149
4	0	0.1807	0.0427	0.0100
4	1	0.1807	0.0427	0.0100
4	2	0.1807	0.0427	0.0100
4	3	0.1807	0.0427	0.0100
4	4	0.1812	0.0452	0.0100

The total tidal potential  $\Phi_{\text{tidal,total}}$  observed at a position  $\boldsymbol{\rho}_0$  fixed in space (not attached to the Earth's surface) is given by the sum of the rigid Earth's tidal potential and the deformation potential:

$$\begin{aligned} \Phi_{\text{tidal,total}}(\boldsymbol{\rho}_0, t) &= \Phi_{\text{tidal}}(\boldsymbol{\rho}_0, t) + \Phi_{\text{tidal,deform}}(\boldsymbol{\rho}_0, t) \\ &= \sum_{n=2}^{\infty} \sum_{m=0}^n \Phi_{\text{tidal},nm} + \sum_{n=2}^{\infty} \sum_{m=0}^n k_{nm} \cdot \Phi_{\text{tidal},nm} \\ &= \sum_{n=2}^{\infty} \sum_{m=0}^n (1 + k_{nm}) \cdot \Phi_{\text{tidal},nm} \end{aligned} \quad (3.153)$$

which is approximately 1.3 times higher or 30% larger than what we would observe on a rigid Earth.

If we now look at the total tidal potential  $\Phi_{\text{tidal,total}}$  observed at a position  $\boldsymbol{\rho}_{\text{Earth}} = \boldsymbol{\rho}_0 + \mathbf{u}$  attached to the Earth's surface, we have to consider the superposition of two phenomena. On the one hand we have again the total tidal potential observed at  $\boldsymbol{\rho}_{\text{Earth}}$  and on the other hand the variation of the apparent potential  $\Phi_{\text{tot}}$  due to the displacement to the position  $\boldsymbol{\rho}_{\text{Earth}}$ . In this case, we have to consider the total potential and we can write:

$$\begin{aligned}\Phi_{\text{tot}}(\boldsymbol{\rho}_{\text{Earth}}, t) &= \Phi_{\text{tot}}(\boldsymbol{\rho}_0 + \mathbf{u}, t) \\ &\approx \Phi_{\text{grav},\delta}(\boldsymbol{\rho}_0 + \mathbf{u}, t) + \Phi_{\text{tidal,total}}(\boldsymbol{\rho}_0 + \mathbf{u}, t)\end{aligned}\quad (3.154)$$

which can be developed using a general first order *Taylor* expansion (see Equation 3.8.3) by:

$$\begin{aligned}\Phi_{\text{tot}}(\boldsymbol{\rho}_0 + \mathbf{u}, t) &\approx \Phi_{\text{grav},\delta}(\boldsymbol{\rho}_0, t) + \underbrace{\nabla \Phi_{\text{grav},\delta}(\boldsymbol{\rho}_0, t) \cdot \mathbf{u}}_{\approx \mathbf{g}} \\ &\quad + \Phi_{\text{tide,total}}(\boldsymbol{\rho}_0, t) + \underbrace{\nabla \Phi_{\text{tide,total}}(\boldsymbol{\rho}_0, t) \cdot \mathbf{u}}_{\approx 0} \\ &= \Phi_{\text{grav},\delta}(\boldsymbol{\rho}_0, t) + \underbrace{\mathbf{g}}_{\approx (0,0,-g)^T} \cdot \mathbf{u} + \Phi_{\text{tide,total}}(\boldsymbol{\rho}_0, t) \\ &= \Phi_{\text{grav},\delta}(\boldsymbol{\rho}_0, t) - g \cdot u_z + \Phi_{\text{tide,total}}(\boldsymbol{\rho}_0, t)\end{aligned}\quad (3.155)$$

with  $u_z$  given by Equation 3.151 and  $\Phi_{\text{tide,total}}$  by Equation 3.153 we find:

$$\begin{aligned}\Phi_{\text{tot}}(\boldsymbol{\rho}_{\text{Earth}}, t) &= \Phi_{\text{grav},\delta}(\boldsymbol{\rho}_0, t) - g \cdot \frac{1}{g} \cdot \sum_{n=2}^{\infty} \sum_{m=0}^n h_{nm} \cdot \Phi_{\text{tidal},nm} \\ &\quad + \sum_{n=2}^{\infty} \sum_{m=0}^n (1 + k_{nm}) \cdot \Phi_{\text{tidal},nm} \\ &= \Phi_{\text{grav},\delta}(\boldsymbol{\rho}_0, t) + \sum_{n=2}^{\infty} \sum_{m=0}^n (1 + k_{nm} - h_{nm}) \cdot \Phi_{\text{tidal},nm}\end{aligned}\quad (3.156)$$

where the total tidal potential at  $\boldsymbol{\rho}_{\text{Earth}}$  is finally given by:

$$\Phi_{\text{tidal,tot}}(\boldsymbol{\rho}_{\text{Earth}}, t) = \sum_{n=2}^{\infty} \sum_{m=0}^n (1 + k_{nm} - h_{nm}) \cdot \Phi_{\text{tidal},nm} \quad (3.157)$$

which reduces the potential we would observe on a rigid Earth by a factor of 0.68.

### 3.8 Geometry of Equipotential Surfaces

As shown in Section 3.7.1, the Eulerian acceleration can be neglected regarding the level of accuracy needed in our application. Thus, the geometry of the liquid-air interface can

be derived directly from the equipotential surface of the apparent gravity field  $\Phi_{\text{stat}}$ , now denoted by  $\Phi_{\text{tot}}$  for the rest of the thesis. When nothing is specified, we are working in the Earth fixed system  $a$ . The liquid-air interface is represented by the set of all position vectors  $\{\boldsymbol{\rho}_{\sim}(t)\}$  which fulfill the following condition:

$$\Phi_{\text{tot}}(\boldsymbol{\rho}_{\sim}(t), t) = \Phi_{\text{tot}}^{\sim}(t) \quad (3.158)$$

where:

$$\begin{aligned} \Phi_{\text{tot}}(\boldsymbol{\rho}, t) \quad \left[ \frac{\text{m}^2}{\text{s}^2} \right] &= \text{Space-time gravity scalar potential field, including the gravitational, the centrifugal and the tidal potential.} \\ \boldsymbol{\rho}_{\sim}(t) \quad [\text{m}] &= \text{Time-dependent position vector of a point at the liquid-air interface } \sim. \\ \Phi_{\text{tot}}^{\sim}(t) \quad \left[ \frac{\text{m}^2}{\text{s}^2} \right] &= \text{Gravity potential at the liquid-air interface at time } t. \end{aligned}$$

and:

$$\Phi_{\text{tot}}(\boldsymbol{\rho}, t) = \Phi_{\text{grav}, \delta}(\boldsymbol{\rho}, t) + \Phi_{\text{centr}}(\boldsymbol{\rho}, t) + \Phi_{\text{tidal}}(\boldsymbol{\rho}, t) \quad (3.159)$$

This shows clearly the different physical components of the gravity potential field but it is not very suited for the determination and the analysis of equipotential surfaces and observables. This comes from the fact that the variations are small compared to the whole signal and that the major part of the signal can be modeled very well by a very simple Earth model.

In geodesy, we usually reformulate the gravity potential, given in Equation 3.159, as the sum of a potential  $U(\boldsymbol{\rho})$  generated by a simple rotating ellipsoidal Earth model, called *Normal Potential*, and a potential  $T_{\text{tot}}(\boldsymbol{\rho}, t)$  which takes into account the remaining part of the whole signal, called *Disturbing Potential*. The tidal potential  $\Phi_{\text{tidal}}(\boldsymbol{\rho}, t)$  remains unchanged:

$$\Phi_{\text{tot}}(\boldsymbol{\rho}, t) = U(\boldsymbol{\rho}) + T_{\text{tot}}(\boldsymbol{\rho}, t) + \Phi_{\text{tidal}}(\boldsymbol{\rho}, t) \quad (3.160)$$

where:

$$\begin{aligned} U(\boldsymbol{\rho}) \quad \left[ \frac{\text{m}^2}{\text{s}^2} \right] &= \text{Time-invariant normal potential field.} \\ T_{\text{tot}}(\boldsymbol{\rho}, t) \quad \left[ \frac{\text{m}^2}{\text{s}^2} \right] &= \text{Space-time disturbing potential field.} \\ \Phi_{\text{tidal}}(\boldsymbol{\rho}, t) \quad \left[ \frac{\text{m}^2}{\text{s}^2} \right] &= \text{Space-time tidal potential field.} \end{aligned}$$

### 3.8.1 Normal Potential and Equipotential Ellipsoid

The normal potential is a non-intuitive and important concept in geodesy. It is a sub-product of an equipotential ellipsoid — also called level ellipsoid — which is used as reference for both, the geometry and the gravity potential of the Earth. As we will see in Section 3.8.3, it is of first importance concerning the linearization of the gravity field and the determination of the geometry of equipotential surfaces or profiles.

### Geophysical Aspects of Equipotential Ellipsoids and Spheroids

From a geophysical point of view, the research on the *figure of the Earth* was always associated with the investigation in theories of *figures of equilibrium*. The presumption that the Earth must be close to a figure of equilibrium was propped by the fact that we can find emerged crustal surfaces all over the world and not at some latitudes only. This becomes obvious by doing the following proof by contradiction. On the one hand we consider that the mean surfaces of oceans are in hydrostatic equilibrium and on the other hand we consider that the solid part of the Earth is not close to equilibrium and less oblate than the figure given by the oceans. In this case we should observe emergent continents only near the poles. In the opposite case, emerging parts would be observed near the equator only.

From this assumption, several famous scientists like *Newton*, *Huygens*, *Clairaut*, *Mac Laurin*, *Jacobi*, *Riemann*, *Poincaré*, *Chandrasekhar* and others, tried to find out what are the possible solutions of equilibrium of rotating bodies subject to gravitational and centrifugal forces. Most of them made the hypothesis of homogeneity for the density field in association with different assumptions for the definition of equilibrium. Today, we would simply define the equilibrium rigorously as the hydrostatic equilibrium, as it is given in Section 3.6.4. However, we must still distinguish two classes of models of Earth's equilibrium which are usually used as reference models for geophysics (first class) or geodetic (second class) applications.

1. The whole Earth is in hydrostatic equilibrium. As we have seen in Section 3.6.4, the main consequence is that equipotential surfaces are parallel to surfaces of equal density everywhere inside and at the surface of the Earth. In this case, the solutions are called *spheroids* which have, in general, not the shape of ellipsoids. There exist only a few particular solutions which have the shape of ellipsoids. The most famous ones are given by *Mac Laurin* and *Jacobi* which have both strictly homogeneous densities. In short, *Mac Laurin ellipsoids* are homogeneous ellipsoids of revolution rotating uniformly around their minor axis and *Jacobi ellipsoids* are homogeneous tri-axial ellipsoids which also rotate around their minor axis. For a given total mass, the body unambiguously takes the shape of a *Mac Laurin* or a *Jacobi* ellipsoid as a function of the angular velocity. At low velocities, the equilibrium is given by the family of *Mac Laurin* ellipsoids and at certain precise velocities, the type of solution bifurcates to *Jacobi* ellipsoids. Afterward, there are other figures of equilibrium which break the ellipsoidal symmetries as it is well summarized in *Chandrasekhar* (1967).

For the Earth, only the ellipsoid of *Mac Laurin* can be considered. In this regard, if we try to see if the Earth can be fitted to a *Mac Laurin* ellipsoid, we can try to compute the mean density of the Earth  $\bar{\rho}_s$  which fulfills the relation of a *Mac Laurin* ellipsoid from the conventional IERS dimensions ( $a, b$ ) and the angular velocity  $\omega_s$  of the reference ellipsoid. The *Mac Laurin* relation can be found in *Chandrasekhar* (1967) and can be easily reformulated in order to find the density:

$$\rho_{\text{ML}} = \frac{\omega_0^2}{\pi G \cdot \left[ \frac{\sqrt{1-e^2}}{e^3} \cdot 2(3-2e^2) \cdot \arcsin(e) - \frac{6}{e^2} \cdot (1-e^2) \right]} \cong 7096 \left[ \frac{\text{kg}}{\text{m}^3} \right] \quad (3.161)$$

where:

$$\begin{aligned}
 \rho_{\text{ML}} \quad \left[ \frac{\text{kg}}{\text{m}^3} \right] &= \text{Density of the Mac Laurin ellipsoid.} \\
 e = \frac{\sqrt{a^2 - b^2}}{a} \quad [-] &= \text{First numerical eccentricity of the IERS reference ellipsoid.} \\
 a \quad [\text{m}] &= \text{Semi-major axis of the IERS reference ellipsoid.} \\
 b \quad [\text{m}] &= \text{Semi-minor axis of the IERS reference ellipsoid.}
 \end{aligned}$$

This density differs significantly from the real mean density of the Earth  $\bar{\rho}_\delta \cong 5515 \frac{\text{kg}}{\text{m}^3}$ . In a similar way, when the density is fixed and the geometrical flattening  $f = \frac{a-b}{a}$  is computed, we find  $f_{\text{ML}} \cong \frac{1}{230}$  — which corresponds to the value predicted by *Newton* — instead  $f_\delta \cong \frac{1}{298}$ . The main part of this large difference comes from the fact that the Earth is not homogeneous. Concerning the hydrostatic equilibrium hypothesis, the deviation is quite small. Numerical models based on global density fields give geometrical flattening values of approximatively  $f_\delta \cong \frac{1}{300}$  which corresponds to a deviation of  $\sim 113 \text{ m}$  between the polar and equatorial radii (*Chambat et al.*, 2010).

2. Only the surface of the Earth is assumed to be in “hydrostatic equilibrium”. In this case, for a given total mass and a given rotation angular velocity, only one condition must be fulfilled. The surface of the Earth has to be an equipotential surface and its geometry can be defined to be a perfect ellipsoid of revolution. The main contributor of the solutions of this kind of problem is *Clairaut* in 1743, who derived many very powerful relations in his famous *Théorie de la Figure de la Terre*, which are still used today. His main contributions are:

- to write the equation of the ellipsoid as a function of the semi-major axis  $a$  and the geometric flattening  $f$ .
- to write the equation of the gravity acceleration of an arbitrary point on the surface of the ellipsoid as a function of the gravity flattening  $f_g = \frac{g_{\text{Pole}} - g_{\text{Equator}}}{g_{\text{Equator}}}$ .
- to relate the purely geometrical flattening  $f$  with the gravity flattening  $f_g$ , the dynamical factor  $J_2$  (which contains the moments of inertia, the total mass and the semi-major axis) and a geodynamic factor  $q$  which especially contains the Earth's angular velocity. This is simply the starting point of the era of physical geodesy.
- to give minimal and maximal possible physical values for the geometrical flattening  $f$ , if the Earth is homogeneous  $f_{\text{max}} \cong \frac{1}{230}$  and if the total mass is concentrated at the center of the Earth  $f_{\text{min}} \cong \frac{1}{576}$ .

Afterward, *Pizzeti* (1894) and *Somigliana* (1929) developed theories which permit to compute the gravity potential, in the outer space, generated by ellipsoids of revolution. Nowadays, from a geophysical point of view, an equipotential ellipsoid of revolution  $\mathcal{E}_0$  is a rotating heterogeneous non-equilibrium ellipsoid of revolution, for which the normal potential  $U(\rho_0)$  on the surface is constant (*Moritz*, 1990). The general non-equilibrium statement comes from the *theorem of Ledersteger* which says that an equipotential ellipsoid cannot be in hydrostatic equilibrium, except for Mac Laurin ellipsoids.

### Normal Potential of Equipotential Ellipsoids

The normal potential is defined as the sum of the gravitational potential generated by the matter inside  $\mathcal{E}_0$  and the centrifugal potential generated by the rotation:

$$U(\boldsymbol{\rho}) = \Phi_{\text{grav}, \mathcal{E}_0}(\boldsymbol{\rho}) + \Phi_{\text{centr}, \omega_0}(\boldsymbol{\rho}) \quad (3.162)$$

From the Stokes-Poincaré theorem (*Torge and Müller, 2012*), the normal potential outside  $\mathcal{E}_0$  is completely determined by four parameters only, usually we use:

- the shape of  $\mathcal{E}_0$ , given by  $a$  and  $b$ .
- the total mass  $M$  inside  $\mathcal{E}_0$ .
- the angular velocity  $\omega_0$  of  $\mathcal{E}_0$ .

An interesting fact is that the determination of the normal potential outside  $\mathcal{E}_0$  depends only on the total mass  $M$  and not on the density field  $\rho(\boldsymbol{\rho})$ . This is also consistent with the inverse problem of potential theory, stating that an infinite set of density fields can generate the same normal potential outside  $\mathcal{E}_0$ . In contrary, concerning the normal potential inside  $\mathcal{E}_0$ , the problem is much more complicated, see *Moritz (1990)*. In fact, the potential is no longer more harmonic, it must fulfill Poisson's equation which depends directly on the density field. In this work, the normal potential inside  $\mathcal{E}_0$  is not treated since the aim of the thesis is to look at equipotential profiles which are certainly in the underground but still above  $\mathcal{E}_0$ .

The analytical computation of  $U(\boldsymbol{\rho})$  outside  $\mathcal{E}_0$  can be realized in different manners *Torge and Müller (2012)* and *Hofmann-Wellenhof and Moritz (2005)*: by a closed formula or by a spherical harmonics expansion. The advantage of the closed formula with respect to a truncated spherical harmonics expansion is that it gives exact values. The main advantage of the spherical harmonics expansion is that it is a function of spherical coordinates, which are convenient in many problems, and completely compatible with the spherical harmonics expansion of the gravity potential.

**Closed Formula.** The closed formula is given as a function of ellipsoidal coordinates<sup>32</sup>, see Figure 3.14, by:

$$\begin{aligned} U(\boldsymbol{\rho}) &= U(\lambda, \beta, u) \\ &= \frac{GM}{\epsilon} \arctan\left(\frac{\epsilon}{u}\right) + \frac{\omega_0^2 \cdot a^2 \cdot q}{2q_0} \cdot \left(\sin^2(\beta) - \frac{1}{3}\right) + \frac{\omega_0^2}{2} \cdot (u^2 + \epsilon^2) \cdot \cos^2(\beta) \end{aligned} \quad (3.163)$$

with:

$$q = \frac{1}{2} \cdot \left[ \left(1 + \frac{3u^2}{\epsilon^2}\right) \cdot \arctan\left(\frac{\epsilon}{u}\right) - \frac{3u}{\epsilon} \right] \quad (3.164)$$

<sup>32</sup>which must not be confounded with the geodetic coordinates  $(\lambda, \phi, h)$

and:

$$q_0 = \frac{1}{2} \cdot \left[ \left( 1 + \frac{3b^2}{\epsilon^2} \right) \cdot \arctan \left( \frac{\epsilon}{b} \right) - \frac{3b}{\epsilon} \right] \quad (3.165)$$

where:

$U$	$\left[ \frac{\text{m}^2}{\text{s}^2} \right]$	=	Normal potential.
$\lambda, \beta, u$	$[\text{deg}], [\text{m}]$	=	Ellipsoidal longitude, latitude, third parameter (semi-minor axis of passing through ellipsoid).
$GM$	$\left[ \frac{\text{m}^3}{\text{s}^2} \right]$	=	Geocentric gravitational constant of the Earth.
$\epsilon = \sqrt{a^2 - b^2}$	$[\text{m}]$	=	Linear eccentricity.
$a, b$	$[\text{m}]$	=	Semi-major and semi-minor axis of the ellipsoid of revolution.
$\omega_0$	$\left[ \frac{\text{rad}}{\text{s}} \right]$	=	Angular velocity of the ellipsoid of revolution.

**Spherical Harmonics Expansion.** The spherical harmonics expansion is given as a function of spherical coordinates by:

$$U(\boldsymbol{\rho}) = U(\lambda, \vartheta, r) \\ = \frac{GM}{r} \cdot \left[ 1 - \sum_{n=1}^{\infty} \left( \frac{a}{r} \right)^{2n} \cdot J_{2n} \cdot P_{2n}(\cos \vartheta) \right] + \frac{\omega_0^2}{2} \cdot r^2 \sin^2 \vartheta \quad (3.166)$$

where:

$U$	$\left[ \frac{\text{m}^2}{\text{s}^2} \right]$	=	Normal potential.
$\lambda, \vartheta, r$	$[\text{deg}], [\text{m}]$	=	Geocentric longitude, co-latitude and radius.
$GM$	$\left[ \frac{\text{m}^3}{\text{s}^2} \right]$	=	Geocentric gravitational constant of the Earth.
$a$	$[\text{m}]$	=	Semi-major axis of the ellipsoid of revolution.
$J_l$	$[-]$	=	Zonal harmonic coefficients of the spherical harmonics expansion.
$P_l$	$[-]$	=	Legendre polynomials.
$\omega_0$	$\left[ \frac{\text{rad}}{\text{s}} \right]$	=	Angular velocity of the ellipsoid of revolution.

### Geometry of Normal Equipotential Surfaces

The geometry of a normal equipotential surface is defined as the locus of position vectors  $\{\boldsymbol{\rho}_o\}$ , where the normal potential  $U(\boldsymbol{\rho})$  is constant. Formally we have:

$$U(\boldsymbol{\rho}_o) = U_{\sim} \quad (3.167)$$



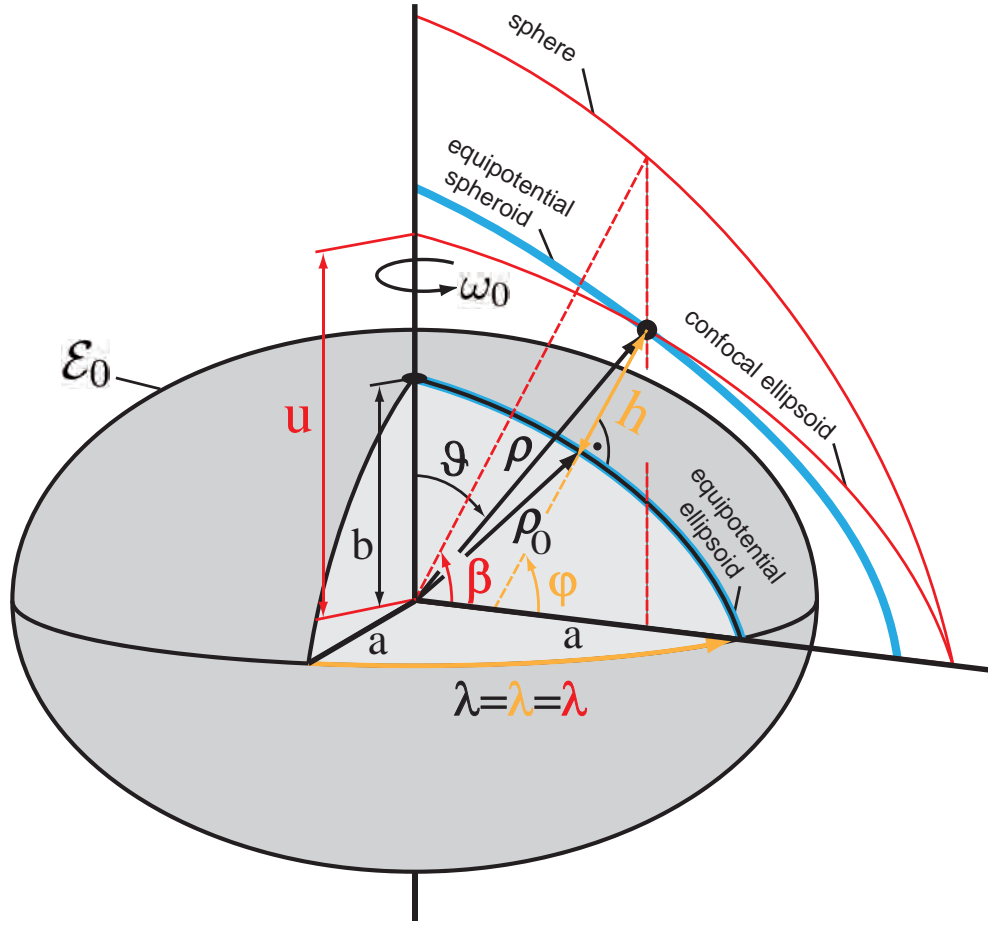


**Figure 3.14:** Earth’s equipotential ellipsoid of revolution with spherical coordinates (black,  $r = |\rho|$ ), geodetic coordinates (orange) and ellipsoidal coordinates (red). On the surface, the solid part of the ellipsoid is identical to the equipotential surface. Elsewhere, the shape of equipotential surfaces is not ellipsoidal. For example, the equipotential surface (blue) passing through the position  $\rho$  differs from its corresponding confocal ellipsoid (red).

As we can see in Equations 3.163 and 3.166, for a given normal potential  $U_\sim$ , it is difficult to isolate explicitly the geometry of its corresponding equipotential surface. Nevertheless, we clearly see that the normal potential does not vary with the longitude but only along meridians without forgetting the strong dependence on height, see Figure 3.15. In (Torge and Müller, 2012) and (Hofmann-Wellenhof and Moritz, 2005) the geometry of the normal potential is described locally by the curvature tensor and the gradient vector of  $U(\rho)$  and not directly in terms of distance separations to a reference surface (e.g. ellipsoid).

Here, the discrepancies between the true normal equipotential surfaces  $\rho_o$  and a simple surface defined by the locus of position vectors which have a constant geodetic height  $h_0$ , are computed numerically in a direct manner from the normal potential function, given in closed form by Equation 3.163, in order to be preserved from any truncation or approximation errors.

When the components  $(\lambda, \varphi)$  of the position vector  $\boldsymbol{\rho}_o$  are provided, the height  $h_o$  which matches the normal potential  $U_\sim$  is computed numerically using a simple Newton iterative method:

1. start with iteration  $k = 1$ .
2. set  $h_{k=1} = 0$ .
3. the position vector  $\boldsymbol{\rho}_{\sim,k}^N$  with geodetic components is given by:

$$\boldsymbol{\rho}_{\sim,k}^N = \begin{pmatrix} \lambda \\ \varphi \\ h_k \end{pmatrix} \quad (3.168)$$

4. convert the geodetic components of  $\boldsymbol{\rho}_{\sim,k}^N$  into ellipsoidal components according to Appendix C:

$$\boldsymbol{\rho}_{\sim,k}^N = \begin{pmatrix} \lambda \\ \varphi \\ h_k \end{pmatrix} \rightarrow \begin{pmatrix} \lambda \\ \beta \\ u_k \end{pmatrix} \quad (3.169)$$

5. compute the normal potential  $U_k(\boldsymbol{\rho}_{\sim,k}^N)$  with Equation 3.163.
6. compute numerically the partial derivative of the normal potential with respect to  $h$  by applying (3) and (4) to an auxiliary position vector with  $h = h_k + \Delta h$  :

$$\left. \frac{\partial U}{\partial h} \right|_{\boldsymbol{\rho}_{o,k}} \quad (3.170)$$

7. compute the updated height  $h_{k+1}$  by:

$$h_{k+1} = h_k - \frac{U_k - U_\sim}{\frac{\partial U}{\partial h}} \quad (3.171)$$

8. if  $|h_{k+1} - h_k| \geq 10^{-7}[\text{m}] \rightarrow$  iterate again from (3), else goto (9).
9. the position vector which is at normal potential  $U_\sim$  is given by:

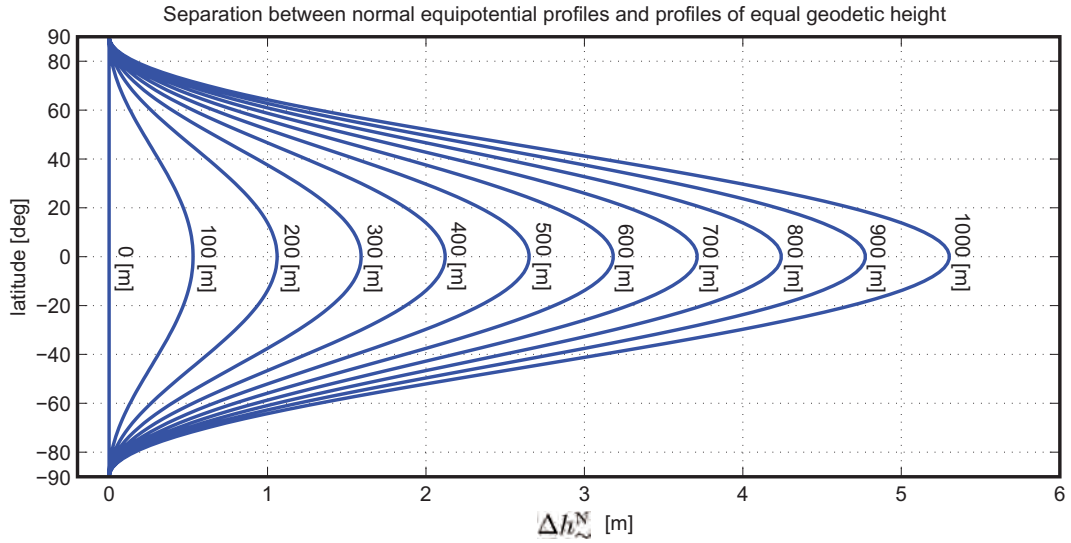
$$\boldsymbol{\rho}_o = \begin{pmatrix} \lambda \\ \varphi \\ h_o = h_{k+1} \end{pmatrix} \quad (3.172)$$

10. stop.

In Table 3.5 and Figure 3.15 we can see some normal equipotential profiles along a fixed meridian for different given normal potentials  $U_\sim(h_0)$  which correspond to different starting heights  $h_0$ . The starting height  $h_0$  is defined as the height of the first position vector (at North pole) of a particular profile. The normal potential is generated using the geocentric equipotential ellipsoid GRS80 (*Moritz, 2000*):

**Table 3.5:** Geodetic height of normal equipotential profiles along the Greenwich meridian,  $\lambda = 0.0$  [deg], for various potential values.

$U_{\sim}$ [ $\frac{\text{m}^2}{\text{s}^2}$ ]	$h_0$ [m]	$h_{\sim, \varphi=+90.0}^N$ [m]	$h_{\sim, \varphi=0.0}^N$ [m]	$h_{\sim, \varphi=-90.0}^N$ [m]	$\Delta h_{\sim, \varphi=0.0}^N$ [m]
62636860.85	+0.000	+0.000	+0.000	+0.000	+0.000
62635877.65	+100.000	+100.000	+100.530	+100.000	+0.530
62634894.47	+200.000	+200.000	+201.060	+200.000	+1.060
62633911.33	+300.000	+300.000	+301.591	+300.000	+1.591
62632928.22	+400.000	+400.000	+402.121	+400.000	+2.121
62631945.14	+500.000	+500.000	+502.651	+500.000	+2.651
62630962.09	+600.000	+600.000	+603.181	+600.000	+3.181
62629979.07	+700.000	+700.000	+703.712	+700.000	+3.712
62628996.09	+800.000	+800.000	+804.242	+800.000	+4.242
62628013.13	+900.000	+900.000	+904.773	+900.000	+4.773
62627030.21	+1000.000	+1000.000	+1005.303	+1000.000	+5.303

**Figure 3.15:** Distance separation  $\Delta h_o$  between normal equipotential profiles and profiles of equal geodetic height for different normal potentials  $U_{\sim}$  corresponding to different heights at the North pole.

### 3.8.2 Disturbing Potential

The disturbing potential  $T_{\text{tot}}(\boldsymbol{\rho}, t)$  is the key concept used for the determination of equipotential surfaces and profiles. It contains the potential generated by all phenomena that are not modeled by the normal potential  $U(\boldsymbol{\rho})$  and the tidal potential  $\Phi_{\text{tidal}}(\boldsymbol{\rho}, t)$ . Formally, this means that it contains all terms of the total gravity potential  $\Phi_{\text{tot}}(\boldsymbol{\rho}, t)$  not contained

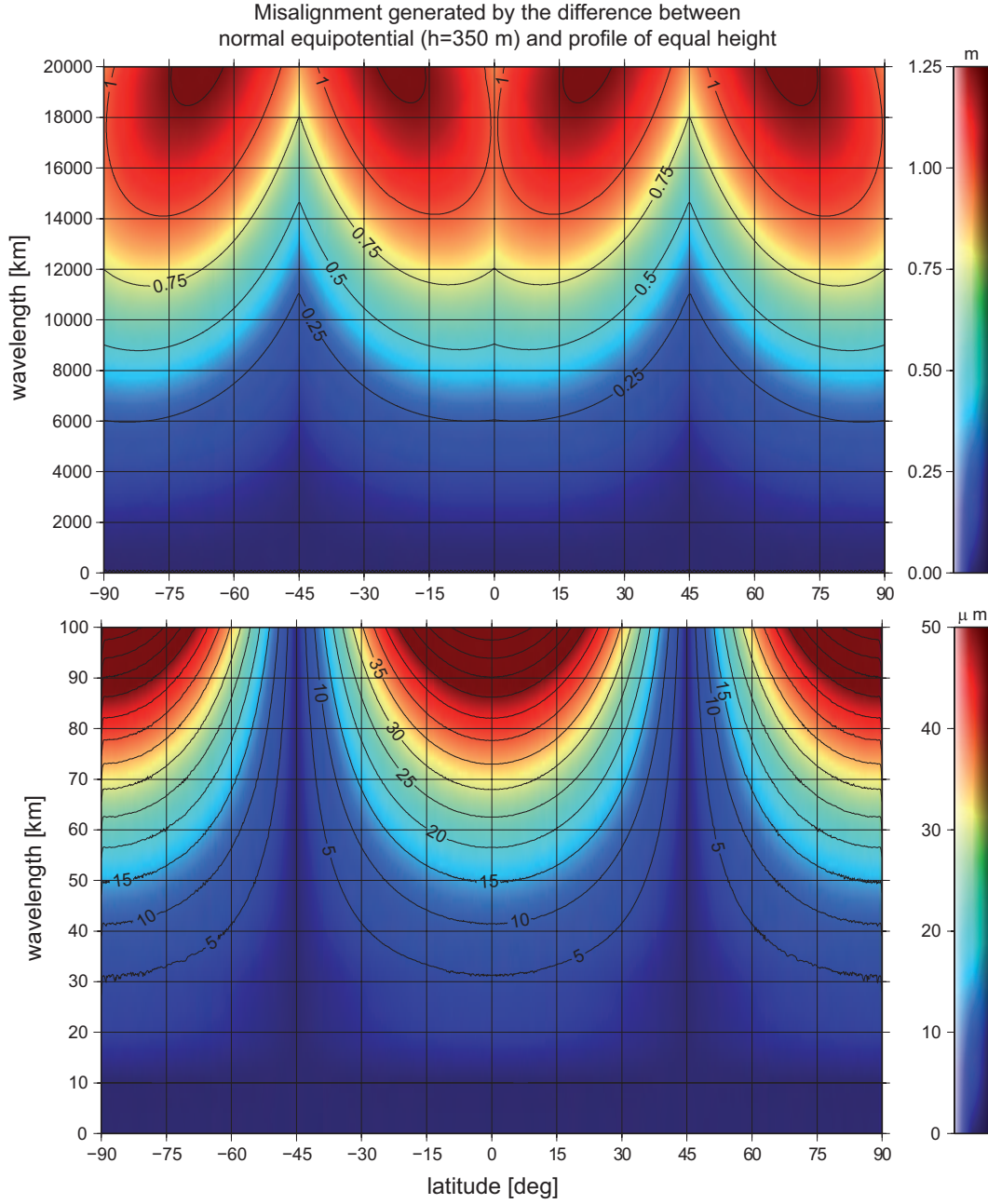


**Figure 3.16:** Misalignment due to the distance separation  $\mathcal{M}_\star^*\{\Delta h_o\}$  between normal equipotential profiles and profiles of equal geodetic height for the normal potentials  $U_\sim$  corresponding to  $h_o = 350$  m at North pole.

in the normal potential  $U(\rho)$ :

$$\begin{aligned}
 T_{\text{tot}}(\rho, t) &= \Phi_{\text{tot}}(\rho, t) - U(\rho) - \Phi_{\text{tidal}}(\rho, t) \\
 &= \Phi_{\text{grav}, \delta}(\rho, t) + \Phi_{\text{centr}}(\rho, t) + \Phi_{\text{tidal}}(\rho, t) \\
 &\quad - \Phi_{\text{grav}, \mathcal{E}_0}(\rho) - \Phi_{\text{centr}, \omega_0}(\rho) - \Phi_{\text{tidal}}(\rho, t)
 \end{aligned} \tag{3.173}$$

which can be rearranged to give:

$$\begin{aligned} T_{\text{tot}}(\boldsymbol{\rho}, t) &= \Phi_{\text{grav}, \delta}(\boldsymbol{\rho}, t) - \Phi_{\text{grav}, \mathcal{E}_0}(\boldsymbol{\rho}) \\ &\quad + \Phi_{\text{centr}}(\boldsymbol{\rho}, t) - \Phi_{\text{centr}, \omega_0}(\boldsymbol{\rho}) \\ &= \Phi_{\text{grav}, \delta - \mathcal{E}_0}(\boldsymbol{\rho}, t) + \delta\Phi_{\text{centr}}(\boldsymbol{\rho}, t) \end{aligned} \quad (3.174)$$

and if the disturbing gravitational potential  $\Phi_{\text{grav}, \delta - \mathcal{E}_0} = \Phi_{\text{grav}, \delta} - \Phi_{\text{grav}, \mathcal{E}_0}$  is decomposed into stationary and non-stationary dynamic terms, we have:

$$T_{\text{tot}}(\boldsymbol{\rho}, t) = \Phi_{\text{grav}, \text{st}}(\boldsymbol{\rho}) + \Phi_{\text{grav}, \text{dyn}}(\boldsymbol{\rho}, t) + \delta\Phi_{\text{centr}}(\boldsymbol{\rho}, t) \quad (3.175)$$

or with a more convenient notation:

$$T_{\text{tot}}(\boldsymbol{\rho}, t) = T_{\text{st}}(\boldsymbol{\rho}) + T_{\text{dyn}}(\boldsymbol{\rho}, t) \quad (3.176)$$

where:

$$\begin{aligned} T_{\text{st}}(\boldsymbol{\rho}) &= \Phi_{\text{grav}, \text{st}}(\boldsymbol{\rho}) \\ T_{\text{dyn}}(\boldsymbol{\rho}, t) &= \Phi_{\text{grav}, \text{dyn}}(\boldsymbol{\rho}, t) + \delta\Phi_{\text{centr}}(\boldsymbol{\rho}, t) \end{aligned} \quad (3.177)$$

In brief, the disturbing field  $T_{\text{tot}}(\boldsymbol{\rho}, t)$  is decomposed into two parts. The stationary part  $T_{\text{st}}(\boldsymbol{\rho})$  represents the gravitational effect of all masses which are not taken into account in  $U(\boldsymbol{\rho})$  and which do not vary with time like:

- geological structures between the equipotential ellipsoid  $\mathcal{E}_0$  and the topography,
- density anomalies inside the equipotential ellipsoid  $\mathcal{E}_0$  compared to the normal density field of  $\mathcal{E}_0$ . This assumption is true but may seem to be confusing. In fact, the normal density field  $U(\boldsymbol{\rho})$  is not defined. In the definition of the normal potential only the whole mass inside  $\mathcal{E}_0$  is fixed, but not the precise distribution of masses. This has an unfortunate consequence concerning the modeling of the disturbing potential from the disturbing density field. There exists an infinite set of possible disturbing density fields because there exist an infinite set of normal density fields which generate the unique normal potential  $U(\boldsymbol{\rho})$ . This problem can be fixed basically in two ways.

Firstly, we could create another normal potential field which would be generated from a predefined normal density field<sup>33</sup>. In this case, the main drawback is that we would loose the nice property that the surface of ellipsoid is an equipotential surface. The new body of reference would certainly not be an equipotential surface anymore.

Secondly, we may assume that the density anomalies inside the normal ellipsoid do not need to be modeled because they generate signals in the potential (of large wavelengths) which are properly caught by the observation. In other words, the spacing of the observables is below the Nyquist's wavelength of the signals.

<sup>33</sup>e.g. with a simple Earth's density model as the Preliminary Reference Earth Model (PREM).

- the lakes at mean level,
- the stationary part of the atmosphere, etc ...

The second part  $T_{\text{dyn}}(\boldsymbol{\rho}, t)$  represents, on the one hand, the gravitational parts of all time-varying masses like:

- geological and geotechnical time-varying phenomena,
- underground water flows,
- the time-varying part of the open water masses like oceans, lakes, etc...
- the time-varying part of the atmosphere, etc ...

and on the other hand, the time varying part of the centrifugal potential  $\Phi_{\text{centr}}(\boldsymbol{\rho}, t)$  due to the variation of the Earth's rotation vector  $\boldsymbol{\omega}_{ia}^a(t)$ .

### 3.8.3 Link between Potential Field and Geometry of Equipotential Surfaces

In this section, the link between total gravity potential field  $\Phi_{\text{tot}}(\boldsymbol{\rho}, t)$  and the geometry of equipotential surface can be realized if the real gravity potential field is approximated by a *Taylor* series expansion in the vicinity of the liquid-air interface represented by the set of positions  $\{\boldsymbol{\rho}_{\sim}\}$  and the position vector of the liquid-air interface is given by:

$$\boldsymbol{\rho}_{\sim} = \boldsymbol{\rho}_o + \Delta\boldsymbol{\rho} \quad (3.178)$$

where  $\Delta\boldsymbol{\rho}$  is an arbitrary relative position vector (see Figure 3.17).

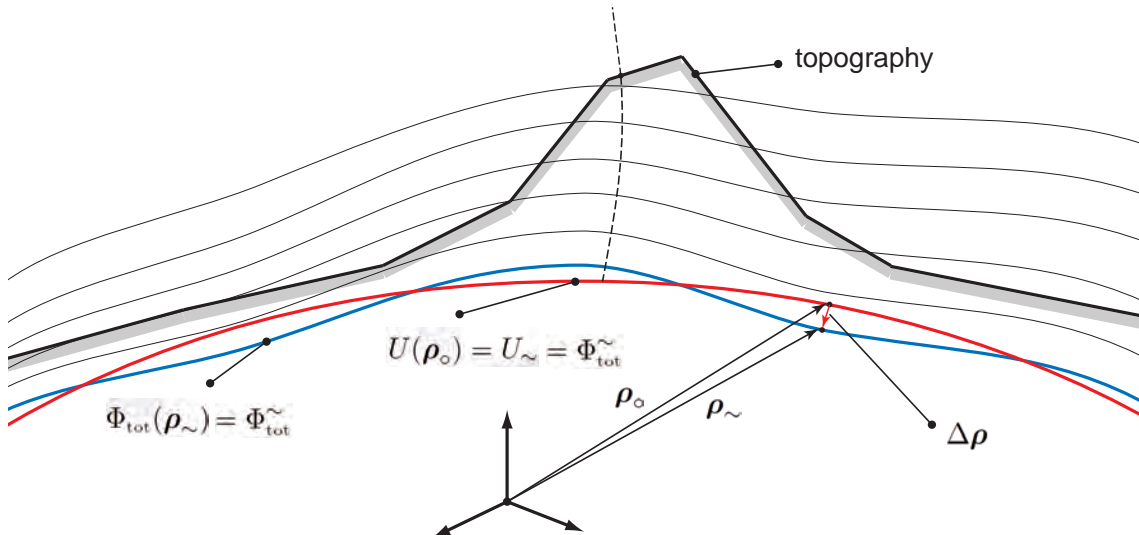


**Figure 3.17:** Schematic representation of the link between potential field and geometry of equipotential surfaces.

### General Taylor Series Expansion of the Gravity Potential

At a given time  $t$ , the *Taylor* series expansion of  $\Phi_{\text{tot}}(\rho_{\sim}, t)$  around  $\rho_o$  is given by:

$$\begin{aligned}\Phi_{\text{tot}}(\rho_{\sim}) &= \Phi_{\text{tot}}(\rho_o) + \nabla \Phi_{\text{tot}}(\rho_o) \cdot \Delta \rho \\ &+ \frac{1}{2} \cdot \Delta \rho^T \cdot \nabla [\nabla \Phi_{\text{tot}}(\rho_o)] \cdot \Delta \rho \\ &+ \mathcal{O}(\Delta \rho^3)\end{aligned}\quad (3.179)$$

Introducing the gravity acceleration vector  $\mathbf{g}_{\text{tot}}(\rho_o)$  and the gravity gradient tensor<sup>34</sup>  $\mathbf{\Gamma}_{\text{tot}}(\rho_o)$  we have:

$$\begin{aligned}\Phi_{\text{tot}}(\rho_{\sim}) &= \Phi_{\text{tot}}(\rho_o) + \mathbf{g}_{\text{tot}}(\rho_o) \cdot \Delta \rho \\ &+ \frac{1}{2} \cdot \Delta \rho^T \cdot \mathbf{\Gamma}_{\text{tot}}(\rho_o) \cdot \Delta \rho \\ &+ \mathcal{O}(\Delta \rho^3)\end{aligned}\quad (3.180)$$

where:

$$\mathbf{g}_{\text{tot}}(\rho_o) = \nabla \Phi_{\text{tot}}(\rho_o) = \left( \begin{array}{c} \frac{\partial \Phi_{\text{tot}}}{\partial x} \\ \frac{\partial \Phi_{\text{tot}}}{\partial y} \\ \frac{\partial \Phi_{\text{tot}}}{\partial z} \end{array} \right) \bigg|_{\rho_o} \quad (3.181)$$

and:

$$\begin{aligned}\mathbf{\Gamma}_{\text{tot}}(\rho_o) &= \nabla [\nabla \Phi_{\text{tot}}(\rho_o)] \\ &= \nabla \left( \begin{array}{c} \frac{\partial \Phi_{\text{tot}}}{\partial x} \\ \frac{\partial \Phi_{\text{tot}}}{\partial y} \\ \frac{\partial \Phi_{\text{tot}}}{\partial z} \end{array} \right) \bigg|_{\rho_o} = \left( \begin{array}{ccc} \frac{\partial^2 \Phi_{\text{tot}}}{\partial x^2} & \frac{\partial^2 \Phi_{\text{tot}}}{\partial x \partial y} & \frac{\partial^2 \Phi_{\text{tot}}}{\partial x \partial z} \\ \frac{\partial^2 \Phi_{\text{tot}}}{\partial y \partial x} & \frac{\partial^2 \Phi_{\text{tot}}}{\partial y^2} & \frac{\partial^2 \Phi_{\text{tot}}}{\partial y \partial z} \\ \frac{\partial^2 \Phi_{\text{tot}}}{\partial z \partial x} & \frac{\partial^2 \Phi_{\text{tot}}}{\partial z \partial y} & \frac{\partial^2 \Phi_{\text{tot}}}{\partial z^2} \end{array} \right) \bigg|_{\rho_o}\end{aligned}\quad (3.182)$$

### Taylor Series Expansion in the Normal Direction of the Equipotential Surface

A special case of the general expansion given in Section 3.8.3 is very useful for the determination of the geometric separation between the normal and the real equipotential surfaces. If the vector  $\Delta \rho$  is chosen to be perpendicular to the gravity equipotential surface and  $N_{\text{tot}}(\rho_o)$  represents the module of  $\Delta \rho$ , we can write:

$$\Delta \rho = \mathbf{n}_{\Phi_{\text{tot}}}(\rho_o) \cdot N_{\text{tot}}(\rho_o) = -\frac{\mathbf{g}_{\text{tot}}(\rho_o)}{|\mathbf{g}_{\text{tot}}(\rho_o)|} \cdot N_{\text{tot}}(\rho_o) \quad (3.183)$$

where  $\mathbf{n}_{\Phi_{\text{tot}}}(\rho_o)$  corresponds to the normal vector of the equipotential surface at  $\rho_o$ . The position vector of the liquid-air interface is given by:

$$\rho_{\sim} = \rho_o + \mathbf{n}_{\Phi_{\text{tot}}}(\rho_o) \cdot N_{\text{tot}}(\rho_o) \quad (3.184)$$

<sup>34</sup>which is the Hessian matrix of the gravity potential and also called *Eötvös* tensor if the coordinates are given in the local topocentric system.

and Equation 3.180 can be written as follows:

$$\begin{aligned}\Phi_{\text{tot}}(\boldsymbol{\rho}_{\sim}) &= \Phi_{\text{tot}}(\boldsymbol{\rho}_o) - |\mathbf{g}_{\text{tot}}(\boldsymbol{\rho}_o)| \cdot N_{\text{tot}}(\boldsymbol{\rho}_o) \\ &+ \frac{1}{2 \cdot |\mathbf{g}_{\text{tot}}(\boldsymbol{\rho}_o)|^2} \cdot \mathbf{g}_{\text{tot}}(\boldsymbol{\rho}_o)^T \cdot \boldsymbol{\Gamma}_{\text{tot}}(\boldsymbol{\rho}_o) \cdot \mathbf{g}_{\text{tot}}(\boldsymbol{\rho}_o) \cdot N_{\text{tot}}^2(\boldsymbol{\rho}_o) \\ &+ \mathcal{O}(N_{\text{tot}}^3)\end{aligned}\quad (3.185)$$

which can be written in a more convenient form as a second order polynomial:

$$\Phi_{\text{tot}}(\boldsymbol{\rho}_{\sim}) = \Phi_{\text{tot}}(\boldsymbol{\rho}_o) + A \cdot N_{\text{tot}}(\boldsymbol{\rho}_o) + B \cdot N_{\text{tot}}^2(\boldsymbol{\rho}_o) + \mathcal{O}(N_{\text{tot}}^3) \quad (3.186)$$

where the coefficients  $A$  and  $B$  are given by:

$$\begin{aligned}A &= -|\mathbf{g}_{\text{tot}}(\boldsymbol{\rho}_o)| \\ B &= \frac{1}{2 \cdot |\mathbf{g}_{\text{tot}}(\boldsymbol{\rho}_o)|^2} \cdot \mathbf{g}_{\text{tot}}(\boldsymbol{\rho}_o)^T \cdot \boldsymbol{\Gamma}_{\text{tot}}(\boldsymbol{\rho}_o) \cdot \mathbf{g}_{\text{tot}}(\boldsymbol{\rho}_o)\end{aligned}\quad (3.187)$$

### Disturbing Potential in Terms of Geometrical Separation

In the previous section, thanks to the *Taylor* series expansion of the gravity potential, the link between the gravity potential and the geometry of the equipotential surface was found. Here, it is the objective to formulate the disturbing potential<sup>35</sup> as a function of the geometric separation. To do this, it is necessary to introduce an additional condition. This condition is the gauge of the gravity potential  $\Phi_{\text{tot}}^{\sim}$  at the liquid-air interface  $\boldsymbol{\rho}_{\sim}$  to the normal potential  $U_{\sim}$  at normal equipotential surface  $\boldsymbol{\rho}_o$ . Formally the following relation is always satisfied:

$$U(\boldsymbol{\rho}_o) = U_{\sim} = \Phi_{\text{tot}}(\boldsymbol{\rho}_{\sim}) = \Phi_{\text{tot}}^{\sim} \quad (3.188)$$

and if this condition is applied to Equation 3.186 combined with Equation 3.160, we get the following remarkable relation:

$$\underbrace{U(\boldsymbol{\rho}_o)}_{=\Phi_{\text{tot}}(\boldsymbol{\rho}_{\sim})} = \underbrace{U(\boldsymbol{\rho}_o) + T_{\text{tot}}(\boldsymbol{\rho}_o) + \Phi_{\text{tidal}}(\boldsymbol{\rho}_o)}_{=\Phi_{\text{tot}}(\boldsymbol{\rho}_o)} + A \cdot N_{\text{tot}}(\boldsymbol{\rho}_o) + B \cdot N_{\text{tot}}^2(\boldsymbol{\rho}_o) + \mathcal{O}(N_{\text{tot}}^3) \quad (3.189)$$

which can be simplified and rearranged as follows:

$$-T_{\text{tot}}(\boldsymbol{\rho}_o) - \Phi_{\text{tidal}}(\boldsymbol{\rho}_o) = +A \cdot N_{\text{tot}}(\boldsymbol{\rho}_o) + B \cdot N_{\text{tot}}^2(\boldsymbol{\rho}_o) + \mathcal{O}(N_{\text{tot}}^3) \quad (3.190)$$

and since all terms (including  $A$  and  $B$ ) are given at position  $\boldsymbol{\rho}_o$  we can write:

$$f(N_{\text{tot}}) = +A \cdot N_{\text{tot}} + B \cdot N_{\text{tot}}^2 + \mathcal{O}(N_{\text{tot}}^3) \quad (3.191)$$

with:

$$f(N_{\text{tot}}) = -(T_{\text{tot}} + \Phi_{\text{tidal}}) \quad (3.192)$$

<sup>35</sup>in this case, the disturbing potential must be understood as being the sum of the standard disturbing potential and the tidal potential  $T_{\text{tot}} + \Phi_{\text{tidal}}$ .



### Geometrical Separation in Terms of the Disturbing Potential

From Equation 3.191, the geometric separation  $N_{\text{tot}}$  as a function of the disturbing potential, represented by  $-f$ , is given by finding the inverse function:

$$f^{-1}(N_{\text{tot}}) = N_{\text{tot}}(f) \quad (3.193)$$

**First order approximation.** Usually, Equation 3.191 is only expanded to the first order and not up to second order as in our case. In the former case, the inverse function is very easy to compute:

$$f(N_{\text{tot}}) = +A \cdot N_{\text{tot}} + \mathcal{O}(N_{\text{tot}}^2) \quad f^{-1}(N_{\text{tot}}) = N_{\text{tot}}(f) = \frac{f}{A} + \mathcal{O}(f^2) \quad (3.194)$$

and by replacing the coefficients using Equations 3.187 and 3.192 we get:

$$N_{\text{tot}}^{\text{1st}}(\rho_o) = \frac{T_{\text{tot}}(\rho_o) + \Phi_{\text{tidal}}(\rho_o)}{|\mathbf{g}_{\text{tot}}(\rho_o)|} + \mathcal{O}(N_{\text{tot}}^2) \quad (3.195)$$

which is very similar, but not exactly identical, to the traditional Brun's formula which can be found in *Torge and Müller (2012)*; *Hofmann-Wellenhof and Moritz (2005)*:

$$N(\rho_o) = \frac{T_{\text{tot}}(\rho_{\sim})}{|\boldsymbol{\gamma}(\rho_o)|} + \mathcal{O}(N^2) \quad (3.196)$$

where  $\boldsymbol{\gamma}(\rho_o)$  corresponds to the normal gravity acceleration vector at  $\rho_o$ .

**Remarks.** The differences between Equations 3.195 and 3.196 are often neglected and in reality very small, but it is still interesting to look at the main theoretical differences of these two approaches.

Firstly, consider the status of the tidal potential part  $\Phi_{\text{tidal}}$ . In fact, in Equation 3.196,  $N(\rho_o)$  is traditionally reduced from the effect of tides. This aspect is not conceptually significant since it would be straightforward and simple to introduce a tidal potential part  $\Phi_{\text{tidal}}(\rho_{\sim})$  to get the more realistic physical undulation  $N_{\text{tot}}(\rho_{\sim})$ .

Secondly, the positions, where the disturbing potentials  $T_{\text{tot}}$  and  $\Phi_{\text{tidal}}$ , as well as the gravity accelerations,  $|\mathbf{g}_{\text{tot}}|$  and  $|\boldsymbol{\gamma}|$ , are determined, are considered to be different. In Equation 3.195, all fields are related to the known position vector  $\rho_o$  which is very convenient for computations, whereas in Equation 3.196, the disturbing potential,  $T_{\text{tot}}$ , is related to the unknown position  $\rho_{\sim}$  and the normal gravity  $|\boldsymbol{\gamma}|$  to known position  $\rho_o$ .

Finally in Equation 3.196, the denominator  $|\boldsymbol{\gamma}|$  has the advantage that it is perfectly known. Whilst, in (3.195), the denominator  $|\mathbf{g}_{\text{tot}}|$ , which represents the real gravity acceleration sensed at  $\rho_o$ , is not directly known. However, it can be directly observed by a gravimeter if access to  $\rho_o$  is possible, which is usually the case in our application.

**Second order approximation using GSK algorithm.** In the case when Equation 3.191 is expanded up to second order, the inverse function  $f^{-1}$  is more complicated to be found. In *Grafarend et al. (1996)* an algorithm (GKS) for computing the approximate inverse function of a univariate polynomial of degree  $n$  which passes through the origin<sup>36</sup> can be found. In *Grafarend et al. (1999)* and *Ardalan and Grafarend (2001)* the GSK algorithm is applied to the formulation of an ellipsoidal and a spheroidal Brun's transformation. For a simple second order polynomial given by:

$$f(x) = a_1 \cdot x + a_2 \cdot x^2 \quad (3.197)$$

the GSK algorithm provides an approximate inverse function:

$$x_{\text{GSK}}(f) = -a_1^{-1} \cdot f + a_1^{-3} a_2 \cdot f^2 \quad (3.198)$$

which has the advantage to be a simple polynomial of second order. Applied to Equation 3.191 gives:

$$f^{-1}(N_{\text{tot}}) = N_{\text{tot}}(f) = A^{-1} \cdot f - A^{-3} B \cdot f^2 + \mathcal{O}(f^3) \quad (3.199)$$

and by replacing the coefficients using Equations 3.187 and 3.192 we get:

$$\begin{aligned} N_{\text{tot}}^{\text{2nd,GSK}}(\rho_o) &= \frac{T_{\text{tot}}(\rho_o) + \Phi_{\text{tidal}}(\rho_o)}{|\mathbf{g}_{\text{tot}}(\rho_o)|} \\ &+ \frac{\mathbf{g}_{\text{tot}}(\rho_o)^T \cdot \mathbf{\Gamma}_{\text{tot}}(\rho_o) \cdot \mathbf{g}_{\text{tot}}(\rho_o)}{2 \cdot |\mathbf{g}_{\text{tot}}(\rho_o)|^5} \cdot [T_{\text{tot}}(\rho_o) + \Phi_{\text{tidal}}(\rho_o)]^2 \\ &+ \mathcal{O}(N_{\text{tot}}^3) \end{aligned} \quad (3.200)$$

**Second order approximation using the exact inverse function.** The exact inverse function of a second order polynomial can be found using the analytic solution of the second order polynomial equation. Equation 3.191 can be written as follows:

$$A \cdot N_{\text{tot}} + B \cdot N_{\text{tot}}^2 - f(N_{\text{tot}}) + \mathcal{O}(N_{\text{tot}}^3) = 0 \quad (3.201)$$

where the solution for  $N_{\text{tot}}$ , which vanishes for  $f = 0$  (since  $-A$  is always positive) is given by:

$$N_{\text{tot}} = \frac{-A - \sqrt{A^2 - 4B \cdot (-f)}}{2B} \quad (3.202)$$

and by replacing the coefficients using Equations 3.187 and 3.192 we get:

$$\begin{aligned} N_{\text{tot}}^{\text{2nd}}(\rho_o) &= \frac{|\mathbf{g}_{\text{tot}}(\rho_o)|^2}{\mathbf{g}_{\text{tot}}(\rho_o)^T \cdot \mathbf{\Gamma}_{\text{tot}}(\rho_o) \cdot \mathbf{g}_{\text{tot}}(\rho_o)} \cdot \left\{ |\mathbf{g}_{\text{tot}}(\rho_o)| \right. \\ &\quad \left. - \sqrt{|\mathbf{g}_{\text{tot}}(\rho_o)|^2 - \frac{2}{|\mathbf{g}_{\text{tot}}(\rho_o)|^2} \cdot \mathbf{g}_{\text{tot}}(\rho_o)^T \cdot \mathbf{\Gamma}_{\text{tot}}(\rho_o) \cdot \mathbf{g}_{\text{tot}}(\rho_o) \cdot [T_{\text{tot}}(\rho_o) + \Phi_{\text{tidal}}(\rho_o)]} \right\} \\ &+ \mathcal{O}(N_{\text{tot}}^3) \end{aligned} \quad (3.203)$$

<sup>36</sup>In *Grafarend et al. (1996)* such polynomials are clumsily called homogeneous. From a mathematical point of view, a homogeneous polynomial, is a polynomial, where all non-zero terms have the same degree.

**Second order omission error.** An empirical estimation of the omission error due to the second order term is computed in order to see up to which level of accuracy the first order approximation is sufficient. In addition, the differences between the solution provided by the GSK algorithm and the exact formula are shown in Figure 3.18 and Table 3.6. This is done by applying Equations 3.195, 3.200 and 3.203 with the following values given in the local topocentric system:

$$\boldsymbol{\rho}_o = \begin{pmatrix} \lambda = 0 \text{ [deg]} \\ \varphi = 45 \text{ [deg]} \\ h = 0 \text{ [m]} \end{pmatrix} \quad \mathbf{g}_{\text{tot}}^{\text{Topo}}(\boldsymbol{\rho}_o) = \begin{pmatrix} 0 \\ 0 \\ -9.81 \end{pmatrix} \left[ \frac{\text{m}}{\text{s}^2} \right] \quad (3.204)$$

$$\boldsymbol{\Gamma}_{\text{tot}}^{\text{Topo}}(\boldsymbol{\rho}_o) = \begin{pmatrix} -1540 & 0 & 8.1 \cdot \sin 2\varphi \\ 0 & -1540 + 10.4 \cdot \cos^2 \varphi & 0 \\ 8.1 \cdot \sin 2\varphi & 0 & 3086 \end{pmatrix} \cdot 10^{-9} \left[ \frac{1}{\text{s}^2} \right] \quad (3.205)$$

These are approximate values provided by the normal gravity field, see *Torge* (1989). Concerning the disturbing potential, the values are chosen as follows:

$$T_{\text{tot}}(\boldsymbol{\rho}_o) + \Phi_{\text{tidal}}(\boldsymbol{\rho}_o) = [-1000, \dots, +1000] \left[ \frac{\text{m}^2}{\text{s}^2} \right] \quad (3.206)$$

This represents values to be expected on the surface of the Earth.

**Table 3.6:** First order and second order geometrical separation of equipotential surface. They are computed for various disturbing potential values and a given normal ellipsoidal potential.

$T_{\text{tot}} + \Phi_{\text{tidal}}$ $\left[ \frac{\text{m}^2}{\text{s}^2} \right]$	$N_{\text{tot}}^{\text{1st}}$ [m]	$N_{\text{tot}}^{\text{2nd}}$ [m]	$N_{\text{tot}}^{\text{2nd,GSK}}$ [m]	$N_{\text{tot}}^{\text{2nd}} - N_{\text{tot}}^{\text{1st}}$ [μm]	$N_{\text{tot}}^{\text{2nd}} - N_{\text{tot}}^{\text{2nd,GSK}}$ [nm]
0.000000	0.000000	0.000000	0.000000	0.0000	0.0000
9.809998	1.000000	1.000000	1.000000	0.1573	0.0000
19.619994	1.999999	2.000000	2.000000	0.6292	0.0004
29.429986	2.999999	3.000000	3.000000	1.4156	0.0013
39.239975	3.999997	4.000000	4.000000	2.5166	0.0032
49.049961	4.999996	5.000000	5.000000	3.9322	0.0062
98.099846	9.999984	10.000000	10.000000	15.7288	0.0495
196.199383	19.999937	20.000000	20.000000	62.9154	0.3958
294.298611	29.999858	30.000000	30.000000	141.5596	1.3359
392.397531	39.999748	40.000000	40.000000	251.6616	3.1667
490.496143	49.999607	50.000000	50.000000	393.2212	6.1849
980.984570	99.998427	100.000000	100.000000	1572.8848	49.4790

**Remarks.** Firstly, we can conclude that, for any point on the Earth, the differences between the exact second order (equation 3.203) and the GSK second order approximation algorithms (equation 3.200) give the same results at the μm level. This permits us to use,

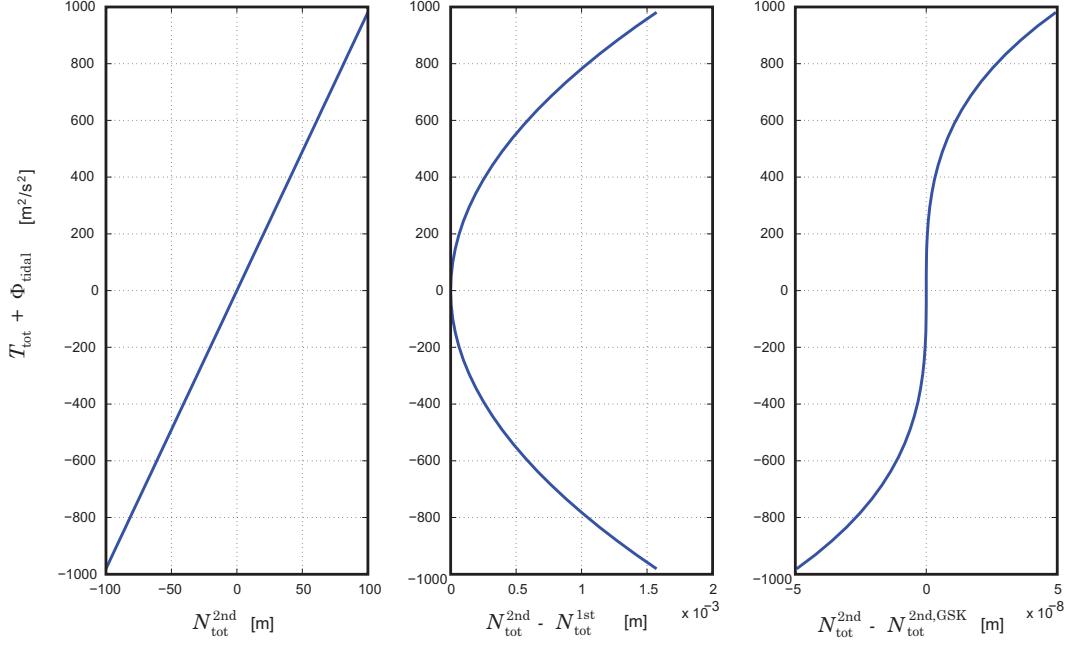


**Figure 3.18:** (Left) geometrical separation of equipotential surface  $N_{\text{tot}}^{2\text{nd}}$  in terms of the disturbing potential computed with the exact second order approximation (see Equation 3.203). (Middle) second order omission error  $N_{\text{tot}}^{2\text{nd}} - N_{\text{tot}}^{1\text{st}}$  (see Equations 3.203 and 3.195). (Right) difference between the exact second order approximation (Equation 3.203) and the GSK second order approximation (see Equation 3.200).

without restriction, the more convenient GSK algorithm.

Secondly, the difference between the second and the first order approximation reaches  $1 \mu\text{m}$  for a disturbing potential of  $T_{\text{tot}} + \Phi_{\text{tidal}} \sim 25 \frac{\text{m}^2}{\text{s}^2}$  or for a geometrical separation of  $N_{\text{tot}}^{2\text{nd}} \sim 2.5 \text{ m}$ .

The main contributor of the second order correction term is the gravity gradient tensor  $\mathbf{\Gamma}_{\text{tot}}$  which contributes in a linear manner. If a local topocentric system is chosen, only the vertical gravity gradient  $\frac{\partial g_z}{\partial z} \sim 3086 \cdot 10^{-9} \frac{1}{\text{s}^2}$  is concerned. In extreme situations, if we assume that  $\frac{\partial g_z}{\partial z}$  could have variations in the order of  $\sim 3000 \cdot 10^{-9} \frac{1}{\text{s}^2}$ , the second order corrections would exceed  $1 \mu\text{m}$  for disturbing potentials larger than  $\sim 12.5 \frac{\text{m}^2}{\text{s}^2}$  or for geometrical separations larger than  $\sim 1.25 \text{ m}$ .

From these findings and regarding the aim of the alignment performance of CLIC, we can assume that the geometrical variations — or the geoid undulation — over some hundred meters will be smaller than one meter and this allows us to consider that the first order approximations given by Equations 3.195 and 3.196 are precise enough.

### Synthesis Formulas

Lastly, according to Equation 3.195, the geometrical separation  $N_{\text{tot}}(t)$  can be approximated — with enough accuracy by:

$$N_{\text{tot}}(t) = \frac{T_{\text{tot}}(\boldsymbol{\rho}_o, t) + \Phi_{\text{tidal}}(\boldsymbol{\rho}_o, t)}{|\mathbf{g}_{\text{tot}}(\boldsymbol{\rho}_o, t)|} \quad (3.207)$$

or, combined with Equation 3.176, by

$$N_{\text{tot}}(t) = \frac{T_{\text{st}}(\boldsymbol{\rho}_o)}{|\mathbf{g}_{\text{tot}}(\boldsymbol{\rho}_o, t)|} + \frac{T_{\text{dyn}}(\boldsymbol{\rho}_o, t)}{|\mathbf{g}_{\text{tot}}(\boldsymbol{\rho}_o, t)|} + \frac{\Phi_{\text{tidal}}(\boldsymbol{\rho}_o, t)}{|\mathbf{g}_{\text{tot}}(\boldsymbol{\rho}_o, t)|} \quad (3.208)$$

and introducing equation 3.177, we find:

$$N_{\text{tot}}(t) = \frac{\Phi_{\text{grav,st}}(\boldsymbol{\rho}_o)}{|\mathbf{g}_{\text{tot}}(\boldsymbol{\rho}_o, t)|} + \frac{\Phi_{\text{grav,dyn}}(\boldsymbol{\rho}_o, t)}{|\mathbf{g}_{\text{tot}}(\boldsymbol{\rho}_o, t)|} + \frac{\delta\Phi_{\text{centr}}(\boldsymbol{\rho}_o, t)}{|\mathbf{g}_{\text{tot}}(\boldsymbol{\rho}_o, t)|} + \frac{\Phi_{\text{tidal}}(\boldsymbol{\rho}_o, t)}{|\mathbf{g}_{\text{tot}}(\boldsymbol{\rho}_o, t)|} \quad (3.209)$$

which can also be written as:

$$N_{\text{tot}}(t) = N_{\text{grav,st}}(t) + N_{\text{grav,dyn}}(t) + \delta N_{\text{centr}}(t) + N_{\text{tidal}}(t) \quad (3.210)$$

By looking at Equations 3.209 and 3.210, it is remarkable that even if the different phenomena are properly splitted in terms of potentials, there still remains a dependence on a non-splitted total quantity,  $|\mathbf{g}_{\text{tot}}(\boldsymbol{\rho}_o, t)|$ . The consequence of a variation of  $|\mathbf{g}_{\text{tot}}(\boldsymbol{\rho}_o, t)|$ , noted  $\delta g_{\text{tot}}$  on a particular  $N_i$ , is given by:

$$\begin{aligned} \delta N_i &= \frac{\partial}{\partial |\mathbf{g}_{\text{tot}}|} \left( \frac{\Phi_i}{|\mathbf{g}_{\text{tot}}|} \right) \cdot \delta g_{\text{tot}} \\ &= - \frac{\Phi_i}{|\mathbf{g}_{\text{tot}}|^2} \cdot \delta g_{\text{tot}} \\ [\text{m}] &\approx - \frac{\Phi_i \left[ \frac{\text{m}^2}{\text{s}^2} \right]}{100 \left[ \frac{\text{m}^2}{\text{s}^4} \right]} \cdot \delta g_{\text{tot}} \left[ \frac{\text{m}}{\text{s}^2} \right] \end{aligned} \quad (3.211)$$

This relation can be used to compute the order of magnitude of acceptable spatio-temporal changes in  $|\mathbf{g}_{\text{tot}}|$  for micrometric relative precision. With the perspective of the determination of a 200 m profile, it is reasonable to expect a maximal total variation of  $N_{\text{tot}}$  smaller than 0.1 m, or equivalently, total variations of  $\Phi_{\text{tot}}$  smaller than  $1.0 \frac{\text{m}^2}{\text{s}^2}$ . Thus, setting  $\delta N_{\text{tot}} \leq 1 \cdot 10^{-6}$  m, we have:

$$\delta g_{\text{tot}} \leq \frac{\delta N_{\text{tot}} \cdot 100}{\Delta \Phi_{\text{tot}}} = \frac{1 \cdot 10^{-6} \cdot 100}{1.0} = 1 \cdot 10^{-4} \left[ \frac{\text{m}}{\text{s}^2} \right] = 10 [\text{mgal}] \quad (3.212)$$

Concerning the largest time-varying part of  $|\mathbf{g}_{\text{tot}}(\boldsymbol{\rho}_o, t)|$ , generated by Earth's tides, of approximately 0.3 [mgal], we can consider the denominators of Equations 3.207, 3.208 and 3.209 as time-invariant and Equation 3.210 can be rewritten as:

$$N_{\text{tot}}(t) = N_{\text{grav,st}} + N_{\text{grav,dyn}}(t) + \delta N_{\text{centr}}(t) + N_{\text{tidal}}(t) \quad (3.213)$$

where the first term  $N_{\text{grav,st}}$  can be considered as stationary.



## Chapter 4

# Determination of Equipotential Surfaces

### 4.1 Introduction

In Section 3.8, it has been shown how to compute rigorously the position vectors  $\boldsymbol{\rho}_{\sim}$  of an equipotential if the total disturbing potential  $T_{\text{tot}}$  is given. In general, we cannot assume that  $T_{\text{tot}}$  can be computed directly. In particular, the most important term,  $T_{\text{st}}$ , which contains the gravitational part of the static mean density field  $\rho_{\text{st}}$ , has to be known. This is not the case usually with respect to the level of precision we are looking for in local gravity field determinations. Therefore, it is necessary to determine the gravity equipotential surface indirectly through gravity observables.

#### 4.1.1 Direct Observation of the Geometry of Equipotentials

In order to determine  $\boldsymbol{\rho}_{\sim}$ , the most direct observable we could imagine is available, if the equipotential surface is somehow materialized and accessible to a geometrical positioning system. Here it is important to understand that the positioning system must be independent of the knowledge of the gravity field. A good and simple example is provided by the observation of sea and ocean surfaces by satellite or airborne altimetry. Once the dynamical effects of the water current etc. are reduced, the surfaces of oceans and seas are direct realizations of  $\boldsymbol{\rho}_{\sim}$ , at sea level, and the positioning system is given by the combination of range measurements between the surface of water and a satellite, and GNSS<sup>1</sup>/SLR<sup>2</sup> positioning for the determination of the orbit of the satellite itself, see *Limpach* (2009).

In a similar way, the combination of measurements provided by a Hydrostatic Measurement System (HLS) and a geometric positioning system gives also a direct access to  $\boldsymbol{\rho}_{\sim}$ . Nowadays, the limiting factor is by far due to insufficient long range geometrical positioning systems. In fact, while highly precise HLS systems are capable to provide micrometric accuracies, differential GNSS positioning is still limited to the cm accuracy in height<sup>3</sup>. Concerning underground facilities, different positioning techniques are conceivable but are

---

<sup>1</sup>Global Navigation Satellite System.

<sup>2</sup>Satellite Laser Ranging.

<sup>3</sup>for applications on the Earth's surface

still in experimental phase. Two classes of systems can be mentioned. Firstly there are systems based on laser beams (*Griffith*, 1989) or x-ray beams (*Yang and Friedsam*, 2006), and secondly, systems based on a mechanical reference like Wire Positioning Systems (*Touzé*, 2011). In practice, the absolute geometrical positioning (at micrometric level) provided by these systems is not guaranteed over distances larger than a few tens of meters, see *Touzé* (2011) and *Stern et al.* (2013). In order to reach micrometric accuracies, some difficulties have to be overcome: on the one hand, there is the necessity to make the beams propagating in vacuum and on the other hand the knowledge of the tension in the wires and variations of humidity content in air in the vicinity of the wire have to be tackled. Nevertheless, improvements of these positioning techniques could have a decisive positive impact on the determination of short-wave gravity equipotential surfaces.

Finally, there is an additional way, speculative for the moment, to realize the locus of equipotentials at arbitrary positions. In fact, since *Einstein* (1916), we know that the proper time  $\tau_1$  and  $\tau_2$  of two observers 1 and 2 at positions  $\boldsymbol{\rho}_1$  and  $\boldsymbol{\rho}_2$  (with no relative velocities) are directly related to their gravitational potential difference by (*Mai*, 2013):

$$\frac{d\tau_2}{d\tau_1} \approx 1 - \frac{\Phi_{\text{grav}}(\boldsymbol{\rho}_2) - \Phi_{\text{grav}}(\boldsymbol{\rho}_1)}{c^2} \quad (4.1)$$

or in terms of relative proper frequency  $f_1$  and  $f_2$  we have:

$$\frac{f_2 - f_1}{f_1} \approx \frac{\Phi_{\text{grav}}(\boldsymbol{\rho}_2) - \Phi_{\text{grav}}(\boldsymbol{\rho}_1)}{c^2} \quad (4.2)$$

where  $c$  is the speed of light. This means that it is theoretically possible to observe directly relative gravitational potential differences by comparing clock rates. According to Equation 4.2, it can be shown that the potential difference corresponding to an orthometric height difference of  $\Delta H = 1$  cm, corresponds to a relative change in proper frequency of approximately  $\frac{f_2 - f_1}{f_1} \approx 1 \cdot 10^{-18}$ . Nowadays, according to *Hinkley et al.* (2013), optical clocks in laboratories are capable of measuring relative frequencies with an accuracy of  $1.6 \cdot 10^{-18}$  by averaging 7 hours of observations. This opens very interesting possibilities for global geoid determination and worldwide height system unification, but will probably stay of limited practical interest for sub-millimeter local applications for a long time.

#### 4.1.2 Determination of Equipotential Surfaces from Gravity Observables

Since the very beginning of the era of physical geodesy, the most common and precise ways to determine the geometry of equipotential surfaces are based on gravity field observables. Here we will distinguish two classes of determination, the *Geodetic Boundary Value Problem* and the *Geometric Solution*.

##### Geodetic Boundary Value Problem

If the objective is to determine the complete gravity potential field  $\Phi_{\text{tot}}$ , it is necessary to solve the *Laplace equation*, with the observations defining the boundary conditions. Mathematically, it corresponds to solving a non-linear elliptic boundary value problem. In geodesy, the problem is usually restricted to the determination of the field outside a certain



boundary which is supposed to enclose all masses. This class of problems is also called the Geodetic Boundary Value Problem (GBVP) and consisting the determination of both the geometry of the boundary surface and the external gravity potential field itself (*Torge and Müller, 2012*).

In order to solve such kind of non-linear problems, the first step consists always in linearizing the gravity field and the geometry of the boundary. Then, several methods are given to find the solution. In history, the first approach is the *Green's method* which leads to *Stokes-like* surface integral formulas which convolve an appropriate Green's Kernel with the boundary values given by the observations. Later, we will find the *method of separation of variables* which results in decomposing the field in spherical harmonics series where the unknown coefficients must be estimated in order to fulfill the boundary conditions given by the observations.

In short, the determination of the geometry of equipotential surfaces based on the GBVP is based on some restrictive assumptions. In order to fulfill the Laplace equation, it is assumed that no masses are located outside the chosen boundary (e.g. the geoid) and that observations are provided on the whole boundary surface (on the whole Earth's surface).

### Geometric Solution

If the objective is to determine the geometry of a certain equipotential surface in a limited region in space, it is not necessary to formulate the GBVP anymore, followed by the restrictive assumptions. In fact, we just need to formulate Brun's equation as a function of appropriate observables (e.g. deflection of the vertical or horizontal gradiometric components) and integrate them along a given path on the surface of reference. Here, we use the intrinsic geometric properties of these observables in a very direct and straightforward way, without worrying about the gravity potential field itself. The *astronomical levelling* (see Figure 4.1) is the most symbolic example of this class of determination.

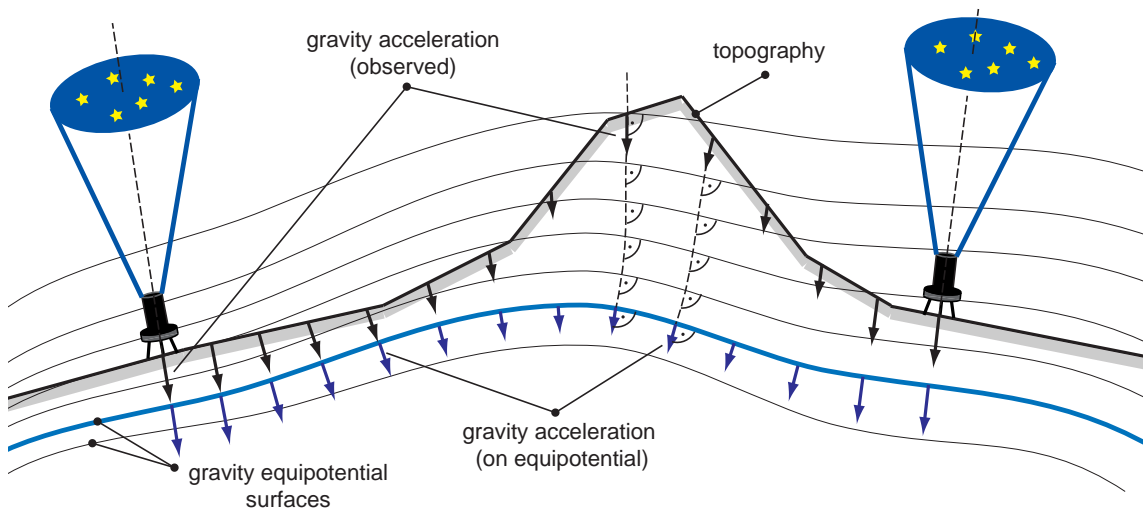


**Figure 4.1:** Astronomical levelling.

## 4.2 Gravity Observables

Here we call gravity field observables the spatial derivatives of the apparent gravity potential  $\Phi_{\text{tot}}$  or linear combination of them. Today, all components of the first and second order spatial derivatives can be directly observed.

### 4.2.1 First order observables

The first derivative — or the gradient — of the apparent gravity potential is the gravity vector:

$$\begin{aligned}\nabla\Phi_{\text{tot}}(\boldsymbol{\rho}) &= \mathbf{g}_{\text{tot}}(\boldsymbol{\rho}) \\ &= g_{\text{tot}}(\boldsymbol{\rho}) \cdot \mathbf{e}_{\mathbf{g}_{\text{tot}}}(\boldsymbol{\rho}) \\ &= \left( \begin{array}{c} \frac{\partial\Phi_{\text{tot}}}{\partial x} \\ \frac{\partial\Phi_{\text{tot}}}{\partial y} \\ \frac{\partial\Phi_{\text{tot}}}{\partial z} \end{array} \right) \bigg|_{\boldsymbol{\rho}}\end{aligned}\tag{4.3}$$

where its module  $g_{\text{tot}}$  can be measured directly by absolute gravimeters or indirectly by relative gravimeters. Its direction  $\mathbf{e}_{\mathbf{g}_{\text{tot}}}$  can be obtained by astrogeodetic observations. In ITRS,  $\mathbf{e}_{\mathbf{g}_{\text{tot}}}$  is given as a function of the astronomical latitude and longitude  $(\Phi, \Lambda)^{\text{ITRS}}$  by:

$$\mathbf{e}_{\mathbf{g}_{\text{tot}}}^{\text{ITRS}}(\boldsymbol{\rho}) = - \left( \begin{array}{c} \cos \Phi \cos \Lambda \\ \cos \Phi \sin \Lambda \\ \sin \Phi \end{array} \right) \bigg|_{\boldsymbol{\rho}}\tag{4.4}$$

Nowadays, the accuracy achieved by absolute and relative gravimeters is in the vicinity of  $2 - 3 \mu\text{gal}$  in the best cases and  $0.07 - 0.08$  arcsec for the astrogeodetic observations.

### 4.2.2 Second order observables

The second derivative is obtained by taking the gradient of  $\mathbf{g}_{\text{tot}}$ , called the gravity gradient tensor:

$$\begin{aligned}\nabla\mathbf{g}_{\text{tot}}(\boldsymbol{\rho}) &= \boldsymbol{\Gamma}_{\text{tot}}(\boldsymbol{\rho}) \\ &= \left( \begin{array}{ccc} \frac{\partial^2\Phi_{\text{tot}}}{\partial x^2} & \frac{\partial^2\Phi_{\text{tot}}}{\partial x\partial y} & \frac{\partial^2\Phi_{\text{tot}}}{\partial x\partial z} \\ \frac{\partial^2\Phi_{\text{tot}}}{\partial y\partial x} & \frac{\partial^2\Phi_{\text{tot}}}{\partial y^2} & \frac{\partial^2\Phi_{\text{tot}}}{\partial y\partial z} \\ \frac{\partial^2\Phi_{\text{tot}}}{\partial z\partial x} & \frac{\partial^2\Phi_{\text{tot}}}{\partial z\partial y} & \frac{\partial^2\Phi_{\text{tot}}}{\partial z^2} \end{array} \right) \bigg|_{\boldsymbol{\rho}} \\ &= \left( \begin{array}{ccc} \Gamma_{\text{tot},xx} & \Gamma_{\text{tot},xy} & \Gamma_{\text{tot},xz} \\ \Gamma_{\text{tot},yx} & \Gamma_{\text{tot},yy} & \Gamma_{\text{tot},yz} \\ \Gamma_{\text{tot},zx} & \Gamma_{\text{tot},zy} & \Gamma_{\text{tot},zz} \end{array} \right) \bigg|_{\boldsymbol{\rho}}\end{aligned}\tag{4.5}$$

which is called *Eötvös tensor* if it is expressed in the local topocentric system. Furthermore, when the *Eötvös tensor* is normalised by  $g_{\text{tot}}$ , it is called the *Marussi tensor*, see *Torge and Müller (2012)*. It can be represented by a  $3 \times 3$  symmetric matrix, where only five elements are independent<sup>4</sup>.

In the literature we can find several gradiometers in use since 100 years (*Jekeli, 2011*). However, we can distinguish two principal classes of gradiometer designs. Historically the torsion balance developed by *Lorand Eötvös*<sup>5</sup> represents the first class. This kind of gradiometer does not have access to all components of  $\mathbf{\Gamma}_{\text{tot}}$ , but only to the following one:

$$\Gamma_{\text{tot},yy}^{\text{Topo}} - \Gamma_{\text{tot},xx}^{\text{Topo}}, \quad \Gamma_{\text{tot},xy}^{\text{Topo}}, \quad \Gamma_{\text{tot},xz}^{\text{Topo}}, \quad \Gamma_{\text{tot},yz}^{\text{Topo}} \quad (4.6)$$

if the components are given in the local topocentric system. In other words, no diagonal elements can be directly measured with a torsion balance. However, if  $\Gamma_{\text{tot},zz}^{\text{Topo}}$  is observed by an other method (e.g. with a gravimeter), if the density  $\rho$  at the station is known (e.g. in the air at  $20^\circ$ ,  $\rho \approx 1.204 \frac{\text{kg}}{\text{m}^3}$ ), and finally if we assume that the Laplacian of the centrifugal  $\Delta\Phi_{\text{centr}}$  and tidal potential  $\Delta\Phi_{\text{tidal}}$  can be well predicted, the diagonal elements are given by:

$$\underbrace{\begin{pmatrix} \Gamma_{\text{tot},yy}^{\text{Topo}} - \Gamma_{\text{tot},xx}^{\text{Topo}} \\ \Gamma_{\text{tot},zz}^{\text{Topo}} \\ -4\pi G\rho + \Delta\Phi_{\text{centr}} + \Delta\Phi_{\text{tidal}} \end{pmatrix}}_{\text{observed}} = \begin{pmatrix} -1 & +1 & 0 \\ 0 & 0 & +1 \\ +1 & +1 & +1 \end{pmatrix} \cdot \begin{pmatrix} \Gamma_{\text{tot},xx}^{\text{Topo}} \\ \Gamma_{\text{tot},yy}^{\text{Topo}} \\ \Gamma_{\text{tot},zz}^{\text{Topo}} \end{pmatrix} \quad (4.7)$$

and can be found by:

$$\begin{aligned} \begin{pmatrix} \Gamma_{\text{tot},xx}^{\text{Topo}} \\ \Gamma_{\text{tot},yy}^{\text{Topo}} \\ \Gamma_{\text{tot},zz}^{\text{Topo}} \end{pmatrix} &= \begin{pmatrix} -1 & +1 & 0 \\ 0 & 0 & +1 \\ +1 & +1 & +1 \end{pmatrix}^{-1} \cdot \begin{pmatrix} \Gamma_{\text{tot},yy}^{\text{Topo}} - \Gamma_{\text{tot},xx}^{\text{Topo}} \\ \Gamma_{\text{tot},zz}^{\text{Topo}} \\ -4\pi G\rho + \Delta\Phi_{\text{centr}} + \Delta\Phi_{\text{tidal}} \end{pmatrix} \\ &= \begin{pmatrix} +\frac{1}{2} & -\frac{1}{2} & +\frac{1}{2} \\ -\frac{1}{2} & -\frac{1}{2} & +\frac{1}{2} \\ 0 & +1 & 0 \end{pmatrix} \cdot \begin{pmatrix} \Gamma_{\text{tot},yy}^{\text{Topo}} - \Gamma_{\text{tot},xx}^{\text{Topo}} \\ \Gamma_{\text{tot},zz}^{\text{Topo}} \\ -4\pi G\rho + \Delta\Phi_{\text{centr}} + \Delta\Phi_{\text{tidal}} \end{pmatrix} \end{aligned} \quad (4.8)$$

Using Equation 4.8, it is easy to find the sensitivity of the estimated diagonal elements with respect to the observed quantities.

- An error in the density of  $\delta\rho = +1.0 \frac{\text{kg}}{\text{m}^3}$  produces a error of  $+0.4 \text{ E}^6$  in the estimation of  $\Gamma_{\text{tot},xx}^{\text{Topo}}$  and  $\Gamma_{\text{tot},yy}^{\text{Topo}}$ .

<sup>4</sup>The gravity gradient tensor is symmetric if the Euler term can be neglected.

<sup>5</sup>Lorand Eötvös, 1848-1919, Hungarian physicist.

<sup>6</sup>In geodesy, the common unit used for gradiometric quantities is represented by E and called eotvos and defined as  $1 \text{ E} = 1 \cdot 10^{-9} \text{ s}^{-2}$ .

- An error in the vertical gradient of  $\delta\Gamma_{\text{tot},zz}^{\text{Topo}} = +3.0 \frac{\mu\text{gal}}{\text{m}} = +30.0 \text{ E}$  produces an error of  $-15.0 \text{ E}$  in  $\Gamma_{\text{tot},xx}^{\text{Topo}}$  and  $\Gamma_{\text{tot},yy}^{\text{Topo}}$ .
- An error in the differential curvature element of  $\delta(\Gamma_{\text{tot},yy}^{\text{Topo}} - \Gamma_{\text{tot},xx}^{\text{Topo}}) = +1.0 \text{ E}$  produces an error of  $+0.5 \text{ E}$  in  $\Gamma_{\text{tot},xx}^{\text{Topo}}$  and  $-0.5 \text{ E}$  in  $\Gamma_{\text{tot},yy}^{\text{Topo}}$ .

The second class of gradiometer design is based on differential linear accelerator measurements and can observe all components of  $\mathbf{\Gamma}_{\text{tot}}$ . The principle is simple in theory but very complicated to realize in practice. It consists in juxtaposing linear accelerometers in their sensing direction and in approximating the gradient by taking the difference and dividing by the baseline length. Nowadays, there is no commercial system available for terrestrial gradiometry and there exist just a few systems for airborne or ship-borne platforms (*Jekeli, 2007*). The accuracy in terms of white noise is announced at approximately  $1.0 \frac{\text{E}}{\sqrt{\text{Hz}}}$ . This corresponds approximately to the accuracy achieved by a stationary torsion balance but with an acquisition rate of 3-6 hours per station instead of a few tens of seconds integration time (*Jekeli, 2007*).

### 4.3 Solutions for the Geometrical Determination

The geometrical determination of equipotential profiles consists in deriving a formula which permits the determination of the difference of the geometrical separation:

$$\Delta N_{\text{tot}} \mathbf{b}_o = N_{\text{tot}}(\mathbf{b}_o) - N_{\text{tot}}(\mathbf{a}_o) \quad (4.9)$$

between two points  $\mathbf{a}_o$  and  $\mathbf{b}_o$  which are elements of the set of the positions on the reference equipotential surface:

$$\mathbf{a}_o, \mathbf{b}_o \in \{\rho_o\} \quad (4.10)$$

The way to find the formula is straightforward. We just have to define a path  $\mathcal{S} \in \{\rho_o\}$  between  $\mathbf{a}_o$  and  $\mathbf{b}_o$ , associated with its differential element  $d\mathbf{s}$ , determine the differential change  $dN_{\text{tot}}$  as a function of the observables when we increment  $d\mathbf{s}$ , and finally integrate over  $\mathcal{S}$ . If we define:

$$\epsilon_{\text{tot}} = -\frac{dN_{\text{tot}}(\rho_o)}{|d\mathbf{s}|} = -\frac{dN_{\text{tot}}(\rho_o)}{ds} \quad (4.11)$$

where the minus sign is included by convention, we have:

$$\Delta N_{\text{tot}} \mathbf{b}_o = -\int_{\mathbf{a}_o}^{\mathbf{b}_o} \epsilon_{\text{tot}} \cdot d\mathbf{s} \quad (4.12)$$

where  $\epsilon_{\text{tot}}$  represents the variation of  $N_{\text{tot}}$  along  $\mathcal{S}$  and at this step, we do not know how it is linked to the observations. Now we have to find:

$$\epsilon_{\text{tot}}(\mathbf{g}_{\text{tot}}, \mathbf{\Gamma}_{\text{tot}}) \quad (4.13)$$

#### 4.3.1 Oriented Normal System

The computation of  $\epsilon_{\text{tot}}$  is simplified when the components of the different vectors are given in the oriented normal system. Its origin is defined at position  $\rho_o$ , with the  $\mathbf{e}_z^S$  basis vector in the opposite direction of the normal gravity vector  $\boldsymbol{\gamma}$  given at position  $\rho_o$ . The basis vector  $\mathbf{e}_x^S$  is colinear with  $d\mathbf{s}$  and  $\mathbf{e}_y^S$  perpendicular to  $\mathbf{e}_x^S$  and  $\mathbf{e}_z^S$ .

### Transformation from ITRS to the Oriented Normal System

Given the geodetic latitude and longitude  $(\varphi, \lambda)^{\text{ITRS}}$  of the position  $\boldsymbol{\rho}_o$  and  $d\mathbf{s}$  which is pointing in the direction of the ellipsoidal azimuth  $\alpha$ , the transformation of a vector  $\mathbf{v}^{\text{ITRS}}$  and a tensor  $\mathbf{V}^{\text{ITRS}}$ , given in ITRS, into the oriented normal system is given by:

$$\mathbf{v}^{\mathcal{S}} = \mathbf{S}_{\text{ITRS}}^{\mathcal{S}} \cdot \mathbf{v}^{\text{ITRS}} \quad (4.14)$$

and:

$$\mathbf{V}^{\mathcal{S}} = \mathbf{S}_{\text{ITRS}}^{\mathcal{S}} \cdot \mathbf{V}^{\text{ITRS}} \cdot \mathbf{S}_{\text{ITRS}}^{\mathcal{S}^T} \quad (4.15)$$

with:

$$\mathbf{S}_{\text{ITRS}}^{\mathcal{S}} = \mathbf{R}_3(\alpha) \cdot \mathbf{T}(\varphi, \lambda) \quad (4.16)$$

where:

$$\mathbf{R}_3(\alpha) = \begin{pmatrix} \cos \alpha & \sin \alpha & 0 \\ -\sin \alpha & \cos \alpha & 0 \\ 0 & 0 & 1 \end{pmatrix}, \quad \mathbf{T}(\varphi, \lambda) = \begin{pmatrix} -\sin \varphi \cos \lambda & -\sin \varphi \sin \lambda & \cos \varphi \\ -\sin \lambda & \cos \lambda & 0 \\ \cos \varphi \cos \lambda & \cos \varphi \sin \lambda & \sin \varphi \end{pmatrix} \quad (4.17)$$

### 4.3.2 Oriented Topocentric System

The oriented topocentric system is defined as follows. Its origin is defined at an arbitrary position  $\boldsymbol{\rho}$ , with the  $\mathbf{e}_z^{\mathcal{G}}$  basis vector in the opposite direction of the gravity vector  $\mathbf{g}_{\text{tot}}$  given at position  $\boldsymbol{\rho}$ . The basis vector  $\mathbf{e}_x^{\mathcal{G}}$  is colinear with  $d\mathbf{s}$  and  $\mathbf{e}_y^{\mathcal{G}}$  perpendicular to  $\mathbf{e}_x^{\mathcal{G}}$  and  $\mathbf{e}_z^{\mathcal{G}}$ .

### Transformation from ITRS to the Oriented Topocentric System

Given the geodetic astronomical latitude and longitude  $(\Phi, \Lambda)^{\text{ITRS}}$  of the position  $\boldsymbol{\rho}$  and  $d\mathbf{s}$  which is pointing into the direction of the astronomical azimuth  $A$ , the transformation of a vector  $\mathbf{v}^{\text{ITRS}}$  and a tensor  $\mathbf{V}^{\text{ITRS}}$ , given in the ITRS, into the local topocentric system is given by:

$$\mathbf{v}^{\mathcal{G}} = \mathbf{S}_{\text{ITRS}}^{\mathcal{G}} \cdot \mathbf{v}^{\text{ITRS}} \quad (4.18)$$

and:

$$\mathbf{V}^{\mathcal{G}} = \mathbf{S}_{\text{ITRS}}^{\mathcal{G}} \cdot \mathbf{V}^{\text{ITRS}} \cdot \mathbf{S}_{\text{ITRS}}^{\mathcal{G}^T} \quad (4.19)$$

with:

$$\mathbf{S}_{\text{ITRS}}^{\mathcal{G}} = \mathbf{R}_3(A) \cdot \mathbf{T}(\Phi, \Lambda) \quad (4.20)$$

where:

$$\mathbf{R}_3(A) = \begin{pmatrix} \cos A & \sin A & 0 \\ -\sin A & \cos A & 0 \\ 0 & 0 & 1 \end{pmatrix}, \quad \mathbf{T}(\Phi, \Lambda) = \begin{pmatrix} -\sin \Phi \cos \Lambda & -\sin \Phi \sin \Lambda & \cos \Phi \\ -\sin \Lambda & \cos \Lambda & 0 \\ \cos \Phi \cos \Lambda & \cos \Phi \sin \Lambda & \sin \Phi \end{pmatrix} \quad (4.21)$$

### 4.3.3 Gravity Vectors and Gradiometric Tensors in the Oriented Normal System

In the oriented normal system, the normal gravity vector  $\gamma^S$  and the normal gradiometric tensor  $\mathbf{U}^S$  at  $\rho_o$  take the special form (*Torge*, 1989):

$$\gamma^S(\rho_o) = \left( \begin{array}{c} 0 \\ 0 \\ \gamma_z^S \end{array} \right) \bigg|_{\rho_o} = \gamma(\rho_o) \cdot \mathbf{e}_\gamma^S(\rho_o) = \gamma(\rho_o) \cdot \left( \begin{array}{c} 0 \\ 0 \\ -1 \end{array} \right) \bigg|_{\rho_o} \quad (4.22)$$

and:

$$\begin{aligned} \mathbf{U}^S(\rho_o) &= \left( \begin{array}{ccc} \mathbf{U}_{xx}^S & \mathbf{U}_{xy}^S & \mathbf{U}_{xz}^S \\ \mathbf{U}_{yx}^S & \mathbf{U}_{yy}^S & \mathbf{U}_{yz}^S \\ \mathbf{U}_{zx}^S & \mathbf{U}_{zy}^S & \mathbf{U}_{zz}^S \end{array} \right) \bigg|_{\rho_o} \\ &\approx \mathbf{R}_3(A) \cdot \left( \begin{array}{ccc} -1540 & 0 & 8.1 \cdot \sin 2\varphi \\ 0 & -1540 + 10.4 \cdot \cos^2 \varphi & 0 \\ 8.1 \cdot \sin 2\varphi & 0 & 3086 \end{array} \right) \cdot \mathbf{R}_3^T(A) \cdot 10^{-9} \left[ \frac{1}{s^2} \right] \end{aligned} \quad (4.23)$$

The gravity vector  $\mathbf{g}_{\text{tot}}^S$  and the gradiometric tensor  $\mathbf{\Gamma}_{\text{tot}}^S$  at an arbitrary position  $\rho$  are given by:

$$\mathbf{g}_{\text{tot}}^S(\rho) = \left( \begin{array}{c} g_{\text{tot},x}^S \\ g_{\text{tot},y}^S \\ g_{\text{tot},z}^S \end{array} \right) \bigg|_{\rho} = g_{\text{tot}}(\rho) \cdot \mathbf{e}_{\mathbf{g}_{\text{tot}}}^S(\rho) = g_{\text{tot}}(\rho) \cdot \left( \begin{array}{c} e_{\mathbf{g}_{\text{tot},x}}^S \\ e_{\mathbf{g}_{\text{tot},y}}^S \\ e_{\mathbf{g}_{\text{tot},z}}^S \end{array} \right) \bigg|_{\rho} \quad (4.24)$$

and:

$$\mathbf{\Gamma}_{\text{tot}}^S(\rho) = \left( \begin{array}{ccc} \Gamma_{\text{tot},xx}^S & \Gamma_{\text{tot},xy}^S & \Gamma_{\text{tot},xz}^S \\ \Gamma_{\text{tot},yx}^S & \Gamma_{\text{tot},yy}^S & \Gamma_{\text{tot},yz}^S \\ \Gamma_{\text{tot},zx}^S & \Gamma_{\text{tot},zy}^S & \Gamma_{\text{tot},zz}^S \end{array} \right) \bigg|_{\rho} \quad (4.25)$$

where  $\gamma = |\gamma|$  and  $g_{\text{tot}} = |\mathbf{g}_{\text{tot}}|$ .

### 4.3.4 Astrogeodetic Levelling

#### Rigorous Geometric Formula

The rigorous purely geometric formula for  $\epsilon_{\text{tot}}$  can be found using the components of  $\mathbf{e}_{\mathbf{g}_{\text{tot}}}^S$  given at  $\rho_{\sim}$ :

$$\epsilon_{\text{tot}} = - \arctan \left( \frac{e_{\mathbf{g}_{\text{tot},x}}^S}{e_{\mathbf{g}_{\text{tot},z}}^S} \right) \bigg|_{\rho_{\sim}} \quad (4.26)$$

which is a rigorous formulation of the *Pizzetti* deflection of the vertical into the direction of  $ds$ . In addition, it is usually more convenient to split the deflection of the vertical in two oriented orthogonal components, North-South ( $\xi_{\text{tot}}$ ), and East-West ( $\eta_{\text{tot}}$ ). These components can be computed in a rigorous way by applying Equation 4.26 to  $ds$  oriented to the North and the East respectively:

$$\begin{aligned}\xi_{\text{tot}} &= -\arctan\left(\frac{e_{\mathbf{g}_{\text{tot}},x}^{\mathcal{N}}}{e_{\mathbf{g}_{\text{tot}},z}^{\mathcal{N}}}\right)\bigg|_{\rho_{\sim}} & \text{with: } \mathbf{e}_{\mathbf{g}_{\text{tot}}}^{\mathcal{N}}(\rho_{\sim}) &= \mathbf{R}_3(0^\circ) \cdot \mathbf{T}(\varphi, \lambda) \cdot \mathbf{e}_{\mathbf{g}_{\text{tot}}}^{\text{ITRS}}(\rho_{\sim}) \\ \eta_{\text{tot}} &= -\arctan\left(\frac{e_{\mathbf{g}_{\text{tot}},x}^{\mathcal{E}}}{e_{\mathbf{g}_{\text{tot}},z}^{\mathcal{E}}}\right)\bigg|_{\rho_{\sim}} & \text{with: } \mathbf{e}_{\mathbf{g}_{\text{tot}}}^{\mathcal{E}}(\rho_{\sim}) &= \mathbf{R}_3(90^\circ) \cdot \mathbf{T}(\varphi, \lambda) \cdot \mathbf{e}_{\mathbf{g}_{\text{tot}}}^{\text{ITRS}}(\rho_{\sim})\end{aligned}\quad (4.27)$$

which can be computed if  $(\Phi, \Lambda)^{\text{ITRS}}$  at  $\rho_{\sim}$ , and  $(\varphi, \lambda)^{\text{ITRS}}$  at  $\rho_o$  are known. Moreover they are related to  $\epsilon_{\text{tot}}$  by:

$$\epsilon_{\text{tot}} = \xi_{\text{tot}} \cdot \cos \alpha + \eta_{\text{tot}} \sin \alpha \quad (4.28)$$

In the literature we can find various approximations of Equation 4.27 which are more or less accurate. In *Voigt* (2013), several approximations are developed and analyzed in a very beautiful and systematic manner. Especially, the most famous, simple and imprecise one is given by:

$$\begin{aligned}\xi_{\text{tot}} &\approx \Phi(\rho_{\sim}) - \varphi(\rho_o) \\ \eta_{\text{tot}} &\approx [\Lambda(\rho_{\sim}) - \lambda(\rho_o)] \cdot \cos[\varphi(\rho_o)]\end{aligned}\quad (4.29)$$

which can deviate, in extreme cases<sup>7</sup>, by  $\sim 0.035$  arcsec from the rigorous formula.

If we come back to the analysis of these geometrical formulas, we can see that only the direction of  $\mathbf{g}_{\text{tot}}$  is used. Nevertheless it is assumed that we are able to observe or reduce  $\mathbf{e}_{\mathbf{g}_{\text{tot}}}$  at  $\rho_{\sim}$ , which is implicitly the position we are looking for. In short, we can say that we have a purely geometric determination only if it is possible to carry out  $\mathbf{e}_{\mathbf{g}_{\text{tot}}}$  at  $\rho_{\sim}$  without knowing explicitly  $\rho_{\sim}$ . It would be true in the case of classical geoid determination, when the measurements are carried out at sea level along the coastline directly.

### Gravity Disturbance based Formula

Using the relation developed in Section 3.8.3 which gives the geometric separation in terms of disturbing potential, it is possible to find  $\epsilon_{\text{tot}}$  from a more physical point of view. The method is simple and consists in applying Equation 4.11 to Equations 3.195 or 3.196.

---

<sup>7</sup>when  $\xi = \eta = 100$  arcsec,  $\phi = 45^\circ$ .

Firstly, if we look at Equation 3.195 (without the tidal component), we can write:

$$\begin{aligned}
 dN_{\text{tot}}(\boldsymbol{\rho}_o) &= \nabla N_{\text{tot}}(\boldsymbol{\rho}_o) \cdot d\mathbf{s} \\
 &= \left[ \frac{1}{|\mathbf{g}_{\text{tot}}|} \cdot \nabla T_{\text{tot}} + \nabla \left( \frac{1}{|\mathbf{g}_{\text{tot}}|} \right) \cdot T_{\text{tot}} \right] \Big|_{\boldsymbol{\rho}_o} \cdot d\mathbf{s} \\
 &= \left[ \frac{1}{|\mathbf{g}_{\text{tot}}|} \cdot \nabla T_{\text{tot}} - \frac{1}{|\mathbf{g}_{\text{tot}}|^2} \cdot \nabla |\mathbf{g}_{\text{tot}}| \cdot T_{\text{tot}} \right] \Big|_{\boldsymbol{\rho}_o} \cdot d\mathbf{s}
 \end{aligned} \tag{4.30}$$

where  $\nabla T_{\text{tot}}$  is the gravity disturbance  $\delta \mathbf{g}_{\text{tot}}$  at  $\boldsymbol{\rho}_o$ :

$$\begin{aligned}
 \nabla T_{\text{tot}}(\boldsymbol{\rho}_o) &= \nabla [\Phi_{\text{tot}}(\boldsymbol{\rho}_o) - U(\boldsymbol{\rho}_o)] = \nabla \Phi_{\text{tot}}(\boldsymbol{\rho}_o) - \nabla U(\boldsymbol{\rho}_o) \\
 &= \mathbf{g}_{\text{tot}}(\boldsymbol{\rho}_o) - \boldsymbol{\gamma}(\boldsymbol{\rho}_o) = \delta \mathbf{g}_{\text{tot}}(\boldsymbol{\rho}_o)
 \end{aligned} \tag{4.31}$$

which takes the following form in the oriented normal system:

$$\delta \mathbf{g}_{\text{tot}}^{\mathcal{S}}(\boldsymbol{\rho}_o) = \mathbf{g}_{\text{tot}}^{\mathcal{S}}(\boldsymbol{\rho}_o) - \boldsymbol{\gamma}^{\mathcal{S}}(\boldsymbol{\rho}_o) = \begin{pmatrix} g_{\text{tot},x}^{\mathcal{S}} \\ g_{\text{tot},y}^{\mathcal{S}} \\ g_{\text{tot},z}^{\mathcal{S}} \end{pmatrix} \Big|_{\boldsymbol{\rho}_o} - \begin{pmatrix} 0 \\ 0 \\ \gamma_z^{\mathcal{S}} \end{pmatrix} \Big|_{\boldsymbol{\rho}_o} = \begin{pmatrix} g_{\text{tot},x}^{\mathcal{S}} \\ g_{\text{tot},y}^{\mathcal{S}} \\ g_{\text{tot},z}^{\mathcal{S}} - \gamma_z^{\mathcal{S}} \end{pmatrix} \Big|_{\boldsymbol{\rho}_o} \tag{4.32}$$

moreover, if Equation 4.30 is given in the oriented normal system, with:

$$d\mathbf{s}^{\mathcal{S}} = \begin{pmatrix} ds \\ 0 \\ 0 \end{pmatrix} \tag{4.33}$$

we have:

$$dN_{\text{tot}}(\boldsymbol{\rho}_o) = \frac{\delta g_{\text{tot},x}^{\mathcal{S}}(\boldsymbol{\rho}_o)}{g_{\text{tot}}(\boldsymbol{\rho}_o)} \cdot ds - \frac{1}{g_{\text{tot}}^2(\boldsymbol{\rho}_o)} \cdot \frac{\partial g_{\text{tot}}}{\partial s} \Big|_{\boldsymbol{\rho}_o} \cdot T_{\text{tot}}(\boldsymbol{\rho}_o) \cdot ds \tag{4.34}$$

and if  $T_{\text{tot}}(\boldsymbol{\rho}_o)$  is replaced by  $N_{\text{tot}}(\boldsymbol{\rho}_o) \cdot g_{\text{tot}}(\boldsymbol{\rho}_o)$  from Equation 3.195 we get:

$$dN_{\text{tot}}(\boldsymbol{\rho}_o) = \frac{\delta g_{\text{tot},x}^{\mathcal{S}}(\boldsymbol{\rho}_o)}{g_{\text{tot}}(\boldsymbol{\rho}_o)} \cdot ds - \frac{N_{\text{tot}}(\boldsymbol{\rho}_o)}{g_{\text{tot}}(\boldsymbol{\rho}_o)} \cdot \frac{\partial g_{\text{tot}}}{\partial s} \Big|_{\boldsymbol{\rho}_o} \cdot ds \tag{4.35}$$

and finally:

$$\epsilon_{\text{tot}} = -\frac{dN_{\text{tot}}(\boldsymbol{\rho}_o)}{ds} = -\frac{\delta g_{\text{tot},x}^{\mathcal{S}}(\boldsymbol{\rho}_o)}{g_{\text{tot}}(\boldsymbol{\rho}_o)} + \frac{N_{\text{tot}}(\boldsymbol{\rho}_o)}{g_{\text{tot}}(\boldsymbol{\rho}_o)} \cdot \frac{\partial g_{\text{tot}}}{\partial s} \Big|_{\boldsymbol{\rho}_o} \tag{4.36}$$

If the same scheme is applied to the traditional Brun's equation given in 3.196, we find:

$$\epsilon_{\text{tot}} = -\frac{dN_{\text{tot}}(\boldsymbol{\rho}_o)}{ds} = -\frac{\delta g_{\text{tot},x}^{\mathcal{S}}(\boldsymbol{\rho}_o)}{\gamma(\boldsymbol{\rho}_o)} + \frac{N_{\text{tot}}(\boldsymbol{\rho}_o)}{\gamma(\boldsymbol{\rho}_o)} \cdot \frac{\partial \gamma}{\partial s} \Big|_{\boldsymbol{\rho}_o} \tag{4.37}$$



### Remarks

- The Equations 4.26, 4.36 and 4.37 provides different way to compute the variation of a equipotential profile between two points. In a purely theoretical way, only the geometric solution (4.26) is absolutely rigorous. This, because the solutions based on the gravity disturbance (4.36, 4.37) are both based on a first order linear approximation of the gravity potential. However, the second order omission error due to the linearization is very small. Some orders of magnitude can be found in Section 3.8.3.
- In Equations 4.36 and 4.37 a second term proportional to the geometric separation  $N_{\text{tot}}$  appears. In Equation 4.36, it represents the plumbline curvature effect between  $\rho_o$  and  $\rho_{\sim}$ . In Equation 4.37 it is the effect of the curvature of the normal plumbline between  $\rho_o$  and  $\rho_{\sim}$ . It follows that Equations 4.26 and 4.37 are almost similar and do not contain conceptual differences. The normal curvature term in 4.37 would be eliminated if we would replace the gravity disturbance  $\delta g_{\text{tot},x}$  by the gravity anomaly  $\Delta g_{\text{tot},x}$ :

$$\epsilon_{\text{tot}} = -\frac{\Delta g_{\text{tot},x}^S(\rho_{\sim})}{\gamma(\rho_o)} \approx -\arctan\left(\frac{e_{\mathbf{g}_{\text{tot},x}}^S}{e_{\mathbf{g}_{\text{tot},z}}^S}\right)\bigg|_{\rho_{\sim}} \quad (4.38)$$

where the gravity anomaly vector is defined as:

$$\Delta \mathbf{g}_{\text{tot}}(\rho_{\sim}) = \mathbf{g}_{\text{tot}}(\rho_{\sim}) - \gamma_{\text{tot}}(\rho_o) \quad (4.39)$$

- The Equation 4.36 provides an interesting formula to compute  $\epsilon_{\text{tot}}$  from observations carried out on the reference equipotential  $\rho_o$  only. However, apart from the observation of  $\mathbf{e}_{\mathbf{g}_{\text{tot}}}$  (e.g. with an astrogeodetic instrument), we need to observe theoretically  $g_{\text{tot}}$  and  $\frac{\partial g_{\text{tot}}}{\partial s}$  (e.g. with a gravimeter).

### 4.3.5 Gradiometric Levelling

In Section 4.3.4, the determination of equipotential profiles is based mainly on *Pizzetti* deflection of the vertical observables. Here we will see that, theoretically, it is also possible make a geometrical determination based on gradiometric observables. The way to find a relation between  $\epsilon_{\text{tot}}$  and  $\mathbf{\Gamma}_{\text{tot}}$  can be found by looking at the derivative of the relation given in Equation 4.38:

$$\begin{aligned} \frac{d\epsilon_{\text{tot}}}{ds} = \dot{\epsilon}_{\text{tot}} &= \frac{d\left[-\frac{\Delta g_{\text{tot},x}^S(\rho_{\sim})}{\gamma(\rho_o)}\right]}{ds} \\ &= -\frac{1}{\gamma(\rho_o)} \cdot \frac{\partial \Delta g_{\text{tot},x}^S}{\partial s}\bigg|_{\rho_{\sim}} - \frac{1}{\gamma^2(\rho_o)} \cdot \frac{\partial \gamma}{\partial s}\bigg|_{\rho_o} \cdot \Delta g_{\text{tot},x}^S(\rho_{\sim}) \\ &= -\frac{1}{\gamma(\rho_o)} \cdot \Delta \Gamma_{\text{tot},xx}^S(\rho_{\sim}) - \frac{\Delta g_{\text{tot},x}^S(\rho_{\sim})}{\gamma(\rho_o)} \cdot \frac{\partial \gamma}{\partial s}\bigg|_{\rho_o} \end{aligned} \quad (4.40)$$

where  $\Delta\Gamma_{\text{tot},xx}^{\mathcal{S}}$  is the first gradiometric anomaly component of the gradiometric tensor given in the oriented normal system by:

$$\Delta\Gamma_{\text{tot}}^{\mathcal{S}} = \mathbf{\Gamma}_{\text{tot}}^{\mathcal{S}}(\boldsymbol{\rho}_{\sim}) - \mathbf{U}^{\mathcal{S}}(\boldsymbol{\rho}_o) \quad (4.41)$$

Then,  $\epsilon_{\text{tot}}$  at position  $\boldsymbol{\rho}_o$  can be computed by integrating 4.40 along  $\mathcal{S}$  from the origin position  $\mathbf{a}_o$ :

$$\begin{aligned} \epsilon_{\text{tot}}(\boldsymbol{\rho}_o) &= \epsilon_{\text{tot}}(\mathbf{a}_o) + \int_{\mathbf{a}_o}^{\boldsymbol{\rho}_o} d\epsilon_{\text{tot}} \\ &= \epsilon_{\text{tot}}(\mathbf{a}_o) + \int_{\mathbf{a}_o}^{\boldsymbol{\rho}_o} \dot{\epsilon}_{\text{tot}} \cdot d\mathbf{s} \end{aligned} \quad (4.42)$$

Finally, the variation of  $N_{\text{tot}}$  between  $\mathbf{a}_o$  and  $\mathbf{b}_o$  is given by inserting 4.42 into 4.12 by:

$$\Delta N_{\text{tot}} \big|_{\mathbf{a}_o}^{\mathbf{b}_o} = -\epsilon_{\text{tot}}(\mathbf{a}_o) \cdot S - \int_{\mathbf{a}_o}^{\mathbf{b}_o} \int_{\mathbf{a}_o}^{\mathbf{b}_o} \dot{\epsilon}_{\text{tot}} \cdot d\mathbf{s} \cdot d\mathbf{s} \quad (4.43)$$

where  $S$  represents the curvilinear distance along  $\mathcal{S}$  between  $\mathbf{a}_o$  and  $\mathbf{b}_o$ .

## 4.4 Reductions of the Gravity Field and Observations

The ultimate aim is to determine the instantaneous geometrical separation  $N_{\text{tot}}(t)$  at any time  $t$ . If we want to determine  $N_{\text{tot}}(t)$  using a particular geometric solution, it is theoretically mandatory to carry out permanently, at any time  $t$ , at any positions  $\boldsymbol{\rho}_o$  along the profile, the corresponding observations. Formally, it means that we need the following observations:

$$l_{\text{tot}}(\boldsymbol{\rho}_o, t) \quad \forall \boldsymbol{\rho}_o, t \quad \implies \quad N_{\text{tot}}(t) \quad (4.44)$$

where  $l_{\text{tot}}$  represents an arbitrary observation (e.g.  $\epsilon_{\text{tot}}$ ,  $g_{\text{tot}}$ , ...). Evidently, this situation is technically and practically impossible. In practice, we only have access to observations carried out at arbitrary locations  $\boldsymbol{\rho}$  and at different epochs  $t_{\text{obs}}$ . Thus, it is impossible to find directly  $N_{\text{tot}}(t)$  from a real set of observations:

$$l_{\text{tot}}(\boldsymbol{\rho}, t_{\text{obs}}) \quad \not\Rightarrow \quad N_{\text{tot}}(t) \quad (4.45)$$

This kind of situation is well known in geodesy and is usually solved in two steps. Firstly,  $N_{\text{tot}}$  is determined at a certain reference epoch  $t_o$  with the actual set of observations, previously reduced in space and time to  $l_{\text{tot}}(\boldsymbol{\rho}_o, t_o)$ , using a predefined space and time-varying gravity potential model  $\Phi_{\text{tot}}^{\text{model}}(\boldsymbol{\rho}, t)$ . Secondly,  $N_{\text{tot}}(t)$  can be predicted, to an arbitrary epoch  $t$ , using the previously determined stationary  $N_{\text{tot}}(t_o)$  and the contribution of  $\Phi_{\text{tot}}^{\text{model}}$  to  $N_{\text{tot}}$ , see Figure 4.2.

The reduced observations are obtained by:

$$l_{\text{tot}}(\boldsymbol{\rho}_o, t_o) = l_{\text{tot}}(\boldsymbol{\rho}, t_{\text{obs}}) - \delta l_{\text{tot}}^{\text{model}}(\boldsymbol{\rho}_o, t_o, \boldsymbol{\rho}, t_{\text{obs}}) \quad (4.46)$$

where the reduction for an arbitrary observable is given by:

$$\delta l_{\text{tot}}^{\text{model}}(\boldsymbol{\rho}_o, t_o, \boldsymbol{\rho}, t_{\text{obs}}) = l_{\text{tot}}^{\text{model}}(\boldsymbol{\rho}, t_{\text{obs}}) - l_{\text{tot}}^{\text{model}}(\boldsymbol{\rho}_o, t_o) \quad (4.47)$$

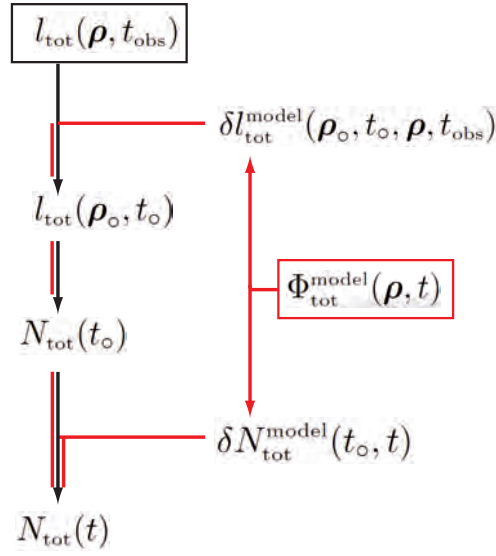


**Figure 4.2:** Schematic representation of the reduction of the observations and the computation of  $N_{\text{tot}}(t)$ . The elements in red are obtained by the gravity potential model, the black elements using observations.

Finally once  $N_{\text{tot}}(t_o)$  is obtained from the reduced observations,  $N_{\text{tot}}(t)$  is given by:

$$N_{\text{tot}}(t) = N_{\text{tot}}(t_o) + \delta N_{\text{tot}}^{\text{model}}(t_o, t) \quad (4.48)$$

where:

$$\delta N_{\text{tot}}^{\text{model}}(t_o, t) = N_{\text{tot}}^{\text{model}}(t) - N_{\text{tot}}^{\text{model}}(t_o) \quad (4.49)$$

can be computed with Equation 4.48.

#### 4.4.1 Reductions in Astronomical Levelling Determinations

Let us assume that only astrogeodetic deflections of the vertical  $\epsilon_{\text{tot}}(\boldsymbol{\rho}_{\text{surf}}, t_{\text{obs}})$  are carried out along a profile, on the surface of topography  $\boldsymbol{\rho}_{\text{surf}}$ , at different epochs  $t_{\text{obs}}$ . According to Equation 4.46, it is necessary to reduce these observations:

$$\epsilon_{\text{tot}}(\boldsymbol{\rho}_{\text{surf}}, t_{\text{obs}}) \rightarrow \epsilon_{\text{tot}}(\boldsymbol{\rho}_o, t_o) \quad (4.50)$$

using a pre-defined space- and time-varying gravity potential model  $\Phi_{\text{tot}}^{\text{model}}(\boldsymbol{\rho}, t)$ . According to Equations 3.160 and 3.177, we know that the actual total potential  $\Phi_{\text{tot}}(\boldsymbol{\rho}, t)$  can be represented by a sum of different parts. If we define a numerical model which tries to model these different parts, we can write :

$$\Phi_{\text{tot}}^{\text{model}}(\boldsymbol{\rho}, t) = U(\boldsymbol{\rho}) + \Phi_{\text{grav, st}}^{\text{model}}(\boldsymbol{\rho}) + \Phi_{\text{grav, dyn}}^{\text{model}}(\boldsymbol{\rho}, t) + \delta\Phi_{\text{centr}}^{\text{model}}(\boldsymbol{\rho}, t) + \Phi_{\text{tidal}}^{\text{model}}(\boldsymbol{\rho}, t) \quad (4.51)$$

where the normal potential  $U(\boldsymbol{\rho})$  is already known and cannot be considered as an approximation of the actual  $U(\boldsymbol{\rho})$ . Concerning the other potentials, we have:

1.  $\Phi_{\text{grav,st}}^{\text{model}}$  represents the stationary gravitational potential generated by a predefined mass model  $\mathcal{M}$  (e.g. topography masses, etc...). A modeling of this potential is absolutely necessary if only surface deflections of the vertical are used in the computation of the equipotential profile. It contributes to the largest spatial reduction  $\rho_{\text{surf}} \rightarrow \rho_o$ .
2.  $\Phi_{\text{grav,dyn}}^{\text{model}}(\rho, t)$  represents the non-stationary gravitational effect generated by time varying masses. For example, time varying underground water tables or mass changes generated by the surface variation of lakes contributes to this potential. In practice, for short-wavelengths, no realistic models are available. Nowadays, this part cannot really be modelled. Thus, the only thing we can do is to simulate some realistic time-varying phenomena and estimate their consequences on the observables and on the equipotential. In the best case, it can be established that they are negligible. Otherwise, they contribute to the limiting factors of the method.
3.  $\delta\Phi_{\text{centr}}^{\text{model}}(\rho, t)$  represents the time-varying centrifugal potential not taken into account in the normal potential. This contribution can be well modeled thanks to Earth Orientation Parameters (EOP) available at the IERS.
4.  $\Phi_{\text{tidal}}^{\text{model}}(\rho, t)$  represents the tidal potential. The available tidal potential models, see Section 3.7.4, are well known and provide accuracies better than 1% (*Torge and Müller, 2012*)<sup>8</sup>. In view of the maximal signals, of 0.05 arcsec, expected on astrogeodetic deflections of the vertical, (*Melchior, 1983*), the tidal effects can be modeled with enough accuracy.

Now, for each single potential, using Equation 4.38, we can compute its contribution to the total reduction (Equation 4.47):

$$\begin{aligned}
 \delta\epsilon_{\text{tot}}^{\text{model}}(\rho_o, t_o, \rho_{\text{surf}}, t_{\text{obs}}) &= \epsilon_{\text{tot}}^{\text{model}}(\rho_{\text{surf}}, t_{\text{obs}}) - \epsilon_{\text{tot}}^{\text{model}}(\rho_o, t_o) \\
 &= \epsilon_{\text{grav,st}}^{\text{model}}(\rho_{\text{surf}}) - \epsilon_{\text{grav,st}}^{\text{model}}(\rho_o) \\
 &\quad + \epsilon_{\text{grav,dyn}}^{\text{model}}(\rho_{\text{surf}}, t_{\text{obs}}) - \epsilon_{\text{grav,dyn}}^{\text{model}}(\rho_o, t_o) \\
 &\quad + \epsilon_{\text{centr}}^{\text{model}}(\rho_{\text{surf}}, t_{\text{obs}}) - \epsilon_{\text{centr}}^{\text{model}}(\rho_o, t_o) \\
 &\quad + \epsilon_{\text{tidal}}^{\text{model}}(\rho_{\text{surf}}, t_{\text{obs}}) - \epsilon_{\text{tidal}}^{\text{model}}(\rho_o, t_o)
 \end{aligned} \tag{4.52}$$

where the term:

$$\delta\epsilon_{\text{st}}^{\rho_o}_{\rho_{\text{surf}}} = \epsilon_{\text{grav,st}}^{\text{model}}(\rho_{\text{surf}}) - \epsilon_{\text{grav,st}}^{\text{model}}(\rho_o) \tag{4.53}$$

represents the traditional curvature of the plumbline. The reduced observations are given by:

$$\epsilon_{\text{tot}}(\rho_o, t_o) = \epsilon_{\text{tot}}(\rho_{\text{surf}}, t_{\text{obs}}) - \delta\epsilon_{\text{tot}}^{\text{model}}(\rho_o, t_o, \rho_{\text{surf}}, t_{\text{obs}}) \tag{4.54}$$

---

<sup>8</sup>Concerning the accurate and consistent prediction of time-varying reductions for astrogeodetic deflections of the vertical, the thesis of *Voigt (2013)* contains very comprehensive and detailed explanations about this issue in relation with to conventions published by IERS. Apart from the tidal and ocean loading effects, his thesis covers also the problem generated by the plate tectonic movements which can introduce systematic effects of the order of a few milliarsec. From my personal point of view, the procedures proposed and applied by *Voigt (2013)* can be considered, for the moment, as the most coherent and accurate ones.

and the equipotential profile  $N_{\text{tot}}(t_o)$  at epoch  $t_o$  can be computed using Equation 4.12.

The final step consists in computing  $N_{\text{tot}}(t)$  at an arbitrary epoch  $t$ . In accordance to Equations 4.48 and 3.210, we have:

$$N_{\text{tot}}(t) = N_{\text{tot}}(t_o) + \delta N_{\text{tot}}^{\text{model}}(t_o, t) \quad (4.55)$$

with:

$$\begin{aligned} \delta N_{\text{tot}}^{\text{model}}(t_o, t) &= N_{\text{grav, dyn}}^{\text{model}}(t) - N_{\text{grav, dyn}}^{\text{model}}(t_o) \\ &\quad + N_{\text{centr}}^{\text{model}}(t) - N_{\text{centr}}^{\text{model}}(t_o) \\ &\quad + N_{\text{tidal}}^{\text{model}}(t) - N_{\text{tidal}}^{\text{model}}(t_o) \end{aligned} \quad (4.56)$$

#### 4.4.2 Orthometric Correction

In this section, in order to simplify the notation, without loss of generality, we consider that all fields and observations are stationary and referred to the epoch  $t_o$ . There is an alternative method for reducing astrogeodetic observations at the level of the equipotential profile  $\rho_o$ . Instead of reducing the astrogeodetic observations individually by the curvature of the plumbline  $\delta\epsilon_{\text{tot}} \frac{\rho_o}{\rho_{\text{surf}}}$  in order to be able to rigorously apply Equation 4.12, the observations are separated in two parts:

$$\begin{aligned} \Delta N_{\text{tot}} \frac{b_o}{a_o} &= - \int_{a_o}^{b_o} \epsilon_{\text{tot}}(\rho_o) \cdot ds \\ &= - \int_{a_o}^{b_o} [\epsilon_{\text{tot}}(\rho_{\text{surf}}) + \delta\epsilon_{\text{tot}} \frac{\rho_o}{\rho_{\text{surf}}}] \cdot ds \\ &= - \int_{a_o}^{b_o} \epsilon_{\text{tot}}(\rho_{\text{surf}}) \cdot ds - \int_{a_o}^{b_o} \delta\epsilon_{\text{tot}} \frac{\rho_o}{\rho_{\text{surf}}} \cdot ds \\ &= - \int_{a_{\text{surf}}}^{b_{\text{surf}}} \epsilon_{\text{tot}}(\rho_{\text{surf}}) \cdot ds - E_{a_o}^{b_o} \end{aligned} \quad (4.57)$$

where:

$$E_{a_o}^{b_o} = + \int_{a_o}^{b_o} \delta\epsilon_{\text{tot}} \frac{\rho_o}{\rho_{\text{surf}}} \cdot ds \quad (4.58)$$

is called the orthometric correction. At this step, there is absolutely no advantage in doing this separation. If the curvature terms are provided (e.g from mass models), it is evident that both formulations of  $\Delta N_{\text{tot}}$  are completely equivalent. The main interest comes from the fact that  $E_{a_o}^{b_o}$  can be determined alternatively, rigorously and without restrictions, from gravimetric quantities by (*Hirt*, 2009):

$$\begin{aligned} E_{a_o}^{b_o} &= \int_{a_{\text{surf}}}^{b_{\text{surf}}} \frac{g_{\text{tot}}(\rho_{\text{surf}}) - \gamma(\rho_o)}{\gamma(\rho_o)} \cdot dn \\ &\quad + \frac{\bar{g}_{\text{tot}} \frac{a_{\text{surf}}}{a_o} - \gamma(a_o)}{\gamma(a_o)} \cdot \Delta H_{a_o}^{a_{\text{surf}}} - \frac{\bar{g}_{\text{tot}} \frac{b_{\text{surf}}}{b_o} - \gamma(b_o)}{\gamma(b_o)} \cdot \Delta H_{b_o}^{b_{\text{surf}}} \end{aligned} \quad (4.59)$$

where  $dn$  represents the differential height element between two consecutive points  $\boldsymbol{\rho}_{\text{surf}}$  on the surface. The quantities  $\bar{g}_{\text{tot}}^{\boldsymbol{a}_{\text{surf}}}$  and  $\bar{g}_{\text{tot}}^{\boldsymbol{b}_{\text{surf}}}$  represent the mean gravity along the plumb lines, and  $\Delta H_{\boldsymbol{a}_{\text{o}}}^{\boldsymbol{a}_{\text{surf}}}$  and  $\Delta H_{\boldsymbol{b}_{\text{o}}}^{\boldsymbol{b}_{\text{surf}}}$  the orthometric height differences between  $\boldsymbol{a}_{\text{o}}$  and  $\boldsymbol{a}_{\text{surf}}$  and  $\boldsymbol{b}_{\text{o}}$  and  $\boldsymbol{b}_{\text{surf}}$ , respectively. In addition, the mean gravity acceleration is given by:

$$\bar{g}_{\text{tot}}^{\boldsymbol{\rho}_{\text{surf}}}_{\boldsymbol{\rho}_{\text{o}}} = \frac{1}{\Delta H_{\boldsymbol{\rho}_{\text{o}}}^{\boldsymbol{\rho}_{\text{surf}}}} \int_{\boldsymbol{\rho}_{\text{o}}}^{\boldsymbol{\rho}_{\text{surf}}} g_{\text{tot}}(\boldsymbol{\rho}) \cdot dH \quad (4.60)$$

Assuming that gravity can be observed on the topography and inside the tunnel only, at  $\boldsymbol{\rho}_{\text{surf}}$  and  $\boldsymbol{\rho}_{\text{o}}$ , the integral part of Equation 4.59 is theoretically unambiguously accessible by surface gravity observations without any additional information. In other words, it can be theoretically determined with an arbitrary high precision. In contrast to the second and the third term containing the mean gravity are fundamentally ambiguous. This ambiguity can be seen by looking carefully at Equation 4.60.

Because  $g_{\text{tot}}(\boldsymbol{\rho})$  is derived from the potential field  $\Phi_{\text{tot}}$ , Equation 4.60 can be written as:

$$\bar{g}_{\text{tot}}^{\boldsymbol{\rho}_{\text{surf}}}_{\boldsymbol{\rho}_{\text{o}}} = - \frac{\Phi_{\text{tot}}(\boldsymbol{\rho}_{\text{surf}}) - \Phi_{\text{tot}}(\boldsymbol{\rho}_{\text{o}})}{\Delta H_{\boldsymbol{\rho}_{\text{o}}}^{\boldsymbol{\rho}_{\text{surf}}}} \quad (4.61)$$

This Equation 4.61 illustrates the equivalence between the mean gravity along the plumb line and the gravity potential difference. In other words, instead of determining a mean gravity along the plumb line from gravity observations, it is equivalent to say that we have to determine the gravity potential difference between  $\boldsymbol{\rho}_{\text{surf}}$  and  $\boldsymbol{\rho}_{\text{o}}$  from the set of all available observations  $\{g_{\text{tot}}(\boldsymbol{\rho}_{\text{o}}), g_{\text{tot}}(\boldsymbol{\rho}_{\text{surf}})\}$ . This type of problem is well known in general potential theory, or more specifically in geodesy or geophysics. Without going into details, the problem is closely related to the determination of the density field which generate the actual gravity field. In fact, if we are able to determine the true density field, the potential difference can be computed unambiguously using Equation 3.133. However, according to *Blakely* (1996), there is definitively no unique solution for the general case. It is possible to find an infinite set of density fields which can generate the actual set of gravity observations. Equivalently, we can say that an infinite set of potential differences are compatible with the actual set of gravity observations. Without supplementary information or assumptions the determination of  $\bar{g}_{\text{tot}}^{\boldsymbol{\rho}_{\text{surf}}}_{\boldsymbol{\rho}_{\text{o}}}$  is simply impossible.

Nevertheless, there is one special case for which the potential field can be determined uniquely from gravity data. From *Green's* third identity, it can be proven that this special case applies, if the gravity data are given on the boundary of a region, where *Laplace's* equation is fulfilled — or equivalently if the density field is equal to  $\rho(\boldsymbol{\rho}) = 0$ . In our specific case, it would be applicable when no masses are present between the surface of the topography and the tunnel. It is obvious that this is physically impossible but mathematically it means that this situation becomes true when the gravitational effects of all masses between the surface of the topography and the tunnel are modeled and removed from the fields. From this point, once the reduced potential field is harmonic and uniquely determined, the reduced mean gravity along the plumb line is provided directly.

### 4.4.3 Mean Gravity along the Plumline from Mass Models

In the literature, we can find several methods for the computation of mean gravity along plumblines. Basically, they can be discriminated by the set of gravity observables which are involved in the computation, the level of refinements in the mass models and the numerical methods used for the prediction of the mean gravity. Let us see now how these quantities are related and can be manipulated. First of all, let us define a total mass model  $\mathcal{M}_{\text{tot}}$ , which generates the true gravity potential  $\Phi_{\text{tot}}$  to which true gravity observables  $g_{\text{tot}}$  are associated. Secondly, we consider that  $\mathcal{M}_{\text{tot}}$  is formed by three parts. The normal ellipsoid  $\mathcal{E}_o$ , the set of all forward modeled masses  $\mathcal{M}$  and the set of all masses  $\delta\mathcal{M}$  which are not modeled so that:

$$\mathcal{M}_{\text{tot}} \equiv \mathcal{E}_o \cup \mathcal{M} \cup \delta\mathcal{M} \quad (4.62)$$

Seen from a different perspective, we can say that  $\mathcal{E}_o$  gives a numerical modelisation of the masses up to the mean sea level, and  $\mathcal{M}$  up to the surface of topography. In addition, their associated gravitational potential fields are:

$$\begin{aligned} \mathcal{M}_{\text{tot}} &\rightarrow \Phi_{\text{tot}}(\boldsymbol{\rho}) \\ \mathcal{E}_o &\rightarrow U(\boldsymbol{\rho}) \\ \mathcal{M} &\rightarrow \Phi_{\mathcal{M}}(\boldsymbol{\rho}) \\ \delta\mathcal{M} &\rightarrow \Phi_{\delta\mathcal{M}}(\boldsymbol{\rho}) \end{aligned} \quad (4.63)$$

Thus, a true gravity observation at an arbitrary position  $\boldsymbol{\rho}$  is given by:

$$g_{\text{tot}}(\boldsymbol{\rho}) = \gamma(\boldsymbol{\rho}) + g_{\mathcal{M}}(\boldsymbol{\rho}) + g_{\delta\mathcal{M}}(\boldsymbol{\rho}) \quad (4.64)$$

and with the very precise approximation that the normal gravity varies linearly between mean sea level and the surface of the topography, we can write Equation 4.64 as:

$$g_{\text{tot}}(\boldsymbol{\rho}) = \gamma_0 + \tau_o \cdot H(\boldsymbol{\rho}) + g_{\mathcal{M}}(\boldsymbol{\rho}) + g_{\delta\mathcal{M}}(\boldsymbol{\rho}) \quad (4.65)$$

where  $\gamma_0 \approx +9.81 \frac{\text{m}}{\text{s}^2}$  is the normal gravity on  $\mathcal{E}_o$ ,  $\tau_o \approx -0.3086 \cdot 10^{-5} \frac{\text{m}}{\text{s}^2}/\text{m}$  the gradient of the normal gravity and  $H(\boldsymbol{\rho})$  the orthometric height of  $\boldsymbol{\rho}$ . Thus, for the specific positions  $\boldsymbol{\rho}_o$  and  $\boldsymbol{\rho}_{\text{surf}}$  we have:

$$\begin{aligned} g_{\text{tot}}(\boldsymbol{\rho}_o) &= \gamma_0 + \tau_o \cdot H(\boldsymbol{\rho}_o) + g_{\mathcal{M}}(\boldsymbol{\rho}_o) + g_{\delta\mathcal{M}}(\boldsymbol{\rho}_o) \\ g_{\text{tot}}(\boldsymbol{\rho}_{\text{surf}}) &= \gamma_0 + \tau_o \cdot H(\boldsymbol{\rho}_{\text{surf}}) + g_{\mathcal{M}}(\boldsymbol{\rho}_{\text{surf}}) + g_{\delta\mathcal{M}}(\boldsymbol{\rho}_{\text{surf}}) \end{aligned} \quad (4.66)$$

Now, if we look at what happens to the true mean gravity between  $\boldsymbol{\rho}_o$  and  $\boldsymbol{\rho}_{\text{surf}}$  by inserting Equation 4.65 into Equation 4.60, we have:

$$\begin{aligned} \bar{g}_{\text{tot}} \big|_{\boldsymbol{\rho}_o}^{\boldsymbol{\rho}_{\text{surf}}} &= \frac{1}{\Delta H_{\boldsymbol{\rho}_o}^{\boldsymbol{\rho}_{\text{surf}}}} \int_{\boldsymbol{\rho}_o}^{\boldsymbol{\rho}_{\text{surf}}} \{ \gamma_0 + \tau_o \cdot H(\boldsymbol{\rho}) + g_{\mathcal{M}}(\boldsymbol{\rho}) + g_{\delta\mathcal{M}}(\boldsymbol{\rho}) \} \cdot dH \\ &= \frac{1}{\Delta H_{\boldsymbol{\rho}_o}^{\boldsymbol{\rho}_{\text{surf}}}} \int_{\boldsymbol{\rho}_o}^{\boldsymbol{\rho}_{\text{surf}}} \{ \gamma_0 + \tau_o \cdot H(\boldsymbol{\rho}) \} \cdot dH \\ &\quad + \frac{1}{\Delta H_{\boldsymbol{\rho}_o}^{\boldsymbol{\rho}_{\text{surf}}}} \int_{\boldsymbol{\rho}_o}^{\boldsymbol{\rho}_{\text{surf}}} g_{\mathcal{M}}(\boldsymbol{\rho}) \cdot dH + \frac{1}{\Delta H_{\boldsymbol{\rho}_o}^{\boldsymbol{\rho}_{\text{surf}}}} \int_{\boldsymbol{\rho}_o}^{\boldsymbol{\rho}_{\text{surf}}} g_{\delta\mathcal{M}}(\boldsymbol{\rho}) \cdot dH \end{aligned} \quad (4.67)$$

where the first term can be integrated easily:

$$\begin{aligned}
 \frac{1}{\Delta H_{\rho_o}^{\rho_{\text{surf}}}} \int_{\rho_o}^{\rho_{\text{surf}}} \{\gamma_0 + \tau_o \cdot H(\rho)\} \cdot dH &= \gamma_0 \cdot \frac{\Delta H_{\rho_o}^{\rho_{\text{surf}}}}{\Delta H_{\rho_o}^{\rho_{\text{surf}}}} + \frac{\tau_o}{2\Delta H_{\rho_o}^{\rho_{\text{surf}}}} [H(\rho_{\text{surf}})^2 - H(\rho_o)^2] \\
 &= \gamma_0 + \frac{\tau_o}{2\Delta H_{\rho_o}^{\rho_{\text{surf}}}} [H(\rho_{\text{surf}}) - H(\rho_o)] \cdot [H(\rho_{\text{surf}}) + H(\rho_o)] \\
 &= \gamma_0 + \tau_o \cdot \frac{H(\rho_{\text{surf}}) + H(\rho_o)}{2} \\
 &= \gamma_0 + \tau_o \cdot \bar{H}_{\rho_o}^{\rho_{\text{surf}}}
 \end{aligned} \tag{4.68}$$

and the second and third term can be given as a function of the corresponding potential so that:

$$\bar{g}_{\text{tot}}^{\rho_{\text{surf}}}_{\rho_o} = \underbrace{\gamma_0 + \tau_o \cdot \bar{H}_{\rho_o}^{\rho_{\text{surf}}}}_{\bar{\gamma}} - \underbrace{\frac{\Phi_{\mathcal{M}}(\rho_{\text{surf}}) - \Phi_{\mathcal{M}}(\rho_o)}{\Delta H_{\rho_o}^{\rho_{\text{surf}}}}}_{\bar{g}_{\mathcal{M}}} - \underbrace{\frac{\Phi_{\delta\mathcal{M}}(\rho_{\text{surf}}) - \Phi_{\delta\mathcal{M}}(\rho_o)}{\Delta H_{\rho_o}^{\rho_{\text{surf}}}}}_{\bar{g}_{\delta\mathcal{M}}} \tag{4.69}$$

In Equation 4.69, the first two terms  $\bar{\gamma}$  and  $\bar{g}_{\mathcal{M}}$  are computed numerically, whereas the third term  $\bar{g}_{\delta\mathcal{M}}$  represents the true omission error in the mean gravity computed by a pure forward modeling of gravity. This is also a formal confirmation of the statement given in the introduction of this section.

#### 4.4.4 Mean Gravity along the Plumblin from Mass Models and Observations

The computation of the mean gravity along the plumblin using mass models and gravimetric observations can be done in several ways. Usually, the methods are based on the set of gravimetric observations  $g_{\text{tot}}(\rho_{\text{surf}})$  carried out at the surface of topography. In this section, we will also consider that gravimetric observations  $g_{\text{tot}}(\rho_o)$  inside the tunnel are available. The aim is to propose a few methods for the computation of the mean gravity using the various sets of gravimetric observations and highlight the consequences on their corresponding omission errors.

##### Gravity Observed at the Surface of Topography

Considering that only the set  $g_{\text{tot}}(\rho_{\text{surf}})$  is available we can obtain a formula for the mean gravity as follows. According to *Wirth* (1990), when the second Equation 4.66 is manipulated in order to isolate the normal gravity  $\gamma_0$  on the left-hand side, we have:

$$\gamma_0 = g_{\text{tot}}(\rho_{\text{surf}}) - \tau_o \cdot H(\rho_{\text{surf}}) - g_{\mathcal{M}}(\rho_{\text{surf}}) - g_{\delta\mathcal{M}}(\rho_{\text{surf}}) \tag{4.70}$$



which can replace the normal gravity in Equation 4.69 so that:

$$\begin{aligned}
\bar{g}_{\text{tot}}^{\text{surf}} \rho_{\text{o}}^{\text{surf}} &= g_{\text{tot}}(\rho_{\text{surf}}) - \tau_{\text{o}} \cdot H(\rho_{\text{surf}}) - g_{\mathcal{M}}(\rho_{\text{surf}}) - g_{\delta\mathcal{M}}(\rho_{\text{surf}}) + \tau_{\text{o}} \cdot \bar{H}_{\rho_{\text{o}}}^{\rho_{\text{surf}}} \\
&\quad - \frac{\Phi_{\mathcal{M}}(\rho_{\text{surf}}) - \Phi_{\mathcal{M}}(\rho_{\text{o}})}{\Delta H_{\rho_{\text{o}}}^{\rho_{\text{surf}}}} - \frac{\Phi_{\delta\mathcal{M}}(\rho_{\text{surf}}) - \Phi_{\delta\mathcal{M}}(\rho_{\text{o}})}{\Delta H_{\rho_{\text{o}}}^{\rho_{\text{surf}}}} \\
&= \underbrace{g_{\text{tot}}(\rho_{\text{surf}})}_{\text{observed}} - \underbrace{\frac{\tau_{\text{o}}}{2} \cdot \Delta H_{\rho_{\text{o}}}^{\rho_{\text{surf}}} - g_{\mathcal{M}}(\rho_{\text{surf}}) - \frac{\Phi_{\mathcal{M}}(\rho_{\text{surf}}) - \Phi_{\mathcal{M}}(\rho_{\text{o}})}{\Delta H_{\rho_{\text{o}}}^{\rho_{\text{surf}}}}}_{\text{forward modeled}} \\
&\quad - \underbrace{\frac{\Phi_{\delta\mathcal{M}}(\rho_{\text{surf}}) - \Phi_{\delta\mathcal{M}}(\rho_{\text{o}})}{\Delta H_{\rho_{\text{o}}}^{\rho_{\text{surf}}}} - g_{\delta\mathcal{M}}(\rho_{\text{surf}})}_{\text{true omission error}}
\end{aligned} \tag{4.71}$$

The first part of Equation 4.71 which contains the observed and forward modeled terms, corresponds, if  $H(\rho_{\text{o}}) = 0$ , to the formula proposed by *Wirth* (1990) also used for the computation of the official orthometric height in Switzerland (*Schlatter*, 2007). Now if we look at the true omission term given in Equation 4.71, it is important to see under which assumption the formula proposed by *Wirth* (1990) gives the actual mean gravity. This happens when the true omission term is equal to zero, or when:

$$- \frac{\Phi_{\delta\mathcal{M}}(\rho_{\text{surf}}) - \Phi_{\delta\mathcal{M}}(\rho_{\text{o}})}{\Delta H_{\rho_{\text{o}}}^{\rho_{\text{surf}}}} = g_{\delta\mathcal{M}}(\rho_{\text{surf}}) \tag{4.72}$$

or equivalently when:

$$\bar{g}_{\delta\mathcal{M}} \rho_{\text{o}}^{\rho_{\text{surf}}} = g_{\delta\mathcal{M}}(\rho_{\text{surf}}) \tag{4.73}$$

Thus the mean gravity along the plumbline generated by the non-modeled masses  $\delta\mathcal{M}$  is equal to the gravity generated by  $\delta\mathcal{M}$  at  $\rho_{\text{surf}}$ , on the surface of the topography. Along a certain profile, this condition is satisfied when  $g_{\delta\mathcal{M}}(\rho)$  is constant for all positions between  $\rho_{\text{o}}$  and  $\rho_{\text{surf}}$ . This corresponds to a single type of mass models  $\delta\mathcal{M}$ : Bouguer plates which do not intersect the region defined by the positions  $\rho_{\text{o}}$  and  $\rho_{\text{surf}}$  (see Figure 4.4). In other words, if we omit to model any kind of masses between the tunnel and the topography (also a Bouguer plate), the mean gravity obtained by Equation 4.71 is distorted in any cases. In addition, we can say that the gravity observations determine only the effect of non-modeled masses which are equivalent to Bouguer plates located entirely below the tunnel or above the topography.

### Gravity Observed inside the Tunnel

If we consider that only gravimetric observations carried out inside the tunnel are used for the computation of the mean gravity, we can easily find a formula similar to Equation

4.71. By proceeding in the same way, we can finally find:

$$\begin{aligned} \bar{g}_{\text{tot}}^{\text{tnl}} \rho_{\text{o}}^{\text{surf}} = & \underbrace{g_{\text{tot}}(\rho_{\text{o}})}_{\text{observed}} + \underbrace{\frac{\tau_{\text{o}}}{2} \cdot \Delta H_{\rho_{\text{o}}}^{\rho_{\text{surf}}} - g_{\mathcal{M}}(\rho_{\text{o}}) - \frac{\Phi_{\mathcal{M}}(\rho_{\text{surf}}) - \Phi_{\mathcal{M}}(\rho_{\text{o}})}{\Delta H_{\rho_{\text{o}}}^{\rho_{\text{surf}}}}}_{\text{forward modeled}} \\ & - \underbrace{\frac{\Phi_{\delta\mathcal{M}}(\rho_{\text{surf}}) - \Phi_{\delta\mathcal{M}}(\rho_{\text{o}})}{\Delta H_{\rho_{\text{o}}}^{\rho_{\text{surf}}}} - g_{\delta\mathcal{M}}(\rho_{\text{o}})}_{\text{true omission error}} \end{aligned} \quad (4.74)$$

which is very similar to Equation 4.71 which gives the actual true mean gravity when:

$$\bar{g}_{\delta\mathcal{M}} \rho_{\text{o}}^{\text{surf}} = g_{\delta\mathcal{M}}(\rho_{\text{o}}) \quad (4.75)$$

which corresponds to the same class of possible mass models  $\delta\mathcal{M}$  mentioned for Equation 4.71 (see Figure 4.4). However, we cannot say that both relations are completely equivalent. In fact, using Equation 4.71, the error is given by the difference between the gravity signals generated at the surface of topography and its mean gravity. Opposed to this, the application of Equation 4.74 gives a result which differs from the truth by the difference between the gravity signals generated inside the tunnel and its mean gravity. Thus, since the gravity effect fades with the square of the distance to  $\delta\mathcal{M}$ , we can consider that the choice of applying Equation 4.71 rather than Equation 4.74 could be argued by the better knowledge of the quality of the mass models  $\mathcal{M}$  in the vicinity of  $\rho_{\text{surf}}$  compared to  $\rho_{\text{o}}$ .

### Gravity Observed at the Surface of Topography and inside the Tunnel

If we consider that both sets of gravimetric observations, at the surface of topography and inside the tunnel, are used for the computation of the mean gravity, the simplest way to obtain a formula which takes into account both observations is given by the average of the mean gravity computed using Equations 4.71 and 4.74 by:

$$\begin{aligned} \bar{g}_{\text{tot}}^{\text{mean}} \rho_{\text{o}}^{\text{surf}} = & \frac{\bar{g}_{\text{tot}}^{\text{tnl}} \rho_{\text{o}}^{\text{surf}} + \bar{g}_{\text{tot}}^{\text{surf}} \rho_{\text{o}}^{\text{surf}}}{2} \\ = & \underbrace{\frac{g_{\text{tot}}(\rho_{\text{o}}) + g_{\text{tot}}(\rho_{\text{surf}})}{2}}_{\text{observed}} - \underbrace{\frac{g_{\mathcal{M}}(\rho_{\text{o}}) + g_{\mathcal{M}}(\rho_{\text{surf}})}{2} - \frac{\Phi_{\mathcal{M}}(\rho_{\text{surf}}) - \Phi_{\mathcal{M}}(\rho_{\text{o}})}{\Delta H_{\rho_{\text{o}}}^{\rho_{\text{surf}}}}}_{\text{forward modeled}} \\ & - \underbrace{\frac{\Phi_{\delta\mathcal{M}}(\rho_{\text{surf}}) - \Phi_{\delta\mathcal{M}}(\rho_{\text{o}})}{\Delta H_{\rho_{\text{o}}}^{\rho_{\text{surf}}}} - \frac{g_{\delta\mathcal{M}}(\rho_{\text{o}}) + g_{\delta\mathcal{M}}(\rho_{\text{surf}})}{2}}_{\text{true omission error}} \end{aligned} \quad (4.76)$$

and provides the actual true mean gravity when:

$$\bar{g}_{\delta\mathcal{M}} \rho_{\text{o}}^{\text{surf}} = \frac{g_{\delta\mathcal{M}}(\rho_{\text{o}}) + g_{\delta\mathcal{M}}(\rho_{\text{surf}})}{2} \quad (4.77)$$

which covers, with respect to the formulas given by Equations 4.71 and 4.74, two additional classes of non-modeled masses  $\delta\mathcal{M}$ :

1. The first class is given by the Bouguer plates which are bounded by  $\rho_{\text{surf}}$  (see Figure 4.4). This is due to the fact that gravity varies linearly inside a Bouguer plate and ensures that the mean gravity is equal to the quantities at the extremities  $\rho_o$  and  $\rho_{\text{surf}}$ .
2. The second class is given by the set of density fields which generate mean gravity equal to zero and at the same time opposite gravity quantities at  $\rho_o$  and  $\rho_{\text{surf}}$ . These conditions are theoretically fulfilled on the one hand, if  $\rho_o$  and  $\rho_{\text{surf}}$  span two horizontal profiles, and on the other hand, if the density field is symmetric in the vertical dimension and centered between  $\rho_o$  and  $\rho_{\text{surf}}$ .

#### 4.4.5 Mean Gravity along the Plumline using Remove and Restore Technique

The methodology described in the following section is more general and ambitious, but can also be more delicate than the methods described in the previous sections. Here the very famous technique of remove and restore is used. The first step consists in removing all modeled signals from the set of observations. For gravimetry observations, using Equation 4.66, we have:

$$\begin{aligned} g_{\delta\mathcal{M}}(\rho_o) &= g_{\text{tot}}(\rho_o) - \gamma_0 - \tau_o \cdot H(\rho_o) - g_{\mathcal{M}}(\rho_o) \\ g_{\delta\mathcal{M}}(\rho_{\text{surf}}) &= g_{\text{tot}}(\rho_{\text{surf}}) - \gamma_0 - \tau_o \cdot H(\rho_{\text{surf}}) - g_{\mathcal{M}}(\rho_{\text{surf}}) \end{aligned} \quad (4.78)$$

For other kinds of observations, as deflections of the vertical or gradients, the reduction must be done in a similar way. Secondly, the non-modeled potential  $\Phi_{\delta\mathcal{M}}$  is estimated from the set of all reduced observations ( $g_{\delta\mathcal{M}}$ ,  $\epsilon_{\delta\mathcal{M}}$ , ...) using a particular estimation methodology based on some assumptions (e.g gravity inversion, least-squares collocation, etc). Finally, the mean gravity is computed by restoring the estimated signal to the modeled one using Equation 4.69.

#### 4.4.6 Non-Modeled Mean Gravity along the Plumline using Least-Squares Collocation

Assuming that we dispose of both sets of reduced gravimetric observations inside the tunnel and on the topography,  $g_{\delta\mathcal{M}}(\rho_o)$  and  $g_{\delta\mathcal{M}}(\rho_{\text{surf}})$ , the aim is to compute the non-modeled potential  $\Phi_{\delta\mathcal{M}}$  at each position  $\rho_{\text{surf}}$  and  $\rho_o$  so that the mean non-modeled gravity can be computed by:

$$\bar{g}_{\delta\mathcal{M}} \frac{\rho_{\text{surf}}}{\rho_o} = - \frac{\Phi_{\delta\mathcal{M}}(\rho_{\text{surf}}) - \Phi_{\delta\mathcal{M}}(\rho_o)}{\Delta H_{\rho_o}^{\rho_{\text{surf}}}} \quad (4.79)$$

#### Mathematical Model of the Non-Modeled Potential

Basically, at a given position  $\rho$ , it is assumed that the non-modeled potential  $\Phi_{\delta\mathcal{M}}$  can be modeled as follows:

$$\Phi_{\delta\mathcal{M}}(\rho) = a_0 + a_1 \cdot H(\rho) + s_{\Phi}(\rho) + n_{\Phi}(\rho) \quad (4.80)$$

where  $a_0$  and  $a_1$  are unknown parameters,  $H$  represents the orthometric height,  $n_{\Phi}$  a non-correlated noise and  $s_{\Phi}$  a purely stochastic signal which is a realization of a stochastic

process  $\Phi$  which is supposed to be *Gaussian* distributed and has the following autocovariance function:

$$\mathcal{C}_{\Phi\Phi}(\boldsymbol{\rho}_i, \boldsymbol{\rho}_j) = \sigma_\Phi^2 \cdot e^{-\frac{|\boldsymbol{\rho}_j - \boldsymbol{\rho}_i|^2}{d^2}} \quad (4.81)$$

where  $\boldsymbol{\rho}_i$  and  $\boldsymbol{\rho}_j$  are two arbitrary positions,  $\sigma_\Phi$  represents the standard deviation of  $s_\Phi$  and  $d$  the correlation length. In Equation 4.81, the autocovariance function represents the statistical behaviour of the random part of the non-modeled potential  $\Phi_{\delta\mathcal{M}}$ . The main reason for choosing this Gaussian form instead of another more sophisticated common function is its simplicity and the absence of singularities. It is also assumed that  $\mathcal{C}_{\Phi\Phi}$  is isotropic even if we can imagine that it is not really the case for non-modeled potential  $\Phi_{\delta\mathcal{M}}$  generated by arbitrary masses  $\delta\mathcal{M}$ . In addition, an empirical estimation of the best function for  $\mathcal{C}_{\Phi\Phi}$  from the simulated field has deliberately not been achieved. As we will show, only the free parameters  $\sigma_\Phi$  and  $d$  are estimated from the observations.

### Mathematical Model of the Reduced Observations

The observation equation for the reduced gravimetric measurements is given by:

$$\begin{aligned} g_{\delta\mathcal{M}}(\boldsymbol{\rho}) &= -\frac{\partial}{\partial z} \{\Phi_{\delta\mathcal{M}}(\boldsymbol{\rho})\} \\ &= -a_1 - \frac{\partial}{\partial z} \{s_\Phi(\boldsymbol{\rho})\} + n_g(\boldsymbol{\rho}) \\ &= -a_1 + s_g(\boldsymbol{\rho}) + n_g(\boldsymbol{\rho}) \end{aligned} \quad (4.82)$$

where  $n_g$  represents the non-correlated noise part of the measurements, whereas  $s_g$  represents the stochastic signals of the gravimetric field which is linked to the potential field through the linear functional  $-\frac{\partial}{\partial z}\{\}$ . This has the huge advantage of relating all possible cross-covariance functions between  $s_\Phi$  and  $s_g$  by the functional covariance propagation law. But first, let us recall how this propagation law is working.

Assuming that a stochastic signal  $s_\beta$  is related to a signal  $s_\alpha$ , with known autocovariance function  $\mathcal{C}_{\alpha\alpha}(\boldsymbol{\rho}_i, \boldsymbol{\rho}_j)$ , by a linear functional  $\mathcal{L}_\beta$ :

$$s_\beta(\boldsymbol{\rho}) = \mathcal{L}_\beta|_{\boldsymbol{\rho}} \{s_\alpha(\boldsymbol{\rho})\} \quad (4.83)$$

the cross-covariance functions are given by:

$$\begin{aligned} \mathcal{C}_{\alpha\beta}(\boldsymbol{\rho}_i, \boldsymbol{\rho}_j) &= \mathcal{L}_\beta|_{\boldsymbol{\rho}_j} \{\mathcal{C}_{\alpha\alpha}(\boldsymbol{\rho}_i, \boldsymbol{\rho}_j)\} \\ \mathcal{C}_{\beta\alpha}(\boldsymbol{\rho}_i, \boldsymbol{\rho}_j) &= \mathcal{L}_\beta|_{\boldsymbol{\rho}_i} \{\mathcal{C}_{\alpha\alpha}(\boldsymbol{\rho}_i, \boldsymbol{\rho}_j)\} \\ \mathcal{C}_{\beta\beta}(\boldsymbol{\rho}_i, \boldsymbol{\rho}_j) &= \mathcal{L}_\beta|_{\boldsymbol{\rho}_i} \{\mathcal{C}_{\alpha\beta}(\boldsymbol{\rho}_i, \boldsymbol{\rho}_j)\} \\ &= \mathcal{L}_\beta|_{\boldsymbol{\rho}_j} \{\mathcal{C}_{\beta\alpha}(\boldsymbol{\rho}_i, \boldsymbol{\rho}_j)\} \end{aligned} \quad (4.84)$$

Applying this to Equation 4.82 and considering 4.81 we get:

$$\begin{aligned}
 \mathcal{C}_{\Phi g}(\rho_i, \rho_j) &= - \frac{\partial}{\partial z} \Big|_{\rho_j} \{ \mathcal{C}_{\Phi \Phi}(\rho_i, \rho_j) \} \\
 &= + \frac{2\sigma_{\Phi}^2}{d^2} \cdot e^{-\frac{|\rho_j - \rho_i|^2}{d^2}} \cdot (z_j - z_i) \\
 \mathcal{C}_{g\Phi}(\rho_i, \rho_j) &= - \frac{\partial}{\partial z} \Big|_{\rho_i} \{ \mathcal{C}_{\Phi \Phi}(\rho_i, \rho_j) \} \\
 &= - \frac{2\sigma_{\Phi}^2}{d^2} \cdot e^{-\frac{|\rho_j - \rho_i|^2}{d^2}} \cdot (z_j - z_i) \\
 \mathcal{C}_{gg}(\rho_i, \rho_j) &= - \frac{\partial}{\partial z} \Big|_{\rho_i} \{ \mathcal{C}_{\Phi g}(\rho_i, \rho_j) \} \\
 &= + \frac{2\sigma_{\Phi}^2}{d^2} \cdot e^{-\frac{|\rho_j - \rho_i|^2}{d^2}} \cdot \left[ 1 - \frac{2 \cdot (z_j - z_i)^2}{d^2} \right]
 \end{aligned} \tag{4.85}$$

A representation of the cross-covariance functions given in Equations 4.81 and 4.85 is shown in Figure 4.3. In general, the free parameters of the covariance functions can be

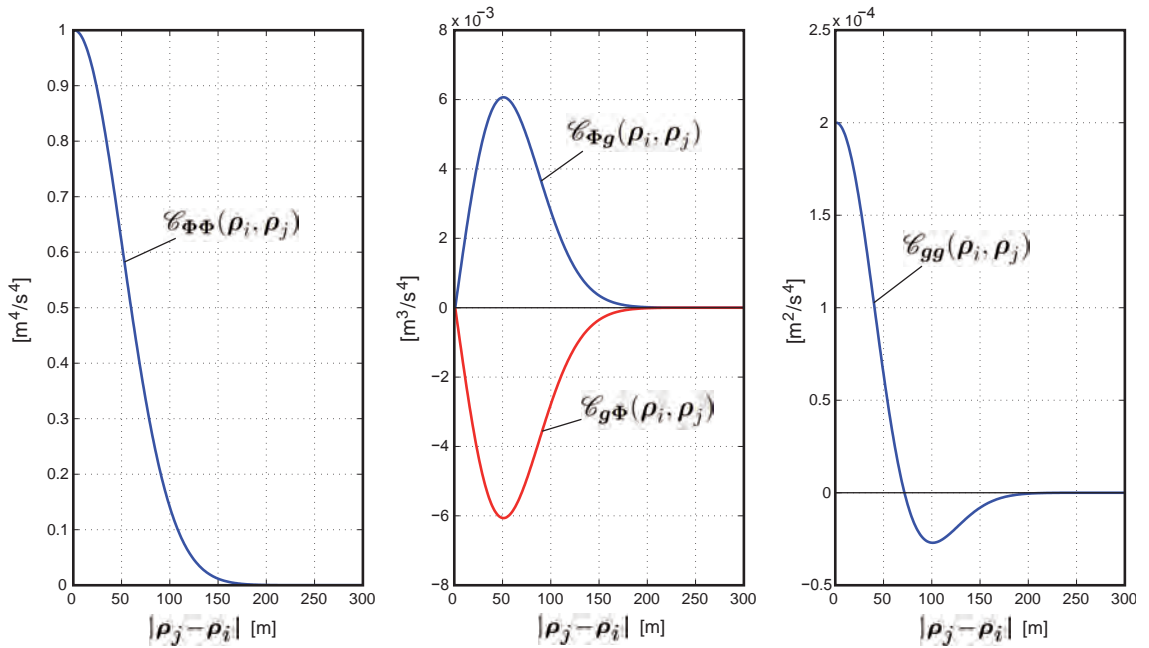


**Figure 4.3:** Autocovariance and cross-covariance functions given in Equations 4.81 and 4.85 for  $\sigma_{\Phi} = 1.0 \left[ \frac{\text{m}^2}{\text{s}^2} \right]$  and  $d = 100$  [m].

fixed in many ways. In our case, the determination of  $\sigma_{\Phi}$  and  $d$  is performed by a usual empirical approach based on the available observations. Since only gravimetric observations are available, only the autocovariance  $\mathcal{C}_{gg}$  is empirically accessible. Then, once  $\mathcal{C}_{gg}$

is provided, it is theoretically possible to determine  $\sigma_\Phi$  and  $d$  by fitting the empirical  $\mathcal{C}_{gg}$  to its analytic form given in Equation 4.85. This ideal procedure is not used here because the large discrepancies which can be expected between the empirical and the analytic forms could make this adjustment unstable and unreliable. Actually, the estimation of both parameters is done by a more pragmatic and stable way.

First, the correlation length  $d$  is estimated by searching for the first minimum of the empirical  $\mathcal{C}_{gg}$  as it is the case in the analytic form (see Figure 4.3).

Secondly,  $\sigma_\Phi$  is simply computed using the quantity of the empirical  $\mathcal{C}_{gg}$  when  $\rho_i = \rho_j$ , or equivalently when  $|\rho_i - \rho_j| = 0$ , so that:

$$\mathcal{C}_{gg}(\rho_i, \rho_i) = + \frac{2\sigma_\Phi^2}{d^2} \quad (4.86)$$

which permits to estimate  $\sigma_\Phi$  by:

$$\sigma_\Phi = \sqrt{\frac{\mathcal{C}_{gg}(\rho_i, \rho_i) \cdot d^2}{2}} \quad (4.87)$$

### Matrix Formulation of the Functional Model

In order to use the standard formulas of the least-squares collocation, the previously developed mathematical models must be integrated in the usual matrix formulation where all observations are incorporated into the following vectorial observation equation:

$$\mathbf{l} = \mathbf{A} \cdot \mathbf{x} + \mathbf{s} + \mathbf{n} \quad (4.88)$$

where  $\mathbf{A} \cdot \mathbf{x}$  represents the deterministic part,  $\mathbf{s}$  the correlated stochastic signals and  $\mathbf{n}$  the non-correlated noises. In our case, considering only potential  $\mathbf{l}_\Phi$  and gravimetric  $\mathbf{l}_g$  observation vectors, we have:

$$\begin{pmatrix} \mathbf{l}_\Phi \\ \mathbf{l}_g \end{pmatrix} = \begin{pmatrix} \mathbf{A}_\Phi \\ \mathbf{A}_g \end{pmatrix} \cdot \mathbf{x} + \begin{pmatrix} \mathbf{s}_\Phi \\ \mathbf{s}_g \end{pmatrix} + \begin{pmatrix} \mathbf{n}_\Phi \\ \mathbf{n}_g \end{pmatrix} \quad (4.89)$$

or more explicitly, from Equations 4.80 and 4.82:

$$\begin{pmatrix} \Phi_{\delta, \mathcal{M}}(\rho_{1_\Phi}) \\ \vdots \\ \Phi_{\delta, \mathcal{M}}(\rho_{m_\Phi}) \\ g_{\delta, \mathcal{M}}(\rho_{1_g}) \\ \vdots \\ g_{\delta, \mathcal{M}}(\rho_{m_g}) \end{pmatrix} = \begin{pmatrix} 1 & H(\rho_{1_\Phi}) \\ \vdots & \vdots \\ 1 & H(\rho_{m_\Phi}) \\ 0 & -1 \\ \vdots & \vdots \\ 0 & -1 \end{pmatrix} \cdot \begin{pmatrix} a_0 \\ a_1 \end{pmatrix} + \begin{pmatrix} s_\Phi(\rho_{1_\Phi}) \\ \vdots \\ s_\Phi(\rho_{m_\Phi}) \\ s_g(\rho_{1_g}) \\ \vdots \\ s_g(\rho_{m_g}) \end{pmatrix} + \begin{pmatrix} n_\Phi(\rho_{1_\Phi}) \\ \vdots \\ n_\Phi(\rho_{m_\Phi}) \\ n_g(\rho_{1_g}) \\ \vdots \\ n_g(\rho_{m_g}) \end{pmatrix} \quad (4.90)$$

assuming that  $m_\Phi$  observations of the potential have been carried out at positions  $\rho_{1_\Phi} \dots \rho_{m_\Phi}$  and  $m_g$  gravimetric observations have been carried out at  $\rho_{1_g} \dots \rho_{m_g}$ . As mentioned before,

in our case, only gravimetric observations are provided. Thus, only one pseudo observation of the potential is introduced in order to fix the singularity that occurs if no potential observation is included.

### Matrix Formulation of the Stochastic Model

First, the non-correlated noise of the  $n$  observations is modeled by the covariance matrix  $\mathbf{C}_{nn}$ , defined as follows:

$$\mathbf{C}_{nn} = \begin{pmatrix} \sigma_{n_1}^2 & 0 & \dots & 0 \\ 0 & \sigma_{n_2}^2 & \ddots & \vdots \\ \vdots & \ddots & \ddots & 0 \\ 0 & \dots & 0 & \sigma_{n_n}^2 \end{pmatrix} \quad (4.91)$$

and for our specific application we have:

$$\mathbf{C}_{nn} = \begin{pmatrix} \mathbf{C}_{\mathbf{n}_\Phi \mathbf{n}_\Phi} & \mathbf{0} \\ \mathbf{0} & \mathbf{C}_{\mathbf{n}_g \mathbf{n}_g} \end{pmatrix} \quad (4.92)$$

where  $\mathbf{C}_{\mathbf{n}_\Phi \mathbf{n}_\Phi}$  is a diagonal matrix containing the variances of the noise of the potential observations,  $\mathbf{C}_{\mathbf{n}_g \mathbf{n}_g}$  a diagonal matrix which contains the variances of the noise of the gravimetric observations.

Concerning the covariance matrices associated to the stochastic signal  $\mathbf{s}$ , we have to complete the matrix  $\mathbf{C}_{ss}$  which can be filled when all cross-covariance functions are known. In our case, we have:

$$\mathbf{C}_{ss} = \begin{pmatrix} \mathbf{C}_{\mathbf{s}_\Phi \mathbf{s}_\Phi} & \mathbf{C}_{\mathbf{s}_\Phi \mathbf{s}_g} \\ \mathbf{C}_{\mathbf{s}_g \mathbf{s}_\Phi} & \mathbf{C}_{\mathbf{s}_g \mathbf{s}_g} \end{pmatrix} \quad (4.93)$$

where the cross-covariance matrices can be filled thanks to the functions given in Equations 4.81 and 4.85 by:

$$\begin{aligned} \mathbf{C}_{\mathbf{s}_\Phi \mathbf{s}_\Phi} &= \begin{pmatrix} \mathcal{C}_{\Phi\Phi}(\rho_{1_\Phi}, \rho_{1_\Phi}) & \dots & \mathcal{C}_{\Phi\Phi}(\rho_{1_\Phi}, \rho_{m_\Phi}) \\ \vdots & \ddots & \vdots \\ \mathcal{C}_{\Phi\Phi}(\rho_{m_\Phi}, \rho_{1_\Phi}) & \dots & \mathcal{C}_{\Phi\Phi}(\rho_{m_\Phi}, \rho_{m_\Phi}) \end{pmatrix} & \mathbf{C}_{\mathbf{s}_\Phi \mathbf{s}_g} &= \begin{pmatrix} \mathcal{C}_{\Phi g}(\rho_{1_\Phi}, \rho_{1_g}) & \dots & \mathcal{C}_{\Phi g}(\rho_{1_\Phi}, \rho_{m_g}) \\ \vdots & \ddots & \vdots \\ \mathcal{C}_{\Phi g}(\rho_{m_\Phi}, \rho_{1_g}) & \dots & \mathcal{C}_{\Phi g}(\rho_{m_\Phi}, \rho_{m_g}) \end{pmatrix} \\ \mathbf{C}_{\mathbf{s}_g \mathbf{s}_\Phi} &= \begin{pmatrix} \mathcal{C}_{g\Phi}(\rho_{1_g}, \rho_{1_\Phi}) & \dots & \mathcal{C}_{g\Phi}(\rho_{1_g}, \rho_{m_\Phi}) \\ \vdots & \ddots & \vdots \\ \mathcal{C}_{g\Phi}(\rho_{m_g}, \rho_{1_\Phi}) & \dots & \mathcal{C}_{g\Phi}(\rho_{m_g}, \rho_{m_\Phi}) \end{pmatrix} & \mathbf{C}_{\mathbf{s}_g \mathbf{s}_g} &= \begin{pmatrix} \mathcal{C}_{gg}(\rho_{1_g}, \rho_{1_g}) & \dots & \mathcal{C}_{gg}(\rho_{1_g}, \rho_{m_g}) \\ \vdots & \ddots & \vdots \\ \mathcal{C}_{gg}(\rho_{m_g}, \rho_{1_g}) & \dots & \mathcal{C}_{gg}(\rho_{m_g}, \rho_{m_g}) \end{pmatrix} \end{aligned} \quad (4.94)$$

### Estimation of the Parameters

According to Möser *et al.* (2000), the vector  $\mathbf{x}$  of parameters, the signals  $\mathbf{s}$  and noises  $\mathbf{n}$  which minimize the following quantity

$$\mathbf{s}^T \cdot \mathbf{Q}_{ss}^{-1} \cdot \mathbf{s} + \mathbf{n}^T \cdot \mathbf{Q}_{nn}^{-1} \cdot \mathbf{n} \quad \text{with:} \quad \begin{aligned} \mathbf{Q}_{ss} &= \frac{1}{\sigma_0^2} \cdot \mathbf{C}_{ss} \\ \mathbf{Q}_{nn} &= \frac{1}{\sigma_0^2} \cdot \mathbf{C}_{nn} \end{aligned} \quad (4.95)$$

are given by

$$\begin{aligned} \hat{\mathbf{x}} &= (\mathbf{A}^T \cdot \mathbf{Q}_{ee}^{-1} \cdot \mathbf{A})^{-1} \cdot \mathbf{A}^T \cdot \mathbf{Q}_{ee}^{-1} \cdot \mathbf{l} \\ \hat{\mathbf{s}} &= \mathbf{Q}_{ss} \cdot \mathbf{Q}_{ee}^{-1} \cdot (\mathbf{l} - \mathbf{A} \cdot \hat{\mathbf{x}}) \\ \hat{\mathbf{n}} &= \mathbf{Q}_{nn} \cdot \mathbf{Q}_{ee}^{-1} \cdot (\mathbf{l} - \mathbf{A} \cdot \hat{\mathbf{x}}) \end{aligned} \quad (4.96)$$

where:

$$\mathbf{Q}_{ee} = \mathbf{Q}_{ss} + \mathbf{Q}_{nn} \quad (4.97)$$

### Prediction of Field Functionals

The least-squares collocation is not only a powerful filtering technique which is able to distinguish between the deterministic and the random parts of observations, it also permits to predict, at any position  $\boldsymbol{\rho}$ , any linear functional  $\mathcal{L}$  of the fundamental field to which all observables are related. In our case, in order to be able to compute the mean gravity along the plumbline using Equation 4.79, it is necessary to predict the non-modeled potential  $\Phi_{\delta, \mathcal{M}}$  only. From Equation 4.80 we can write:

$$\Phi_{\delta, \mathcal{M}}^*(\boldsymbol{\rho}^*) = \hat{a}_0 + \hat{a}_1 \cdot H(\boldsymbol{\rho}^*) + s_{\Phi}^*(\boldsymbol{\rho}^*) \quad (4.98)$$

where the superscript  $*$  means that the corresponding quantity is not observed nor computed using Equation 4.96 at  $\boldsymbol{\rho}^*$ . For  $p$  different positions and using the matrix formulation, we have:

$$\mathbf{t}_{\Phi}^* = \mathbf{A}_{\Phi}^* \cdot \hat{\mathbf{x}} + \mathbf{s}_{\Phi}^* \quad (4.99)$$

or more explicitly:

$$\begin{pmatrix} \Phi_{\delta, \mathcal{M}}^*(\boldsymbol{\rho}_1^*) \\ \vdots \\ \Phi_{\delta, \mathcal{M}}^*(\boldsymbol{\rho}_p^*) \end{pmatrix} = \begin{pmatrix} 1 & H(\boldsymbol{\rho}_1^*) \\ \vdots & \vdots \\ 1 & H(\boldsymbol{\rho}_p^*) \end{pmatrix} \cdot \begin{pmatrix} \hat{a}_0 \\ \hat{a}_1 \end{pmatrix} + \begin{pmatrix} s_{\Phi}^*(\boldsymbol{\rho}_1^*) \\ \vdots \\ s_{\Phi}^*(\boldsymbol{\rho}_p^*) \end{pmatrix} \quad (4.100)$$

where only the vector  $\mathbf{s}_{\Phi}^*$ , containing the signals, is not yet available and can be determined by:

$$\hat{\mathbf{s}}_{\Phi}^* = \mathbf{Q}_{s_{\Phi}^* s} \cdot \mathbf{Q}_{ee}^{-1} \cdot (\mathbf{l} - \mathbf{A} \cdot \hat{\mathbf{x}}) \quad (4.101)$$



with:

$$\mathbf{Q}_{\mathbf{s}_{\Phi}^* \mathbf{s}} = \frac{1}{\sigma_0^2} \cdot \mathbf{C}_{\mathbf{s}_{\Phi}^* \mathbf{s}} \quad (4.102)$$

where:

$$\begin{aligned} \mathbf{C}_{\mathbf{s}_{\Phi}^* \mathbf{s}} &= \begin{pmatrix} \mathbf{C}_{\mathbf{s}_{\Phi}^* \mathbf{s}_{\Phi}} & \mathbf{C}_{\mathbf{s}_{\Phi}^* \mathbf{s}_g} \end{pmatrix} \\ &= \left( \begin{array}{ccc|ccc} \mathcal{C}_{\Phi\Phi}(\rho_1^*, \rho_{1\Phi}) & \dots & \mathcal{C}_{\Phi\Phi}(\rho_1^*, \rho_{m\Phi}) & \mathcal{C}_{\Phi g}(\rho_1^*, \rho_{1g}) & \dots & \mathcal{C}_{\Phi g}(\rho_1^*, \rho_{mg}) \\ \vdots & \ddots & \vdots & \vdots & \ddots & \vdots \\ \mathcal{C}_{\Phi\Phi}(\rho_p^*, \rho_{1\Phi}) & \dots & \mathcal{C}_{\Phi\Phi}(\rho_p^*, \rho_{m\Phi}) & \mathcal{C}_{\Phi g}(\rho_p^*, \rho_{1g}) & \dots & \mathcal{C}_{\Phi g}(\rho_p^*, \rho_{mg}) \end{array} \right) \end{aligned} \quad (4.103)$$

### Final Remarks

The extension of the least-squares collocation model developed in this section to other kinds of observables is, in principle, straightforward. Surface deflections of the vertical or gradiometric observations are both also related to the potential through linear functionals. Nevertheless, it is not guaranteed that the results become better by just adding supplementary information. In fact, in the frame of this thesis, some rudimentary computations which also included the surface deflection observations were not very successful. However, it would be interesting for sure to investigate further along this way. In addition, the indicators of precision which are provided by the least-squares collocation methodology have also not been investigated, although it would be interesting to investigate their validity. Nevertheless, as it will be shown, the quality of the predictions is realized by comparisons with true values directly.

### 4.4.7 Comparisons of the Various Methods

In order to illustrate the different methods exposed in the previous sections for the computation of the mean gravity along the plumbline, two revealing synthetic mass models are used to generate theoretical mean gravity values and their corresponding true observations. We assume that the observations are carried out at the surface of a flat topography ( $H(\rho_{\text{surf}}) = 450$  m), and inside a tunnel 150 meters below ground ( $H(\rho_o) = 300$  m), along a 1'200 m long profile, see Figures 4.6 and 4.9. In addition, we consider that the gravity field contributions generated by the normal ellipsoid  $\mathcal{E}_o$  and all modeled masses  $\mathcal{M}$  have already been reduced from all available observations. Thus, the problem of the determination of the mean gravity along the plumbline  $\bar{g}_{\text{tot}} \frac{\rho_{\text{surf}}}{\rho_o}$  can be reduced to the determination of the mean gravity  $\bar{g}_{\delta\mathcal{M}} \frac{\rho_{\text{surf}}}{\rho_o}$  generated by the non-modeled masses  $\delta\mathcal{M}$ .

In the following two examples the non-modeled masses are given by homogeneous sinusoidal prisms of density  $\rho_{\text{SIN}} = 500 \frac{\text{kg}}{\text{m}^3}$  as defined in Section 6.3. As it can be seen in Figures 4.6 and 4.9, the wavelength is equal to  $\lambda_{\text{SIN}} = 200$  meters in both cases, and the amplitudes  $A_{\text{SIN}}$  are equal to 50 and 40 meters for the first case and second case, respectively. Their bottom is delimited by a horizontal plane at  $H = 0$ , and their upper surface by the sinusoidal surface. Along the axis perpendicular to the axis defined by the tunnel,

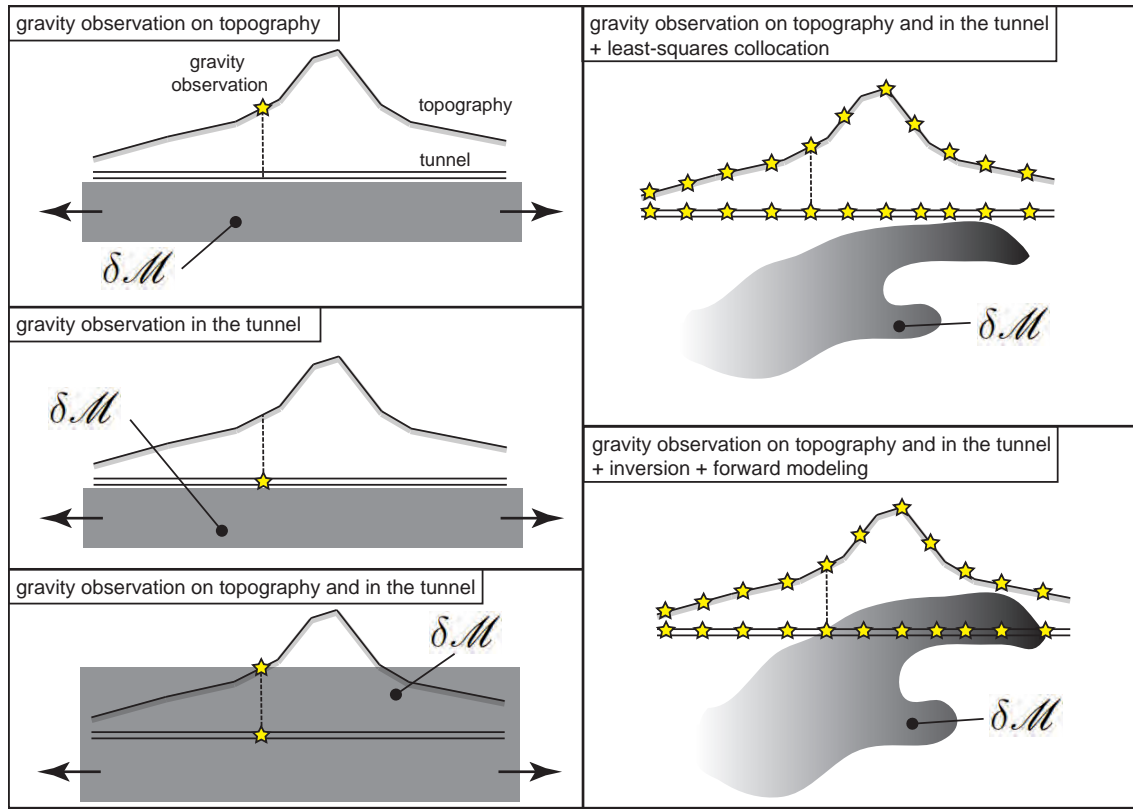


**Figure 4.4:** Graphical representation of the non-modeled masses which generate changes in the mean gravity along the plumbline that can be theoretically observed by the different strategies exposed in this section.

the prism extends over 5 kilometers in both directions, see Figure 4.5.

## Observations

In both cases, we assume that noise-free gravimetric observations are carried out on the topography and inside the tunnel along the profile every 5 meters. In Figures 4.6 and 4.9, the positions of the gravimetric observations are represented by the blue dots. The main reason to work with noise-free observations is motivated by the fact that the objective is to show the fundamental differences and artifacts inherent to the various methodologies without the suspicion that they could come from some noise sources. Moreover, in order to have a better idea of the variation of the gravity field between the tunnel and topography, the gravity field component  $g_{z,\delta\mathcal{M}}(\rho) = -g_{\delta\mathcal{M}}(\rho)$  is shown in Figures 4.7 and 4.10.

## Methods

The following methods are used for the computation of the mean gravity along the plumbline:

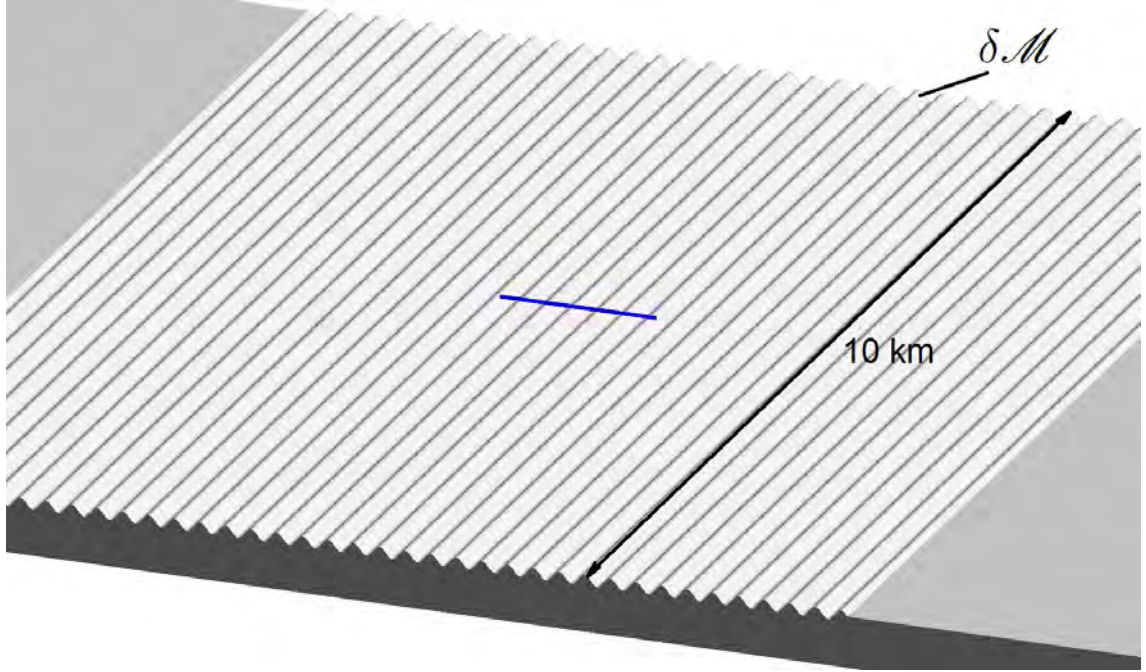


**Figure 4.5:** Perspective view of a sinusoidal prism used for the comparison of the different methods for the computation of the mean gravity along the plumbline. The line in blue represents the positions considered at the surface of the topography.

1. using the simulated non-modeled potential. According to Equation 4.69 we have:

$$\bar{g}_{\delta\mathcal{M}}^{\text{true}} \frac{\rho_{\text{surf}}}{\rho_o} = -\frac{\Phi_{\delta\mathcal{M}}(\rho_{\text{surf}}) - \Phi_{\delta\mathcal{M}}(\rho_o)}{\Delta H_{\rho_o}^{\rho_{\text{surf}}}} \quad (4.104)$$

which corresponds to the true mean gravity used as reference.

2. using only the observations on topography. From Equations 4.71 and 4.69 we have:

$$\bar{g}_{\delta\mathcal{M}}^{\text{surf}} \frac{\rho_{\text{surf}}}{\rho_o} = g_{\delta\mathcal{M}}(\rho_{\text{surf}}) \quad (4.105)$$

3. using only the observations inside the tunnel. From Equations 4.74 and 4.69 we have:

$$\bar{g}_{\delta\mathcal{M}}^{\text{tnl}} \frac{\rho_{\text{surf}}}{\rho_o} = g_{\delta\mathcal{M}}(\rho_o) \quad (4.106)$$

4. using all observations. From Equations 4.76 and 4.69 we have:

$$\bar{g}_{\delta\mathcal{M}}^{\text{mean}} \frac{\rho_{\text{surf}}}{\rho_o} = \frac{g_{\delta\mathcal{M}}(\rho_o) + g_{\delta\mathcal{M}}(\rho_{\text{surf}})}{2} \quad (4.107)$$

5. using all observations in a least-squares collocation estimation. According to Equation 4.99, a prediction of the non-modeled potential  $\Phi_{\delta\mathcal{M}}^{\text{lsc}}$  gives the possibility to compute the mean gravity as follows:

$$\bar{g}_{\delta\mathcal{M}}^{\text{lsc}} \frac{\rho_{\text{surf}}}{\rho_o} = -\frac{\Phi_{\delta\mathcal{M}}^{\text{lsc}}(\rho_{\text{surf}}) - \Phi_{\delta\mathcal{M}}^{\text{lsc}}(\rho_o)}{\Delta H_{\rho_o}^{\rho_{\text{surf}}}} \quad (4.108)$$

### Case 1

In this case, the sinusoidal surface is centered at  $H = 200$  meters, so that  $\delta\mathcal{M}$  is located completely below the tunnel (Figure 4.6). In this case, the gravitational potential between the tunnel and the topography satisfies the *Laplace* equation and is therefore harmonic. This means that according to the *Stokes-Poincaré theorem* (Torge and Müller, 2012), a non-ambiguous downward continuation of the potential field is theoretically possible.

The results of the different methods are shown in Figure 4.8. By comparing to the true mean gravity, we can see that the most accurate results are given by far, by the least-squares collocation  $\bar{g}_{\delta\mathcal{M}}^{\text{isc}}$ . At first glance, this is not surprising. In contrast to the other methods, the least-squares collocation uses not only superposed observations in order to compute the mean gravity at a single position, but all observations together. In addition, since the Laplace equation is fulfilled, the downward continuation — or the estimation of the potential field — can be realised by a projection on a set of appropriate harmonic basis functions. But from another viewpoint, it might be surprising that it works so well considering that the least-squares collocation gives only optimal results if signals are *Gaussian* distributed and if the theoretical covariance function fits the actual one. In this case, it is obvious that both conditions are not fulfilled. Concerning the other methods, we can see that  $\bar{g}_{\delta\mathcal{M}}^{\text{mean}}$  recovers a correct signature but over-estimates the amplitude for the centered mean gravity by a factor two compared to that given by  $\bar{g}_{\delta\mathcal{M}}^{\text{true}}$ . Finally, the methods using only one set of observations show that the errors in the estimation of the lateral variation are smaller for  $\bar{g}_{\delta\mathcal{M}}^{\text{surf}}$  than for  $\bar{g}_{\delta\mathcal{M}}^{\text{tnl}}$ . This can be explained by the fact that the gravity field on the topography looks more like a *Bouguer* plate field than that inside the tunnel, see Figure 4.7.

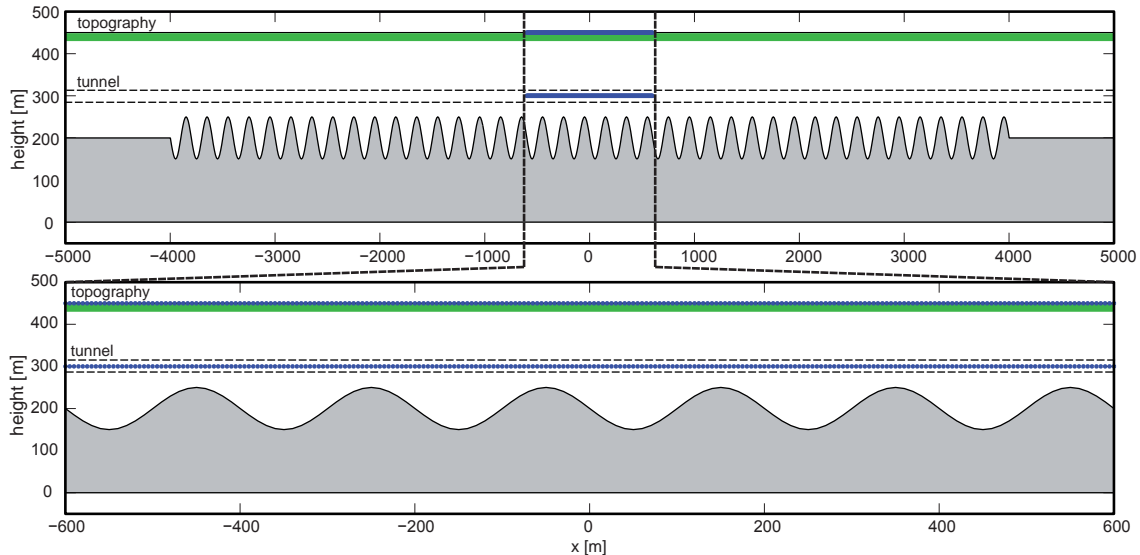


**Figure 4.6:** Vertical profile of the non-modeled mass model  $\delta\mathcal{M}$  and the positions of the gravimetric observations used in **Case 1**. The blue dots represent the positions of the observations.

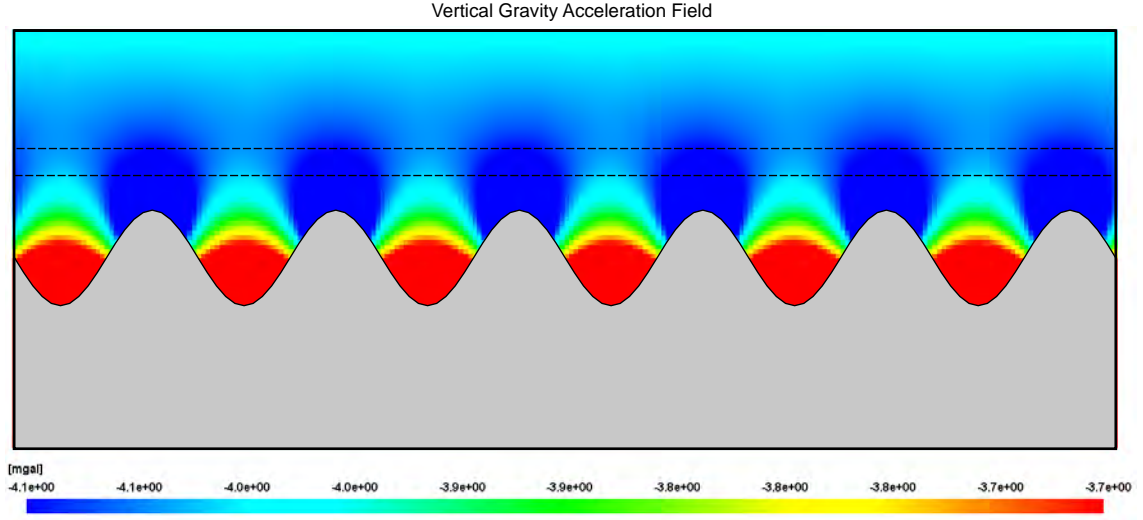


**Figure 4.7:** Simulated gravity field component  $g_{z, \delta \mathcal{M}}(\rho) = -g_{\delta \mathcal{M}}(\rho)$ , generated by the non-modeled mass  $\delta \mathcal{M}$  in **Case 1**. The simulation was computed with the software QGravity. The black dashed lines represent the tunnel.

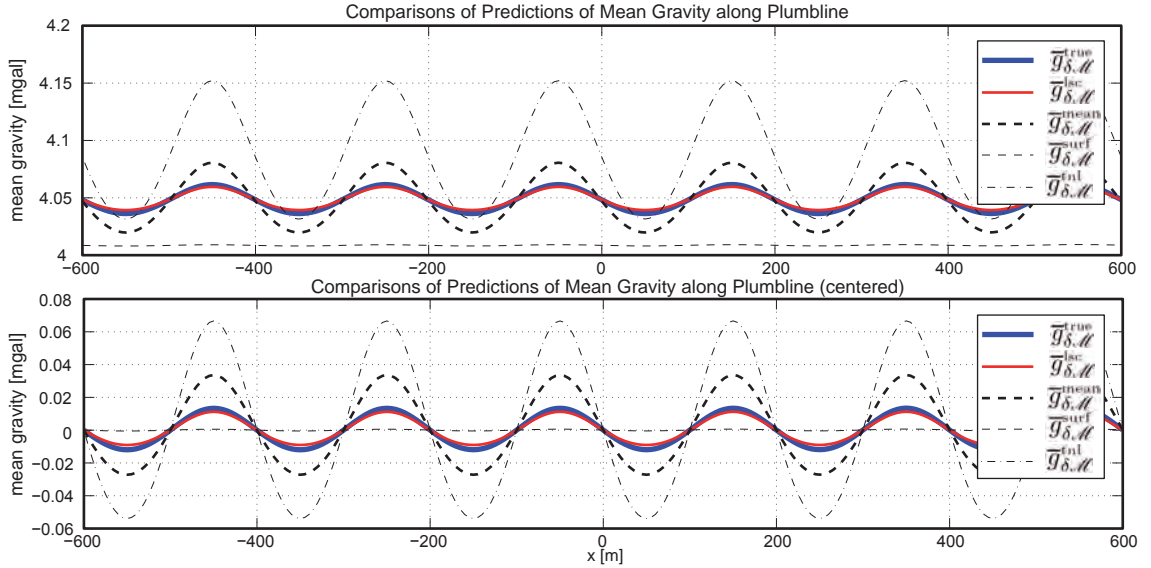


**Figure 4.8:** Mean gravity along the plumblines for **Case 1**, according to the different methods exposed in Section 4.4.7.

### Case 2

In this second example, the sinusoidal surface is centered at  $H = 400$  meters, so that  $\delta\mathcal{M}$  contains the tunnel but stays below the surface of topography (Figure 4.9). In this case, the gravitational potential no longer satisfies *Laplace* equation and is therefore not harmonic. A downward non-ambiguous continuation of the potential field is theoretically not more possible.

The results of the different methods are shown in Figure 4.11. They demonstrate several interesting non-intuitive aspects. Firstly, if we look at the absolute values provided by the different methods, the superiority of  $\bar{g}_{\delta\mathcal{M}}^{\text{lsc}}$  and  $\bar{g}_{\delta\mathcal{M}}^{\text{mean}}$  is evident and corresponds to the common sense. In this case, two methods are able to estimate the mean gravity with a relative accuracy of approximately 10 % whereas  $\bar{g}_{\delta\mathcal{M}}^{\text{surf}}$  and  $\bar{g}_{\delta\mathcal{M}}^{\text{tnl}}$  lead to a relative accuracy of 30 % only. Compared to the results obtained in **Case 1**, we clearly see a first bad consequence of the presence of non-modeled masses inside the field which must be estimated.

Secondly, if we look at the errors with respect to the centered values the comparisons are more surprising. Now, the best estimation is given by  $\bar{g}_{\delta\mathcal{M}}^{\text{tnl}}$ . This solution is the only one which recovers the true signature with an acceptable amplitude. By contrast, all other methods are not able to recover the true signature. They show a kind of opposite phase shift which provokes a supplementary amplification of the errors. This effect is very pronounced for  $\bar{g}_{\delta\mathcal{M}}^{\text{surf}}$  with amplitude errors larger than a factor 10. Concerning  $\bar{g}_{\delta\mathcal{M}}^{\text{lsc}}$  and  $\bar{g}_{\delta\mathcal{M}}^{\text{mean}}$  the amplitude errors stay approximately in the order of magnitude of the true value but are also disappointing.

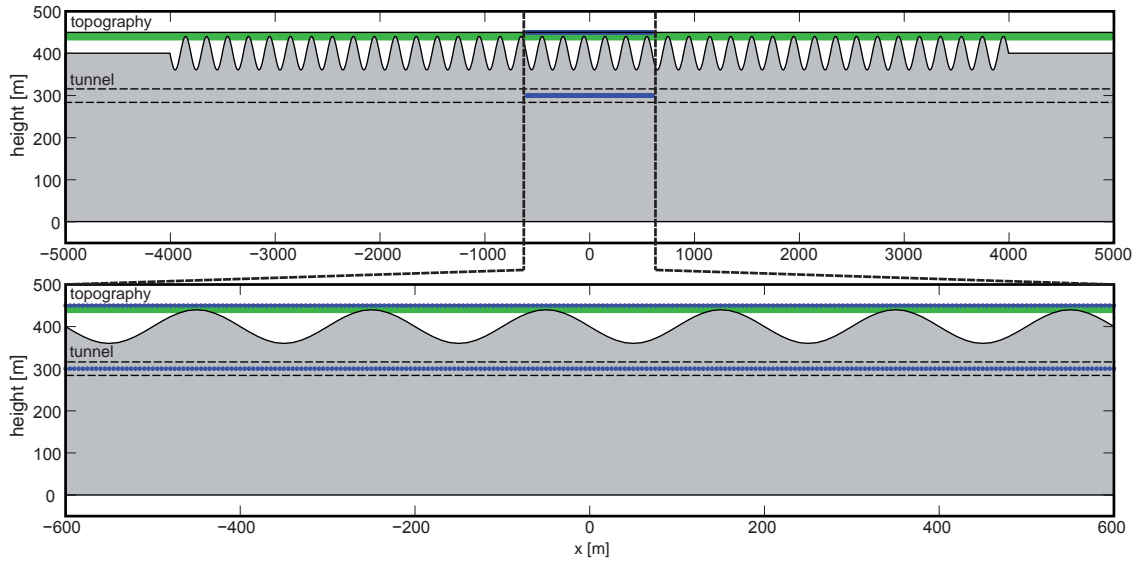


**Figure 4.9:** Vertical profile of the non-modeled mass model  $\delta\mathcal{M}$  and the positions of the gravimetric observations used in **Case 2**. The blue dots represent the positions of the observations.

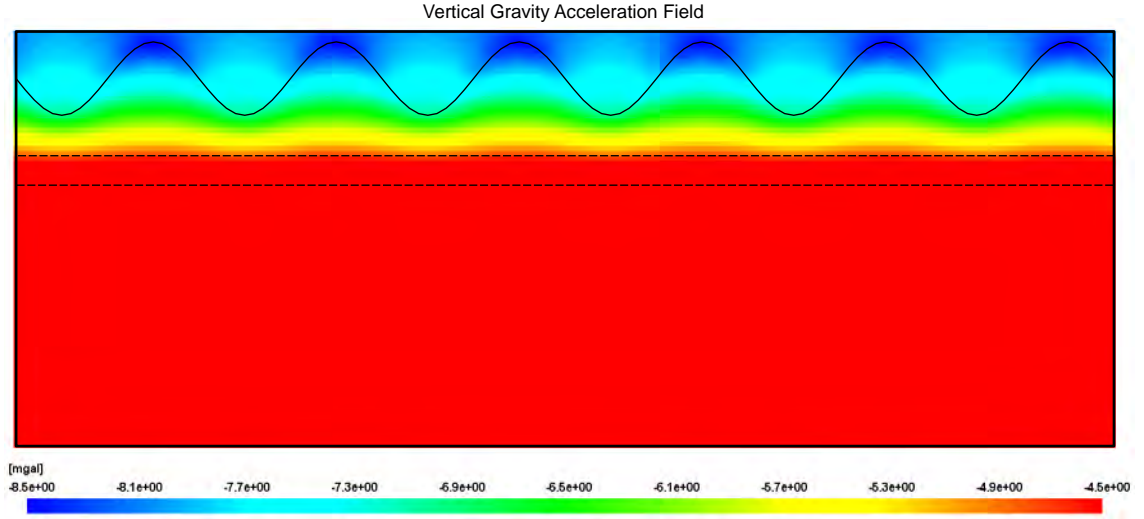


**Figure 4.10:** Simulated gravity field component  $g_{z, \delta \mathcal{M}}(\rho) = -g_{\delta \mathcal{M}}(\rho)$ , generated by the non-modeled mass  $\delta \mathcal{M}$  in **Case 2**. The color scale is optimized to see the variations between the tunnel and the topography. The red homogeneous field below the tunnel does not correspond to a homogeneous gravity field. It means that the values are larger than 4.5 [mgal]. The simulation was computed with the software QGravity. The black dashed lines represent the tunnel.

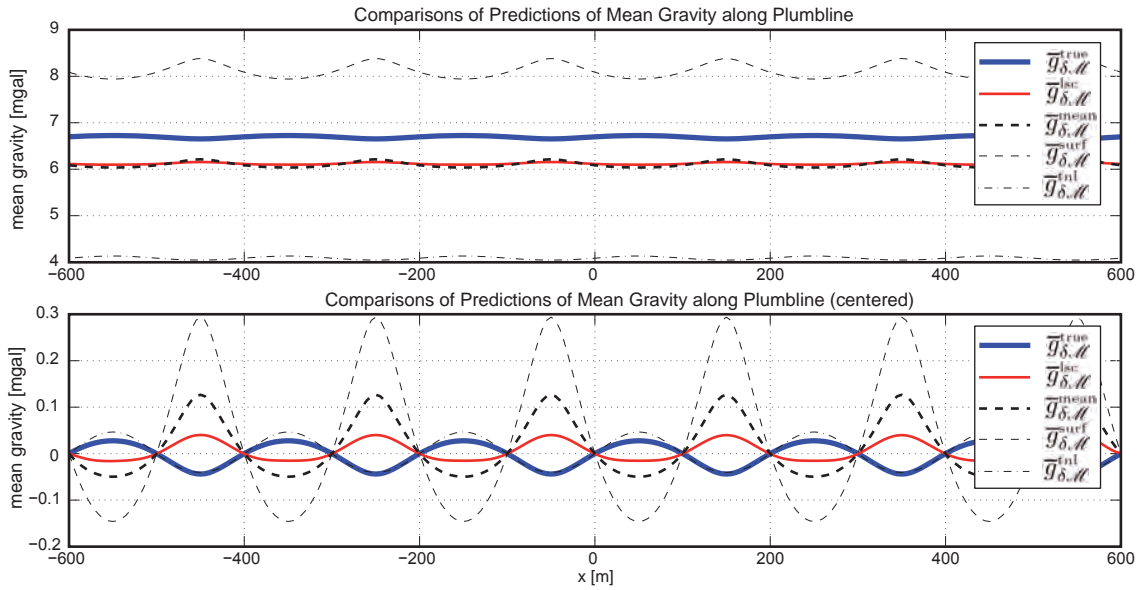


**Figure 4.11:** Mean gravity along the plumblines, for **Case 2**, according to the different methods exposed in Section 4.4.7.

**Concluding Remarks**

As shown in examples, the quality of the determination of the mean gravity along the plumbline is primary governed by the quality of the modeled masses situated between the tunnel and the topography. This aspect is by far the most crucial one, since additional and more accurate observations cannot help to make the determination of the gravity field unambiguous. Furthermore, the unpredictable impact of non-modeled masses between the tunnel and the topography can be limited using  $\bar{g}_{\delta, \mathcal{M}}^{\text{isc}}$  and  $\bar{g}_{\delta, \mathcal{M}}^{\text{mean}}$ . In addition, in order to estimate the irreducible accuracy which can be realistically obtained without supplementary geophysical or geological density field investigations, some gravity field simulations must be computed. This can be done using some assumptions about the order of magnitude and the size of the non-modeled masses.



## 4.5 Alignment Accuracy of Geometric Determinations

In this section, the accuracy of the astronomical and gradiometric levelling are treated separately, using Equations 4.12 and 4.43, in terms of alignment introduced in Section 2.1. The analyses focus on the accuracy of the determination of equipotential profiles of  $S = 200$  meters in length according to the alignment constraints given by the CLIC studies. In order to simplify the models, we assume that  $\epsilon_{\text{tot}}$ ,  $g_{\text{tot}}$  and  $\frac{d\epsilon_{\text{tot}}}{ds}$  are directly observed at regular a spacing  $\Delta s_{\text{obs}}$  and affected by systematic, random and correlated noise as explained in Section 4.5.3. The omission errors due to the finite spacing between the observations are neglected in the following simulations but treated in detail in Chapter 6.

### 4.5.1 Definition of the Misalignment Accuracy

In order to rigorously formulate the misalignment accuracy, it is necessary to define some useful random variables. For a given observable model  $\Sigma(l_{\text{obs}}, \Delta s_{\text{obs}})$ , which contains the noisy observables  $l_{\text{obs}}$  and the spacing  $\Delta s_{\text{obs}}$ , the discretized equipotential profile  $\rho_{\sim}(s)$  is represented by a random vector  $\mathcal{P}(\Sigma)$ , for which a single realization  $k$  is represented as follows:

$$\mathcal{P}_k(\Sigma) \equiv \left( N_{\text{tot}}(s_1 = 0) \quad \dots \quad N_{\text{tot}}(s_i = (i-1) \cdot \Delta s) \quad \dots \quad N_{\text{tot}}(s_n = 200) \right)_k^T \quad (4.109)$$

where  $s$  represents the curvilinear coordinate along the profile. The misalignment error for a wavelength of 200 meters of  $\mathcal{P}_k(\Sigma)$  is given by:

$$x_k(\Sigma) = \mathcal{M}_{\star}^{200} \{ \mathcal{P}_k(\Sigma) \} \quad (4.110)$$

where  $x_k(\Sigma)$  is a realization of the random variable  $\mathcal{X}(\Sigma)$  which represents the misalignment error for a wavelength of 200 meters. Finally, the alignment accuracy  $\sigma_{\mathcal{M}(\Sigma)}$  is defined as:

$$\sigma_{\mathcal{M}(\Sigma)} = x : P(\mathcal{X}(\Sigma) \leq x) = 0.68 \quad (4.111)$$

which covers the same probability as the bilateral univariate Gaussian random variable  $\mathcal{N}(0, \sigma^2)$  at one sigma ( $\pm 1\sigma$ ):

$$P(-\sigma \leq \mathcal{N}(0, \sigma^2) \leq +\sigma) = 0.68 \quad (4.112)$$

In the case of fixing a confidence level  $1 - \alpha$  differing from 68%, the alignment accuracy will be denoted by  $\sigma_{\mathcal{M}(\Sigma)}^{1-\alpha}$  and corresponds to:

$$\sigma_{\mathcal{M}(\Sigma)}^{1-\alpha} = x : P(\mathcal{X}(\Sigma) \leq x) = 1 - \alpha \quad (4.113)$$

In an equivalent manner, we can say that  $\sigma_{\mathcal{M}(\Sigma)}^{1-\alpha}$  is the  $(1 - \alpha)$ -quantile of  $\mathcal{X}(\Sigma)$ .

### 4.5.2 Monte-Carlo Simulation

Since the misalignment operator  $\mathcal{M}$  has strong non-linear behaviors, the development of a closed analytic formula of the probability density of the random variable  $\mathcal{X}(\Sigma)$  is not conceivable. Thus, it must be computed in an empirical way. In this thesis this is done using Monte-Carlo simulations. The basic principle is very simple and consists of the following steps (see Figure 4.12):

1. simulate noisy observations from the error model of the observables  $\Sigma(l_{\text{obs}}, \Delta s_{\text{obs}})$ .
2. realize numerically a large<sup>9</sup> number  $K$  of discretized equipotential profiles  $\mathcal{P}_k(\Sigma)$ , from simulated noisy observations  $\Sigma$ .
3. for each profile  $k$  compute the misalignment:

$$x_k(\Sigma) = \mathcal{M}_0^{200} \{ \mathcal{P}_k(\Sigma) \} \quad (4.114)$$

4. compute numerically the cumulative probability density function  $\text{CDF}_{\mathcal{X}(\Sigma)}(x)$  of  $\mathcal{X}(\Sigma)$  with all  $x_k(\Sigma)$ .
5. compute the empirical misalignment accuracy  $\sigma_{\mathcal{M}(\Sigma)}^{1-\alpha}$  from the CDF  $F_{\mathcal{X}(\Sigma)}(x)$  using a linear interpolation.

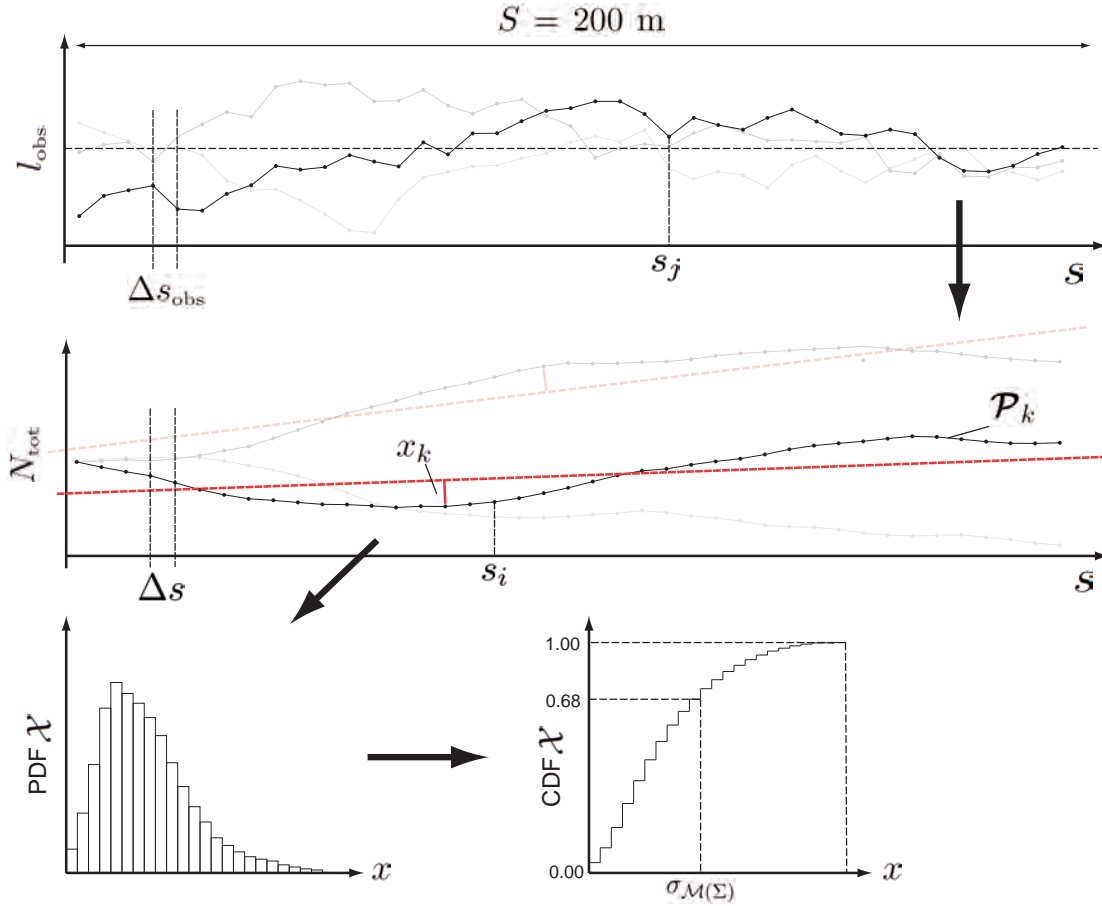


**Figure 4.12:** Schematic representation of the steps defined in Sections 4.5.1 and 4.5.2 for the computation of the misalignment accuracy in geometric determinations with Monte-Carlo simulations.

<sup>9</sup>In this thesis, if not mentioned,  $K=10'000$ .

### 4.5.3 Generation of Noisy Observables

The generation of a noisy observable  $l_{\text{obs}}(s_j)$ , at position  $s_j$  is done by adding a noise-free observable  $\tilde{l}_{\text{obs}}(s_j)$ , computed from an error-free equipotential profile  $\tilde{\mathcal{P}}$ , and an error  $\delta l(s_j)$ , computed from a pre-defined error model:

$$l_{\text{obs}}(s_j) = \tilde{l}(s_j) + \delta l(s_j) \quad (4.115)$$

#### Noise-free Observables

The error-free equipotential profile is assumed to match exactly the normal equipotential so that:

$$\tilde{\mathcal{P}} \equiv \left( \tilde{N}_{\text{tot}}(s_1 = 0) = 0 \quad \dots \quad \tilde{N}_{\text{tot}}(s_i = (i-1) \cdot \Delta s) = 0 \quad \dots \quad \tilde{N}_{\text{tot}}(s_n = 200) = 0 \right)^T \quad (4.116)$$

which implies that the following noise-free observable  $\tilde{l}(s_j)$  are equal to zero:

$$\tilde{l}(s_j) = \tilde{\epsilon}_{\text{tot}}(s_j) = \frac{d\tilde{\epsilon}_{\text{tot}}}{ds}(s_j) = 0 \quad (4.117)$$

and the noise-free gravimetric observations are equal to the normal gravity:

$$\tilde{l}(s_j) = \tilde{g}_{\text{tot}}(H_j, s_j) = \gamma(H_j) \quad (4.118)$$

where  $H_j$  represents the orthometric height of a particular position on the plumbline passing through  $s_j$ .

#### General Observable Noise Model

The noise — or stochastic — model of the observations is the most important part of the current analysis. There are many ways to model or represent noise. Here,  $\delta l(s_j)$  is formed by systematic, random and correlated noise as:

$$\begin{aligned} \delta l(s_j) = & \delta l_{\text{Bias}} + \delta l_{\text{Rnd Bias}} \\ & + \delta l_{\text{Drift}} + \delta l_{\text{Rnd Drift}} \\ & + \delta l_{\text{White}} + \delta l_{\text{Corr}} \end{aligned} \quad (4.119)$$

where:

- $\delta l_{\text{Bias}}$  = A systematic non-calibrated bias.
- $\delta l_{\text{Rnd Bias}}$  = A systematic bias which is occurring randomly at each realization of the full process. The randomness is modeled by a Gaussian random bias stochastic process  $\mathcal{X}_{\text{Rnd Bias}}$  parametrized by the standard deviation  $\sigma_{\text{Rnd Bias}}$ .
- $\delta l_{\text{Drift}}$  = A systematic non-calibrated drift, proportional to  $s_j$ :

$$\delta l_{\text{Drift}}(s_j) = \dot{\delta} l_{\text{Drift}} \cdot s_j \quad (4.120)$$

where  $\dot{\delta} l_{\text{Drift}} = \frac{d\delta l_{\text{Drift}}(s_j)}{ds}$  is the constant drift parameter.

- $\delta l_{\text{Rnd Drift}}$  = A systematic drift, proportional to  $s_j$  which is occurring randomly at each realization of the full process. The randomness is modeled by a Gaussian random drift stochastic process  $\mathcal{X}_{\text{Rnd Drift}}$  parametrized by the standard deviation  $\sigma_{\text{Rnd Drift}}$ .
- $\delta l_{\text{White}}$  = A non-correlated random noise modeled by a Gaussian white noise stochastic process  $\mathcal{X}_{\text{White}}$  parametrized by the standard deviation  $\sigma_{\text{White}}$ .
- $\delta l_{\text{Corr}}$  = A correlated random noise modeled by a first-order stationary Gaussian-Markov stochastic process  $\mathcal{X}_{\text{Corr}}$  parametrized by the standard deviation  $\sigma_{\text{Corr}}$  and the correlation length  $d_{\text{Corr}}$ .

A formal description of these stochastic processes is given in Appendix D.

#### 4.5.4 Alignment Accuracy of Astrogeodetic Levelling

The following analyses are based each time on  $K = 10'000$  Monte-Carlo generated equipotential profiles  $\mathcal{P}^{\text{astro}}(\Sigma)$ .

##### Noise Model for Astrogeodetic Observations

Here we suppose that only  $\epsilon_{\text{tot}}$  is observed at a regular spacing  $\Delta s_{\text{obs}}$ . According to Equation 4.119, the observations are generated by taking into account the following noise sources:

$$\begin{aligned} \delta\epsilon_{\text{tot}} = & \underbrace{\delta\epsilon_{\text{Bias}}}_{=0} + \underbrace{\delta\epsilon_{\text{Rnd Bias}}}_{=0} \\ & + \delta\epsilon_{\text{Drift}} + \delta\epsilon_{\text{Rnd Drift}} \\ & + \delta\epsilon_{\text{White}} + \delta\epsilon_{\text{Corr}} \end{aligned} \quad (4.121)$$

where:

- $\delta\epsilon_{\text{Bias}}$  Is not taken into account because a bias in  $\epsilon_{\text{tot}}$  provokes a constant tilting of  $\mathcal{P}^{\text{astro}}$  but no misalignment.
- $\delta\epsilon_{\text{Rnd Bias}}$  Is not taken into account for the same reason as in the case of  $\delta\epsilon_{\text{Bias}}$ .
- $\delta\epsilon_{\text{Drift}}$  This is a purely systematic noise effect which depends linearly on  $s$ . This kind of systematic effect is very difficult to identify because it is, per definition, also constant in time. We can imagine a large number of stationary phenomena coupled indirectly with variables which change linearly with  $s$  that might provoke such effects. However, in astrogeodetic observations the most likely might be due to stationary anomalous refraction effects highly correlated with the topography or insufficient plumbline curvature reductions highly correlated with the underground density field.
- $\delta\epsilon_{\text{Rnd Drift}}$  This systematic effect depends linearly on  $s$ , but it might take a different value in repeated determination of  $\mathcal{P}^{\text{astro}}$  separated in time. In opposition to  $\delta\epsilon_{\text{Drift}}$ , it renders possible an empirical estimation by repeated determination of  $\mathcal{P}^{\text{astro}}$ . This noise corresponds also to a correlated noise  $\delta\epsilon_{\text{Corr}}$  with infinite correlation length. In astrogeodetic observations, the most likely sources of this class of noise are similar to those in  $\delta\epsilon_{\text{Drift}}$ , with the difference that we consider that the effects are only stationary during the observation time of  $\mathcal{P}^{\text{astro}}$ .
- $\delta\epsilon_{\text{White}}$  The sources of white noise in astrogeodetic observations are mainly due to the noise in the astrometry caused by high frequency refraction signal in the atmosphere and the noise generated by the tiltmeters. The determination of the level of white noise can be evaluated and its impact is mitigated by repeated observations.
- $\delta\epsilon_{\text{Corr}}$  The correlated noise models the impact of phenomena that generate noise having a statistical behavior bounded by the white noise and the random bias.

### Computation of $\mathcal{P}^{\text{astro}}(\Sigma)$

The observations generated at each discrete position  $s_j$  (separated by  $\Delta s_{\text{obs}}$ ), are firstly predicted at each discrete position  $s_i$  (separated by  $\Delta s = 10$  m) by linear interpolation. Finally, one realization of  $\mathcal{P}^{\text{astro}}(\Sigma)$  is computed by a numerical solution of Equation 4.12 using a trapeze rule scheme for the integration:

$$N_{\text{tot}}(s_{ii}) = \sum_{i=2}^{ii} \frac{1}{2} [\epsilon_{\text{tot}}(s_{i-1}) + \epsilon_{\text{tot}}(s_i)] \cdot \Delta s \quad (4.122)$$

### Summary of the Impact of Observable's Noises on Misalignment

A summary of the various noises which generate a misalignment of 10 microns over 200 meters is shown in Table 4.1. More detailed results can be found in the Appendix F.1.

**Table 4.1:** Summary of the alignment accuracy of astrogeodetic levelling. The maximal allowed noises are given regarding to a misalignement of 10 microns over 200 meters for a level of confidence  $1 - \alpha$ .

noise	additional parameters	depends on $\Delta s_{\text{obs}}$	depends on $\alpha$	max noise		unit	critical
				68%	95%		
$\delta\epsilon_{\text{Bias}}$	—	no	no	—	—	[arcsec]	no
$\delta\epsilon_{\text{Rnd Bias}}$	—	no	yes	—	—	[arcsec]	no
$\delta\epsilon_{\text{Drift}}$	—	no	no	0.07	0.06	$\left[\frac{\text{arcsec}}{100 \text{ m}}\right]$	yes
$\delta\epsilon_{\text{Rnd Drift}}$	—	no	yes	0.07	0.02	$\left[\frac{\text{arcsec}}{100 \text{ m}}\right]$	yes
$\delta\epsilon_{\text{White}}$	$\Delta s_{\text{obs}} = 10$ m	yes	yes	0.09	0.06	[arcsec]	yes
$\delta\epsilon_{\text{White}}$	$\Delta s_{\text{obs}} = 40 - 100$ m	yes	yes	0.06	0.04	[arcsec]	yes
$\delta\epsilon_{\text{Corr}}$	$\Delta s_{\text{obs}} = 10$ m, $d_{\text{Corr}} = 0$ m	yes	yes	0.09	0.06	[arcsec]	yes
$\delta\epsilon_{\text{Corr}}$	$\Delta s_{\text{obs}} = 10$ m, $d_{\text{Corr}} = 40$ m	yes	yes	0.06	0.04	[arcsec]	yes
$\delta\epsilon_{\text{Corr}}$	$\Delta s_{\text{obs}} = 10$ m, $d_{\text{Corr}} = 500$ m	yes	yes	0.1	0.06	[arcsec]	yes

### 4.5.5 Alignment Accuracy of the Orthometric Corrections

The analyses of the alignment accuracy of the orthometric correction are divided into two different parts. The first part  $E1$  concerns the integral term of Equation 4.59, the second part  $E2$  the remaining terms:

$$\begin{aligned}
 E_{a_o}^{b_o} = & \underbrace{\int_{a_{\text{surf}}}^{b_{\text{surf}}} \frac{g_{\text{tot}}(\rho_{\text{surf}}) - \gamma(\rho_o)}{\gamma(\rho_o)} \cdot dn}_{E1} \\
 & + \underbrace{\frac{\bar{g}_{\text{tot}} a_{\text{surf}} - \gamma(a_o)}{\gamma(a_o)} \cdot \Delta H_{a_o}^{a_{\text{surf}}} - \frac{\bar{g}_{\text{tot}} b_{\text{surf}} - \gamma(b_o)}{\gamma(b_o)} \cdot \Delta H_{b_o}^{b_{\text{surf}}}}_{E2}
 \end{aligned} \tag{4.123}$$

This separation is due to the fact that:

- $E1$  and  $E2$  have a different error propagation behavior.
- $E1$  depends directly on  $dn$ , the change in height of topography.
- Unlike  $E2$ , the quantities in  $E1$  are observables without ambiguities.

The analyses are based each time on  $K = 10'000$  generated orthometric corrections profiles  $\mathcal{P}^{E1}(\Sigma)$  and  $\mathcal{P}^{E2}(\Sigma)$ .

### Noise Model

It is assumed that  $g_{\text{tot}}$  is directly observed, and  $\bar{g}_{\text{tot}}$  estimated by an arbitrary method, at a regular spacing  $\Delta s_{\text{obs}}$ . According to Equation 4.119, the observed gravity observations on topography  $g_{\text{tot}}$  are generated by taking into account the following noise sources:

$$\begin{aligned}
 \delta g_{\text{tot}} = & \underbrace{\delta g_{\text{Bias}}}_{=0} + \underbrace{\delta g_{\text{Rnd Bias}}}_{=0} \\
 & + \delta g_{\text{Drift}} + \delta g_{\text{Rnd Drift}} \\
 & + \delta g_{\text{White}} + \delta g_{\text{Corr}}
 \end{aligned} \tag{4.124}$$

where:

$\delta g_{\text{Bias}}$  Is not taken into account because a bias in  $g_{\text{tot}}$  provokes a constant tilting on  $\mathcal{P}^{E1}$  but no misalignment.

$\delta g_{\text{Rnd Bias}}$  Is not taken into account for the same reason as for  $\delta g_{\text{Bias}}$ .

$\delta g_{\text{Drift}}$  This purely systematic noise effect depends linearly on  $s$ . In relative gravimetric measurements, time drifts are common and could produce drifts which depend linearly on  $s$ , if the measurements are carried out sequentially along the profile.

- $\delta g_{\text{Rnd Drift}}$  This systematic effect depends linearly on  $s$  but might take a different value in repeated determinations of  $\mathcal{P}^{E1}$  separated in time. For gravimetric observations, the most likely sources of this class of noise are similar to those for  $\delta g_{\text{Drift}}$ , with the difference that we consider that the effects are only stationary during the observation time of  $\mathcal{P}^{E1}$ .
- $\delta g_{\text{White}}$  The sources of white noise in gravimetric observations on the surface of topography are mainly due to high-frequency perturbations caused by traffic or wind.
- $\delta g_{\text{Corr}}$  The correlated noise models the impact of phenomena that generate noise having a statistical behavior bounded by the white noise and the random bias. For gravimetric measurements, it could be generated by all systematic errors of the gravimeter which are coupled with the local environment or which change slowly in time. For example, errors in the scaling factor and changes of the hysteresis behavior of the instrument can be imagined.

The mean gravity estimations  $\bar{g}_{\text{tot}}$  by:

$$\begin{aligned} \delta \bar{g}_{\text{tot}} = & \underbrace{\delta \bar{g}_{\text{Bias}}}_{=0} + \underbrace{\delta \bar{g}_{\text{Rnd Bias}}}_{=0} \\ & + \underbrace{\delta \bar{g}_{\text{Drift}}}_{=0} + \underbrace{\delta \bar{g}_{\text{Rnd Drift}}}_{=0} \\ & + \delta \bar{g}_{\text{White}} + \delta \bar{g}_{\text{Corr}} \end{aligned} \quad (4.125)$$

- $\delta \bar{g}_{\text{Bias}}$  Is not taken into account because a bias in  $\bar{g}_{\text{tot}}$  provokes no changes in  $\mathcal{P}^{E2}$ .
- $\delta \bar{g}_{\text{Rnd Bias}}$  Is not taken into account for the same reason as for  $\delta \bar{g}_{\text{Bias}}$ .
- $\delta \bar{g}_{\text{Drift}}$  Is not taken into account because a drift in  $\bar{g}_{\text{tot}}$  provokes a constant tilting on  $\mathcal{P}^{E2}$  but no misalignment.
- $\delta \bar{g}_{\text{Rnd Drift}}$  Is not taken into account for the same reason as for  $\delta \bar{g}_{\text{Drift}}$ .
- $\delta \bar{g}_{\text{White}}$  The source of white noise in the mean gravity is mainly due to the white noise contained in the observations used for the determination of the mean gravity.
- $\delta \bar{g}_{\text{Corr}}$  The correlated noise models the impact of phenomena that generate noise having a statistical behavior bounded by the white noise and the random bias. For the mean gravity, the correlated noise is implicitly generated by the estimation process of the mean gravity from observations and the intrinsic ambiguous nature of this estimation. It is probably the most problematic noise source.

### Computation of $\mathcal{P}^{E1}(\Sigma)$ and $\mathcal{P}^{E2}(\Sigma)$

The observations generated at each discrete position  $s_j$  (separated by  $\Delta s_{\text{obs}}$ ), are firstly predicted at each discrete position  $s_i$  (separated by  $\Delta s = 10$  m) by linear interpolation. In addition it is assumed that the topography is fixed at  $s_1$  with  $H_1^{\text{surf}} = 150$  m and with a slope of  $\frac{\Delta n}{\Delta s} = +10\%$  in order to have a non-zero and significant effect. The tunnel is



fixed at  $H_i^{\text{tnl}} = 0$  m. One realization of  $\mathcal{P}^{E1}(\Sigma)$  is computed by a numerical solution of Equation 4.59 using a trapeze rule scheme for the integration:

$$E1(s_{ii}) = \sum_{i=2}^{ii} \frac{1}{2} \left[ \frac{g_{\text{tot}}(H_{i-1}^{\text{surf}}, s_{i-1}) - \gamma(0)}{\gamma(0)} + \frac{g_{\text{tot}}(H_i^{\text{surf}}, s_i) - \gamma(0)}{\gamma(0)} \right] \cdot \Delta n \quad (4.126)$$

Concerning the computation of  $\mathcal{P}^{E2}(\Sigma)$ , it is assumed that the topography is fixed at  $H_i^{\text{surf}} = 150$  m, without slope, in order to have a clear separation from  $E1$ . The tunnel is fixed at  $H_i^{\text{tnl}} = 0$  m. One realization of  $\mathcal{P}^{E2}(\Sigma)$  is computed by:

$$E2(s_i) = \frac{\bar{g}_{\text{tot}}(s_1) - \gamma(0)}{\gamma(0)} \cdot (H_1^{\text{surf}} - H_1^{\text{tnl}}) - \frac{\bar{g}_{\text{tot}}(s_i) - \gamma(0)}{\gamma(0)} \cdot (H_i^{\text{surf}} - H_i^{\text{tnl}}) \quad (4.127)$$

### Summary of the Impact of Observable's Noises on Misalignment ( $\mathcal{P}^{E1}$ and $\mathcal{P}^{E2}$ )

A summary of the various noises which generate a misalignment of 10 microns overs 200 meters is shown in Table 4.2 and 4.3. More detailed results can be found in the Appendix F.2.

**Table 4.2:** Summary of the alignment accuracy of the ortometric corrections  $\mathcal{P}^{E1}$ . The maximal allowed noises are given regarding to a misalignement of 10 microns over 200 meters for a level of confidence  $1 - \alpha$ .

noise	additional parameters	depends on $\Delta s_{\text{obs}}$	depends on $\alpha$	max noise		unit	critical
				68%	95%		
$\delta g_{\text{Bias}}$	—	no	no	—	—	mgal	no
$\delta g_{\text{Rnd Bias}}$	—	no	yes	—	—	mgal	no
$\delta g_{\text{Drift}}$	$\Delta s_{\text{obs}} = 10 - 100$ m	no	no	30	30	$\frac{\text{mgal}}{100 \text{ m}}$	no
$\delta g_{\text{Rnd Drift}}$	$\Delta s_{\text{obs}} = 10 - 100$ m	no	yes	30	15	$\frac{\text{mgal}}{100 \text{ m}}$	no
$\delta g_{\text{White}}$	$\Delta s_{\text{obs}} = 10$ m	yes	yes	4	3	mgal	no
$\delta g_{\text{White}}$	$\Delta s_{\text{obs}} = 40 - 100$ m	yes	yes	3	2	mgal	no
$\delta g_{\text{Corr}}$	$\Delta s_{\text{obs}} = 10$ m, $d_{\text{Corr}} = 0$ m	yes	yes	4	3	mgal	no
$\delta g_{\text{Corr}}$	$\Delta s_{\text{obs}} = 10$ m, $d_{\text{Corr}} = 40$ m	yes	yes	3	2	mgal	no
$\delta g_{\text{Corr}}$	$\Delta s_{\text{obs}} = 10$ m, $d_{\text{Corr}} = 500$ m	yes	yes	5	3	mgal	no

**Table 4.3:** Summary of the alignment accuracy of the ortometric corrections  $\mathcal{P}^{E2}$ . The maximal allowed noises are given regarding to a misalignement of 10 microns over 200 meters for a level of confidence  $1 - \alpha$ .

noise	additional parameters	depends on $\Delta s_{\text{obs}}$	depends on $\alpha$	max noise		unit	critical
				68%	95%		
$\delta\bar{g}_{\text{Bias}}$	—	no	no	—	—	mgal	no
$\delta\bar{g}_{\text{Rnd Bias}}$	—	no	yes	—	—	mgal	no
$\delta\bar{g}_{\text{Drift}}$	—	no	no	—	—	$\frac{\text{mgal}}{100 \text{ m}}$	no
$\delta\bar{g}_{\text{Rnd Drift}}$	—	no	yes	—	—	$\frac{\text{mgal}}{100 \text{ m}}$	no
$\delta\bar{g}_{\text{White}}$	$\Delta s_{\text{obs}} = 10 \text{ m}$	yes	yes	0.03	0.025	mgal	no
$\delta\bar{g}_{\text{White}}$	$\Delta s_{\text{obs}} = 100 \text{ m}$	yes	yes	0.1	0.05	mgal	no
$\delta\bar{g}_{\text{Corr}}$	$\Delta s_{\text{obs}} = 10 \text{ m}, d_{\text{Corr}} = 0 \text{ m}$	yes	yes	0.03	0.025	mgal	no
$\delta\bar{g}_{\text{Corr}}$	$\Delta s_{\text{obs}} = 10 \text{ m}, d_{\text{Corr}} = 1 \text{ km}$	yes	yes	0.175	0.125	mgal	yes
$\delta\bar{g}_{\text{Corr}}$	$\Delta s_{\text{obs}} = 10 \text{ m}, d_{\text{Corr}} = 16 \text{ km}$	yes	yes	0.5	0.8	mgal	yes

### 4.5.6 Alignment Accuracy of Gradiometric Levelling

The following analyses are based each time on  $K = 10'000$  Monte-Carlo generated equipotential profiles  $\mathcal{P}(\Sigma)$ .

#### Noise Model for Gradiometric Observations

Here we suppose that only  $\Delta\Gamma_{\text{tot},xx}^S$ , denoted by  $\Delta\Gamma_{\text{tot}}$  for the convenience, is observed at a regular spacing  $\Delta s_{\text{obs}}$ . According to Equation 4.119, the observations are generated by taking into account the following noise sources:

$$\begin{aligned}\delta\Delta\Gamma_{\text{tot}} &= \delta\Delta\Gamma_{\text{Bias}} + \delta\Delta\Gamma_{\text{Rnd Bias}} \\ &\quad + \delta\Delta\Gamma_{\text{Drift}} + \delta\Delta\Gamma_{\text{Rnd Drift}} \\ &\quad + \delta\Delta\Gamma_{\text{White}} + \delta\Delta\Gamma_{\text{Corr}}\end{aligned}\tag{4.128}$$

where:

- $\delta\Delta\Gamma_{\text{Bias}}$  A systematic bias which might come from non-calibrated effects or systematic biases in the reductions.
- $\delta\Delta\Gamma_{\text{Rnd Bias}}$  A bias which is assumed to be constant for a single determination of  $\mathcal{P}$  only. This might occurs when the gradiometer is affected by a different bias at each start. An other possibility might come from time varying environmental effects which can be seen as constant during the duration of the observation of  $\mathcal{P}$ , e.g., hydrogeological changes.
- $\delta\Delta\Gamma_{\text{Drift}}$  As for astrogeodetic measurements, a systematic drift source might be of instrumental or environmental origin.
- $\delta\Delta\Gamma_{\text{Rnd Drift}}$  As for astrogeodetic measurements, a random drift source might be of instrumental or environmental origin.
- $\delta\Delta\Gamma_{\text{White}}$  Nowadays, regarding the performance of torsion balance measurements (*Völgyesi*, 2001) and airborne gradiometric measurements (*Jekeli*, 2011) it might be possible to achieve a white noise of the order of 1 – 2 E.
- $\delta\Delta\Gamma_{\text{Corr}}$  As for astrogeodetic measurements, a correlated noise source might be of instrumental or environmental origin.

#### Computation of $\mathcal{P}(\Sigma)$

The observations generated at each discrete position  $s_j$  (separated by  $\Delta s_{\text{obs}}$ ), are firstly predicted at each discrete position  $s_i$  (separated by  $\Delta s = 10$  m) by linear interpolation. Afterwards, one realization of  $\mathcal{P}(\Sigma)$  is computed by a numerical solution of Equation 4.43 in three steps. Firstly,  $\Delta\Gamma_{\text{tot}}$  is converted into  $\dot{\epsilon}_{\text{tot}}$  using a simplified form of Equation 4.40:

$$\dot{\epsilon}_{\text{tot}} = -\frac{1}{\gamma} \cdot \Delta\Gamma_{\text{tot}} \quad \text{with: } \gamma = 9.81 \left[ \frac{\text{m}}{\text{s}^2} \right] \tag{4.129}$$

Secondly,  $\epsilon_{\text{tot}}$  is computed from Equation 4.42 using the trapeze rule for integration:

$$\epsilon_{\text{tot}}(s_{ii}) = \sum_{i=2}^{ii} \frac{1}{2} [\dot{\epsilon}_{\text{tot}}(s_{i-1}) + \dot{\epsilon}_{\text{tot}}(s_i)] \cdot \Delta s \quad (4.130)$$

Finally,  $\mathcal{P}(\Sigma)$  is computed as for the astrogeodetic levelling in Equation 4.122:

$$N_{\text{tot}}(s_{ii}) = \sum_{i=2}^{ii} \frac{1}{2} [\epsilon_{\text{tot}}(s_{i-1}) + \epsilon_{\text{tot}}(s_i)] \cdot \Delta s \quad (4.131)$$

### Summary of the Impact of Observable's Noises on Misalignment

A summary of the various noises which generate a misalignment of 10 microns overs 200 meters is shown in Table 4.4. More detailed results can be found in the Appendix F.3.

**Table 4.4:** Summary of the alignment accuracy of gradiometric levelling. The maximal allowed noises are given regarding to a misalignement of 10 microns over 200 meters for a level of confidence  $1 - \alpha$ .

noise	additional parameters	depends on $\Delta s_{\text{obs}}$	depends on $\alpha$	max noise		unit	critical
				68%	95%		
$\delta\Delta\Gamma_{\text{Bias}}$	$\Delta s_{\text{obs}} = 10 - 100 \text{ m}$	no	no	31	31	E	no
$\delta\Delta\Gamma_{\text{Rnd Bias}}$	$\Delta s_{\text{obs}} = 10 - 100 \text{ m}$	no	yes	31	18	E	no
$\delta\Delta\Gamma_{\text{Drift}}$	$\Delta s_{\text{obs}} = 10 - 100 \text{ m}$	no	no	26	26	$\frac{\text{E}}{100 \text{ m}}$	no
$\delta\Delta\Gamma_{\text{Rnd Drift}}$	$\Delta s_{\text{obs}} = 10 - 100 \text{ m}$	no	yes	26	15	$\frac{\text{E}}{100 \text{ m}}$	no
$\delta\Delta\Gamma_{\text{White}}$	$\Delta s_{\text{obs}} = 10 \text{ m}$	yes	yes	100	58	E	no
$\delta\Delta\Gamma_{\text{White}}$	$\Delta s_{\text{obs}} = 100 \text{ m}$	yes	yes	40	20	E	no
$\delta\Delta\Gamma_{\text{Corr}}$	$\Delta s_{\text{obs}} = 10 \text{ m}, d_{\text{Corr}} = 0 \text{ m}$	yes	yes	100	58	E	no
$\delta\Delta\Gamma_{\text{Corr}}$	$\Delta s_{\text{obs}} = 10 \text{ m}, d_{\text{Corr}} = 40 \text{ m}$	yes	yes	40	20	E	no
$\delta\Delta\Gamma_{\text{Corr}}$	$\Delta s_{\text{obs}} = 10 \text{ m}, d_{\text{Corr}} > 100 \text{ m}$	yes	yes	30	15	E	no

## 4.6 Alignment Accuracy with Several Zenith Camera Systems

In the previous section, the alignment accuracy of the astrogravimetric levelling method has been analysed in a systematic manner, with respect to different kinds of errors, treated separately. Here, the analyses are less general but are governed by some present-day knowledge about the noise sources entering the budget of modern astrogeodetic observations. In addition, the analyses are extended to the explicit modeling of several zenith cameras measuring in parallel. As we shall see, it increases not only the productivity, but permits also to mitigate the impact of anomalous refraction, which is nowadays, the largest source of error of standard astrogeodetic observations (*Hirt, 2006, 2008*).

### 4.6.1 Observation Setup and Noise Model

We consider  $n_{zc}$  zenith cameras operating in parallel during  $\Delta t_{\text{obs}}$  hours on points which follow, separated by a spacing  $\Delta s$ , see Figure 4.13. After  $\Delta t_{\text{obs}}$ , these  $n_{zc}$  deflections of the vertical  $\epsilon_{\text{tot}}$ , denoted  $\epsilon$ , are grouped into the set  $\mathbb{DOV}_j$ :

$$\mathbb{DOV}_j \equiv \left\{ \epsilon_j^1, \epsilon_j^2, \dots, \epsilon_j^i, \epsilon_j^{n_{zc}} \right\} \quad (4.132)$$

We consider that the observations  $\epsilon_j^i$  are affected by two different noise sources:

$$\delta \epsilon_i^j = \delta \epsilon_{i \text{ White}}^j + \delta \epsilon_{\text{Rnd Bias}}^j \quad (4.133)$$

where the first  $\delta \epsilon_{i \text{ White}}^j$  is a white noise, different for each camera, which models the pure non-correlated part of the total error  $\delta \epsilon_i^j$ . The second is a random bias  $\delta \epsilon_{\text{Rnd Bias}}^j$ , common to the set  $\mathbb{DOV}_j$ , which models the anomalous refraction. Here it is assumed that all zenith cameras, which are measuring in parallel, are affected by the same anomalous refraction. This can be supported by the fact that the duration of the observations is not too short, i.e., larger than 15 minutes, and that the stations are located at short distances  $< 1$  kilometer. Thus there is a good chance that the mean anomalous refraction behaves similarly for each station.

Once a set  $\mathbb{DOV}_j$  has been carried out, the cameras are displaced to the next points, with an overlap  $\mathcal{O}$  with respect to the previous set  $\mathbb{DOV}_j$ , in order to make the acquisition of the next set  $\mathbb{DOV}_{j+1}$ . The overlap is an integer which corresponds to the number of stations of  $\mathbb{DOV}_j$  and  $\mathbb{DOV}_{j+1}$ , located at the same position. This procedure is repeated  $n_{\mathbb{DOV}}$  times, until the whole profile has been observed.

### 4.6.2 Mathematical Models

Before applying Equation 4.122 of the astronomical levelling for the computation of  $N_{\text{tot}}$ , a single deflection  $\epsilon(s_{ii})$  must be obtained from the sets  $\left\{ \mathbb{DOV}_1, \dots, \mathbb{DOV}_{n_{\mathbb{DOV}}} \right\}$ . This can be done in several ways. Here two approach are described. The first is obvious and consists in taking the average of the observations  $\epsilon_j^i$  located at identical positions. The second way is uncommon and consists in estimating a constant bias for each set  $\mathbb{DOV}_j$ .

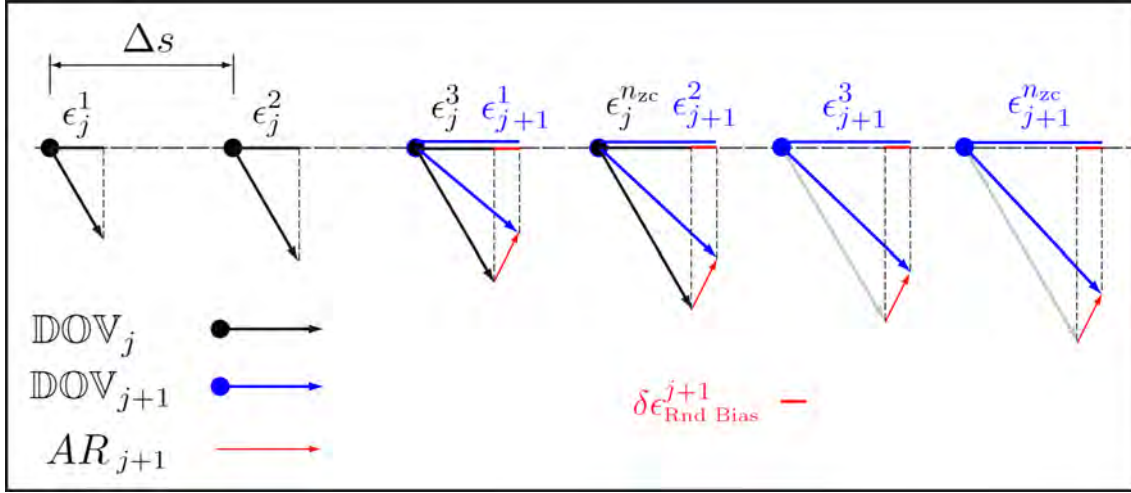


**Figure 4.13:** Schema of the observation setup with several zenith cameras operating in parallel. Here, the number of available cameras is  $n_{zc} = 4$ , the overlap  $\mathcal{O} = 2$  and the anomalous refraction is assumed to be equal to 0 for the set  $\mathbb{DOV}_j$ .

### Functional Model (without bias)

The observation equation of the first approach is given by:

$$\epsilon_j^i(s_{ii}) + \hat{v}_{\epsilon_j^i(s_{ii})} = \hat{\epsilon}(s_{ii}) \quad (4.134)$$

where  $\epsilon_j^i(s_{ii})$  represents the observation of the zenith camera  $i$  of the set  $\mathbb{DOV}_j$ , located at position  $s_{ii}$ . The quantity  $\hat{v}_{\epsilon_j^i(s_{ii})}$  is the adjusted residual and the adjusted deflection of the vertical is given by  $\hat{\epsilon}(s_{ii})$ . In matrix formulation we have:

$$\mathbf{l} + \hat{\mathbf{v}}_1 = \mathbf{A}_1 \cdot \hat{\mathbf{x}}_1 \quad (4.135)$$

with:

$$\mathbf{l} = \begin{pmatrix} \epsilon_1^1(s_1) \\ \vdots \\ \epsilon_1^{n_{zc}}(s_{n_{zc}}) \\ \epsilon_2^1(s_{n_{zc}-\mathcal{O}}) \\ \vdots \\ \epsilon_2^{n_{zc}}(s_{2n_{zc}-\mathcal{O}}) \\ \vdots \\ \epsilon_{n_{\mathbb{DOV}}}^{n_{zc}}(s_{n_{\epsilon}}) \end{pmatrix}, \hat{\mathbf{v}}_1 = \begin{pmatrix} \hat{v}_{\epsilon_1^1(s_1)} \\ \vdots \\ \hat{v}_{\epsilon_1^{n_{zc}}(s_{n_{zc}})} \\ \hat{v}_{\epsilon_2^1(s_{n_{zc}-\mathcal{O}})} \\ \vdots \\ \hat{v}_{\epsilon_2^{n_{zc}}(s_{2n_{zc}-\mathcal{O}})} \\ \vdots \\ \hat{v}_{\epsilon_{n_{\mathbb{DOV}}}^{n_{zc}}(s_{n_{\epsilon}})} \end{pmatrix}, \mathbf{A}_1 = \begin{pmatrix} 1 & \dots & 0 & \dots & 0 & \dots & 0 \\ \vdots & \ddots & \vdots & \ddots & \vdots & \ddots & \vdots \\ 0 & \dots & 1 & \dots & 0 & \dots & 0 \\ 0 & \dots & 1 & \dots & 0 & \dots & 0 \\ \vdots & \ddots & \vdots & \ddots & \vdots & \ddots & \vdots \\ 0 & \dots & 0 & \dots & 1 & \dots & 0 \\ \vdots & \ddots & \vdots & \ddots & \vdots & \ddots & \vdots \\ 0 & \dots & 0 & \dots & 0 & \dots & 1 \end{pmatrix}, \hat{\mathbf{x}}_1 = \begin{pmatrix} \hat{\epsilon}(s_1) \\ \vdots \\ \hat{\epsilon}(s_{n_{zc}}) \\ \hat{\epsilon}(s_{n_{zc}-\mathcal{O}}) \\ \vdots \\ \hat{\epsilon}(s_{2n_{zc}-\mathcal{O}}) \\ \vdots \\ \hat{\epsilon}(s_{n_{\epsilon}}) \end{pmatrix} \quad (4.136)$$

where  $n_{\epsilon}$  represents the number of points forming the astrogeodetic levelling profile.

**Functional Model (with bias)**

The observation equation of the second approach is given by:

$$\epsilon_j^i(s_{ii}) + \hat{v}_{\epsilon_j^i(s_{ii})} = \hat{\epsilon}(s_{ii}) + \hat{b}_j \quad (4.137)$$

where the bias  $\hat{b}_j$  is introduced as unknown parameter. In matrix formulation we have:

$$\mathbf{l} + \hat{\mathbf{v}}_2 = \mathbf{A}_2 \cdot \hat{\mathbf{x}}_2 \quad (4.138)$$

with:

$$\mathbf{l} = \begin{pmatrix} \epsilon_1^1(s_1) \\ \vdots \\ \epsilon_1^{n_{zc}}(s_{n_{zc}}) \\ \hline \epsilon_2^1(s_{n_{zc}-\mathcal{O}}) \\ \vdots \\ \epsilon_2^{n_{zc}}(s_{2n_{zc}-\mathcal{O}}) \\ \hline \vdots \\ \epsilon_{n_{DOV}}^{n_{zc}}(s_{n_{\epsilon}}) \end{pmatrix}, \hat{\mathbf{v}}_2 = \begin{pmatrix} \hat{v}_{\epsilon_1^1(s_1)} \\ \vdots \\ \hat{v}_{\epsilon_1^{n_{zc}}(s_{n_{zc}})} \\ \hline \hat{v}_{\epsilon_2^1(s_{n_{zc}-\mathcal{O}})} \\ \vdots \\ \hat{v}_{\epsilon_2^{n_{zc}}(s_{2n_{zc}-\mathcal{O}})} \\ \hline \vdots \\ \hat{v}_{\epsilon_{n_{DOV}}^{n_{zc}}(s_{n_{\epsilon}})} \end{pmatrix} \quad (4.139)$$

and:

$$\mathbf{A}_2 = \begin{pmatrix} 1 & \dots & 0 & \dots & 0 & \dots & 0 & | & 1 & 0 & \dots & 0 \\ \vdots & \ddots & \vdots & \ddots & \vdots & \ddots & \vdots & | & \vdots & \vdots & \dots & \vdots \\ 0 & \dots & 1 & \dots & 0 & \dots & 0 & | & 1 & 0 & \dots & 0 \\ \hline 0 & \dots & 1 & \dots & 0 & \dots & 0 & | & 0 & 1 & \dots & 0 \\ \vdots & \ddots & \vdots & \ddots & \vdots & \ddots & \vdots & | & \vdots & \vdots & \dots & \vdots \\ 0 & \dots & 0 & \dots & 1 & \dots & 0 & | & 0 & 1 & \dots & 0 \\ \hline \vdots & \ddots & \vdots & \ddots & \vdots & \ddots & \vdots & | & \vdots & \vdots & \dots & \vdots \\ 0 & \dots & 0 & \dots & 0 & \dots & 1 & | & 0 & 0 & \dots & 1 \end{pmatrix}, \hat{\mathbf{x}}_2 = \begin{pmatrix} \hat{\epsilon}(s_1) \\ \vdots \\ \hat{\epsilon}(s_{n_{zc}}) \\ \hline \hat{\epsilon}(s_{n_{zc}-\mathcal{O}}) \\ \vdots \\ \hat{\epsilon}(s_{2n_{zc}-\mathcal{O}}) \\ \hline \vdots \\ \hat{\epsilon}(s_{n_{\epsilon}}) \\ \hline \hat{b}_1 \\ \hat{b}_2 \\ \vdots \\ \hat{b}_{n_{DOV}} \end{pmatrix} \quad (4.140)$$

**Stochastic Model (with and without bias)**

The stochastic model is identical for both approaches and assumes uncorrelated Gaussian-distributed observations:

$$\epsilon_j^i(s_{ii}) \sim \mathcal{N}(\check{\epsilon}(s_{ii}), \sigma_{\epsilon}^2) \quad \rightarrow \quad \mathbf{C}_{11} = \sigma_{\epsilon}^2 \cdot \mathbf{I} \quad (4.141)$$

where  $\check{\epsilon}(s_{ii})$  represents the true deflection at  $s_{ii}$  and  $\mathbf{I}$  the identity matrix.

### Parameter Estimation

The maximum likelihood unknown vectors  $\mathbf{x}_{1,2}$  are given by the well-known least-squares condition, and are estimated by:

$$\hat{\mathbf{x}}_{1,2} = (\mathbf{A}_{1,2}^T \cdot \mathbf{Q}_{\text{II}}^{-1} \cdot \mathbf{A}_{1,2})^{-} \cdot \mathbf{A}_{1,2}^T \cdot \mathbf{Q}_{\text{II}}^{-1} \cdot \mathbf{1} \quad (4.142)$$

where  $\mathbf{Q}_{\text{II}} = \frac{1}{\sigma_0^2} \cdot \mathbf{C}_{\text{II}}$ , and the matrix operator  $()^{-}$  represents the *Moore-Penrose* pseudo-inverse. Here, only the estimation of  $\mathbf{x}_2$  needs the use of a generalized inverse. Because all biases  $\hat{b}_j$ , are set as unknown parameters, its normal matrix is singular. This choice is not relevant for misalignment analyses and corresponds to the solution which minimizes  $\mathbf{x}_2^T \cdot \mathbf{x}_2$ .

### 4.6.3 Monte-Carlo Simulation Scheme

In order to analyse the impact of different configurations on the misalignment, some Monte-Carlo simulations are realized. In opposition to the previous simulations, the observations are generated for a whole CLIC profile of 50 kilometers because the overlapping of the different sets  $\text{DOV}_j$  exceeds 200 meters. Moreover, the simulations are based on the generation of a single profile instead of 10'000. This can be argued if the processes are assumed to be ergodic. The simulations are based on the following steps:

1. Generate noisy observations according to Equation 4.133 to the predefined error model and observation setting, as the spacing  $\Delta s$  and the overlap  $\mathcal{O}$ , over 50 kilometers:

$$\epsilon_i^j(s_{ii}) = \delta \epsilon_i^j \text{ White} + \delta \epsilon_{\text{Rnd Bias}}^j \quad (4.143)$$

where the white and the random bias noise is parametrized by its standard deviation  $\sigma_{\text{White}}$  and  $\sigma_{\text{Rnd Bias}}$ , respectively.

2. using Equation 4.142, compute the deflections of the vertical  $\hat{\mathbf{x}}_{1,2}$  at each point of the profile, for both approaches, with and without the estimation of biases  $\hat{b}_j$ .
3. Realize numerically, the discretized equipotential profiles  $\mathcal{P}_{1,2}$  using  $\hat{\mathbf{x}}_{1,2}$  and Equation 4.122.
4. Analyse  $\mathcal{P}_{1,2}$  in terms of misalignment, especially the quantities  $\mathcal{M}_{\star}^{200} \{\mathcal{P}_{1,2}\}$  from which the empirical cumulative distributions  $CDF_{1,2}$  can be computed, with their associated  $(1 - \alpha)$ -quantiles  $\sigma_{\mathcal{M}\{\mathcal{P}_{1,2}\}}^{1-\alpha}$ .
5. The productivity is quantified by the number of working days needed for the acquisition of the whole 50 kilometers profile. This indicator is denoted by  $\#\mathcal{C}$  and computed from the total number of clear sky hours  $T_{\text{obs}}$  needed for the whole profile, assuming that in average, 8 hours per day are available for astrogeodetic observations.



**Table 4.5:** Parameters and results of the simulations of astrogeodetic determinations of an equipotential profile of 50 kilometers according to the two approaches described in Section 4.6.

$n_{zc}$ [#]	$\mathcal{O}$ [#]	$\sigma_{\text{Rnd Bias}}$ [arcsec]	$\sigma_{\text{White}}$ [arcsec]	$\Delta t_{\text{obs}}$ [hour]	$\Delta s$ [m]	$T_{\text{obs}}$ [hour]	$\#\mathfrak{C}$ [day]	$\sigma_{\mathcal{M}\{\mathcal{P}_1\}}^{0.68}$ [ $\mu\text{m}$ ]	$\sigma_{\mathcal{M}\{\mathcal{P}_1\}}^{0.95}$ [ $\mu\text{m}$ ]	$\sigma_{\mathcal{M}\{\mathcal{P}_2\}}^{0.68}$ [ $\mu\text{m}$ ]	$\sigma_{\mathcal{M}\{\mathcal{P}_2\}}^{0.95}$ [ $\mu\text{m}$ ]
2	1	0.08	0.03	2.0	50	2000	250.0	10.2	17.4	7.8	14.5
2	1	0.08	0.03	2.0	100	1000	125.0	8.0	13.1	5.4	9.6
2	1	0.08	0.05	1.0	50	1000	125.0	11.2	19.3	13.1	23.7
2	1	0.08	0.05	1.0	100	500	62.5	9.0	16.3	8.1	15.8
5	1	0.08	0.03	2.0	50	500	62.5	9.7	19.0	5.4	9.9
5	2	0.08	0.03	2.0	50	668	83.5	9.4	16.0	4.8	8.1
5	1	0.08	0.03	2.0	100	250	31.3	6.7	13.8	4.4	8.3
5	2	0.08	0.03	2.0	100	334	41.8	5.8	11.3	3.6	6.6
5	1	0.08	0.05	1.0	50	250	31.3	10.7	21.1	8.4	15.3
5	2	0.08	0.05	1.0	50	334	41.8	10.6	19.2	7.6	13.2
5	1	0.08	0.05	1.0	100	125	15.6	9.0	16.4	7.6	13.6
5	2	0.08	0.05	1.0	100	167	20.9	8.4	15.3	6.7	11.9
10	1	0.08	0.03	2.0	50	224	28.0	6.4	16.5	5.0	8.4
10	2	0.08	0.03	2.0	50	250	31.3	6.8	15.2	4.7	7.6
10	5	0.08	0.03	2.0	50	400	50.0	4.9	12.2	3.4	5.4
10	1	0.08	0.03	2.0	100	112	14.0	5.0	11.2	4.3	7.7
10	2	0.08	0.03	2.0	100	126	15.8	5.2	10.6	4.2	7.4
10	5	0.08	0.03	2.0	100	200	25.0	3.9	8.1	3.1	5.7
10	1	0.08	0.05	1.0	50	112	14.0	9.9	19.2	8.9	15.6
10	2	0.08	0.05	1.0	50	125	15.6	9.2	17.3	7.9	13.1
10	5	0.08	0.05	1.0	50	200	25.0	7.0	13.3	5.8	9.6
10	1	0.08	0.05	1.0	100	56	7.0	8.2	15.2	7.7	13.6
10	2	0.08	0.05	1.0	100	63	7.9	7.2	12.7	7.1	12.3
10	5	0.08	0.05	1.0	100	100	12.5	6.1	11.2	5.6	9.6

#### 4.6.4 Results of the Simulations

The different sets of parameters and the results of the various simulations are listed in Table 4.5. The standard deviation of the random biases, which model the anomalous refraction, are fixed at  $\sigma_{\text{Rnd Bias}} = 0.08$  arcsec. This value is computed by:

$$\sigma_{\text{Rnd Bias}} = \frac{AR_{\text{Hirt}}}{2.5} \quad (4.144)$$

where  $AR_{\text{Hirt}} = 0.2$  arcsec corresponds to the amplitude of the expected anomalous refraction in zenith at periods of some hours, quantified by *Hirt* (2006) from high-quality time series of deflections of the vertical data. The division by 2.5 is chosen in order to generate 95% of  $\delta\epsilon_{\text{Rnd Bias}}^j < AR_{\text{Hirt}}$ . The standard deviation of the white noise is fixed at  $\sigma_{\text{White}} = 0.03$  arcsec assuming an observation duration  $\Delta t_{\text{obs}} = 2$  hours, or  $\sigma_{\text{White}} = 0.05$  arcsec assuming an observation duration  $\Delta t_{\text{obs}} = 1$  hour. These values are indirectly derived from *Hirt and Seeber* (2008). The spacing is fixed at  $\Delta s = 50$  or 100, meters since it no observable real anomalies of wavelength shorter than 100 or 200 meters can generate significant misalignment signals larger than 10 micrometers, see Chapter 6.

In order to see the differences between the two approaches, two simulations are presented

in detail in Figures 4.14 and 4.15.

### Simulation 1

**Table 4.6:** Parameters and results of **Simulation 1**.

$n_{zc}$	$\mathcal{O}$	$\sigma_{\text{Rnd Bias}}$	$\sigma_{\text{White}}$	$\Delta t_{\text{obs}}$	$\Delta s$	$T_{\text{obs}}$	$\#\mathcal{C}$	$\sigma_{\mathcal{M}\{\mathcal{P}_1\}}^{0.68}$	$\sigma_{\mathcal{M}\{\mathcal{P}_1\}}^{0.95}$	$\sigma_{\mathcal{M}\{\mathcal{P}_2\}}^{0.68}$	$\sigma_{\mathcal{M}\{\mathcal{P}_2\}}^{0.95}$
[#]	[#]	[arcsec]	[arcsec]	[hour]	[m]	[hour]	[day]	[ $\mu\text{m}$ ]	[ $\mu\text{m}$ ]	[ $\mu\text{m}$ ]	[ $\mu\text{m}$ ]
5	1	0.08	0.03	2.0	50	500	62.5	9.7	19.0	5.4	9.9

The parameters and the results of the first simulation are summarized in Table 4.6 and shown in Figure 4.14. In this case, thanks to significant number of zenith cameras  $n_{zc} = 5$  operating in parallel, the misalignment over 200 meters, generated by the solution, which estimates biases, is approximately two times smaller than the classical approach:

$$\sigma_{\mathcal{M}\{\mathcal{P}_1\}}^{0.68} = 9.7 \rightarrow \sigma_{\mathcal{M}\{\mathcal{P}_2\}}^{0.68} = 5.4 \quad [\mu\text{m}]$$

The price to pay for this short-wavelength improvements is the significant reduction of accuracy for long wavelengths. This comes from the fact that the deflections adjusted together with the biases loose their absolute referencing with respect to the reference system in favor of the relative accuracy. This is clearly shown in the upper-right plot of Figure 4.14, where the equipotential  $\mathcal{P}_1$  stays closer to zero but contains more noise for short periods than  $\mathcal{P}_2$ . This evidence appears equivalently in adjusted deflections shown in the upper-left plot of Figure 4.14. In other words, we can also say that the second approach acts like a filter, which reduces short period noise and generates long period correlated noise.

Finally, we can say that compared to the case of measuring the whole profile with a single zenith camera, the availability of five cameras increases both the productivity and the achievable accuracy. According to the parameters given in Table 4.6, the whole CLIC profile of 50 kilometers needs  $T_{\text{obs}} = 500$  hours of clear night, corresponding to  $\#\mathcal{C} = 62.5$  field working days (8 hours per day).

### Simulation 2

**Table 4.7:** Parameters and results of **Simulation 2**.

$n_{zc}$	$\mathcal{O}$	$\sigma_{\text{Rnd Bias}}$	$\sigma_{\text{White}}$	$\Delta t_{\text{obs}}$	$\Delta s$	$T_{\text{obs}}$	$\#\mathcal{C}$	$\sigma_{\mathcal{M}\{\mathcal{P}_1\}}^{0.68}$	$\sigma_{\mathcal{M}\{\mathcal{P}_1\}}^{0.95}$	$\sigma_{\mathcal{M}\{\mathcal{P}_2\}}^{0.68}$	$\sigma_{\mathcal{M}\{\mathcal{P}_2\}}^{0.95}$
[#]	[#]	[arcsec]	[arcsec]	[hour]	[m]	[hour]	[day]	[ $\mu\text{m}$ ]	[ $\mu\text{m}$ ]	[ $\mu\text{m}$ ]	[ $\mu\text{m}$ ]
2	1	0.08	0.05	1.0	50	1000	125.0	11.2	19.3	13.1	23.7

The parameters and the results of the second simulation are summarized in Table 4.7 and shown in Figure 4.15. In this case, only two zenith cameras  $n_{zc} = 2$  are operating in parallel and the second approach presents no advantages, for short as well as for long

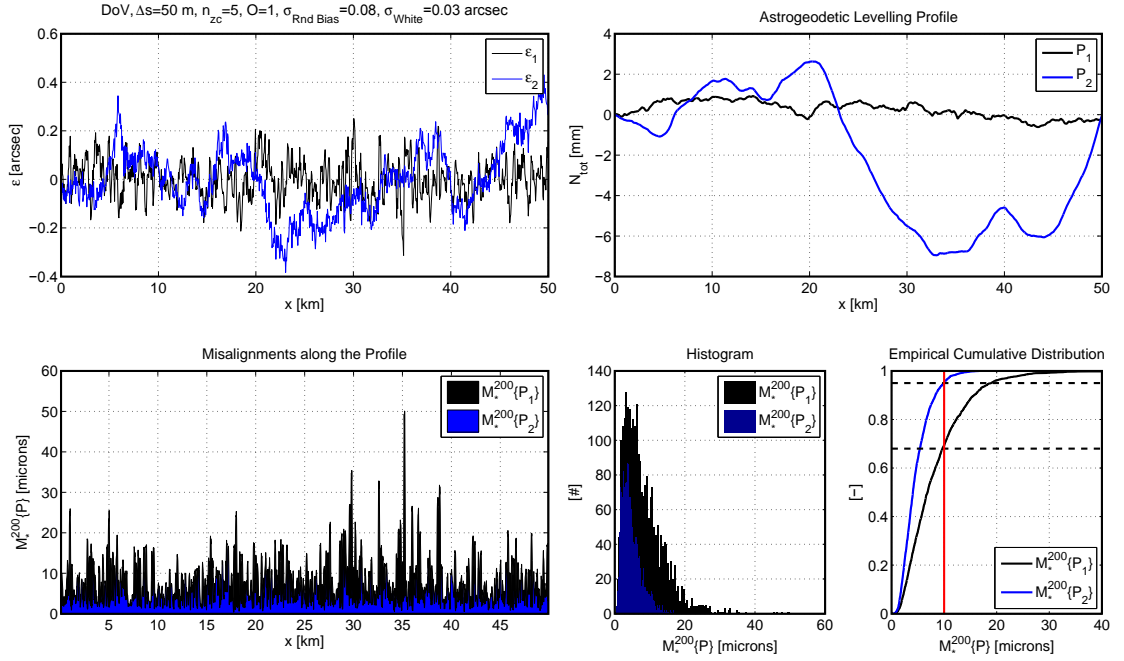


**Figure 4.14:** Results of **Simulation 1**. (Upper, left) adjusted deflections of the verticals. (Upper, right) equipotential profiles. (Lower, left) misalignments  $\mathcal{M}_{\star}^{200}\{\mathcal{P}_{1,2}\}$ . (Lower, right) histogram and empirical cumulative distribution of  $\mathcal{M}_{\star}^{200}\{\mathcal{P}_{1,2}\}$ .

wavelengths. Compared to the case of measuring the whole profile with a single zenith camera, the availability of two zenith cameras mainly increases the productivity, but not the achievable accuracy.

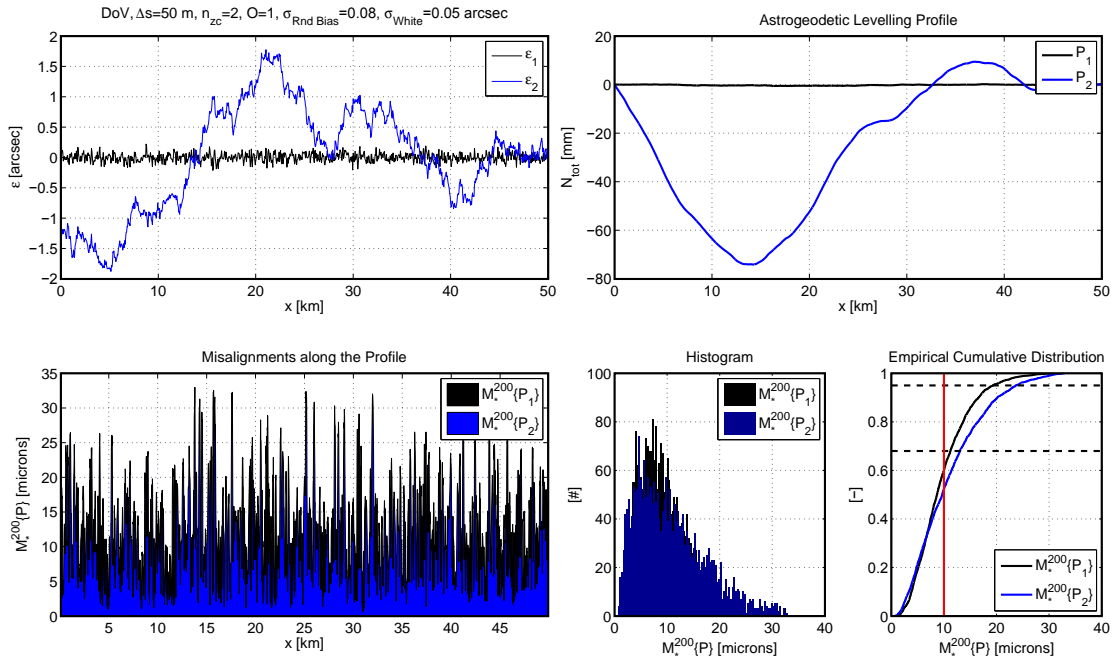


**Figure 4.15:** Results of **Simulation 2**. (Upper, left) adjusted deflections of the verticals. (Upper, right) equipotential profiles. (Lower, left) misalignments  $\mathcal{M}_*^{200}\{\mathcal{P}_{1,2}\}$ . (Lower, right) histogram and empirical cumulative distribution of  $\mathcal{M}_*^{200}\{\mathcal{P}_{1,2}\}$ .

## 4.7 Cloud Cover in Geneva

This short section addresses an important practical aspect of astrogeodetic observations, the estimation of the number of clear nights available during a given time span in Geneva. It is obvious that this number depends strongly on the location and the time of the year.

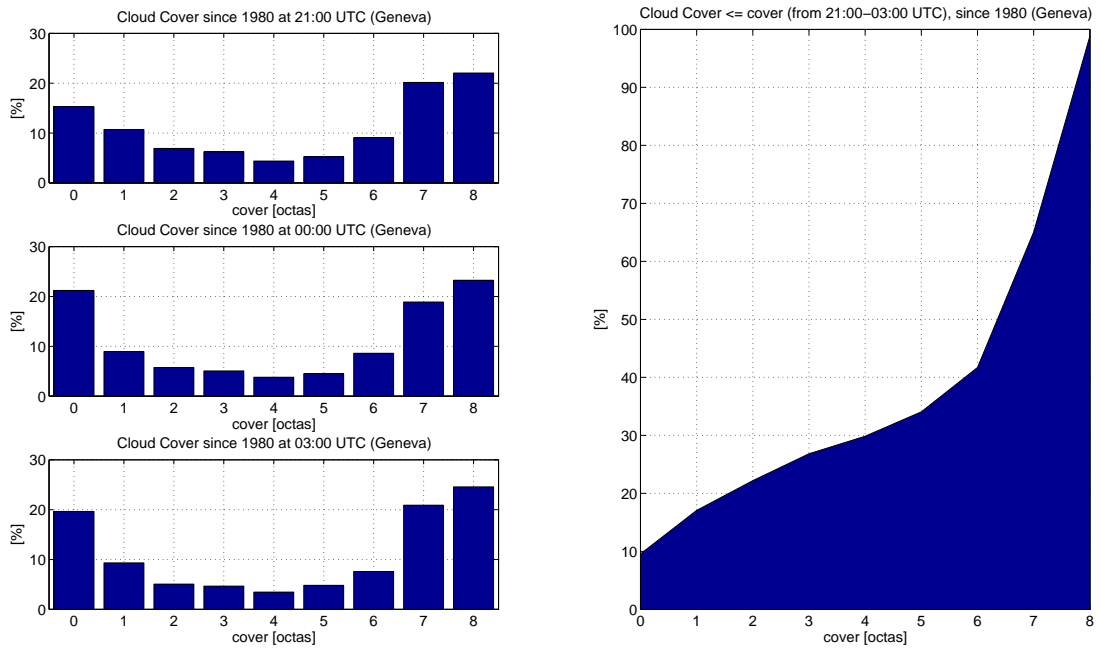


**Figure 4.16:** (Left) histogram of cloud cover in Geneva at 21:00, 00:00 and 03:00 UTC from data between 1980 and 2014. (Right) probability of having a cloud cover  $\leq$  than a given cover (between 21:00 and 03:00 UTC). A night with a cover of  $\frac{2}{8}$  should be adequate for astrogeodetic observations. Source of data: MeteoSwiss.

## 4.8 Concluding Remarks

The principal findings of this chapter concerns the analyses of the precision of the geometric determinations of equipotential surfaces with respect to the misalignment over 200 meters. In particular, performances which can be expected with the astrogravimetric levelling were treated in details. It is well-known that the astrogravimetric levelling is formed by two main parts. The first is given by the integration of surface deflections of the vertical along the profile, the second by the orthometric correction. The precision of the determination of the first part, called astrogeodetic part, is limited by the accuracy of the deflections of the vertical, while the second part, called orthometric part, is mainly limited by the precision of the determination of the mean gravity along the plumbline which strongly depends on the knowledge of the density field between the surface of topography and the location of the equipotential surface we want to determine.

According to the various Monte-Carlo simulations presented in this chapter, the feasi-

bility of the determination of the astrogeodetic part with sufficient alignment accuracy (compared to the constraints of CLIC) is demonstrated.

- If a single zenith camera is engaged for the measurements, the misalignment accuracy of 10 microns over 200 meters is reached when deflections of the vertical measurements — assuming a noise of 0.09 arcsec, free of correlations for distances between 0 and 300 meters — are carried out with a spacing of 10 meters. Assuming that a single station needs 30 minutes, the whole profile can be measured in 2'500 hours of clear night sky, which corresponds to 312.5 working days (8 hours per day). Moreover, according to Section 4.7, because approximately 75 days per year are suited for astronomical observations in the region of Geneva, the campaign will last about 4.2 years! For a larger spacing of 50 meters, the noise must not exceed 0.06 arcsec, free of correlations for distances between 0 and 75 meters. In this case, the duration of a single observation must probably be increased to 2-3 hours and would not be advantageous compared to the working days needed for the whole campaign.
- If several zenith camera systems are engaged in parallel, the performance of the astrogeodetic determination increases with respect to productivity and alignment accuracy. In particular, if an adequate observation setting is chosen, it may be possible to reduce the impact of the anomalous refraction on the alignment. A realistic configuration which consists of determining the deflections of the vertical in parallel, with 5 zenith cameras during 2 hours on successive stations separated by 50 meters and an overlap of one station, the alignment accuracy is expected at about 5.4 microns. In addition, the whole profile can be measured in 62.5 working days, less than 1 year.

Concerning the determination of the orthometric correction, it has been shown that only the determination of the second part *E2*, which depends on the mean gravity along the plumbline at each point of the profile, is critical and ambiguous. According to the results of the Monte-Carlo simulations, for an equipotential surface located 150 meters below the surface of topography, the mean gravity should be affected by a white noise larger than 30  $\mu\text{gal}$ , a correlated noise of 125 or 5'000  $\mu\text{gal}$  if the correlation length is equal to 1'000 or 16'000 meters, respectively. From this matter of fact, in opposition to the astrogeodetic part, the correlated noise of the mean gravity is not directly related to the noise of gravimetric observations<sup>10</sup>. The precision depends mainly on the knowledge of the density field between the surface of topography and the location of the equipotential surface, but also on the methodology used for the determination. It is obvious that the methods based on observations carried out on the surface of topography as well as in the tunnel are superior. In this chapter, two methods have been presented. The method consisting of averaging superposed gravity measurements is certainly not as optimal as the least-squares collocation approach, but has the benefit to be straightforward, without needing to fix a subjective parameter, and to provide determinations which have limited and predictable errors. Nevertheless, the estimation of the accuracy of the orthometric correction achievable by a given method can only be analysed seriously by gravity field

<sup>10</sup>it would be if gravimetric measurements could be carried out along the whole plumbline between the surface of topography and the equipotential.

---

simulations. They do not allow better determinations but permit it to classify anomalies which generate significant and/or observable signals. This kind of analyses is performed in Chapter 6.





## Chapter 5

# Computation of Gravitational Fields

This chapter presents the methods used for the computation of gravitational fields. It also includes the description of the software **QGravity** developed in the frame of this thesis. In theory, it exists two main approaches to compute the fields based on differential or the integral formulation of the gravitational field respectively. The former consists in solving Poisson's partial differential equation:

$$\Delta\Phi_{\text{grav}}(\mathbf{r}) = -4\pi G \cdot \rho(\mathbf{r}) \quad (5.1)$$

the latter consists in integrating Newton's gravitational potential.

In this thesis, all computations are based on the second approach. This is due to several reasons. The main reason is due to the fact that, in the case of a Poisson solver, it is necessary to define and to discretize the complete domain of interest before starting the solver. The three-dimensional domain must include, in a continuous manner, the bodies of interest, the positions where the field must be computed and the positions associated to the boundary conditions. This is not only time-consuming but might also be problematic concerning the memory allocation. Moreover, the results are always approximate due to the mesh size. The advantage of this approach could be really interesting only, if the domain is limited, if the density field of the bodies varies continuously and irregularly, and if the field must be computed at all points of the domain. In contrary, the methods based on the integral formulation do not need any domain to be defined and the computations can be realized independently for each point of interest.

Formally, the problem to solve is as follows: given a body  $\mathcal{B}$ , delimited by the surface  $\partial\mathcal{B}$ , which contains matter described by a density field  $\rho$ . Compute the gravitational scalar potential  $\Phi_{\text{grav}}$ , the gravitational acceleration vector  $\mathbf{g}_{\text{grav}}$ , and the tensor  $\mathbf{\Gamma}_{\text{grav}}$ , at a given position vector  $\mathbf{r}$ . The scalar potential is given by:

$$\Phi_{\text{grav}}(\mathbf{r}) = +G \cdot \iiint_{\mathcal{B}} \frac{1}{|\mathbf{r} - \mathbf{r}'|} \cdot \rho(\mathbf{r}') \cdot dV \quad (5.2)$$

the acceleration vector is given by:

$$\begin{aligned}
 \mathbf{g}_{\text{grav}}(\mathbf{r}) &= \nabla \Phi_{\text{grav}}(\mathbf{r}) \\
 &= -G \cdot \iiint_{\mathcal{B}} \frac{\mathbf{r} - \mathbf{r}'}{|\mathbf{r} - \mathbf{r}'|^3} \cdot \rho(\mathbf{r}') \cdot dV \\
 &= -G \cdot \begin{pmatrix} \iiint_{\mathcal{B}} \frac{r_x - r'_x}{|\mathbf{r} - \mathbf{r}'|^3} \cdot \rho(\mathbf{r}') \cdot dV \\ \iiint_{\mathcal{B}} \frac{r_y - r'_y}{|\mathbf{r} - \mathbf{r}'|^3} \cdot \rho(\mathbf{r}') \cdot dV \\ \iiint_{\mathcal{B}} \frac{r_z - r'_z}{|\mathbf{r} - \mathbf{r}'|^3} \cdot \rho(\mathbf{r}') \cdot dV \end{pmatrix}
 \end{aligned} \tag{5.3}$$

and the gravitational tensor is given by:

$$\begin{aligned}
 \mathbf{\Gamma}_{\text{grav}}(\mathbf{r}) &= \nabla [\nabla \Phi_{\text{grav}}(\mathbf{r})] = \nabla \mathbf{g}_{\text{grav}}(\mathbf{r}) \\
 &= \frac{\partial \mathbf{g}_{\text{grav}}(\mathbf{r})}{\partial x} \otimes \mathbf{e}_x + \frac{\partial \mathbf{g}_{\text{grav}}(\mathbf{r})}{\partial y} \otimes \mathbf{e}_y + \frac{\partial \mathbf{g}_{\text{grav}}(\mathbf{r})}{\partial z} \otimes \mathbf{e}_z \\
 &= -G \cdot \iiint_{\mathcal{B}} \nabla \left[ \frac{\mathbf{r} - \mathbf{r}'}{|\mathbf{r} - \mathbf{r}'|^3} \right] \cdot \rho(\mathbf{r}') \cdot dV \\
 &= -G \cdot \iiint_{\mathcal{B}} \frac{\partial \left( \frac{\mathbf{r} - \mathbf{r}'}{|\mathbf{r} - \mathbf{r}'|^3} \right)}{\partial x} \cdot \rho(\mathbf{r}') \cdot dV \otimes \mathbf{e}_x \\
 &\quad - G \cdot \iiint_{\mathcal{B}} \frac{\partial \left( \frac{\mathbf{r} - \mathbf{r}'}{|\mathbf{r} - \mathbf{r}'|^3} \right)}{\partial y} \cdot \rho(\mathbf{r}') \cdot dV \otimes \mathbf{e}_y \\
 &\quad - G \cdot \iiint_{\mathcal{B}} \frac{\partial \left( \frac{\mathbf{r} - \mathbf{r}'}{|\mathbf{r} - \mathbf{r}'|^3} \right)}{\partial z} \cdot \rho(\mathbf{r}') \cdot dV \otimes \mathbf{e}_z
 \end{aligned} \tag{5.4}$$

or more explicitly after developing the tensor products:

$$\begin{aligned}
 \mathbf{\Gamma}_{\text{grav}}(\mathbf{r}) &= +G \cdot \begin{pmatrix} \iiint_{\mathcal{B}} \frac{|\mathbf{r} - \mathbf{r}'|^2 - 3 \cdot (r_x - r'_x)^2}{|\mathbf{r} - \mathbf{r}'|^5} \cdot dV & 0 & 0 \\ \iiint_{\mathcal{B}} \frac{-3 \cdot (r_x - r'_x) \cdot (r_y - r'_y)}{|\mathbf{r} - \mathbf{r}'|^5} \cdot dV & 0 & 0 \\ \iiint_{\mathcal{B}} \frac{-3 \cdot (r_x - r'_x) \cdot (r_z - r'_z)}{|\mathbf{r} - \mathbf{r}'|^5} \cdot dV & 0 & 0 \end{pmatrix} \\
 &\quad + G \cdot \begin{pmatrix} 0 & \iiint_{\mathcal{B}} \frac{-3 \cdot (r_y - r'_y) \cdot (r_x - r'_x)}{|\mathbf{r} - \mathbf{r}'|^5} \cdot dV & 0 \\ 0 & \iiint_{\mathcal{B}} \frac{|\mathbf{r} - \mathbf{r}'|^2 - 3 \cdot (r_y - r'_y)^2}{|\mathbf{r} - \mathbf{r}'|^5} \cdot dV & 0 \\ 0 & \iiint_{\mathcal{B}} \frac{-3 \cdot (r_y - r'_y) \cdot (r_z - r'_z)}{|\mathbf{r} - \mathbf{r}'|^5} \cdot dV & 0 \end{pmatrix} \\
 &\quad + G \cdot \begin{pmatrix} 0 & 0 & \iiint_{\mathcal{B}} \frac{-3 \cdot (r_z - r'_z) \cdot (r_x - r'_x)}{|\mathbf{r} - \mathbf{r}'|^5} \cdot dV \\ 0 & 0 & \iiint_{\mathcal{B}} \frac{-3 \cdot (r_z - r'_z) \cdot (r_y - r'_y)}{|\mathbf{r} - \mathbf{r}'|^5} \cdot dV \\ 0 & 0 & \iiint_{\mathcal{B}} \frac{|\mathbf{r} - \mathbf{r}'|^2 - 3 \cdot (r_z - r'_z)^2}{|\mathbf{r} - \mathbf{r}'|^5} \cdot dV \end{pmatrix}
 \end{aligned} \tag{5.5}$$

## 5.1 Numerical Computation of the Gravitational Field

It is obvious that only a few bodies exist which have closed formulas for the computation of their gravitational field components. In the literature, under the keywords *gravity forward modeling*, we can find various formulas associated to homogeneous simple bodies as point mass, finite and infinite wire, homogeneous sphere, homogeneous spherical shell, homogeneous cylinder, etc..., which are described by a few parameters and are simple to be implemented in a software. In addition, also analytic formulas exist for the computation of more complex bodies as homogeneous rectangular or triangular prisms or arbitrary shaped homogeneous polyhedra.

Here, only the formulas for the point mass, the homogeneous sphere and the homogeneous polyhedron are used and described. The point mass and the polyhedron formulas are used for the modeling of gravitational effects of interesting bodies while the homogeneous sphere is mainly used for the validation of the polyhedron routines.

### 5.1.1 Point Mass

If the body  $\mathcal{B}$  is modeled by a point mass of mass  $M_{\mathcal{B}}$  at position  $\mathbf{r}_{\mathcal{B}}$ , the gravitational scalar potential  $\Phi_{\text{grav}}$ , the gravitational acceleration vector  $\mathbf{g}_{\text{grav}}$ , and tensor  $\mathbf{\Gamma}_{\text{grav}}$ , at a given position vector  $\mathbf{r}$ , are given by:

#### Gravitational Potential

$$\Phi_{\text{grav}}(\mathbf{r}) = + \frac{GM_{\mathcal{B}}}{|\mathbf{r} - \mathbf{r}_{\mathcal{B}}|} \quad \text{if: } \mathbf{r} \neq \mathbf{r}_{\mathcal{B}} \quad (5.6)$$

#### Gravitational Acceleration

$$\mathbf{g}_{\text{grav}}(\mathbf{r}) = -GM_{\mathcal{B}} \cdot \begin{pmatrix} \frac{r_x - r_{x,\mathcal{B}}}{|\mathbf{r} - \mathbf{r}_{\mathcal{B}}|^3} \\ \frac{r_y - r_{y,\mathcal{B}}}{|\mathbf{r} - \mathbf{r}_{\mathcal{B}}|^3} \\ \frac{r_z - r_{z,\mathcal{B}}}{|\mathbf{r} - \mathbf{r}_{\mathcal{B}}|^3} \end{pmatrix} \quad \text{if } \mathbf{r} \neq \mathbf{r}_{\mathcal{B}} \quad (5.7)$$

#### Gravitational Tensor

$$\mathbf{\Gamma}_{\text{grav}}(\mathbf{r}) = -GM_{\mathcal{B}} \cdot \begin{pmatrix} \frac{|\mathbf{r} - \mathbf{r}_{\mathcal{B}}|^2 - 3 \cdot (r_x - r_{x,\mathcal{B}})^2}{|\mathbf{r} - \mathbf{r}_{\mathcal{B}}|^5} & \frac{-3 \cdot (r_y - r_{y,\mathcal{B}}) \cdot (r_x - r_{x,\mathcal{B}})}{|\mathbf{r} - \mathbf{r}_{\mathcal{B}}|^5} & \frac{-3 \cdot (r_z - r_{z,\mathcal{B}}) \cdot (r_x - r_{x,\mathcal{B}})}{|\mathbf{r} - \mathbf{r}_{\mathcal{B}}|^5} \\ \frac{-3 \cdot (r_x - r_{x,\mathcal{B}}) \cdot (r_y - r_{y,\mathcal{B}})}{|\mathbf{r} - \mathbf{r}_{\mathcal{B}}|^5} & \frac{|\mathbf{r} - \mathbf{r}_{\mathcal{B}}|^2 - 3 \cdot (r_y - r_{y,\mathcal{B}})^2}{|\mathbf{r} - \mathbf{r}_{\mathcal{B}}|^5} & \frac{-3 \cdot (r_z - r_{z,\mathcal{B}}) \cdot (r_y - r_{y,\mathcal{B}})}{|\mathbf{r} - \mathbf{r}_{\mathcal{B}}|^5} \\ \frac{-3 \cdot (r_x - r_{x,\mathcal{B}}) \cdot (r_z - r_{z,\mathcal{B}})}{|\mathbf{r} - \mathbf{r}_{\mathcal{B}}|^5} & \frac{-3 \cdot (r_y - r_{y,\mathcal{B}}) \cdot (r_z - r_{z,\mathcal{B}})}{|\mathbf{r} - \mathbf{r}_{\mathcal{B}}|^5} & \frac{|\mathbf{r} - \mathbf{r}_{\mathcal{B}}|^2 - 3 \cdot (r_z - r_{z,\mathcal{B}})^2}{|\mathbf{r} - \mathbf{r}_{\mathcal{B}}|^5} \end{pmatrix} \quad (5.8)$$

if  $\mathbf{r} \neq \mathbf{r}_{\mathcal{B}}$

### 5.1.2 Homogeneous Sphere

If the body  $\mathcal{B}$  is modeled by a homogeneous sphere of radius  $R_{\mathcal{B}}$ , density  $\rho_{\mathcal{B}}$  and centered at position  $\mathbf{r}_{\mathcal{B}}$ , the gravitational scalar potential  $\Phi_{\text{grav}}$ , the gravitational acceleration vector  $\mathbf{g}_{\text{grav}}$ , and tensor  $\mathbf{\Gamma}_{\text{grav}}$ , at a given position vector  $\mathbf{r}$ , are given by:

#### Gravitational Potential

$$\Phi_{\text{grav}}(\mathbf{r}) = \begin{cases} +G\frac{4}{3}\pi R_{\mathcal{B}}^3\rho_{\mathcal{B}} \cdot \frac{1}{|\mathbf{r} - \mathbf{r}_{\mathcal{B}}|} & \text{if: } |\mathbf{r} - \mathbf{r}_{\mathcal{B}}| > R_{\mathcal{B}} \\ +2\pi G\rho_{\mathcal{B}} \cdot \left( R_{\mathcal{B}}^2 - \frac{|\mathbf{r} - \mathbf{r}_{\mathcal{B}}|^2}{3} \right) & \text{if } |\mathbf{r} - \mathbf{r}_{\mathcal{B}}| \leq R_{\mathcal{B}} \end{cases} \quad (5.9)$$

#### Gravitational Acceleration

$$\mathbf{g}_{\text{grav}}(\mathbf{r}) = \begin{cases} -G\frac{4}{3}\pi R_{\mathcal{B}}^3\rho_{\mathcal{B}} \cdot \begin{pmatrix} \frac{r_x - r_{x,\mathcal{B}}}{|\mathbf{r} - \mathbf{r}_{\mathcal{B}}|^3} \\ \frac{r_y - r_{y,\mathcal{B}}}{|\mathbf{r} - \mathbf{r}_{\mathcal{B}}|^3} \\ \frac{r_z - r_{z,\mathcal{B}}}{|\mathbf{r} - \mathbf{r}_{\mathcal{B}}|^3} \end{pmatrix} & \text{if: } |\mathbf{r} - \mathbf{r}_{\mathcal{B}}| > R_{\mathcal{B}} \\ -G\frac{4}{3}\pi\rho_{\mathcal{B}} \cdot \begin{pmatrix} r_x - r_{x,\mathcal{B}} \\ r_y - r_{y,\mathcal{B}} \\ r_z - r_{z,\mathcal{B}} \end{pmatrix} & \text{if } |\mathbf{r} - \mathbf{r}_{\mathcal{B}}| \leq R_{\mathcal{B}} \end{cases} \quad (5.10)$$

#### Gravitational Tensor

$$\mathbf{\Gamma}_{\text{grav}}(\mathbf{r}) = -G\frac{4}{3}\pi R_{\mathcal{B}}^3\rho_{\mathcal{B}} \cdot \begin{pmatrix} \frac{|\mathbf{r} - \mathbf{r}_{\mathcal{B}}|^2 - 3 \cdot (r_x - r_{x,\mathcal{B}})^2}{|\mathbf{r} - \mathbf{r}_{\mathcal{B}}|^5} & \frac{-3 \cdot (r_y - r_{y,\mathcal{B}}) \cdot (r_x - r_{x,\mathcal{B}})}{|\mathbf{r} - \mathbf{r}_{\mathcal{B}}|^5} & \frac{-3 \cdot (r_z - r_{z,\mathcal{B}}) \cdot (r_x - r_{x,\mathcal{B}})}{|\mathbf{r} - \mathbf{r}_{\mathcal{B}}|^5} \\ \frac{-3 \cdot (r_x - r_{x,\mathcal{B}}) \cdot (r_y - r_{y,\mathcal{B}})}{|\mathbf{r} - \mathbf{r}_{\mathcal{B}}|^5} & \frac{|\mathbf{r} - \mathbf{r}_{\mathcal{B}}|^2 - 3 \cdot (r_y - r_{y,\mathcal{B}})^2}{|\mathbf{r} - \mathbf{r}_{\mathcal{B}}|^5} & \frac{-3 \cdot (r_z - r_{z,\mathcal{B}}) \cdot (r_y - r_{y,\mathcal{B}})}{|\mathbf{r} - \mathbf{r}_{\mathcal{B}}|^5} \\ \frac{-3 \cdot (r_x - r_{x,\mathcal{B}}) \cdot (r_z - r_{z,\mathcal{B}})}{|\mathbf{r} - \mathbf{r}_{\mathcal{B}}|^5} & \frac{-3 \cdot (r_y - r_{y,\mathcal{B}}) \cdot (r_z - r_{z,\mathcal{B}})}{|\mathbf{r} - \mathbf{r}_{\mathcal{B}}|^5} & \frac{|\mathbf{r} - \mathbf{r}_{\mathcal{B}}|^2 - 3 \cdot (r_z - r_{z,\mathcal{B}})^2}{|\mathbf{r} - \mathbf{r}_{\mathcal{B}}|^5} \end{pmatrix} \quad (5.11)$$

if  $|\mathbf{r} - \mathbf{r}_{\mathcal{B}}| > R_{\mathcal{B}}$

and:

$$\mathbf{\Gamma}_{\text{grav}}(\mathbf{r}) = -G\frac{4}{3}\pi\rho_{\mathcal{B}} \cdot \begin{pmatrix} 1 & 0 & 0 \\ 0 & 1 & 0 \\ 0 & 0 & 1 \end{pmatrix} \quad \text{if } |\mathbf{r} - \mathbf{r}_{\mathcal{B}}| \leq R_{\mathcal{B}} \quad (5.12)$$

### 5.1.3 Homogeneous Polyhedron

The modeling of bodies with homogeneous polyhedra is very useful. Compared to rectangular prisms, it permits to model bodies with complicated shapes in a much better way. For example, the modeling of the topography in 3D with rectangular prisms, based on a digital terrain model (DTM), is not ideal, the discretization is not continuous, and not

straightforward if the Earth's curvature should be taken into account. In contrary, if the topography is modeled by a polyhedron, the body is continuous and the consideration of the Earth's curvature is simply given, if the coordinates of the vertices are provided in a 3D Cartesian coordinate system. In addition, once the topology of the polyhedron is defined, the body can be deformed very easily by changing the coordinates of the vertices only. This gives the possibility to automatically generate sequences of deformed versions of a given body.

In the literature, many publications deal with the computation of gravitational fields of homogeneous polyhedra. The algorithms proposed by the various authors are not equivalent and can be evaluated according to the following characteristics:

- homogeneous or linearly varying density.
- based on approximate methods or given by exact analytic formulas.
- cope with triangular meshes or with arbitrary polygonal meshes.
- gravitational functionals which can be computed (e.g., potential, acceleration vector and tensor).
- allowed positions of the points to be computed (outside, inside or at the boundary of the body).
- provide formulas for the treatment of singularities.

In Table 5.1, a non-exhaustive list of references is given together with some of their principal characteristics. Regardless of the density model, it is obvious that the formulas provided on the one hand by *Petrovic* (1996); *Tsouliis and Petrovic* (2001); *Tsouliis* (2012) and on the other hand by *D'Urso* (2013, 2014) are superior to the other models, since they give the possibility to compute all gravitational field functionals, at arbitrary positions, using analytical formulas. However, because the formulas provided by *D'Urso* were only published after the development of **QGravity** and since those ones provided by *Petrovic* and *Tsouliis* are very comprehensive and easy to implement, the computations are solely based on the publications of *Petrovic* (1996); *Tsouliis and Petrovic* (2001), summarized in *Tsouliis* (2012).

Basically, the way used by *Petrovic* (1996) to find the formulas for all functionals of the gravitational field is very elegant and is based on two subsequent applications of the divergence theorem<sup>1</sup> on simplified versions of Equations 5.2, 5.3 and 5.5 in order to transform the volume integrals into line integrals which have analytic expressions for straight line segments. The simplifications of Equations 5.2, 5.3 and 5.5 consists on the one hand in assuming a constant density field  $\rho_{\mathcal{B}}$  and on the other hand in defining the origin of

<sup>1</sup>also called the Green-Ostrogradski's theorem, or the Gauss theorem.

the coordinate system at the computation point  $\mathbf{r} \equiv \mathcal{O}$ :

$$\begin{aligned}
 \Phi_{\text{grav}} &= +G\rho_{\mathcal{B}} \cdot \iiint_{\mathcal{B}} \frac{1}{|\mathbf{r}'|} \cdot dV \\
 \mathbf{g}_{\text{grav}} &= +G\rho_{\mathcal{B}} \cdot \begin{pmatrix} \iiint_{\mathcal{B}} \frac{\partial}{\partial x} \left( \frac{1}{|\mathbf{r}'|} \right) \cdot dV \\ \iiint_{\mathcal{B}} \frac{\partial}{\partial y} \left( \frac{1}{|\mathbf{r}'|} \right) \cdot dV \\ \iiint_{\mathcal{B}} \frac{\partial}{\partial z} \left( \frac{1}{|\mathbf{r}'|} \right) \cdot dV \end{pmatrix} \\
 \mathbf{\Gamma}_{\text{grav}} &= +G\rho_{\mathcal{B}} \cdot \begin{pmatrix} \iiint_{\mathcal{B}} \frac{\partial^2}{\partial x \partial x} \left( \frac{1}{|\mathbf{r}'|} \right) \cdot dV & \iiint_{\mathcal{B}} \frac{\partial^2}{\partial x \partial y} \left( \frac{1}{|\mathbf{r}'|} \right) \cdot dV & \iiint_{\mathcal{B}} \frac{\partial^2}{\partial x \partial z} \left( \frac{1}{|\mathbf{r}'|} \right) \cdot dV \\ \iiint_{\mathcal{B}} \frac{\partial^2}{\partial y \partial x} \left( \frac{1}{|\mathbf{r}'|} \right) \cdot dV & \iiint_{\mathcal{B}} \frac{\partial^2}{\partial y \partial y} \left( \frac{1}{|\mathbf{r}'|} \right) \cdot dV & \iiint_{\mathcal{B}} \frac{\partial^2}{\partial y \partial z} \left( \frac{1}{|\mathbf{r}'|} \right) \cdot dV \\ \iiint_{\mathcal{B}} \frac{\partial^2}{\partial z \partial x} \left( \frac{1}{|\mathbf{r}'|} \right) \cdot dV & \iiint_{\mathcal{B}} \frac{\partial^2}{\partial z \partial y} \left( \frac{1}{|\mathbf{r}'|} \right) \cdot dV & \iiint_{\mathcal{B}} \frac{\partial^2}{\partial z \partial z} \left( \frac{1}{|\mathbf{r}'|} \right) \cdot dV \end{pmatrix}
 \end{aligned} \tag{5.13}$$

**Table 5.1:** Non-exhaustive list of references to algorithms allowing the computation of gravitational field functionals of an arbitrary shaped polyhedron.

references	density	formulas	gravitational functionals	allowed position	treatment of singularities
<i>Petrovic (1996); Tsoulis and Petrovic (2001); Tsoulis (2012)</i>	homog.	exact	$\Phi, \mathbf{g}, \mathbf{\Gamma}$	all	yes
<i>D'Urso (2013, 2014)</i>	homog.	exact	$\Phi, \mathbf{g}, \mathbf{\Gamma}$	all	yes
<i>Arnet (1992)</i>	homog.	exact	$\Phi, \mathbf{g}, \mathbf{\Gamma}$	all*	no
<i>Pohanka (1988)</i>	homog.	approx	$\mathbf{g}$	all	yes
<i>Pohanka (1998)</i>	linear	approx	$\mathbf{g}$	all	yes
<i>Hamayun et al. (2009)</i>	linear	approx	$\Phi$	all	yes
<i>Talwani and Ewing (1960)</i>	homog.	approx	$g_z$	external	no
<i>Tsoulis et al. (2009)</i>	homog.	approx	$C_{nm}, S_{nm}$ **	external	no

\* spherical harmonic coefficients of the gravitational potential.

\*\* position inside the body not allowed for the gravitational tensor only.

### Transformations of Volume Integrals into Surface Integrals

In the three-dimensional space  $\mathbb{R}^3$ , the divergence theorem is given by:

$$\iiint_{\mathcal{V}} (\nabla \cdot \mathbf{u}) \cdot dV = \iint_{\partial \mathcal{V}} (\mathbf{u} \cdot \mathbf{n}) \cdot dS \tag{5.14}$$

where  $\mathcal{V}$  is a compact<sup>2</sup> volume which has the piecewise smooth boundary  $\partial\mathcal{V}$ . The vector field  $\mathbf{u}$  must be continuously differentiable in the neighborhood of  $\mathcal{V}$  and  $\mathbf{n}$  represents the unit normal field of the boundary  $\partial\mathcal{V}$ <sup>3</sup> pointing outward.

In order to apply Equation 5.14 to a particular integral given by Equation 5.13, it is necessary to find a vector field  $\mathbf{u}$  which has its divergence corresponding to the integrand. For the potential, *Petrovic* (1996) found the following field:

$$\mathbf{u}_\Phi = \frac{\mathbf{r}'}{2|\mathbf{r}'|} \implies \nabla \cdot \mathbf{u}_\Phi = \frac{1}{|\mathbf{r}'|} \quad (5.15)$$

for the acceleration vector *Petrovic* (1996) proposes:

$$\begin{aligned} \mathbf{u}_{g_x} = \frac{\mathbf{e}_x}{|\mathbf{r}'|} &\implies \nabla \cdot \mathbf{u}_{g_x} = \frac{\partial}{\partial x} \left( \frac{1}{|\mathbf{r}'|} \right) \\ \mathbf{u}_{g_y} = \frac{\mathbf{e}_y}{|\mathbf{r}'|} &\implies \nabla \cdot \mathbf{u}_{g_y} = \frac{\partial}{\partial y} \left( \frac{1}{|\mathbf{r}'|} \right) \\ \mathbf{u}_{g_z} = \frac{\mathbf{e}_z}{|\mathbf{r}'|} &\implies \nabla \cdot \mathbf{u}_{g_z} = \frac{\partial}{\partial z} \left( \frac{1}{|\mathbf{r}'|} \right) \end{aligned} \quad (5.16)$$

and for the gravitational tensor:

$$\begin{aligned} \mathbf{u}_{\Gamma_{xx}} = \frac{\partial}{\partial x} \left( \frac{\mathbf{e}_x}{|\mathbf{r}'|} \right) &\implies \nabla \cdot \mathbf{u}_{\Gamma_{xx}} = \frac{\partial^2}{\partial x \partial x} \left( \frac{1}{|\mathbf{r}'|} \right) \\ \mathbf{u}_{\Gamma_{yy}} = \frac{\partial}{\partial y} \left( \frac{\mathbf{e}_y}{|\mathbf{r}'|} \right) &\implies \nabla \cdot \mathbf{u}_{\Gamma_{yy}} = \frac{\partial^2}{\partial y \partial y} \left( \frac{1}{|\mathbf{r}'|} \right) \\ \mathbf{u}_{\Gamma_{zz}} = \frac{\partial}{\partial z} \left( \frac{\mathbf{e}_z}{|\mathbf{r}'|} \right) &\implies \nabla \cdot \mathbf{u}_{\Gamma_{zz}} = \frac{\partial^2}{\partial z \partial z} \left( \frac{1}{|\mathbf{r}'|} \right) \\ \mathbf{u}_{\Gamma_{xy}} = \mathbf{u}_{\Gamma_{yx}} = \frac{\partial}{\partial y} \left( \frac{\mathbf{e}_x}{|\mathbf{r}'|} \right) &\implies \nabla \cdot \mathbf{u}_{\Gamma_{xy}} = \frac{\partial^2}{\partial x \partial y} \left( \frac{1}{|\mathbf{r}'|} \right) \\ \mathbf{u}_{\Gamma_{xz}} = \mathbf{u}_{\Gamma_{zx}} = \frac{\partial}{\partial z} \left( \frac{\mathbf{e}_x}{|\mathbf{r}'|} \right) &\implies \nabla \cdot \mathbf{u}_{\Gamma_{xz}} = \frac{\partial^2}{\partial x \partial z} \left( \frac{1}{|\mathbf{r}'|} \right) \\ \mathbf{u}_{\Gamma_{yz}} = \mathbf{u}_{\Gamma_{zy}} = \frac{\partial}{\partial z} \left( \frac{\mathbf{e}_y}{|\mathbf{r}'|} \right) &\implies \nabla \cdot \mathbf{u}_{\Gamma_{yz}} = \frac{\partial^2}{\partial y \partial z} \left( \frac{1}{|\mathbf{r}'|} \right) \end{aligned} \quad (5.17)$$

<sup>2</sup>in  $\mathbb{R}^n$ , compact means that the volume is closed and bounded.

<sup>3</sup>The boundary  $\partial\mathcal{V}$  must be an orientable two-dimensional manifold.

which permits to transform, with Equation 5.14, the volume integrals 5.13 into surface integrals as follows:

$$\begin{aligned}
 \Phi_{\text{grav}} &= +\frac{G\rho_{\mathcal{B}}}{2} \cdot \iint_{\partial\mathcal{B}} \left( \frac{\mathbf{r}'}{|\mathbf{r}'|} \cdot \mathbf{n} \right) \cdot dS \\
 \mathbf{g}_{\text{grav}} &= +G\rho_{\mathcal{B}} \cdot \begin{pmatrix} \iint_{\partial\mathcal{B}} \left( \frac{\mathbf{e}_x}{|\mathbf{r}'|} \cdot \mathbf{n} \right) \cdot dS \\ \iint_{\partial\mathcal{B}} \left( \frac{\mathbf{e}_y}{|\mathbf{r}'|} \cdot \mathbf{n} \right) \cdot dS \\ \iint_{\partial\mathcal{B}} \left( \frac{\mathbf{e}_z}{|\mathbf{r}'|} \cdot \mathbf{n} \right) \cdot dS \end{pmatrix} \\
 \mathbf{\Gamma}_{\text{grav}} &= +G\rho_{\mathcal{B}} \cdot \begin{pmatrix} \iint_{\partial\mathcal{B}} \frac{\partial}{\partial x} \left( \frac{\mathbf{e}_x}{|\mathbf{r}'|} \right) \cdot \mathbf{n} \cdot dS & \iint_{\partial\mathcal{B}} \frac{\partial}{\partial y} \left( \frac{\mathbf{e}_x}{|\mathbf{r}'|} \right) \cdot \mathbf{n} \cdot dS & \iint_{\partial\mathcal{B}} \frac{\partial}{\partial z} \left( \frac{\mathbf{e}_x}{|\mathbf{r}'|} \right) \cdot \mathbf{n} \cdot dS \\ \iint_{\partial\mathcal{B}} \frac{\partial}{\partial y} \left( \frac{\mathbf{e}_x}{|\mathbf{r}'|} \right) \cdot \mathbf{n} \cdot dS & \iint_{\partial\mathcal{B}} \frac{\partial}{\partial y} \left( \frac{\mathbf{e}_y}{|\mathbf{r}'|} \right) \cdot \mathbf{n} \cdot dS & \iint_{\partial\mathcal{B}} \frac{\partial}{\partial z} \left( \frac{\mathbf{e}_y}{|\mathbf{r}'|} \right) \cdot \mathbf{n} \cdot dS \\ \iint_{\partial\mathcal{B}} \frac{\partial}{\partial z} \left( \frac{\mathbf{e}_x}{|\mathbf{r}'|} \right) \cdot \mathbf{n} \cdot dS & \iint_{\partial\mathcal{B}} \frac{\partial}{\partial z} \left( \frac{\mathbf{e}_y}{|\mathbf{r}'|} \right) \cdot \mathbf{n} \cdot dS & \iint_{\partial\mathcal{B}} \frac{\partial}{\partial z} \left( \frac{\mathbf{e}_z}{|\mathbf{r}'|} \right) \cdot \mathbf{n} \cdot dS \end{pmatrix}
 \end{aligned} \tag{5.18}$$

### Polyhedral Discretization of the Surface Integrals

The next step consists in formulating the surface integrals given in Equation 5.18 as a function of the geometry defined by a polyhedron. It consists in replacing the general boundary  $\partial\mathcal{B}$  by a discretized polyhedral surface  $\mathbb{S}$ , which is defined as the union of  $n$  polygons  $\mathbb{S}_i$ :

$$\partial\mathcal{B} \equiv \mathbb{S} = \bigcup_{i=1}^n \mathbb{S}_i \tag{5.19}$$

associated with their constant outer unit normal  $\mathbf{n}_i$  and their Hessian plane equation:

$$\mathbb{S}_i \equiv \mathbf{n}_i \cdot \mathbf{r}' = h_i \tag{5.20}$$

where  $h_i$  represents the signed orthogonal distance between the computation point  $\mathbf{r}$  and the plane defined by  $\mathbb{S}_i$ . Per definition,  $h_i < 0$  if  $\mathbf{r}$  is inside the half-space defined by  $\mathbf{n}_i$  and  $h_i > 0$  otherwise.

Now, Equation 5.18 can be reformulated when replacing  $\partial\mathcal{B}$  is replaced by  $\mathbb{S}$ . This makes it possible to express the integral on  $\partial\mathcal{B}$  by a discrete sum of surface integrals defined on the polygons  $\mathbb{S}_i$ . And together with Equation 5.20, this permits to replace  $\mathbf{n}_i \cdot \mathbf{r}'$  by  $h_i$  and to take these out of the integral. Finally, since the scalar products  $(\mathbf{e}_x \cdot \mathbf{n}_i)$ ,  $(\mathbf{e}_y \cdot \mathbf{n}_i)$  and



$(\mathbf{e}_z \cdot \mathbf{n}_i)$  are constant on a particular polygon  $\mathbb{S}_i$ , we have:

$$\begin{aligned}\Phi_{\text{grav}} &= +\frac{G\rho_{\mathcal{B}}}{2} \cdot \sum_{i=1}^n h_i \cdot \iint_{\mathbb{S}_i} \frac{1}{|\mathbf{r}'|} \cdot dS \\ \mathbf{g}_{\text{grav}} &= +G\rho_{\mathcal{B}} \cdot \begin{pmatrix} \sum_{i=1}^n \mathbf{e}_x \cdot \mathbf{n}_i \cdot \iint_{\mathbb{S}_i} \frac{1}{|\mathbf{r}'|} \cdot dS \\ \sum_{i=1}^n \mathbf{e}_y \cdot \mathbf{n}_i \cdot \iint_{\mathbb{S}_i} \frac{1}{|\mathbf{r}'|} \cdot dS \\ \sum_{i=1}^n \mathbf{e}_z \cdot \mathbf{n}_i \cdot \iint_{\mathbb{S}_i} \frac{1}{|\mathbf{r}'|} \cdot dS \end{pmatrix} \\ \mathbf{\Gamma}_{\text{grav}} &= +G\rho_{\mathcal{B}} \cdot \begin{pmatrix} \sum_{i=1}^n \mathbf{e}_x \cdot \mathbf{n}_i \cdot \iint_{\mathbb{S}_i} \frac{\partial}{\partial x} \left( \frac{1}{|\mathbf{r}'|} \right) \cdot dS & \dots & \vdots \\ \sum_{i=1}^n \mathbf{e}_x \cdot \mathbf{n}_i \cdot \iint_{\mathbb{S}_i} \frac{\partial}{\partial y} \left( \frac{1}{|\mathbf{r}'|} \right) \cdot dS & \sum_{i=1}^n \mathbf{e}_y \cdot \mathbf{n}_i \cdot \iint_{\mathbb{S}_i} \frac{\partial}{\partial y} \left( \frac{1}{|\mathbf{r}'|} \right) \cdot dS & \vdots \\ \sum_{i=1}^n \mathbf{e}_x \cdot \mathbf{n}_i \cdot \iint_{\mathbb{S}_i} \frac{\partial}{\partial z} \left( \frac{1}{|\mathbf{r}'|} \right) \cdot dS & \dots & \ddots \end{pmatrix}\end{aligned}\quad (5.21)$$

which shows that the non-geometric quantities, which have still to be solved, are:

$$\mathcal{A}_i = \iint_{\mathbb{S}_i} \frac{1}{|\mathbf{r}'|} \cdot dS \quad (5.22)$$

and:

$$\mathcal{B}_i = \iint_{\mathbb{S}_i} \frac{\partial}{\partial x} \left( \frac{1}{|\mathbf{r}'|} \right) \cdot dS; \quad \mathcal{C}_i = \iint_{\mathbb{S}_i} \frac{\partial}{\partial y} \left( \frac{1}{|\mathbf{r}'|} \right) \cdot dS; \quad \mathcal{D}_i = \iint_{\mathbb{S}_i} \frac{\partial}{\partial z} \left( \frac{1}{|\mathbf{r}'|} \right) \cdot dS \quad (5.23)$$

which allows it to reformulate Equation 5.21 in a more compact way by:

$$\begin{aligned}\Phi_{\text{grav}} &= +\frac{G\rho_{\mathcal{B}}}{2} \cdot \sum_{i=1}^n h_i \cdot \mathcal{A}_i \\ \mathbf{g}_{\text{grav}} &= +G\rho_{\mathcal{B}} \cdot \begin{pmatrix} \sum_{i=1}^n \mathbf{e}_x \cdot \mathbf{n}_i \cdot \mathcal{A}_i \\ \sum_{i=1}^n \mathbf{e}_y \cdot \mathbf{n}_i \cdot \mathcal{A}_i \\ \sum_{i=1}^n \mathbf{e}_z \cdot \mathbf{n}_i \cdot \mathcal{A}_i \end{pmatrix} \\ \mathbf{\Gamma}_{\text{grav}} &= +G\rho_{\mathcal{B}} \cdot \begin{pmatrix} \sum_{i=1}^n \mathbf{e}_x \cdot \mathbf{n}_i \cdot \mathcal{B}_i & \sum_{i=1}^n \mathbf{e}_y \cdot \mathbf{n}_i \cdot \mathcal{B}_i & \sum_{i=1}^n \mathbf{e}_z \cdot \mathbf{n}_i \cdot \mathcal{B}_i \\ \sum_{i=1}^n \mathbf{e}_x \cdot \mathbf{n}_i \cdot \mathcal{C}_i & \sum_{i=1}^n \mathbf{e}_y \cdot \mathbf{n}_i \cdot \mathcal{C}_i & \sum_{i=1}^n \mathbf{e}_z \cdot \mathbf{n}_i \cdot \mathcal{C}_i \\ \sum_{i=1}^n \mathbf{e}_x \cdot \mathbf{n}_i \cdot \mathcal{D}_i & \sum_{i=1}^n \mathbf{e}_y \cdot \mathbf{n}_i \cdot \mathcal{D}_i & \sum_{i=1}^n \mathbf{e}_z \cdot \mathbf{n}_i \cdot \mathcal{D}_i \end{pmatrix}\end{aligned}\quad (5.24)$$

### Transformations of Surface Integrals into Curvilinear Integrals

In the two-dimensional space  $\mathbb{R}^2$ , the divergence theorem is given by:

$$\iint_{\mathcal{S}} (\nabla \cdot \boldsymbol{\mu}) \cdot dS = \oint_{\partial\mathcal{S}} (\boldsymbol{\mu} \cdot \boldsymbol{\eta}) \cdot ds \quad (5.25)$$

where  $\mathcal{S}$  is a region in  $\mathbb{R}^2$  which has the piecewise smooth boundary curve  $\partial\mathcal{S}$ . The two-dimensional vector field  $\boldsymbol{\mu}$  must be continuously differentiable in the neighborhood of  $\mathcal{S}$  and  $\boldsymbol{\eta}$  represents the outer unit normals at the boundary curve  $\partial\mathcal{S}$ . In addition, the curvilinear integral must be computed in the counterclockwise direction.

In order to apply Equation 5.25 to Equations 5.22 and 5.23 it is again necessary to find 2D vector fields which have divergences corresponding to the integrands of the Equations 5.22 and 5.23. In a first step, *Petrovic* (1996) defines a new coordinate system, with basis vectors  $(\mathbf{e}_x^i, \mathbf{e}_y^i, \mathbf{e}_z^i)$  for each polygon  $\mathbb{S}_i$ . Basically it is so that the origin  $\mathbf{o}^{\mathbb{S}_i}$  is placed at the orthogonal projection of the computation point  $\mathbf{r}$  on the plane  $\mathbb{S}_i$ . And the basis vectors are defined such that:

$$\mathbf{e}_z^i = \mathbf{n}_i \quad \text{and} \quad \mathbf{e}_x^i \perp \mathbf{e}_y^i \perp \mathbf{e}_z^i \quad (5.26)$$

and if the three-dimensional vector  $\mathbf{r}'$  is given in the new two-dimensional coordinate system as:

$$\boldsymbol{\rho}' = \begin{pmatrix} (\mathbf{r}' - \mathbf{o}^{\mathbb{S}_i}) \cdot \mathbf{e}_x^i \\ (\mathbf{r}' - \mathbf{o}^{\mathbb{S}_i}) \cdot \mathbf{e}_y^i \end{pmatrix} \quad (5.27)$$

*Petrovic* (1996) proposes for  $\mathcal{A}_i$ :

$$\boldsymbol{\mu}_{\mathcal{A}_i} = \frac{\boldsymbol{\rho}'}{|\mathbf{r}'|} + \frac{h_i^2 \cdot \boldsymbol{\rho}'}{|\boldsymbol{\rho}'|^2 \cdot |\mathbf{r}'|} \implies \nabla \cdot \boldsymbol{\mu}_{\mathcal{A}_i} = \frac{1}{|\mathbf{r}'|} \quad (5.28)$$

which permits to transform, with Equation 5.25, the surface integrals of Equation 5.22 into curvilinear integrals as follows:

$$\mathcal{A}_i = \oint_{\partial\mathbb{S}_i} \left( \frac{\boldsymbol{\rho}'}{|\mathbf{r}'|} + \frac{h_i^2 \cdot \boldsymbol{\rho}'}{|\boldsymbol{\rho}'|^2 \cdot |\mathbf{r}'|} \right) \cdot \boldsymbol{\eta}_i \cdot d\mathbf{s} \quad (5.29)$$

Concerning the surface integrals  $\mathcal{B}_i, \mathcal{C}_i, \mathcal{D}_i$ , the derivation of the vector fields are a little bit more tricky. In fact, *Petrovic* (1996) decomposes the integrands in order to get:

$$\begin{aligned} \mathcal{B}_i &= \iint_{\mathbb{S}_i} \frac{\partial}{\partial x} \left( \frac{1}{|\mathbf{r}'|} \right) \cdot d\mathbf{S} \\ &= -|\mathbf{n}_i \times \mathbf{e}_x| \cdot \iint_{\mathbb{S}_i} \frac{\partial}{\partial x^i} \left( \frac{1}{|\mathbf{r}'|} \right) \cdot d\mathbf{S} + \mathbf{n}_i \cdot \mathbf{e}_x \cdot \iint_{\mathbb{S}_i} \frac{\partial}{\partial z^i} \left( \frac{1}{|\mathbf{r}'|} \right) \cdot d\mathbf{S} \\ \mathcal{C}_i &= \iint_{\mathbb{S}_i} \frac{\partial}{\partial y} \left( \frac{1}{|\mathbf{r}'|} \right) \cdot d\mathbf{S} \\ &= -|\mathbf{n}_i \times \mathbf{e}_y| \cdot \iint_{\mathbb{S}_i} \frac{\partial}{\partial x^i} \left( \frac{1}{|\mathbf{r}'|} \right) \cdot d\mathbf{S} + \mathbf{n}_i \cdot \mathbf{e}_y \cdot \iint_{\mathbb{S}_i} \frac{\partial}{\partial z^i} \left( \frac{1}{|\mathbf{r}'|} \right) \cdot d\mathbf{S} \\ \mathcal{D}_i &= \iint_{\mathbb{S}_i} \frac{\partial}{\partial z} \left( \frac{1}{|\mathbf{r}'|} \right) \cdot d\mathbf{S} \\ &= -|\mathbf{n}_i \times \mathbf{e}_z| \cdot \iint_{\mathbb{S}_i} \frac{\partial}{\partial x^i} \left( \frac{1}{|\mathbf{r}'|} \right) \cdot d\mathbf{S} + \mathbf{n}_i \cdot \mathbf{e}_z \cdot \iint_{\mathbb{S}_i} \frac{\partial}{\partial z^i} \left( \frac{1}{|\mathbf{r}'|} \right) \cdot d\mathbf{S} \end{aligned} \quad (5.30)$$

which implies the search for two vector fields common to all integrands  $\mathcal{B}_i, \mathcal{C}_i, \mathcal{D}_i$ :

$$\begin{aligned}\boldsymbol{\mu}_1 &= \frac{1}{|\mathbf{r}'|} \begin{pmatrix} 1 \\ 0 \end{pmatrix} \Rightarrow \nabla \cdot \boldsymbol{\mu}_1 = \frac{\partial}{\partial x^i} \left( \frac{1}{|\mathbf{r}'|} \right) \\ \boldsymbol{\mu}_2 &= \frac{h_i \cdot \boldsymbol{\rho}'}{|\boldsymbol{\rho}'|^2 \cdot |\mathbf{r}'|} \Rightarrow \nabla \cdot \boldsymbol{\mu}_2 = \frac{\partial}{\partial z^i} \left( \frac{1}{|\mathbf{r}'|} \right)\end{aligned}\quad (5.31)$$

and permits the transformation of the surface integrals in Equation 5.23 into the following curvilinear integrals:

$$\begin{aligned}\mathcal{B}_i &= -|\mathbf{n}_i \times \mathbf{e}_x| \cdot \oint_{\partial \mathbb{S}_i} \frac{1}{|\mathbf{r}'|} \begin{pmatrix} 1 \\ 0 \end{pmatrix} \cdot \boldsymbol{\eta}_i \cdot d\mathbf{s} + \mathbf{n}_i \cdot \mathbf{e}_x \cdot \oint_{\partial \mathbb{S}_i} \frac{h_i \cdot \boldsymbol{\rho}'}{|\boldsymbol{\rho}'|^2 \cdot |\mathbf{r}'|} \cdot \boldsymbol{\eta}_i \cdot d\mathbf{s} \\ \mathcal{C}_i &= -|\mathbf{n}_i \times \mathbf{e}_y| \cdot \oint_{\partial \mathbb{S}_i} \frac{1}{|\mathbf{r}'|} \begin{pmatrix} 1 \\ 0 \end{pmatrix} \cdot \boldsymbol{\eta}_i \cdot d\mathbf{s} + \mathbf{n}_i \cdot \mathbf{e}_y \cdot \oint_{\partial \mathbb{S}_i} \frac{h_i \cdot \boldsymbol{\rho}'}{|\boldsymbol{\rho}'|^2 \cdot |\mathbf{r}'|} \cdot \boldsymbol{\eta}_i \cdot d\mathbf{s} \\ \mathcal{D}_i &= -|\mathbf{n}_i \times \mathbf{e}_z| \cdot \oint_{\partial \mathbb{S}_i} \frac{1}{|\mathbf{r}'|} \begin{pmatrix} 1 \\ 0 \end{pmatrix} \cdot \boldsymbol{\eta}_i \cdot d\mathbf{s} + \mathbf{n}_i \cdot \mathbf{e}_z \cdot \oint_{\partial \mathbb{S}_i} \frac{h_i \cdot \boldsymbol{\rho}'}{|\boldsymbol{\rho}'|^2 \cdot |\mathbf{r}'|} \cdot \boldsymbol{\eta}_i \cdot d\mathbf{s}\end{aligned}\quad (5.32)$$

### Polygonal Discretization of the Curvilinear Integrals

The last steps consists in the discretization of the curvilinear integrals and the analytic solving of the resulting linear integrals. Here the polygonal boundaries  $\partial \mathbb{S}_i$  are replaced by the union of  $m$  linear segments  $\mathbb{L}_{ij}$ :

$$\mathbb{S}_i \equiv \mathbb{L}_i = \bigcup_{j=1}^m \mathbb{L}_{ij} \quad (5.33)$$

and with the Hessian form of the equation of the line:

$$\mathbb{L}_{ij} \equiv \boldsymbol{\eta}_{ij} \cdot \boldsymbol{\rho}' = h_{ij} \quad (5.34)$$

where  $h_{ij}$  represents the signed orthogonal distance between the point  $\boldsymbol{\rho}'$  and the line defined by  $\mathbb{L}_{ij}$ . Per definition,  $h_{ij} < 0$  if  $\boldsymbol{\rho}'$  is inside the half-plane defined by  $\boldsymbol{\eta}_{ij}$  and  $h_{ij} > 0$  otherwise.

Now, similarly to the discretization of the surface integrals, Equations 5.29 and 5.32 can be reformulate, when replacing  $\partial \mathbb{S}_i$  by  $\mathbb{L}_i$ . This renders possible to express the integral on  $\partial \mathbb{S}_i$  by a discrete sum of linear integrals defined on the segments of lines  $\mathbb{L}_{ij}$ . Together with Equation 5.34, this permits to replace  $\boldsymbol{\eta}_{ij} \cdot \boldsymbol{\rho}'$  by  $h_{ij}$  and take these out of the integral. For the integral  $\mathcal{A}_i$  this step is easy to follow and gives:

$$\mathcal{A}_i = \sum_{j=1}^m \left\{ h_{ij} \cdot \int_{\mathbb{L}_{ij}} \frac{1}{|\mathbf{r}'|} \cdot d\mathbf{s} + h_i^2 h_{ij} \cdot \int_{\mathbb{L}_{ij}} \frac{1}{|\boldsymbol{\rho}'|^2 \cdot |\mathbf{r}'|} \cdot d\mathbf{s} \right\} \quad (5.35)$$

For the integrals  $\mathcal{B}_i$ ,  $\mathcal{C}_i$  and  $\mathcal{D}_i$  the discretization is more complicated and *Petrovic* (1996) gives finally:

$$\begin{aligned}\mathcal{B}_i &= \sum_{j=1}^m \left\{ \boldsymbol{\eta}_{ij} \cdot \mathbf{e}_x \cdot \int_{\mathbb{L}_{ij}} \frac{1}{|\mathbf{r}'|} \cdot ds + h_i h_{ij} \cdot \mathbf{n}_i \cdot \mathbf{e}_x \cdot \int_{\mathbb{L}_{ij}} \frac{1}{|\boldsymbol{\rho}'|^2 \cdot |\mathbf{r}'|} \cdot ds \right\} \\ \mathcal{C}_i &= \sum_{j=1}^m \left\{ \boldsymbol{\eta}_{ij} \cdot \mathbf{e}_y \cdot \int_{\mathbb{L}_{ij}} \frac{1}{|\mathbf{r}'|} \cdot ds + h_i h_{ij} \cdot \mathbf{n}_i \cdot \mathbf{e}_y \cdot \int_{\mathbb{L}_{ij}} \frac{1}{|\boldsymbol{\rho}'|^2 \cdot |\mathbf{r}'|} \cdot ds \right\} \\ \mathcal{D}_i &= \sum_{j=1}^m \left\{ \boldsymbol{\eta}_{ij} \cdot \mathbf{e}_z \cdot \int_{\mathbb{L}_{ij}} \frac{1}{|\mathbf{r}'|} \cdot ds + h_i h_{ij} \cdot \mathbf{n}_i \cdot \mathbf{e}_z \cdot \int_{\mathbb{L}_{ij}} \frac{1}{|\boldsymbol{\rho}'|^2 \cdot |\mathbf{r}'|} \cdot ds \right\}\end{aligned}\quad (5.36)$$

It appears that the four relations given in Equations 5.35 and 5.36 contain just the two integrals:

$$\mathcal{L}1_{ij} = \int_{\mathbb{L}_{ij}} \frac{1}{|\mathbf{r}'|} \cdot ds \quad \text{and} \quad \mathcal{L}2_{ij} = \int_{\mathbb{L}_{ij}} \frac{1}{|\boldsymbol{\rho}'|^2 \cdot |\mathbf{r}'|} \cdot ds \quad (5.37)$$

which makes it possible to simplify Equations 5.35 and 5.36 in:

$$\begin{aligned}\mathcal{A}_i &= \sum_{j=1}^m \{ h_{ij} \cdot \mathcal{L}1_{ij} + h_i^2 h_{ij} \cdot \mathcal{L}2_{ij} \} \\ \mathcal{B}_i &= \sum_{j=1}^m \{ \boldsymbol{\eta}_{ij} \cdot \mathbf{e}_x \cdot \mathcal{L}1_{ij} + h_i h_{ij} \cdot \mathbf{n}_i \cdot \mathbf{e}_x \cdot \mathcal{L}2_{ij} \} \\ \mathcal{C}_i &= \sum_{j=1}^m \{ \boldsymbol{\eta}_{ij} \cdot \mathbf{e}_y \cdot \mathcal{L}1_{ij} + h_i h_{ij} \cdot \mathbf{n}_i \cdot \mathbf{e}_y \cdot \mathcal{L}2_{ij} \} \\ \mathcal{D}_i &= \sum_{j=1}^m \{ \boldsymbol{\eta}_{ij} \cdot \mathbf{e}_z \cdot \mathcal{L}1_{ij} + h_i h_{ij} \cdot \mathbf{n}_i \cdot \mathbf{e}_z \cdot \mathcal{L}2_{ij} \}\end{aligned}\quad (5.38)$$

### Final Analytical Formulas

If the origin  $\mathbf{o}^{\mathbb{L}_{ij}}$  of the axis  $\mathbf{e}_s$  is defined at the point defined as the orthogonal projection of  $\mathbf{o}^{\mathbb{S}_i}$  on the line  $\mathbb{L}_{ij}$ , the integrals 5.37 can be written as a function of the signed distances  $h_i$  and  $h_{ij}$  by:

$$\mathcal{L}1_{ij} = \int_{s_{1ij}}^{s_{2ij}} \frac{1}{\sqrt{h_i^2 + h_{ij}^2 + s^2}} \cdot ds \quad \text{and} \quad \mathcal{L}2_{ij} = \int_{s_{1ij}}^{s_{2ij}} \frac{1}{(h_{ij}^2 + s^2) \sqrt{h_i^2 + h_{ij}^2 + s^2}} \cdot ds \quad (5.39)$$

where  $s_{1ij}$  and  $s_{2ij}$  are the abscisse of the first and the second vertices of  $\mathbb{L}_{ij}$ . And their analytic solutions are given by:

$$\begin{aligned}\mathcal{L}1_{ij} &= \ln(s_{2ij} + l_{2ij}) - \ln(s_{1ij} + l_{1ij}) \\ \mathcal{L}2_{ij} &= \frac{1}{h_i h_{ij}} \cdot \left[ \arctan\left(\frac{h_i s_{2ij}}{h_{ij} l_{2ij}}\right) - \arctan\left(\frac{h_i s_{1ij}}{h_{ij} l_{1ij}}\right) \right]\end{aligned}\quad (5.40)$$

where  $l_{1ij} = |\mathbf{r}'_{1ij}|$  and  $l_{2ij} = |\mathbf{r}'_{2ij}|$ . Finally, by introducing 5.40 into 5.38, and 5.38 in 5.24, we have the analytical formulas for the gravitational potential, acceleration and tensor, found by *Petrovic* (1996), for a homogeneous polyhedron:

$$\begin{aligned}
 \Phi_{\text{grav}} &= +\frac{G\rho_{\mathcal{B}}}{2} \cdot \sum_{i=1}^n h_i \cdot \sum_{j=1}^m \{h_{ij} \cdot \mathcal{L}1_{ij} + h_i^2 h_{ij} \cdot \mathcal{L}2_{ij}\} \\
 \mathbf{g}_{\text{grav}} &= +G\rho_{\mathcal{B}} \cdot \begin{pmatrix} \sum_{i=1}^n \mathbf{e}_x \cdot \mathbf{n}_i \cdot \sum_{j=1}^m \{h_{ij} \cdot \mathcal{L}1_{ij} + h_i^2 h_{ij} \cdot \mathcal{L}2_{ij}\} \\ \sum_{i=1}^n \mathbf{e}_y \cdot \mathbf{n}_i \cdot \sum_{j=1}^m \{h_{ij} \cdot \mathcal{L}1_{ij} + h_i^2 h_{ij} \cdot \mathcal{L}2_{ij}\} \\ \sum_{i=1}^n \mathbf{e}_z \cdot \mathbf{n}_i \cdot \sum_{j=1}^m \{h_{ij} \cdot \mathcal{L}1_{ij} + h_i^2 h_{ij} \cdot \mathcal{L}2_{ij}\} \end{pmatrix} \\
 \mathbf{\Gamma}_{\text{grav}} &= +G\rho_{\mathcal{B}} \cdot \begin{pmatrix} \sum_{i=1}^n \mathbf{e}_x \cdot \mathbf{n}_i \cdot \sum_{j=1}^m \{\eta_{ij} \cdot \mathbf{e}_x \cdot \mathcal{L}1_{ij} + h_i h_{ij} \cdot \mathbf{n}_i \cdot \mathbf{e}_x \cdot \mathcal{L}2_{ij}\} & \dots \\ \vdots & \ddots \end{pmatrix}
 \end{aligned} \tag{5.41}$$

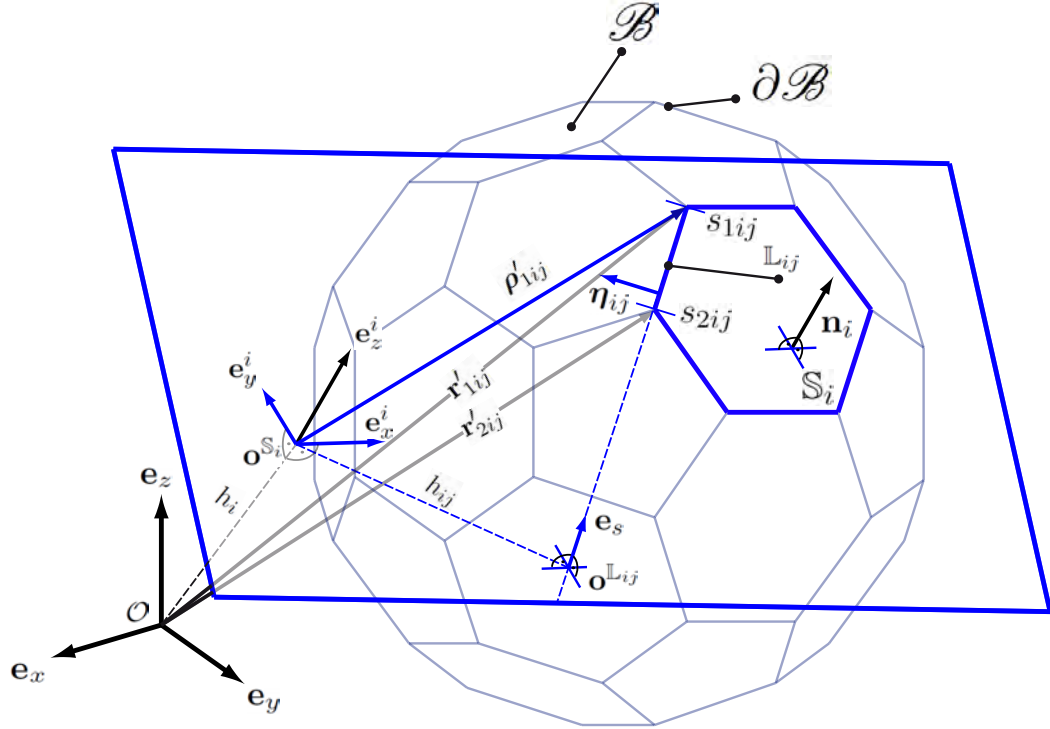


**Figure 5.1:** Vectorial and geometrical quantities in the derivation of the gravitational potential, acceleration vector and tensor for a homogeneous polyhedron. The vectors and lines drawn in blue belong to the plane defined by the polygon  $S_i$ .

### Treatment of Singularities

In the previous developments, the problem of singularities has been neglected. However, there are some configurations where the divergence theorem cannot be directly applied. This happens when the derivatives of the vector fields  $\mathbf{u}$  and  $\boldsymbol{\mu}$  are not continuous inside the corresponding regions of integration. Thanks to the publication of *Tsoulis and Petrovic* (2001), the singularities occurring in the formulation of *Petrovic* (1996) have been identified and treated in a proper way in order to provide a general formulation which is appropriate for a software implementation, as it is well summarized in *Tsoulis* (2012) .

## 5.2 Development of QGravity

QGravity is a software developed in the frame of this thesis in order to compute gravitational fields from density models. The decision to start an own development arose, when looking at an existing software, who gives the possibility to compute the gravitational potential, up to its second spatial derivatives of homogeneous polyhedral bodies, was not satisfying.

In the geophysical community there are several very efficient and powerful software packages which permit to generate complex density models. But unfortunately, because the traditional gravity observable is provided by gravimeters, they only provide the possibility to compute the vertical component  $g_z$  of the acceleration vector. In addition, they usually only provide interactive functionality, in contrast to batch processing, to generate density models and to compute gravity fields.

Finally, there are many advantages of having the full control of the source code. In our special case, we can mention that it permits to integrate optimal algorithms for the generation of density models and the computation of gravity field components. And it allows the integration of all pre-processing (such as coordinate transformations) in the main code in order to avoid non-optimal external pre-processing routines (costly in term of computer resources, e.g., pre-processing of millions of DTM<sup>4</sup> points).

### 5.2.1 Software Overview

QGravity is a software with a GUI<sup>5</sup> coded in C++. The GUI is based on the libraries of Qt (*Qt Company*, 2014). The software is divided in four main parts which interact with each other (see Figure 5.2):

1. Mass models
2. Geometric computations
3. Gravity fields
4. 3D visualization

---

<sup>4</sup>Digital terrain model.

<sup>5</sup>Graphical user interface

In addition, a coordinate transformation pipeline can be defined and applied to the data which are imported — or exported — from the different modules. This is mainly necessary to apply some coordinate transformations to the raw data because they are usually not given in 3D Cartesian coordinates, which are needed for the exact gravitational computations. Finally, all functionality provided by the GUI can be used for batch processing using an appropriate script protocol.

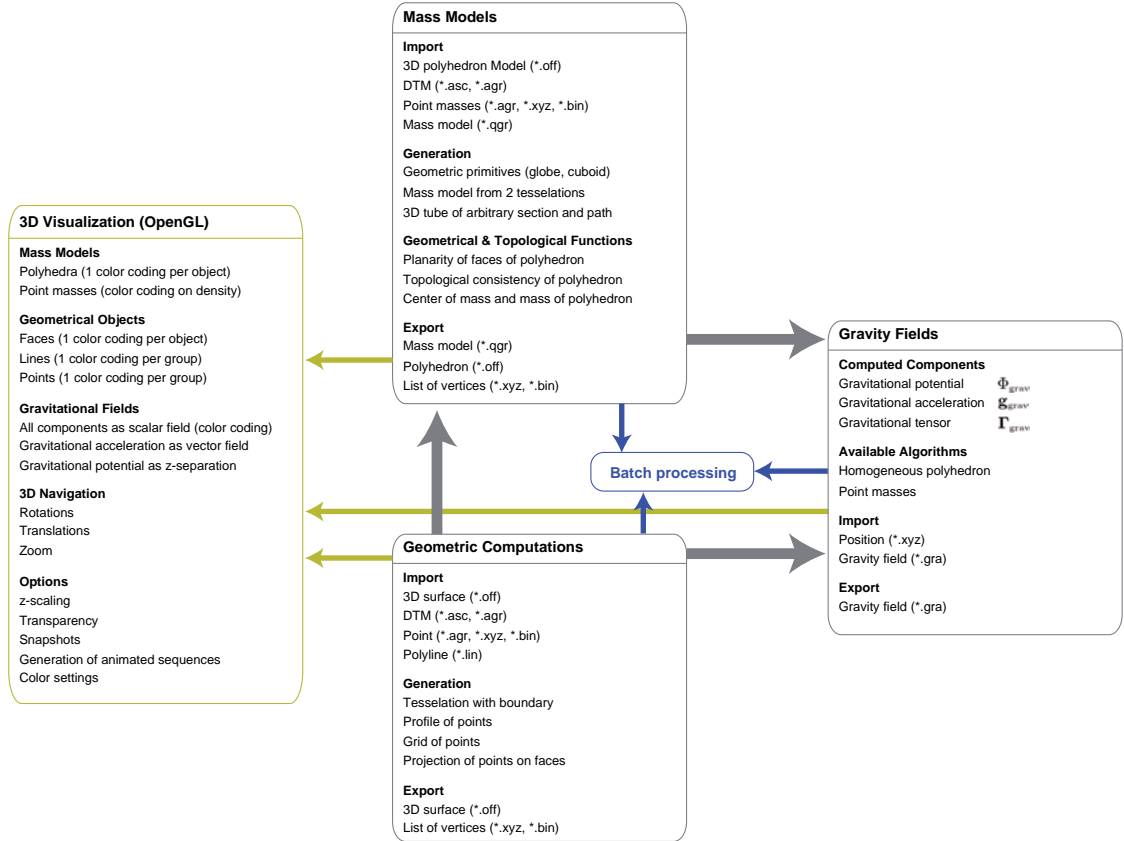


**Figure 5.2:** Overview of the main structures and functionality implemented in the software QGravity.

### 5.2.2 Coordinate Transformation Pipeline

The coordinate transformation pipeline allows to transform rigorously the coordinates of points given in a specific system to an other system. The pipeline consists in the application of four optional successive transformations:

1. projective coordinates<sup>6</sup> to ellipsoidal coordinates<sup>7</sup>:

$$\{\text{East, North, } h_{\text{ell}}\} \longrightarrow \{\lambda, \phi, h_{\text{ell}}\} \quad (5.42)$$

<sup>6</sup>Swiss grid 03, Swiss grid 95 or French Lambert 93.

<sup>7</sup>Defined by the projection.

2. ellipsoidal coordinates to geocentric Cartesian coordinates:

$$\{\lambda, \phi, h_{\text{ell}}\} \longrightarrow \{X, Y, Z\} \quad (5.43)$$

3. 3D similarity transformation of geocentric Cartesian coordinates:

$$\{X, Y, Z\} \longrightarrow \{X_2, Y_2, Z_2\} \quad (5.44)$$

4. geocentric Cartesian coordinates to topocentric coordinates:

$$\{X_2, Y_2, Z_2\} \longrightarrow \{y, x, z\} \quad (5.45)$$

The transformations are applied in this order when points or objects are imported, and in the opposite order when points or objects are exported. In addition, each transformation can be applied optionally in order to import and export data from various coordinate systems with this transformation pipeline. The parameters of the pipelines are stored in specific text files and they are applied, once they have been selected in the main menu of **QGravity**. For example, the file which defines the transformation pipeline between the Swiss grid 03 and the CCS<sup>8</sup> (*Jones, 2000*) is defined as follows:

```
# Transformation pipeline parameters for QGravity #
#####
projection yes
LBh.to.XYZ yes
HELMERT_3D yes
XYZ.to.topo yes

-----

proj_name LV03

-----

a_datum_proj 6377397.155
e2_datum_proj 0.006674372230614

-----

transl_X_m 626.447
transl_Y_m 45.100
transl_Z_m 378.788
rotX_arcsec 0.000
rotY_arcsec 0.000
rotZ_arcsec 0.000
scale_ppm 1.000

-----

X0_datum_2 4395400.36378
Y0_datum_2 465785.056736
Z0_datum_2 4583458.22601
```

<sup>8</sup>CERN Coordinate System



```

a_datum_2 6378137.000
e2_datum_2 0.006694380023011
Xi0_datum_2 0.000
Eta0_datum_2 0.000
east_0_topoc 2000.00000
north_0_topoc 2097.79265
z_0_topoc 2433.66000
az_0_deg 34.000776
-----

```

### 5.2.3 Mass Models

The mass model part contains the functionalities for the import, the generation and the storage of the bodies, the gravity fields of which must be computed. Basically, there are two kind of bodies which can be treated, point masses and homogeneous polyhedra. In QGravity a `MassModel` object is a set of `PointMass` and `Polyhedron` objects.

A `PointMass` object is formed by a `Vertex` object in association with a `Mass`. A `Polyhedron` is basically formed by a set of `Face` objects which are formed by a set of `Vertex` objects. In addition, the attribute `Density` is associated to the geometry. Internally, a `Polyhedron` is represented by a vector containing all `Vertex` objects and a vector containing all `Face` objects which are related to the `Vertex` objects by indices. In addition, if the polyhedron is seen from the outside, the indices of `Vertex` objects of a given `Face` object must be given in a counterclockwise order. This implicitly gives the right direction of the normal of faces, crucial for all computations.

#### Import

QGravity allows the import of various data sources:

**3D polyhedron model (\*.off)** The Object File Format (OFF) is a standard common ASCII format used for the exchange of the geometry of arbitrary 3D polyhedra. It has the advantage of being very simply and easily editable. Moreover, the meshes have the same structure as the `Polyhedron` objects in QGravity and render the creation of `Polyhedron` objects in a straight forward way.

```

OFF
2452 2500
6.279052 0.000000 -99.802673
6.229540 0.786974 -99.802673
6.081784 1.561537 -99.802673
5.838115 2.311473 -99.802673
5.502375 3.024956 -99.802673
:
:

```

```

4 0 1 51 50
4 1 2 52 51
4 2 3 53 52
4 3 4 54 53
4 4 5 55 54
4 5 6 56 55
4 6 7 57 56
4 7 8 58 57
:

```

**Digital terrain model (\*.asc, \*.agr)** One of the most common formats used for Digital terrain models (DTM) is the ESRI ASCII raster format (\*.asc, \*.agr). It is a 2D+1 format which provides the heights of points on a regular grid. This regular grid represents the horizontal positions in a predefined projection system. From this kind of data, the creation a properly closed polyhedron in the Euclidean 3D Cartesian space needs to look carefully at different geometrical aspects. Firstly, because the data only provides the upper part of the geometry, it is necessary to define an appropriate floor and find a way to link both parts. In **QGravity** the floor is defined as a surface of equal heights discretized by a rectangular grid defined in the projection system of the DTM file. The number of discretization points must be given explicitly and depends on the horizontal extension of the DTM. Thus, because once the points are transformed into the 3D Cartesian system, the points defining the floor are no longer on a plane but also have to approximate the Earth curvature. Concerning the link between the upper part and the floor, four polygons are sufficient in order to close the polyhedron (see Figure 5.3).

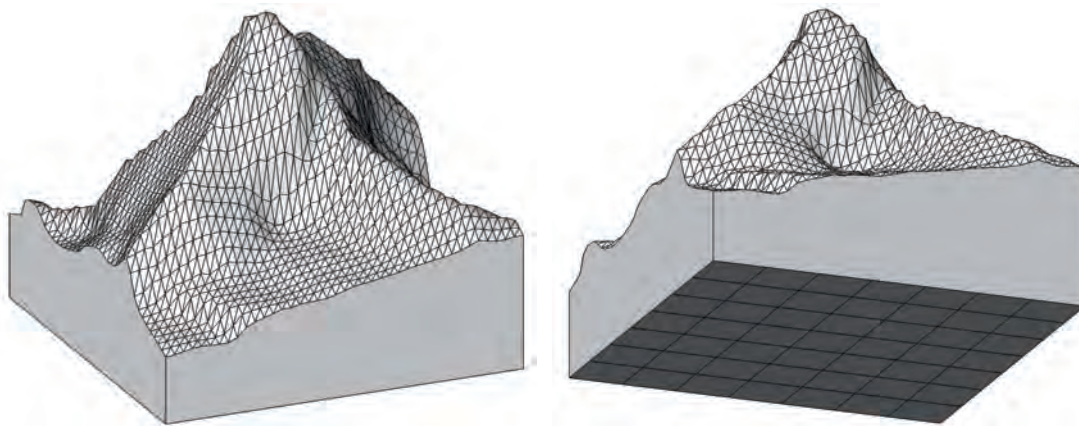


**Figure 5.3:** Polyhedron created with **QGravity** from a digital terrain model ESRI ASCII raster format. Source of raw data: Swiss Federal Office of Topography.

**QGravity** provides a further way to import a DTM by creating a set of **PointMass** objects instead of a single **Polyhedron**. In this case, each cell is discretized in the height component by **PointMass** objects (see Figure 5.4). The position and the mass of these objects are

computed from adjacent four-sided polyhedra. The main interest of importing a DTM with this method is that it permits to model complicated density variations in a straightforward way.

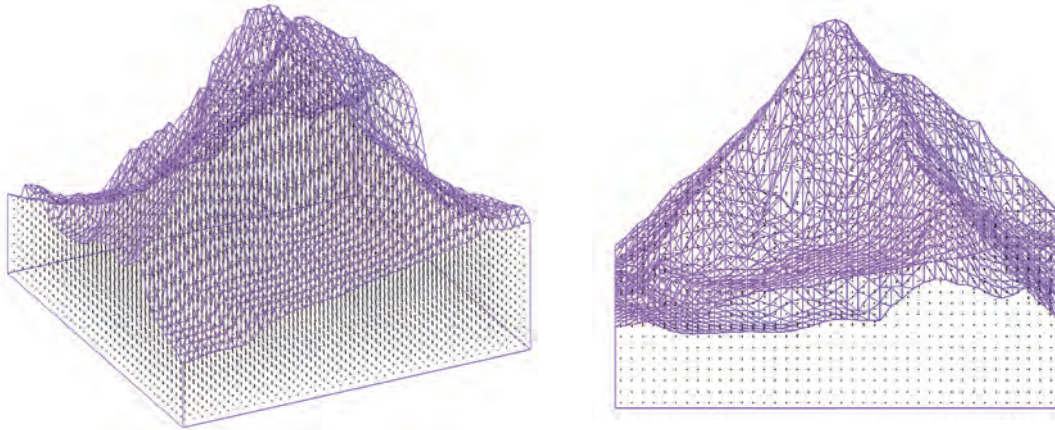


**Figure 5.4:** Polyhedron created with QGravity from a digital terrain model ESRI ASCII raster format. Source of raw data: Swiss Federal Office of Topography.

```

NCOLS 701
NROWS 481
XLLCORNER 550000.0
YLLCORNER 254000.0
CELLSIZE 25
NODATA_VALUE -9999
353.4 353.4 352.6 351.7 350.9 350.0 349.7 349.2 342.5 338.3 335.6 332.9 ...
355.6 355.4 354.5 353.7 352.8 351.9 351.2 348.6 341.9 338.0 335.4 333.2 ...
357.9 357.3 356.5 355.6 354.2 352.4 350.6 346.0 340.5 337.9 335.5 333.0 ...
360.1 359.0 357.2 355.4 353.6 351.8 349.9 344.1 339.5 337.5 335.2 333.2 ...
361.3 359.1 357.2 355.4 353.5 351.6 349.4 344.8 340.5 338.0 335.5 333.0 ...
362.6 359.1 357.3 355.4 353.5 351.8 350.6 347.9 343.4 339.4 336.9 334.4 ...
:
:

```

**Point masses (\*.xyz)** PointMass objects can be imported from an ASCII file (\*.xyz) which contains 5 columns:

1. Text identification
2.  $x$ -coordinate in meter
3.  $y$ -coordinate in meter
4.  $z$ -coordinate in meter
5. the mass in kilogram

```

0 616025.000 92675.000 2725.000 333750000.000
1 616025.000 92675.000 2775.000 333750000.000
2 616025.000 92675.000 2825.000 333750000.000
3 616025.000 92675.000 2875.000 333750000.000
4 616025.000 92675.000 2925.000 333750000.000
5 616025.000 92675.000 2975.000 333750000.000
6 616025.000 92675.000 3025.000 333750000.000
7 616025.000 92675.000 3075.000 333750000.000
8 616025.000 92675.000 3125.000 333750000.000
:

```

## Generation

The generation of bodies using various and specific methods is an essential part of this thesis. It permits to simulate the gravitational field of uncommon objects with a high level of automation and flexibility. Three features have been implemented in order to generate **Polyhedron** objects:

**Geometric primitives** Two kinds of geometric primitives can generate **Polyhedron** objects: globes and four-sided cuboids. The main utility of creating this kind of simple **Polyhedron** objects is related to the validation process of the complex algorithms implemented in **QGravity**. In fact, because the homogeneous sphere has a well-known gravitational field in the whole space, the fields computed from a **Polyhedron** object which approximate a sphere must converge to the exact solution when the discretization is refined, as it is shown in Section 5.2.8.

**Polyhedron from 2 tessellations** The generation of **Polyhedron** objects using two tessellations is a kind of surface reconstruction algorithm<sup>9</sup> developed in the frame of this thesis, which does not need the knowledge of the surface normal at each vertex. This method is very powerful for the generation of 3D bodies when we dispose of three specific sets of **Vertex** objects. The first set,  $\{\text{Vertex}\}_{\text{upper}}$ , represents a 2D+1 point cloud which approximates the upper boundary of a given body. The second set,  $\{\text{Vertex}\}_{\text{lower}}$ , represents a 2D+1 point cloud which approximate the lower boundary of the same body. The upper and lower parts of this body are discriminated by a common boundary curve, represented by the third set  $\{\text{Vertex}\}_{\text{boundary}}$ . In Figure 5.5 an example of the surface reconstruction of the Lake of Geneva is shown.

Once the sets  $\{\text{Vertex}\}_{\text{upper}}$ ,  $\{\text{Vertex}\}_{\text{lower}}$  and  $\{\text{Vertex}\}_{\text{boundary}}$  are provided, two separate constrained Delaunay tessellations are processed. In **QGravity**, the very powerful routines of *Shewchuk* (1996) and *Shewchuk* (2002) have been implemented to do this

<sup>9</sup>In the computational geometry community, the most famous 3D surface reconstruction algorithm is the *Poisson surface reconstruction algorithm*, discovered by *Kazhdan et al.* (2006). It consists in generating a mesh from 3D oriented vertices (the surface normals is known at each vertex).

difficult task. The first tessellation,  $\mathbb{T}_{\text{upper}}$ , is computed with the following input:

$$\mathbb{T}_{\text{upper}} \equiv \begin{cases} \{\text{Vertex}\}_{\text{upper}} \cup \{\text{Vertex}\}_{\text{boundary}}, & \text{as vertices.} \\ \{\text{Vertex}\}_{\text{boundary}}, & \text{as boundary.} \end{cases} \quad (5.46)$$

and the second tessellation,  $\mathbb{T}_{\text{lower}}$ , is computed with the following input:

$$\mathbb{T}_{\text{lower}} \equiv \begin{cases} \{\text{Vertex}\}_{\text{lower}} \cup \{\text{Vertex}\}_{\text{boundary}}, & \text{as vertices.} \\ \{\text{Vertex}\}_{\text{boundary}}, & \text{as boundary.} \end{cases} \quad (5.47)$$

Finally, the **Polyhedron** object can be generated from the union of the two tessellations using the common boundary (see Figure 5.6):

$$\text{Polyhedron} \equiv \mathbb{T}_{\text{upper}} \cup \mathbb{T}_{\text{lower}} \quad (5.48)$$

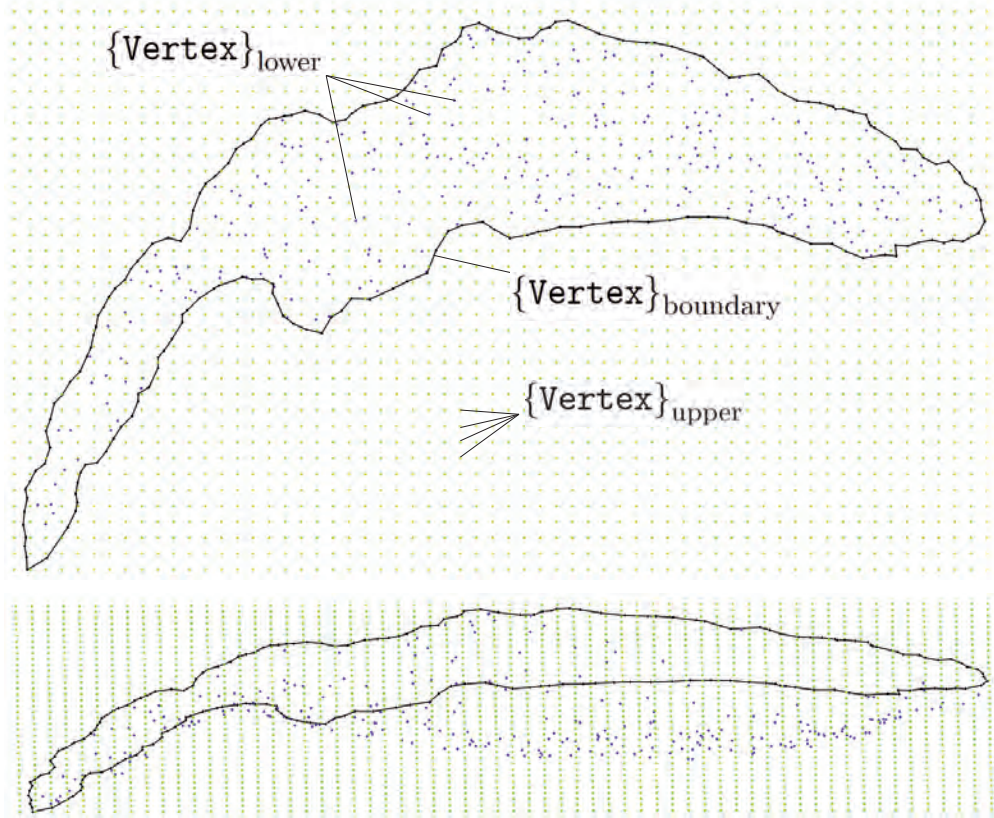


**Figure 5.5:** Plane view (upper) and perspective view (lower) of the three sets used for the generation of a **Polyhedron** object.  $\{\text{Vertex}\}_{\text{upper}}$  in blue,  $\{\text{Vertex}\}_{\text{lower}}$  in green and  $\{\text{Vertex}\}_{\text{boundary}}$  in black. The z-component is scaled by a factor of 20 with respect to the x,y-components.



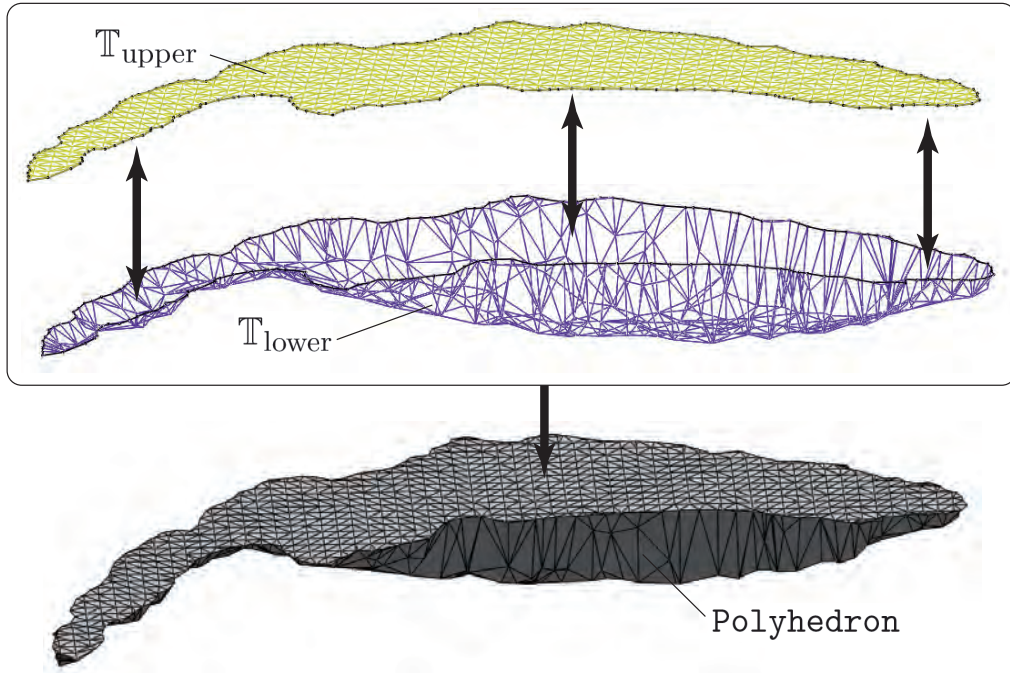


**Figure 5.6:** (Upper) perspective view of the two tessellation  $T_{upper}$  and  $T_{lower}$ . (Lower) final Polyhedron object. The z-component is scaled by a factor of 20 with respect to the x,y-components.

**3D tube of arbitrary section and path** This functionality is based on a three-dimensional path  $\mathbf{r}(s)$  and cross section  $\rho(s)$  in order to generate a Polyhedron object. The former is given by the set  $\mathbf{r}(s) \equiv \{\text{Vertex}\}_{\text{path}}$  and the former by the set  $\rho(s) \equiv \{\text{Vertex}\}_{\text{section}}$ . As illustrated in Figures 5.7 and 5.8, the idea consists in constructing a closed tube of constant cross section  $\rho(s)$  which follows the trajectory defined by the path  $\mathbf{r}(s)$ .

The tube is build by sequential extrude operations of  $\rho(s)$  along  $\mathbf{r}(s)$ . In order to do this operation, it is necessary to transform the  $\rho(s)$  into a particular the local moving frame  $\{\mathbf{e}_1(s), \mathbf{e}_2(s), \mathbf{e}_3(s)\}$  attached to  $\mathbf{r}(s)$ . There are several possibilities in order to compute a local moving frame. For physical applications the most natural one is the *Frenet* frame which has the particularities to be orthogonal, has  $\mathbf{e}_1(s)$  tangent to  $\mathbf{r}(s)$  and  $\mathbf{e}_2(s)$  pointing to the center of the local osculating circle of  $\mathbf{r}(s)$ . In addition, the *Frenet* frame is subjected to a non-zero torsion which would generate unwanted twists which negatively affect both the orientation and the topology of the tube. From this point of view, instead of the *Frenet* frame, a *parallel transport* moving frame is used. It is orthogonal and has its first basis vector  $\mathbf{e}_1(s)$  also tangential to  $\mathbf{r}(s)$ . Moreover,  $\mathbf{e}_2(s)$  and  $\mathbf{e}_3(s)$  are defined in such a way that the torsion is equal to zero everywhere (*Hanson and Ma, 1995*). In addition, it is necessary to define a vector  $\mathbf{n}$ , which defines a constant direction in space to which  $\mathbf{e}_2(s)$  is always perpendicular. Formally, this particular *parallel transport* moving

frame is defined by:

$$\begin{aligned} \mathbf{e}_1(s) &= \frac{d\mathbf{r}(s)}{ds} \\ \mathbf{e}_2(s) &= \frac{\mathbf{n} \times \mathbf{e}_1(s)}{|\mathbf{n} \times \mathbf{e}_1(s)|} \\ \mathbf{e}_3(s) &= \mathbf{e}_1(s) \times \mathbf{e}_2(s) \end{aligned} \quad (5.49)$$

where, in QGravity,  $\mathbf{n} = \mathbf{e}_z$ .

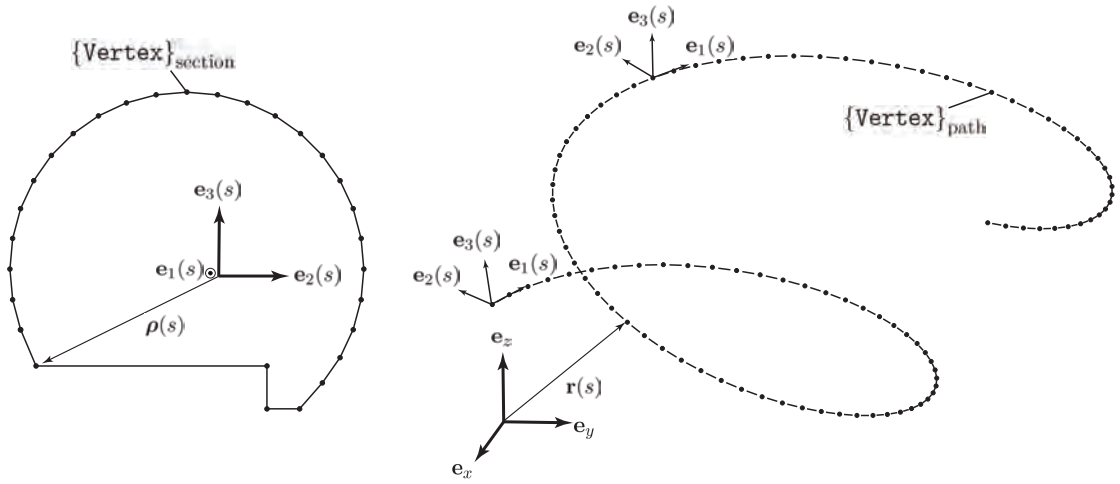


**Figure 5.7:** Input data used for the generation of 3D tubes of arbitrary section and path. (Right) the section  $\rho(s)$  approximated by  $\{\text{Vertex}\}_{\text{section}}$ . (Right) the path  $\mathbf{r}(s)$  approximated by  $\{\text{Vertex}\}_{\text{path}}$ .



**Figure 5.8:** 3D tube generated by the section and the path given in Figure 5.7.

## Geometrical & Topological Functions

In the perspective of the computation of the gravity field according to the formulas given in Section 5.1.3, the class of objects which can be considered is restricted to closed oriented manifolds. In our discretized case, it means that a **Polyhedron** object must be a closed oriented manifold-mesh, or, according to *Hoffmann* (1989), a **Polyhedron** represented by its boundary is also called: *a manifold B-rep solid*.

Now the question is how to be sure that a given **Polyhedron** object, generated or imported by the various ways described above, is a valid closed oriented manifold-mesh? The answer requires both, geometrical and topological validation procedures which are largely treated in the geometrical computing community. The validation procedures and algorithms which are proposed are more or less restrictive and depend on the definition of what is a solid — or a polyhedron (*Ledoux*, 2013). A rigorous validation procedure is given by *Hoffmann* (1989) in three steps based on geometrical and topological tests which are beyond the scope of this thesis. A more practical description of a possible validation procedure can be found in *Ledoux* (2013). This procedure is based on the international standard ISO 19107<sup>10</sup> which is based on hierarchical validation procedures. Objects with the lowest dimension as vertices and edges are validated before the faces and the shell. In a similar way, when only a *closed composite surface* is considered, *Gröger and Plümer* (2011) propose a hierarchical validation procedure based on 13 axioms.

**Topological consistency of polyhedron** Concerning **QGravity**, an exhaustive and rigorous geometrical and topological validation has not been implemented. This is mainly due to the complexity and the time which would have been consumed by this task. In addition, in the case of a suspicious object, it is always possible to make an export and to perform proceed the validation in an external software. Nevertheless, an important topological consistency test, which covers a large amount of possible topological error sources, is implemented. It checks if any two adjacent faces have compatible orientation. This is done by checking that for each edge  $\text{Edge}_i(\text{Vertex}_1, \text{Vertex}_2)$ , given by a start vertex  $\text{Vertex}_1$  and on end vertex  $\text{Vertex}_2$ , there exists one edge  $\text{Edge}_j(\text{Vertex}_2, \text{Vertex}_1)$  which contains the same vertices but in the opposite order.

**Planarity of faces of polyhedron** A **Polyhedron** object is supposed to have planar faces. For a particular face, if the number of vertices is larger than 3, the orthogonal distance between the middle plane of the polygon and all vertices are checked so that the maximal value does not exceed a certain threshold. In the frame of this thesis, the limit is fixed at 0.01 meters.

**Center of mass and mass of polyhedron** The center of mass coordinates and the mass of a **Polyhedron** object can be computed according to *Mirtich* (1996) who provides also a c-code which was migrated to C++ and adapted to the data structure of **QGravity**.

<sup>10</sup>Geographic information – Spatial schema



### Export

The `MassModel` objects can be exported — or stored — in different file formats for further utilization.

**File format \*.qgr** This is a binary format created specifically in this thesis for the storage of a `MassModel` object which can contain an arbitrary number of `Polyhedron` and `PointMass` objects.

**File format \*.off** See Section 5.2.3.

**File format \*.xyz** See Section 5.2.3.

### 5.2.4 Geometric Computations

The geometric computation part contains the functionalities for the import, the generation and the export of geometric objects. The main purpose of this part is to generate specific `Vertex` objects for which the gravitational field must be computed. They are generated using various geometrical operations which are sometimes related to other geometric objects. In `QGravity` three kind of geometric objects are available: `Vertex`, `Vector`, `Polyline` and `Face`.

### Import

The following files can be imported in order to generate geometric objects:

**Surfaces (\*.off)** Compared to the import explained in Section 5.2.3, the Object File Format (OFF) is not only reserved for the storage of polyhedra but also for arbitrary non-closed surfaces. In `QGravity` a list of `Face` objects is generated when importing an \*.off file.

**Digital terrain model (\*.asc,\*.agr)** Here the ESRI ASCII raster format can be imported as a list of `Face` or `Vertex` objects.

**Point (\*.xyz)** A simple list of points can be imported as a list of `Vertex` objects.

**Vector (\*.vec)** A list of vectors can be imported as a list of `Vector` objects. The ASCII file format \*.vec contains 7 columns defined as follows:

1. Text identification
2.  $x$ -coordinate of the position in meter
3.  $y$ -coordinate of the position in meter
4.  $z$ -coordinate of the position in meter
5.  $v_x$ -component of the vector in meter

6.  $v_y$ -component of the vector in meter

7.  $v_z$ -component of the vector in meter

```
0 0.252878000 -0.055721333 0.007564000 0.944801978 -0.314949797 0.090309729
1 0.248432333 -0.045806000 0.016476000 0.666637215 -0.246646983 0.703391846
2 0.243834333 -0.043640667 0.020519333 0.228209929 -0.124779121 0.965582932
3 0.250284667 -0.051260333 0.014404667 0.691658967 0.198972366 0.694275069
4 0.246126000 -0.056589000 0.014456667 0.060768494 -0.535409527 0.842403602
5 0.245525000 -0.064299667 0.003354667 0.454855373 -0.882888997 0.116677369
6 0.246641000 -0.058992333 0.000937667 -0.250161009 0.089299555 -0.964077310
:
```

**Polyline (\*.lin)** A polyline can be imported as a **Polyline** object. The ASCII file format \*.lin is identical to the format \*.xyz. The points are simply interpreted as forming a path instead of individual positions.

## Generation

In this section, five methods implemented in **QGravity** for generating geometrical objects are exposed:

**Profile of points** This functionality permits to generate a list of **Vertex** objects, separated by a constant distance, along an arbitrary 3D straight line defined by its start and end positions.

**Grid of points** This functionality permits to generate a list of **Vertex** objects which represents a sequence of regular grids. Any spacing, position and orientation of the grids can be specified.

**Tessellation with boundary** A list of **Face** objects can be generated by a constrained 2D *Delaunay* tessellation. The input data are a point cloud and a boundary given by two different lists of **Vertex** objects. The tessellation is processed using the  $(x, y)$ -components. As for the generation of **Polyhedron**, the computation is done with the routines of *Shewchuk* (1996) and *Shewchuk* (2002).

**Projection of points on faces** This functionality generates **Vertex** objects. They are projections of predefined **Vertex** objects on a surface defined by a list of **Face** objects, along  $\mathbf{e}_z$ . If it is necessary to project a point along the height component  $\mathbf{e}_H$  instead of  $\mathbf{e}_z$ , a transformation pipeline can be applied before the projection in order to have  $\mathbf{e}_z$  corresponding to  $\mathbf{e}_H$ .

**Normal vectors of faces** This functionality generates **Vector** objects from a surface given by a list of **Face** objects. For each **Face** object a **Vector** object is generated. The position is the mean position of the **Face** object. The vector itself is the normalized normal vector of the **Face** object.

### Export

Every geometric object can be exported in the corresponding ASCII file format:

**File format \*.off** See Section 5.2.4.

**File format \*.xyz** See Section 5.2.4.

**File format \*.vec** See Section 5.2.4.

**File format \*.lin** See Section 5.2.4.

### 5.2.5 Gravity Fields

The gravity fields part contains the functionalities for the import, the computation and the export of the gravity fields. In **QGravity** a gravity field is modeled by a **GravityField** object which contains a list of **Gravity** objects. The object **Gravity** contains the components of the position vector **r** and the values of the different components of the gravitational field as described in Table 5.2.

**Table 5.2:** Components stored in an object **Gravity**.

index	component	symbol	unit
1	identification	ID	string
2	position	$x$	[m]
3	position	$y$	[m]
4	position	$z$	[m]
5	gravitational potential	$\Phi_{\text{grav}}$	$\left[\frac{\text{m}^2}{\text{s}^2}\right]$
6	gravitational acceleration	$g_{x,\text{grav}}$	$[\text{mgal}] = \left[\frac{\text{m}}{\text{s}^2}\right] \cdot 10^{-5}$
7	gravitational acceleration	$g_{y,\text{grav}}$	[mgal]
8	gravitational acceleration	$g_{z,\text{grav}}$	[mgal]
9	gravitational tensor	$\Gamma_{xx,\text{grav}}$	$[\text{E}] = \left[\frac{1}{\text{s}^2}\right] \cdot 10^{-9}$
10	gravitational tensor	$\Gamma_{yy,\text{grav}}$	[E]
11	gravitational tensor	$\Gamma_{zz,\text{grav}}$	[E]
12	gravitational tensor	$\Gamma_{xy,\text{grav}}$	[E]
13	gravitational tensor	$\Gamma_{xz,\text{grav}}$	[E]
14	gravitational tensor	$\Gamma_{yz,\text{grav}}$	[E]

### Available Algorithms

The gravitational field components given in Table 5.2 are computed by the formulas given in Section 5.1.1 for the **PointMass** objects. And for the **Polyhedron** objects the formulas of *Petrovic* (1996) and *Tsoulis and Petrovic* (2001), exposed in Section 5.1.3, are implemented.

### Import and Export

Once **MassModel** objects have been defined, it is necessary to define at which positions the gravitational field has to be computed. These positions can be imported from an \*.xyz file. After the computation, the gravitational field can be exported to the ASCII file format \*.gra. Each line corresponds to one position and each column contains the components given in Table 5.2.

### 5.2.6 Batch Processing

In order to increase the automation of systematic computations and to allow for parallel computations, the principal functionalities of **QGravity** for the generation of mass models and for the computation of gravity fields can be executed in a batch processing mode. Basically a batch process can be started from a shell as follows:

```
>> QGravity.exe FUNCTION input_batch_file.txt
```

where **FUNCTION** is a keyword which defines the function to be executed. According to the particular **FUNCTION**, a simple ASCII file **input\_batch\_file.txt** containing all batch processing commands must be given. A summary of all available **FUNCTION** is given in Table G.1.

For example, using the function **MASS2GRAVITY**, for some points given in the file **points.xyz**, we want to compute the gravitational field of two bodies  $\mathcal{B}_1$  and  $\mathcal{B}_2$ , generated by:

- A body  $\mathcal{B}_1$  of density  $\rho_{\mathcal{B}_1} = 2670 \left[ \frac{\text{kg}}{\text{m}^3} \right]$  given by the file **body1.off**.
- A body  $\mathcal{B}_2$  of density  $\rho_{\mathcal{B}_2} = 1000 \left[ \frac{\text{kg}}{\text{m}^3} \right]$  which has to be generated by two tessellations. The points of the upper and lower surfaces are given by the files **upper.xyz** and **lower.xyz**. The points of the common boundary are given by the file **boundary.xyz**.

In addition, the results should be output into the file **field.gra**. Assuming that all files are placed in a folder with the path **c:\QGravity\data**, the input file **input\_batch\_file.txt** is defined as follows:

```
INPUT_PATH
c:\QGravity\data
INPUT_LIST_PTS_TO_COMPUTE
\points.xyz
```

```
INPUT_OFF
\body1.off 2670.0
INPUT_MASS_FROM_2_TESSELATIONS
\lower.xyz \upper.xyz \boundary.xyz 1000.0
OUTPUT
\field.gra
END
```

### 5.2.7 3D Visualization

The development of the 3D visualization tool was initiated in order to increase the interactivity and, most importantly, in order to undertake comfortable visual checks of the various objects imported, generated and computed in **QGravity**. In addition, since the objects which have to be rendered are usually formed of several thousand primitives, the standard 3D visualization tools provided by standard software as **Matlab** are not powerful enough. For these reasons, the tool is based on the open source library OpenGL<sup>11</sup> which permits high-performance hardware-accelerated rendering.

All objects described in the previous section can be visualized (see Figure 5.9). Depending on their geometrical properties, they can be rendered as solids, meshes, vectors or points. The navigation in the 3D scene can be done easily by standard tools as rotations, translations and zooming.

---

<sup>11</sup>Open Graphics Library.

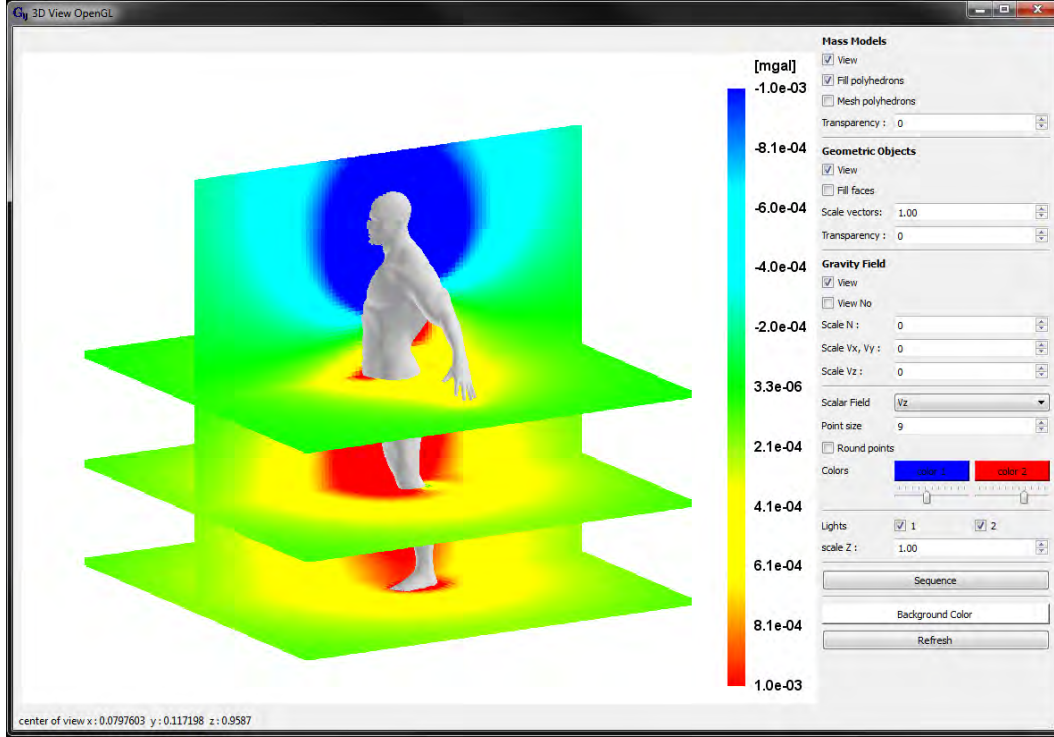


**Figure 5.9:** Print screen of the 3D visualization tool of QGravity which shows the  $g_{z,\text{grav}}$  component of the gravitational field generated by a human body. The body is actually a homogeneous polyhedron of density  $\rho = 1000 \left[ \frac{\text{kg}}{\text{m}^3} \right]$ .

### 5.2.8 Validation of the Polyhedron Algorithm

It is obvious that the validation of the algorithms implemented in QGravity for the computation of gravity fields generated by a polyhedron, described in Section 5.1.3, is a crucial task. The validation can be done in several ways that are more or less reliable and more or less time-consuming. In the literature we can find some authors comparing their results with known analytic fields (Arnet, 1992; Tsoulis, 2012) or with fields which have already been computed and published by other authors (D’Urso, 2013). Moreover, some validation procedures also tried to look at the results at some points which are critical in terms of singularities (D’Urso, 2013; Tsoulis, 2012).

In this thesis, the validation is realized by comparing the analytic solution of the gravitational field generated by a sphere  $\mathcal{S}$  (Section 5.1.2) and the results of three different polyhedra  $\mathcal{S}_{25}$ ,  $\mathcal{S}_{50}$  and  $\mathcal{S}_{100}$ , which approximate  $\mathcal{S}$  with an increasing level of resolution. They approximate  $\mathcal{S}$  with  $25 \times 25$ ,  $50 \times 50$  and  $100 \times 100$  meridians and parallels, respectively. In order to validate the results inside and outside the body, the fields are computed for points belonging to three different planes  $\mathbb{P}_{-50}$ ,  $\mathbb{P}_0$  and  $\mathbb{P}_{+50}$ , of  $1000 \times 1000$  meters extend (see Figure 5.10). The sphere has a radius of 100 meters and a density  $\rho = 2670 \frac{\text{kg}}{\text{m}^3}$ . The comparisons are computed for each point and for each component of the gravitational field. The relative errors  $\epsilon$  are visualized in Figures H.1 to H.10 and a summary is provided in Table 5.3. As expected, the results converge to the true values

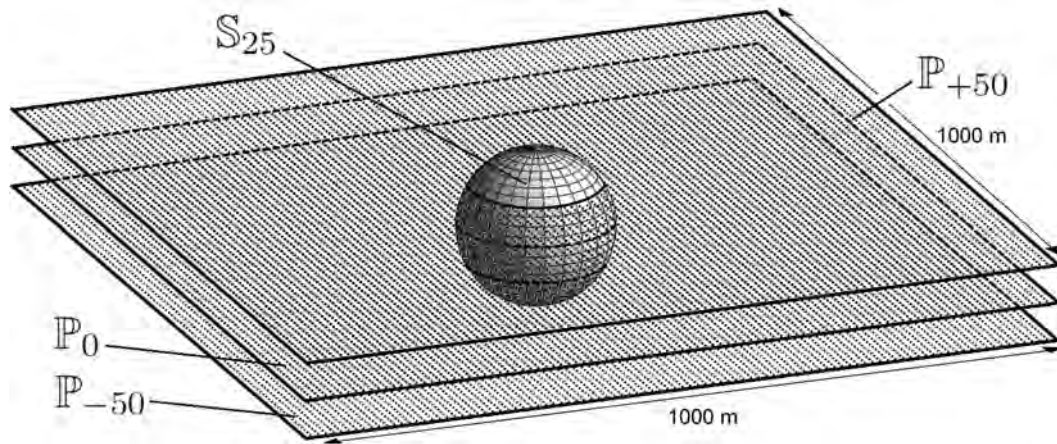


**Figure 5.10:** Representation of the objects used for the validation of the algorithms implemented in QGravity for the computation of gravitational fields of homogeneous polyhedra.

with the square of the resolution.

**Table 5.3:** Summary of the comparison between the gravity field generated by an analytic sphere  $\mathcal{S}$  and three different approximations  $\mathbb{S}_{25}$ ,  $\mathbb{S}_{50}$  and  $\mathbb{S}_{100}$ . The fields are computed for three different planes  $\mathbb{P}_{-50}$ ,  $\mathbb{P}_0$  and  $\mathbb{P}_{+50}$  (see Figure 5.10). The relative errors  $\epsilon$  are given in percent. The fields having no value are due to signals equal to zero which implies undefined relative errors.

component	plane	$\mathbb{S}_{25}$			$\mathbb{S}_{50}$			$\mathbb{S}_{100}$		
		$\epsilon$ [%]	min $\epsilon$ [%]	max $\epsilon$ [%]	$\epsilon$ [%]	min $\epsilon$ [%]	max $\epsilon$ [%]	$\epsilon$ [%]	min $\epsilon$ [%]	max $\epsilon$ [%]
$\Phi_{\text{grav}}$	$\mathbb{P}_{-50}$	1.443	1.014	1.475	0.362	0.254	0.370	0.091	0.064	0.093
	$\mathbb{P}_0$	1.444	0.965	1.555	0.362	0.242	0.388	0.091	0.060	0.097
	$\mathbb{P}_{+50}$	1.443	1.014	1.475	0.362	0.254	0.370	0.091	0.064	0.093
$g_{x,\text{grav}}$	$\mathbb{P}_{-50}$	1.433	0.061	2.171	0.360	0.022	0.667	0.090	0.002	0.167
	$\mathbb{P}_0$	1.436	0.013	2.436	0.360	0.029	0.511	0.090	0.002	0.132
	$\mathbb{P}_{+50}$	1.433	0.061	2.171	0.360	0.022	0.667	0.090	0.002	0.167
$g_{y,\text{grav}}$	$\mathbb{P}_{-50}$	1.435	0.005	6.733	0.360	0.028	0.379	0.090	0.002	0.167
	$\mathbb{P}_0$	1.437	0.001	4.478	0.360	0.019	0.549	0.090	0.002	0.132
	$\mathbb{P}_{+50}$	1.435	0.005	6.733	0.360	0.028	0.379	0.090	0.002	0.167
$g_{z,\text{grav}}$	$\mathbb{P}_{-50}$	1.504	0.347	2.332	0.378	0.012	0.526	0.095	0.026	0.128
	$\mathbb{P}_0$	—	—	—	—	—	—	—	—	—
	$\mathbb{P}_{+50}$	1.504	0.347	2.332	0.378	0.012	0.526	0.095	0.026	0.128
$\Gamma_{xx,\text{grav}}$	$\mathbb{P}_{-50}$	1.657	0.019	222.882	0.380	0.030	7.400	0.094	0.006	1.858
	$\mathbb{P}_0$	1.609	0.025	269.978	0.398	0.019	22.962	0.100	0.005	6.066
	$\mathbb{P}_{+50}$	1.657	0.019	222.882	0.380	0.030	7.400	0.094	0.006	1.858
$\Gamma_{yy,\text{grav}}$	$\mathbb{P}_{-50}$	1.597	0.014	220.023	0.378	0.007	7.400	0.094	0.006	1.858
	$\mathbb{P}_0$	1.626	0.025	267.824	0.388	0.019	20.891	0.100	0.005	6.066
	$\mathbb{P}_{+50}$	1.597	0.014	220.023	0.378	0.007	7.400	0.094	0.006	1.858
$\Gamma_{zz,\text{grav}}$	$\mathbb{P}_{-50}$	1.555	0.019	73.288	0.371	0.007	7.782	0.093	0.007	0.939
	$\mathbb{P}_0$	1.519	0.416	5.330	0.381	0.015	2.910	0.096	0.019	1.039
	$\mathbb{P}_{+50}$	1.555	0.019	73.288	0.371	0.007	7.782	0.093	0.007	0.939
$\Gamma_{xy,\text{grav}}$	$\mathbb{P}_{-50}$	—	0.099	—	—	0.018	—	—	0.068	—
	$\mathbb{P}_0$	—	0.019	—	—	0.070	—	—	0.091	—
	$\mathbb{P}_{+50}$	—	0.099	—	—	0.018	—	—	0.068	—
$\Gamma_{xz,\text{grav}}$	$\mathbb{P}_{-50}$	—	0.481	—	—	0.369	—	—	0.092	—
	$\mathbb{P}_0$	—	—	—	—	—	—	—	—	—
	$\mathbb{P}_{+50}$	—	0.481	—	—	0.369	—	—	0.092	—
$\Gamma_{yz,\text{grav}}$	$\mathbb{P}_{-50}$	—	0.156	—	—	0.178	—	—	0.092	—
	$\mathbb{P}_0$	—	—	—	—	—	—	—	—	—
	$\mathbb{P}_{+50}$	—	0.156	—	—	0.178	—	—	0.092	—



## Chapter 6

# Expected Gravity Field Signals and Observability at Short Wavelengths

### 6.1 Introduction

This chapter contains some studies about gravity field signals which can be expected on the Earth's surface or in the near underground — at approximately hundred meters underground — at very small wavelengths, from a couple of meters to some kilometers. These studies have multiple objectives which are all related to the perspective of realizing a straight line, using HLS systems, with a relative precision of ten micrometers over two hundred meters.

The first objective is to estimate the geometrical consequences, on equipotential profiles, of the different phenomena which affect the gravity field. Are they significant? Are they negligible? When do they become problematic? A first trivial example is to consider that a profile realized by a HLS can be assumed to be straight, without even taking into consideration a basic spherical model for the Earth. Regarding the alignment constraints, up to which wavelength can this model be assumed to be sufficient?

The second objective is to estimate the consequences of different phenomena on gravity field observables and their respective reductions. Primary because the observations are usually not carried out at the same positions as the equipotential profile which must be determined. In addition, since the observations are not carried out at the same time, time-varying phenomena can theoretically also introduce random, correlated and/or systematic errors.

But maybe the most important aspect is the introduction of the concept of **observability**. Here, the observability is always related to a certain methodology or strategy for the determination of underground equipotential profiles. It consists in testing the ability of this particular strategy, assuming error-free observations, to determine, with sufficient accuracy, the geometry of the equipotential profile generated by a certain mass anomaly. For example, the observability of the astrogravimetric levelling methodology is limited by the fact that the orthometric corrections, even computed from error-free gravimetric

observations, can only be theoretically determined in very special cases, see Section 4.4.2. Furthermore, depending on the mass anomaly and the strategy for determining the mean gravity along the plumbline, we saw that there are cases which are counterproductive. Thus, given a certain mass anomaly, it is possible to simulate on the one hand the true equipotential in the tunnel, and on the other hand, error-free observations of the deflection of the vertical on the topography and gravimetric observations on the topography and in the tunnel which can be used to compute the equipotential profile according to a given strategy. Finally, the latter equipotential profile can be compared to the true one in order to see if they match at a sufficient level of accuracy.

The main difficulty of this kind of analysis is related to the choice of the environments which are considered. If the analyses are concentrated on a very precise emplacement, the advantage is that it is possible to model several phenomena with very good, precise and realistic a priori information as topography, geology, water table levels, etc... But on the other hand, the results can always be suspected to be only reliable for the considered emplacement and not very general. They are usually hardly transferable to different environmental conditions. In a diametrically opposite point of view, if the objective is to produce very general and universal statements, it becomes very difficult to consider all possibilities as it is hard to generate precise and useful predictions. For these reasons, both of these complementary approaches are considered.

In the first section, a systematic and general analysis of expected signals generated by underground anomalies is tempted. Afterwards, the analysis will focus in the vicinity of Geneva along the projected emplacement of the futur CLIC facilities.

But first of all, it is necessary to recall some fundamental assumptions which are considered for the coming computations.

### 6.1.1 Shape of Fluid-Air Interface

We want to determine the time-dependent fluid-air interface of a HLS. We assume that this interface corresponds to the particular equipotential profile of the gravity field at the level of the HLS. This profile is a set of three-dimensional position vectors  $\boldsymbol{\rho}_{\sim}(t)$  denoted by  $\{\boldsymbol{\rho}_{\sim}(t)\}$ . According to Equation 3.184, each vector  $\boldsymbol{\rho}_{\sim}(t)$  can be expressed as the sum of two vectors:

$$\boldsymbol{\rho}_{\sim}(t) = \boldsymbol{\rho}_o + \mathbf{n}_{\Phi_{\text{tot}}}(t) \cdot N_{\text{tot}}(t) \quad (6.1)$$

where  $\boldsymbol{\rho}_o$  is the time-invariant position vector of the normal equipotential,  $\mathbf{n}_{\Phi_{\text{tot}}}(t)$  is the time-dependent normalized normal vector to the total equipotential surface at position  $\boldsymbol{\rho}_o$  and  $N_{\text{tot}}(t)$  is the time-dependent geometrical separation between normal and the real equipotential at position  $\boldsymbol{\rho}_o$ <sup>1</sup>.

According to the formulas given in Section 3.8.1, for a given starting position vector  $\boldsymbol{\rho}_o(\lambda, \phi, h_0)$  — or equivalently for a given normal potential  $U_{\sim}$  — it is possible to compute  $\boldsymbol{\rho}_o$  with an arbitrary good precision so that it can be considered as perfectly known.

<sup>1</sup>If  $\boldsymbol{\rho}_o \equiv$  position at mean sea level  $\implies N_{\text{tot}}(t) \equiv$  geoid undulation.

Concerning the computation of the normalized normal vector  $\mathbf{n}_{\Phi_{\text{tot}}}(t)$ , according to Equation 3.183, it is theoretically necessary to know the total gravity vector  $\mathbf{g}_{\text{tot}}$ . Practically, assuming that a first order linearization of the total potential  $\Phi_{\text{tot}}$  is sufficient and that the time variations of  $\mathbf{g}_{\text{tot}}$  are negligible<sup>2</sup>, we can replace  $\mathbf{n}_{\Phi_{\text{tot}}}(t)$  by the time-invariant normalized normal vector to the normal potential  $\mathbf{n}_U$  which is perfectly known — for the same reason as for  $\rho_o$ .

Lastly, according to Equation 3.209, the geometrical separation  $N_{\text{tot}}(t)$  can be approximated by:

$$N_{\text{tot}}(t) = \frac{\Phi_{\text{grav,st}}(\rho_o)}{|\mathbf{g}_{\text{tot}}(\rho_o)|} + \frac{\Phi_{\text{grav,dyn}}(\rho_o, t)}{|\mathbf{g}_{\text{tot}}(\rho_o)|} + \frac{\delta\Phi_{\text{centr}}(\rho_o, t)}{|\mathbf{g}_{\text{tot}}(\rho_o)|} + \frac{\Phi_{\text{tidal}}(\rho_o, t)}{|\mathbf{g}_{\text{tot}}(\rho_o)|} \quad (6.2)$$

which can also be written as:

$$N_{\text{tot}}(t) = N_{\text{grav,st}} + N_{\text{grav,dyn}}(t) + \delta N_{\text{centr}}(t) + N_{\text{tidal}}(t) \quad (6.3)$$

### 6.1.2 Determination of Equipotential Surfaces

The observables presented in Section 4.2 can be carried out at different positions along the plumbline passing through a particular  $\rho_o$ . Here, three different possibilities are considered:

1.  $\rho_o$ , the position where the normal potential is equal to the potential at the fluid-air interface.
2.  $\rho_{\sim}$ , the position at the fluid-air interface of the HLS inside the tunnel.
3.  $\rho_{\text{surf}}$ , the position on the Earth surface.

However, for the following analyses of observables, no distinction between observations carried out at  $\rho_o$  or  $\rho_{\sim}$  are considered. In addition, it is assumed that gravimetric observations can be carried out at  $\rho_o$  and  $\rho_{\text{surf}}$ . By contrast, it is evident that astro-geodetic observations can only be carried out on the Earth's surface at  $\rho_{\text{surf}}$ . This implies that we can consider two main scenarios concerning the analyses of the determination of equipotential profiles using observations.

1. The first scenario consists in assuming that only astro-geodetic observations are carried out. In this case, it is assumed that the observations  $\epsilon_{\text{tot}}(\rho_{\text{surf}})$  are reduced to  $\epsilon_{\text{tot}}(\rho_o)$  by known mass models only. The change in the equipotential profile between  $\mathbf{a}_o$  and  $\mathbf{b}_o$  is computed according to Equation 4.12 by:

$$\Delta N_{\text{tot}} \frac{\mathbf{b}_o}{\mathbf{a}_o} = - \int_{\mathbf{a}_o}^{\mathbf{b}_o} \epsilon_{\text{tot}}(\rho_o) \cdot d\mathbf{s} \quad (6.4)$$

On the one hand, non-modeled or badly modeled reductions  $\delta\epsilon_{\text{tot}} = \epsilon_{\text{tot}}(\rho_o) - \epsilon_{\text{tot}}(\rho_{\text{surf}})$  can be treated, as an additional correlated noise on  $\epsilon_{\text{tot}}(\rho_o)$ , for which

---

<sup>2</sup>as it will be demonstrated in this chapter.

the impact on the misalignment can be analyzed using the simulations described in Section 4.5. And on the other hand the impact on the misalignment can be analyzed in a more direct manner by looking directly at the integrated  $\delta\epsilon_{\text{tot}}$  which is equivalent to the true orthometric correction term (see Equation 4.58).

2. The second scenario consists in assuming that astro-geodetic observations and gravimetric observations are carried out. The former on the Earth's surface only ( $\epsilon_{\text{tot}}(\boldsymbol{\rho}_{\text{surf}})$ ), the latter on the Earth's surface ( $g_{\text{tot}}(\boldsymbol{\rho}_{\text{surf}})$ ) and inside the tunnel ( $g_{\text{tot}}(\boldsymbol{\rho}_{\text{o}})$ ). The change in the equipotential profile between  $\mathbf{a}_{\text{o}}$  and  $\mathbf{b}_{\text{o}}$  is computed according to Equation 4.59 by:

$$\Delta N_{\text{tot}}^{\mathbf{b}_{\text{o}}}_{\mathbf{a}_{\text{o}}} = - \int_{\mathbf{a}_{\text{surf}}}^{\mathbf{b}_{\text{surf}}} \epsilon_{\text{tot}}(\boldsymbol{\rho}_{\text{surf}}) \cdot d\mathbf{s} - E_{\mathbf{a}_{\text{o}}}^{\mathbf{b}_{\text{o}}} \quad (6.5)$$

with the orthometric correction term:

$$\begin{aligned} E_{\mathbf{a}_{\text{o}}}^{\mathbf{b}_{\text{o}}} = & \int_{\mathbf{a}_{\text{surf}}}^{\mathbf{b}_{\text{surf}}} \frac{g_{\text{tot}}(\boldsymbol{\rho}_{\text{surf}}) - \gamma(\boldsymbol{\rho}_{\text{o}})}{\gamma(\boldsymbol{\rho}_{\text{o}})} \cdot d\mathbf{n} \\ & + \frac{\bar{g}_{\text{tot}}(\mathbf{a}_{\text{o}}) - \gamma(\boldsymbol{\rho}_{\text{o}})}{\gamma(\boldsymbol{\rho}_{\text{o}})} \cdot \Delta H_{\mathbf{a}_{\text{o}}}^{\mathbf{a}_{\text{surf}}} - \frac{\bar{g}_{\text{tot}}(\mathbf{b}_{\text{o}}) - \gamma(\boldsymbol{\rho}_{\text{o}})}{\gamma(\boldsymbol{\rho}_{\text{o}})} \cdot \Delta H_{\mathbf{b}_{\text{o}}}^{\mathbf{b}_{\text{surf}}} \end{aligned} \quad (6.6)$$

where the mean gravity  $\bar{g}_{\text{tot}}(\mathbf{a}_{\text{o}})$  and  $\bar{g}_{\text{tot}}(\mathbf{b}_{\text{o}})$  has to be computed using a predefined more or less sophisticated estimation process exposed in Section 4.4.3.

### 6.1.3 Gravity Field Modeling for the Simulation of Stationary Mass Anomalies

In order to be able to directly use the formalism and the formulas provided in this thesis, it is necessary to clarify some additional aspects. From a geological point of view, the following simulations can be seen as a rigorous modeling of an hypothetical Earth which is formed by the union of a normal ellipsoid  $\mathcal{E}_0$  and a stationary mass anomaly  $\delta\mathcal{M}$ . From a geodetic point of view, the total potential is simply given by:

$$\begin{aligned} \Phi_{\text{tot}}(\boldsymbol{\rho}) &= U(\boldsymbol{\rho}) + \Phi_{\text{grav,st}}(\boldsymbol{\rho}) \\ &= U(\boldsymbol{\rho}) + \Phi_{\delta\mathcal{M}}(\boldsymbol{\rho}) \end{aligned} \quad (6.7)$$

thus, gravimetric  $g_{\text{tot}}$  and astrogeodetic observations  $\epsilon_{\text{tot}}$  are given by:

$$\begin{aligned} g_{\text{tot}}(\boldsymbol{\rho}) &= \gamma(\boldsymbol{\rho}) - g_{z,\delta\mathcal{M}}(\boldsymbol{\rho}) \\ &\approx 9.81 - 0.3 \cdot 10^{-5} \cdot H(\boldsymbol{\rho}) - g_{z,\delta\mathcal{M}}(\boldsymbol{\rho}) \\ \epsilon_{\text{tot}}(\boldsymbol{\rho}) &= -\arctan\left(\frac{g_{x,\delta\mathcal{M}}(\boldsymbol{\rho})}{g_{\text{tot}}(\boldsymbol{\rho})}\right) \end{aligned} \quad (6.8)$$

### 6.1.4 Outputs of the Simulations

The following output is computed given a specific mass anomaly,  $\delta\mathcal{M}$ , and the set of positions,  $\{\boldsymbol{\rho}_o, \boldsymbol{\rho}_{\text{surf}}\}$ , for which observations are supposed to be carried out:

$$\{\delta\mathcal{M}, \boldsymbol{\rho}_o, \boldsymbol{\rho}_{\text{surf}}\} \rightarrow \begin{cases} N_{\text{true}} \equiv \text{the true equipotential } N_{\text{tot}} \text{ at tunnel level, Eq. 3.209.} \\ N_{\text{quasi}} \equiv N_{\text{tot}} \text{ with } \epsilon_{\text{tot}}(\boldsymbol{\rho}_{\text{surf}}), \text{ Eq. 6.4.} \\ N_{\text{surf}} \equiv N_{\text{tot}} \text{ with } \epsilon_{\text{tot}}(\boldsymbol{\rho}_{\text{surf}}), g_{\text{tot}}(\boldsymbol{\rho}_{\text{surf}}), \text{ Eq. 6.5, 4.71.} \\ N_{\text{tnl}} \equiv N_{\text{tot}} \text{ with } \epsilon_{\text{tot}}(\boldsymbol{\rho}_{\text{surf}}), g_{\text{tot}}(\boldsymbol{\rho}_{\text{surf}}), g_{\text{tot}}(\boldsymbol{\rho}_o), \text{ Eq. 6.5, 4.74.} \\ N_{\text{mean}} \equiv N_{\text{tot}} \text{ with } \epsilon_{\text{tot}}(\boldsymbol{\rho}_{\text{surf}}), g_{\text{tot}}(\boldsymbol{\rho}_{\text{surf}}), g_{\text{tot}}(\boldsymbol{\rho}_o), \text{ Eq. 6.5, 4.76.} \\ N_{\text{lsc}} \equiv N_{\text{tot}} \text{ with } \epsilon_{\text{tot}}(\boldsymbol{\rho}_{\text{surf}}), g_{\text{tot}}(\boldsymbol{\rho}_{\text{surf}}), g_{\text{tot}}(\boldsymbol{\rho}_o), \text{ Eq. 6.5, 4.69, 4.98.} \end{cases} \quad (6.9)$$

where the differences between the output are mainly due to the different manner of computing the mean gravity along the plumbline  $\bar{g}_{\text{tot}}$  which is the most crucial quantity used for the computation of the orthometric corrections. Furthermore, except  $N_{\text{true}}$ , all other quantities can be determined by real observations.

Thus, the equipotential profiles given in Equation 6.9 are analysed in terms of misalignments. On the one hand, the analysis of  $N_{\text{true}}$  permits to identify if a given mass anomaly  $\delta\mathcal{M}$  generates misalignments larger than 10 micrometers over 200 meters. This is done by looking if:

$$\max [\mathcal{M}_{\star}^{200} \{N_{\text{true}}\}] \leq 10 \text{ [microns]} \quad (6.10)$$

On the other hand, the observability of a given strategy is tested by looking if the true equipotential generated by a given mass anomaly  $\delta\mathcal{M}$  can be determined by a given set of observations and a specific strategy with sufficient accuracy. This is done by looking if:

$$\max [\mathcal{M}_{\star}^{200} \{\delta N_{\text{xxxx}}\}] \leq 10 \text{ [microns]} \quad (6.11)$$

where:

$$\delta N_{\text{xxxx}} = N_{\text{xxxx}} - N_{\text{true}} \quad \text{with:} \quad \begin{cases} \delta N_{\text{quasi}} = N_{\text{quasi}} - N_{\text{true}} \\ \delta N_{\text{surf}} = N_{\text{surf}} - N_{\text{true}} \\ \delta N_{\text{tnl}} = N_{\text{tnl}} - N_{\text{true}} \\ \delta N_{\text{mean}} = N_{\text{mean}} - N_{\text{true}} \\ \delta N_{\text{lsc}} = N_{\text{lsc}} - N_{\text{true}} \end{cases} \quad (6.12)$$

## 6.2 Normal Equipotential

The largest component responsible for the non-straightness of the geometry  $\rho_{\sim}$  of gravity equipotentials is, by far, due to the potential generated by the normal ellipsoid  $\mathcal{E}_{\circ}$ . The geometry of the normal equipotential  $\rho_{\circ}$  is rigorously given in Section 3.8.1. However, in order to compute some order of magnitudes of misalignment generated by  $\rho_{\circ}$ , for short wavelengths, it is reasonable to approximate the normal equipotential profile by the following well-known linearized spherical approximation:

$$\rho_{\circ}(x) = \begin{pmatrix} x \\ 0 \\ -\frac{x^2}{2R} \end{pmatrix} \quad (6.13)$$

where  $x$  represents a topocentric horizontal coordinate and  $R \approx 6'380'000$  meters the Earth radius. Thus, it is trivial to compute the misalignment errors generated by neglecting the Earth's normal curvature, for a given wavelength  $\lambda$ . Formally, using the misalignment operator  $\mathcal{M}$ , this is given by:

$$\mathcal{M}_0^* \{\rho_{\circ}\} \quad (6.14)$$

Figure 6.1 illustrates these misalignments for wavelengths between  $\lambda = 0.1$  and  $\lambda = 1000$

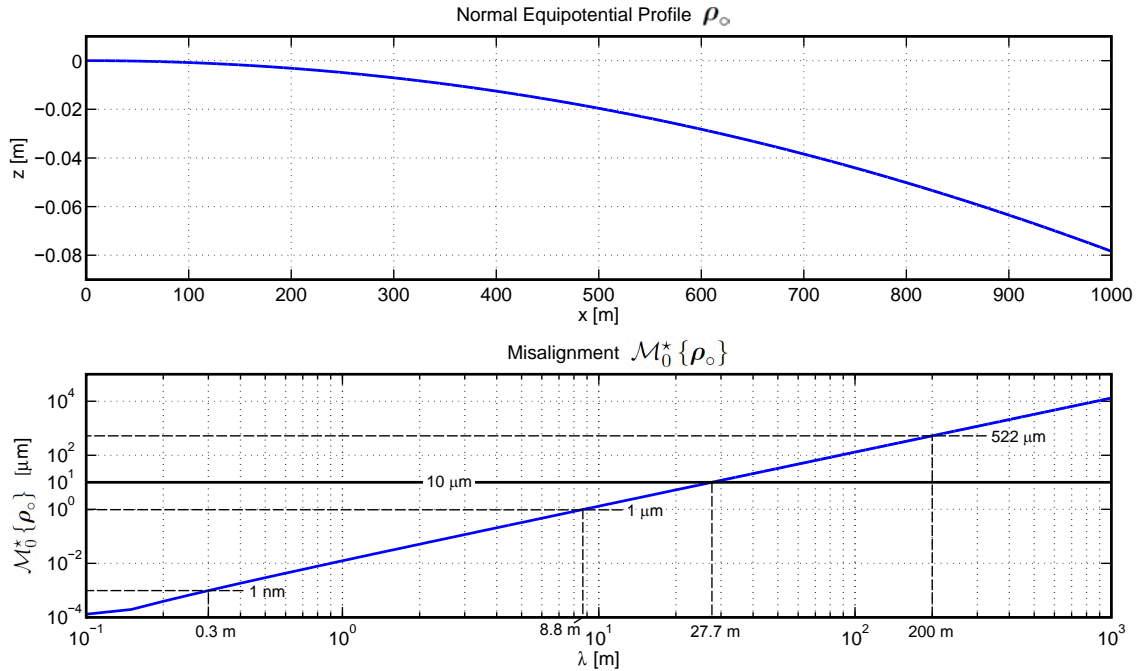


**Figure 6.1:** Normal equipotential profile  $\rho_{\circ}(x)$  (upper) represented in a local topocentric system. Misalignments generated by  $\rho_{\circ}$  as a function of the wavelength  $\lambda$  (lower).

meters. In Table 6.1, some interesting points are listed. For example, we can see that a hydrostatic water reference can realize a straight line — or a plane — at nanometer level for wavelengths  $\leq 0.3$  meters. The micrometer level is guaranteed up to 8.8 meters,

and 10 microns are reached already at approximately 27.7 meters. Finally, regarding the alignment accuracy over 200 meters, we can see that the misalignment  $\mathcal{M}_0^{200}\{\boldsymbol{\rho}_o\}$  reaches 522 micrometers, more than 50 times the objective of 10 microns. The latter finding is a very trivial one but a first necessary justification of not considering the fluid-air interface of a hydrostatic system as straight enough for the alignment of the CLIC.

**Table 6.1:** Misalignments generated by the normal equipotential as a function of the wavelength  $\lambda$ .

$\lambda$ [m]	$\Delta z$ [m]	$\mathcal{M}_0^\lambda\{\boldsymbol{\rho}_o\}$ [ $\mu\text{m}$ ]
0.3	$-7 \cdot 10^{-9}$	$1.0 \cdot 10^{-3}$
8.8	$-6 \cdot 10^{-6}$	$1.0 \cdot 10^0$
27.7	$-6 \cdot 10^{-5}$	$1.0 \cdot 10^1$
100.0	$-8 \cdot 10^{-4}$	$1.3 \cdot 10^2$
200.0	$-3 \cdot 10^{-3}$	$5.2 \cdot 10^2$
1000.0	$-8 \cdot 10^{-2}$	$1.3 \cdot 10^4$

### 6.3 Systematic Analysis of Lateral Varying Anomalies

The aim is to determine the order of magnitude and characteristics of the shape of underground equipotential profiles exited by anomalous density fields which can be expected at very high frequencies ( $\lambda \sim 200$  m). In addition, error-free gravimetric and astrogeodetic deflection of the vertical observations are simulated on the surface of topography and inside a tunnel in order to test the strategies, exposed in Section 6.1.2, for the determination of equipotential profiles in tunnels.

It is obvious that the exploration of all possible mass anomalies is hopeless. However, firstly, we know that the endless space of mathematical possibilities and configurations can be reduced by a priori realistic geological and topographical bounds. Subsequently, by choosing extreme but realistic configurations, the analyses can pretend to encompass most of the case which may arise in reality.

The following numerical simulations of the gravity field are based on homogenous polyhedra computed with **QGravity**. It is well known that only horizontal density variations produce curvature variations of equipotentials. For this reason, a systematic analysis of extreme – but geologically admissible – periodic anomalous density fields, which produce modifications of the gravity field, is realized in order to approach the extremal bounds which can be expected by unmodeled or unobservable phenomena. The density anomalies are based on two classes of mass anomalies, connected slabs **SLAB** and sinusoidal prisms **SIN**.

In order to illustrate the analysis of the consequences of **SLAB** and **SIN** anomalies on the misalignment, four symptomatic cases (two per class) are exposed. The first demonstrate that there exist **SLAB** and **SIN** which generate significant misalignments which can be properly determined by astrogravimetric levelling. In opposition, the second two cases show that there exist **SLAB** and **SIN** for which astro-gravimetric determinations cannot help and more seriously, lead to totally wrong results. The anomalies analyzed in the first cases are called **observable** by astrogravimetric levelling. The anomalies analyzed in the second cases are called **not observable**. Finally, an attempt to systematically analyse several representative **SLAB** and **SIN** is conducted in order to classify problematic and non-problematic configurations without forgetting to quantify their consequences on the misalignment.



### 6.3.1 Connected Slab Anomalies SLAB

A connected slab anomaly is a homogeneous polyhedron represented as a function of some parameters:

$$\text{SLAB}(H_{0\text{SLAB}}, H_{\text{SLAB}}, \Delta H_{\text{SLAB}}, \beta_{\text{SLAB}}, \rho_{\text{SLAB}}) \quad (6.15)$$

with a fixed depth equal to 30 kilometers, a fixed foundation at height  $H_{0\text{SLAB}} = 0$  meters, a variable height difference  $= \Delta H_{\text{SLAB}}$  of the slab, slope of the slab connection  $\beta_{\text{SLAB}}$ , height  $H_{\text{SLAB}}$  and the density  $\rho_{\text{SLAB}}$ , as shown in Figure 6.2. The density of a SLAB represents the realistic density contrasts with respect to a mean rock density  $\rho_{\text{topo}} = 2670 \frac{\text{kg}}{\text{m}^3}$  which can be expected in upper layers. The connected slab anomalies with their respective variable parameters used for the simulations are listed in Table 6.2.

It is assumed that error-free observations are carried out every 10 meters inside a horizontal tunnel, at  $H = 300$  meters, and on the surface of a flat topography at  $H = 450$  meters, for all anomalies for which  $H_{\text{SLAB}} < 450$  meters. When  $H_{\text{SLAB}} \geq 450$  meters, the upper boundary of the highest slab is considered as the topography itself and the observations on the topography are simulated accordingly.

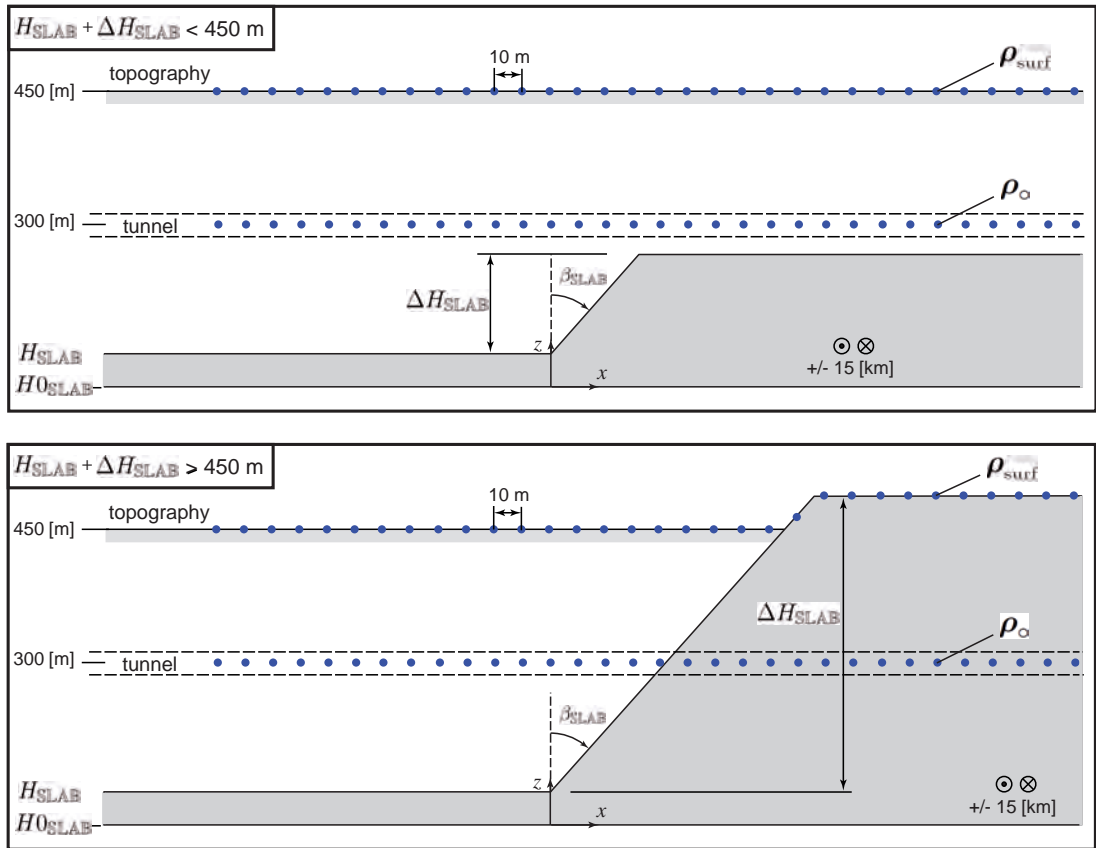


**Figure 6.2:** Schematic view of the parameters defining a slab anomaly  $\text{SLAB}(H_{0\text{SLAB}}, H_{\text{SLAB}}, \Delta H_{\text{SLAB}}, \beta_{\text{SLAB}}, \rho_{\text{SLAB}})$  with the definition of the topography for  $H_{\text{SLAB}} + \Delta H_{\text{SLAB}} < 450$  meters (upper) and for  $H_{\text{SLAB}} + \Delta H_{\text{SLAB}} \geq 450$  meters (lower).

### 6.3.2 Sinusoidal Prism Anomalies $\text{SIN}$

A sinusoidal prism anomaly is a homogeneous polyhedron represented as a function of some parameters:

$$\text{SIN}(H0_{\text{SIN}}, H_{\text{SIN}}, A_{\text{SIN}}, \lambda_{\text{SIN}}, \rho_{\text{SIN}}) \quad (6.16)$$

with a fixed depth equal to 10 kilometers, a foundation located at  $H0_{\text{SIN}} = 0$  or  $H0_{\text{SIN}} = -3'000$  meters, and a variable amplitude  $= A_{\text{SIN}}$ , wavelength  $\lambda_{\text{SIN}}$ , height  $H_{\text{SIN}}$  and a variable density  $\rho_{\text{SIN}}$ , as shown in Figure 6.3. The densities of the various  $\text{SIN}$  represent realistic density contrasts with respect to a mean rock density  $\rho_{\text{topo}} = 2670 \frac{\text{kg}}{\text{m}^3}$  which can be expected in upper layers. The anomalies with their respective variable parameters used for the simulations are listed in Table 6.5.

It is assumed that error-free observations are carried out every 10 meters inside a horizontal tunnel at  $H = 300$  meters and on a flat topography at  $H = 450$  meters, for all anomalies for which  $H_{\text{SIN}} < 450$  meters. When  $H_{\text{SIN}} \geq 450$  meters, the sinusoidal upper boundary of  $\text{SIN}$  is considered as the topography itself and the observations on the topography are simulated accordingly.

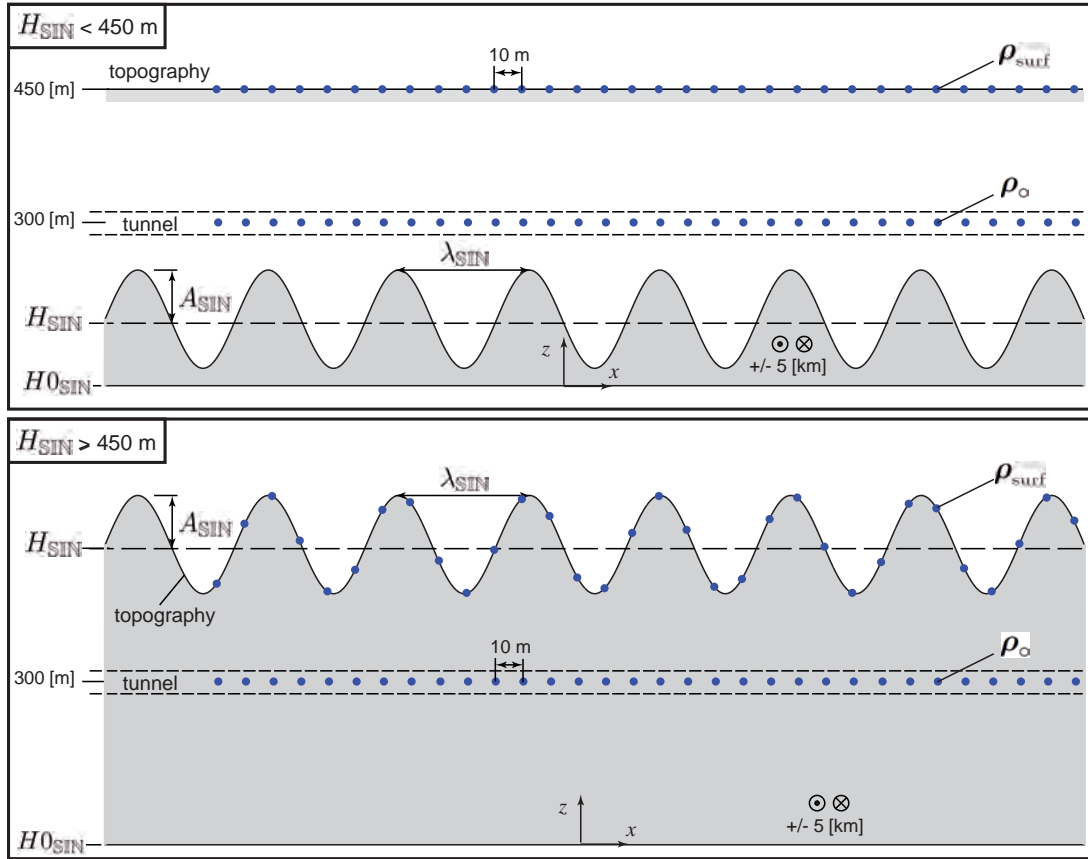


**Figure 6.3:** Schematic view of the parameters defining a sinus anomaly  $\text{SIN}(H0_{\text{SIN}}, H_{\text{SIN}}, A_{\text{SIN}}, \lambda_{\text{SIN}}, \rho_{\text{SIN}})$  with the definition of the topography for  $H_{\text{SIN}} < 450$  meters (upper) and for  $H_{\text{SIN}} \geq 450$  meters (lower).

### 6.3.3 Misalignment Analyses due to SLAB Anomalies

#### A Significant Observable Anomaly

The anomaly  $\text{SLAB}(-3000 \text{ m}, -2950 \text{ m}, +3200 \text{ m}, +45 \text{ deg}, +500 \frac{\text{kg}}{\text{m}^3})$  produces significant misalignments over 200 meters and can be determined by astrogravimetric levelling with sufficient accuracy.

The anomaly, the different solutions of the equipotential profile and the differences with respect to the true profile are shown in Figure 6.4.

In Figure 6.5, the misalignments of the true equipotential  $\mathcal{M}_\star^\star\{N_{\text{true}}\}$  are represented as a function of the wavelength (middle), the position, and for the particular wavelength equal to 200 meters  $\mathcal{M}_\star^{200}\{N_{\text{true}}\}$  (lower). The latter shows clearly that this anomaly cannot be neglected because it generates significant misalignments, larger than 10 micrometers over 200 meters.

The remaining misalignments  $\mathcal{M}_\star^\star\{\delta N_{\text{mean}}\}$  and  $\mathcal{M}_\star^{200}\{\delta N_{\text{mean}}\}$ , generated by the difference between the equipotential surface determined by astrogravimetric levelling  $N_{\text{mean}}$  and the true equipotential  $N_{\text{true}}$  are shown in Figure 6.6. The latter shows clearly that it is theoretically possible, in this specific case, to determine the equipotential profile with sufficient accuracy when astrogeodetic deflections of the vertical and gravimetric measurements are carried out on the topography and in the tunnel.

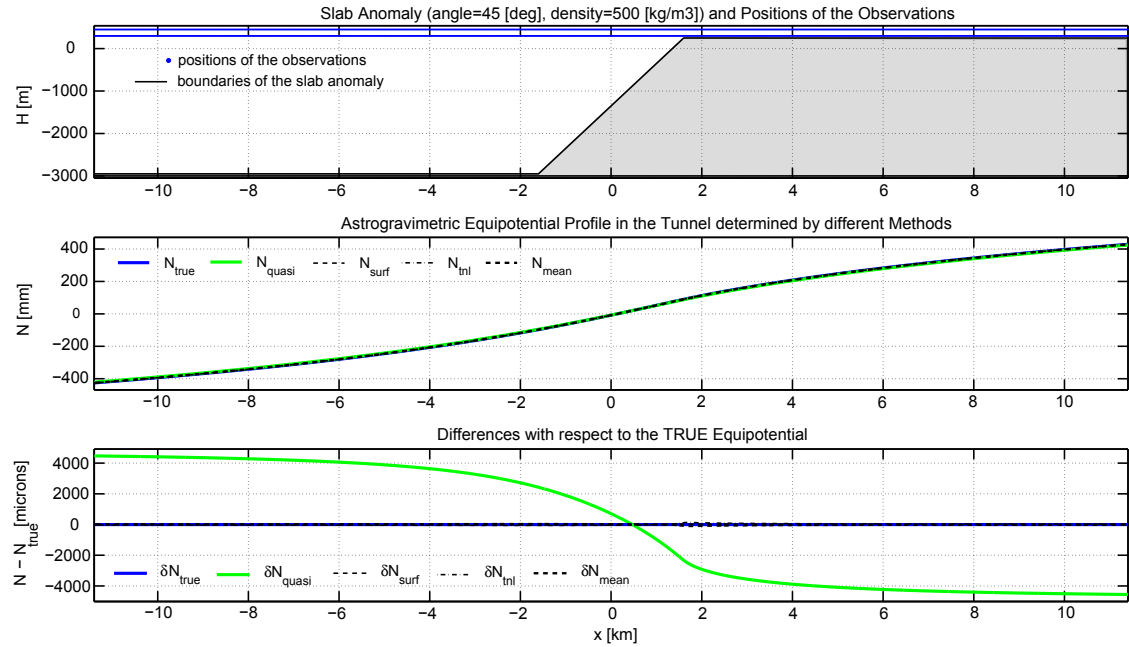


**Figure 6.4:** (Upper)  $\text{SLAB}(-3000 \text{ m}, -2950 \text{ m}, +3200 \text{ m}, +45 \text{ deg}, +500 \frac{\text{kg}}{\text{m}^3})$  in black and  $\rho_o, \rho_{\text{surf}}$  in blue. (Middle) equipotential profiles  $N_{\text{true}}, N_{\text{quasi}}, N_{\text{surf}}, N_{\text{tnl}}, N_{\text{mean}}$ . (Lower) equipotential profile errors  $\delta N_{\text{true}}, \delta N_{\text{quasi}}, \delta N_{\text{surf}}, \delta N_{\text{tnl}}, \delta N_{\text{mean}}$ .

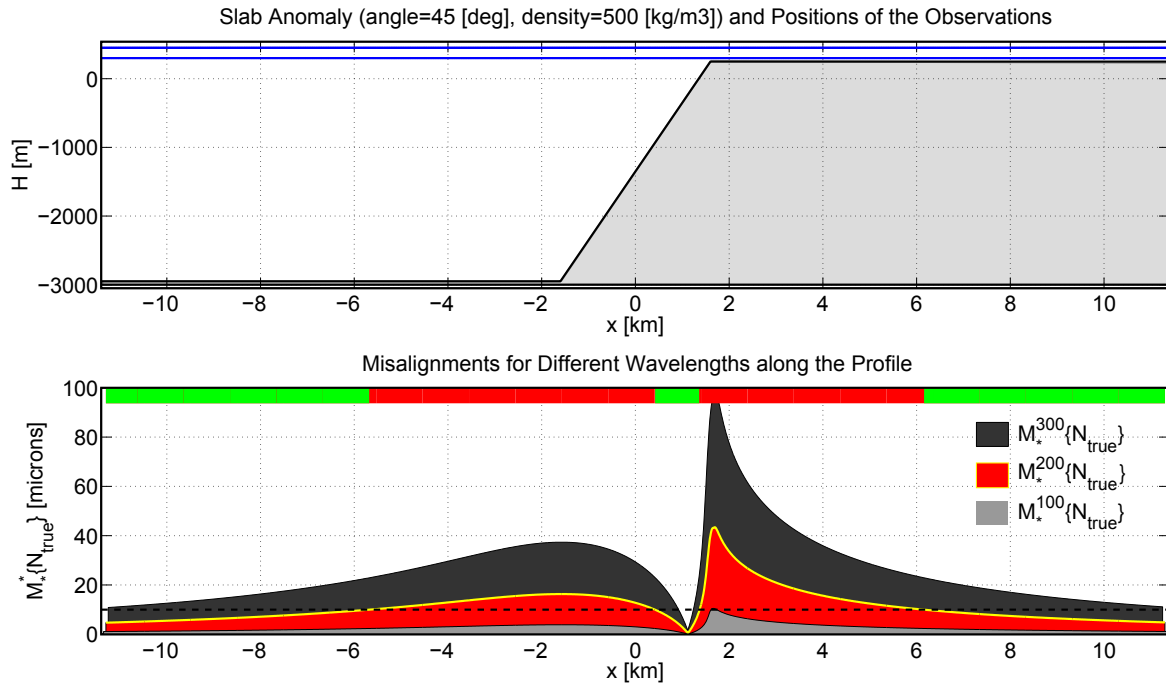


**Figure 6.5:** Misalignment of the true equipotential  $\mathcal{M}_*^*\{N_{\text{true}}\}$  as a function of several wavelengths, and for the wavelength equal to 200 meters  $\mathcal{M}_*^{200}\{N_{\text{true}}\}$  (lower) generated by SLAB(−3000 m, −2950 m, +3200 m, +45 deg, +500  $\frac{\text{kg}}{\text{m}^3}$ ).

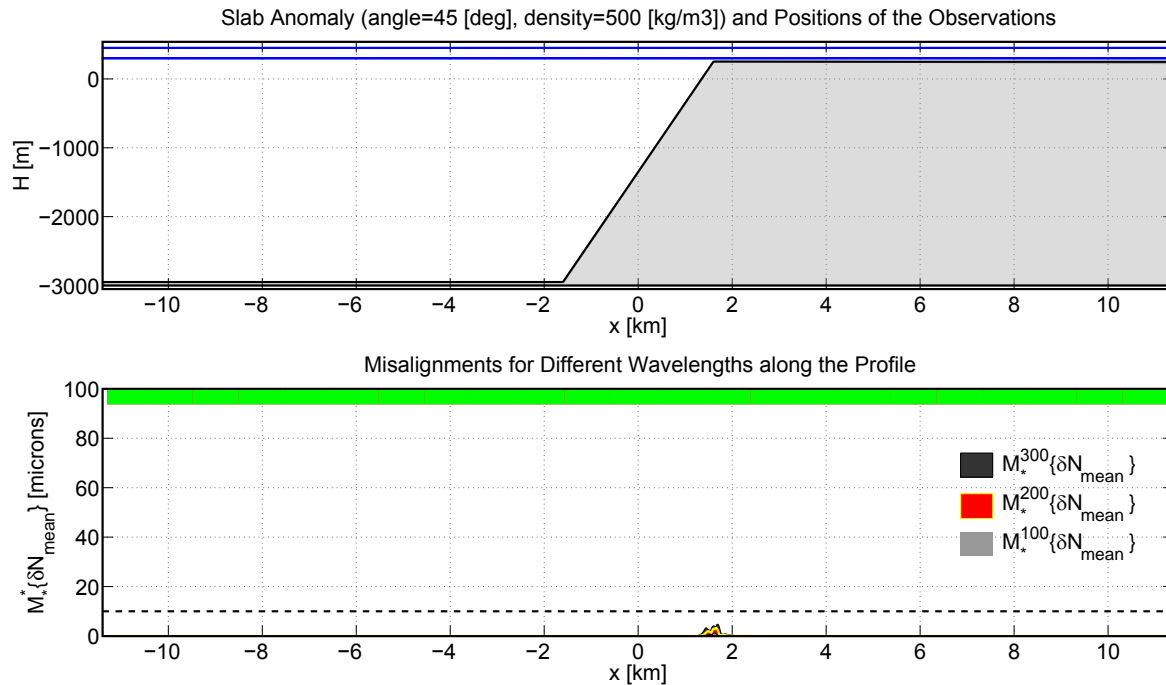


**Figure 6.6:** Remaining misalignment  $\mathcal{M}_*^*\{\delta N_{\text{mean}}\}$  as a function of several wavelengths, and for the wavelength equal to 200 meters  $\mathcal{M}_*^{200}\{\delta N_{\text{mean}}\}$  (lower) generated by SLAB(−3000 m, −2950 m, +3200 m, +45 deg, +500  $\frac{\text{kg}}{\text{m}^3}$ ).

### A Significant Not Observable Anomaly $\Rightarrow$ Significant Artifacts

As in the previous case, the anomaly  $\text{SLAB}(+0 \text{ m}, +50 \text{ m}, +200 \text{ m}, +50 \text{ deg}, +200 \frac{\text{kg}}{\text{m}^3})$  produces significant misalignments over 200 meters. However, it is shown that the various astrogravimetric strategies proposed in this thesis are not able to determine the equipotential profile with enough accuracy. Worse still, they produce significant artifacts.

The anomaly, the different solutions and the differences with respect to the true profile are shown in Figure 6.7. It appears that all determinations generate larger signal-to-error ratios compared to  $N_{\text{true}}$  (middle).

Regarding the misalignment over 200 meters, Figures 6.8 and 6.9 show clearly that the true equipotential  $N_{\text{true}}$  cannot be observed with sufficient accuracy, and a maximal misalignment is produced that is twice as large as if no determination would be tempted.

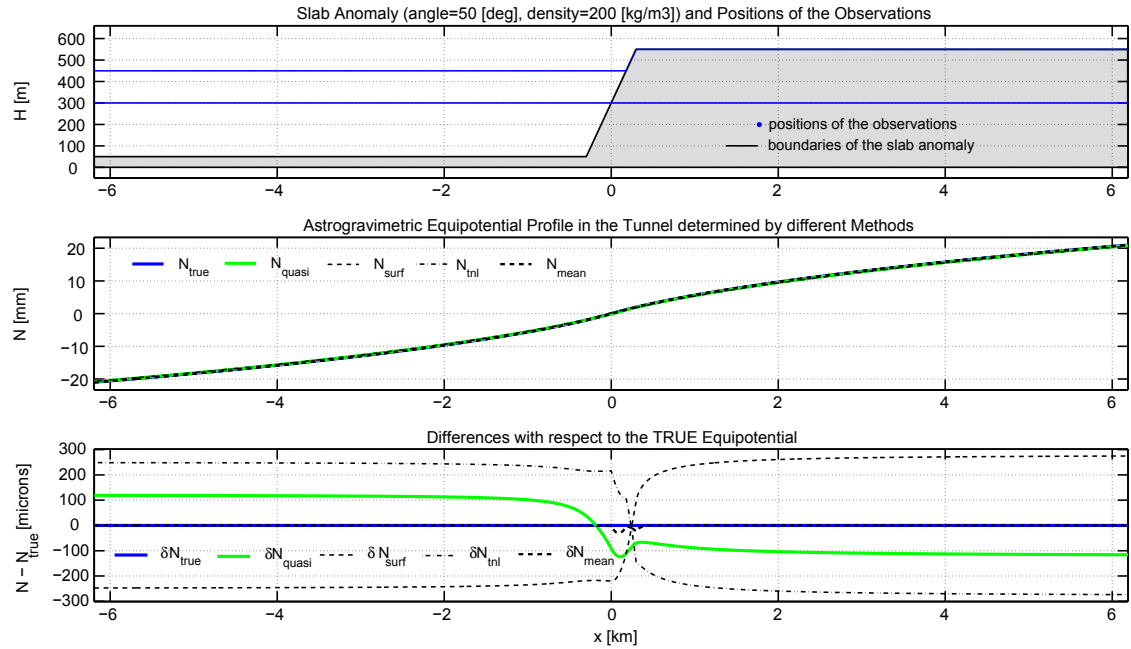


**Figure 6.7:** (Upper)  $\text{SLAB}(+0 \text{ m}, +50 \text{ m}, +200 \text{ m}, +50 \text{ deg}, +200 \frac{\text{kg}}{\text{m}^3})$  in black and  $\rho_o, \rho_{\text{surf}}$  in blue. (Middle) equipotential profiles  $N_{\text{true}}, N_{\text{quasi}}, N_{\text{surf}}, N_{\text{tnl}}, N_{\text{mean}}$ . (Lower) equipotential profile errors  $\delta N_{\text{true}}, \delta N_{\text{quasi}}, \delta N_{\text{surf}}, \delta N_{\text{tnl}}, \delta N_{\text{mean}}$ .

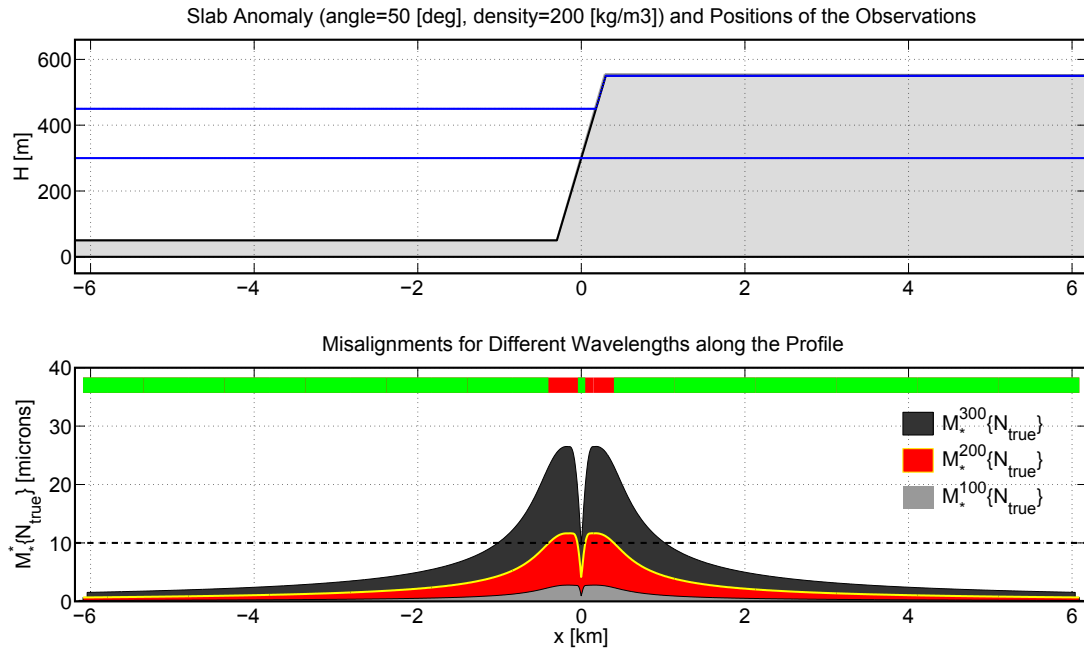


**Figure 6.8:** Misalignment of the true equipotential  $\mathcal{M}_{\star}\{N_{\text{true}}\}$  as a function of several wavelengths, and for the wavelength equal to 200 meters  $\mathcal{M}_{\star}^{200}\{N_{\text{true}}\}$  (lower) generated by SLAB(+0 m, +50 m, +200 m, +50 deg, +200  $\frac{\text{kg}}{\text{m}^3}$ ).

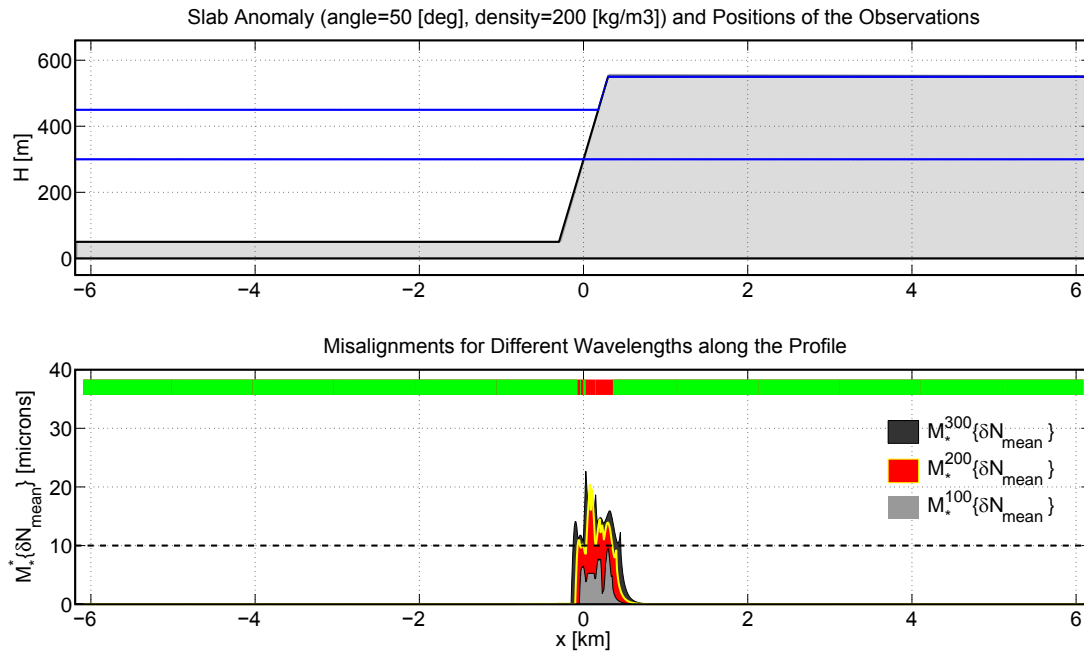


**Figure 6.9:** Remaining misalignment  $\mathcal{M}_{\star}\{\delta N_{\text{mean}}\}$  as a function of several wavelengths, and for the wavelength equal to 200 meters  $\mathcal{M}_{\star}^{200}\{\delta N_{\text{mean}}\}$  (lower) generated by SLAB(+0 m, +50 m, +200 m, +50 deg, +200  $\frac{\text{kg}}{\text{m}^3}$ ).

### Systematic Analysis of SLAB Anomalies

In this section, several SLAB anomalies are analyzed:

**Table 6.2:** List of SLAB anomalies used for systematic analyses. Here an object  $\text{SLAB}_i$  does not represents a single SLAB anomaly but represents a set of slab anomalies.

$\{\text{SLAB}\}$	$H_{0\text{SLAB}}$	$H_{\text{SLAB}}$	$\Delta H_{\text{SLAB}}$	$\beta_{\text{SLAB}}$	$\rho_{\text{SLAB}}$	$H_{\text{SLAB}} + \Delta H_{\text{SLAB}} - H(\rho_o)$	topography	mass between $\rho_o \rightarrow \rho_{\text{surf}}$
	[m]	[m]	[m]	[deg]	$\left[\frac{\text{kg}}{\text{m}^3}\right]$	[m]		
$\text{SLAB}_1$	0	50	50	[0, 85]	[50, 500]	-200	flat	no
$\text{SLAB}_2$	0	50	150	[0, 85]	[50, 500]	-100	flat	no
$\text{SLAB}_3$	0	50	200	[0, 85]	[50, 500]	-50	flat	no
$\text{SLAB}_4$	0	50	250	[0, 85]	[50, 500]	0	flat	no
$\text{SLAB}_5$	0	50	325	[0, 85]	[50, 500]	75	flat	yes
$\text{SLAB}_6$	0	50	400	[0, 85]	[50, 500]	150	flat	yes
$\text{SLAB}_7$	0	50	450	[0, 85]	[50, 500]	200	flat/oblique	yes
$\text{SLAB}_8$	0	50	500	[0, 85]	[50, 500]	250	flat/oblique	yes
$\text{SLAB}_{11}$	-3000	-2950	2750	[0, 85]	[50, 500]	-500	flat	no
$\text{SLAB}_{12}$	-3000	-2950	3150	[0, 85]	[50, 500]	-100	flat	no
$\text{SLAB}_{13}$	-3000	-2950	3200	[0, 85]	[50, 500]	-50	flat	no
$\text{SLAB}_{14}$	-3000	-2950	3250	[0, 85]	[50, 500]	0	flat	no
$\text{SLAB}_{15}$	-3000	-2950	3325	[0, 85]	[50, 500]	75	flat	yes
$\text{SLAB}_{16}$	-3000	-2950	3400	[0, 85]	[50, 500]	150	flat	yes
$\text{SLAB}_{17}$	-3000	-2950	3450	[0, 85]	[50, 500]	200	flat/oblique	yes
$\text{SLAB}_{18}$	-3000	-2950	3500	[0, 85]	[50, 500]	250	flat/oblique	yes

The results are presented in Tables 6.3 and 6.4, and in Figures 6.10 and 6.11.

**Table 6.3:** Systematic misalignment analyses of SLAB<sub>1</sub> → SLAB<sub>8</sub>. The maximal misalignments larger than 10 microns are listed for  $N_{\text{true}}$ ,  $\delta N_{\text{quasi}}$  and  $\delta N_{\text{mean}}$  only.

{SLAB}	$\max [\mathcal{M}_{\star}^{200} \{N_{\text{true}}\}]$ $> 10\mu\text{m}$			$\max [\mathcal{M}_{\star}^{200} \{\delta N_{\text{quasi}}\}]$ $> 10\mu\text{m}$			$\max [\mathcal{M}_{\star}^{200} \{\delta N_{\text{mean}}\}]$ $> 10\mu\text{m}$			best
	$\rho_{\text{SLAB}}, \beta_{\text{SLAB}}, \mathcal{M}_{\star}^{200}$ $\left[\frac{\text{kg}}{\text{m}^3}\right], [\text{deg,deg}], [\mu\text{m}]$			$\rho_{\text{SLAB}}, \beta_{\text{SLAB}}, \mathcal{M}_{\star}^{200}$ $\left[\frac{\text{kg}}{\text{m}^3}\right], [\text{deg,deg}], [\mu\text{m}]$			$\rho_{\text{SLAB}}, \beta_{\text{SLAB}}, \mathcal{M}_{\star}^{200}$ $\left[\frac{\text{kg}}{\text{m}^3}\right], [\text{deg,deg}], [\mu\text{m}]$			
SLAB <sub>1</sub>	✓			✓			✓			$N_{\text{mean}}$
SLAB <sub>2</sub>	500	[0,45]	10.5	✓			✓			$N_{\text{mean}}$
SLAB <sub>3</sub>	300	[0,60]	10.6							
	400	[0,75]	14.2	500	[0,50]	11.5		✓		$N_{\text{mean}}$
	500	[0,80]	17.7							
SLAB <sub>4</sub>	200	[0,60]	12.8							
	300	[0,75]	19.3	300	[0,60]	13.8	300	[0,10]	10.3	$N_{\text{mean}}$
	400	[0,80]	25.7	400	[0,70]	18.4	400	[0,40]	13.8	
	500	[0,80]	32.1	500	[0,75]	23.0	500	[0,50]	17.2	
SLAB <sub>5</sub>	200	[0,65]	18.8	200	[0,50]	14.0	200	[20,65]	13.0	$N_{\text{mean}}$
	300	[0,75]	28.2	300	[0,60]	20.9	300	[0,75]	19.4	
	400	[0,80]	37.8	400	[0,65]	27.9	400	[0,80]	25.9	
	500	[0,80]	46.9	500	[0,70]	34.9	500	[0,80]	32.4	
SLAB <sub>6</sub>	100	[0,15]	10.3				100	[45,45]	10.4	$N_{\text{quasi}}$
	200	[0,60]	20.6	200	[10,55]	15.5	200	[25,65]	20.9	
	300	[0,70]	31.0	300	[0,65]	23.2	300	[0,75]	31.3	
	400	[0,75]	41.3	400	[0,70]	31.0	400	[0,80]	41.7	
	500	[0,80]	51.6	500	[0,70]	38.7	500	[0,80]	52.2	
SLAB <sub>7</sub>	100	[0,20]	10.6				100	[50,50]	10.1	$N_{\text{quasi}}$
	200	[0,60]	21.2	200	[0,60]	19.4	200	[30,70]	20.2	
	300	[0,70]	31.8	300	[0,65]	29.2	300	[0,75]	30.2	
	400	[0,75]	42.5	400	[0,70]	38.9	400	[0,80]	40.3	
	500	[0,80]	53.1	500	[0,75]	48.6	500	[0,80]	50.4	
SLAB <sub>8</sub>	100	[0,20]	10.9	100	[30,45]	10.8	100	[50,50]	10.2	$N_{\text{mean}}$
	200	[0,55]	21.7	200	[0,60]	21.5	200	[0,65]	20.4	
	300	[0,65]	32.6	300	[0,65]	32.3	300	[0,75]	30.5	
	400	[0,75]	43.5	400	[0,70]	43.0	400	[0,80]	40.7	
	500	[0,75]	54.3	500	[0,75]	53.8	500	[0,80]	50.9	



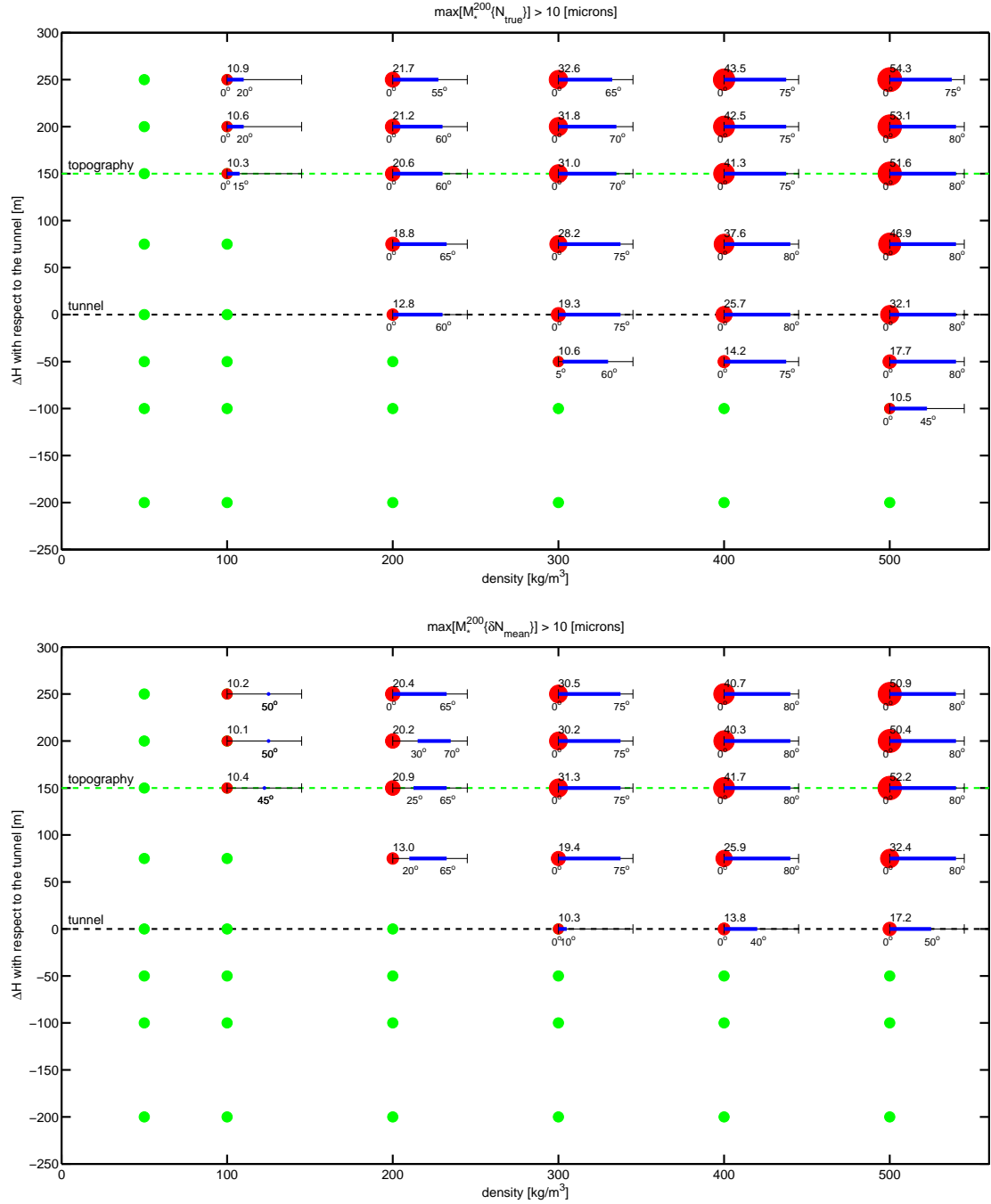


**Figure 6.10:** Representation of the misalignment analyses contained in Table 6.3 for  $N_{\text{true}}$  (upper) and  $\delta N_{\text{mean}}$  (lower) only. Each dot represents the results of a subset of  $\text{SLAB}_i(\beta_{\text{SLAB}})$  simulations. A dot is positioned as a function of its density  $\rho_{\text{SLAB}}$  (x-axis) and its height separation with respect to the tunnel (y-axis),  $H_{\text{SLAB}} + \Delta H_{\text{SLAB}} - H(\rho_o)$ . A green dot means that the maximal misalignment is smaller than 10 microns for all angles  $\beta_{\text{SLAB}}$ . In opposition, the red dots represent  $\text{SLAB}$  which contain maximal misalignments larger than 10 microns. They are scaled proportionally to the maximal misalignment. In addition, the horizontal blue bar represents the angle  $\beta_{\text{SLAB}}$  for which the maximal misalignment is larger than 10 microns.

**Table 6.4:** Systematic misalignment analyses of  $\text{SLAB}_{11} \rightarrow \text{SLAB}_{18}$ . The maximal misalignment larger as 10 microns are listed for  $N_{\text{true}}$ ,  $\delta N_{\text{quasi}}$  and  $\delta N_{\text{mean}}$  only.

$\{\text{SLAB}\}$	$\max [\mathcal{M}_{\star}^{200} \{N_{\text{true}}\}]$ $> 10\mu\text{m}$ $\rho_{\text{SLAB}}, \beta_{\text{SLAB}}, \mathcal{M}_{\star}^{200}$ $\left[\frac{\text{kg}}{\text{m}^3}\right], [\text{deg}, \text{deg}], [\mu\text{m}]$			$\max [\mathcal{M}_{\star}^{200} \{\delta N_{\text{quasi}}\}]$ $> 10\mu\text{m}$ $\rho_{\text{SLAB}}, \beta_{\text{SLAB}}, \mathcal{M}_{\star}^{200}$ $\left[\frac{\text{kg}}{\text{m}^3}\right], [\text{deg}, \text{deg}], [\mu\text{m}]$			$\max [\mathcal{M}_{\star}^{200} \{\delta N_{\text{mean}}\}]$ $> 10\mu\text{m}$ $\rho_{\text{SLAB}}, \beta_{\text{SLAB}}, \mathcal{M}_{\star}^{200}$ $\left[\frac{\text{kg}}{\text{m}^3}\right], [\text{deg}, \text{deg}], [\mu\text{m}]$			best
SLAB <sub>11</sub>	300	[0,65]	12.0	✓			✓			$N_{\text{mean}}$
	400	[0,75]	15.9							
	500	[0,80]	19.9							
SLAB <sub>12</sub>	200	[0,70]	14.8	500 [0,50] 11.2			✓			$N_{\text{mean}}$
	300	[0,80]	22.1							
	400	[0,80]	29.5							
	500	[0,80]	36.9							
SLAB <sub>13</sub>	200	[0,75]	18.9	400 [0,55] 13.1 500 [0,65] 16.4			✓			$N_{\text{mean}}$
	300	[0,80]	28.4							
	400	[0,80]	37.8							
	500	[0,85]	47.3							
SLAB <sub>14</sub>	100	[20,55]	12.2	200 [5,45] 12.4 300 [0,65] 18.5 400 [0,70] 24.7 500 [0,75] 30.9	300 [0,10] 10.5 400 [0,40] 14.0 500 [0,50] 17.5			$N_{\text{mean}}$		
	200	[0,75]	24.3							
	300	[0,80]	36.5							
	400	[0,80]	48.7							
	500	[0,85]	60.8							
SLAB <sub>15</sub>	100	[0,60]	14.2	200 [0,55] 16.1 300 [0,65] 24.1 400 [0,70] 32.1 500 [0,70] 40.1	200 [20,65] 12.4 300 [0,75] 18.5 400 [0,80] 24.7 500 [0,80] 30.9			$N_{\text{mean}}$		
	200	[0,75]	28.4							
	300	[0,80]	42.7							
	400	[0,80]	56.9							
	500	[0,85]	71.1							
SLAB <sub>16</sub>	100	[0,55]	14.5	200 [5,60] 17.7 300 [0,65] 26.6 400 [0,70] 35.5 500 [0,70] 44.4	100 [45,45] 10.3 200 [25,65] 20.6 300 [0,75] 31.0 400 [0,80] 41.3 500 [0,80] 51.6			$N_{\text{quasi}}$		
	200	[0,75]	28.9							
	300	[0,80]	43.4							
	400	[0,80]	57.8							
	500	[0,80]	72.3							
SLAB <sub>17</sub>	100	[0,55]	14.3	100 [35,45] 10.6 200 [0,60] 21.2 300 [0,65] 31.8 400 [0,70] 42.4 500 [0,75] 53.0	100 [50,50] 10.0 200 [30,70] 20.0 300 [0,75] 30.0 400 [0,80] 40.0 500 [0,80] 50.0			$N_{\text{mean}}$		
	200	[0,70]	28.5							
	300	[0,80]	42.6							
	400	[0,80]	57.1							
	500	[0,80]	71.3							
SLAB <sub>18</sub>	100	[0,50]	14.1	100 [0,45] 15.6 200 [0,60] 31.2 300 [0,65] 46.7 400 [0,70] 62.3 500 [0,75] 77.9	200 [0,65] 20.0 300 [0,75] 29.9 400 [0,80] 39.9 500 [0,80] 49.9			$N_{\text{mean}}$		
	200	[0,70]	28.2							
	300	[0,75]	42.3							
	400	[0,80]	55.4							
	500	[0,80]	70.5							

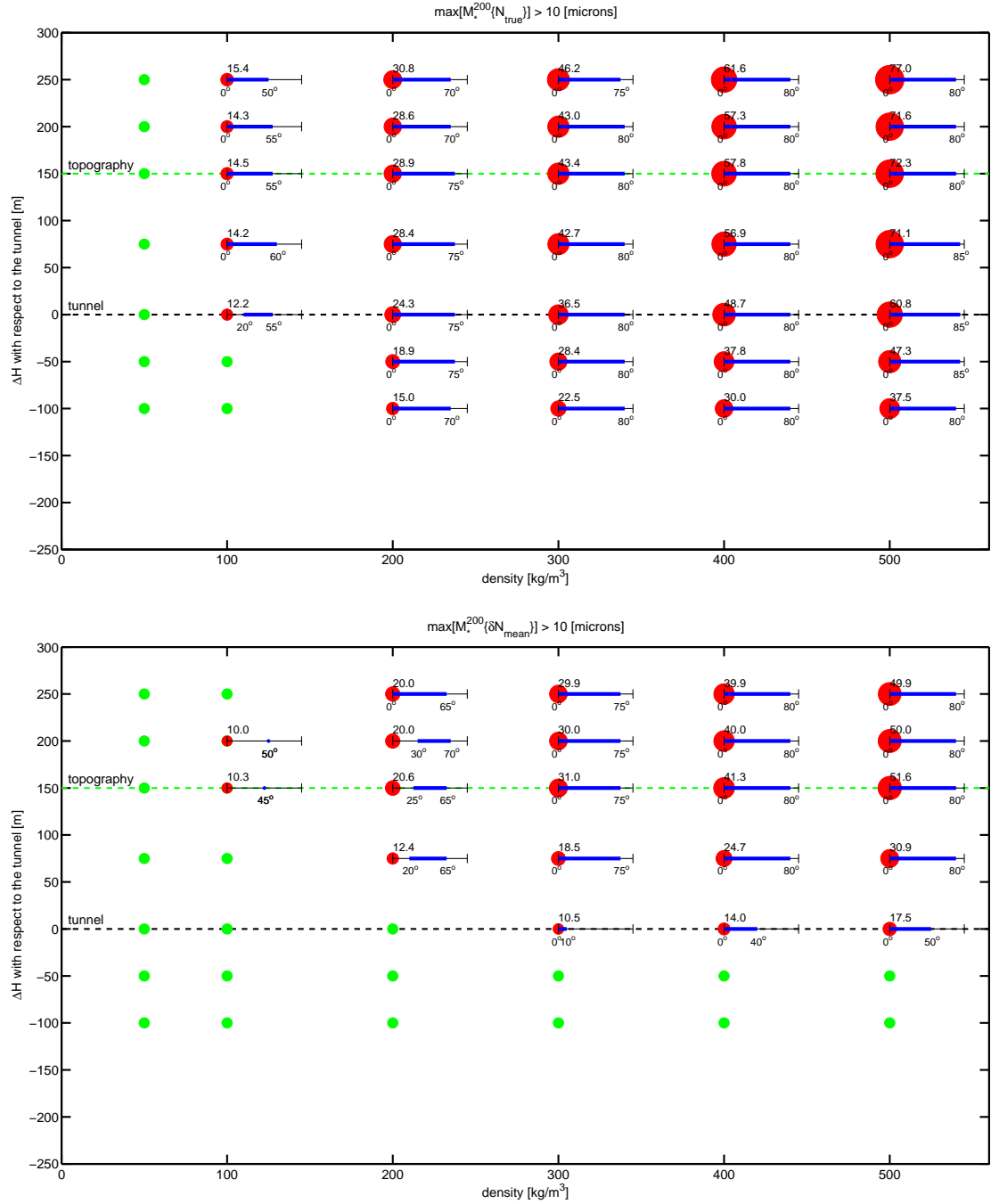


**Figure 6.11:** Representation of the misalignment analyses contained in Table 6.4 for  $N_{\text{true}}$  (upper) and  $\delta N_{\text{mean}}$  (lower) only. Each dot represents the results of a subset of  $\text{SLAB}_i(\beta_{\text{SLAB}})$  simulations. A dot is positioned as a function of its density  $\rho_{\text{SLAB}}$  (x-axis) and its height separation with respect to the tunnel (y-axis),  $H_{\text{SLAB}} + \Delta H_{\text{SLAB}} - H(\rho_o)$ . A green dot means that the maximal misalignment is smaller than 10 microns for all angles  $\beta_{\text{SLAB}}$ . In opposition, the red dots represent  $\text{SLAB}$  which contain maximal misalignments larger than 10 microns. They are scaled proportionally to the maximal misalignment. In addition, the horizontal blue bar represents the angle  $\beta_{\text{SLAB}}$  for which the maximal misalignment is larger than 10 microns.

### 6.3.4 Misalignment Analyses due to SIN Anomalies

#### A Significant Observable Anomaly

The anomaly  $\text{SIN}(+0 \text{ m}, +150 \text{ m}, +140 \text{ m}, 850 \text{ m}, +500 \frac{\text{kg}}{\text{m}^3})$  produces a significant misalignment over 200 meters but can be determined with sufficient accuracy.

The anomaly, the different solutions of the equipotential profile and the differences with respect to the true profile are shown in Figure 6.12.

The misalignments of the true equipotential  $\mathcal{M}_\star^\star\{N_{\text{true}}\}$  are represented as a function of the wavelength (middle), the position, and for the particular wavelength equal to 200 meters  $\mathcal{M}_\star^{200}\{N_{\text{true}}\}$  (lower) in Figure 6.13. The latter shows clearly that this anomaly cannot be neglected, because it generates significant misalignments larger than 10 micrometers over 200 meters.

The remaining misalignments  $\mathcal{M}_\star^\star\{\delta N_{\text{mean}}\}$  and  $\mathcal{M}_\star^{200}\{\delta N_{\text{mean}}\}$ , generated by the difference between the equipotential surface determined by astrogravimetric levelling  $N_{\text{mean}}$ , and the true equipotential  $N_{\text{true}}$  are shown in Figure 6.14. The latter shows clearly that it is theoretically possible to determine the equipotential profile with sufficient accuracy when astrogeodetic deflections of the vertical and gravimetric measurements are carried out on the topography and in the tunnel.

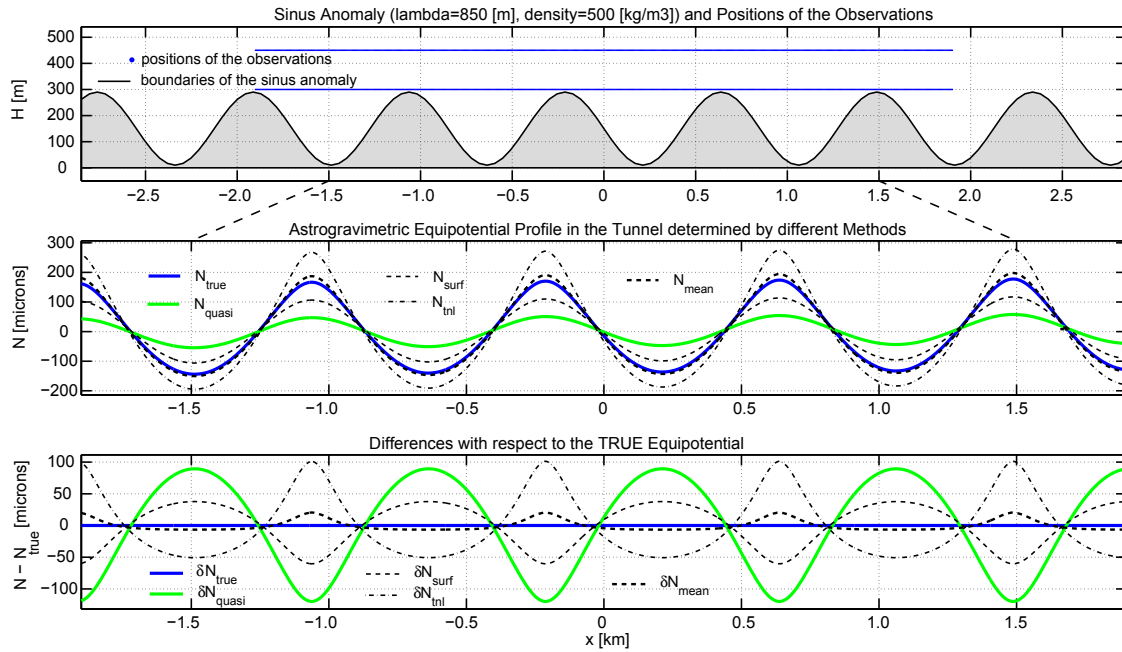


**Figure 6.12:** (Upper)  $\text{SIN}(+0 \text{ m}, +150 \text{ m}, +140 \text{ m}, 850 \text{ m}, +500 \frac{\text{kg}}{\text{m}^3})$  in black and  $\rho_o, \rho_{\text{surf}}$  in blue. (Middle) equipotential profiles  $N_{\text{true}}, N_{\text{quasi}}, N_{\text{surf}}, N_{\text{tnl}}, N_{\text{mean}}$ . (Lower) equipotential profile errors  $\delta N_{\text{true}}, \delta N_{\text{quasi}}, \delta N_{\text{surf}}, \delta N_{\text{tnl}}, \delta N_{\text{mean}}$ .

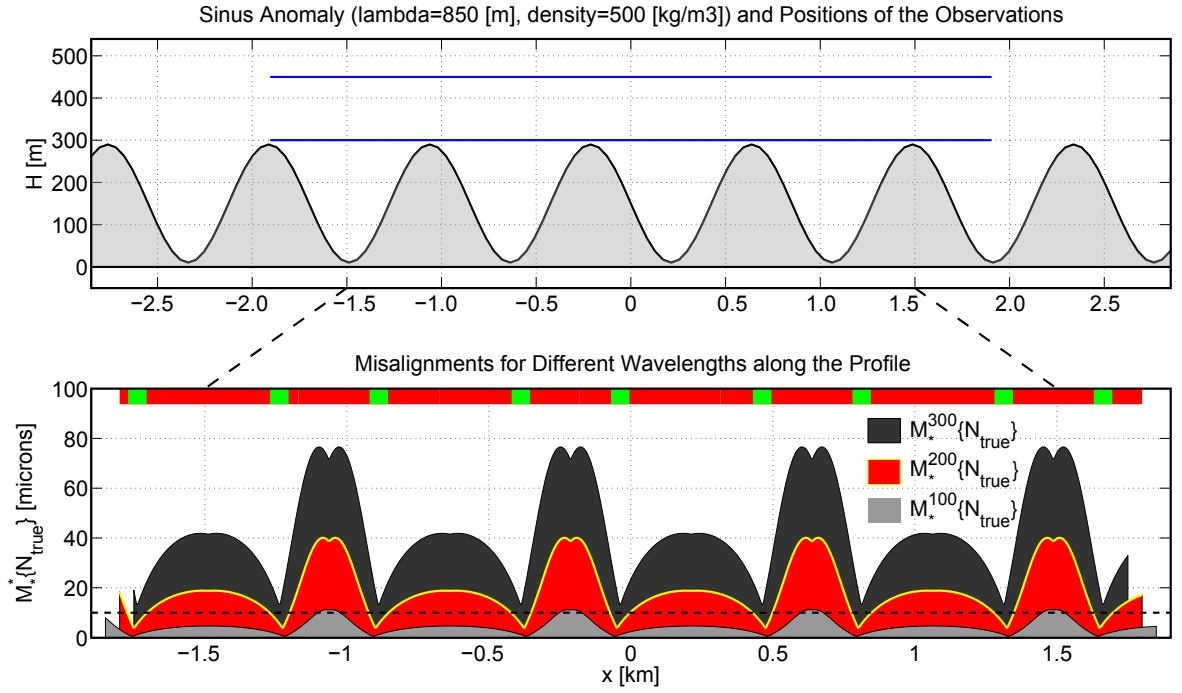


**Figure 6.13:** Misalignment of the true equipotential  $\mathcal{M}_{\star}^*\{N_{true}\}$  as a function of several wavelengths (middle), and for the wavelength equal to 200 meters  $\mathcal{M}_{\star}^{200}\{N_{true}\}$  (lower) generated by  $\text{SIN}(+0 \text{ m}, +150 \text{ m}, +140 \text{ m}, 850 \text{ m}, +500 \frac{\text{kg}}{\text{m}^3})$ .

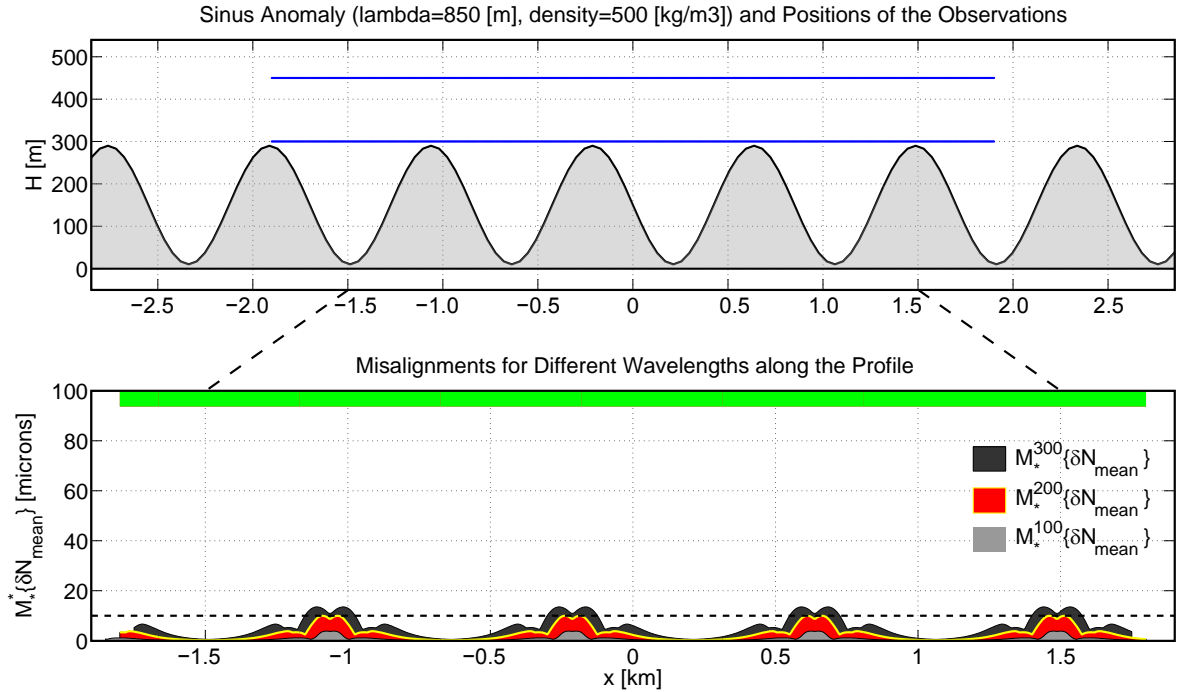


**Figure 6.14:** Remaining misalignment  $\mathcal{M}_{\star}^*\{\delta N_{mean}\}$  as a function of several wavelengths (middle), and for the wavelength equal to 200 meters  $\mathcal{M}_{\star}^{200}\{\delta N_{mean}\}$  (lower) generated by  $\text{SIN}(+0 \text{ m}, +150 \text{ m}, +140 \text{ m}, 850 \text{ m}, +500 \frac{\text{kg}}{\text{m}^3})$ .

### A non-Significant non-Observable Anomaly $\Rightarrow$ Significant Artifacts

On the one hand, the anomaly  $\text{SIN}(+0 \text{ m}, +450 \text{ m}, +100 \text{ m}, 240 \text{ m}, +200 \frac{\text{kg}}{\text{m}^3})$  produces non-significant misalignment over 200 meters. But on the other hand, it also implies that the various astrogravimetric strategies proposed in this thesis, give completely wrong results and produce significant artifacts.

The anomaly, the different solutions of the equipotential profiles and the differences with respect to the true profile are shown in Figure 6.15 .

The misalignments of the true equipotential  $\mathcal{M}_\star^\star\{N_{\text{true}}\}$  are represented in figure 6.16, as a function of the wavelength (middle), the position, and for the particular wavelength equal to 200 meters  $\mathcal{M}_\star^{200}\{N_{\text{true}}\}$  (lower). The latter shows clearly that this anomaly generates non-significant misalignments, smaller than 10 micrometers, over 200 meters.

In Figure 6.17, the remaining misalignments  $\mathcal{M}_\star^\star\{\delta N_{\text{mean}}\}$  and  $\mathcal{M}_\star^{200}\{\delta N_{\text{mean}}\}$ , generated by the difference between the equipotential surface determined by observations  $N_{\text{mean}}$  and the true equipotential  $N_{\text{true}}$ . The latter shows clearly that the determination  $N_{\text{mean}}$  is wrong and cannot determine this equipotential profile with sufficient accuracy. In this specific case, it may sound like a paradox, but a tentative of determining the equipotential profile from observation is counterproductive! The unique source of errors comes from the determination of the mean gravity along the plumbline as it can be expected and as it has been explained in Section 4.4.3.

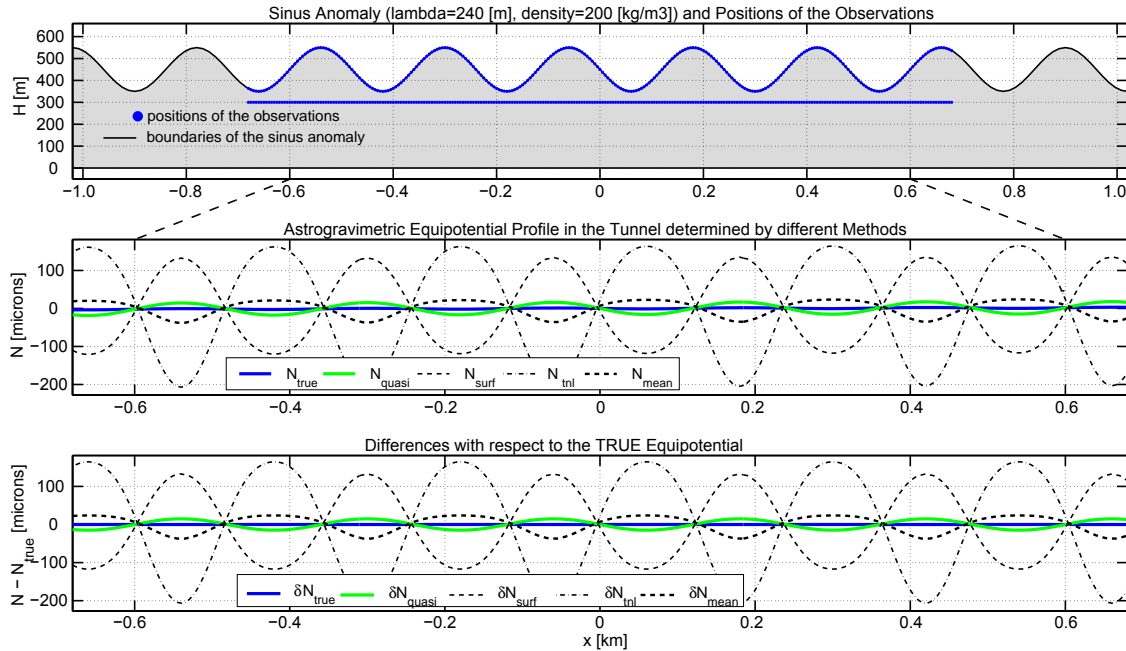


**Figure 6.15:** (Upper)  $\text{SIN}(+0 \text{ m}, +450 \text{ m}, +100 \text{ m}, 240 \text{ m}, +200 \frac{\text{kg}}{\text{m}^3})$  in black and  $\rho_o, \rho_{\text{surf}}$  in blue. (Middle) equipotential profiles  $N_{\text{true}}, N_{\text{quasi}}, N_{\text{surf}}, N_{\text{tnl}}, N_{\text{mean}}, N_{\text{lsc}}$ . (Lower) equipotential profile errors  $\delta N_{\text{true}}, \delta N_{\text{quasi}}, \delta N_{\text{surf}}, \delta N_{\text{tnl}}, \delta N_{\text{mean}}, \delta N_{\text{lsc}}$ .

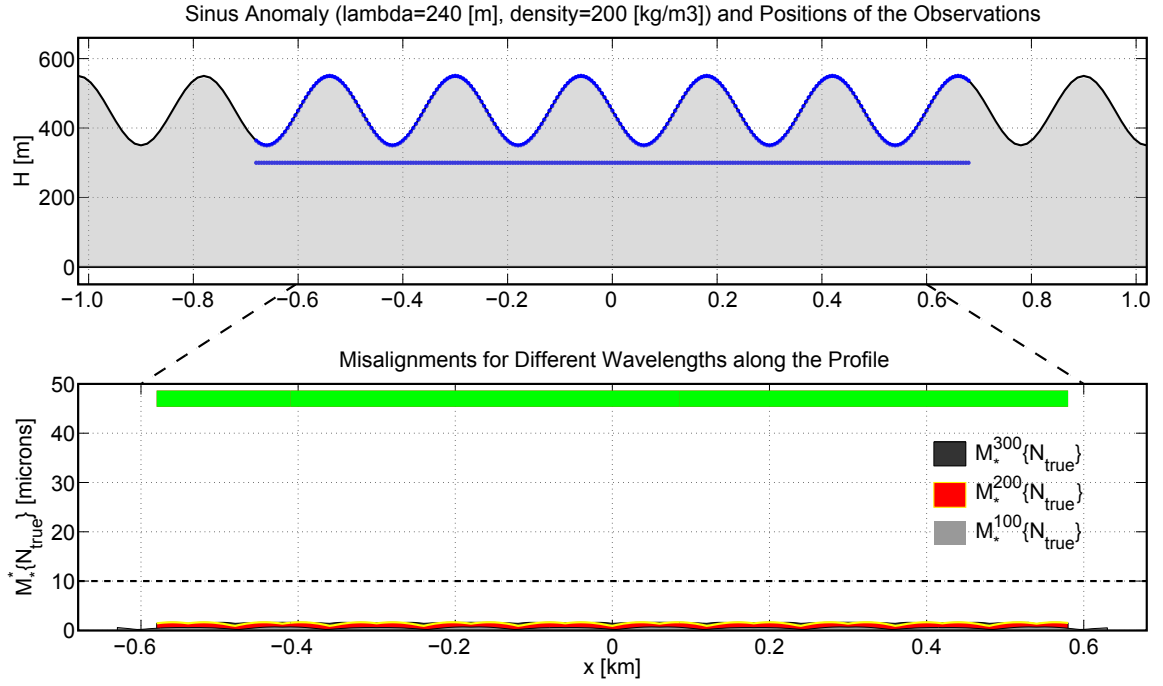


**Figure 6.16:** Misalignment of the true equipotential  $\mathcal{M}_*^*\{N_{true}\}$  as a function of several wavelengths (middle), and for the wavelength equal to 200 meters  $\mathcal{M}_*^{200}\{N_{true}\}$  (lower) generated by  $\text{SIN}(+0 \text{ m}, +450 \text{ m}, +100 \text{ m}, 240 \text{ m}, +200 \frac{\text{kg}}{\text{m}^3})$ .

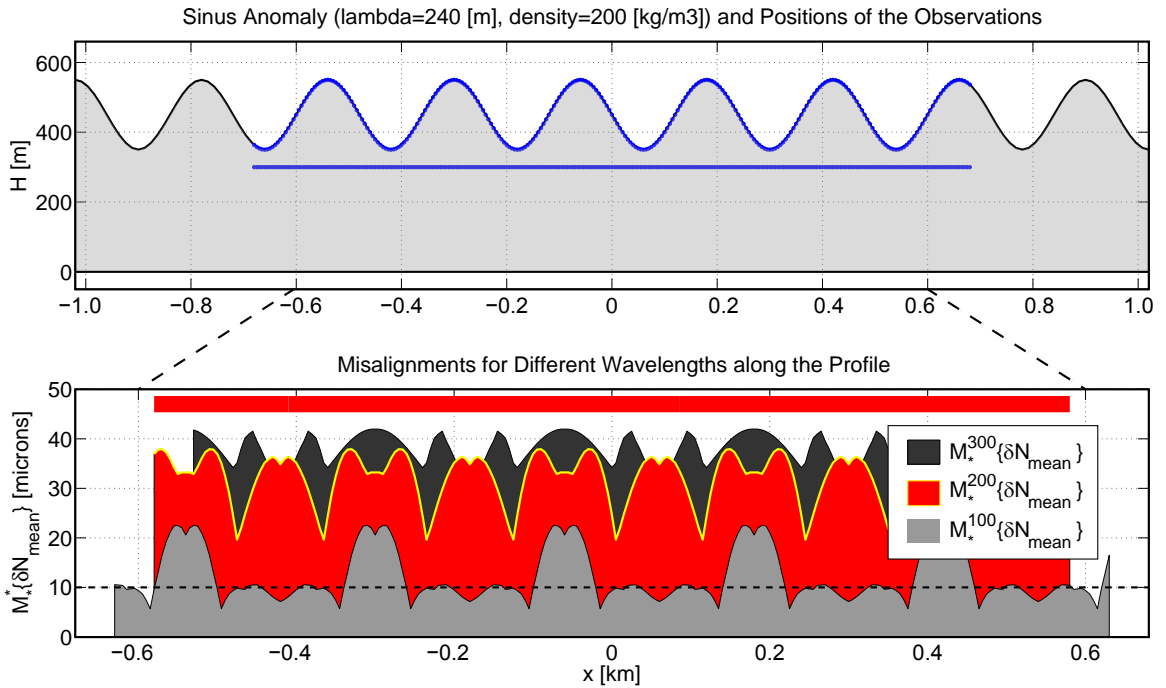


**Figure 6.17:** Remaining misalignment  $\mathcal{M}_*^*\{\delta N_{mean}\}$  as a function of several wavelengths (middle), and for the wavelength equal to 200 meters  $\mathcal{M}_*^{200}\{\delta N_{mean}\}$  (lower) generated by  $\text{SIN}(+0 \text{ m}, +450 \text{ m}, +100 \text{ m}, 240 \text{ m}, +200 \frac{\text{kg}}{\text{m}^3})$ .

### Systematic Analysis of SIN Anomalies

In this section, several SIN anomalies are analyzed:

**Table 6.5:** List of SIN anomalies used for systematic analyses. Here an object  $\text{SIN}_i$  does not represents a single SIN anomaly but represents a set of sinus anomalies.

$\{\text{SIN}\}$	$H0_{\text{SIN}}$	$H_{\text{SIN}}$	$A_{\text{SIN}}$	$\lambda_{\text{SIN}}$	$\rho_{\text{SIN}}$	$H_{\text{SIN}} + \Delta H_{\text{SIN}} - H(\rho_o)$	topography	mass between $\rho_o \rightarrow \rho_{\text{surf}}$
	[m]	[m]	[m]	[deg]	$\left[\frac{\text{kg}}{\text{m}^3}\right]$	[m]		
$\text{SIN}_1$	0	150	10	[60,10000]	[50,500]	-140	flat	no
$\text{SIN}_2$	0	150	50	[60,10000]	[50,500]	-100	flat	no
$\text{SIN}_3$	0	150	100	[60,10000]	[50,500]	-50	flat	no
$\text{SIN}_4$	0	150	140	[60,10000]	[50,500]	-10	flat	no
$\text{SIN}_5$	0	200	10	[60,10000]	[50,500]	-90	flat	no
$\text{SIN}_6$	0	200	50	[60,10000]	[50,500]	-50	flat	no
$\text{SIN}_7$	0	200	75	[60,10000]	[50,500]	-25	flat	no
$\text{SIN}_8$	0	200	90	[60,10000]	[50,500]	-10	flat	no
$\text{SIN}_9$	0	250	10	[60,10000]	[50,500]	-40	flat	no
$\text{SIN}_{10}$	0	250	20	[60,10000]	[50,500]	-30	flat	no
$\text{SIN}_{11}$	0	250	30	[60,10000]	[50,500]	-20	flat	no
$\text{SIN}_{12}$	0	250	40	[60,10000]	[50,500]	-10	flat	no
$\text{SIN}_{13}$	0	300	10	[60,10000]	[50,500]	10	flat	yes
$\text{SIN}_{14}$	0	300	50	[60,10000]	[50,500]	50	flat	yes
$\text{SIN}_{15}$	0	300	100	[60,10000]	[50,500]	100	flat	yes
$\text{SIN}_{16}$	0	300	140	[60,10000]	[50,500]	140	flat	yes
$\text{SIN}_{17}$	0	375	10	[60,10000]	[50,500]	85	flat	yes
$\text{SIN}_{18}$	0	375	25	[60,10000]	[50,500]	100	flat	yes
$\text{SIN}_{19}$	0	375	50	[60,10000]	[50,500]	125	flat	yes
$\text{SIN}_{20}$	0	375	70	[60,10000]	[50,500]	145	flat	yes
$\text{SIN}_{21}$	0	450	10	[60,10000]	[50,500]	160	sinus	yes
$\text{SIN}_{22}$	0	450	25	[60,10000]	[50,500]	175	sinus	yes
$\text{SIN}_{23}$	0	450	50	[60,10000]	[50,500]	200	sinus	yes
$\text{SIN}_{24}$	0	450	70	[60,10000]	[50,500]	220	sinus	yes
$\text{SIN}_{25}$	0	800	10	[60,10000]	[50,500]	510	sinus	yes
$\text{SIN}_{26}$	0	800	25	[60,10000]	[50,500]	525	sinus	yes
$\text{SIN}_{27}$	0	800	50	[60,10000]	[50,500]	550	sinus	yes
$\text{SIN}_{28}$	0	800	70	[60,10000]	[50,500]	570	sinus	yes

The results are presented in Tables 6.6, 6.7, 6.8, 6.9, 6.10, 6.11 and 6.12, and in Figures 6.18, 6.19, 6.20, 6.21, 6.22, 6.23 and 6.24.



**Table 6.6:** Systematic misalignment analyses of  $\text{SIN}_1 \rightarrow \text{SIN}_4$ . The maximal misalignments larger than 10 microns are listed for  $N_{\text{true}}$ ,  $\delta N_{\text{quasi}}$  and  $\delta N_{\text{mean}}$  only.

$\{\text{SIN}\}$	$\max [\mathcal{M}_{\star}^{200} \{N_{\text{true}}\}]$ $> 10\mu\text{m}$ $\left[\frac{\rho_{\text{SIN}}}{\frac{\text{kg}}{\text{m}^3}}, [\text{m}, \text{m}], [\mu\text{m}]\right]$			$\max [\mathcal{M}_{\star}^{200} \{\delta N_{\text{quasi}}\}]$ $> 10\mu\text{m}$ $\left[\frac{\rho_{\text{SIN}}}{\frac{\text{kg}}{\text{m}^3}}, [\text{m}, \text{m}], [\mu\text{m}]\right]$			$\max [\mathcal{M}_{\star}^{200} \{\delta N_{\text{mean}}\}]$ $> 10\mu\text{m}$ $\left[\frac{\rho_{\text{SIN}}}{\frac{\text{kg}}{\text{m}^3}}, [\text{m}, \text{m}], [\mu\text{m}]\right]$			best
$\text{SIN}_1$	✓			✓			✓			$N_{\text{mean}}$
$\text{SIN}_2$	✓			✓			✓			$N_{\text{mean}}$
$\text{SIN}_3$	300	[500,2000]	13.6	400	[450,1000]	13.3	✓			$N_{\text{mean}}$
	400	[400,3000]	18.1	500	[360,1000]	16.6				
	500	[360,3000]	22.6							
$\text{SIN}_4$	200	[400,2000]	16.0	200	[450,1000]	12.6	400 [240,700] 12.5 500 [180,800] 15.6			$N_{\text{mean}}$
	300	[300,3000]	24.0	300	[320,1000]	18.9				
	400	[260,4000]	32.0	400	[280,1000]	25.2				
	500	[240,6000]	40.1	500	[240,2000]	31.5				

**Table 6.7:** Systematic misalignment analyses of  $\text{SIN}_5 \rightarrow \text{SIN}_8$ . The maximal misalignments larger than 10 microns are listed for  $N_{\text{true}}$ ,  $\delta N_{\text{quasi}}$  and  $\delta N_{\text{mean}}$  only.

$\{\text{SIN}\}$	$\max [\mathcal{M}_{\star}^{200} \{N_{\text{true}}\}]$ $> 10\mu\text{m}$ $\left[\frac{\rho_{\text{SIN}}}{\frac{\text{kg}}{\text{m}^3}}, [\text{m}, \text{m}], [\mu\text{m}]\right]$			$\max [\mathcal{M}_{\star}^{200} \{\delta N_{\text{quasi}}\}]$ $> 10\mu\text{m}$ $\left[\frac{\rho_{\text{SIN}}}{\frac{\text{kg}}{\text{m}^3}}, [\text{m}, \text{m}], [\mu\text{m}]\right]$			$\max [\mathcal{M}_{\star}^{200} \{\delta N_{\text{mean}}\}]$ $> 10\mu\text{m}$ $\left[\frac{\rho_{\text{SIN}}}{\frac{\text{kg}}{\text{m}^3}}, [\text{m}, \text{m}], [\mu\text{m}]\right]$			best
$\text{SIN}_5$	✓			✓			✓			$N_{\text{mean}}$
$\text{SIN}_6$	400	[500,1000]	11.4	500	[400,800]	11.6	✓			$N_{\text{mean}}$
	500	[380,1000]	14.3							
$\text{SIN}_7$	300	[360,1000]	14.7	300	[380,900]	12.2	500 [300,400] 10.5			$N_{\text{mean}}$
	400	[300,2000]	24.5	400	[300,1000]	16.2				
	500	[260,3000]	24.5	500	[280,1000]	20.3				
$\text{SIN}_8$	200	[400,1000]	13.0	200	[450,750]	10.9	400 [200,550] 12.2 500 [160,650] 15.2			$N_{\text{mean}}$
	300	[300,2000]	19.5	300	[300,1000]	16.4				
	400	[260,3000]	26.0	400	[260,1000]	21.9				
	500	[220,3000]	32.5	500	[220,1000]	27.3				

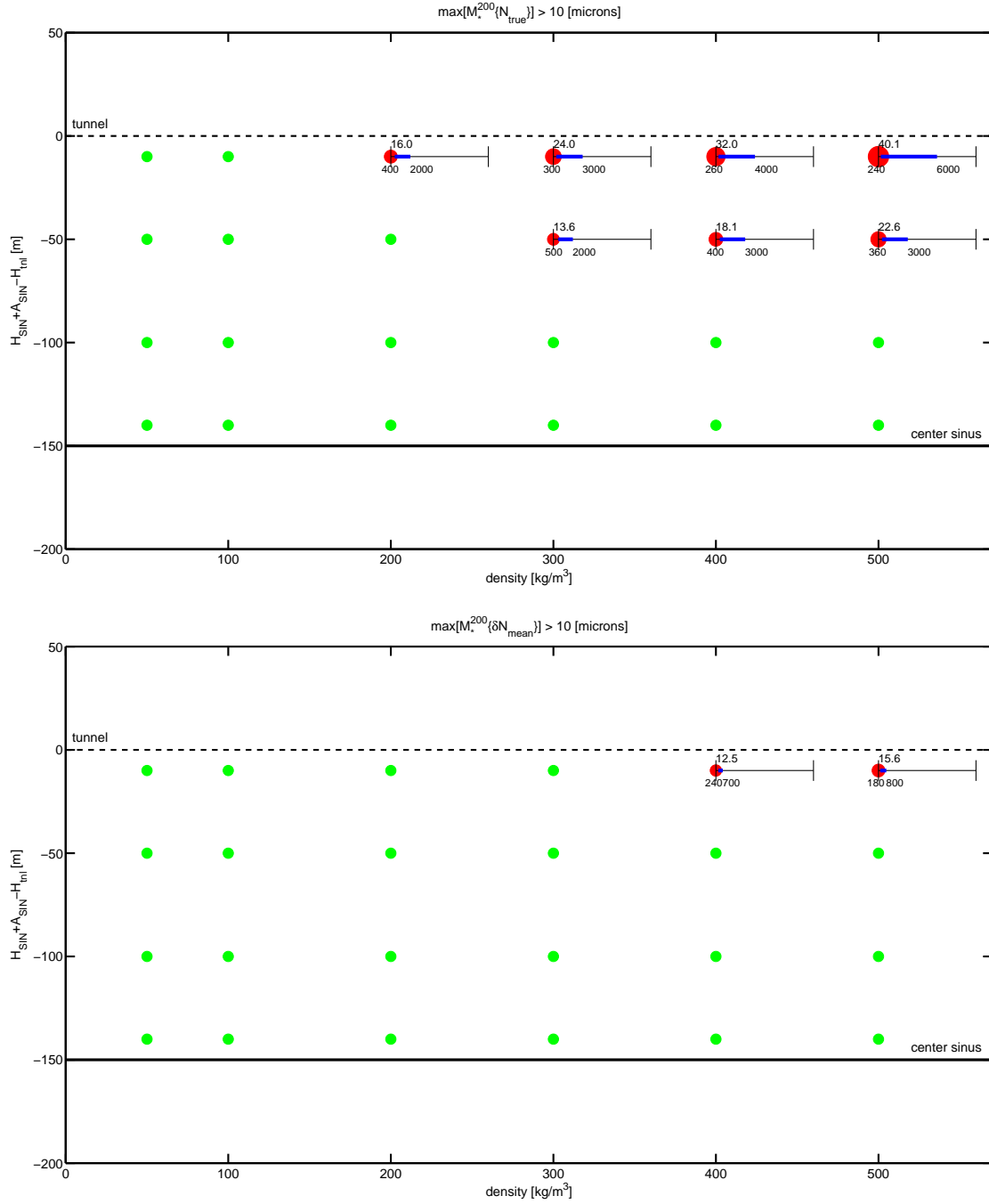


**Figure 6.18:** Representation of the misalignment analyses contained in Table 6.6 for  $N_{\text{true}}$  (upper) and  $\delta N_{\text{mean}}$  (lower) only. Each dot represents the results of a subset of  $\text{SIN}_i(\lambda_{\text{SIN}})$ . A dot is positioned as a function of its density  $\rho_{\text{SIN}}$  (x-axis) and its height separation with respect to the tunnel (y-axis),  $H_{\text{SIN}} + A_{\text{SLAB}} - H(\rho_o)$ . The position of the center of the sinus is represented by a black line. A green dot means that the maximal misalignment is smaller than 10 microns for all wavelengths  $\lambda_{\text{SIN}}$ . In opposition, the red dots represent  $\text{SIN}$  which contain maximal misalignments larger than 10 microns. They are scaled proportionally to the maximal misalignment. In addition, the horizontal blue bar represents the wavelength  $\lambda_{\text{SIN}}$  for which the maximal misalignment is larger than 10 microns.

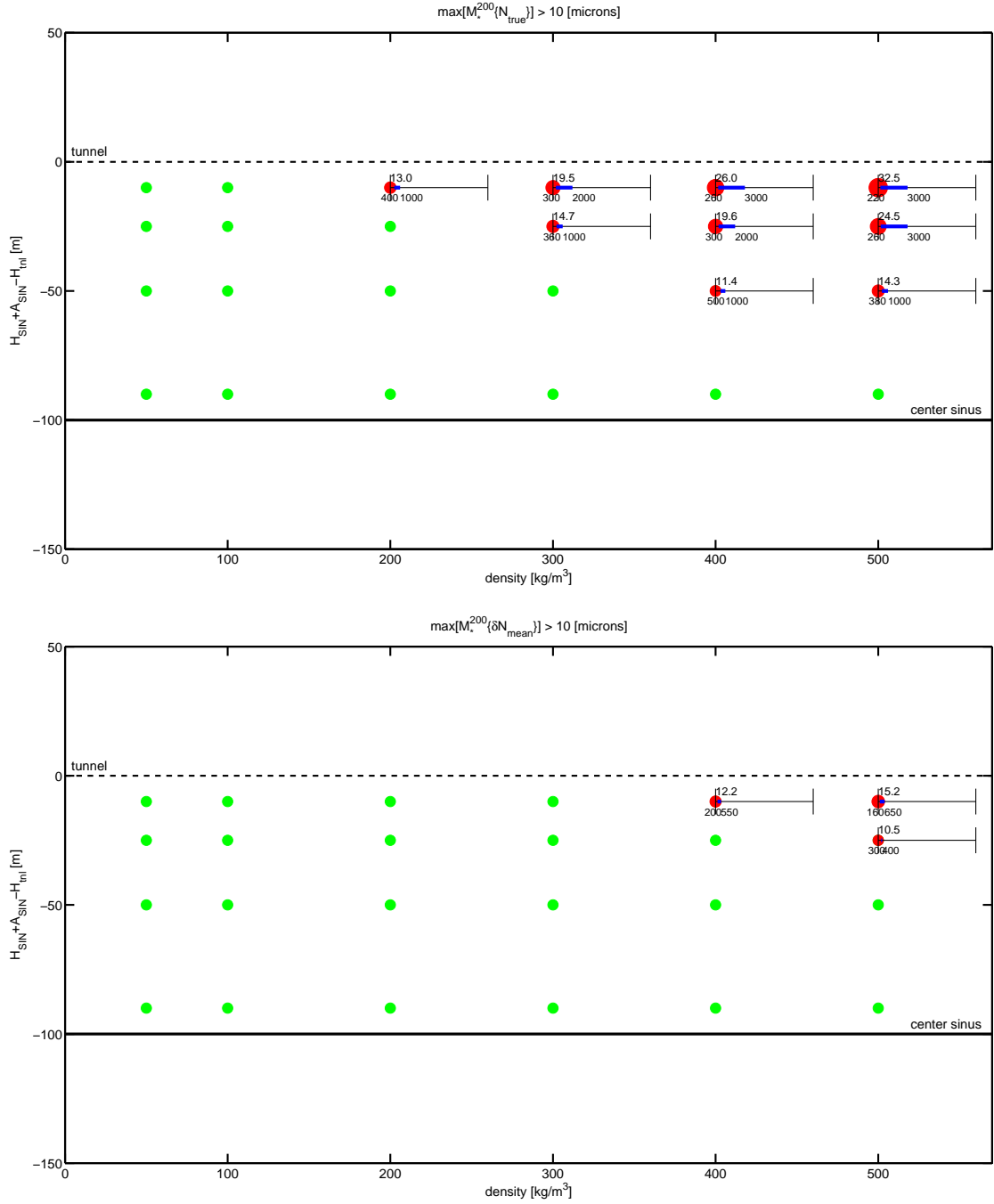


**Figure 6.19:** Representation of the misalignment analyses contained in Table 6.7 for  $N_{\text{true}}$  (upper) and  $\delta N_{\text{mean}}$  (lower) only. Each dot represents the results of a subset of  $\text{SIN}_i(\lambda_{\text{SIN}})$ . A dot is positioned as a function of its density  $\rho_{\text{SIN}}$  (x-axis) and its height separation with respect to the tunnel (y-axis),  $H_{\text{SIN}} + A_{\text{SLAB}} - H(\rho_0)$ . The position of the center of the sinus is represented by a black line. A green dot means that the maximal misalignment is smaller than 10 microns for all wavelengths  $\lambda_{\text{SIN}}$ . In opposition, the red dot represents SIN which contain maximal misalignments larger than 10 microns. They are scaled proportionally to the maximal misalignment. In addition, the horizontal blue bar represents the wavelength  $\lambda_{\text{SIN}}$  for which the maximal misalignment is larger than 10 microns.

**Table 6.8:** Systematic misalignment analyses of  $\text{SIN}_9 \rightarrow \text{SIN}_{12}$ . The maximal misalignment larger as 10 microns are listed for  $N_{\text{true}}$ ,  $\delta N_{\text{quasi}}$  and  $\delta N_{\text{mean}}$  only.

$\{\text{SIN}\}$	$\max [\mathcal{M}_{\star}^{200} \{N_{\text{true}}\}]$ $> 10\mu\text{m}$ $\rho_{\text{SIN}}, \lambda_{\text{SIN}}, \mathcal{M}_{\star}^{200}$ $\left[\frac{\text{kg}}{\text{m}^3}\right], [\text{m}, \text{m}], [\mu\text{m}]$			$\max [\mathcal{M}_{\star}^{200} \{\delta N_{\text{quasi}}\}]$ $> 10\mu\text{m}$ $\rho_{\text{SIN}}, \lambda_{\text{SIN}}, \mathcal{M}_{\star}^{200}$ $\left[\frac{\text{kg}}{\text{m}^3}\right], [\text{m}, \text{m}], [\mu\text{m}]$			$\max [\mathcal{M}_{\star}^{200} \{\delta N_{\text{mean}}\}]$ $> 10\mu\text{m}$ $\rho_{\text{SIN}}, \lambda_{\text{SIN}}, \mathcal{M}_{\star}^{200}$ $\left[\frac{\text{kg}}{\text{m}^3}\right], [\text{m}, \text{m}], [\mu\text{m}]$			best
$\text{SIN}_9$	✓			✓			✓			$N_{\text{mean}}$
$\text{SIN}_{10}$	✓			✓			✓			$N_{\text{mean}}$
$\text{SIN}_{11}$	400	[320,750]	11.8	400	[360,500]	10.5	✓			$N_{\text{mean}}$
	500	[280,1000]	14.8	500	[280,650]	13.1				
$\text{SIN}_{12}$	300	[320,800]	12.6	300	[320,550]	11.2	400 [180,320] 11.6 500 [140,400] 14.5			$N_{\text{mean}}$
	400	[260,1000]	16.8	400	[260,800]	14.9				
	500	[220,1000]	21.0	500	[220,950]	18.6				

**Table 6.9:** Systematic misalignment analyses of  $\text{SIN}_{13} \rightarrow \text{SIN}_{16}$ . The maximal misalignment larger than 10 microns are listed for  $N_{\text{true}}$ ,  $\delta N_{\text{quasi}}$  and  $\delta N_{\text{mean}}$  only.

$\{\text{SIN}\}$	$\max [\mathcal{M}_{\star}^{200} \{N_{\text{true}}\}]$ $> 10\mu\text{m}$ $\rho_{\text{SIN}}, \lambda_{\text{SIN}}, \mathcal{M}_{\star}^{200}$ $\left[\frac{\text{kg}}{\text{m}^3}\right], [\text{m}, \text{m}], [\mu\text{m}]$			$\max [\mathcal{M}_{\star}^{200} \{\delta N_{\text{quasi}}\}]$ $> 10\mu\text{m}$ $\rho_{\text{SIN}}, \lambda_{\text{SIN}}, \mathcal{M}_{\star}^{200}$ $\left[\frac{\text{kg}}{\text{m}^3}\right], [\text{m}, \text{m}], [\mu\text{m}]$			$\max [\mathcal{M}_{\star}^{200} \{\delta N_{\text{mean}}\}]$ $> 10\mu\text{m}$ $\rho_{\text{SIN}}, \lambda_{\text{SIN}}, \mathcal{M}_{\star}^{200}$ $\left[\frac{\text{kg}}{\text{m}^3}\right], [\text{m}, \text{m}], [\mu\text{m}]$			best
$\text{SIN}_{13}$	✓			✓			300	[320,360]	10.1	$N_{\text{quasi}}$
							400	[200,450]	13.5	
							500	[180,500]	16.8	
$\text{SIN}_{14}$	200	[200,600]	14.2	200	[220,400]	13.2	200	[200,650]	19.7	$N_{\text{quasi}}$
	300	[180,1000]	21.4	300	[180,650]	19.8	300	[160,1000]	29.6	
	400	[140,1000]	28.5	400	[140,800]	26.4	400	[140,2000]	39.4	
	500	[140,1000]	35.6	500	[140,950]	33.0	500	[120,2000]	49.3	
$\text{SIN}_{15}$	100	[300,400]	10.4	200	[200,650]	17.6	200	[200,1000]	19.2	$N_{\text{quasi}}$
	200	[180,1000]	20.9				300	[160,2000]	28.7	
	300	[160,2000]	31.3				400	[140,4000]	38.3	
	400	[140,3000]	41.8				500	[120,5000]	47.9	
	500	[120,3000]	52.2							
$\text{SIN}_{16}$	100	[260,550]	11.8	200	[200,1000]	17.2	200	[260,550]	18.2	$N_{\text{quasi}}$
	200	[180,1000]	23.7	300	[180,1000]	25.8	300	[180,1000]	27.2	
	300	[160,2000]	35.5	400	[140,2000]	34.4	400	[160,2000]	36.3	
	400	[140,4000]	47.3	500	[140,2000]	43.0	500	[180,7000]	46.4	
	500	[120,5000]	59.2							

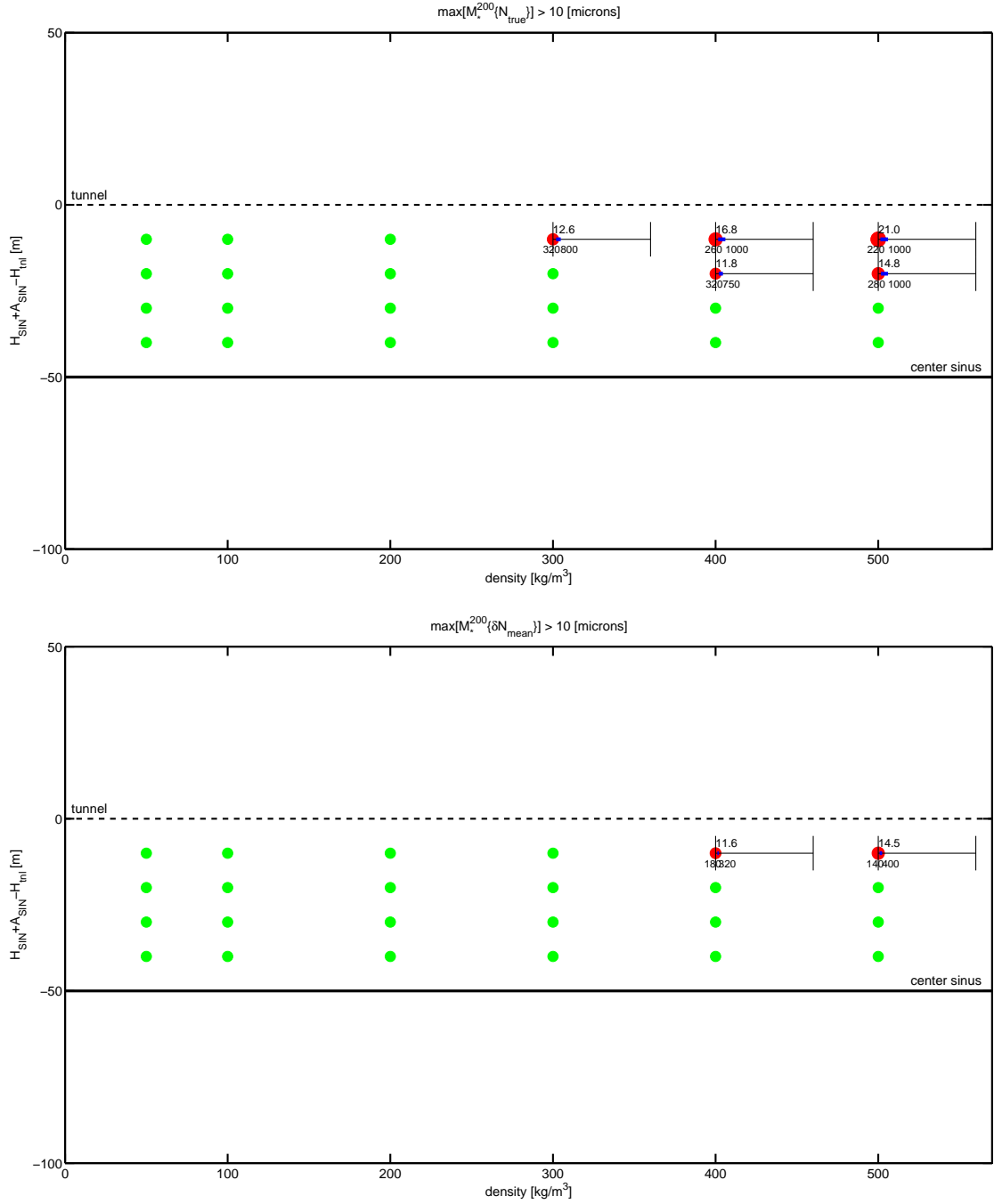


**Figure 6.20:** Representation of the misalignment analyses contained in table 6.8 for  $N_{\text{true}}$  (upper) and  $\delta N_{\text{mean}}$  (lower) only. Each dot represents the results of a subset of  $\text{SIN}_i(\lambda_{\text{SIN}})$ . A dot is positioned in function its density  $\rho_{\text{SIN}}$  (x-axis) and its height separation with respect to the tunnel (y-axis),  $H_{\text{SIN}} + A_{\text{SLAB}} - H(\rho_o)$ . The position of the center of the sinus is represented by a black line. A green dot means that the maximal misalignment is smaller than 10 microns for all wavelengths  $\lambda_{\text{SIN}}$ . In opposition, the red dots represents  $\text{SIN}$  which contains maximal misalignment larger than 10 microns. They are scaled proportionally to the maximal misalignment. In addition, the horizontal blue bar represents the wavelength  $\lambda_{\text{SIN}}$  for which the maximal misalignment is larger than 10 microns.

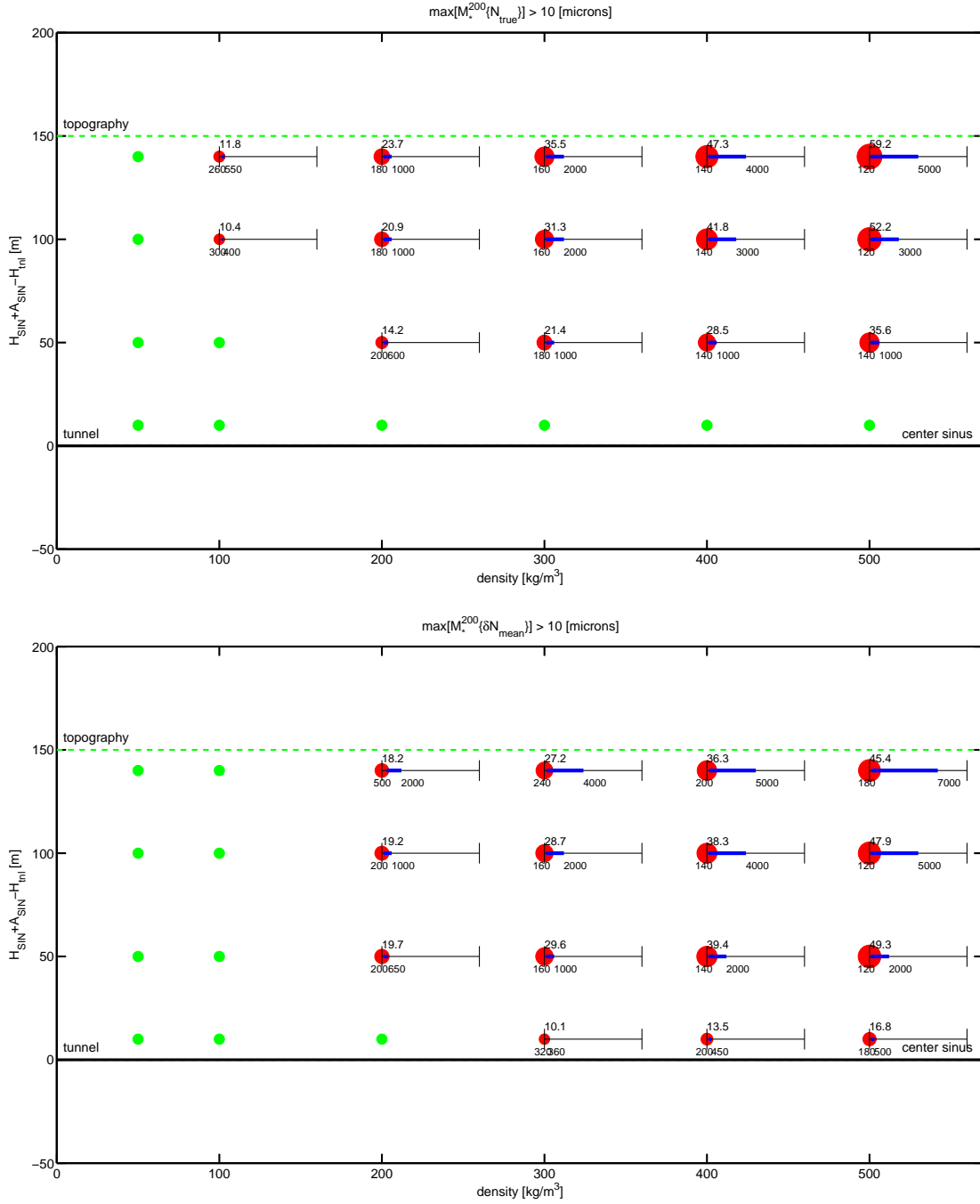


**Figure 6.21:** Representation of the misalignment analyses contained in Table 6.9 for  $N_{\text{true}}$  (upper) and  $\delta N_{\text{mean}}$  (lower) only. Each dot represents the results of a subset of  $\text{SIN}_i(\lambda_{\text{SIN}})$ . A dot is positioned as a function of its density  $\rho_{\text{SIN}}$  (x-axis) and its height separation with respect to the tunnel (y-axis),  $H_{\text{SIN}} + A_{\text{SIN}} - H(\rho_o)$ . The position of the center of the sinus is represented by a black line. A green dot means that the maximal misalignment is smaller than 10 microns for all wavelengths  $\lambda_{\text{SIN}}$ . In opposition, the red dot represents  $\text{SIN}$  which contain maximal misalignments larger than 10 microns. They are scaled proportionally to the maximal misalignment. In addition, the horizontal blue bar represents the wavelength  $\lambda_{\text{SIN}}$  for which the maximal misalignment is larger than 10 microns.

**Table 6.10:** Systematic misalignment analyses of  $\text{SIN}_{17} \rightarrow \text{SIN}_{20}$ . The maximal misalignment larger than 10 microns are listed for  $N_{\text{true}}$ ,  $\delta N_{\text{quasi}}$  and  $\delta N_{\text{mean}}$  only.

$\{\text{SIN}\}$	$\max [\mathcal{M}_{\star}^{200} \{N_{\text{true}}\}]$ $> 10\mu\text{m}$ $\rho_{\text{SIN}}, \lambda_{\text{SIN}}, \mathcal{M}_{\star}^{200}$ $\left[\frac{\text{kg}}{\text{m}^3}\right], [\text{m}, \text{m}], [\mu\text{m}]$			$\max [\mathcal{M}_{\star}^{200} \{\delta N_{\text{quasi}}\}]$ $> 10\mu\text{m}$ $\rho_{\text{SIN}}, \lambda_{\text{SIN}}, \mathcal{M}_{\star}^{200}$ $\left[\frac{\text{kg}}{\text{m}^3}\right], [\text{m}, \text{m}], [\mu\text{m}]$			$\max [\mathcal{M}_{\star}^{200} \{\delta N_{\text{mean}}\}]$ $> 10\mu\text{m}$ $\rho_{\text{SIN}}, \lambda_{\text{SIN}}, \mathcal{M}_{\star}^{200}$ $\left[\frac{\text{kg}}{\text{m}^3}\right], [\text{m}, \text{m}], [\mu\text{m}]$			best
$\text{SIN}_{17}$	✓			✓			✓			$N_{\text{mean}}$
$\text{SIN}_{18}$	✓			✓			✓			$N_{\text{mean}}$
$\text{SIN}_{19}$	300	[450,1000]	11.9	✓			400	[380,800]	12.9	$N_{\text{quasi}}$
	400	[300,1000]	15.8				500	[340,1000]	16.2	
	500	[260,1000]	19.8							
$\text{SIN}_{20}$	200	[380,1000]	12.7				200	[320,850]	14.3	$N_{\text{quasi}}$
	300	[260,1000]	19.0				300	[240,1000]	21.4	
	400	[220,2000]	25.4				400	[200,1000]	28.5	
	500	[200,2000]	31.7				500	[180,1000]	35.7	

**Table 6.11:** Systematic misalignment analyses of  $\text{SIN}_{21} \rightarrow \text{SIN}_{24}$ . The maximal misalignment larger than 10 microns are listed for  $N_{\text{true}}$ ,  $\delta N_{\text{quasi}}$  and  $\delta N_{\text{mean}}$  only.

$\{\text{SIN}\}$	$\max [\mathcal{M}_{\star}^{200} \{N_{\text{true}}\}]$ $> 10\mu\text{m}$ $\rho_{\text{SIN}}, \lambda_{\text{SIN}}, \mathcal{M}_{\star}^{200}$ $\left[\frac{\text{kg}}{\text{m}^3}\right], [\text{m}, \text{m}], [\mu\text{m}]$			$\max [\mathcal{M}_{\star}^{200} \{\delta N_{\text{quasi}}\}]$ $> 10\mu\text{m}$ $\rho_{\text{SIN}}, \lambda_{\text{SIN}}, \mathcal{M}_{\star}^{200}$ $\left[\frac{\text{kg}}{\text{m}^3}\right], [\text{m}, \text{m}], [\mu\text{m}]$			$\max [\mathcal{M}_{\star}^{200} \{\delta N_{\text{mean}}\}]$ $> 10\mu\text{m}$ $\rho_{\text{SIN}}, \lambda_{\text{SIN}}, \mathcal{M}_{\star}^{200}$ $\left[\frac{\text{kg}}{\text{m}^3}\right], [\text{m}, \text{m}], [\mu\text{m}]$			best
$\text{SIN}_{21}$	✓			✓			400	[60,200]	12.7	$N_{\text{quasi}}$
							500	[60,240]	15.9	
$\text{SIN}_{22}$	✓			300	[200,450]	13.8	200	[60,240]	16.7	no determ.
				400	[160,600]	18.4	300	[60,300]	25.0	
				500	[140,700]	23.0	400	[60,360]	33.3	
							500	[60,380]	41.5	
$\text{SIN}_{23}$	✓			200	[200,550]	15.6	100	[60,240]	16.3	no determ.
				300	[160,800]	23.4	200	[60,360]	32.6	
				400	[140,1000]	31.2	300	[60,450]	48.9	
				500	300	39.0	400	[60,500]	65.2	
							400	[60,550]	81.4	
$\text{SIN}_{24}$				100	[280,450]	10.7	50	[60,220]	14.0	no determ.
				300	[500,2000]	14.2	100	[60,400]	27.9	
				400	[450,3000]	18.9	200	[60,550]	55.9	
				500	[360,3000]	23.7	300	[60,700]	83.8	
							400	[60,800]	111.8	
							500	[60,850]	139.7	

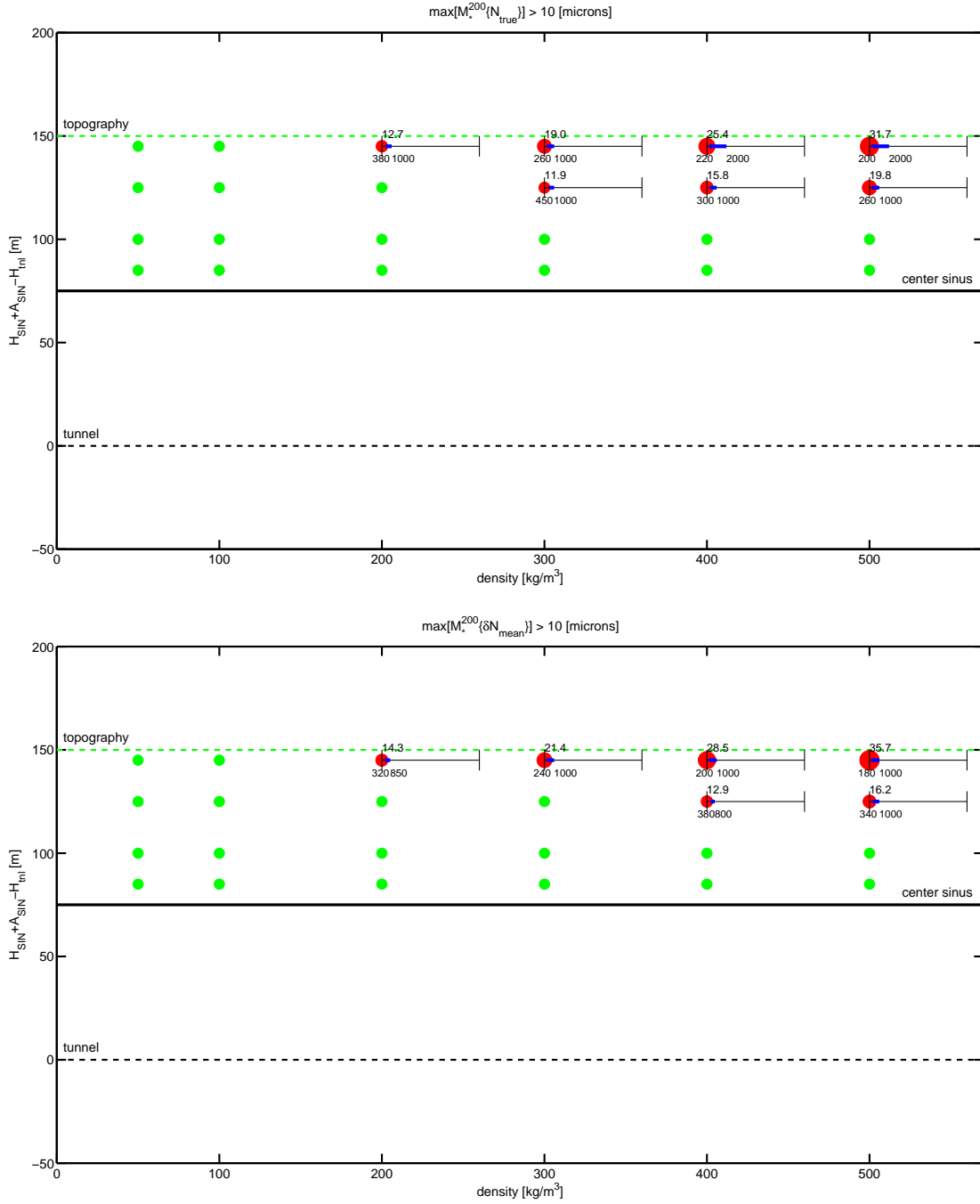


**Figure 6.22:** Representation of the misalignment analyses contained in Table 6.10 for  $N_{\text{true}}$  (upper) and  $\delta N_{\text{mean}}$  (lower) only. Each dot represents the results of a subset of  $\text{SIN}_i(\lambda_{\text{SIN}})$ . A dot is positioned as a function of its density  $\rho_{\text{SIN}}$  (x-axis) and its height separation with respect to the tunnel (y-axis),  $H_{\text{SIN}} + A_{\text{SLAB}} - H(\rho_o)$ . The position of the center of the sinus is represented by a black line. A green dot means that the maximal misalignment is smaller than 10 microns for all wavelengths  $\lambda_{\text{SIN}}$ . In opposition, the red dot represents  $\text{SIN}$  which contain maximal misalignments larger than 10 microns. They are scaled proportionally to the maximal misalignment. In addition, the horizontal blue bar represents the wavelength  $\lambda_{\text{SIN}}$  for which the maximal misalignment is larger than 10 microns.



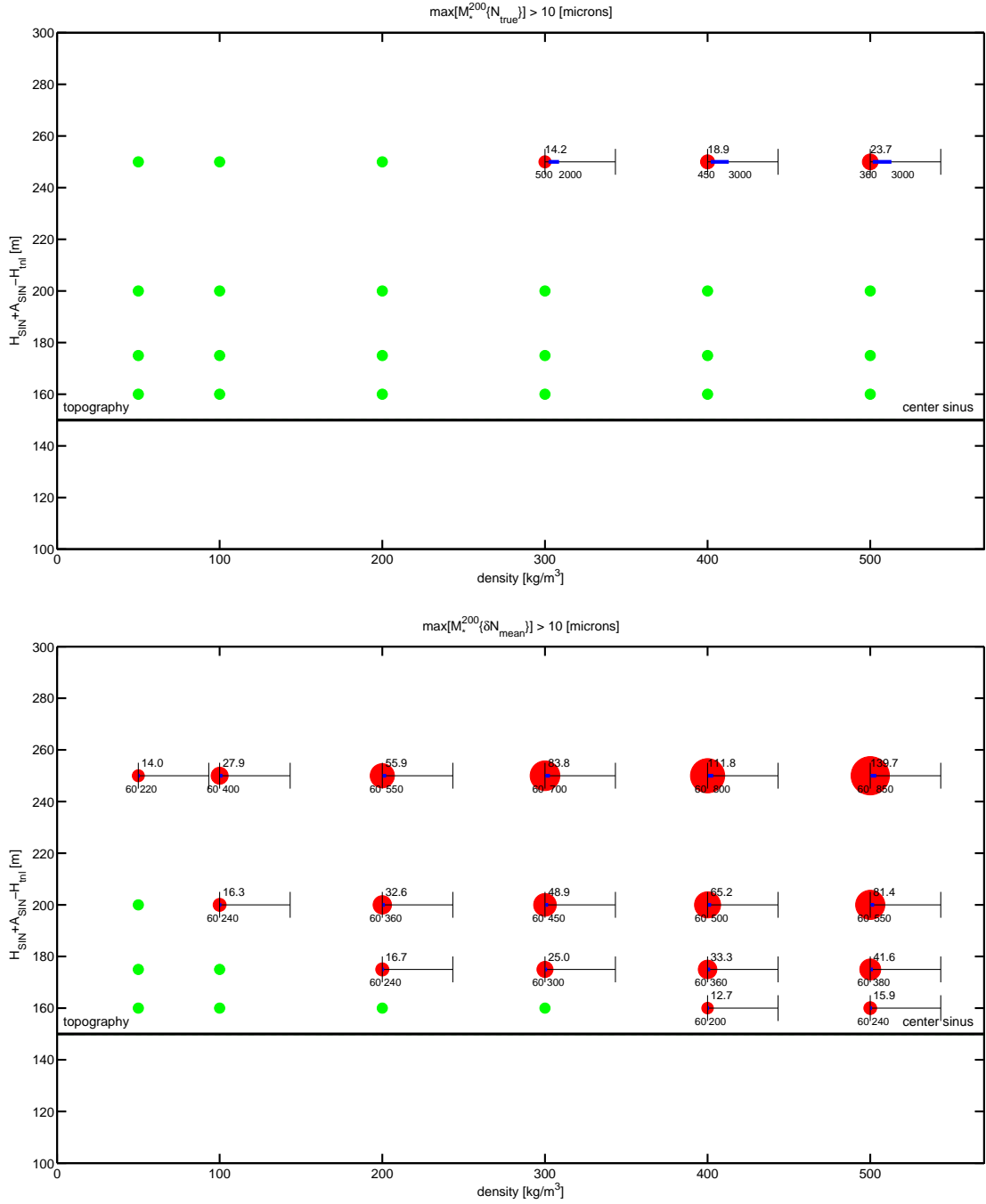


**Figure 6.23:** Representation of the misalignment analyses contained in Table 6.11 for  $N_{\text{true}}$  (upper) and  $\delta N_{\text{mean}}$  (lower) only. Each dot represents the results of a subset of  $\text{SIN}_i(\lambda_{\text{SIN}})$ . A dot is positioned as a function of its density  $\rho_{\text{SIN}}$  (x-axis) and its height separation with respect to the tunnel (y-axis),  $H_{\text{SIN}} + A_{\text{SLAB}} - H(\rho_o)$ . The position of the center of the sinus is represented by a black line. A green dot means that the maximal misalignment is smaller than 10 microns for all wavelengths  $\lambda_{\text{SIN}}$ . In opposition, the red dot represents  $\text{SIN}$  which contain maximal misalignments larger than 10 microns. They are scaled proportionally to the maximal misalignment. In addition, the horizontal blue bar represents the wavelength  $\lambda_{\text{SIN}}$  for which the maximal misalignment is larger than 10 microns.

**Table 6.12:** Systematic misalignment analyses of  $\text{SIN}_{25} \rightarrow \text{SIN}_{28}$ . The maximal misalignment larger than 10 microns are listed for  $N_{\text{true}}$ ,  $\delta N_{\text{quasi}}$  and  $\delta N_{\text{mean}}$  only.

$\{\text{SIN}\}$	$\max [\mathcal{M}_{\star}^{200} \{N_{\text{true}}\}]$ $> 10\mu\text{m}$ $\rho_{\text{SIN}}, \lambda_{\text{SIN}}, \mathcal{M}_{\star}^{200}$ $[\frac{\text{kg}}{\text{m}^3}], [\text{m}, \text{m}], [\mu\text{m}]$			$\max [\mathcal{M}_{\star}^{200} \{\delta N_{\text{quasi}}\}]$ $> 10\mu\text{m}$ $\rho_{\text{SIN}}, \lambda_{\text{SIN}}, \mathcal{M}_{\star}^{200}$ $[\frac{\text{kg}}{\text{m}^3}], [\text{m}, \text{m}], [\mu\text{m}]$			$\max [\mathcal{M}_{\star}^{200} \{\delta N_{\text{mean}}\}]$ $> 10\mu\text{m}$ $\rho_{\text{SIN}}, \lambda_{\text{SIN}}, \mathcal{M}_{\star}^{200}$ $[\frac{\text{kg}}{\text{m}^3}], [\text{m}, \text{m}], [\mu\text{m}]$			best
$\text{SIN}_{25}$	$\checkmark$			100	[240,700]	12.5	50	[60,650]	61.9	no determ.
				200	[180,1000]	25.1	100	[60,850]	123.9	
				300	[140,2000]	37.6	200	[60,1000]	247.8	
				400	[120,2000]	50.2	300	[60,1000]	371.7	
				500	[120,2000]	52.7	400	[60,1000]	495.6	
$\text{SIN}_{26}$	500	[2000,5000]	12.4				500	[60,1000]	619.5	no determ.
				100	[220,1000]	16.2	50	[60,950]	113.7	
				200	[160,2000]	32.4	100	[60,1000]	227.4	
				300	[140,3000]	48.6	200	[60,1000]	454.8	
				400	[120,4000]	64.8	300	[60,2000]	682.1	
$\text{SIN}_{27}$	300	[2000,5000]	12.7	500	[120,4000]	81.0	400	[60,4000]	909.5	no determ.
							500	[60,6000]	1136.9	
				100	[220,1000]	17.6	50	[60,1000]	153.5	
				200	[160,3000]	35.2	100	[60,1000]	307.1	
				300	[140,4000]	52.7	200	[60,3000]	614.2	
$\text{SIN}_{28}$	400	[2000,8000]	17.0	400	[120,5000]	70.3	300	[60,6000]	921.3	no determ.
				500	[120,6000]	87.9	400	[60,9000]	1228.3	
							500	[60,1000]	1535.1	
				200	[220,1000]	17.8	50	[60,1000]	181.9	
				300	[850,9000]	20.3	100	[60,2000]	363.7	
$\text{SIN}_{28}$	400	[750,10000]	27.0	200	[160,3000]	35.5	200	[60,5000]	727.4	no determ.
				300	[140,5000]	53.3	300	[60,10000]	1091.1	
				400	[120,7000]	71.1	400	[60,10000]	1454.8	
$\text{SIN}_{28}$	500	[650,10000]	33.8	500	[120,8000]	88.8	500	[60,10000]	1818.6	

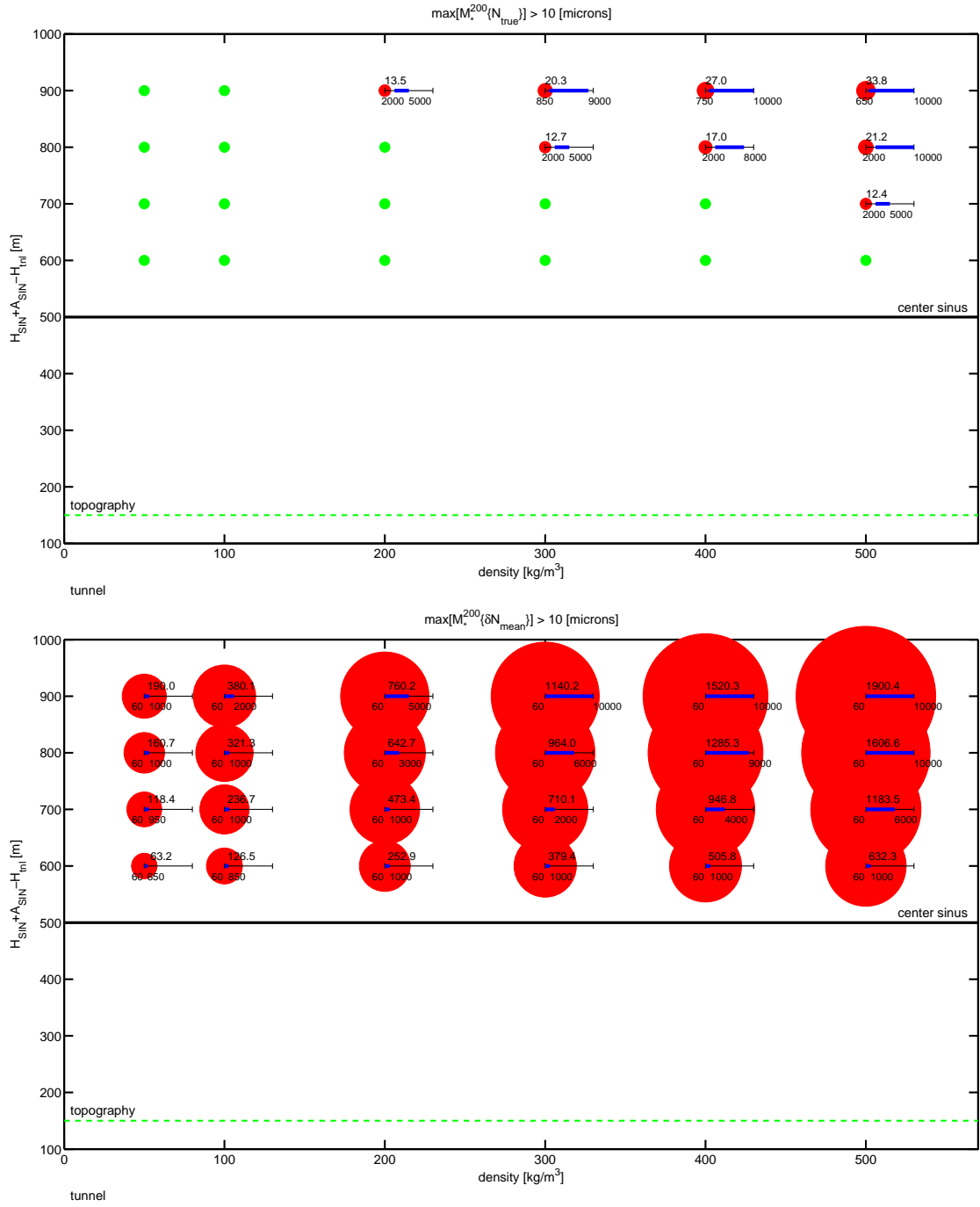


**Figure 6.24:** Representation of the misalignment analyses contained in Table 6.12 for  $N_{\text{true}}$  (upper) and  $\delta N_{\text{mean}}$  (lower) only. Each dot represents the results of a subset of  $\text{SIN}_i(\lambda_{\text{SIN}})$ . A dot is positioned as a function of its density  $\rho_{\text{SIN}}$  (x-axis) and its height separation with respect to the tunnel (y-axis),  $H_{\text{SIN}} + A_{\text{SLAB}} - H(\rho_o)$ . The position of the center of the sinus is represented by a black line. A green dot means that the maximal misalignment is smaller than 10 microns for all wavelengths  $\lambda_{\text{SIN}}$ . In opposition, the red dots represent  $\text{SIN}$  which contain maximal misalignments larger than 10 microns. They are scaled proportionally to the maximal misalignment. In addition, the horizontal blue bar represents the wavelength  $\lambda_{\text{SIN}}$  for which the maximal misalignment is larger than 10 microns.

## 6.4 Topography

In this section, the analyses are focusing on the region of Geneva, in Switzerland, close to the existing CERN facilities, where a location for the future CLIC is proposed *Aicheler et al.* (2012). The collider consists of two main linear accelerators (both 24.65 kilometers) which are laser straight but not collinear in the vertical plane. They have a crossing angle of 20 milliradians, see Figure 1.3. The tunnels are situated at approximately 350 meters in height above sea level. Both extremities are placed at 358.67 meters and the collision point at 350.0 meters. This means that the tunnel which contains CLIC is laser straight and is represented by two curved profiles in a Cartesian plot, if the y-axis corresponds to the usual height component as it can be seen in Figure 6.25. Along the whole profile, the tunnel is passing through minimal and maximal heights of about 343 and 359 meters, respectively, and its mean height is around 347 meters. From this point of view, because the height variations stay small along the profile, only the equipotential profile at  $H = 350$  meters is considered.

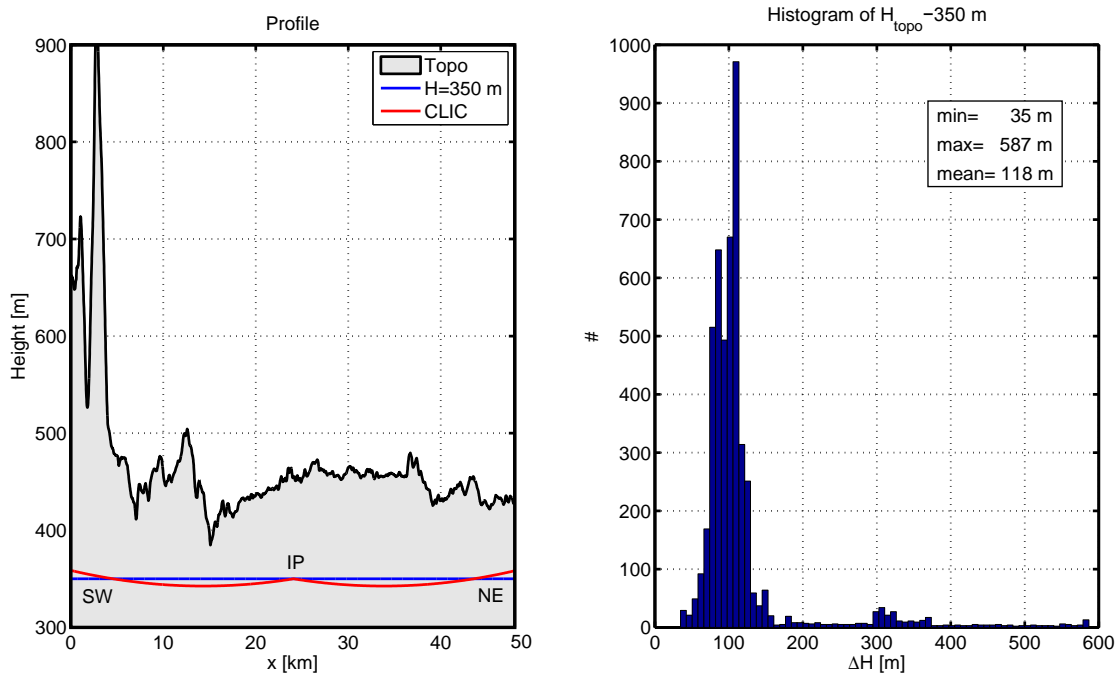


**Figure 6.25:** Longitudinal profile of CLIC (left) and the histogram of the height differences between topography and a profile of constant height  $H = 350$  meters.

### 6.4.1 Topography Anomalies TOPO

In the literature and in practice, the gravitational signals generated by topography are computed in various ways. An exhaustive overview of all already proposed solutions is very difficult and almost impossible to be done. These various approaches exist only because the available computing power is still very low compared to the amount of data available for topography. From this point of view, it is impossible to numerically integrate the

masses over the whole Earth with the level of detail provided by the modern digital terrain models. Simplified formulas, data reductions, filtering techniques are therefore proposed according to specific applications, causing at the same time artifacts and approximations, advantages and drawbacks.

Nowadays, the most successful global forward gravitational topography computation is probably due to the work of *Hirt et al.* (2014); *Hirt* (2013) which use adequately the advantages of several methods developed among others by *Forsberg* (1984). For local geoid computations, for example in Switzerland (*Marti*, 1997), similar methods are used. They always consist in defining a new discretization of topography for each computed point. This approach is very efficient and has the advantage to provide different resolutions for the near and far fields equivalently for all points. However, it can introduces some discontinuities and artifacts which can be crippling for short wavelengths analysis. Especially for the potential for which the dependency mitigates slowly. For this reason, in order to ensure the continuity and the consistency of the fields and because only small wavelengths are considered in this thesis, the effects due to topography are computed for all points with a single mass model. This strategy is only possible thanks to the fact that the area of our interest is limited to the region where the CLIC facilities are projected.

Concerning the following simulations, the choice of the digital terrain model was mainly motivated by its availability for the region surrounding CLIC up to 100 kilometers. The choice fell on the free digital terrain data set ASTER GDEM, provided by METI and NASA, providing 30 meters resolution. Unfortunately, according to *Rexer* (2014), it is probable that this choice is not optimal. The data set SRTM CGIAR-CSI<sup>3</sup> seems to be of better quality. However, since the data set is not used for reduction of real observations or computation of real geoid, but for some preliminary feasibility analyses and simulations of the determination of the gravity field, it can be considered that ASTER GDEM is sufficient. Here, a topography anomaly is given by a single homogeneous polyhedron which have a single variable parameter, its density  $\rho_{\text{TOPO}}$ :

$$\text{TOPO}(\rho_{\text{TOPO}}) \quad (6.17)$$

Using **QGravity**, the polyhedron is generated from two tessellations, see Section 5.2.3. The vertices of the upper tessellation  $\mathbb{T}_{\text{superior}}$  approximate the actual topography with decreasing resolution with respect to the horizontal distance to the CLIC profile. The resolution is equal to 90 meters up to a distance of 20 kilometers from every points of the CLIC profile, 300 meters up to 50 kilometers and 900 meters up to 100 kilometers as it is represented in Figure 6.26. The vertices of the lower tessellation  $\mathbb{T}_{\text{lower}}$  are given by a regular 1 kilometer grid at  $H = 0$  meters. The common boundary is given by the external boundary of  $\mathbb{T}_{\text{upper}}$ . For the upcoming simulations, it is assumed that error-free astrogravimetric observations have been carried out every 10 meters inside the CLIC tunnel at  $H = 350$  meters and on the topography. This is done for the following densities:

$$\rho_{\text{TOPO}} : \{50, 100, 200, 300, 400, 500, 2670\} \quad \left[ \frac{\text{kg}}{\text{m}^3} \right]$$

<sup>3</sup>by the Consortium for Spatial Information (CSI), Consultative Group for International Agricultural Research (CGIAR).

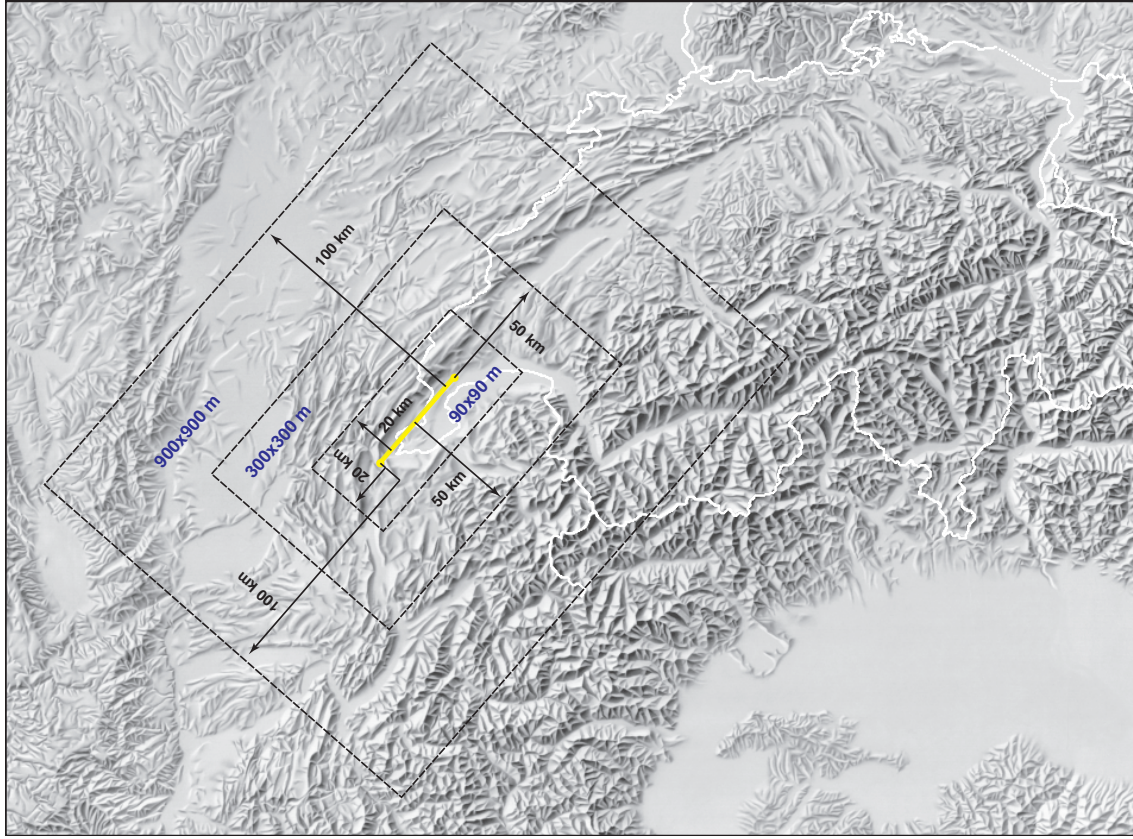


**Figure 6.26:** Overview map showing the different decreasing resolutions areas around CLIC (yellow) used for topographic mass models TOPO. Source of relief: Swiss Federal Office of Topography.

From this set, the anomaly  $\text{TOPO}(2670)$  is used in order to model the full signals expected by topography, while the others,  $\text{TOPO}(50) \rightarrow \text{TOPO}(500)$ , are useful for analyzing the consequences of non-modeled density contrasts in reductions and predictions.

#### 6.4.2 Misalignment Analyses due to $\text{TOPO}(2670)$ Anomaly

The results of the simulations of the mass anomaly  $\text{TOPO}(2670)$  are given in Figure 6.27. They give some interesting orders of magnitudes of expected gravity signals along the CLIC profile on topography and in the tunnel. It is not surprising that large variations of DoVs and free-air anomalies are highly correlated with the local variation in topography. In particular, the variations of plumbline curvature, with changes between  $-2$  to  $+2$  arcsec over less than 1 kilometer, clearly highlight that the first 5 kilometres will be subjected to the great difficulties.

In Figures 6.28 and 6.29, the expected misalignment  $\mathcal{M}_\star^\lambda \{N_{\text{true}}\}$  and  $\mathcal{M}_\star^\lambda \{\delta N_{\text{mean}}\}$  along the profile are given for the wavelengths  $\lambda = 100, 200$  and  $300$  meters. The expected misalignment  $\mathcal{M}_\star^\lambda \{N_{\text{true}}\}$  shows clearly that topography generates significant misalignments over 200 meters from the beginning to the 18th kilometer approximately. However, if the whole profile is considered, only 17.8% of the profile is affected by misalignments

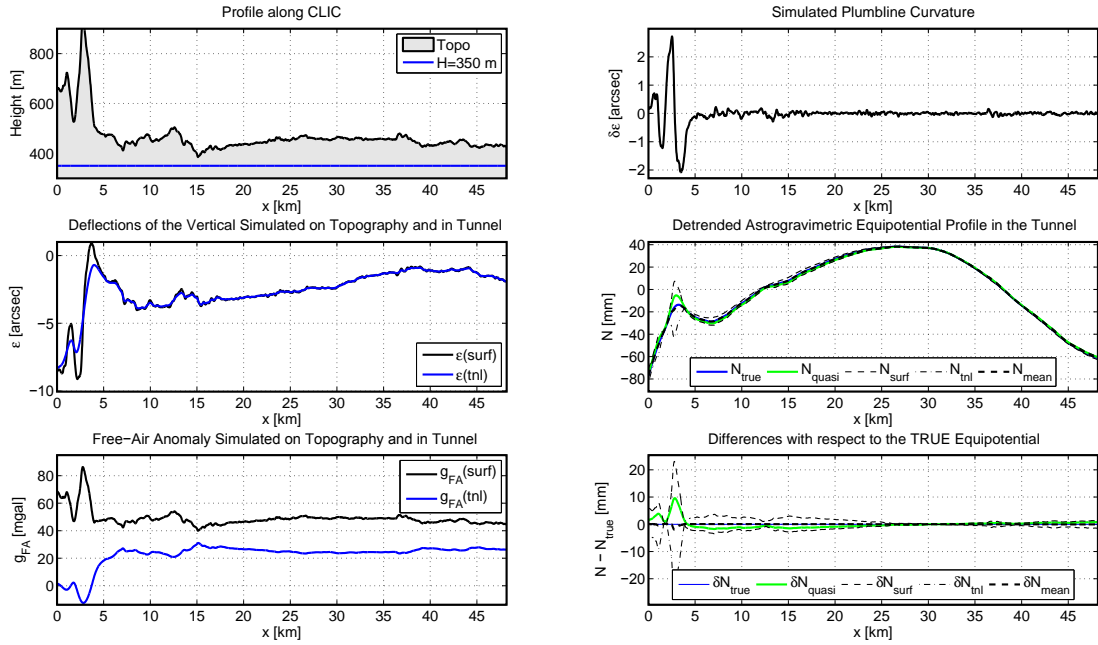


**Figure 6.27:** Results of the simulations of the mass anomaly TOPO(2670). (Upper, left) profile along CLIC with topography and tunnel. (Middle, left) error-free deflections of the vertical on topography and in the tunnel. (Lower, left) error-free free-air anomaly on the topography and in the tunnel. (Upper, right) error-free curvature of plumblin. (Middle, right) equipotential profiles in the tunnel. (Lower, right) Differences of the different strategies with respect to the true equipotential surface  $N_{\text{true}}$ .

larger than 10 microns. This can be seen in Figure 6.30 or in Table 6.13. Afterwards, they stay always below 10 microns.

From this fact, it is now crucial to see, if these significant signals can be observed directly with a sufficient accuracy. If so, the determination of the equipotential variations generated by topography could be theoretically determined directly without using any mass model reductions. If not, some hypotheses about the masses are unavoidable for the determination. This kind of quantification of observability is done by comparing  $\mathcal{M}_{\star}^{\lambda}\{N_{\text{true}}\}$  and  $\mathcal{M}_{\star}^{\lambda}\{\delta N_{\text{mean}}\}$ . This comparison is shown in Figure 6.30 and demonstrates that the determination of the equipotential surface by the strategy  $N_{\text{mean}}$  is efficient ( $\lambda = 200$  meters) for the major part of the profile but remains ineffective for the first 5 kilometers. In this region, the determination  $N_{\text{mean}}$  generates a misalignment which reaching 313.4 microns! The reason for this inefficiency is due to the bad estimation of the mean gravity along the plumblin, crucial for the determination of the orthometric corrections. Nevertheless, for the wavelength  $\lambda = 200$  meters, a determination according to  $N_{\text{mean}}$  can theoretically reduce the part of misalignment larger than 10 microns, over the whole profile, from 17.8% (no determination) up to 7.9%, an improvement of +10.1%, see Table 6.13. If we consider the misalignment for other wavelengths, it also can be seen that the efficiency of the determination increases significantly with increasing wavelength. For  $\lambda = 100$  meters,



the improvement is negative  $-2.5\%$ , while for  $\lambda = 300$  meters, it reaches  $+30.1\%$ . This statement also can be confirmed by figure 6.31, where the misalignment  $\mathcal{M}_\star^\lambda\{N_{\text{true}}\}$  and  $\mathcal{M}_\star^\lambda\{\delta N_{\text{mean}}\}$  are superposed and compared.

**Table 6.13:** Statistics of  $\mathcal{M}_\star^\lambda\{N_{\text{true}}\}$  and  $\mathcal{M}_\star^\lambda\{\delta N_{\text{mean}}\}$  due to TOPO(2670).

$\lambda$ [m]	$\mathcal{M}_\star^\lambda\{N_{\text{true}}\}$					$\mathcal{M}_\star^\lambda\{\delta N_{\text{mean}}\}$					impr. [%]
	min [ $\mu\text{m}$ ]	max [ $\mu\text{m}$ ]	mean [ $\mu\text{m}$ ]	RMS [ $\mu\text{m}$ ]	$\leq 10[\mu\text{m}]$ [%]	min [ $\mu\text{m}$ ]	max [ $\mu\text{m}$ ]	mean [ $\mu\text{m}$ ]	RMS [ $\mu\text{m}$ ]	$\leq 10[\mu\text{m}]$ [%]	
100	0.0	19.4	1.7	3.4	97.2	0.0	158.8	2.9	9.9	94.7	-2.5
<b>200</b>	<b>0.1</b>	<b>81.9</b>	<b>7.4</b>	<b>14.5</b>	<b>82.0</b>	<b>0.2</b>	<b>313.4</b>	<b>6.8</b>	<b>23.4</b>	<b>92.1</b>	<b>+10.1</b>
300	0.1	186.9	17.0	33.3	60.2	0.3	523.8	11.5	43.2	90.3	+30.1

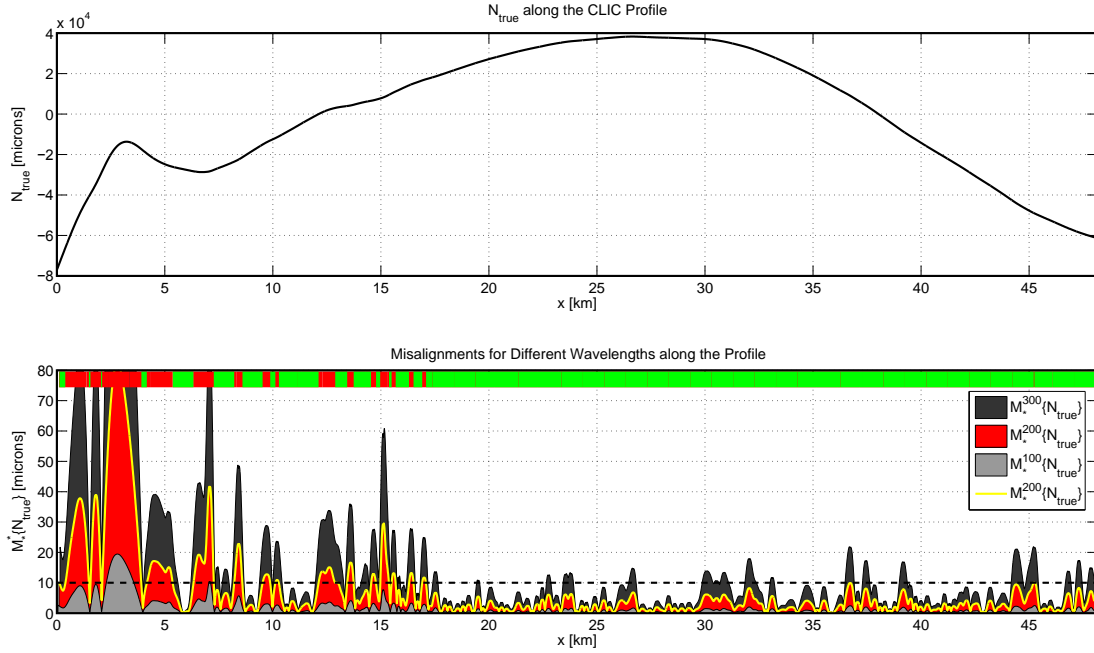


**Figure 6.28:**  $N_{\text{true}}$  (upper) and  $\mathcal{M}_\star^\lambda\{N_{\text{true}}\}$  (lower) along the CLIC profile due to TOPO(2670). The green-red bold line on top of the lower plot indicates the positions for which the determination  $\mathcal{M}_\star^{200}\{N_{\text{true}}\} < 10$  microns (green), and where  $\mathcal{M}_\star^{200}\{N_{\text{true}}\} \geq 10$  microns (red).



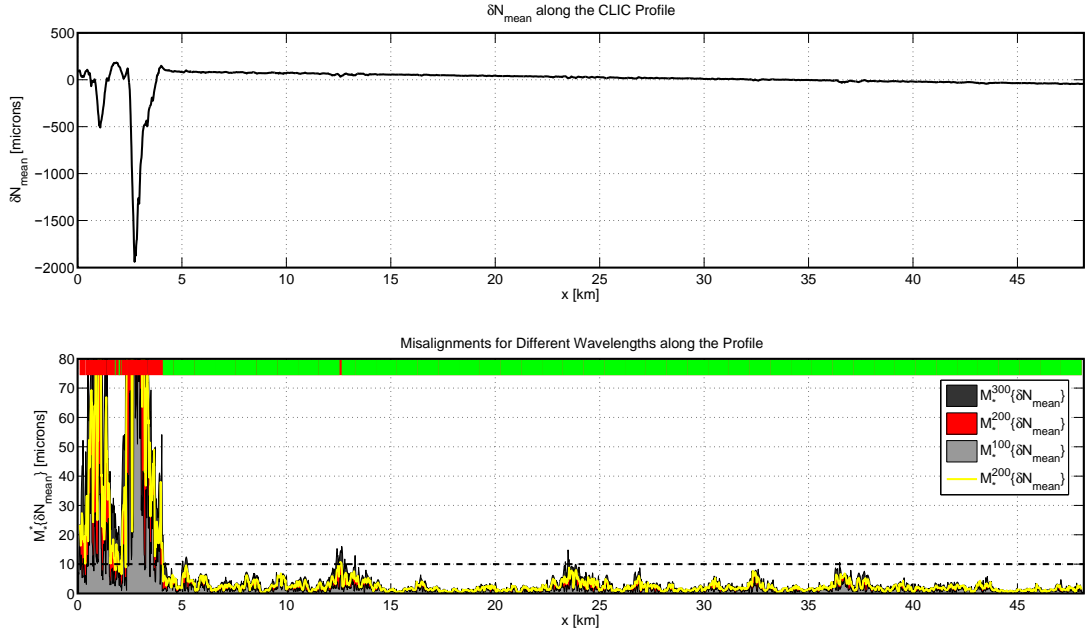


**Figure 6.29:**  $\delta N_{\text{mean}}$  (upper) and  $\mathcal{M}_\star^\lambda \{\delta N_{\text{mean}}\}$  (lower) along the CLIC profile due to TOPO(2670). The green-red bold line on top of the lower plot indicates the positions for which the determination  $\mathcal{M}_\star^{200} \{\delta N_{\text{mean}}\} < 10$  microns (green), and where  $\mathcal{M}_\star^{200} \{\delta N_{\text{mean}}\} \geq 10$  microns (red)

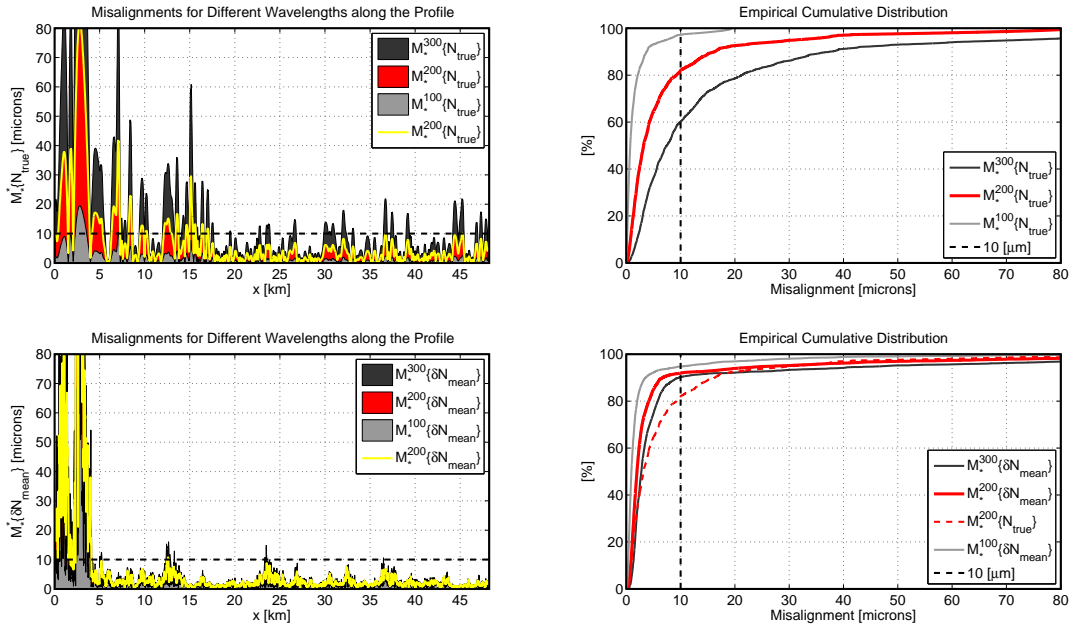


**Figure 6.30:** Comparisons of the misalignment  $\mathcal{M}_\star^\lambda \{N_{\text{true}}\}$  (upper) and  $\mathcal{M}_\star^\lambda \{\delta N_{\text{mean}}\}$  (lower) due to TOPO(2670). The right column shows the empirical cumulative distributions of misalignment CDF ( $\mathcal{M}_\star^\lambda \{N_{\text{true}}\}$ ) (upper) and CDF ( $\mathcal{M}_\star^\lambda \{\delta N_{\text{mean}}\}$ ) (lower), considering the whole profile.

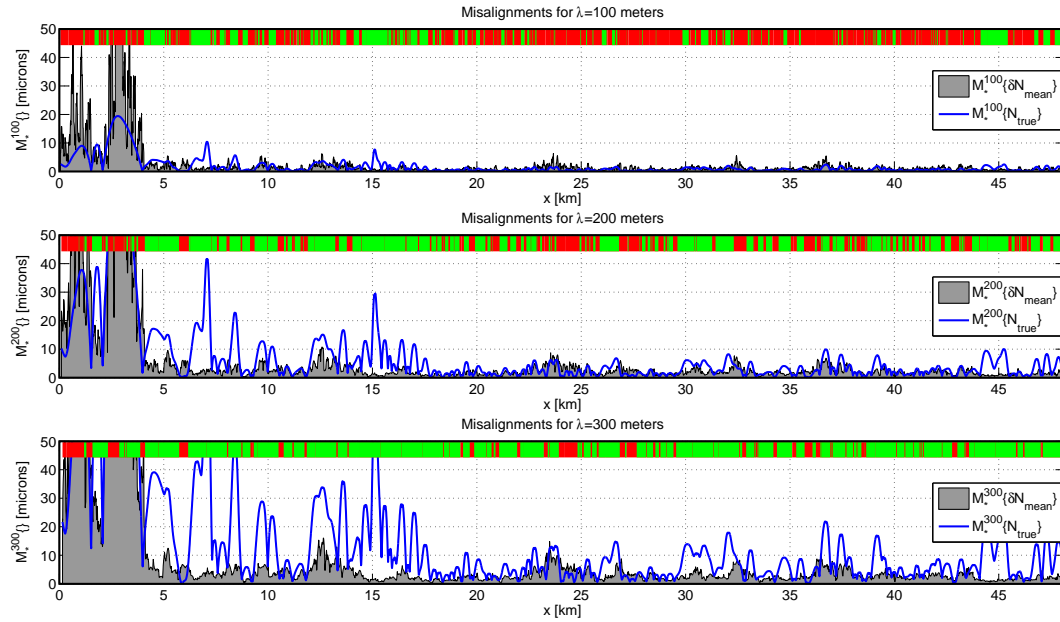


**Figure 6.31:** Comparisons of  $\mathcal{M}_*^\lambda\{N_{\text{true}}\}$  and  $\mathcal{M}_*^\lambda\{\delta N_{\text{mean}}\}$  for different wavelengths,  $\lambda = 100, 200, 300$  due to TOPO(2670). The green-red bold line on top of each plot indicates the positions for which the determination  $N_{\text{mean}}$  improves (green) or degrades (red) the misalignment with respect to  $N_{\text{true}}$ .

### 6.4.3 Misalignment Analyses due to TOPO(50) $\rightarrow$ TOPO(500) Anomalies

The following analyses are useful in order to quantify expected gravity signals generated by non-modeled density contrasts in topography. Because all gravity functionals are proportional to density, every field quantity generated by TOPO(50)  $\rightarrow$  TOPO(500) can be directly computed from TOPO(2670). However, because the most important statements are given regarding a threshold of 10 microns, it is still necessary to show explicitly the statistics for each density. They are given in Table 6.14 and show that, for a wavelength  $\lambda = 200$  meters, no misalignments  $\mathcal{M}_\star^{200}\{N_{\text{true}}\}$  larger than 10 micrometers are expected up to a density contrast of  $300 \frac{\text{kg}}{\text{m}^3}$ . Concerning the consequences for a determination by  $N_{\text{mean}}$ , we can see that density contrasts smaller than  $100 \frac{\text{kg}}{\text{m}^3}$  generate misalignment  $\mathcal{M}_\star^{200}\{\delta N_{\text{mean}}\}$  which stay below 11.7 microns.

**Table 6.14:** Statistics of  $\mathcal{M}_\star^\lambda\{N_{\text{true}}\}$  and  $\mathcal{M}_\star^\lambda\{\delta N_{\text{mean}}\}$  due to TOPO(50)  $\rightarrow$  TOPO(500).

$\lambda$ [m]	min [ $\mu\text{m}$ ]	max [ $\mu\text{m}$ ]	$\mathcal{M}_\star^\lambda\{N_{\text{true}}\}$		$\leq 10[\mu\text{m}]$ [%]	min [ $\mu\text{m}$ ]	max [ $\mu\text{m}$ ]	$\mathcal{M}_\star^\lambda\{\delta N_{\text{mean}}\}$		$\leq 10[\mu\text{m}]$ [%]	impr. [%]
			mean [ $\mu\text{m}$ ]	RMS [ $\mu\text{m}$ ]				mean [ $\mu\text{m}$ ]	RMS [ $\mu\text{m}$ ]		
TOPO(50)											
100	0.0	0.4	0.0	0.1	100.0	0.0	3.0	0.1	0.2	100.0	0.0
<b>200</b>	<b>0.0</b>	<b>1.5</b>	<b>0.1</b>	<b>0.3</b>	<b>100.0</b>	<b>0.0</b>	<b>5.9</b>	<b>0.1</b>	<b>0.4</b>	<b>100.0</b>	<b>0.0</b>
300	0.0	3.5	0.3	0.6	100.0	0.0	9.8	0.2	0.8	100.0	0.0
TOPO(100)											
100	0.0	0.7	0.1	0.1	100.0	0.0	5.9	0.1	0.4	100.0	0.0
<b>200</b>	<b>0.0</b>	<b>3.1</b>	<b>0.3</b>	<b>0.5</b>	<b>100.0</b>	<b>0.0</b>	<b>11.7</b>	<b>0.3</b>	<b>0.9</b>	<b>99.9</b>	<b>-0.1</b>
300	0.0	7.0	0.6	1.2	100.0	0.0	19.6	0.4	1.6	99.2	-0.8
TOPO(200)											
100	0.0	1.5	0.1	0.3	100.0	0.0	11.9	0.2	0.7	99.9	-0.1
<b>200</b>	<b>0.0</b>	<b>6.1</b>	<b>0.6</b>	<b>1.1</b>	<b>100.0</b>	<b>0.0</b>	<b>23.5</b>	<b>0.5</b>	<b>1.8</b>	<b>99.3</b>	<b>-0.7</b>
300	0.0	14.0	1.3	2.5	98.0	0.0	39.2	0.9	3.2	98.3	0.3
TOPO(300)											
100	0.0	2.2	0.2	0.4	100.0	0.0	17.8	0.3	1.1	99.7	-0.3
<b>200</b>	<b>0.0</b>	<b>9.2</b>	<b>0.8</b>	<b>1.6</b>	<b>100.0</b>	<b>0.0</b>	<b>35.2</b>	<b>0.8</b>	<b>2.6</b>	<b>98.4</b>	<b>-1.6</b>
300	0.0	21.0	1.9	3.7	97.1	0.0	58.9	1.3	4.9	97.2	0.1
TOPO(400)											
100	0.0	2.9	0.3	0.5	100.0	0.0	23.8	0.4	1.5	99.5	-0.5
<b>200</b>	<b>0.0</b>	<b>12.3</b>	<b>1.1</b>	<b>2.2</b>	<b>98.4</b>	<b>0.0</b>	<b>47.0</b>	<b>1.0</b>	<b>3.5</b>	<b>97.7</b>	<b>-0.7</b>
300	0.0	28.0	2.6	5.0	94.5	0.0	78.5	1.7	6.5	96.0	1.5
TOPO(500)											
100	0.0	3.6	0.3	0.6	100.0	0.0	29.7	0.6	1.9	99.1	-0.9
<b>200</b>	<b>0.0</b>	<b>15.3</b>	<b>1.4</b>	<b>2.7</b>	<b>97.8</b>	<b>0.0</b>	<b>58.7</b>	<b>1.3</b>	<b>4.4</b>	<b>97.1</b>	<b>-0.7</b>
300	0.0	35.0	3.2	6.2	93.3	0.1	98.1	2.1	8.1	95.4	2.1

Nevertheless, the regions of which  $\mathcal{M}_\star^\lambda \{\delta N_{\text{mean}}\} \geq 10$  microns are restricted to the first 3 kilometers for  $\text{TOPO}(50) \rightarrow \text{TOPO}(500)$ . For the rest of the profile,  $\mathcal{M}_{3 \rightarrow 49}^\lambda \{\delta N_{\text{mean}}\}$  are negligible and stay below 3 microns, see Figure 6.32.

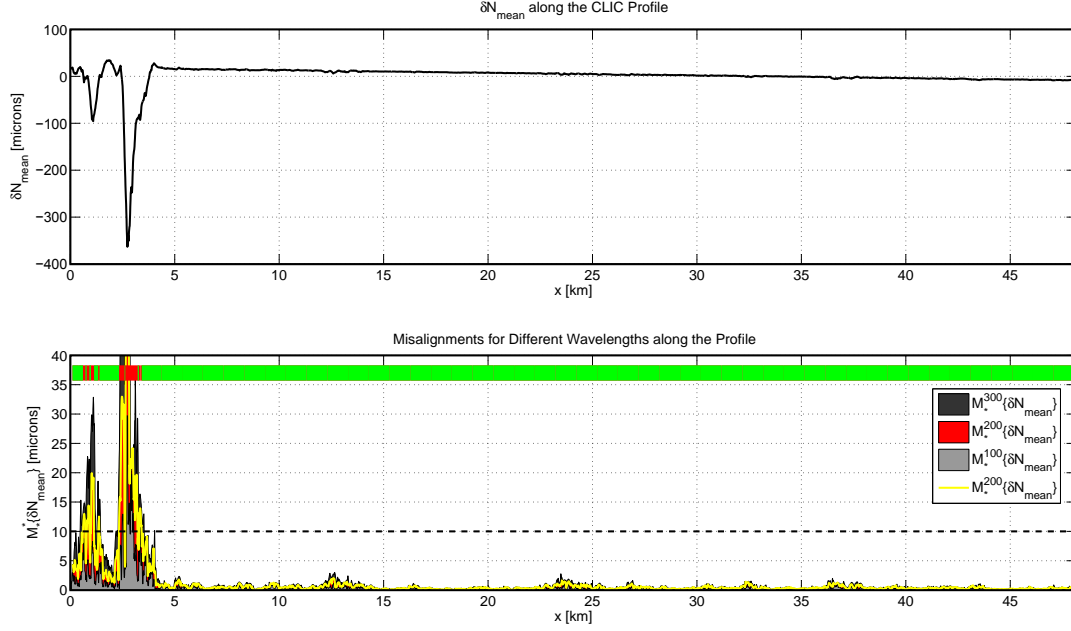


**Figure 6.32:**  $\delta N_{\text{mean}}$  (upper) and  $\mathcal{M}_\star^\lambda \{\delta N_{\text{mean}}\}$  (lower) along the CLIC profile due to  $\text{TOPO}(50)$ . The green-red bold line on top of the lower plot indicates the positions for which the determination  $\mathcal{M}_\star^{200} \{\delta N_{\text{mean}}\} < 10$  microns (green), and where  $\mathcal{M}_\star^{200} \{\delta N_{\text{mean}}\} \geq 10$  microns (red)

## 6.5 Time-Varying Centrifugal Effects

This section concerns the analysis of signals generated by the varying disturbing centrifugal potential as presented in Section 3.8.2. According to Equation 3.174, the disturbing centrifugal potential is defined as:

$$\delta\Phi_{\text{centr}}(\boldsymbol{\rho}, t) = \Phi_{\text{centr}}(\boldsymbol{\rho}, t) - \Phi_{\text{centr}, \omega_0}(\boldsymbol{\rho}) \quad (6.18)$$

where the centrifugal potential terms on the right-hand side, in ITRS, are given by Equation 3.136:

$$\begin{aligned} \Phi_{\text{centr}}(\boldsymbol{\rho}^{\text{ITRS}}, t) &= +\frac{1}{2} \cdot \left\{ |\boldsymbol{\omega}_{\delta}^{\text{ITRS}}(t)|^2 \cdot |\boldsymbol{\rho}^{\text{ITRS}}|^2 - (\boldsymbol{\rho}^{\text{ITRS}} \cdot \boldsymbol{\omega}_{\delta}^{\text{ITRS}}(t))^2 \right\} \\ \Phi_{\text{centr}, \omega_0}(\boldsymbol{\rho}^{\text{ITRS}}) &= +\frac{1}{2} \cdot \left\{ |\boldsymbol{\omega}_0 \cdot \mathbf{e}_z^{\text{ITRS}}|^2 \cdot |\boldsymbol{\rho}^{\text{ITRS}}|^2 - (\boldsymbol{\rho}^{\text{ITRS}} \cdot \boldsymbol{\omega}_0 \cdot \mathbf{e}_z^{\text{ITRS}})^2 \right\} \end{aligned} \quad (6.19)$$

from which the change in the equipotential is given by Equation 3.209:

$$\delta N_{\text{centr}}(\boldsymbol{\rho}_o^{\text{ITRS}}, t) = \frac{\delta\Phi_{\text{centr}}(\boldsymbol{\rho}_o^{\text{ITRS}}, t)}{|\mathbf{g}_{\text{tot}}(\boldsymbol{\rho}_o^{\text{ITRS}})|} \quad (6.20)$$

The following analyses are based on a numerically computed global time series of the disturbing centrifugal potential, between 1980 and 2013, from which the Earth rotation vector time series  $\boldsymbol{\omega}_{\delta}^{\text{ITRS}}(t)$  is generated from the Earth orientation parameter data EOP 08 C04 (IAU1980), and shown in Figure 6.33, and with more details in Appendix B.

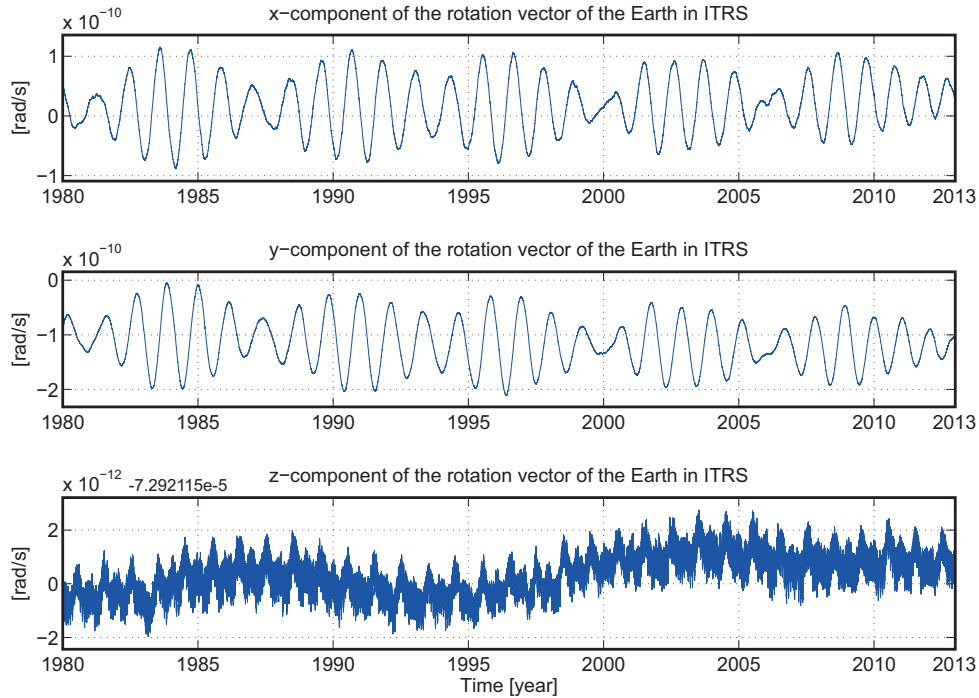


**Figure 6.33:** Time series of the x-y-z components of the Earth rotation vector  $\boldsymbol{\omega}_{\delta}^{\text{ITRS}}$  generated from the Earth orientation parameter data EOP 08 C04 (IAU1980).

### 6.5.1 Global Variations

A typical mapping of the absolute variation of  $\delta N_{\text{centr}}$  is shown in Figure 6.34. Globally, the amplitudes of the variation of the equipotential stay below 0.03 meters. In Geneva at the location of CLIC, they stay below 0.015 meters and for the relative variations over the whole CLIC profile, they reach only 0.1 millimeters, see Figure 6.35. The spatial pattern is always formed by two maxima and minima located at approximately  $+50$  and  $-50$  degrees of latitude. This is due to the fact that time series of the  $y$ -component of the Earth rotation vector  $\omega_{\delta}^{\text{ITRS}}$  is not centered and contains an offset of approximately  $1 \cdot 10^{-10} \frac{\text{rad}}{\text{s}}$ . Concerning the deflections of the vertical, the maximal variations are in the order of 0.002-0.003 arcsec.

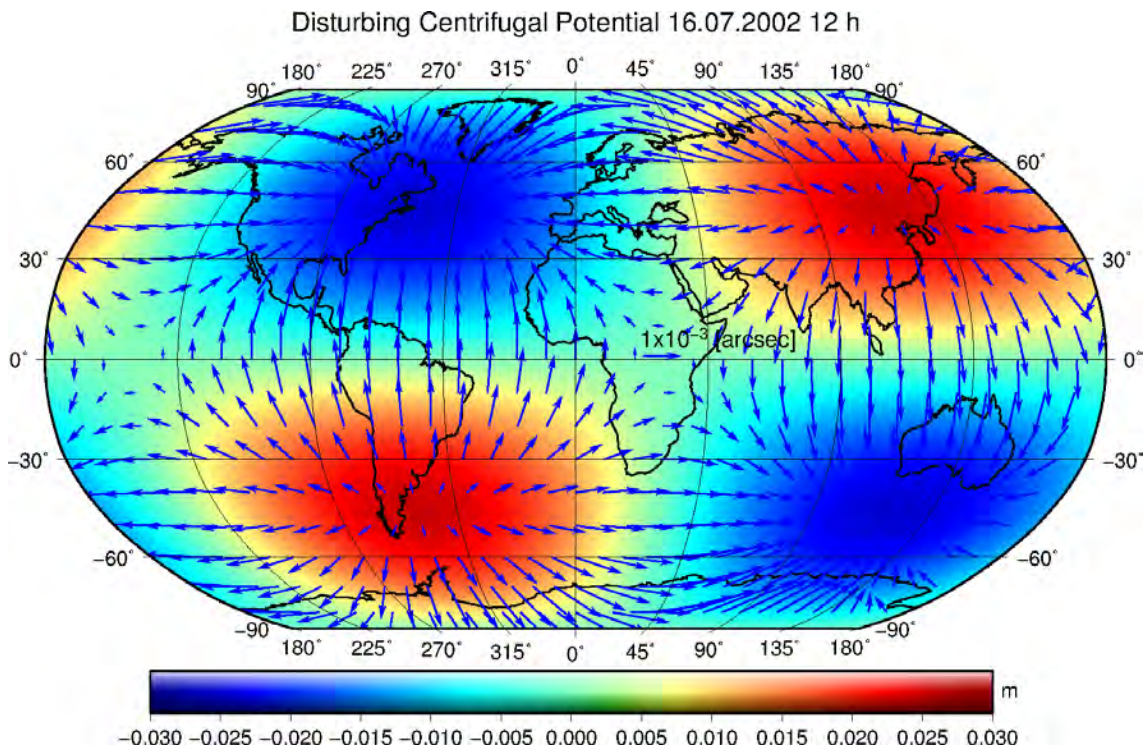


**Figure 6.34:** Typical equipotential  $\delta N_{\text{centr}}$  and deflections of the vertical  $(\xi, \eta)$  variations and due to the disturbing centrifugal potential on the profile on 16.07.2002 at 12:00 UTC.

### 6.5.2 Misalignment Analyses for CLIC

If we look at the impact on misalignments for CLIC, we can see that they are by far negligible. They have maximal values below 0.15 microns for all wavelengths  $\lambda \leq 50$  km, see Figure 6.36. The maximal amplitude is generated by the pole wobble with a periodicity of 420 days, see Table 6.15.

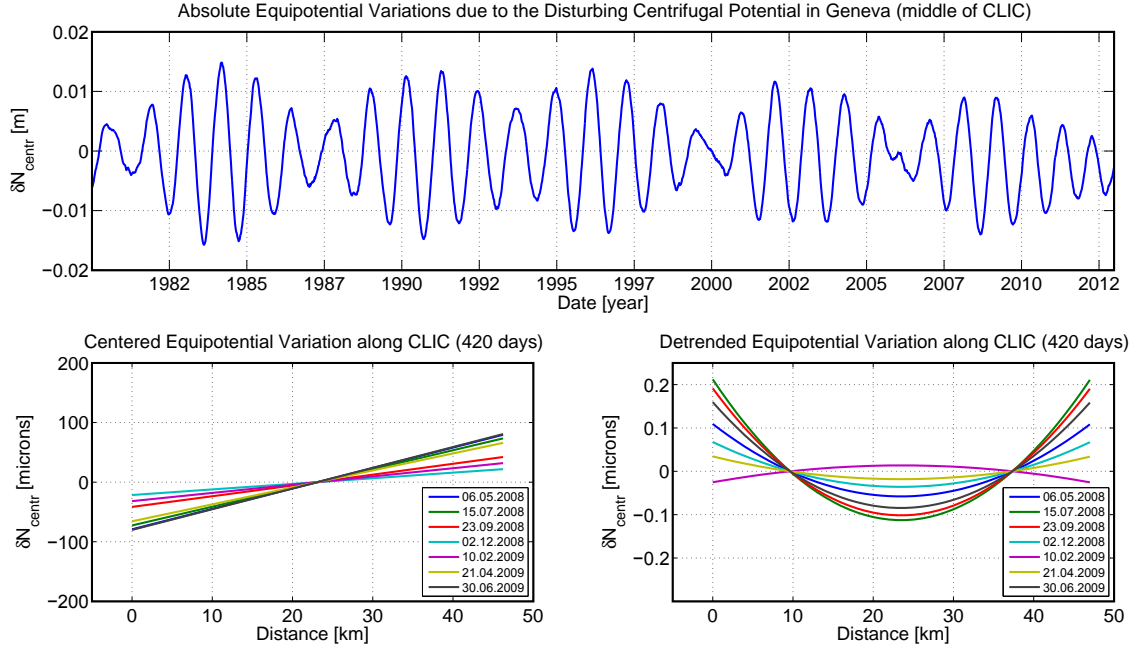


**Figure 6.35:** (Upper) time series  $\delta N_{\text{centr}}$  generated by the disturbing centrifugal potential computed for the position in the middle of the profile of CLIC, from 1980 to 2013, according to the Earth orientation parameters time series EOP 08 C04 (IAU1980). (Lower) centered (left) and detrended (right) equipotential along the profile of CLIC at different epochs during a cycle of 420 days.

**Table 6.15:** List of the main periods of the components of the maximal misalignment  $\max[\mathcal{M}_{\star}^{\star}\{\delta N_{\text{centr}}\}]$  generated by the disturbing centrifugal potential on the profile of CLIC.

Rank	Period	Amplitude
[-]	[day]	[ $\mu\text{m}$ ]
1	$\infty$	0.100
2	430.0	0.028
3	364.8	0.016
4	2408.0	0.014
5	197.3	0.011
6	445.9	0.011
7	218.9	0.011
8	215.0	0.011
9	376.2	0.007
10	2006.6	0.006

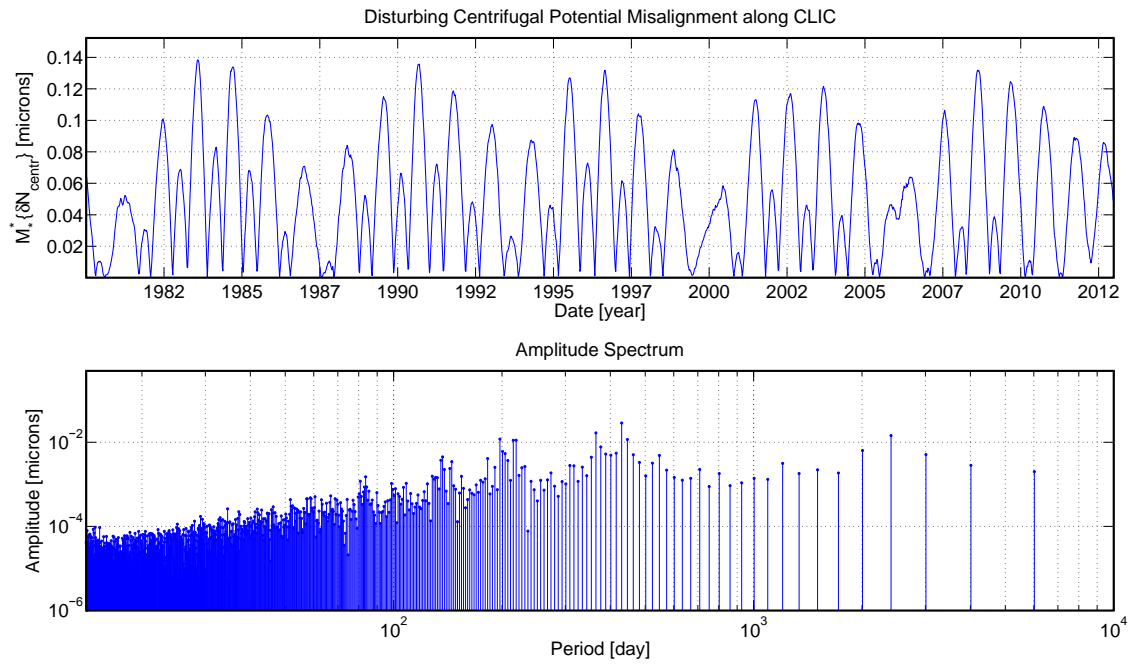


**Figure 6.36:** Time series (upper) and amplitude spectrum (lower) of the maximal misalignment  $\mathcal{M}_* \{\delta N_{\text{centr}}\}$  generated by the disturbing centrifugal potential on the profile of CLIC, from 1980 to 2013, with the Earth orientation parameters time series EOP 08 C04 (IAU1980).



## 6.6 Earth Tides

Since the signal of the Earth tides is treated abundantly in geodetic books and literature, only the computation of misalignments along the profile of CLIC are discussed in this section. Concerning the problem of the tidal signals for the reduction of geodetic observations, please refer to Section 4.4. As seen in Section 3.7.4, the tidal potential of a deformable Earth can be computed on the one hand for positions fixed in space or on the other hand for points fixed on the Earth's surface. Here, only the latter case is argued. From the potential given in Equation 3.157 the change in the equipotential is given by:

$$N_{\text{tidal}}(\boldsymbol{\rho}_o^{\text{ITRS}}, t) = \frac{\Phi_{\text{tidal}}(\boldsymbol{\rho}_o^{\text{ITRS}}, t)}{|\mathbf{g}_{\text{tot}}(\boldsymbol{\rho}_o^{\text{ITRS}})|} \quad (6.21)$$

The analyses are based on a hourly time series between 2012 and 2013, computed with the software **ETERNA** (Wenzel, 1993) provided by the *International Center for Earth Tides* (ICET), for 20 positions uniformly distributed along the profile of CLIC. In Figure 6.37, (upper) the time series of the absolute equipotential variations  $N_{\text{tidal}}$  for the position in the middle of the profile of CLIC is shown. As expected the absolute changes can reach 0.3 meters. The centered and detrended variations along the profile are shown in Figure 6.37, (lower) for a cycle of 12 hours. Finally, the consequences of the tides on the misalignments are shown in Figures 6.38 and 6.39. They reach maximum 1.0 and 6.6 microns for the wavelengths  $\lambda = 15$  and  $\lambda = 48$  km respectively. In addition, these misalignments occur mostly with periodicities below 26 hours.

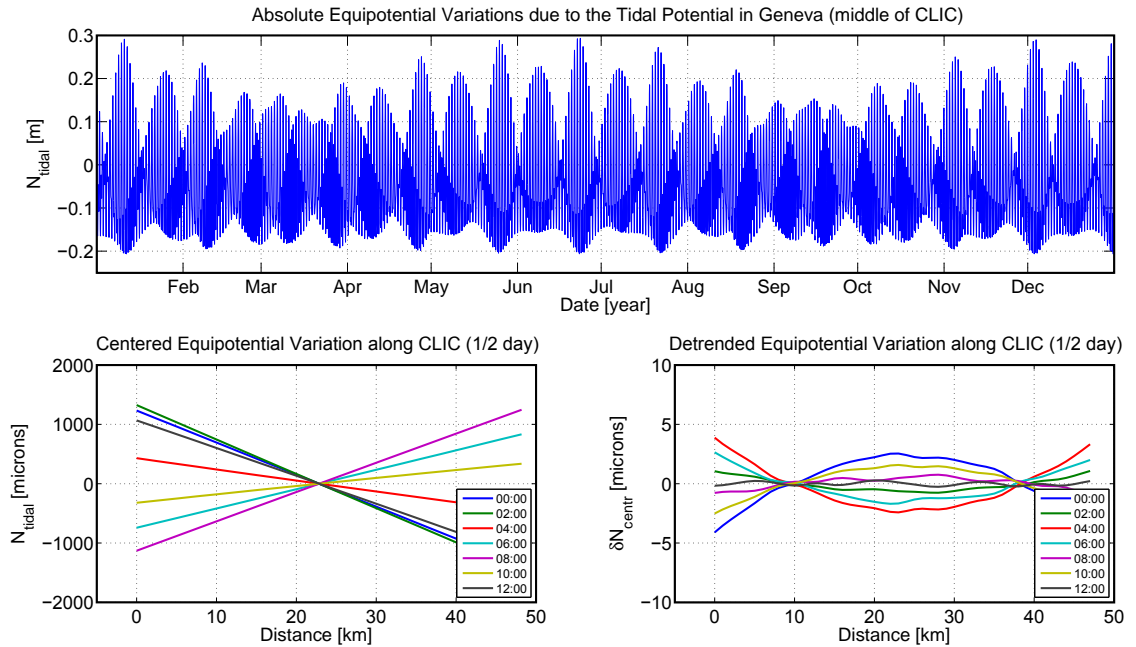


**Figure 6.37:** (Upper) time series  $N_{\text{tidal}}$  generated by the tidal potential computed for the position in the middle of the profile of CLIC, from 2012 to 2013, computed with the software **ETERNA**. (Lower) centered (left) and detrended (right) equipotential along the profile of CLIC at different epochs during a cycle of half a day of the 23.06.2012.

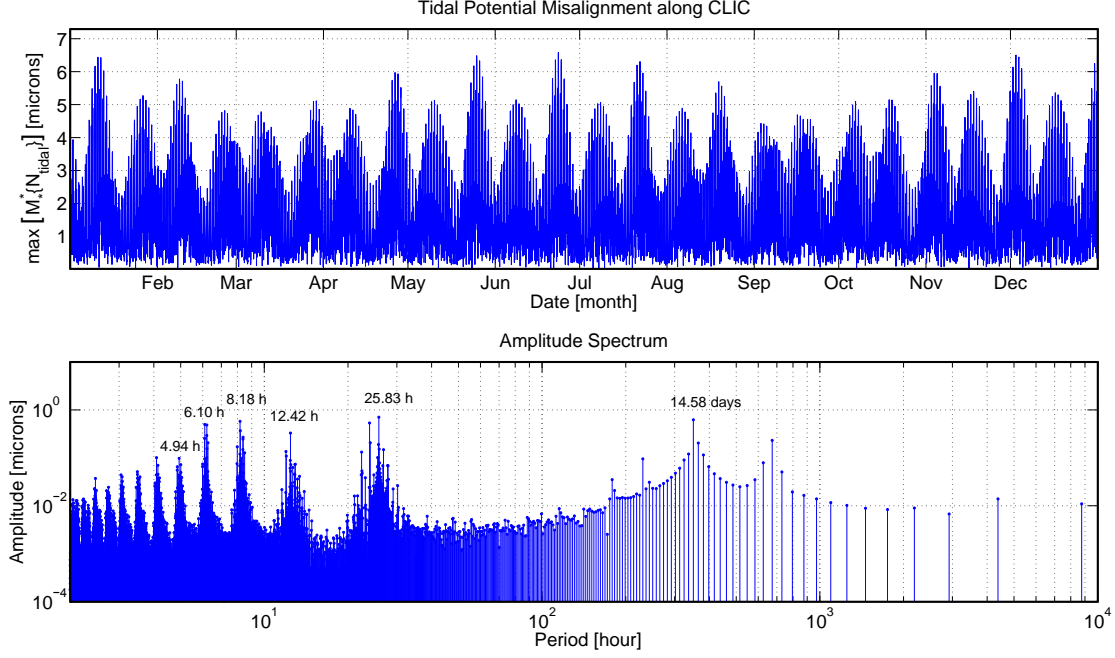


**Figure 6.38:** Time series (upper) and amplitude spectrum (lower) of the maximal misalignment  $\mathcal{M}_\star\{N_{\text{tidal}}\}$  generated by the tidal potential on the profile of CLIC, from 2012 to 2013, computed with the software ETERNA.

**Table 6.16:** List of the main periods of the components of the maximal misalignment  $\max[\mathcal{M}_\star\{N_{\text{tidal}}\}]$  generated by the tidal potential on the profile of CLIC.

Rank	Period	Amplitude
[-]	[hour]	[ $\mu\text{m}$ ]
1	$\infty$	3.90
2	25.8	0.70
3	350.2	0.62
4	8.2	0.58
5	23.9	0.53
6	6.1	0.49
7	6.2	0.48
8	8.2	0.36
9	12.42	0.33
10	6.2	0.29

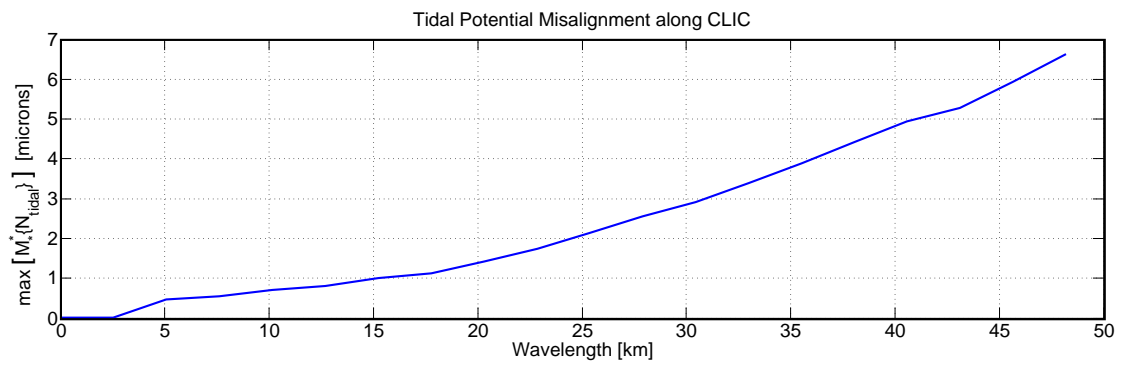


**Figure 6.39:** Maximal misalignments  $\max [\mathcal{M}_* \{N_{\text{tidal}}\}]$  generated by the tidal potential on the profile of CLIC, as a function of the wavelength along the profile of CLIC.

## 6.7 Lake of Geneva

This section considers signals generated by the Lake of Geneva, mainly at the location of the projected CLIC facilities. According to *Graf* (1983), the origin of the Lake of Geneva seems to be due to several geological processes as fluvial erosion, tectonic deformation and glacial remodeling. The water level is regulated in Geneva at approximately  $\bar{H}_{\text{Lake}} = 372$  meters, with variations of about 1.0 meter, see Figure 6.40. Its maximal depth is equal to 309.7 meters, the mean depth is equal to 152.7 meters, and it covers an area of 582 km<sup>2</sup>. The lengths along the major and minor axis are equal to 72.3 km and 13.8 km respectively. The volume reaches 89 km<sup>3</sup> with a mean outflow of 240  $\frac{\text{m}^3}{\text{s}}$ . It is crossed by the Rhône river from East to West.

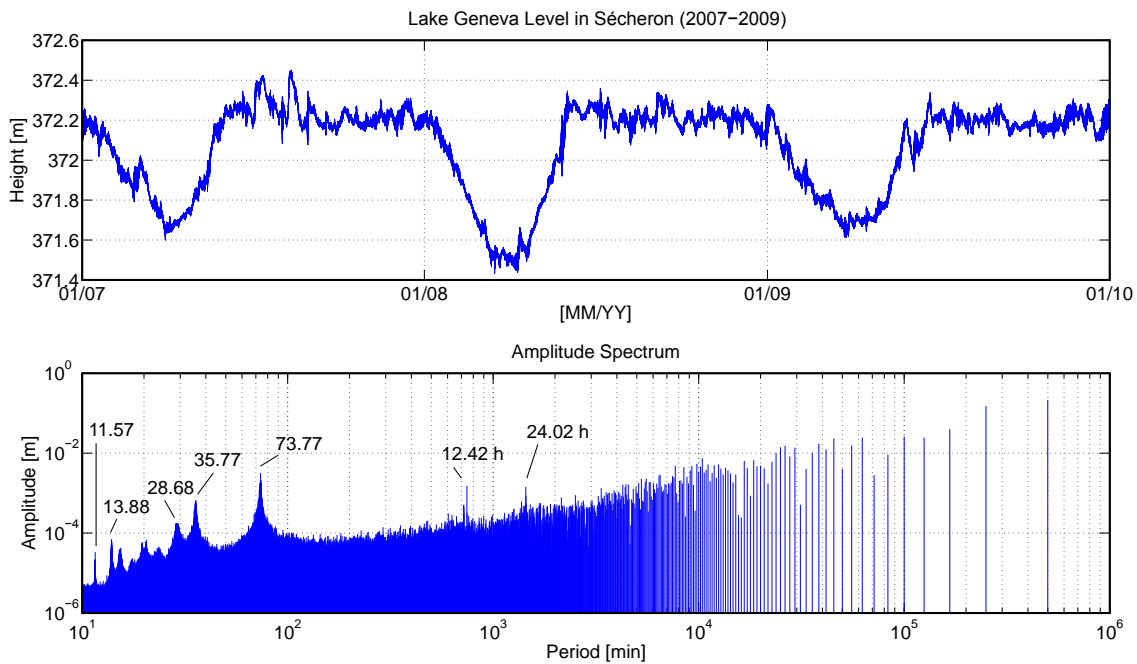


**Figure 6.40:** (Upper) time series of Lake of Geneva Level in Sécheron between 2007 and 2009. (Lower) Amplitude spectrum. Source of data: Federal Office for the Environment FOEN.

From a geodetic point of view, the interesting aspects are related to the corresponding gravity field generated by the lake. In Switzerland, the first considerations of lakes for geoid computations can be found in *Marti* (1997). He considered stationary lake models of density contrast equal to  $-1'670 \frac{\text{kg}}{\text{m}^3}$  with respect to topography, for the geoid computation based on the remove-restore technique. Here, the aim is to go a little further in the modeling and to consider the Lake of Geneva as a time-varying body, and look at the consequences on the time varying gravity field. Despite the fact that the surface of lakes seems to vary in a very chaotic manner, it can be shown that the largest mass movements satisfy simple laws which can be used to encompass the major phenomena. Here, the surface of the lake is considered in two ways:

1. The overall rise and descent of the water surface. As we can see in Figure 6.40,

the water level is regulated and variations of about 1.0 meters, once per year, are expected.

2. Stationary waves or *Seiches*, established and observed by *Forel* (1895). Usually, Seiches happen when a lake is excited by the friction of wind or storm on its surface. In the Lake of Geneva, they have periods of some minutes up to approximately 74 minutes, the period of the uninodal longitudinal mode. The amplitudes are quite small in the Lake of Geneva, usually smaller than 20 centimeters *Bauer* (1979). The amplitude spectrum of Figure 6.40 shows several significant peaks which correspond to normal modes of Seiches.

In the following section, the gravity field generated by the different mass models are simulated on the one hand for gridded points in a square region encompassing CLIC at  $H = 350$  meters, and on the other hand, at the projected location of CLIC, at  $H = 350$  meters and on the surface of topography as it is shown in Figure 6.41.

### 6.7.1 Overall Lake Level Variation

Here, two homogeneous polyhedra, noted LAKE<sub>371</sub> and LAKE<sub>373</sub>, of density  $\rho_{\text{water}} = 1'000 \frac{\text{kg}}{\text{m}^3}$ , are considered for the following simulations. They are both generated from two tessellations where  $T_{\text{lower}}$  is given by the actual bathymetry of the Lake of Geneva.  $T_{\text{upper}}$  is given by a horizontal plane, at  $H_{\text{Lake}} = 371.0$  and  $H_{\text{Lake}} = 373.0$  meters for LAKE<sub>371</sub> and LAKE<sub>373</sub>, respectively. The height difference of 2 meters, twice the actual one, is chosen in order to estimate the consequences of an extreme level change. Before analyzing the consequence of the lake level change, let us begin with the computation of signals and misalignments generated by the whole mass of the Lake of Geneva, seen as stationary.

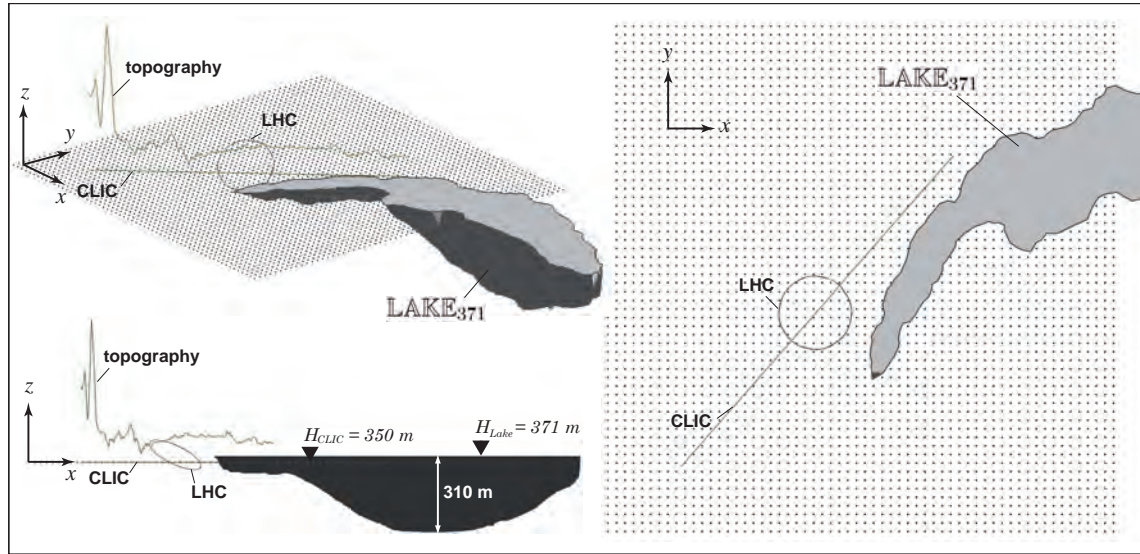


**Figure 6.41:** LAKE<sub>371</sub>. The  $z$ -component is scaled by a factor 40 with respect to  $x$  and  $y$ .

**Misalignment Analyses due to LAKE<sub>371</sub>**

The consequences on the gravity field generated by LAKE<sub>371</sub> are shown in Figures 6.42, 6.44 and 6.45. In Figure 6.42, the absolute variations of the equipotential surface in the region of Geneva, at  $H = 350$  meters, are represented and show that the lake provokes a change of about 2 cm along the profile of CLIC. This can be better seen in Figure 6.44 where the equipotential profile along CLIC and its respective misalignments are represented. They reach maximal 3 and 10 microns for the wavelengths  $\lambda = 1.0$  and  $\lambda = 2.4$  km, respectively. For  $\lambda = 200$  meters, the misalignment is negligible and the plumbline curvature stays below 0.01 arcsec, see Figure 6.45.

**Misalignment Analyses due to LAKE<sub>373</sub> - LAKE<sub>371</sub>**

The consequences of the gravity field generated by an overall lake level variation of 2 meters are shown in Figures 6.43, 6.44 and 6.45. The gravity field representing the variation is obtained by subtracting the gravity fields generated by LAKE<sub>373</sub> and LAKE<sub>371</sub>. In Figure 6.43, the absolute variations of the equipotential surface in the region of Geneva, at  $H = 350$  meters, are represented and show that an overall lake level variation of 2 meters provokes a change of about 0.4 mm along the profile of CLIC. In Figure 6.44, the equipotential profile along CLIC and its respective misalignments are represented. They reach maximal 1 and 10 microns for the wavelengths  $\lambda = 4.2$  and  $\lambda = 15$  km, respectively. For  $\lambda = 200$  meters, the misalignment is negligible and the plumbline curvature stay below 0.01 arcsec, see Figure 6.45. The latter value is computed from, on the one hand, the predicted deflections of the vertical on the surface of topography generated by LAKE<sub>371</sub>, and on the other hand with the deflections in the tunnel generated by LAKE<sub>373</sub>.



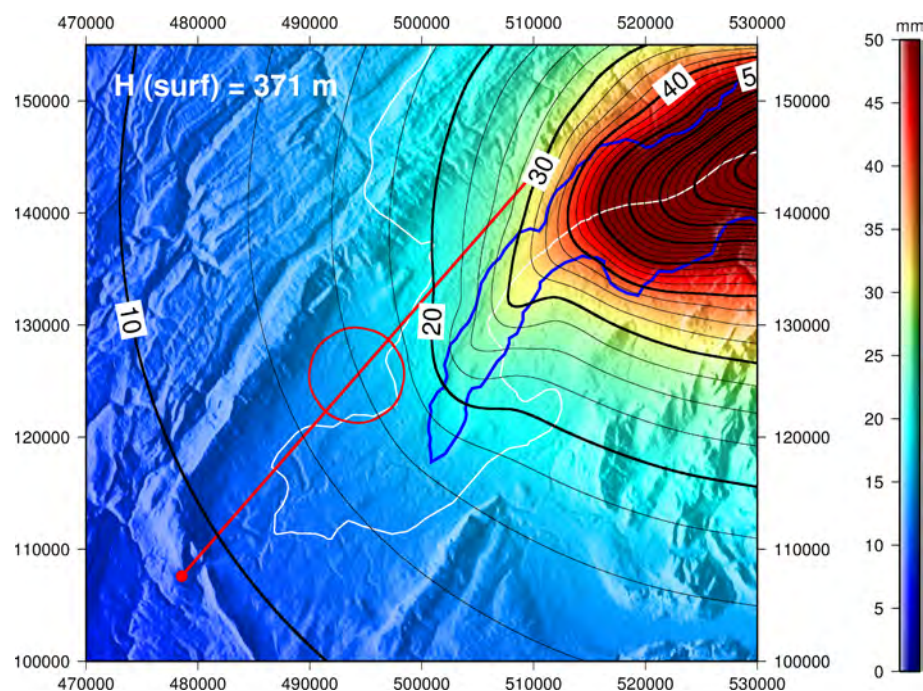


**Figure 6.42:** Absolute variations of the equipotential surface in the region of Geneva generated by the whole Lake of Geneva LAKE<sub>371</sub>.

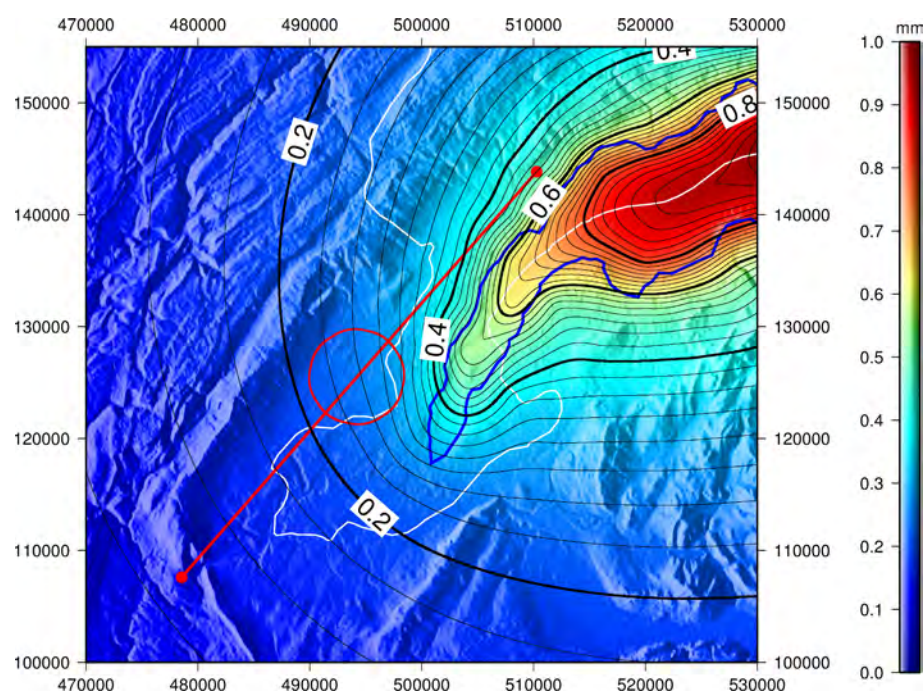


**Figure 6.43:** Absolute variations of the equipotential surface in the region of Geneva generated by an overall variation of the Lake of Geneva by 2 meters, LAKE<sub>373</sub>-LAKE<sub>371</sub>.

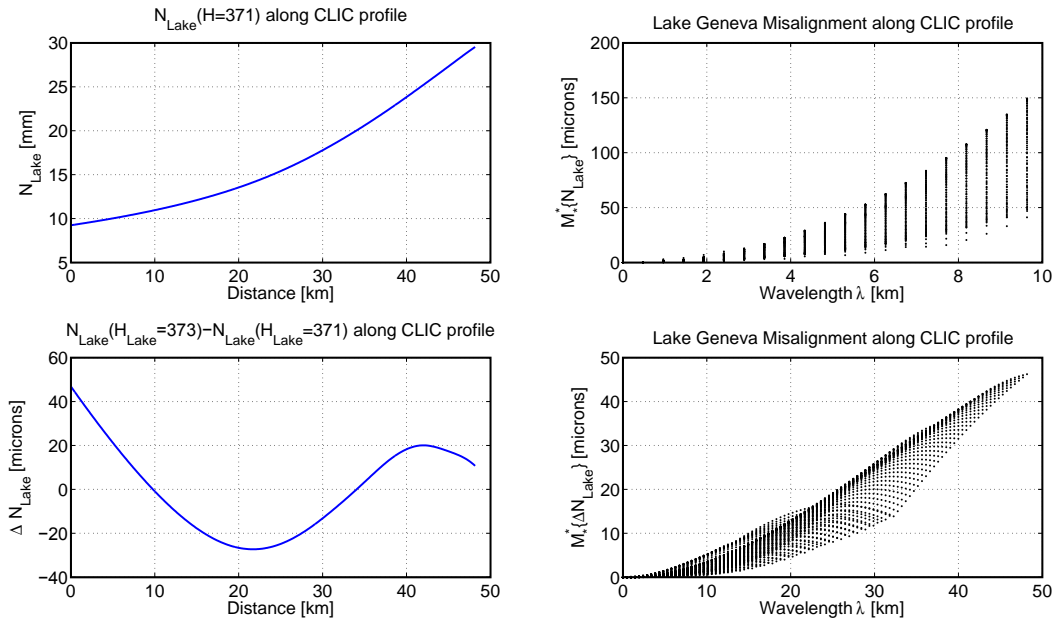


**Figure 6.44:** (Upper, left) equipotential profile generated by the whole Lake of Geneva along the CLIC profile. (Upper, right) misalignments  $\mathcal{M}_* \{N_{\text{Lake}}\}$ . (Lower, left) equipotential profile generated by an overall variation of the Lake of Geneva by 2 meters along the CLIC profile. (Lower, right) misalignments  $\mathcal{M}_* \{\Delta N_{\text{Lake}}\}$ .

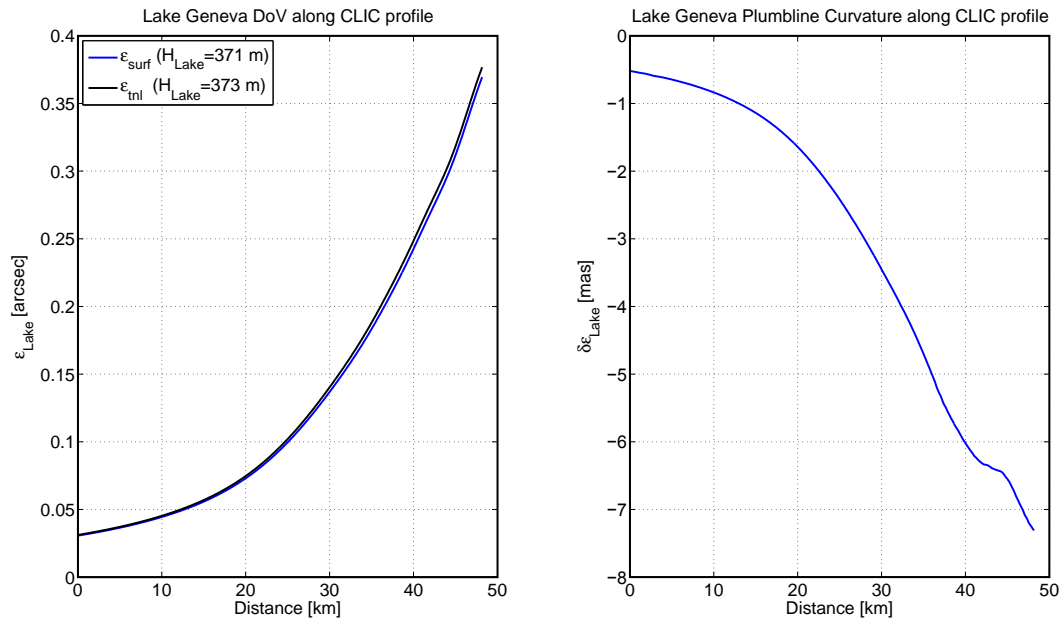


**Figure 6.45:** (Left) deflection of the vertical on the surface of topography generated by LAKE<sub>371</sub> and deflection of the vertical in the tunnel generated by LAKE<sub>373</sub>, along the CLIC profile. (right) curvature of the plumblines generated by LAKE<sub>371</sub> and LAKE<sub>373</sub>.



### 6.7.2 Seiches

From a physical point of view, since the vertical dimension of the Lake of Geneva is very small compared to the horizontal ones, the shallow water equations, presented in Section 3.6.2, provide a very good hydrodynamic model. They parameterize the water by three 2D time-varying fields, the 2D field of water surface heights and the 2D velocity field. As input they need the geometry of the basin, the initial state of the water and eventually forcing terms. For example, in *Bauer* (1979), we can find several numerical hydrodynamic simulations of the Lake of Geneva, forced by wind friction, based on the shallow water equations, which reproduce observations of the lake level oscillations with good precision.

In order to generate homogeneous polyhedra for gravity field simulations, the most precise way to generate the surface of the Lake of Geneva at successive epochs, is certainly provided by numerical simulations similar to those provided in *Bauer* (1979). However, this solution has not been retained. Apart from the fact that such simulations are beyond the scope of this thesis, the aim is to estimate some order of magnitude of extreme events and a high accuracy is not needed. The privileged solution for generating the surface of the Lake of Geneva is a mixture between some information provided by *Bauer* (1979), and parts of the analytic solutions of the linear shallow water equations for rectangular flat basins. In particular since there exist resonant modes, standing waves solutions are provided.

#### Solution of the Linear Shallow Water Equation in Rectangular Basins

Basically, for a basin of length  $L_x$ , width  $L_y$  and a flat depth  $h_r$ , the three 2D fields are given by the superposition of normal modes of the linear shallow water equations:

$$\begin{aligned} h(x, y, t) &= \sum_{N=0}^{\infty} \sum_{M=0}^{\infty} h_{N,M}(x, y, t) \\ v_x(x, y, t) &= \sum_{N=0}^{\infty} \sum_{M=0}^{\infty} v_{x,N,M}(x, y, t) \\ v_y(x, y, t) &= \sum_{N=0}^{\infty} \sum_{M=0}^{\infty} v_{y,N,M}(x, y, t) \end{aligned} \quad (6.22)$$

where  $h$  represents the field of water surface heights and  $v_x$  and  $v_y$  the horizontal velocity fields in  $x$  and  $y$ . The normal modes are given by:

$$\begin{aligned} h_{N,M}(x, y, t) &= A_{N,M} \cdot \cos(k_N \cdot x) \cos(k_M \cdot y) \cos(k_{N,M} \cdot c_r \cdot t) \\ v_{x,N,M}(x, y, t) &= A_{N,M} \cdot \frac{g \cdot k_N}{c_r \cdot k} \cdot \sin(k_N \cdot x) \cos(k_M \cdot y) \sin(k_{N,M} \cdot c_r \cdot t) \\ v_{y,N,M}(x, y, t) &= A_{N,M} \cdot \frac{g \cdot k_M}{c_r \cdot k} \cdot \cos(k_N \cdot x) \sin(k_M \cdot y) \sin(k_{N,M} \cdot c_r \cdot t) \end{aligned} \quad (6.23)$$

with:

$$k_N = \frac{\pi N}{L_x}, \quad k_M = \frac{\pi M}{L_y}, \quad k_{N,M} = \sqrt{k_N^2 + k_M^2}, \quad c_r = \sqrt{g \cdot h_r} \quad (6.24)$$

and  $A_{N,M}$  the initial height amplitude of the mode  $N, M$  and  $g$  the acceleration of gravity. Equations 6.23 show time and space periodic features from which the modal period  $T_{N,M}$  is given by:

$$T_{N,M} = \frac{2\pi}{k_{N,M} \cdot c_r} \quad (6.25)$$

For example, the periods related to a rectangular flat basin corresponding to the Lake of Geneva, of dimensions:  $L_x = 75$  km,  $L_y = 7$  km and  $h_r = 150$  m, are listed in Table 6.17.

**Table 6.17:** Periods, in minutes, corresponding of the resonant modes of a rectangular flat basin of  $L_x = 75$  km,  $L_y = 7$  km and  $h_r = 150$  m.

M \ N	N			
	0	1	2	3
0	$\infty$	65.17	32.59	21.72
1	6.08	6.06	5.98	5.86
2	3.04	3.04	3.03	3.01
3	2.02	2.03	2.02	2.02

In particular, if we look at the period of the principal longitudinal mode  $T_{1,0} = 65.17$  minutes, we can see that it corresponds approximately to the actual one, observed at 73.77 minutes, see Figure 6.40.

### Modified Rectangular Basin Solution for the Lake of Geneva

The solution retained for the generation of the surface of the Lake of Geneva is an adaptation of the formula of the height field of the rectangular basin. The adaptation is simple and consists in replacing, in Equation 6.23, the terms which model the profile of the longitudinal wave by the profile given by in *Bauer* (1979). In addition, the period is no longer computed from the dimension of the basin but just taken from the observation. Only the first longitudinal mode, of period  $T_{1,0} = 73.77$  minutes, containing the major part of the energy, is considered. The initial amplitude is fixed at 1.0 meters, an extreme case for the Lake of Geneva. The equation for the surface of the Lake of Geneva is given by:

$$h(x, y, t) = \sum_{N=0}^{\infty} \sum_{M=0}^{\infty} h_{N,M}(x, y, t) = \sum_{N=0}^1 \sum_{M=0}^0 h_{N,M}(x, y, t) \quad (6.26)$$

with:

$$h_{N,M}(x, y, t) = \text{Bauer}_{N,M}(x) \cdot \cos(k_M \cdot y) \cos\left(\frac{2\pi}{T_{N,M}} \cdot t\right) \quad (6.27)$$

where the function  $\text{Bauer}_{N,M}(x)$  represents the longitudinal profile given in *Bauer* (1979). The first two modes are represented in Figure 6.46 (left), at  $t = 0$  minutes.

### Misalignment Analyses due to Seiches

The gravity fields generated by the Seiches model, given in the previous section, are computed for epochs separated by 5 minutes, for a complete cycle of approximately 75

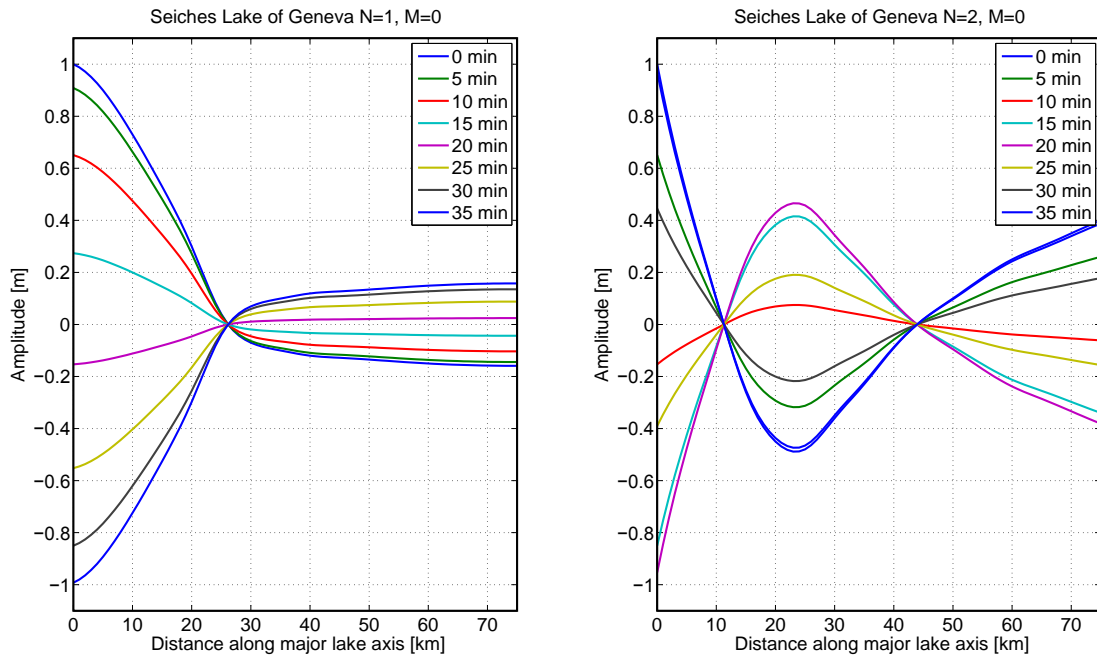


**Figure 6.46:** Seiches profile, from Geneva (West) to Montreux (East) of the first (left) and second (right) longitudinal mode at different epochs according to *Bauer* (1979).

minutes. Perspective views of the mass models, for a half-cycle, are shown in Figure 6.49, and the corresponding consequences on the variation of the equipotential surface at  $H = 350$  meters are shown in Figure 6.50. They show that the absolute variations are of the order of some 0.1 mm. Concerning the effects on the profile of CLIC, Figure 6.47 confirms that the changes are very small and negligible. The maximal misalignments only reach 0.07, 1.0 and 10.0 microns for the wavelengths  $\lambda = 1$ ,  $\lambda = 5$  and 20 km, respectively. The absolute variations of the deflection of the vertical are in the order of some milliarcsec, see Figure 6.48.

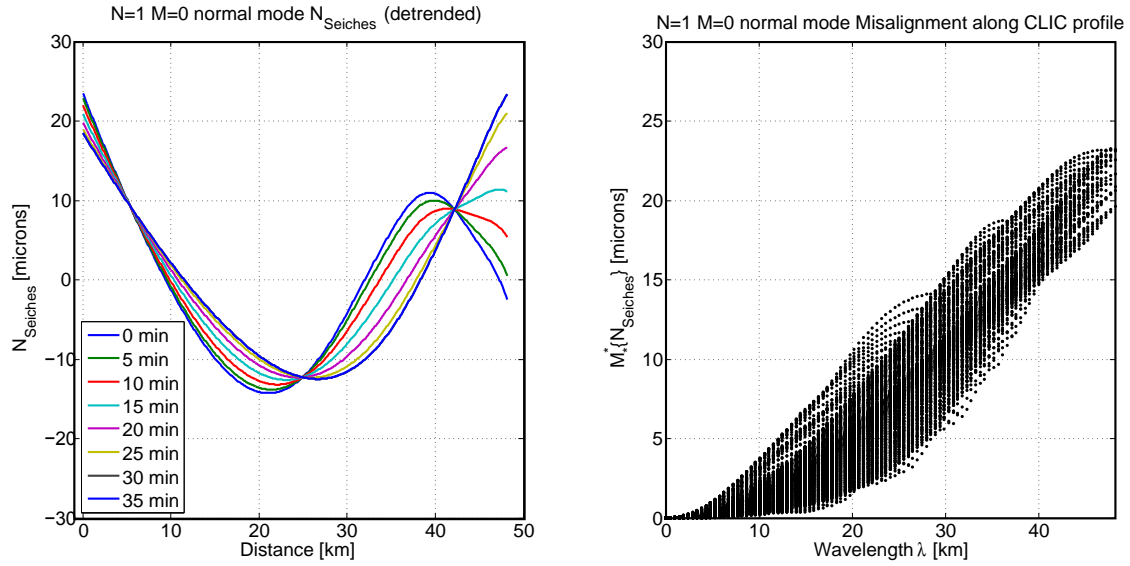


**Figure 6.47:** (Left) equipotential profile generated by the first longitudinal normal mode ( $N = 1, M = 0$ ) of an extreme Seiches event in the Lake of Geneva along the CLIC profile, at different epochs, during a half-cycle. (Right) misalignments  $M_{\star}\{N_{\text{Seiches}}\}$ .

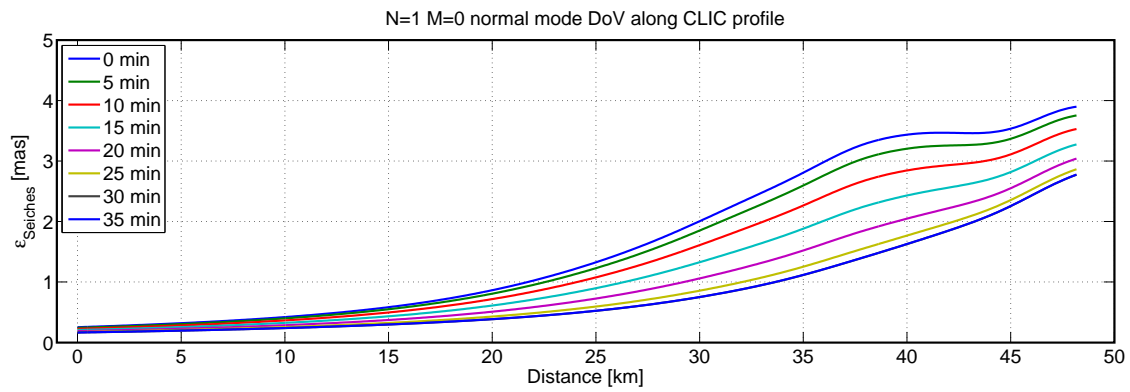


**Figure 6.48:** Deflections of the vertical on the surface generated by the first longitudinal normal mode ( $N = 1, M = 0$ ) of an extreme Seiches event in the Lake of Geneva along the CLIC profile, at different epochs, during a half-cycle.

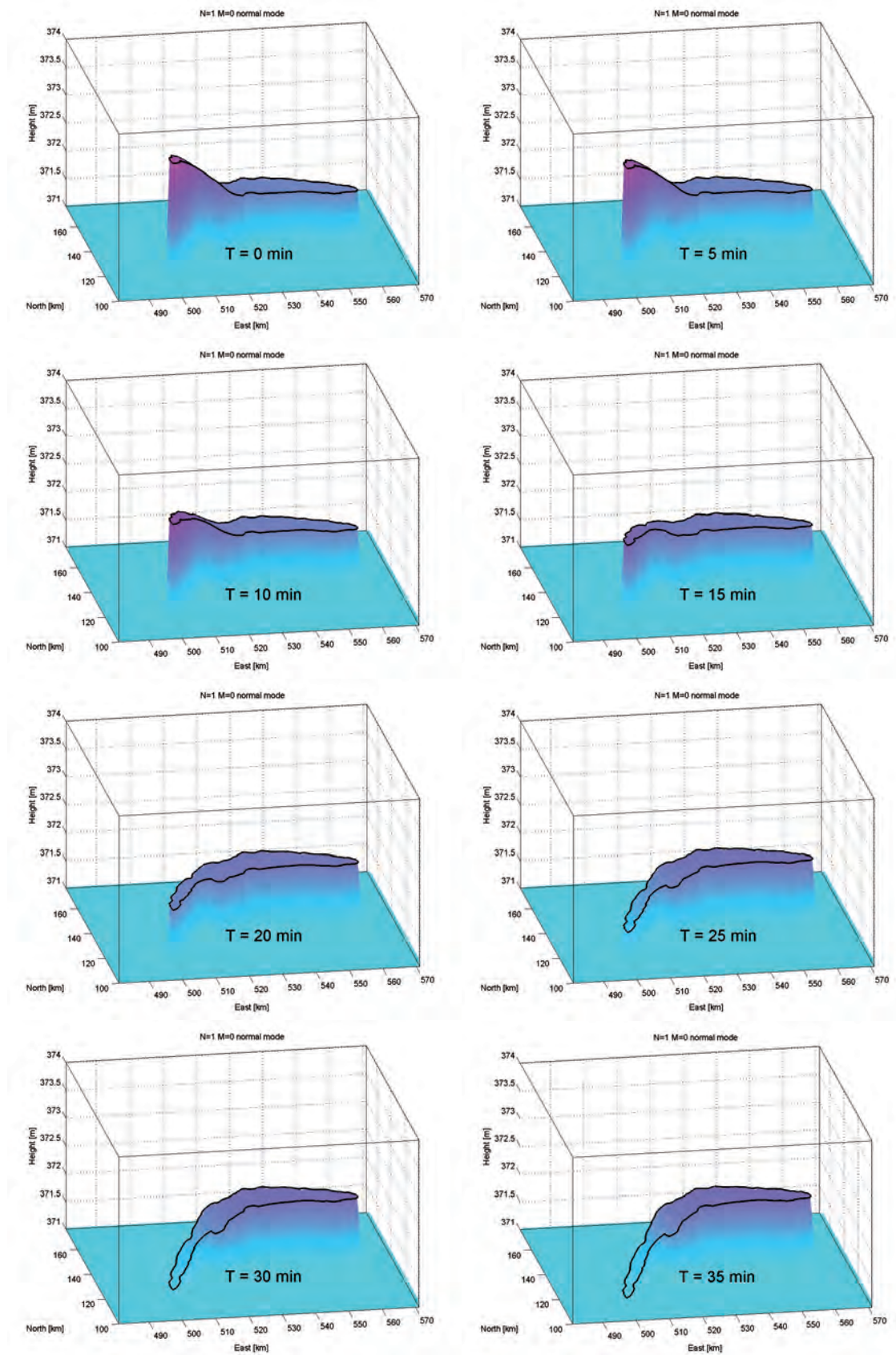


**Figure 6.49:** First longitudinal normal mode ( $N = 1, M = 0$ ) of an extreme Seiches event in the Lake of Geneva along the CLIC profile, at different epochs, during a half-cycle.



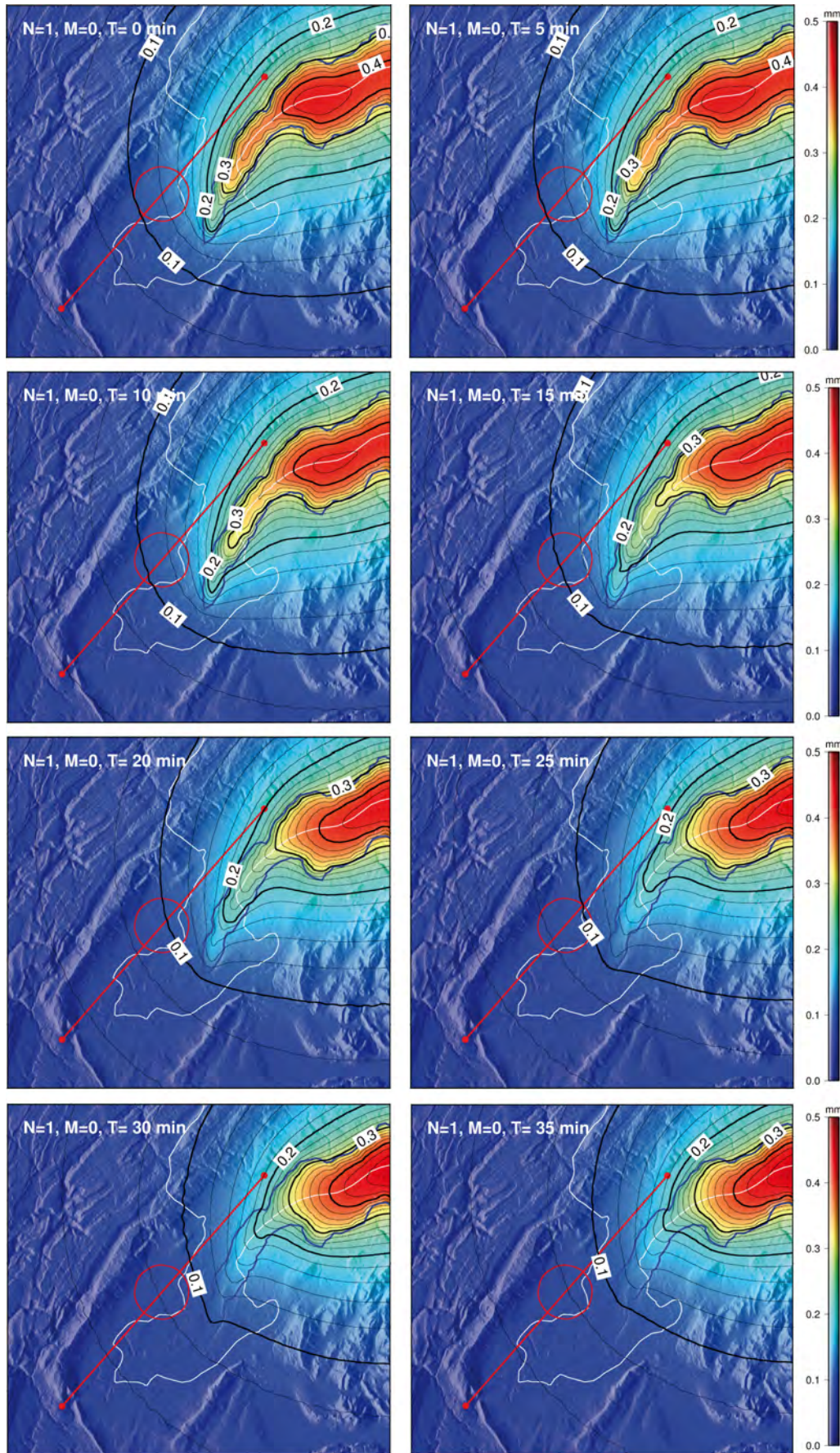


**Figure 6.50:** Equipotential surface variations, at  $H = 350$  meters, generated by the first longitudinal normal mode ( $N = 1, M = 0$ ) of an extreme Seiches event in the Lake of Geneva along the CLIC profile, at different epochs, during a half-cycle.

## 6.8 Concluding Remarks

The main findings of this chapter can be separated into two distinct parts. The first part concerns the systematic analyses of lateral varying anomalies. The second part concerns the analyses related to the CLIC profile situated in the region of Geneva. If nothing is stated more precisely, the term *significant signal* is used instead of the *misalignment larger than 10 microns for a wavelength of 200 meters*.

### Lateral Varying Anomalies

The first conclusion is that it is very difficult to draw precise general conclusions from the large amount of simulations performed in this chapter. However, we can still say that:

- Anomalies located entirely below the tunnel:
  - can generate significant signals for density contrasts larger than  $200 \frac{\text{kg}}{\text{m}^3}$ .
  - of wavelengths between 220 and 6000 meters can generate significant anomalies.
  - (connected slabs) are observable if gravimetric measurements are carried out on the topography and in the tunnel.
  - (sinus) are partially observable if gravimetric measurements are carried out on the topography and in the tunnel. Large amplitude anomalies approaching the tunnel to less than 10 meters are not observable.
- Anomalies with masses between the tunnel and a flat topography:
  - can generate significant signals for density contrasts larger than  $100 \frac{\text{kg}}{\text{m}^3}$ .
  - of wavelengths between 120 and 5000 meters can generate significant anomalies.
  - (connected slabs) are partially observable if gravimetric measurements are carried out on the topography and in the tunnel. Anomalies of density contrast larger than  $200 \frac{\text{kg}}{\text{m}^3}$  are not observable.
  - (sinus) are partially observable if gravimetric measurements are carried out on the topography and in the tunnel. Anomalies of density contrast larger than  $200 \frac{\text{kg}}{\text{m}^3}$  are not observable.
- Anomalies with masses between the tunnel and a non-flat topography ( $\text{SIN}_{25 \rightarrow 28}$  not considered):
  - (connected slabs) can generate significant signals for density contrasts larger than  $100 \frac{\text{kg}}{\text{m}^3}$ .
  - (sinus) can generate significant signals for density contrasts larger than  $300 \frac{\text{kg}}{\text{m}^3}$ .
  - of wavelengths between 360 and 3000 meters can generate significant anomalies (for amplitudes larger than 100 meters).
  - (connected slabs) are partially observable if gravimetric measurements are carried out on topography and in the tunnel. Anomalies of density contrast larger than  $200 \frac{\text{kg}}{\text{m}^3}$  are not observable.

- (sinus) are partially observable if gravimetric measurements are carried out on the topography and in the tunnel. Anomalies with amplitudes larger than 50 meters and density contrast larger than  $100 \frac{\text{kg}}{\text{m}^3}$  are not observable.

These findings can also be summarized as follows. The shorter wavelengths which can generate significant signals is equal to 120 meters. This means that observations must be carried out with a spacing shorter than 60 meters. In addition, the density field between the tunnel and the topography must be known with a precision better than  $100\text{-}200 \frac{\text{kg}}{\text{m}^3}$ .

### CLIC Profile

The topographic masses generate significant signals for 17.8% of the profile, all located in the first 17 kilometers. In addition it has been demonstrated that only 60% of these signals are directly observable by astrogravimetric levelling (with gravimetric measurements carried out on the topography and in the tunnel). This means that 7.9% of the whole profile, located in the first 4 kilometers, are not directly observable.

The analysis concerning the signals generated by non-modeled topographic density contrasts shows that no signals are generated for density contrasts lower than  $300 \frac{\text{kg}}{\text{m}^3}$ . Nevertheless, the first 3 kilometers still remain not observable and problematic for density contrasts larger than  $100 \frac{\text{kg}}{\text{m}^3}$ .

The impact of time-varying phenomena as the disturbing centrifugal potential and extreme variations of the surface of the Lake of Geneva do not generate significant gravity signals which must be modeled, for the equipotential as well for observations. Finally, the impact of the Earth's tides signals is small and can well be taken into account with the standard existing models.



## Chapter 7

# Astrogeodetic Determination of Deflections of the Vertical

This chapter deals with the astrogeodetic determination of deflections of the vertical. More specifically, it looks at the determination of the direction of the local gravity acceleration vector in the ITRS, being more fundamental than the deflection of the vertical itself. According to (*Jekeli*, 1999), the deflection of the vertical is defined as the angular difference between the local gravity direction and a reference direction. This reference direction can be the perpendicular to a reference ellipsoid or the direction of the normal gravity vector, defining the *Helmert* and *Molodensky* deflections of the vertical, respectively. Rigorous formulas and relations for the determination of equipotential profiles are given in Section 4.3.4.

After a short introduction to basic principles of astrogeodetic determinations of the local gravity acceleration vector in the ITRS, two high-precision zenith camera systems are presented. The first system DIADEM (Digital Astronomical Deflection Measuring System) was initially constructed within a collaborative project of ETH Zurich together with the Geodetic Institute at the Leibniz University of Hannover. During more than three decades, the system has been deployed in numerous countries in Europe and North America. Specially it was deployed in the astrogravimetric campaign TZ32 at CERN as exposed in Chapter 8.

Based on the experiences gained with DIADEM, a second camera system CODIAC (Compact Digital Astrometric Camera) has been designed, developed and manufactured at ETH Zurich. As already DIADEM in 2011 (*Smith et al.*, 2013), the new system CODIAC has been successfully deployed 2014 in the project Geoid slope validation survey (GSVS14) in the state of Iowa, conducted by the US National Geodetic Survey (NGS) from NOAA.

### 7.1 Astrogeodetic Determination of the Local Gravity Unit Vector

Astrogeodetic determinations of the local gravity unit vector in the ITRS, denoted by  $\mathbf{e}_{\text{g}_{\text{tot}}}^{\text{ITRS}}$ , became possible at the moment when two elements reached sufficient accuracy.

The first one was the prediction of topocentric apparent places of celestial bodies with respect to a global Earth-fixed reference system. The second condition was fulfilled, when directional observations of celestial bodies related to gravity became possible. Formally, if the apparent place of a celestial body with respect to the ITRS, denoted by  $\mathbf{s}_\star^{\text{ITRS}}$ , is known, a gravity-dependent directional observation is a function  $\mathcal{L}$  of  $\mathbf{s}_\star^{\mathcal{G}}$ , but expressed in the local astronomical topocentric system  $\mathcal{G}$ . The observation equations are based on the following relation:

$$\mathcal{L}(\mathbf{s}_\star^{\mathcal{G}}) = \mathbf{T}_{\text{ITRS}}^{\mathcal{G}}(\Phi, \Lambda) \cdot \mathbf{s}_\star^{\text{ITRS}} \quad (7.1)$$

with:

$$\mathbf{T}_{\text{ITRS}}^{\mathcal{G}}(\Phi, \Lambda) = \begin{pmatrix} -\sin \Phi \cos \Lambda & -\sin \Phi \sin \Lambda & \cos \Phi \\ -\sin \Lambda & \cos \Lambda & 0 \\ \cos \Phi \cos \Lambda & \cos \Phi \sin \Lambda & \sin \Phi \end{pmatrix} \quad (7.2)$$

where the unknown parameters are the astronomical longitude and latitude  $(\Phi, \Lambda)$  which completely define  $\mathbf{e}_{\text{g}_{\text{tot}}}^{\text{ITRS}}$  by:

$$\mathbf{e}_{\text{g}_{\text{tot}}}^{\text{ITRS}} = - \begin{pmatrix} \cos \Phi \cos \Lambda \\ \cos \Phi \sin \Lambda \\ \sin \Phi \end{pmatrix} \quad (7.3)$$

In practice, the observation Equation 7.1 is not sufficient and must be completed because real measurements are always affected by a variety of systematic errors. Some of them are invariant during one or several nights and can be estimated by an appropriate calibration procedure (e.g. for zenith camera, scale factors and orientations of tiltmeters with respect to the CCD camera, estimated within a celestial calibration procedure). Others are assumed to be unchanged only during a single setup or even during some minutes (e.g. zenith camera, absolute offset of tiltmeters). The modern acquisition setup, calibration and data processing details are exposed in *Hirt* (2004), successfully taken over by *Somieski* (2008) for the ETH system DIADEM, and summarized by *Hirt* (2010).

### 7.1.1 Topocentric Apparent Places of Celestial Bodies (Stars)

The computation of topocentric apparent places of celestial bodies, also called topocentric *proper direction* (*van Altena*, 2012), is an ancestral challenge, still closely related to fundamental advances in theoretical and experimental physics. In fact, this very hard task is directly related to ultimate definitions, formalization and realizations of space-time reference systems, transformations in-between, modeling of motion and propagation of electromagnetic signals between objects and observers. Modern atmosphere-free astrometric computations are all based on the general relativistic framework and allow predictions at  $\mu\text{arcsec}$  level (*Klioner and Kopeikin*, 1992; *Klioner*, 2002).

If we restrict the problem to the proper direction of a particular star, the aim is to predict the topocentric proper direction  $\mathbf{s}_\star^{\text{ITRS}}$  of its incoming photons<sup>1</sup>, for an observer on

<sup>1</sup>It may be confusing and contradictory that we want to compute a topocentric proper direction in the ITRS, and not in the local topocentric system. Here it is important to understand that *topocentric* signifies

Earth, located at a known ITRS position  $\boldsymbol{\rho}_{\text{obs}}^{\text{ITRS}}$ , who reads the time  $t_{\text{obs}}^{\text{UTC}}$  on his watch. Assuming that the position of the star  $\mathbf{r}_{\star}^{\text{ICRS}}(t_0^{\text{TT}})$  is precisely known in the ICRS, at a certain reference epoch<sup>2</sup>  $t_0^{\text{TT}}$ , the following function has to be found:

$$\mathbf{s}_{\star}^{\text{ITRS}} \left\{ \mathbf{r}_{\star}^{\text{ICRS}}(t_0^{\text{TT}}), \boldsymbol{\rho}_{\text{obs}}^{\text{ITRS}}, t_{\text{obs}}^{\text{UTC}} \right\} \quad (7.4)$$

and according to *Kaplan et al.* (1989), this function can take the form:

$$\mathbf{s}_{\star}^{\text{ITRS}}(t_{\text{obs}}^{\text{TT}}) = \mathbf{S}_{\text{GCRS}}^{\text{ITRS}}(t_{\text{obs}}^{\text{TDB}}) \cdot f \left\{ g \left[ \mathbf{r}_{\star/\text{obs}}^{\text{ICRS}}(t_{\text{obs}}^{\text{TDB}}) \right] \right\} \quad (7.5)$$

where the barycentric vector of the star from which we subtracted the barycentric vector of the observer<sup>3</sup> is given by:

$$\mathbf{r}_{\star/\text{obs}}^{\text{ICRS}}(t_{\text{obs}}^{\text{TDB}}) = \mathbf{r}_{\star}^{\text{ICRS}}(t_0^{\text{TDB}}) + \dot{\mathbf{r}}_{\star}^{\text{ICRS}}(t_0^{\text{TDB}}) \cdot (t_{\text{obs}}^{\text{TDB}} - t_0^{\text{TDB}}) - \mathbf{r}_{\text{obs}}^{\text{ICRS}}(t_{\text{obs}}^{\text{TDB}}) \quad (7.6)$$

which is related to the known Earth-fixed geocentric position of the observer by:

$$\mathbf{r}_{\text{obs}}^{\text{ICRS}}(t_{\text{obs}}^{\text{TDB}}) = \mathbf{r}_{\delta}^{\text{ICRS}}(t_{\text{obs}}^{\text{TDB}}) + \mathbf{S}_{\text{GCRS}}^{\text{ITRS}^T}(t_{\text{obs}}^{\text{TDB}}) \cdot \boldsymbol{\rho}_{\text{obs}}^{\text{ITRS}} \quad (7.7)$$

where:

---

only that we want to compute the proper direction for an observer fixed on the Earth's surface and not at geocenter. It does not mean that the axes are defined as a traditional local topocentric system. In fact, the axes are defined to be parallel to the axes of ITRS.

<sup>2</sup>According to *Kaplan* (2005), for modern stars catalogs, the reference epoch  $t_0^{\text{TT}}$  is J2000.0 in the TT timescale.

<sup>3</sup>This relation models the linear proper motion of the star as well as the classical yearly and daily parallax.

- $t_{\text{obs}}^{\text{TT}}$  = epoch of observation in terrestrial time TT. The time TT runs at the same rate as a time scale based on SI seconds on the surface of the Earth.
- $t_{\text{obs}}^{\text{TDB}}$  = epoch of observation in the barycentric dynamical time TDB. The TDB is a correct timescale for equations of motion referred to the barycenter of the solar system (*Kaplan, 2005*).
- $t_0^{\text{TDB}}$  = reference epoch of the star catalog in TDB.
- $\mathbf{s}_{\star}^{\text{ITRS}}$  = atmosphere-free non-normalized topocentric proper direction vector of the star  $\star$  in the ITRS.
- $\mathbf{r}_{\star}^{\text{ICRS}}$  = position vector of the star in the ICRS.
- $\dot{\mathbf{r}}_{\star}^{\text{ICRS}}$  = space motion vector of the star in the ICRS.
- $\mathbf{r}_{\text{obs}}^{\text{ICRS}}$  = position vector of the observer in the ICRS.
- $\mathbf{r}_{\delta}^{\text{ICRS}}$  = position vector of the geocenter in the ICRS.
- $\boldsymbol{\rho}_{\text{obs}}^{\text{ITRS}}$  = position vector of the observer in the ITRS.
- $\mathbf{S}_{\text{GCRS}}^{\text{ITRS}}$  = Rotation matrix which transforms a vector given in the GCRS into the ITRS.
- $g[\dots]$  = function which models the general relativistic gravitational deflection of light.
- $f\{\dots\}$  = Lorentz transformation between BCRS (ICRS) and GCRS. Models the aberration of light.

### 7.1.2 Atmospheric Refraction

For an observer located on the surface of the Earth, the topocentric proper direction  $\mathbf{s}_{\star}^{\text{ITRS}}$ , given in the previous section, is not yet the real apparent direction of the star. In fact, in Equation 7.5, the interactions with the atmosphere are not considered. From a physical point of view, the effect of the atmosphere on the apparent direction can be addressed by two ways: the propagation of electromagnetic waves in a refractive medium and the principle of *Fermat*. In the first approach, the apparent direction corresponds to the perpendicular to the wavefront at the location of the observer, and for the second, light is treated in the geometrical optics framework as rays for which trajectories satisfy paths of stationary optical length with respect to variations of the path (*Ghatak, 2005*). The good thing is, that both approaches lead to the same second order differential equation, called *eikonal*, which gives, in an Euclidean system, for a particular wavelength  $\lambda$ , the trajectory of a light ray path  $\boldsymbol{\rho}$  as a function of the refractive index field  $n_{\lambda}(\boldsymbol{\rho}(s))$ :

$$\frac{d}{ds} \left[ n_{\lambda}(\boldsymbol{\rho}(s)) \cdot \frac{d\boldsymbol{\rho}(s)}{ds} \right] = \nabla n_{\lambda}(\boldsymbol{\rho}(s)) \quad (7.8)$$

where  $s$  represents the curvilinear coordinate along the trajectory. According to *Wunderlin* (1979), Equation 7.8 is given in a more explicit form by:

$$\frac{d^2 \boldsymbol{\rho}(s)}{ds^2} = \nabla n_\lambda(\boldsymbol{\rho}(s)) - \frac{1}{n_\lambda(\boldsymbol{\rho}(s))} \cdot \frac{dn_\lambda(\boldsymbol{\rho}(s))}{ds} \cdot \frac{d\boldsymbol{\rho}(s)}{ds} \quad (7.9)$$

where the refractive index field is the ratio between the speed of light in vacuum  $c$ , and in the medium  $v_\lambda(\boldsymbol{\rho}(s))$  :

$$n_\lambda(\boldsymbol{\rho}(s)) = \frac{c}{v_\lambda(\boldsymbol{\rho}(s))} \quad (7.10)$$

In the optical range, the refractive index can be derived directly from a meteorological field which comprises the temperature  $T(\boldsymbol{\rho})$ , pressure  $p(\boldsymbol{\rho})$  and partial water vapor pressure  $e(\boldsymbol{\rho})$  fields. According to *Stone and Zimmerman* (2011), formulas providing similar precision of about  $10^{-7}$  are given in *Birch and Downs* (1993) and *Ciddor* (1996). Once the refractive index field  $n_\lambda(\boldsymbol{\rho})$  is provided, the trajectory of a ray can be computed by integrating Equation 7.8 or 7.9. For arbitrary complex fields  $n_\lambda(\boldsymbol{\rho})$ , a numerical integrator has to be used. Otherwise, for simple cases as vertical stratified atmosphere models (e.g. *Geiger* (1988)), analytic solutions can be found.

For the computation of the proper direction, the trajectory  $\boldsymbol{\rho}(s)$  is not primarily of interest. In fact, the proper direction is given by its tangential vector  $\mathbf{t}(s_{\text{obs}})$  at the location of the observer, see Figure 7.1. By definition, the tangential vector is given by:

$$\mathbf{t}(s_{\text{obs}}) = \left. \frac{d\boldsymbol{\rho}(s)}{ds} \right|_{s_{\text{obs}}} \quad (7.11)$$

and the system of second order differential equations 7.9 can be reformulated as a system of first order differential equations as follows:

$$\begin{cases} \frac{d\boldsymbol{\rho}(s)}{ds} = \mathbf{t}(s) \\ \frac{d\mathbf{t}(s)}{ds} = \nabla n_\lambda(\boldsymbol{\rho}(s)) - \frac{1}{n_\lambda(\boldsymbol{\rho}(s))} \cdot \frac{dn_\lambda(\boldsymbol{\rho}(s))}{ds} \cdot \mathbf{t}(s) \end{cases} \quad (7.12)$$

which can be solved as a boundary or initial values problem.

### Algorithm for Numerical Integration

In our case, we have two boundary conditions. The position of the observer  $\boldsymbol{\rho}_{\text{obs}}^{\text{ITRS}}$  and the proper direction of the star in vacuum  $\mathbf{s}_\star^{\text{ITRS}}$ . A simple way to compute this boundary value problem and finally  $\mathbf{t}(s_{\text{obs}})$  is to solve Equation 7.12 as an initial value problem, and iterate the initial proper direction until the proper direction in vacuum  $\mathbf{s}_\star^{\text{ITRS}}$  is reached. If the vectors are given in the ITRS, the algorithm can proceed as follows:

1. for the iteration  $k$ , set the initial values to:

$$\begin{cases} \boldsymbol{\rho}_k^{\text{ITRS}}(s = s_{\text{obs}}) = \boldsymbol{\rho}_{\text{obs}}^{\text{ITRS}} \\ \mathbf{t}_k^{\text{ITRS}}(s = s_{\text{obs}}) = \frac{\mathbf{s}_\star^{\text{ITRS}}}{|\mathbf{s}_\star^{\text{ITRS}}|} \end{cases} \quad (7.13)$$

2. integrate Equation 7.12 until the limit of the tropopause ( $\approx H=12$  km) is reached  
 $\implies \mathbf{t}_k^{\text{ITRS}}(s_\star)$ .
3. compute the correction term for the initial direction by comparing the normalized directions  $\mathbf{t}_k^{\text{ITRS}}(s_\star)$  and  $\mathbf{s}_\star^{\text{ITRS}}$ :

$$\delta \mathbf{t}_k^{\text{ITRS}} = \frac{\mathbf{s}_\star^{\text{ITRS}}}{|\mathbf{s}_\star^{\text{ITRS}}|} - \frac{\mathbf{t}_k^{\text{ITRS}}(s_\star)}{|\mathbf{t}_k^{\text{ITRS}}(s_\star)|} \quad (7.14)$$

4. if the correction  $|\delta \mathbf{t}_k^{\text{ITRS}}|$  is larger than a fixed abort criterion, the new initial direction is set to:

$$\mathbf{t}_{k+1}^{\text{ITRS}}(s = s_{\text{obs}}) = \mathbf{t}_k^{\text{ITRS}}(s_{\text{obs}}) + \delta \mathbf{t}_k^{\text{ITRS}} \quad (7.15)$$

and a new iteration is started. Otherwise, if the correction  $|\delta \mathbf{t}_k^{\text{ITRS}}|$  is smaller than the abort criterion, the final proper direction of the star is given by:

$$\mathbf{t}_\star^{\text{ITRS}} \equiv \mathbf{t}_k^{\text{ITRS}}(s_{\text{obs}}) \quad (7.16)$$

### Total Refraction Signal

The total signal generated by refraction on the proper direction is the directional difference between the proper direction in vacuum  $\mathbf{s}_\star^{\text{ITRS}}$  and the proper direction after interaction with the real atmosphere  $\mathbf{t}_\star^{\text{ITRS}}$ . Formally, it is given by:

$$\delta \mathbf{s}_{\text{refr,tot}}^{\text{ITRS}} = \frac{\mathbf{t}_\star^{\text{ITRS}}}{|\mathbf{t}_\star^{\text{ITRS}}|} - \frac{\mathbf{s}_\star^{\text{ITRS}}}{|\mathbf{s}_\star^{\text{ITRS}}|} \quad (7.17)$$

### Standard Refraction

We call standard refraction, the refraction generated by a standard atmosphere. Here, the ICAO 1976 standard atmosphere (ICAO, 1976) provided by the *International Civil Aviation Organization* (ICAO) is used. In Table 7.1, only the significant optical refracting part of the standard atmosphere is shown.

region	height $H$ [km]	temperature $T$ [°C]	pressure $p$ [hPa]	rel. hum. [%]
sea level	0	15.0	1013.25	0
troposphere	0 → 11	15.0 – 6.5 · $H$ [km]	$1013.25 \cdot \left(1 - \frac{6.5 \cdot H \text{ [km]}}{288.15}\right)^{5.2581}$	0
low stratosphere	11 → 20	-56.5	$1013.25 \cdot \left(1 - \frac{6.5 \cdot H \text{ [km]}}{288.15}\right)^{5.2581}$	0

**Table 7.1:** Lowest parts of the ICAO 1976 standard atmosphere.

And the standard refraction is formally defined as:

$$\delta \mathbf{s}_{\text{refr,std}}^{\text{ITRS}} = \left. \frac{\mathbf{t}_\star^{\text{ITRS}}}{|\mathbf{t}_\star^{\text{ITRS}}|} \right|_{\text{std}} - \frac{\mathbf{s}_\star^{\text{ITRS}}}{|\mathbf{s}_\star^{\text{ITRS}}|} \quad (7.18)$$

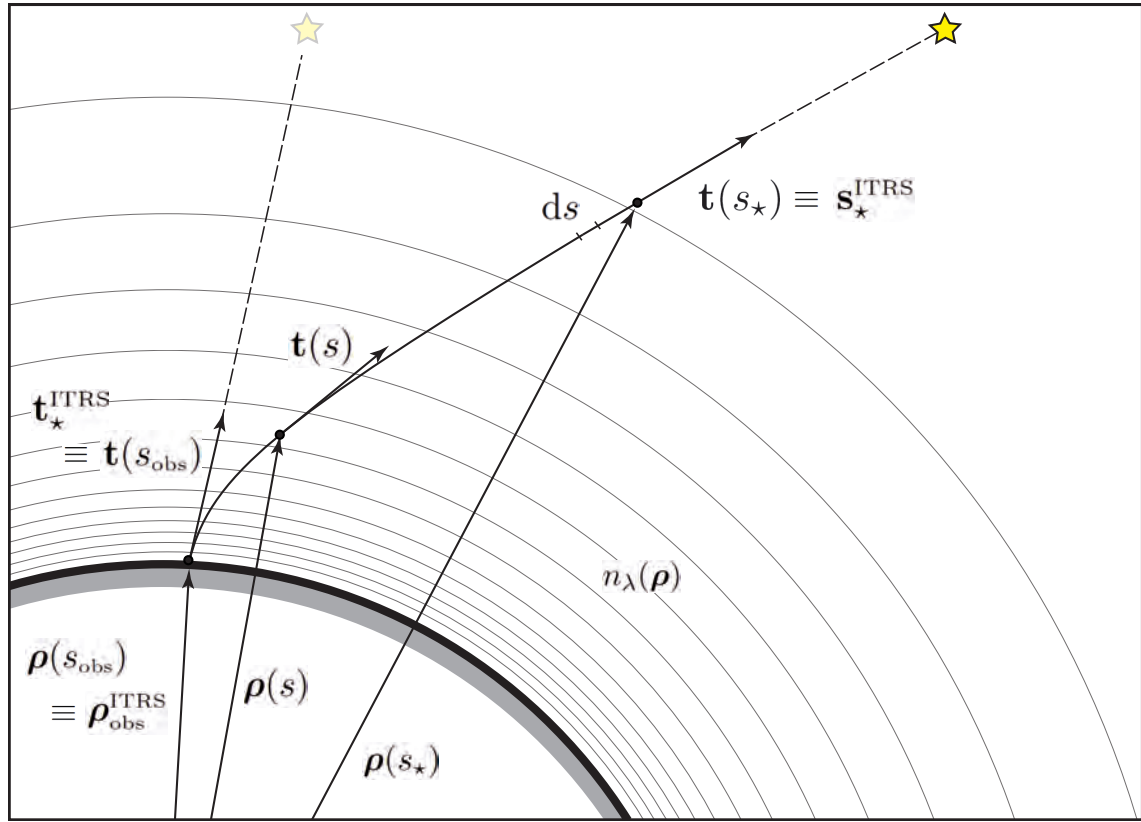


Figure 7.1: Computation of the refraction in the atmosphere.

### Anomalous Refraction

According to *Hirt* (2006), anomalous refraction is defined as the part of astronomical (here total) refraction which cannot be explained by radially symmetric refraction models. This definition is univocal only if the radially symmetric refraction model is clearly defined, which is not obvious if it depends on ground-based meteorological quantities. Here, the anomalous refraction is simply and univocally defined as the difference between the total and the standard refraction:

$$\delta \mathbf{s}_{\text{refr,anom}}^{\text{ITRS}} = \delta \mathbf{s}_{\text{refr,tot}}^{\text{ITRS}} - \delta \mathbf{s}_{\text{refr,std}}^{\text{ITRS}} \quad (7.19)$$

In zenith, while the standard refraction is equal to zero, the anomalous refraction is equal to the total refraction. Moreover, it can be demonstrated that the anomalous refraction is mainly driven by horizontal temperature gradients.

### Estimation of Anomalous Refraction in Zenith with Ray Tracing in 3D Meteo Models

This section presents briefly some results of the first determination of the anomalous refraction in zenith by ray tracing through a 3D numerical weather model. The motivation for exploring this new approach comes principally from the conclusions reached by (*Hirt*, 2004, 2006), who argues that the limiting accuracy factor of deflection of the vertical

determinations, by modern zenith camera systems, is due to non-modeled anomalous refraction signals. As usual in the case of such problems, the goal is to develop a method allowing to model a significant part of the signal in order to perform useful reductions. Here, the objectives are less ambitious, they are restricted to the computation of some statistical quantities. This can be argued by the fact that time series of observed and predicted anomalous refraction are difficult to generate. This requires high-quality observations of the deflection of the vertical and high-resolution 3D numerical weather models at the same location and time. Since no homogeneous continuous deflections are available in Switzerland, only anomalous refraction signals estimated from models are treated here and compared to the amplitudes suggested by *Hirt* (2004).

The following estimations are computed by the software `Ray_Tracing` developed in the frame of this thesis. Based on the high-resolution COSMO-2 3D numerical weather model<sup>4</sup> provided by MeteoSwiss and described in *Doms and Schättler* (2002), the numerical integration of the system 7.9 is performed with the Runge-Kutta DOPRI5 routine developed at University of Geneva by *Hairer and Wanner* (1993) and translated from the programming language FORTRAN to c++ by *Ashby* (2003). In order to take advantage of all variations of the model, the maximal adaptive integration step is fixed to 20 meters. The formulas of *Birch and Downs* (1993) are used for the computation of the index of refraction field for a wavelength of 600 nm. A trilinear interpolation scheme is used for the estimation of the field and its gradients at arbitrary positions.

In order to have a better idea of the resolution, the complexity of the model and the variation of zenith anomalous refraction, profiles along the projected CLIC (see Figure 1.2) are represented in Figure 7.2. They show the refraction field and the evolution of the anomalous refraction along zenith for six successive epochs, separated by one hour, during a night of January 2008. They outline the location of air layers contributing to the anomalous refraction. The layers higher than 3000 meters do not contribute significantly.

More quantitative results are shown in Figure 7.3. They result from ray tracing computations based on hourly COSMO-2 fields, for three months, April, July and October, in the year 2008. The mean values over one month and the hourly standard deviations of anomalous refraction (only for nightly data) provide interesting aspects. As expected, the statistical behavior of anomalous refraction depends strongly on the season and the topographic relief. The anomalous refraction is stronger in summer time and in regions along the boundaries between the Alps, basin and Jura. The reason is probably that these regions are more exposed to the mixture of air masses than other regions. The monthly systematic bias is mostly below 0.025 arcsec and the standard deviation varies between 0.1 and 0.3 arcsec, confirming the order of magnitude presented by *Hirt* (2006).

Due to the complexity of the refraction fields and the strong dependency of the refraction on the local temperature gradients, the generation of reliable epoch-wise predictions might remain an utopic wish. Nevertheless, middle-waves (5-10 km) and middle-period (2-3 hours) time-space estimations of anomalous refraction from numerical weather models

<sup>4</sup>The model COSMO-2 provides a horizontal resolution of 2.2 km, 60 layers with varying separations in the vertical, and a resolution of 15 minutes in time.



certainly deserves to be more systematically explored.

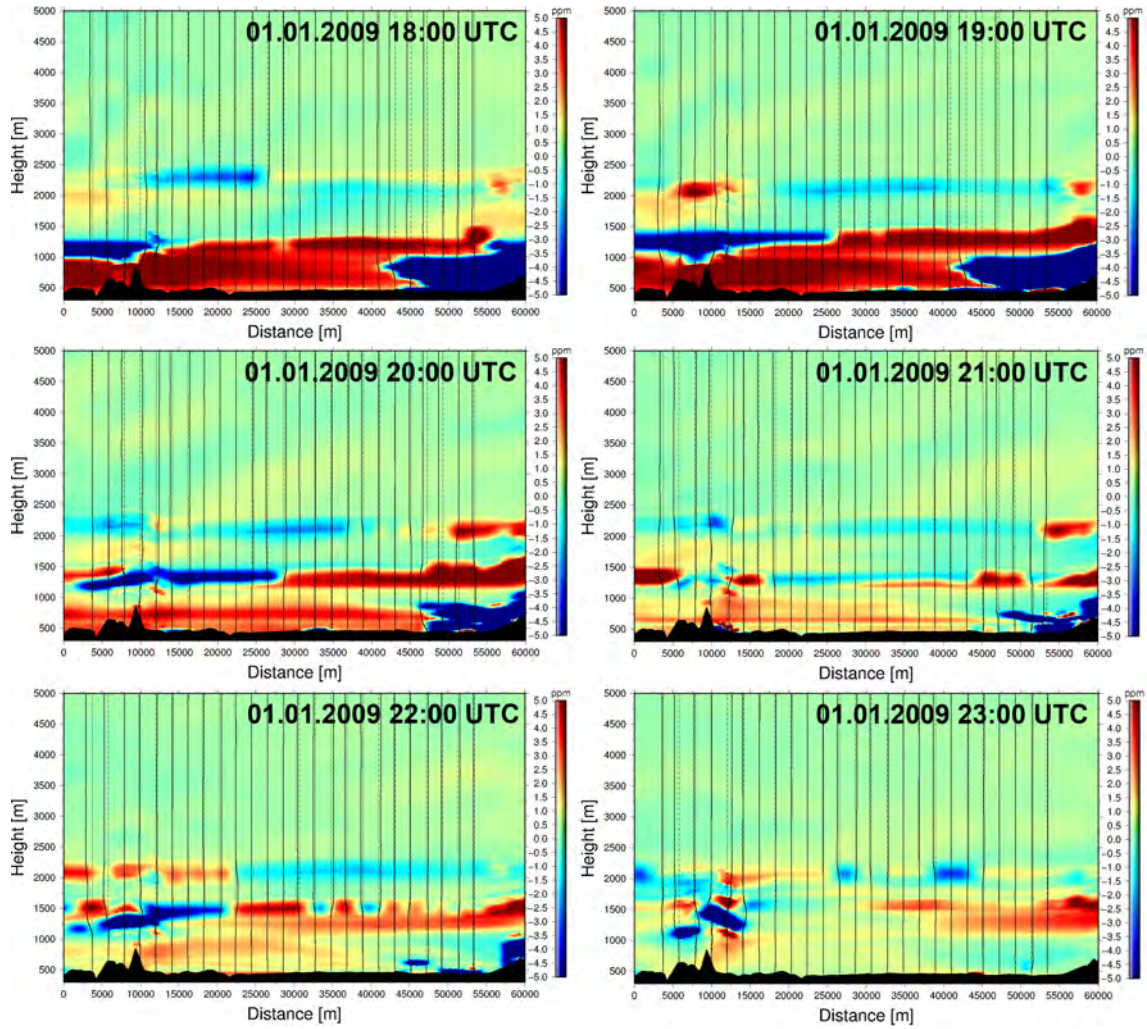


**Figure 7.2:** Refractive index field (color in ppm) and anomalous refraction in zenith along the CLIC profile estimated with ray tracing and the COSMO-2 numerical weather model. In order to represent the horizontal variations in refractive index field, at each height, the mean value is subtracted from the actual one. The black line represents the evolution of anomalous refraction in the vertical dimension, not the trajectories of light rays.

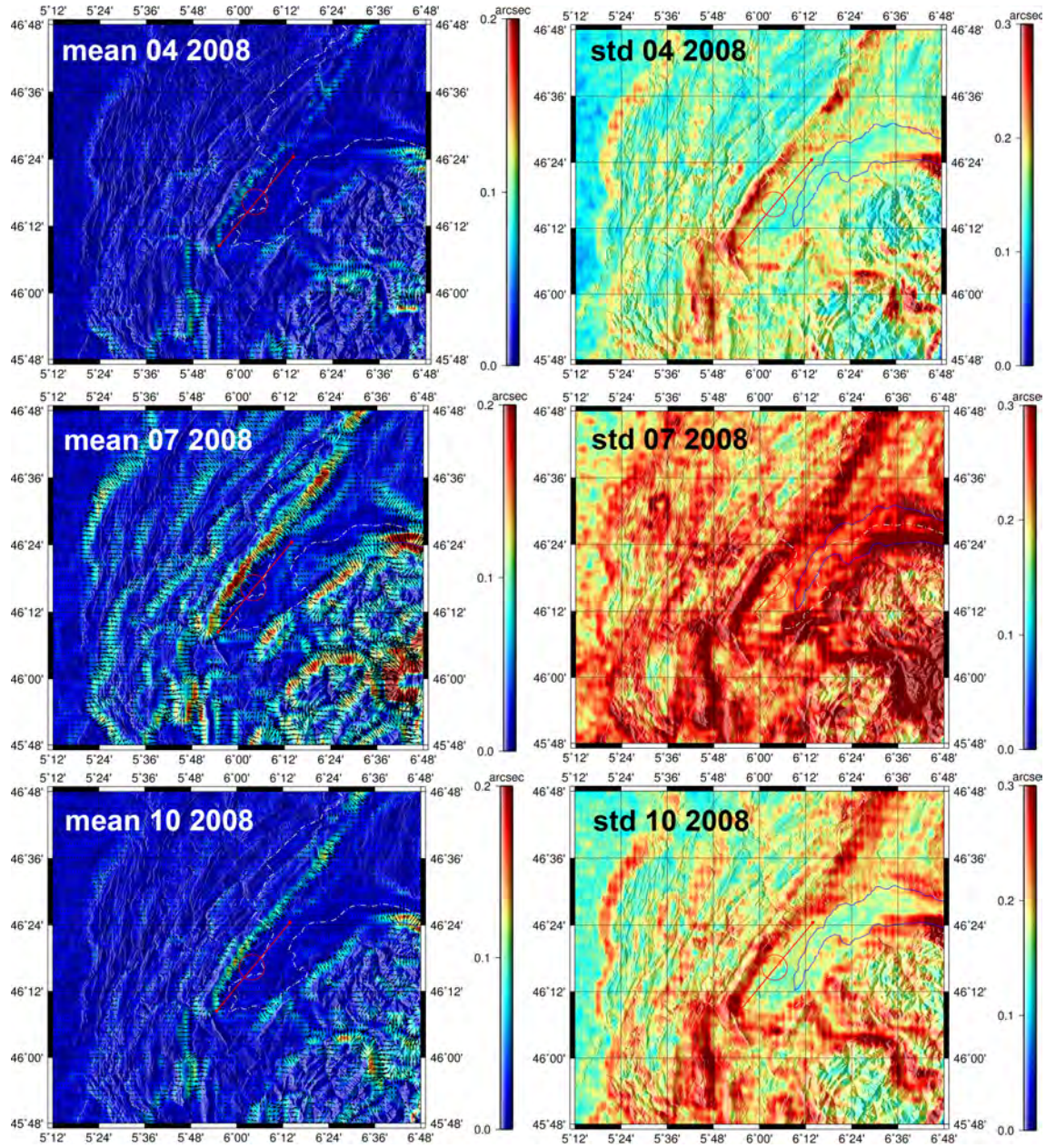


**Figure 7.3:** (Left) monthly mean value of anomalous refraction estimated with ray tracing and COSMO-2 numerical weather models. (Right) standard deviation of hourly data. Only nightly data are used for the computations.



## 7.2 The Digital Astronomical Deflection System DIADEM

The Digital Astronomical Deflection Measuring System (DIADEM) is a zenith camera system developed at ETH Zurich in a fruitful collaboration with the Institut für Erdmessung (IfE) at the Leibniz University of Hannover. While IfE designed the main part of the mechanical components, some important supplements in mechanics and electronics were carried out at ETH Zurich. The first version of the system denoted as Transportable Zenitkamera TZK3 was imaging the stars onto analogue films (*Bürki*, 1989). During about two decades the system TZK3 was deployed in numerous national and international campaigns in Europe and North America. Several hard- and software components were permanently re-designed in order to upgrade the system.

Thanks to the advent of suitable CCD cameras on the market, DIADEM was transformed from an analogue to a digital system in the year 2000 *Somieski* (2008). This important step helped not only to improve the system accuracy but also to significantly reduce the time needed for the processing chain. While the evaluation of the analogue films requested time consuming measurements on a dedicated measuring machine to determine the image coordinates of the stars, the CCD technique delivers this information quasi online. Furthermore the integration of precise tiltmeters for a better link to the local gravity direction (plumb line) and the motorization of all moving elements helped to drastically increase the level of system automation *Hirt* (2010). Last but not least the implementation of the processing software AURIGA (Automatic Realtime Image Processing System for Geodetic Astronomy) provided by C. Hirt contributed significantly to improve the performance of the zenith camera system in terms of accuracy, efficiency, and reliability. The transformation from analogue to digital allowed to win almost one order of magnitude in precision and accuracy for the determination of deflections of the vertical, from approximately 0.4 to 0.5 arcsec, for the first analogue generation, to 0.07-0.08 arcsec for the digital version. The system was deployed during more than three decades, from 1982 until 2014, when the last measurements were carried out in Austria. As described later, DIADEM has been replaced by CODIAC, the new generation of digital zenith cameras.

### 7.2.1 Instrumental Design

At a first glance, the instrument consists of an optical system pointing to the zenith, mounted on a turnable superstructure on which tiltmeters are fixed. The latest version of DIADEM (2014) is presented in Figure 7.4.

#### Optical System

The optical system is formed by:

- 1 catadioptric telescope MIROTAR of 1020 mm focal length and aperture of 200 mm, providing a focal ratio of  $f/5.6$  and a field of view of  $3.6^\circ$ .
- 1 Apogee ALTA CCD camera with an array size of  $2184 \times 1472$  pixels, providing a field of view of approximately  $0.85^\circ \times 0.57^\circ$ . The pixel size is equal to  $6.8 \times 6.8$  microns

and provides an angular resolution of  $1.4 \frac{\text{arcsec}}{\text{pixel}}$ . The digital resolution is equal to 16 bits and the mechanical shutter can be remotely triggered with an LVTTTL<sup>5</sup> signal.

- 1 FLI PDF focuser with a resolution step of 1.25 microns and a range of 8.75 mm.
- 1  $\mu$ blox GNSS receiver for the precise absolute timing of the CCD remote triggering.

### Tiltmeters

Three pairs of tiltmeters are mounted on the superstructure of DIADEM:

- 2 Wyler Zerotronic mounted orthogonally on the superstructure. The measuring range is about  $1^\circ$  and the precision is approximately 0.15 arcsec. The digitalization is realized by the sensors themselves which send tilt measurements via a RS232 interface at a rate of approximately 2 Hz.
- 2x2 HRTM (High Resolution TiltMeters), manufactured by Lippmann company for Geophysical Instruments, mounted orthogonally on the superstructure. The measuring range is about 200 arcsec and the precision is approximately 0.05 arcsec. The digitalization is realized with an external 16 bits digital acquisition board at a rate of 100 Hz.

### Mechanical Automation

The automation is guaranteed by 8 motors which allow to control the extension of the legs for the setup, to level the system automatically with a precision better than 5 arcsec, and to rotate the superstructure around its vertical axis. The major electronic components are deported in an appropriate box placed close to the camera.

### Software

The automatic acquisition comprising the levelling of the system, the focusing of the star field, the data acquisition and the visual checking of the raw data is realized with the LabView software DIADEM developed at ETH Zurich by (*Somieski*, 2008) and adapted to the new sensors (CCD camera, DAQ HRTM, focuser) in the frame of the present thesis. As mentioned previously, the data were processed with the software AURIGA.

---

<sup>5</sup>Low voltage TTL.



**Figure 7.4:** The Digital Astronomical Deflection System DIADEM in its last version (2014).

### 7.3 The Compact Digital Astrometric Camera CODIAC

The Compact Digital Astrometric Camera CODIAC is a new zenith camera system entirely designed, developed and manufactured at the Institute of Geodesy and Photogrammetry of ETH Zurich. The principal objective behind the development of a new system was to replace the system DIADEM with a system of reduced size and costs, based on commercial modern components, that provides the same level of accuracy as DIADEM. In addition, it is designed with almost industrial standards in order to facilitate the use by non-astrogeodetic experts, to increase the performance in terms of productivity, and if necessary, to provide the possibility to build additional instruments.

#### 7.3.1 Instrumental Design

As shown in Figure 7.5, the design is very similar to the system DIADEM. However, the interfaces of CODIAC are drastically improved and permit a complete steering by a single laptop connected to the instrument by only 2 USB cables. The main components are described as follows:

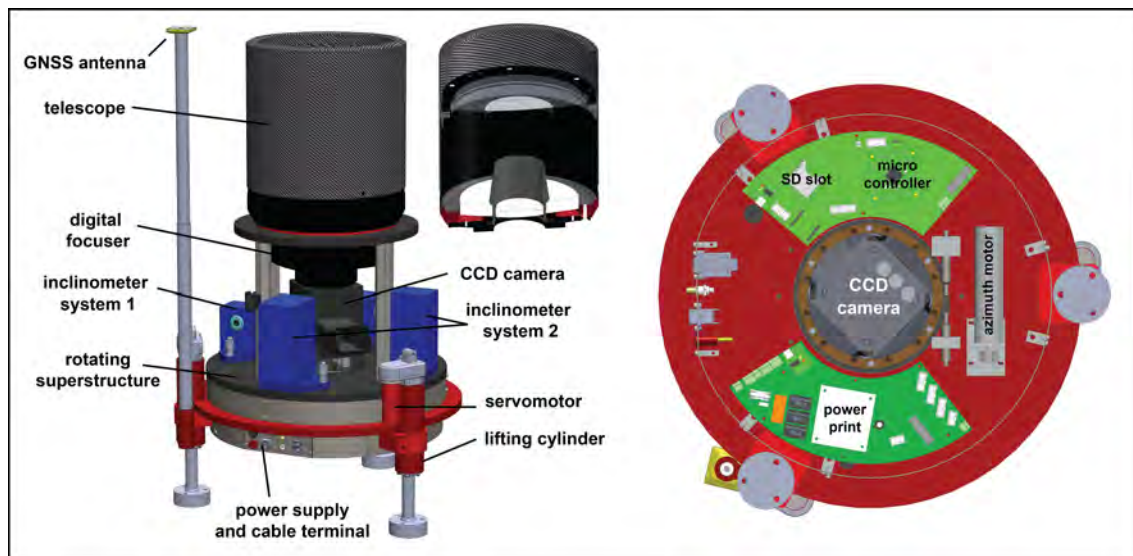


Figure 7.5: Main components of the Compact Digital Astrometric Camera CODIAC

#### Optical System

The optical system is formed by:

- 1 Veloce RH 200AT Riccardi-Honders Astrograph of 600 mm focal length and a aperture of 216 mm, providing a focal ratio of  $f/3$ .
- 1 FLI MicroLine ML8300 CCD camera with an array size of  $3326 \times 2504$  pixels, providing a field of view of approximately  $1^\circ 43' \times 1^\circ 17'$ . The pixel size is equal to  $5.4 \times 5.4$  microns and provides an angular resolution of  $1.86 \frac{\text{arcsec}}{\text{pixel}}$ . The digital resolution is



**Figure 7.6:** CODIAC deployed on the roof of the Geodesy and Geodynamics Lab of ETH Zurich.

equal to 16 bits and the mechanical shutter can be remotely triggered with a TTL signal.

- 1 FLI ATLAS focuser with a resolution step of 85 nm and a range of 8.9 mm.
- 1  $\mu$ blox GNSS receiver for the precise absolute timing of the CCD remote triggering.

### Tiltmeters

Two pairs of tiltmeters are mounted on the superstructure of CODIAC:

- 2 Wyler Zerotronic mounted orthogonally on the superstructure. The measuring range is about  $1^\circ$  and the precision is approximately 0.15 arcsec. The digitalization is realized by the sensors themselves which send tilt measurements via an RS232 interface at a rate of approximately 10 Hz.
- 2 HRTM (High Resolution TiltMeters), manufactured by Lippmann company for Geophysical Instruments (Germany), mounted orthogonally on the superstructure. The measuring range is about 200 arcsec and the precision is approximately 0.05 arcsec. The digitalization is done by the sensors themselves which send already filtered tilt measurements via an RS232 interface at a rate of approximately 10 Hz.

### Mechanical Automation

The automation is guaranteed by 4 motors which allow to control the extension of the legs for the setup, to level the system automatically with a precision better than 5 arcsec, and to rotate the superstructure around its vertical axis. All electronic components are integrated on the superstructure of the camera.

### $\mu$ Controller

CODIAC is equipped with a built-in 32 bit  $\mu$ Controller of type PIC 32. With this  $\mu$ Controller it is possible to manage important tasks locally within the camera, thus relieving the steering software. The  $\mu$ Controller is able to carry out an automatic leveling of the camera in a closed-loop control by reading the inclination sensors and activating the lifting cylinders until a predefined tolerance is reached. This independent capability helps to accelerate the observation process and to relieve of the steering software. Further tasks of the  $\mu$ Controller are the management of the power supply and the rotation of the objective into its second face or any other heading. The steering laptop communicates with the  $\mu$ Controller by means of a dedicated command set.

### Softwares

The automatic acquisition comprising the levelling of the system, the focusing of the star field, the data acquisition and the visual checking of the raw data is realized with a new software QCodiAC developed in Qt and c++ at ETH Zurich in the frame of the present thesis. The final processing is still realized with the software AURIGA.

### 7.3.2 First CODIAC Validation in Corbin USA

The first validation of CODIAC was performed in summer 2014 in the training center of the National Geodetic Survey (NGS) in Corbin USA. Standard measurements of approximately 30 minutes for each station were carried out by non-expert instructed surveyors at 6 stations separated by some 100 meters during 4 different nights. In order to estimate the performance of the system in terms of precision and repeatability, each station was re-observed several times. The results are listed in Table 7.2 and presented in Figure 7.7. Without going too much into details, each station shows a very good repeatability, almost always better than 0.05 arcsec. In addition, since two independent tiltmeter systems are available on CODIAC, it is possible to analyze the precision of the tiltmeters' contributions. They show excellent agreement in the order of 0.02-0.03 arcsec. To have a better idea of the performance of CODIAC at small scales, the lower plot in Figure 7.7, representing the deflections of the vertical reduced to the station **center**, seems to show significant signals with very low amplitudes of approximately 0.1 arcsec.



**Table 7.2:** Results of the deflections of the vertical determined by CODIAC in Corbin (USA).

$\Phi$ [deg min sec]	$\Lambda$ [deg min sec]	$\varphi$ (WGS84) [deg min sec]	$\lambda$ (WGS84) [deg min sec]	$\xi$ [arcsec]	$\eta$ [arcsec]	$v_\xi$ [arcsec]	$v_\eta$ [arcsec]	$\xi, \eta, \text{Lip.} - \text{Wyler}$ [arcsec]	
<b>west</b>									
+38 12 7.155	-77 22 23.208	+38 12 7.092	-77 22 26.832	+0.063	+2.848	+0.080	+0.036	+0.037	+0.007
+38 12 7.173	-77 22 23.142	+38 12 7.092	-77 22 26.832	+0.081	+2.900	+0.062	-0.016	-0.013	-0.036
+38 12 7.212	-77 22 23.071	+38 12 7.092	-77 22 26.832	+0.120	+2.955	+0.023	-0.071	-0.031	-0.029
+38 12 7.263	-77 22 23.111	+38 12 7.092	-77 22 26.832	+0.171	+2.924	-0.028	-0.040	+0.011	-0.035
+38 12 7.374	-77 22 23.279	+38 12 7.092	-77 22 26.832	+0.282	+2.792	-0.139	+0.092	-0.005	+0.009
				<b>+0.143</b>	<b>+2.884</b>				
<b>center</b>									
+38 12 7.164	-77 22 20.700	+38 12 7.038	-77 22 24.420	+0.126	+2.923	+0.045	+0.028	-0.020	+0.004
+38 12 7.228	-77 22 20.561	+38 12 7.038	-77 22 24.420	+0.190	+3.032	-0.019	-0.081	+0.033	+0.046
+38 12 7.234	-77 22 20.731	+38 12 7.038	-77 22 24.420	+0.196	+2.899	-0.025	+0.052	+0.014	+0.020
				<b>+0.171</b>	<b>+2.951</b>				
<b>north</b>									
+38 12 11.922	-77 22 20.545	+38 12 11.743	-77 22 24.247	+0.179	+2.909	+0.025	+0.017	-0.002	-0.023
+38 12 11.971	-77 22 20.504	+38 12 11.743	-77 22 24.247	+0.228	+2.942	-0.025	-0.017	+0.038	-0.006
				<b>+0.204</b>	<b>+2.926</b>				
<b>south</b>									
+38 12 5.374	-77 22 20.727	+38 12 5.267	-77 22 24.485	+0.107	+2.953	-0.057	-0.010	+0.014	+0.001
+38 12 5.290	-77 22 20.658	+38 12 5.267	-77 22 24.485	+0.023	+3.007	+0.027	-0.064	-0.007	+0.019
+38 12 5.331	-77 22 20.885	+38 12 5.267	-77 22 24.485	+0.064	+2.829	-0.014	+0.115	-0.008	+0.010
+38 12 5.273	-77 22 20.686	+38 12 5.267	-77 22 24.485	+0.006	+2.985	+0.044	-0.042	+0.001	-0.005
				<b>+0.050</b>	<b>+2.944</b>				
<b>east</b>									
+38 12 6.870	-77 22 9.430	+38 12 6.786	-77 22 13.404	+0.084	+3.123	+0.071	-0.034	+0.022	+0.012
+38 12 7.011	-77 22 9.515	+38 12 6.786	-77 22 13.404	+0.225	+3.056	-0.071	+0.034	+0.006	+0.017
				<b>+0.155</b>	<b>+3.090</b>				
<b>cq4</b>									
+38 12 5.105	-77 22 20.498	+38 12 5.090	-77 22 24.215	+0.015	+2.921	+0.055	+0.026	+0.018	+0.014
+38 12 5.186	-77 22 20.440	+38 12 5.090	-77 22 24.215	+0.095	+2.967	-0.025	-0.020	+0.018	+0.006
+38 12 5.174	-77 22 20.493	+38 12 5.090	-77 22 24.215	+0.084	+2.925	-0.014	+0.022	+0.001	-0.024
+38 12 5.175	-77 22 20.429	+38 12 5.090	-77 22 24.215	+0.085	+2.975	-0.015	-0.028	+0.001	-0.081
				<b>+0.070</b>	<b>+2.947</b>	<b>+0.054</b>	<b>+0.052</b>	<b>+0.018</b>	<b>+0.028</b>

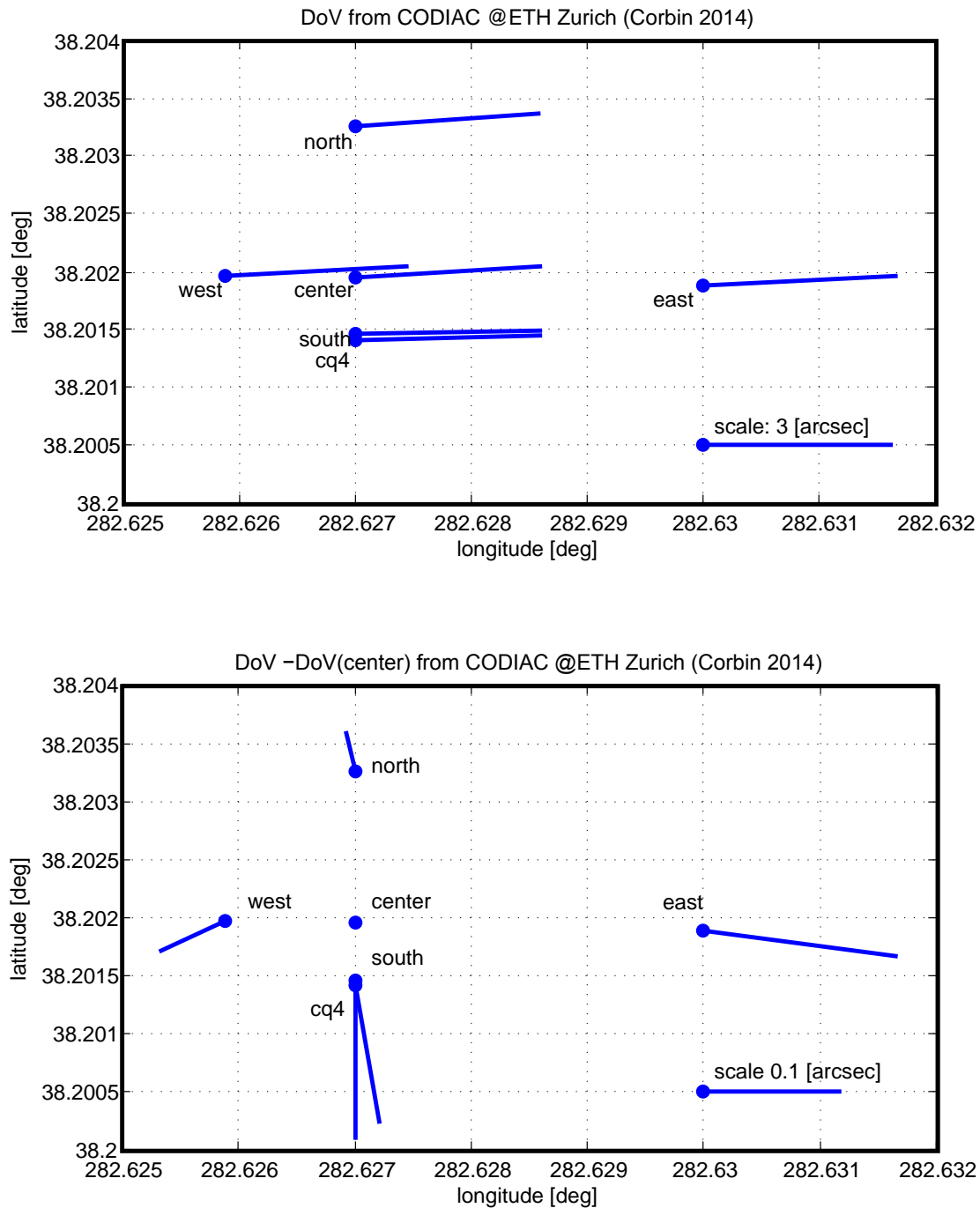


**Figure 7.7:** (Upper) deflections of the vertical determined by CODIAC in Corbin (USA). (Lower) deflections of the vertical reduced to the station **center**.

## Chapter 8

# Astro-Gravimetric Campaign at CERN (TZ32)

Thanks to the continuous development of astrogeodetic instruments at ETH Zurich and the availability of a linear underground tunnel (TZ32, which is linked to the LHC, 850 m in length, at a depth of 80 m) at CERN, see Figures 8.1 and 8.2, it was possible to perform a very special gravity measurement campaign for the determination of a high-precision underground equipotential profile. This determination is compared to a gravity model based on a high-precision multi-resolution DTM combined with a bathymetric model of Lake Geneva, near-field geological density data and a detailed 3D model of the tunnels including TZ32 and LHC.

Deflections of the vertical were carried out every 10 m directly above the tunnel with the Digital Astronomical Deflection Measuring System (DIADDEM) from ETH Zurich. Moreover, gravimetric measurements were carried out with a Scintrex CG-5 relative gravimeter every 10 m on the surface of the topography and inside the tunnel. They are linked to an absolute gravimetric network determined with a Micro-g FG-5 absolute gravimeter provided by the Swiss Federal Office of Metrology (METAS).

After a brief description of the measurements, the complete mass model is exposed and used for an analysis of observability of the equipotential profile by astro-gravimetric levelling. It demonstrates that a direct determination, without mass model reductions, is possible along TZ32. This allows to compare the astro-gravimetric determination of the equipotential profile in the tunnel with a solution computed uniquely from the mass model.

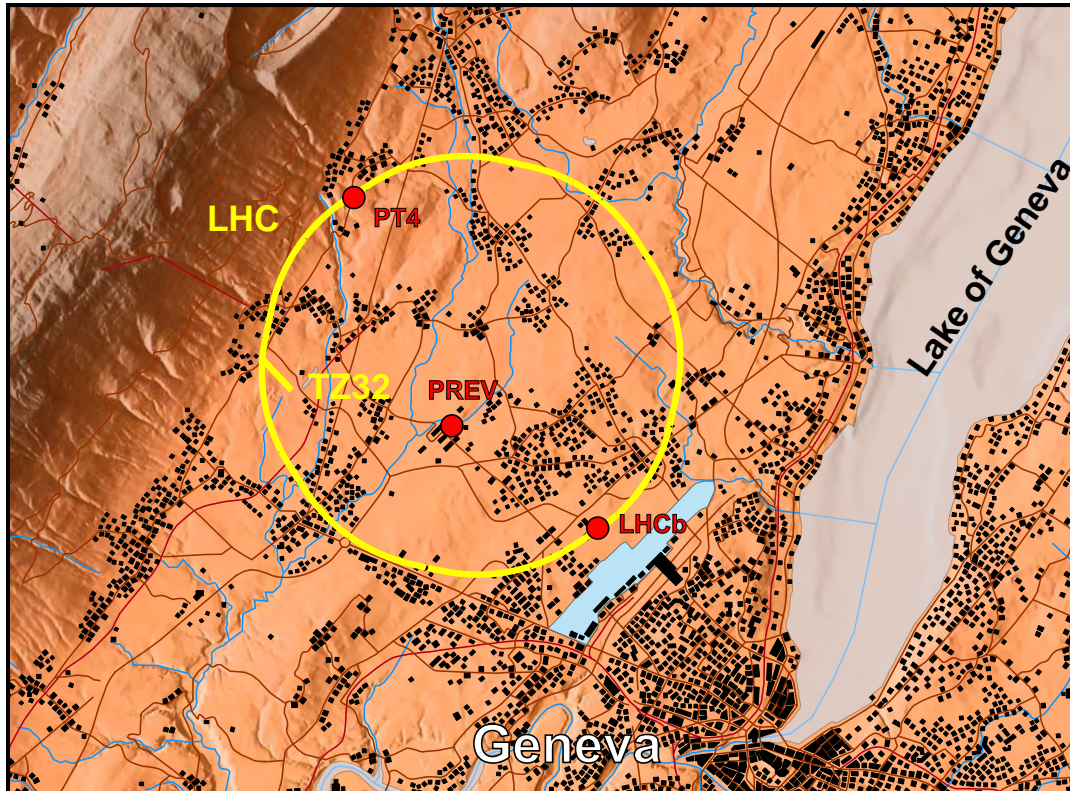


**Figure 8.1:** Map of the region near Geneva. The existing LHC and TZ32 tunnels are represented in yellow. The points in red represent the location of the absolute gravimetric reference network. Source of data: Swisstopo (DTM25, VECTOR200).

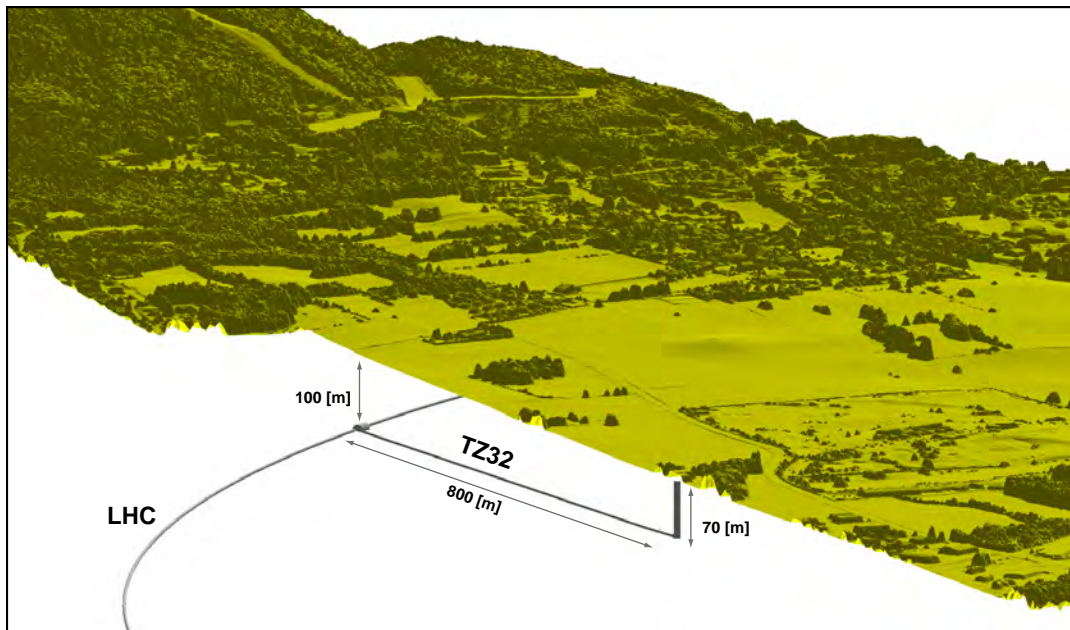


**Figure 8.2:** Perspective view of the tunnels TZ32 and LHC with topography. Source of digital surface model: système d'information du territoire à Genève (SITG).

## 8.1 Gravimetric Observations

In order to produce high-quality gravity measurement sets along the TZ32 profile on the topography and in the tunnel, it is necessary construct a precise, stable and accessible absolute gravimetric reference network, which is used for the calibration and for the periodic control of the relative gravimeter. In addition, since 3 mm in height represent 1 microgal change in gravity, it is also necessary to have a precise and homogeneous reference positioning network on topography and in the tunnel in order to measure the precise location of gravimetric observations. During this campaign, both reference networks were determined with sufficient accuracy and served as basis for all determinations.

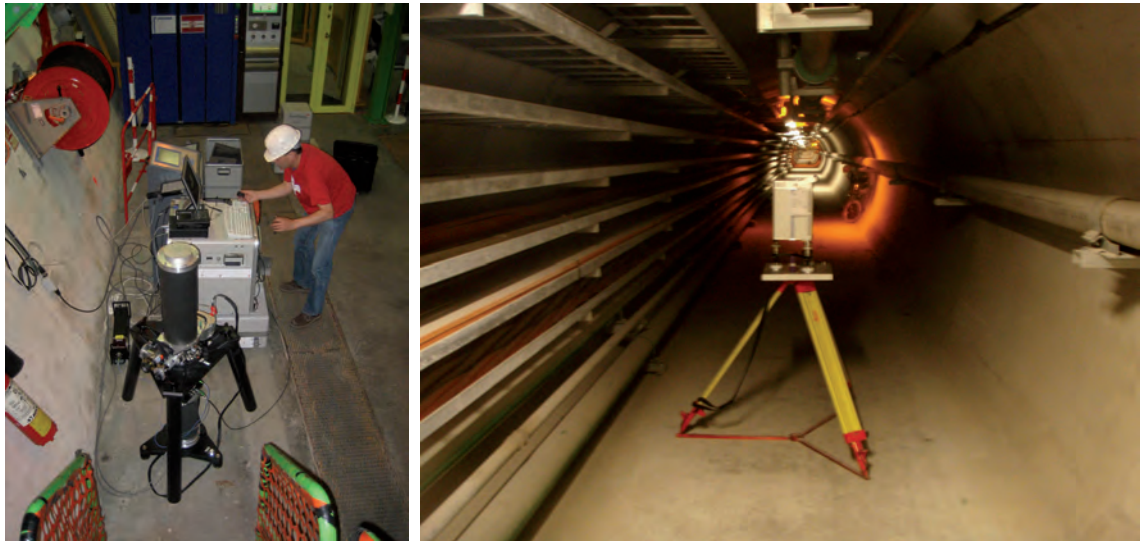


**Figure 8.3:** (Left) Dr. Henri Baumann (METAS) in the LHCb cavern, preparing the Micro-g FG-5 for data acquisition. (Right) The relative gravimeter Scintrex CG-5 in TZ32 during data acquisition.

### 8.1.1 Absolute Gravimetric Reference Network

The absolute reference network is formed by 3 points chosen in stable and accessible locations in the vicinity of the CERN installations in Prévessin. In Figure 8.1, the locations of PREV, PT4 and LHCb are shown. In order to make possible a good determination of the scale factor of the relative gravimeter, they span a contrast of approximately 30 mgal. All points were determined gratefully by METAS and its Micro-g FG-5 absolute gravimeter. The acquisition time was of about 12 hours and the local vertical gradients were determined by CG-5 measurements with superposed measurements separated by 1 meters. The observations used for the least-squares adjustment of the absolute reference network are listed in table 8.1. The mathematical model of the *Gauss-Markov* adjustment is based on a functional model which provide the following equations of observations:

$$\begin{aligned}\Delta g_i + \hat{v}_{\Delta g_i} &= \hat{m} \cdot \hat{g}_i + \hat{c}_0 \\ g_i + \hat{v}_{g_i} &= \hat{g}_i\end{aligned}\tag{8.1}$$

**Table 8.1:** Observations integrated into the computation of the absolute reference network.

Pt	type	value [mgal]	$\Delta H$ [m]	$\frac{\partial g}{\partial H}$ $\frac{[\text{mgal}]}{[\text{m}]}$	reduced obs. [mgal]	$\sigma_{\Delta g_i}/\sigma_{g_i}$ [mgal]
PREV	$\Delta g$	0	0	-0.258	0	0.003
PT4	$\Delta g$	-18.888	0	-0.298	-18.888	0.003
LHCb	$\Delta g$	11.427	0	-0.178	11.427	0.003
PREV	$g$	980576.039	1.3	-0.258	980576.374	0.003
PT4	$g$	980557.105	1.3	-0.298	980557.493	0.003
LHCb	$g$	980587.573	1.3	-0.178	980587.804	0.003

where the relative and absolute observations are given by  $\Delta g_i$  and  $g_i$ , and their associated residuals by  $\hat{v}_{\Delta g_i}$  and  $\hat{v}_{g_i}$ . The unknown parameters are the absolute value of gravity  $\hat{g}_i$ , the scaling factor  $\hat{m}$  and the offset  $\hat{c}_0$  between the relative and the absolute gravimeter. It is important to notice that in Equation 8.1, no time drifts are parameterized for the relative measurements while the observations  $\Delta g_i$  come from the combination of several adjustments of purely relative gravimetric networks which filtered out linear time drifts. The final results of the adjustment are resumed in table 8.2 and shows that we can assume that the points of the reference network are known with an accuracy better than 5 microgals.

**Table 8.2:** Adjusted parameters from the absolute gravimetric reference network.

unknown	$\hat{x}_i$	$\sigma_{x_i}$	unit
$\hat{g}_{\text{PREV}}$	980576.376	0.002	[mgal]
$\hat{g}_{\text{PT4}}$	980557.492	0.002	[mgal]
$\hat{g}_{\text{LHCb}}$	980587.803	0.002	[mgal]
$\hat{c}_0$	979423.548	0.087	[mgal]
$\hat{m}$	0.999869	0.000151	[-]

### 8.1.2 Gravimetric Measurements along the TZ32 Profile

The relative gravimetric campaign took place along the axis of the TZ32, on topography and in the tunnel, with a spacing of 10 meters. Depending on the instantaneous measurement conditions (e.g. vibrations, wind), each point was observed once, one after the other, between 2 and 5 minutes. In between, some points are re-observed in order to be able to estimate the time drift. During the acquisition time, the position of the gravimeter is precisely determined with a total station previously positioned with respect to the reference network. In addition, the first and the last measurement of a half-day are always done on the absolute reference PREV.

The raw measurements carried out during 1 day are firstly pre-processed (outliers filtering, etc...) and reduced from tides using the software **ETERNA** (Wenzel, 1993). The final absolute gravity values are obtained by least-squares adjustment, where a linear time



drift factor is estimated for each half-day. The accuracy of the final absolute values are estimated to be in the order of 5-8 microgals. They are shown in Figure 8.4 and listed in Tables I.1 and I.4.

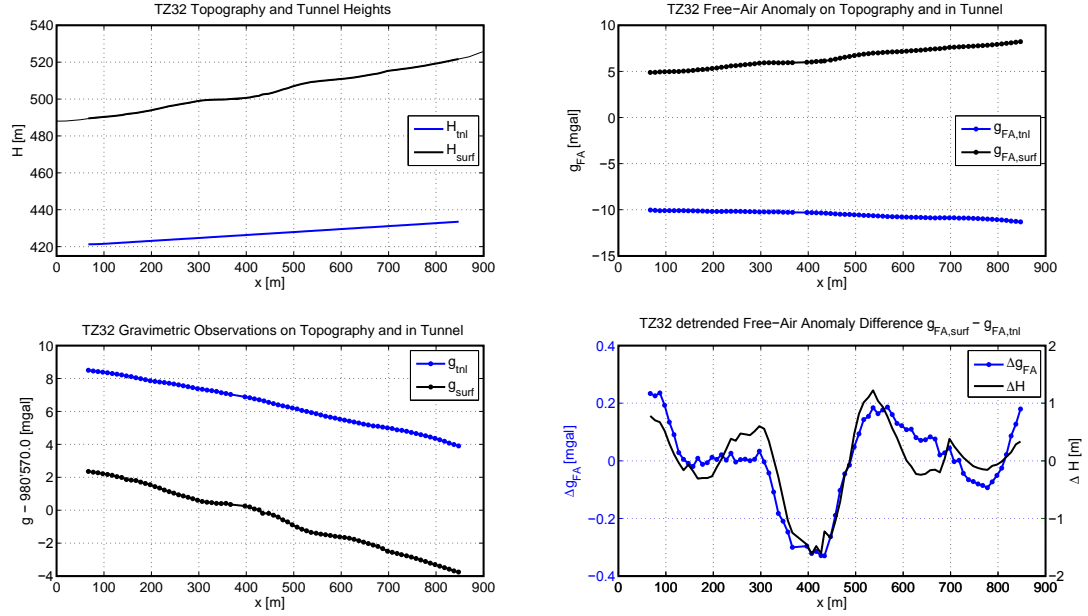


**Figure 8.4:** (Upper, left) profile along the TZ32 of the topography and the tunnel. (Left, lower) absolute gravimetric observations on topography and in the tunnel. (Upper, right) free-air anomalies. (Lower, right) detrended free-air anomalies differences between the values on the topography and in the tunnel, and height differences.

## 8.2 Astrogeodetic Observations

The astrogeodetic deflection of the vertical were carried out every 10 meters along the TZ32 profile with the system DIADEM developed at ETH Zurich (Somieski, 2008). One of the main difficulty in opposition to previous campaigns or standard modern measurements (Voigt, 2013), comes from the necessity to install the instrument on a precise locations along the TZ32 which are almost exclusively on soft ground. This can be potentially a problem when the system is tilting too much during the measurements. It is well-known that the performance of the system depends strongly on the absolute values of tiltmeter measurements (Hirt, 2004). Intuitively it is easy to understand that all accelerations of the system provoke also non-gravitational responses in the tiltmeters, in addition since the synchronization of tiltmeter measurements and the image acquisition are not realized on hardware level in DIADEM, the variation of tilt in time generate systematic errors in proportion. Finally, small tiltmeters values are also proportionally less affected by the uncertainty of the calibration parameters determined with the celestial calibration (Hirt, 2008). For these reasons, the system developed by (Somieski, 2008) was upon other terms augmented by a third pair of HRTM Lippmann tiltmeters in order to increase the reliability and the precision of the unique link of the system to gravity.

The problem of the transportation of DIADEM off-road was also an issue. Finally the solution adopted can be seen in Figure 8.5 and consisted into modify a trailer in order to let the tripod legs pass through the floor and to permit driving to the points and deploy the system without taking off the instrument from the trailer.

The acquisition of the 77 stations took place during 16 nights in total. One station measurement results from approximately 60 individual solutions acquired during 45 minutes approximately. The duration was larger than expected under normal condition because the levelling process had to be started several times. The data were processed according to the standard procedures, using the software of Dr. Christian Hirt, AURIGA, developed during his thesis (*Hirt, 2004*) at the University of Hannover. The tides are corrected according to (*Voigt, 2013*), but since the absolute deflection values are not really of interest in this experiment, the corrections concerning the plate tectonics, proposed by Voigt were not applied. The final deflections are shown in Figure 8.6. With respect to the difficult conditions for acquisition, the achieved accuracy is between 0.06-0.08 arcsec, very close to what can be expected for acquisition under normal conditions. This accuracy was only possible to achieve when the camera was stabilized by putting conscientiously small blocks of wood between the feet of the tripod and the ground. As we can see in Figure 8.7, the three pairs of tiltmeters mounted on DIADEM agree mostly below 0.04 arcsec.



**Figure 8.5:** (Left) The astrogeodetic system DIADEM installed on the trailer for the field experiments at CERN. (Right) Monique Dupont (CERN) and Sébastien Guillaume (ETH) during a DIADEM data acquisition.



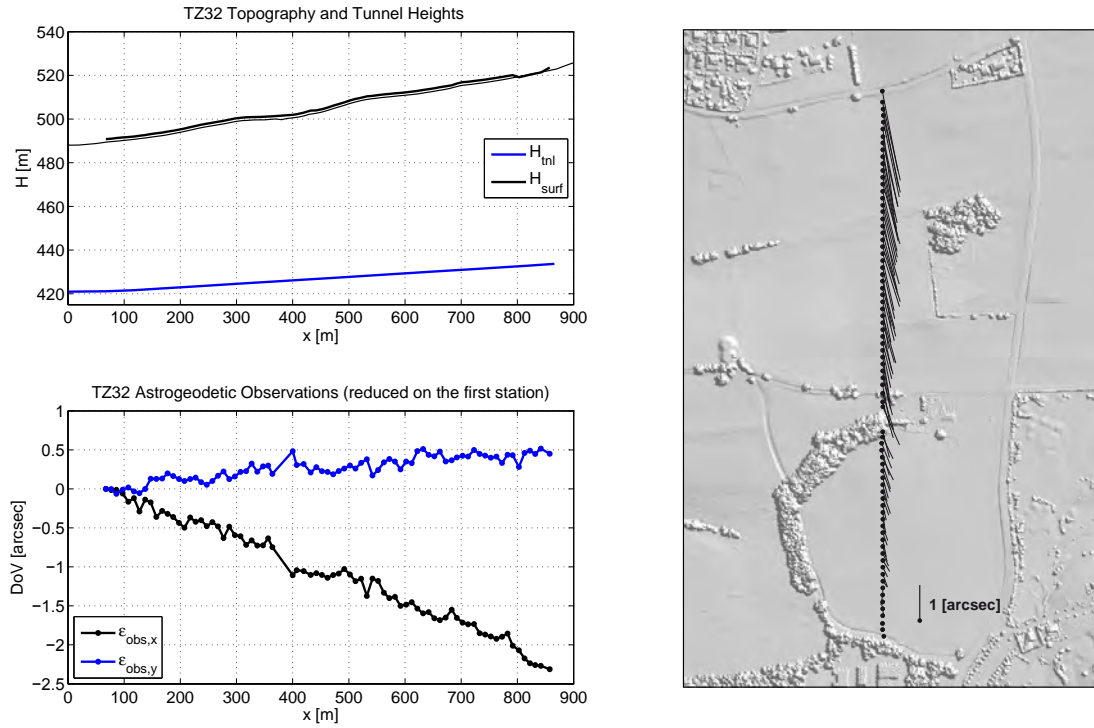


**Figure 8.6:** (Upper, left) profile along the TZ32 of the topography and the tunnel. (Lower, left) deflection of the vertical observations projected along the TZ32 profile. (Right) map representation of the deflections of the vertical. The relief map was computed from DSM data provided by SITG.

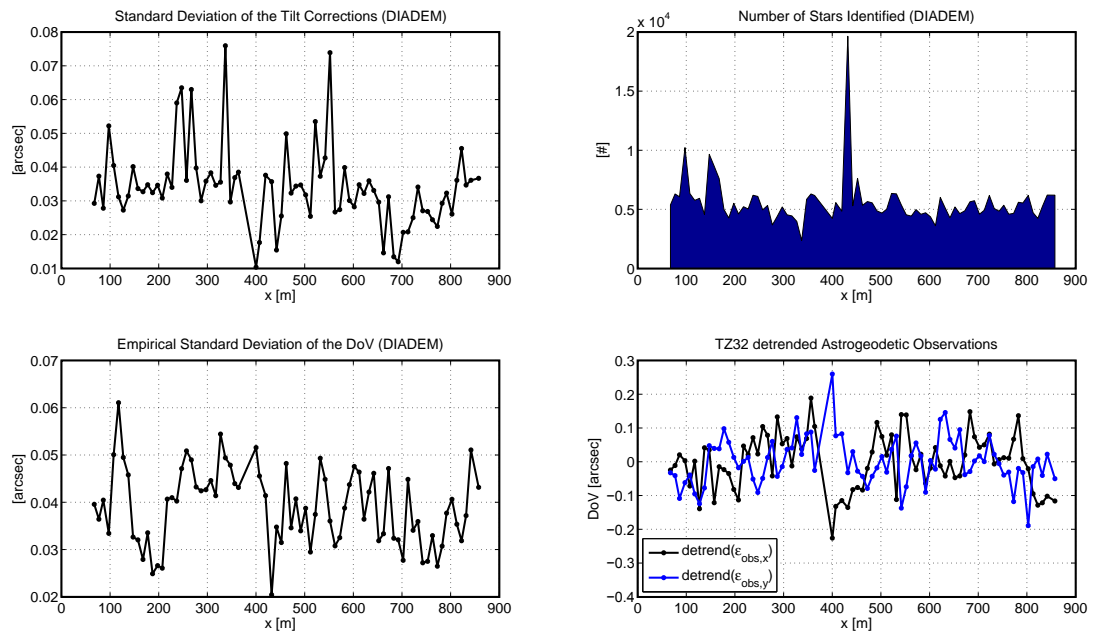


**Figure 8.7:** (Upper, left) empirical standard deviation of the tilt corrections computed from the three independent pairs of tiltmeters. (Lower, left) empirical standard deviation of the deflection of the vertical observations. (Upper, right) number of stars identified and used in total. (Lower, right) detrended deflection of the vertical observations.

### 8.3 Mass Models

A precise 3D mass model for the TZ32 region is now presented. It is formed by a model for topography, the lake of Geneva, near-field geological density contrasts and a detailed 3D model of the tunnels including TZ32 and LHC. The modeling is done in a rigorous local Cartesian topocentric system, centered on the floor of the access well. The  $x$ -axis is defined to be along the tunnel and the  $z$ -axis in zenith direction as shown in Figure 8.8.

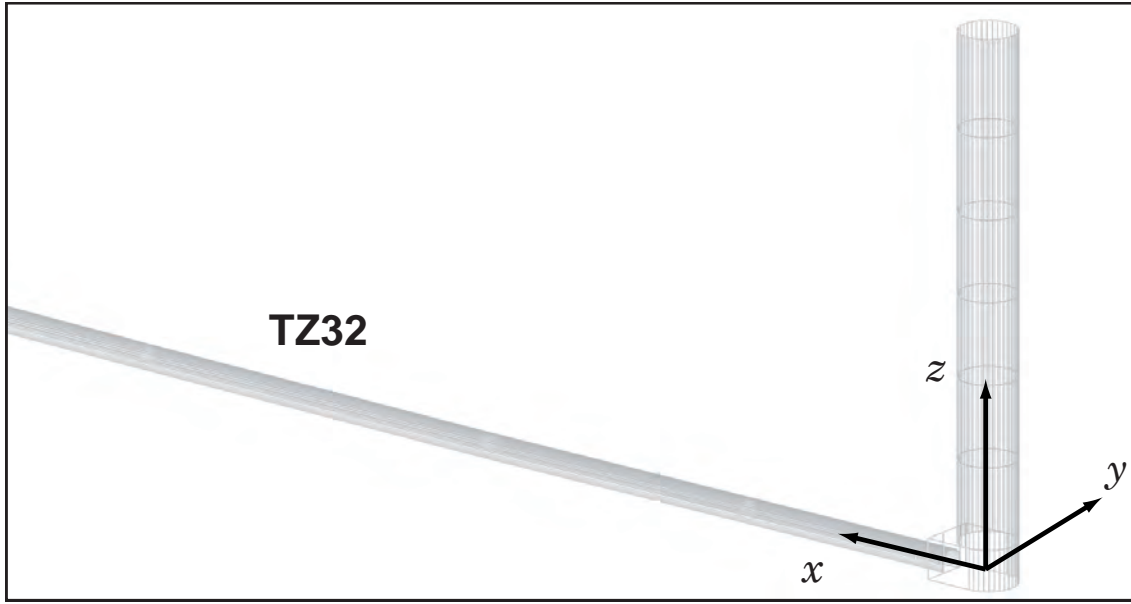


Figure 8.8: Topocentric TZ32 coordinate system.

#### 8.3.1 Topography

The polyhedron is generated from two tessellations, see Section 5.2.3. The vertices of the upper tessellation  $\mathbb{T}_{\text{upper}}$  approximate the actual topography with a resolution decreasing with the horizontal distance to the TZ32 profile. The resolution is equal to 2x2 meters up to a distance of 500 meters (DTM, SITG), 8x8 meters up to 3 kilometers (DTM, SITG), 25x25 meters up to 10 kilometers (DTM, Swisstopo), 90x90 meters up to 50 kilometers (DTM, ASTER) and 300x300 up to 100 kilometers (DTM, ASTER). The vertices of the lower tessellation  $\mathbb{T}_{\text{lower}}$  are given by a regular 1 kilometer grid at  $H = 0$  meters. The common boundary is given by the external boundary of  $\mathbb{T}_{\text{upper}}$ . The density is fixed to  $\rho_{\text{topo}} = 2'670 \frac{\text{kg}}{\text{m}^3}$ .

#### 8.3.2 Lake of Geneva

The lake of Geneva is modeled by a homogeneous polyhedron of density  $\rho_{\text{lake}} = 1'000 \frac{\text{kg}}{\text{m}^3}$  as shown in Figure 8.9.

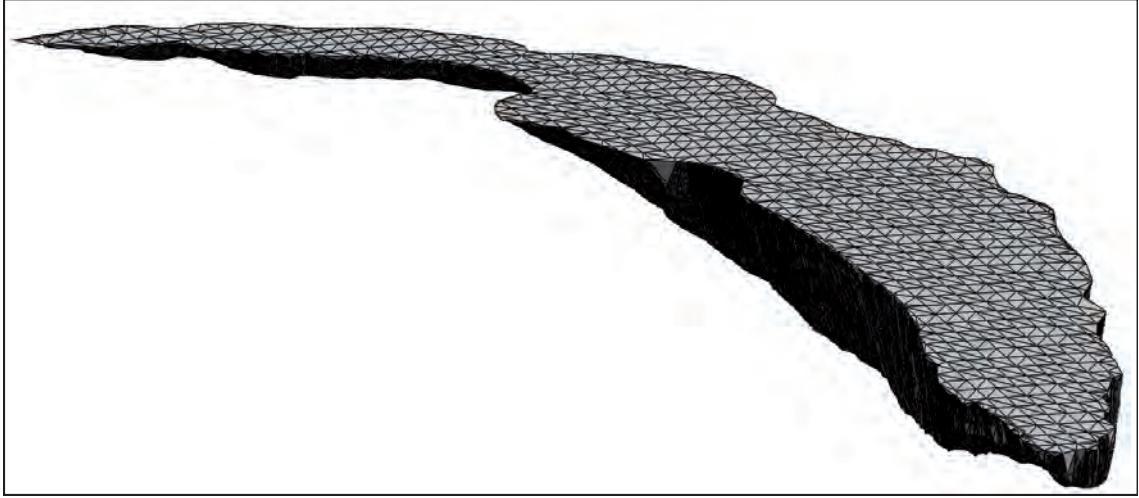


**Figure 8.9:** Lake of Geneva is modeled by a homogeneous polyhedron. The  $z$ -component is scaled by a factor 20 with respect to  $x$  and  $y$ .

### 8.3.3 Near-Field Geology

The near-field geology is formed by three homogeneous polyhedrons which have the following density contrasts with respect to the density of topography:

1. quaternary sediments,  $\Delta\rho_{\text{quaternary}} = -300 \frac{\text{kg}}{\text{m}^3}$ ,
2. the molasse basin,  $\Delta\rho_{\text{molasse}} = -200 \frac{\text{kg}}{\text{m}^3}$ ,
3. gompholite stone,  $\Delta\rho_{\text{gompholite}} = -100 \frac{\text{kg}}{\text{m}^3}$ .

They are constructed according to data and maps collected in 1980 on the base of geological soundings realized in the frame of the studies for the construction of the LEP tunnel. A reproduction of a geological profile in the vicinity of the TZ32 tunnel is shown in Figure 8.11. In addition, the Table 8.3 gives a summary of density data observed by the sounding L135.

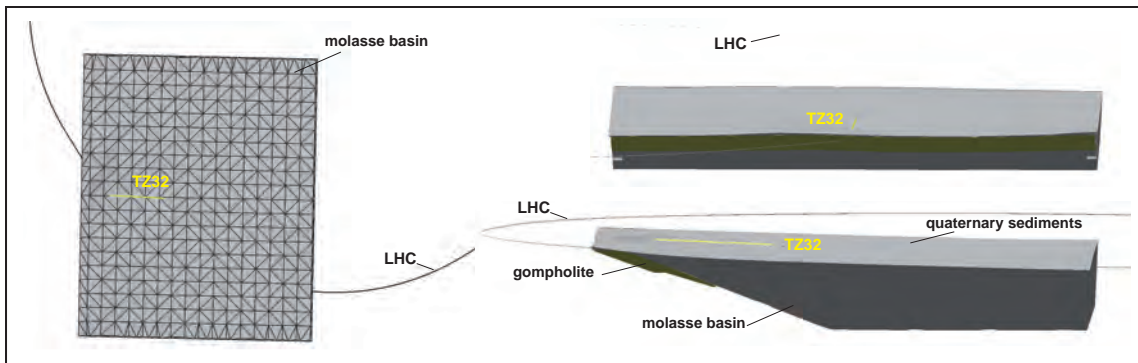


**Figure 8.10:** Homogeneous polyhedra which model the near-field geology in the vicinity of the TZ32.

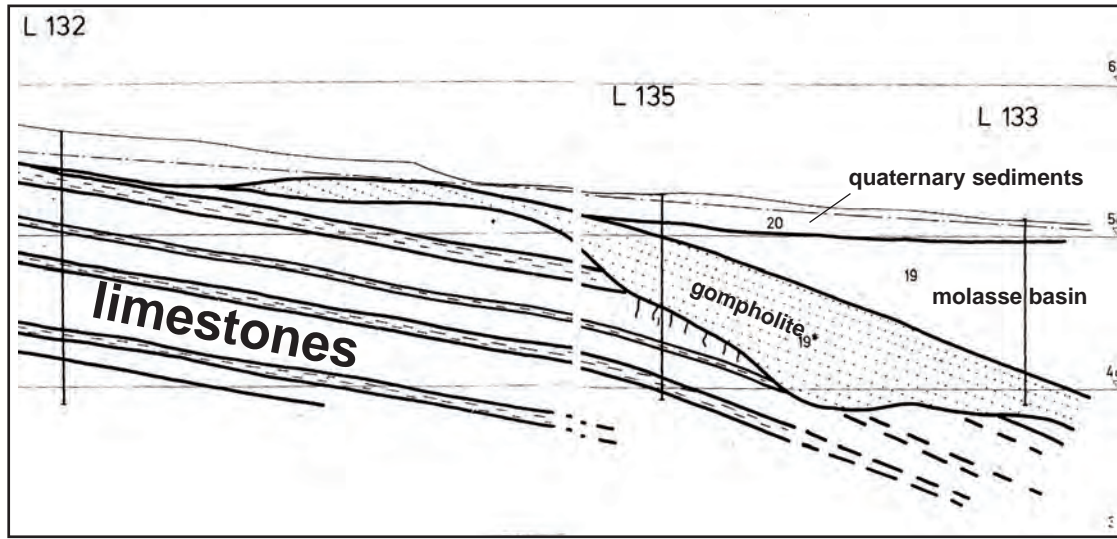


**Figure 8.11:** Reproduction of a geological profile along the axis of TZ32.

**Table 8.3:** Density data from the geological sounding L135 located at: East=489'900, North=125'690, H=527.231 meters (LV03).

$H$	depth	$\frac{\text{water}}{\text{rock}}$	apparent density	dry density	grain density	void ratio
[m]	[m]	[%]	$\left[\frac{\text{kg}}{\text{m}^3}\right]$	$\left[\frac{\text{kg}}{\text{m}^3}\right]$	$\left[\frac{\text{kg}}{\text{m}^3}\right]$	[-]
513.231	14.0	6.7	2'450	2'330	2'720	0.166
488.231	39.0	3.3	2'600	2'520	2'750	0.093
485.231	42.0	6.0	2'470	2'330	2'770	0.189
480.231	47.0	4.5	2'570	2'460	2'770	0.126
469.231	58.0	2.6	2'550	2'490	2'750	0.106
462.231	65.0	6.4	2'490	2'340	2'770	0.184
450.231	77.0	1.0	2'630	2'600	2'740	0.052
446.531	80.7	8.2	2'410	2'230	2'760	0.237
435.231	92.0	2.7	2'580	2'510	2'740	0.091
429.231	98.0	3.6	2'560	2'470	2'740	0.109
428.231	99.0	4.0	2'530	2'430	2'740	0.126
420.231	107.0	1.0	2'650	2'620	2'740	0.044
415.231	112.0	1.8	2'650	2'570	2'740	0.066
409.731	117.5	1.2	2'610	2'580	2'740	0.062
405.831	121.4	10.6	2'320	2'100	2'780	0.335
402.431	124.8	5.5	2'550	2'420	2'780	0.150
399.231	128.0	4.4	2'570	2'460	2'780	0.129
396.231	131.0	1.3	2'670	2'640	2'740	0.040

### 8.3.4 Underground Infrastructure

The LHC and TZ32 tunnels are modeled rigorously, by homogeneous polyhedra of density contrast  $\Delta\rho_{\text{tunnels}} = -2'670 \frac{\text{kg}}{\text{m}^3}$ . The geometry of the tunnels and the access well are based on the official construction plans available at CERN. In **QGravity**, the polyhedra could be

generated in an easy manner using the functionality "3D tube of arbitrary section and path", see Section 5.2.3.

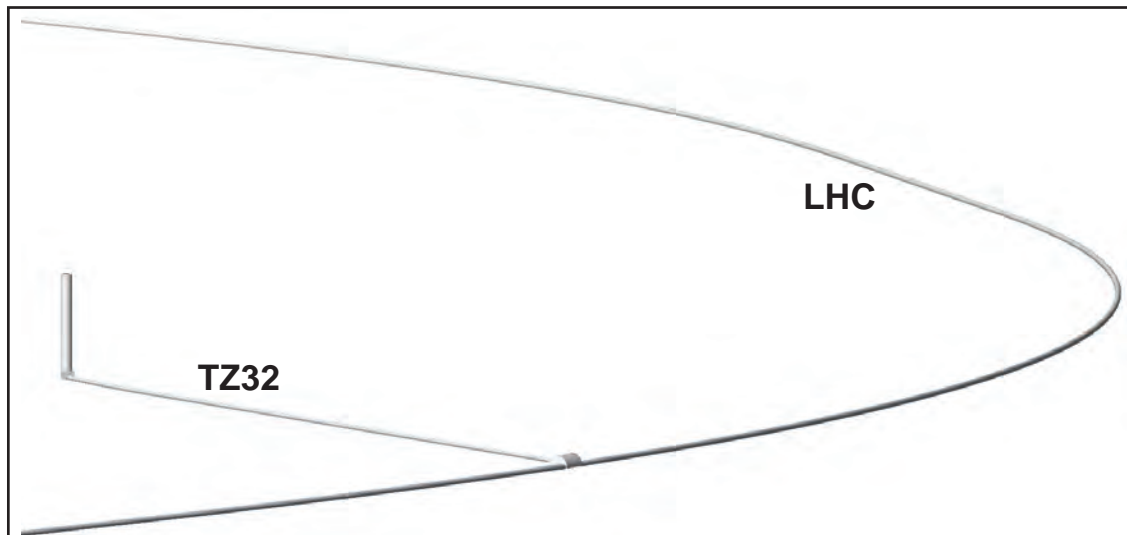


**Figure 8.12:** Homogeneous polyhedra which model the underground infrastructure.

## 8.4 Expected Gravity Fields and Observability

The expected gravity fields and the observability of the equipotential profile by astrogravimetric levelling are computed according to the principles exposed in Chapter 6.

### 8.4.1 Expected Gravity Field and Error-Free Observations

In a first step the equipotential profile in the TZ32 tunnel and error-free observables (Figure 8.13) are computed with QGravity from the mass models exposed in Section 8.3.

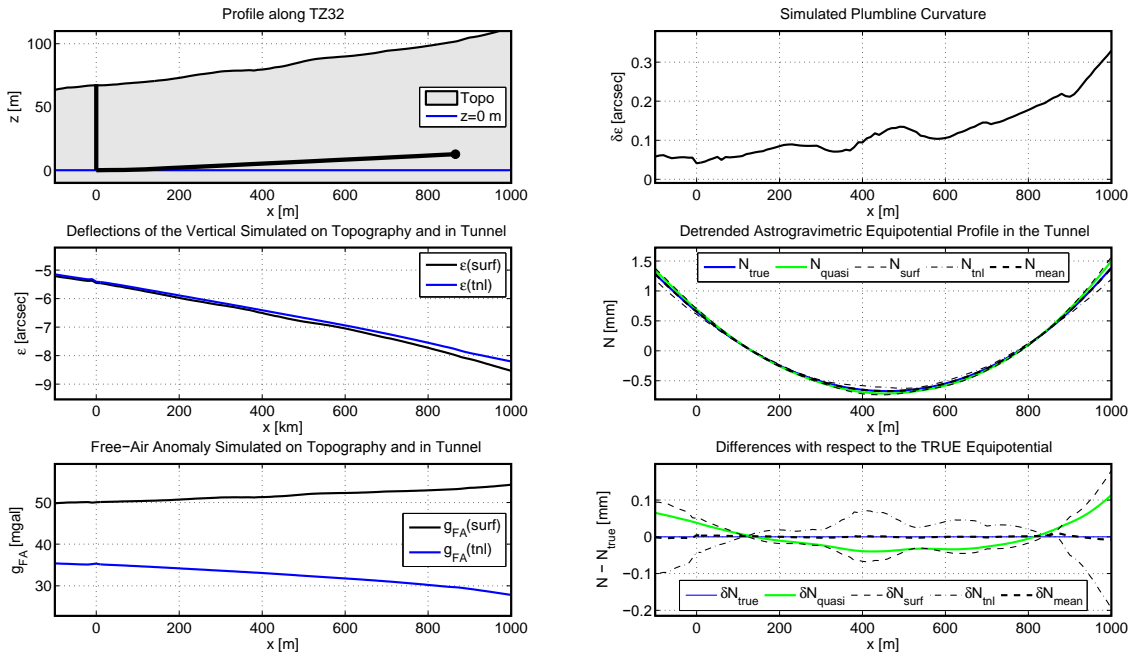


**Figure 8.13:** Results of the simulations of the mass models for the TZ32. (Upper, left) profile along the TZ32 with topography and tunnel. (Middle, left) error-free deflections of the vertical on the topography and in the tunnel. (Lower, left) error-free free-air anomaly on the topography and in the tunnel. (Upper, right) error-free curvature of plumline. (Middle, right) equipotential profiles in tunnel. (Lower, right) Differences with respect to the true equipotential  $N_{\text{true}}$  for the different strategies.

### 8.4.2 Expected Misalignments Generated by known Masses

The second step consists in determining the equipotential profile (at  $z = 0.000 \equiv H_0 = 420.950$  meters) from the error-free observations using a strategy of astrogravimetric levelling. Finally, misalignment analyses are applied to both, the true equipotential profile  $N_{\text{true}}$  (Figure 8.14) and the astrogravimetric equipotential error  $\delta N_{\text{xxxx}}$  (Figures 8.15, 8.16 and 8.17).

The misalignments  $\mathcal{M}_\star^\lambda \{N_{\text{true}}\}$  generated by the mass models for the wavelengths  $\lambda = 100, 200$  and  $300$  meters are shown in Figure 8.14. They are significant for all wavelengths and along the entire profile. In particular, for  $\mathcal{M}_\star^{200} \{N_{\text{true}}\}$ , values between

40 and 50 microns can be expected. In addition, it can be noted that  $\mathcal{M}_\star^\lambda \{N_{\text{true}}\}$  increases more than proportionally with respect to  $\lambda$ . From  $\lambda = 200 \rightarrow 300$ , we have  $\mathcal{M}_\star^{200} \{N_{\text{true}}\} \approx 40 \rightarrow \mathcal{M}_\star^{300} \{N_{\text{true}}\} \approx 90$  microns.

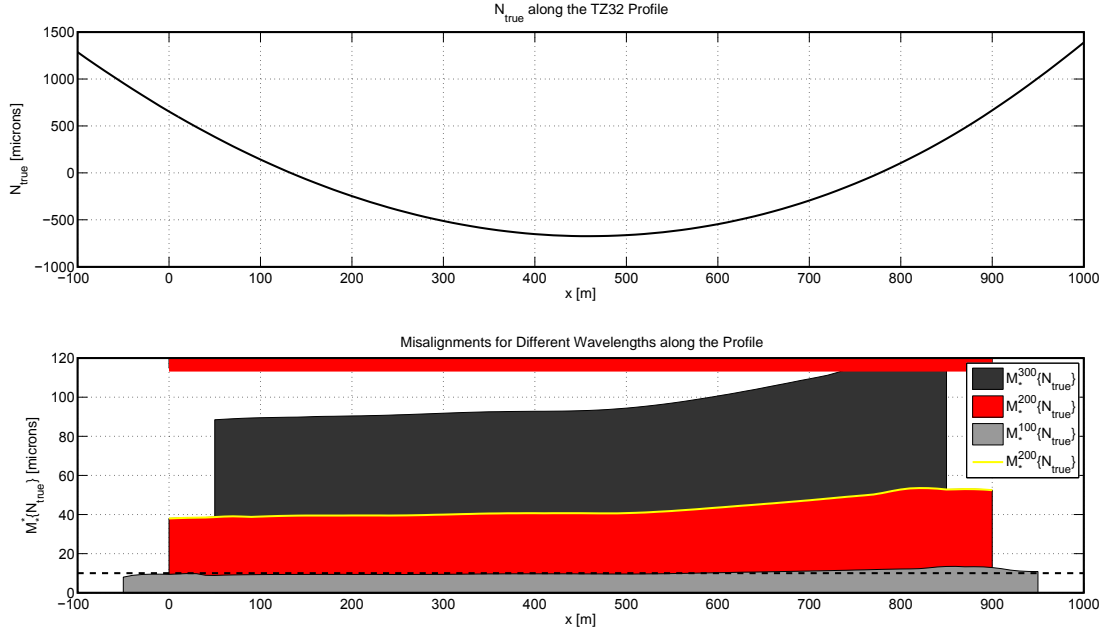


**Figure 8.14:**  $N_{\text{true}}$  (upper) and  $\mathcal{M}_\star^\lambda \{N_{\text{true}}\}$  (lower) along the TZ32 profile due to known mass models. The bold line on top of the lower plot indicates the positions for which the determination  $\mathcal{M}_\star^{200} \{N_{\text{true}}\} < 10$  microns (green), and where  $\mathcal{M}_\star^{200} \{N_{\text{true}}\} \geq 10$  microns (red).

### 8.4.3 Observability by Astrogravimetric Levelling

The observability of the equipotential profile simulated from the known mass models by different astrogravimetric levelling strategies is shown in Figures 8.15, 8.16 and 8.17. As expected, the best solution is given by  $N_{\text{mean}}$ , where the mean gravity along the plumbline is observed on the topography and in the tunnel, and computed by a simple mean value (Figure 8.17). Fortunately, this strategy seems to be able to observe directly the equipotential profile in the tunnel without any mass model assumptions — or reductions. It allows an independent comparison between the equipotential profile predicted from mass models and that determined uniquely from astrogravimetric measurements.

Concerning the other strategies, the solution  $N_{\text{quasi}}$ , which consists of observing only deflections of the vertical, permits also to observe the equipotential profile with sufficient accuracy (Figure 8.15). However, this method is, from a conceptual point of view, not satisfactory. It can only be used if all masses in the vicinity are reliably known, and if the height difference between topography and the tunnel is shorter than 100 meters. And for the standard strategy  $N_{\text{surf}}$ , which consists in observing deflections of the vertical and gravity on the topography only, Figure 8.15 shows clearly that this strategy is insufficient over the major part of the profile.



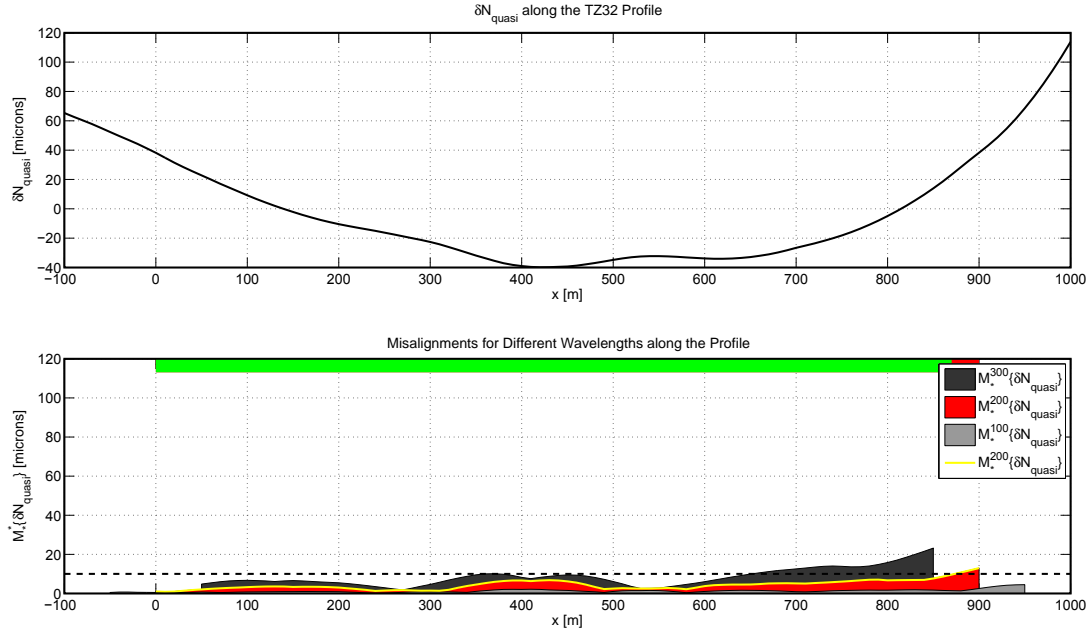


**Figure 8.15:**  $\delta N_{\text{quasi}}$  (upper) and  $\mathcal{M}_{\star}^{\lambda} \{\delta N_{\text{quasi}}\}$  (lower) along the TZ32 profile due to known mass models. The green-red bold line on top of the lower plot indicates the positions for which the determination  $\mathcal{M}_{\star}^{200} \{\delta N_{\text{quasi}}\} < 10$  microns (green), and where  $\mathcal{M}_{\star}^{200} \{\delta N_{\text{quasi}}\} \geq 10$  microns (red)

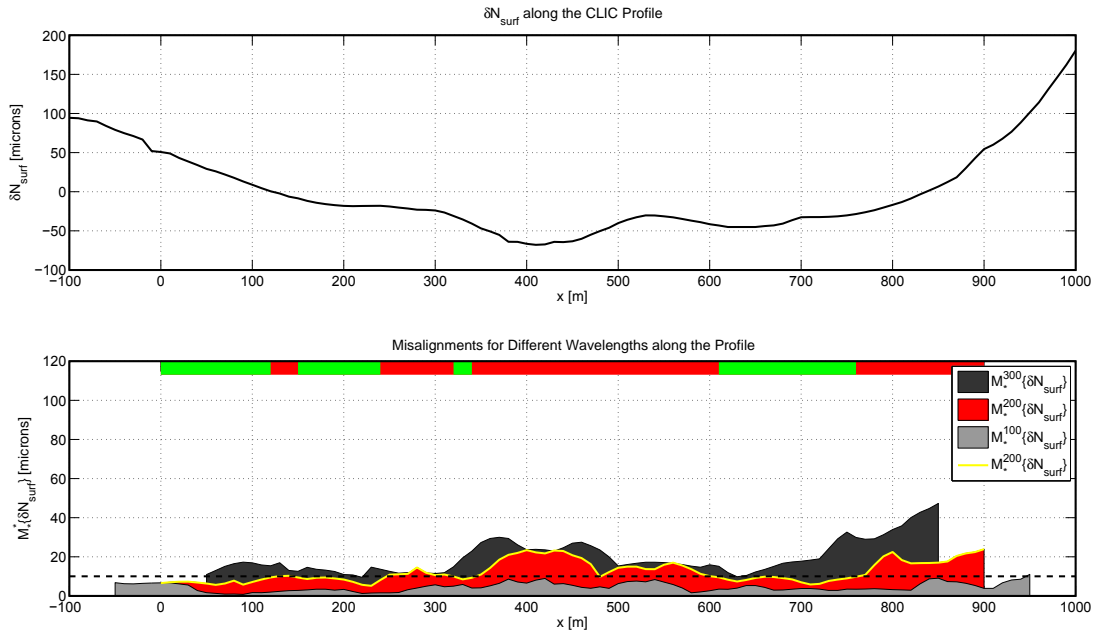


**Figure 8.16:**  $\delta N_{\text{surf}}$  (upper) and  $\mathcal{M}_{\star}^{\lambda} \{\delta N_{\text{surf}}\}$  (lower) along the TZ32 profile due to known mass models. The green-red bold line on top of the lower plot indicates the positions for which the determination  $\mathcal{M}_{\star}^{200} \{\delta N_{\text{surf}}\} < 10$  microns (green), and where  $\mathcal{M}_{\star}^{200} \{\delta N_{\text{surf}}\} \geq 10$  microns (red)



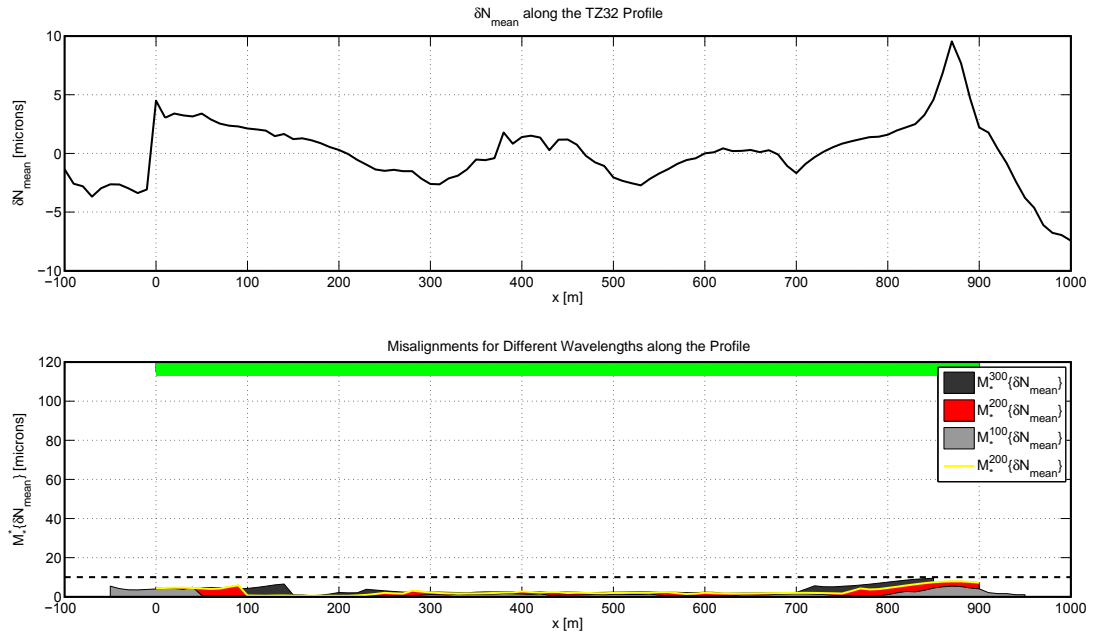


**Figure 8.17:**  $\delta N_{\text{mean}}$  (upper) and  $\mathcal{M}_*^{\lambda} \{ \delta N_{\text{mean}} \}$  (lower) along the TZ32 profile due to known mass models. The green-red bold line on top of the lower plot indicates the positions for which the determination  $\mathcal{M}_*^{200} \{ \delta N_{\text{mean}} \} < 10$  microns (green), and where  $\mathcal{M}_*^{200} \{ \delta N_{\text{mean}} \} \geq 10$  microns (red)

## 8.5 Predicted versus Observed Measurements

In Figures 8.18 and 8.19, the gravimetric and astrogeodetic observations are compared with the predictions computed from the mass models. In order to be able to compare the observations with the model, the gravimetric observations and predictions are reduced to the first observation of the profile. For the deflections of the vertical, a similar reduction is applied. In addition, some statistical indicators are given in Tables 8.4 and 8.5. They show that the model agrees well with the observations. For the deflections, we can

**Table 8.4:** Statistics of the comparison between the observed and predicted gravimetric observations.

quantity	min	max	mean	std	RMS
	[mgal]	[mgal]	[mgal]	[mgal]	[mgal]
$g_{\text{obs}}(\boldsymbol{\rho}_{\text{surf}}) - g_{\text{model}}(\boldsymbol{\rho}_{\text{surf}})$	-0.378	0.000	-0.198	0.103	0.223
$g_{\text{obs}}(\boldsymbol{\rho}_{\text{tnl}}) - g_{\text{model}}(\boldsymbol{\rho}_{\text{tnl}})$	-0.339	0.000	-0.163	0.100	0.191
$g_{\text{obs}}(\boldsymbol{\rho}_{\text{surf}}) - g_{\text{model}}(\boldsymbol{\rho}_{\text{surf}}), \text{detrended}$	-0.101	0.046	0.000	0.027	0.027
$g_{\text{obs}}(\boldsymbol{\rho}_{\text{tnl}}) - g_{\text{model}}(\boldsymbol{\rho}_{\text{tnl}}), \text{detrended}$	-0.138	0.218	0.000	0.083	0.082

**Table 8.5:** Statistics of the comparison between the observed and predicted deflections of the vertical.

quantity	min	max	mean	std	RMS
	[arcsec]	[arcsec]	[arcsec]	[arcsec]	[arcsec]
$\epsilon_{x,\text{obs}}(\boldsymbol{\rho}_{\text{surf}}) - \epsilon_{x,\text{model}}(\boldsymbol{\rho}_{\text{surf}})$	-0.166	0.262	0.055	0.083	0.099
$\epsilon_{y,\text{obs}}(\boldsymbol{\rho}_{\text{surf}}) - \epsilon_{y,\text{model}}(\boldsymbol{\rho}_{\text{surf}})$	-0.176	0.277	0.027	0.074	0.078
$\epsilon_{x,\text{obs}}(\boldsymbol{\rho}_{\text{surf}}) - \epsilon_{x,\text{model}}(\boldsymbol{\rho}_{\text{surf}}), \text{centered}$	-0.208	0.152	0.000	0.072	0.072
$\epsilon_{y,\text{obs}}(\boldsymbol{\rho}_{\text{surf}}) - \epsilon_{y,\text{model}}(\boldsymbol{\rho}_{\text{surf}}), \text{centered}$	-0.185	0.247	0.000	0.073	0.073

admit that the differences between the model and the observations are of the order of magnitude of the expected accuracy of the astrogeodetic determination, i.e. 0.07-0.08 arcsec. Concerning the gravimetric measurements, disregarding the trend, the agreement of the observations on the topography is of the order of 30 microgals, which is remarkable. For the observations in the tunnel, the differences are larger and show significant non-modeled signals of about 80 to 100 microgals, probably due to non-modeled masses close to the tunnel. Here we see clearly the higher sensitivity of gravimetric observations with respect to near-field anomalies and the absolute necessity of observing the gravity in the tunnel, not only for the computation of the mean gravity, but also to be able to estimate the accuracy and reliability of a given mass model. From this point, further investigations could be done with the gravimetric signals in order to estimate possible realistic geological mass anomalies which could generate these observations, and which can be finally used to compute their consequence on the misalignment of the equipotential profile. Nevertheless, as a first estimation of the order of magnitude of the consequence of these differences on the determination of the equipotential profile, we can make the hypothesis that the error on the mean gravity is of the same order as the discrepancies between the model and the observations, i.e. about 100 microgals. We know from the analyses of the misalignment

due to correlated noise for the orthometric corrections (see Section F.2.6, Figure F.13) that no significant misalignments ( $> 10$  microns) are generated when the correlation length of the mean gravity is larger than 300 meters.

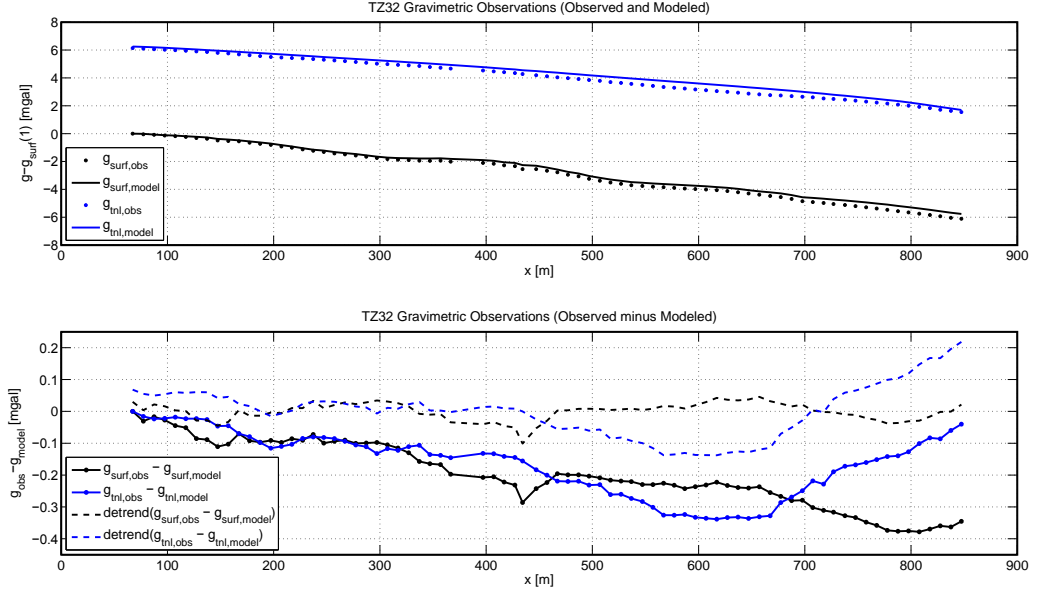


**Figure 8.18:** (Upper) observed and predicted gravimetric observations. (Lower) differences between observed and predicted gravimetric observations.

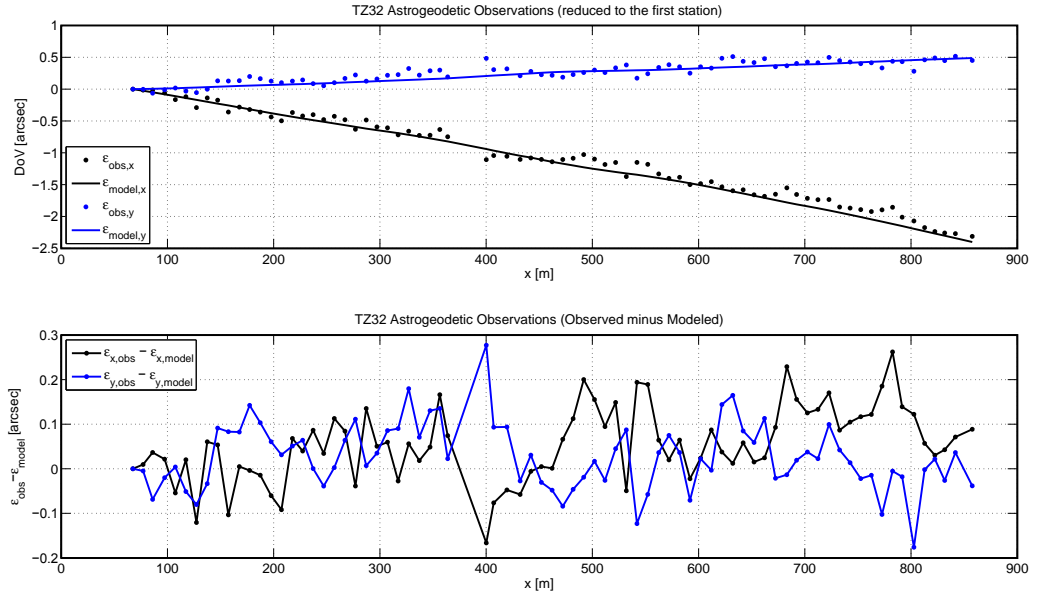


**Figure 8.19:** (Upper) observed and predicted deflection of the vertical observations. (Lower) differences between observed and predicted deflection of the vertical observations.

## 8.6 Computation of the Equipotential Profile in the Tunnel

Using the observations exposed in the previous section, the equipotential profile in the TZ32 at  $H_0 = 420.95$  meters is determined using the strategies  $N_{\text{mean}}$  and  $N_{\text{quasi}}$ , without any previous mass model reductions or filtering. In a first step, all observations are linearly interpolated along the profile for points spaced by 2 meters. In addition, since the observed gravity in the tunnel is not located at  $H_0 = 420.95$  meters, the gravity at  $H_0$  along the profile are predicted using a simple linear extrapolation based on the vertical gradient computed from the superposed observations on the topography and in the tunnel.

The results are shown in Figure 8.20. The equipotential profile and the orthometric corrections are compared with the prediction based only on the mass models. The differences between the solutions  $N_{\text{mean}}$  and  $N_{\text{model}}$  stay between -12 and + 32 microns along the 850 meters. The larger differences are concentrated between 450 and 500 meters and can be observed in  $N_{\text{mean}}$  and  $N_{\text{quasi}}$ . This means that they are caused by the deflections of the vertical observations. It is highly probable that this signal is not real but comes from correlated errors in the astrogeodetic observations. In fact, the equipotential varies between -12 and + 32 microns over a very short distance of 100 meters. And according to the systematic analysis presented in Chapter 6, it is difficult to construct a realistic anomaly which can generate a signals of this amplitude for so short wavelengths. Furthermore, in this region, the gravimetric observations match the prediction very well and do not indicate a strong non-modeled anomaly. The optimal solution for a direct determination of the equipotential profile is certainly given when the observations are previously appropriately filtered. The design of the filter could be based on the one hand on the statistical error modeling of the instruments and on the other hand on the amplitude of realistic expected signals given by systematic simulations and geological data. An other way would be to improve the models by realistic inversion techniques which consider all available gravity observables, gravimetric and deflection of the vertical data.

The misalignment analyses are shown in Figures 8.21, 8.22 and 8.23. As expected from the observability analysis, the actual equipotential profile generates significant misalignments  $\mathcal{M}_{\star}^{200}\{N_{\text{mean}}\}$  reaching 40-50 microns. Concerning the analysis of the difference  $N_{\text{mean}} - N_{\text{model}}$  in terms of misalignment, Figure 8.21 shows that  $\mathcal{M}_{\star}^{\lambda}\{N_{\text{mean}}\}$  is below 20 microns for the entire profile if the segment between 400 and 500 meters is not taken into account.

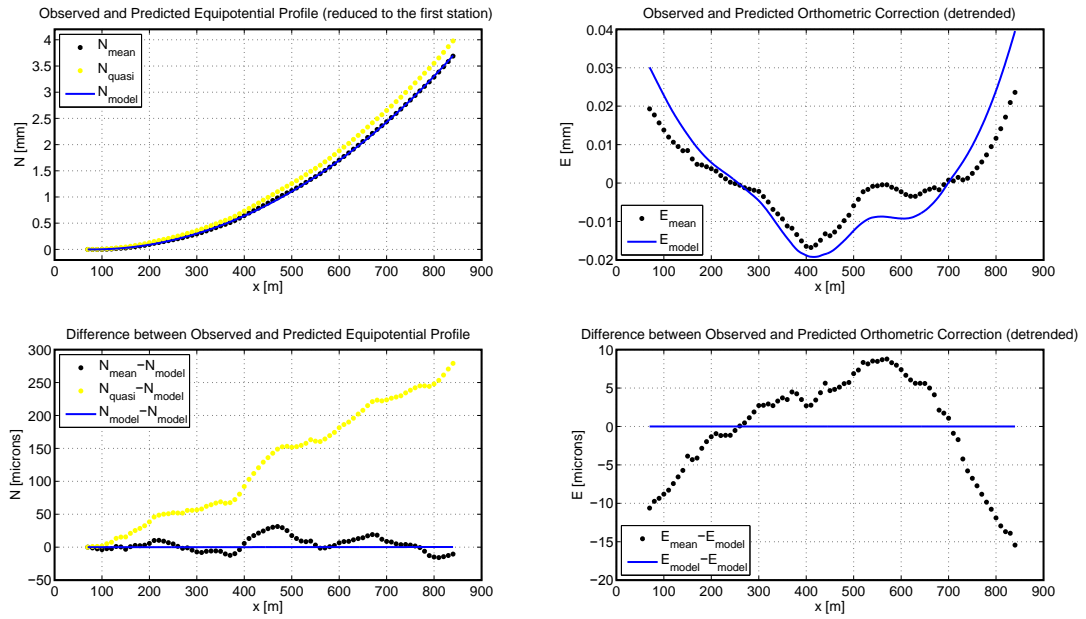


**Figure 8.20:** (Upper, left) observed and predicted equipotential profile in TZ32. The deflection of the vertical are reduced to the first point. (Lower, left) difference between the observed and the predicted equipotential profiles. (Upper, right) detrended observed and predicted orthometric correction. (Lower, right) difference between the observed and the predicted orthometric correction.

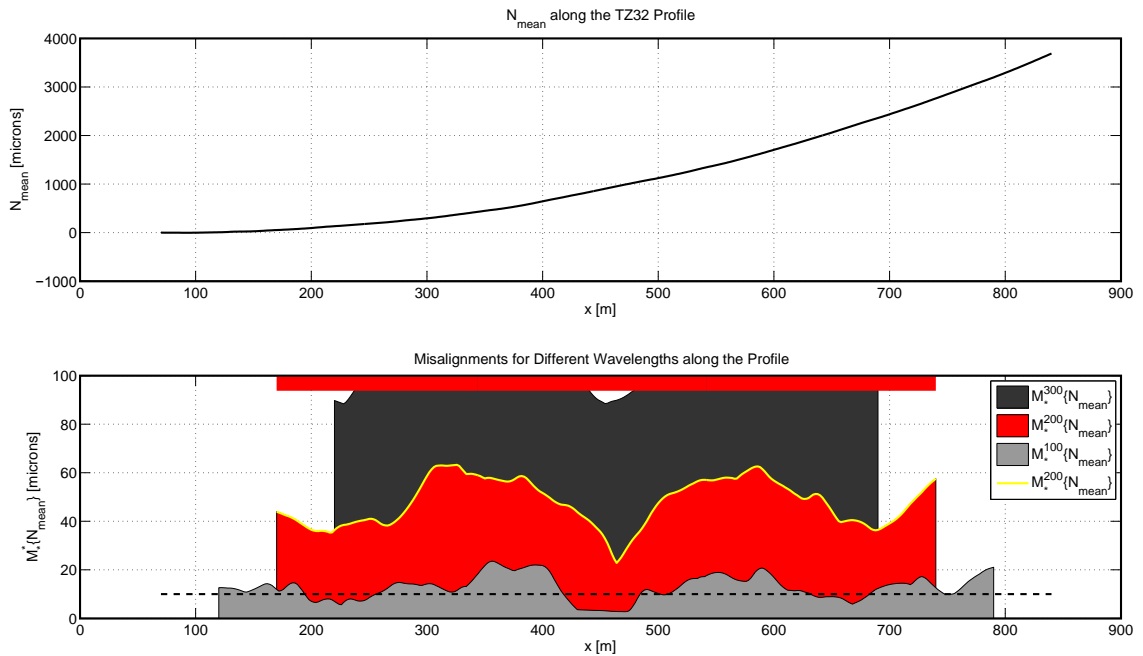


**Figure 8.21:** (Upper) equipotential profile  $N_{\text{mean}}$ . Misalignments  $\mathcal{M}_{\star}^{\lambda}\{N_{\text{mean}}\}$  for the wavelengths  $\lambda = 100, 200$  and 300 meters.

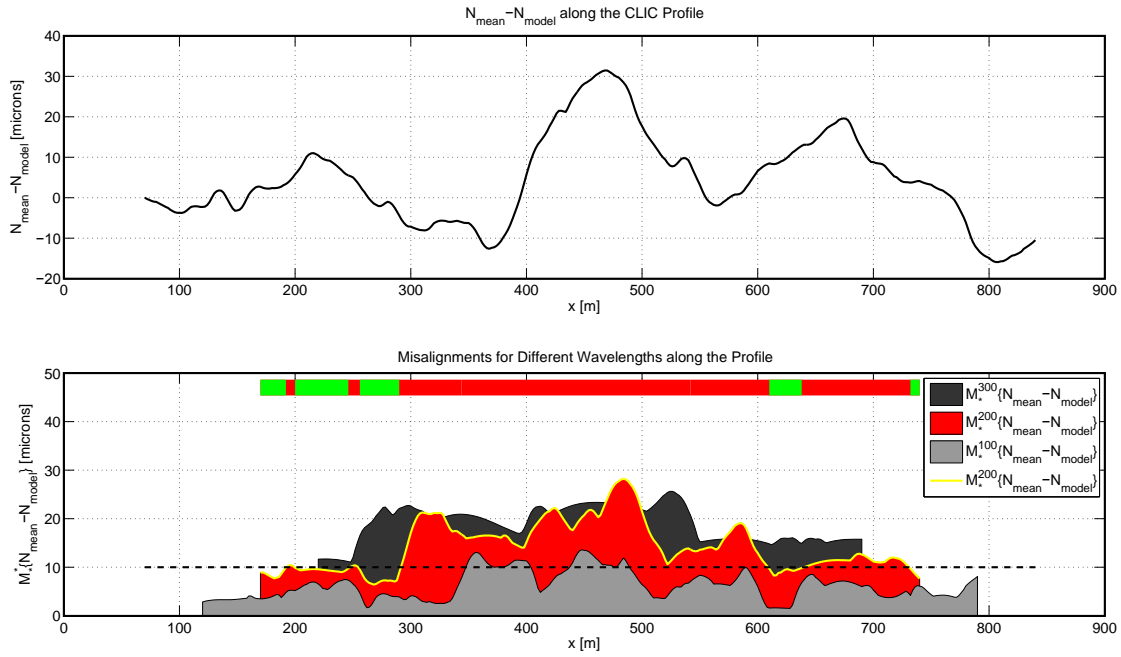


**Figure 8.22:** (Upper) difference between the observed and the predicted equipotential profile  $N_{\text{mean}} - N_{\text{model}}$ . Misalignments  $\mathcal{M}_{\star}^{\lambda} \{N_{\text{mean}} - N_{\text{model}}\}$  for the wavelengths  $\lambda = 100, 200$  and  $300$  meters.

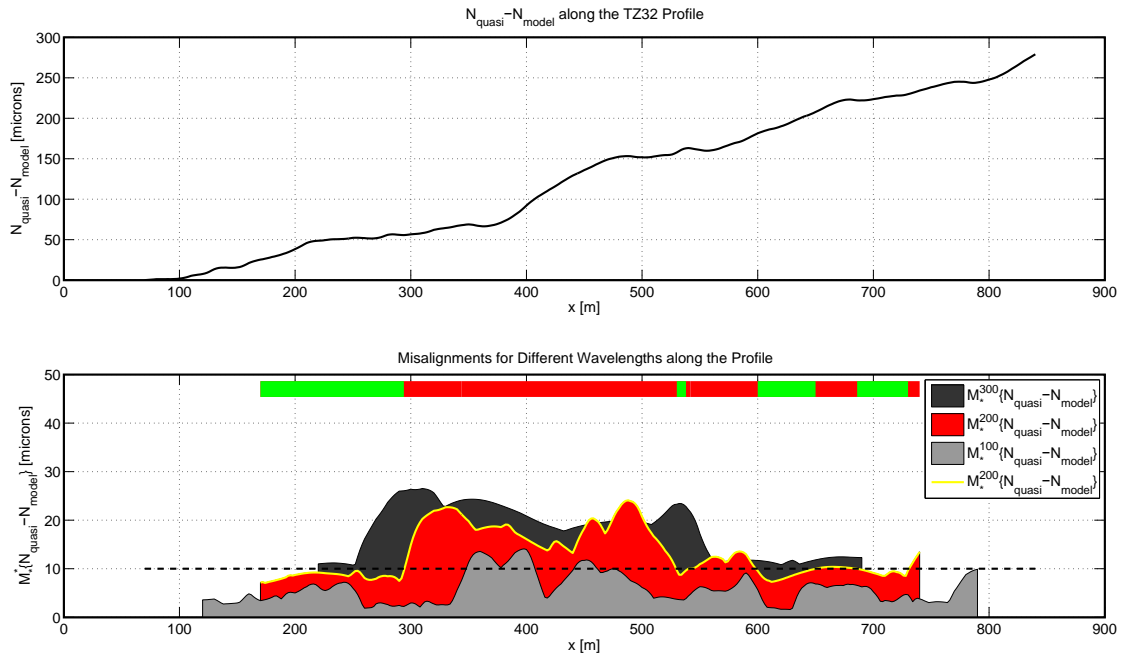


**Figure 8.23:** (Upper) difference between the observed and the predicted equipotential profile  $N_{\text{quasi}} - N_{\text{model}}$ . Misalignments  $\mathcal{M}_{\star}^{\lambda} \{N_{\text{quasi}} - N_{\text{model}}\}$  for the wavelengths  $\lambda = 100, 200$  and  $300$  meters.

## Chapter 9

# Development of a Differential Geodetic Interferometric Deflectometer

This chapter is a reproduction of the peer-reviewed paper *Guillaume et al.* (2014b) published by the author of this thesis.

### 9.1 Introduction

A new system for measuring underground variations of the deflection of the vertical is presented. Based on geodetic and interferometric tilt measurements along a profile, it is designed to finally determine variations of equipotential profiles to better than  $10\text{ }\mu\text{m}$  over 200 m with respect to a straight line. In the first part of this chapter, the basic principle is described and a mathematical model of the system is developed in order to estimate, using Monte-Carlo simulations, theoretical precisions achievable by the system in various configurations. In the second part, the first 12 m long prototype, designed and assembled at the European Organization for Nuclear Research (CERN) in Geneva, is presented. From the first experiments, it is not yet possible to validate the concept, nevertheless they permit us to identify the weaknesses which have to be solved in order to achieve the performance anticipated.

The idea is to measure the direction of the vertical with respect to a perfect straight line, with an accuracy better than  $0.05\text{ arcsec} = 0.25\text{ }\mu\text{rad}$ , at different points along the profile of the tunnel where the accelerator must be aligned. These measurements would be carried out with an innovative new instrument named High-Precision Interferometric Deflectometer.

The basic principle is to simultaneously measure the tilt of a moving platform placed in a vacuum tube, with both an angular interferometer and a gravity sensitive inclinometer. Assuming that both systems are rigidly fixed together, at any given position along the profile the measurements should only differ by a constant initial offset, and the variation of the direction of the vertical with respect to the straight line realized by the laser beams

of the interferometric measurement system. We present the realization of a 12 m long prototype assembled in the metrological calibration building of the survey section of the Accelerators & Beams Physics group of the European Organization for Nuclear Research, CERN, in Geneva. The calibration procedure and the first measurements are presented and discussed.

## 9.2 Basic Principle

Inspired by Astronomical Levelling *Hirt* (2009), the principle is very simple. The idea is to measure the variation of the direction of the vertical with respect to a straight line at different places along a profile. Basically, the inclination in length of a moving cart is measured on the one hand by a high-precision geodetic inclinometer and on the other hand by an angular interferometer. The variation of the direction of the vertical is simply the difference between the measurements carried out by both systems (see Figure 9.1). Although the analogy with astro-geodetic measurements, it is obvious that this new system does not provide absolute deflections of the vertical – as with zenith camera systems – but relative deflections with respect to the straight line defined by the laser beams of the interferometer system. Due to the very high precision of the angular measurements which are necessary for both systems, optimum observation conditions along the profile have to be fulfilled. As a first approximation, the precision of the geodetic tiltmeter should not be dependent upon its place along the profile. In contrast, the performance of the angular interferometer system is significantly dependent on the distance to the target. This is mainly due to the influence of the air which produces refraction and scintillation, degrading the precision. This implies that the moving cart must be enclosed by a vacuum vessel so that the perturbations of the laser beams due to the atmosphere are almost cancelled out.

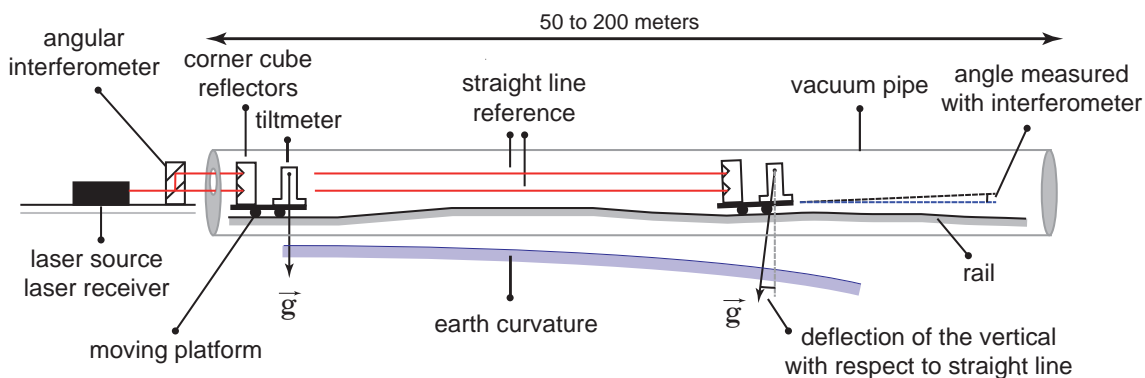


**Figure 9.1:** Functional sketch of the High Precision Interferometric Deflectometer.



### 9.3 Analysis of the Precision by Simulations

#### 9.3.1 Mathematical Model

The raw observations consist of the angles measured by the angular interferometer,  $\alpha_i^{\mathcal{I}}(t)$ , and by the geodetic inclinometer,  $\alpha_i^{\mathcal{G}}(t)$ , at time  $t$ , and at positions  $i = 1 \dots n + 1$ , inside the deflectometer. Assuming that they are both affected by a constant offset  $c^{\mathcal{I}}$  and  $c^{\mathcal{G}}$  and a temporal linear drift  $m^{\mathcal{I}}$  and  $m^{\mathcal{G}}$ , we can write:

$$\begin{aligned}\alpha_i^{\mathcal{I}}(t) &= c^{\mathcal{I}} + m^{\mathcal{I}} \cdot t + \alpha_i^{\mathcal{C}}(t) + \mathcal{N}(0, \sigma_{\alpha^{\mathcal{I}}}^2) \\ \alpha_i^{\mathcal{G}}(t) &= c^{\mathcal{G}} + m^{\mathcal{G}} \cdot t + \alpha_i^{\mathcal{C}}(t) + \epsilon_i + \mathcal{N}(0, \sigma_{\alpha^{\mathcal{G}}}^2)\end{aligned}\tag{9.1}$$

where  $\epsilon_i$  is the difference between the direction of the vertical of the first position  $i = 1$  and the direction of the vertical at position  $i$ . The tilt of the moving cart with respect to the direction of the vertical of the first position is represented by  $\alpha_i^{\mathcal{C}}(t)$ . If we take the difference between  $\alpha_i^{\mathcal{G}}(t)$  and  $\alpha_i^{\mathcal{I}}(t)$  we have:

$$\begin{aligned}\underbrace{\alpha_i^{\mathcal{G}}(t) - \alpha_i^{\mathcal{I}}(t)}_{\alpha_i(t)} &= \underbrace{(c^{\mathcal{G}} - c^{\mathcal{I}})}_c + \underbrace{(m^{\mathcal{G}} - m^{\mathcal{I}})}_m \cdot t + \epsilon_i \\ &\quad + \mathcal{N}(0, \underbrace{\sigma_{\alpha^{\mathcal{I}}}^2 + \sigma_{\alpha^{\mathcal{G}}}^2}_{\sigma_{\alpha}^2})\end{aligned}\tag{9.2}$$

Now an equipotential profile of length  $S = 200$  m could be determined using observations carried out with a single deflectometer of length  $L$  which is displaced  $m$  times along the profile so that a certain overlapping  $\mathcal{O} = ]0; 1[$  exists. Let us consider various overlapping positions  $j = 1 \dots m$  of the deflectometer:

$$\alpha_i^j(t) = \epsilon_i^j + c^j + m^j \cdot t + \mathcal{N}(0, \sigma_{\alpha}^2)\tag{9.3}$$

Two consecutive observations  $i$  are separated by a space interval  $\Delta s = \frac{L}{n}$  and a time interval  $\Delta t$ . Two consecutive deflectometer positions are separated by  $\Delta n = \lfloor (1 - \mathcal{O}) \cdot n \rfloor$  positions. Moreover, all positions inside the deflectometer are observed successively on the outward and return journey of the cart so that the time drift factors  $m^j$  can be estimated (see Figure 9.2). From (9.3) we can write a linear system of equations in the form:

$$\begin{cases} \mathbf{1} + \hat{\mathbf{v}} &= \mathbf{A} \cdot \hat{\mathbf{x}} \\ \mathbf{B} \cdot \hat{\mathbf{x}} &= \mathbf{t} \end{cases}\tag{9.4}$$

where  $\hat{\mathbf{l}}$  represents the vector of the true observations;  $\mathbf{l} \sim \mathcal{N}(\hat{\mathbf{l}}, \mathbf{C}_{\mathbf{l}} = \sigma_0^2 \cdot \mathbf{Q}_{\mathbf{l}})$  is the vector of observations;  $\hat{\mathbf{v}}$  the vector of the estimated residuals;  $\mathbf{A}$  the design matrix;  $\hat{\mathbf{x}}$  the vector of the estimated unknowns. Conditions between unknowns are expressed using the matrix  $\mathbf{B}$  and the vector  $\mathbf{t}$  in order to fix the first constant offset to  $c^1 = 0$ . In (9.5) and

(9.6) a simple case is shown, when  $n = 4$ ,  $m = 2$  and  $\mathcal{O} = 0.5 \Rightarrow \Delta n = 2$ .

$$\underbrace{\begin{pmatrix} \alpha_1^1(0 \cdot \Delta t) \\ \alpha_2^1(1 \cdot \Delta t) \\ \alpha_3^1(2 \cdot \Delta t) \\ \alpha_4^1(3 \cdot \Delta t) \\ \alpha_5^1(4 \cdot \Delta t) \\ \alpha_5^1(5 \cdot \Delta t) \\ \alpha_4^1(6 \cdot \Delta t) \\ \alpha_3^1(7 \cdot \Delta t) \\ \alpha_2^1(8 \cdot \Delta t) \\ \alpha_1^1(9 \cdot \Delta t) \\ \hline \alpha_1^2(0 \cdot \Delta t) \\ \alpha_2^2(1 \cdot \Delta t) \\ \alpha_3^2(2 \cdot \Delta t) \\ \alpha_4^2(3 \cdot \Delta t) \\ \alpha_5^2(4 \cdot \Delta t) \\ \alpha_5^2(5 \cdot \Delta t) \\ \alpha_4^2(6 \cdot \Delta t) \\ \alpha_3^2(7 \cdot \Delta t) \\ \alpha_2^2(8 \cdot \Delta t) \\ \alpha_1^2(9 \cdot \Delta t) \end{pmatrix}}_{\mathbf{I}} ; \underbrace{\begin{pmatrix} 1 & 0 & 0 & 0 & 0 & 0 & 0 & 0 & 1 & 0 & 0 \cdot \Delta t & 0 \\ 0 & 1 & 0 & 0 & 0 & 0 & 0 & 0 & 1 & 0 & 1 \cdot \Delta t & 0 \\ 0 & 0 & 1 & 0 & 0 & 0 & 0 & 0 & 1 & 0 & 2 \cdot \Delta t & 0 \\ 0 & 0 & 0 & 1 & 0 & 0 & 0 & 0 & 1 & 0 & 3 \cdot \Delta t & 0 \\ 0 & 0 & 0 & 0 & 1 & 0 & 0 & 0 & 1 & 0 & 4 \cdot \Delta t & 0 \\ 0 & 0 & 0 & 0 & 0 & 1 & 0 & 0 & 1 & 0 & 5 \cdot \Delta t & 0 \\ 0 & 0 & 0 & 1 & 0 & 0 & 0 & 0 & 1 & 0 & 6 \cdot \Delta t & 0 \\ 0 & 0 & 1 & 0 & 0 & 0 & 0 & 0 & 1 & 0 & 7 \cdot \Delta t & 0 \\ 0 & 1 & 0 & 0 & 0 & 0 & 0 & 0 & 1 & 0 & 8 \cdot \Delta t & 0 \\ 1 & 0 & 0 & 0 & 0 & 0 & 0 & 0 & 1 & 0 & 9 \cdot \Delta t & 0 \\ \hline 0 & 0 & 1 & 0 & 0 & 0 & 0 & 0 & 0 & 1 & 0 & 0 \cdot \Delta t \\ 0 & 0 & 0 & 1 & 0 & 0 & 0 & 0 & 0 & 1 & 0 & 1 \cdot \Delta t \\ 0 & 0 & 0 & 0 & 1 & 0 & 0 & 0 & 0 & 1 & 0 & 2 \cdot \Delta t \\ 0 & 0 & 0 & 0 & 0 & 1 & 0 & 0 & 0 & 1 & 0 & 3 \cdot \Delta t \\ 0 & 0 & 0 & 0 & 0 & 0 & 1 & 0 & 0 & 1 & 0 & 4 \cdot \Delta t \\ 0 & 0 & 0 & 0 & 0 & 0 & 0 & 1 & 0 & 1 & 0 & 5 \cdot \Delta t \\ 0 & 0 & 0 & 0 & 0 & 1 & 0 & 0 & 0 & 1 & 0 & 6 \cdot \Delta t \\ 0 & 0 & 0 & 0 & 1 & 0 & 0 & 0 & 0 & 1 & 0 & 7 \cdot \Delta t \\ 0 & 0 & 0 & 1 & 0 & 0 & 0 & 0 & 0 & 1 & 0 & 8 \cdot \Delta t \\ 0 & 0 & 1 & 0 & 0 & 0 & 0 & 0 & 0 & 1 & 0 & 9 \cdot \Delta t \end{pmatrix}}_{\mathbf{A}} ; \underbrace{\begin{pmatrix} \epsilon_1 \\ \epsilon_2 \\ \epsilon_3 \\ \epsilon_4 \\ \epsilon_5 \\ \epsilon_6 \\ \epsilon_7 \\ \hline c^1 \\ c^2 \\ \hline m^1 \\ m^2 \end{pmatrix}}_{\mathbf{x}} \quad (9.5)$$

$$\mathbf{B} = \left( \begin{array}{cccccccc|cc} 0 & 0 & 0 & 0 & 0 & 0 & 0 & 0 & 1 & 0 & 0 & 0 \end{array} \right); \mathbf{t} = \left( \begin{array}{c} 0 \end{array} \right) \quad (9.6)$$

The maximum likelihood solution of (9.4) can be found when *Möser et al.* (2000):

$$\hat{\mathbf{v}}^T \cdot \mathbf{Q}_{\Pi}^{-1} \cdot \hat{\mathbf{v}} + 2 \cdot \mathbf{k}^T (\mathbf{B} \cdot \hat{\mathbf{x}} - \mathbf{t}) \rightarrow \min \quad (9.7)$$

or:

$$\begin{pmatrix} \hat{\mathbf{x}} \\ \mathbf{k} \end{pmatrix} = \left( \begin{array}{c|c} \mathbf{A}^T \cdot \mathbf{Q}_{\Pi}^{-1} \cdot \mathbf{A} & \mathbf{B}^T \\ \hline \mathbf{B} & \mathbf{0} \end{array} \right)^{-1} \begin{pmatrix} \mathbf{A}^T \cdot \mathbf{Q}_{\Pi}^{-1} \cdot \mathbf{1} \\ \mathbf{t} \end{pmatrix} \quad (9.8)$$

$$= \left( \begin{array}{c|c} \mathbf{Q}_{\hat{\mathbf{x}}\hat{\mathbf{x}}} & \dots \\ \hline \dots & \dots \end{array} \right) \begin{pmatrix} \mathbf{A}^T \cdot \mathbf{Q}_{\Pi}^{-1} \cdot \mathbf{1} \\ \mathbf{t} \end{pmatrix}$$

where the variance-covariance matrix of  $\hat{\mathbf{x}}$  can be computed by  $\mathbf{C}_{\hat{\mathbf{x}}\hat{\mathbf{x}}} = \sigma_0^2 \cdot \mathbf{Q}_{\hat{\mathbf{x}}\hat{\mathbf{x}}}$ .

Finally, the variation of the equipotential profile  $\Delta N_{\mathbf{r}_{\text{beg}}}^{\mathbf{r}_K}$  between the beginning  $\mathbf{r}_{\text{beg}}$  and the position  $\mathbf{r}_K$  with respect to the straight line can be computed as:

$$\Delta N_{\mathbf{r}_{\text{beg}}}^{\mathbf{r}_K} = - \int_{\mathbf{r}_{\text{beg}}}^{\mathbf{r}_K} \epsilon \cdot ds \cong - \sum_{k=1}^K \epsilon_k \cdot \Delta s \quad (9.9)$$

and the path  $\mathcal{P}_{\Delta N}$  representing the equipotential profile can be computed with:

$$\mathcal{P}_{\Delta N} \equiv \Delta \mathbf{N} = \mathbf{F} \cdot \hat{\mathbf{x}} \quad (9.10)$$

with:

$$\mathbf{F} = -\Delta s \cdot \begin{pmatrix} 1 & 0 & 0 & 0 & 0 & 0 & 0 & 0 & 0 & 0 & 0 \\ 1 & 1 & 0 & 0 & 0 & 0 & 0 & 0 & 0 & 0 & 0 \\ 1 & 1 & 1 & 0 & 0 & 0 & 0 & 0 & 0 & 0 & 0 \\ 1 & 1 & 1 & 1 & 0 & 0 & 0 & 0 & 0 & 0 & 0 \\ 1 & 1 & 1 & 1 & 1 & 0 & 0 & 0 & 0 & 0 & 0 \\ 1 & 1 & 1 & 1 & 1 & 1 & 0 & 0 & 0 & 0 & 0 \\ 1 & 1 & 1 & 1 & 1 & 1 & 1 & 0 & 0 & 0 & 0 \\ 1 & 1 & 1 & 1 & 1 & 1 & 1 & 1 & 0 & 0 & 0 \\ 1 & 1 & 1 & 1 & 1 & 1 & 1 & 1 & 1 & 0 & 0 \\ 1 & 1 & 1 & 1 & 1 & 1 & 1 & 1 & 1 & 1 & 0 \end{pmatrix} \quad (9.11)$$

The probability density of  $\mathcal{P}_{\Delta N}$  can be computed with the variance-covariance propagation law:

$$\mathcal{P}_{\Delta N} \sim \mathcal{N}(\Delta \mathbf{N}, \sigma_0^2 \cdot \mathbf{F} \cdot \mathbf{Q}_{\hat{\mathbf{x}}\hat{\mathbf{x}}} \cdot \mathbf{F}^T) \quad (9.12)$$

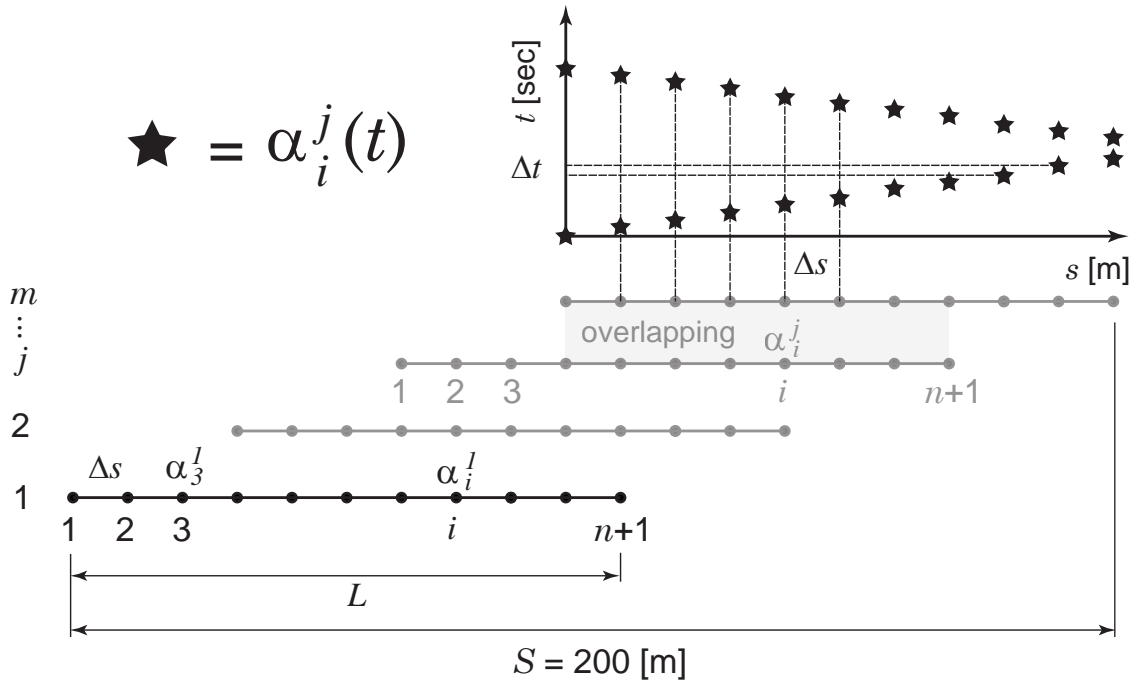


**Figure 9.2:** The mathematical modelling of the High Precision Interferometric Deflectometer.

### 9.3.2 Monte-Carlo Simulations

In Equation 9.12 the probability density of  $\Delta\mathbf{N}$  can be computed analytically if  $\mathbf{C}_{\Pi}$ ,  $\mathbf{A}$  and  $\mathbf{B}$  are known, see Equation 9.8. This gives the uncertainty with respect to the straight line reference in an absolute way. Nevertheless, in our application, we are not interested in the probability density of the absolute value of  $\Delta\mathbf{N}$  but in the probability density of the misalignment produced by the system. This density is represented by the random variable  $\mathcal{X}$ . Because of the non-linear behaviour of the misalignment operator  $\mathcal{M}$ , it is not possible to compute it analytically. However, it is possible to estimate it in an empirical way, using Monte-Carlo simulations. The simulations are computed according to the parameters given in Table 9.1.

Basically, for one set of parameters  $p(\sigma_\alpha, L, \mathcal{O})$ , and using the operator  $\mathcal{M}$  introduced in Section 2.1, the  $k^{th}$  realization of  $\mathcal{X}_p$  can be formulated as  $x_k = \mathcal{M}_0^{200}\{\Delta\mathbf{N}_k\}$ . If we produce  $K$  realizations of  $\mathcal{X}_p$ , it is now possible to compute empirically the cumulative distribution function (CDF)  $F_{\mathcal{X}_p}(x) = P(\mathcal{X}_p \leq x)$ . Finally, we define:

$$\sigma_{\mathcal{M}_p} = x : P(\mathcal{X}_p \leq x) = 0.68 \quad (9.13)$$

which covers the same probability as the bilateral univariate Gaussian CDF at one sigma ( $\pm 1\sigma$ ):

$$P(-\sigma \leq \mathcal{N}(0, \sigma^2) \leq +\sigma) = 0.68 \quad (9.14)$$

The results of  $K = 2000$  simulations for all combinations  $p(\sigma_\alpha, L, \mathcal{O})$  given in Table 9.1 can be seen in Figure 9.3 and give a better idea of the theoretical alignment accuracies which can be expected in various combinations.

**Table 9.1:** Monte-Carlo simulation parameters

variable	type	value
$\alpha_i^j$	observation	formed by Equation 9.3
$\epsilon_i^j$	unknown	0.0 [arcsec]
$c^j$	unknown	0.0 [arcsec]
$m^j$	unknown	1.0 [ $\frac{\text{arcsec}}{\text{hour}}$ ]
$\mathcal{N}(0, \sigma_\alpha^2)$	random nbr.	$\mathcal{RN}(0, \sigma_\alpha^2)$
$\sigma_\alpha$	constant	0.02...0.10 [arcsec]
$\Delta t$	constant	5.0 [min]
$L$	constant	50, 100, 150, 200 [m]
$\Delta s$	constant	10 [m]
$\mathcal{O}$	constant	25%, 50%, 75%
$m$	constant	: $L + (m - 1) \cdot \Delta s > 200$ [m]
$\Delta\mathbf{N}$	path	simulated by Equation 9.8 and 9.10

Moreover, for every combination  $(L, \mathcal{O})$ , a first estimation of the duration of the observation can be predicted. In Table 9.2,  $T^j = [2 \cdot (n + 1) - 1] \cdot \Delta t$  represents the duration of the observations of the deflectometer at one position  $j$ . This value gives an important order of magnitude for the time for which the temporal drift of the sensors must have a

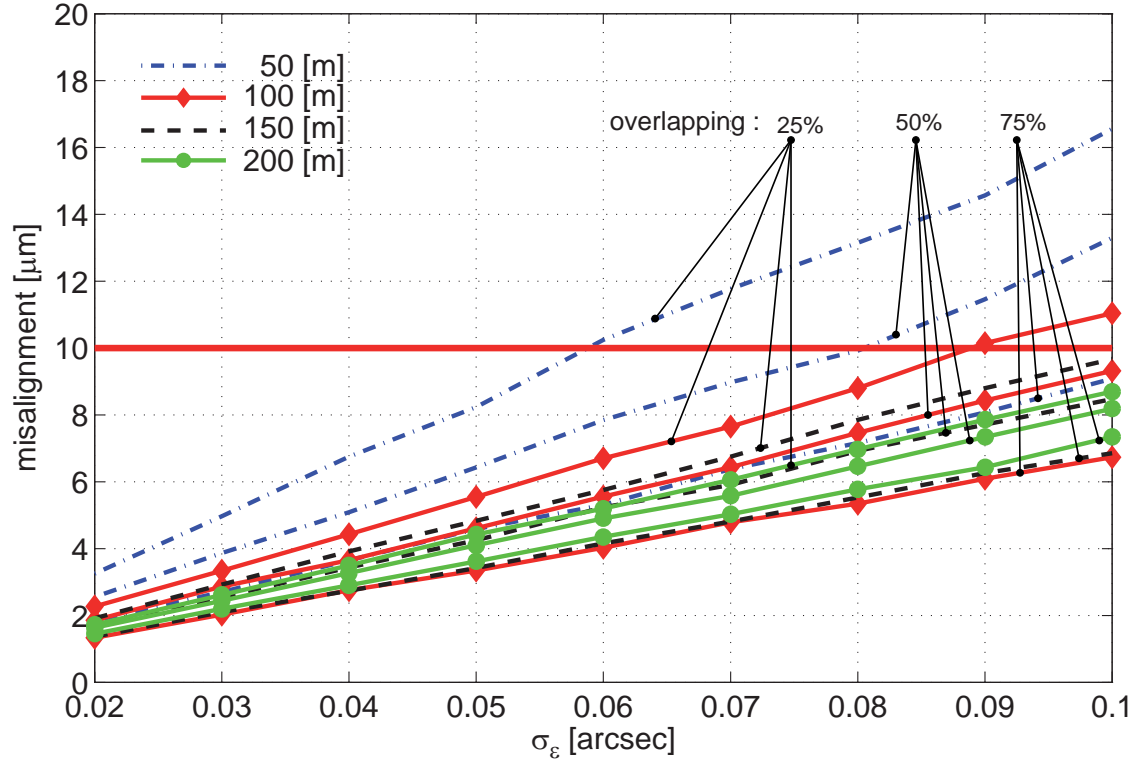


**Figure 9.3:** Simulated alignment accuracy of an equipotential profile of 200 m length determined by overlapping deflectometers of different length  $L$ , different overlapping  $\mathcal{O}$  and different measurement noise  $\sigma_\alpha$ .

linear behaviour, modelled by  $m^j \cdot t$ .

The approximate total time which would be necessary to observe a profile of 200 m is represented by  $T_{\text{tot}} = m \cdot T^j + (m - 1) \cdot T_{\text{disp}}$  assuming that  $T_{\text{disp}} = 5$  [hours] represents the duration which is needed to displace the deflectometer from a position  $j$  to  $j + 1$ . This value gives a first estimation of the productivity obtained by a certain set of parameters.

## 9.4 Development of the first Prototype

A first prototype, 12 m in length, was designed and assembled in the metrological calibration building of the survey section of the Accelerators & Beams Physics group of the European Organization for Nuclear Research, CERN, in Geneva. This instrument must meet several challenges. Firstly, it should demonstrate the technical feasibility of making angular interferometric and geodetic measurements in a vacuum vessel on a moving cart operated externally to the vessel. Secondly, the accuracy of the system in terms of systematic and random noise and its stability over time should be demonstrated.

**Table 9.2:** Estimated duration of the observations for a profile of 200, m where  $\Delta s = 10$  m. The number of positions  $m$  is determined so that the total length of the profile which is determined, is strictly greater than 200 m.

$L$ [m]	$\mathcal{O}$ [%]	$n$ #	$m$ #	$T^j$ [min]	$T_{\text{tot}}$ [hours]
50	25%	5	7	55	36.4
50	50%	5	9	55	48.3
50	75%	5	17	55	95.6
100	25%	10	3	105	15.3
100	50%	10	4	105	22.0
100	75%	10	7	105	42.3
150	25%	15	2	155	10.2
150	50%	15	2	155	17.8
150	75%	15	3	155	11.8
200	25%	20	2	205	11.8
200	50%	20	2	205	11.8
200	75%	20	2	205	11.8

### 9.4.1 Main Components

The main components of the prototype are described in Table 9.3. They consist of a vacuum tube, in which a cart can be manually displaced with a crank, on a monorail. The tilt of the cart can be controlled by two stepping motors. This is essential for the realization of the calibration in vacuum and to ensure the levelling of the cart over the entire length of the deflectometer. The tolerance for the levelling is fixed to 5 arcsec in order to make systematic errors due to the calibration and crosswise tilt negligible. Two single-axis geodetic inclinometers, one arranged along and the second transverse to the direction of displacement and the double corner cube of the angular interferometer are mounted on the cart.

### 9.4.2 Calibration Process

The calibration consists of the determination of the scale factor of the geodetic inclinometer with respect to the angular interferometer. This can be achieved by making measurements in vacuum, for different tilt angles of the cart (see Figure 9.4). Considering that the measurements are carried out at a fixed position in the tube ( $i = 1$ ), the interferometric measurements are taken as reference, and that the geodetic inclinometer  $\mathcal{G}$  is affected by a scaling factor  $s^{\mathcal{G}}$ , Equation 9.2 can be reformulated as:

$$\alpha_1^{\mathcal{G}}(t) = \frac{\alpha_1^{\mathcal{I}}(t)}{s^{\mathcal{G}}} + \frac{c + \epsilon_1}{s^{\mathcal{G}}} + \frac{m}{s^{\mathcal{G}}} \cdot t + \frac{\mathcal{N}(0, \sigma_{\alpha}^2)}{s^{\mathcal{G}}} \quad (9.15)$$

or:

$$\alpha^{\mathcal{G}}(t) = \alpha^{\mathcal{I}}(t) \cdot s_{\text{cal}} + c_{\text{cal}} + m_{\text{cal}} \cdot t + \mathcal{N}\left(0, \sigma_{\alpha}^2 \cong \frac{\sigma_{\alpha}^2}{s^{\mathcal{G}}}\right) \quad (9.16)$$

where  $s^{\mathcal{G}} = s_{\text{cal}}^{-1}$ .

**Table 9.3:** Main Components of the Prototype Deflectometer

Component	Origin	Description		
Vacuum Tube	CERN	length:	12	[m]
		rail tilt:	$\pm 200$	[arcsec]
		diameter:	225	[mm]
		pressure:	$10^{-2}$	[mbar]
		porthole:	60	[mm]
		electric interface	$3 \cdot 10$	[pin]
Movable cart	CERN ETHZ	displ.:	manual	
		tilt corr.:	2 step motors	
		range:	$\pm 0.25$	[deg]
		resol.:	0.2	[arcsec]
Angular Interfero.	HP Agilent	type:	heterodyne	
		range:	$\pm 30$	[deg]
		resol.:	$5 \cdot 10^{-3}$	[arcsec]
		inter-beam:	32.61	[mm]
		aquis. rate	10	[Hz]
Geodetic Tiltmeter	Lippmann HRTM	filtering	none	
		type:	1-axis pendulum	
		range:	$\pm 200$	[arcsec]
		resol.:	$1 \cdot 10^{-3}$	[arcsec]
		aquis. rate	1000	[Hz]
		filtering:	1.0	[Hz]

Assuming that  $\mathbf{l} \sim \mathcal{N}(\tilde{\mathbf{l}}, \mathbf{C}_{\mathbf{l}})$  and  $\mathbf{C}_{\mathbf{l}} = \sigma_{\alpha}^2 \cdot \mathbf{I}$ , affect only the geodetic observations  $\alpha^{\mathcal{G}}(t)$ , and further that observations are carried out at  $N$  different epochs, then we can write the linear system of equations as:

$$\mathbf{l} + \hat{\mathbf{v}} = \mathbf{A} \cdot \hat{\mathbf{x}} \quad (9.17)$$

with:

$$\mathbf{l} = \begin{pmatrix} \alpha^{\mathcal{G}}(t_1) \\ \vdots \\ \alpha^{\mathcal{G}}(t_N) \end{pmatrix}; \mathbf{A} = \begin{pmatrix} \alpha^{\mathcal{I}}(t_1) & 1 & t_1 \\ \vdots & \vdots & \vdots \\ \alpha^{\mathcal{I}}(t_N) & 1 & t_N \end{pmatrix}; \hat{\mathbf{x}} = \begin{pmatrix} s_{\text{cal}} \\ c_{\text{cal}} \\ m_{\text{cal}} \end{pmatrix} \quad (9.18)$$

which can be solved according to (9.8). The results of a calibration process is summarized in Table 9.4. It shows that the calibration process in vacuum is successful and permits an estimation of the scale factor  $s_{\text{cal}}$  with a precision of 0.1% which corresponds to a systematic error of  $\sim 0.01$  arcsec if we measure tilts smaller than 10 arcsec which can be easily achieved by the levelling process of the cart.

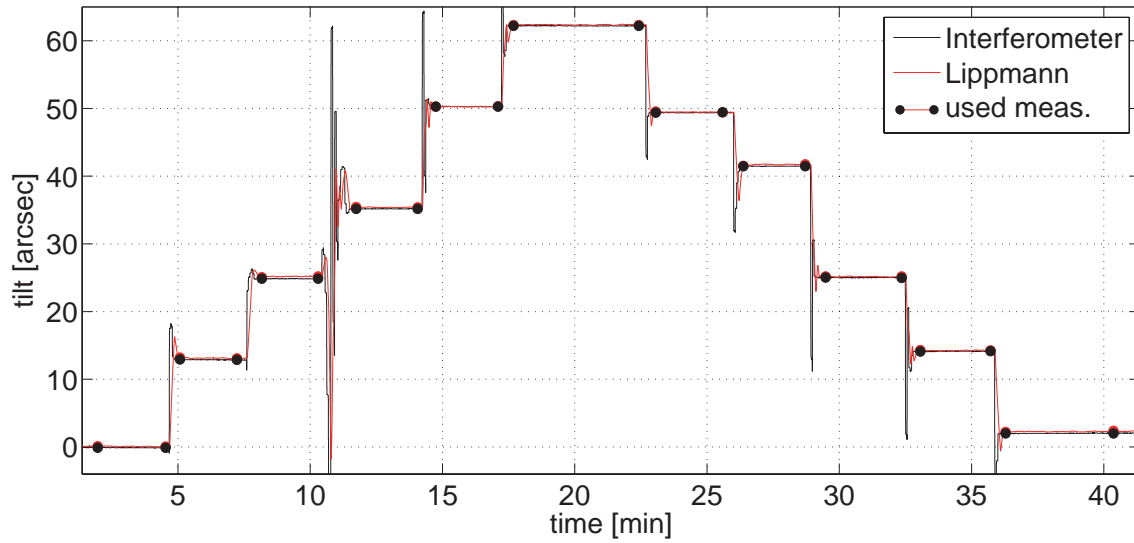


**Figure 9.4:** Time series of the Lippmann tiltmeter and the HP Agilent angular interferometer for the calibration.

**Table 9.4:** Deflectometer Calibration Process Results

parameter	value	unit
# observations	$2 \cdot 11 = 22$	
# unknowns	3	
# conditions	0	
# outliers	0	
# redundancy	19	
duration	$\sim 42$	[min]
$s_{\text{cal}}$	$0.9978 \pm 0.001$	[-]
$c_{\text{cal}}$	$0.2676 \pm 0.047$	[arcsec]
$m_{\text{cal}}$	$9.2805^{-5} \pm 0.002$	[arcsec]/[min]

### 9.4.3 Measurement of a Profile

Finally, the validation of the system can only be done by determining deflections along the deflectometer which should match those predicted from a simple spherical Earth model. In this example, the aim is to determine deflections at 0, 5 and 10 m using observations carried out at the following sequence of distance:

$$0 \rightarrow 5 \rightarrow 10 \rightarrow 5 \rightarrow 0 \rightarrow 5 \rightarrow 10 \rightarrow 5 \rightarrow 0 \text{ [m]} \quad (9.19)$$

After levelling, the observations were carried out over 5 min with an acquisition rate of  $\sim 2$  Hz. The raw data, which represent  $\alpha_i^{\mathcal{G}}(t)$  and  $\alpha_i^{\mathcal{T}}(t)$ , can be seen in Figure 9.5. In Figure 9.6, we can see the time series of  $\alpha_i^1(t)$  obtained from (9.2). At this stage, the observations  $\alpha_i^1(t)$  are averaged before forming the matrix according to (9.5) and the final adjustment.



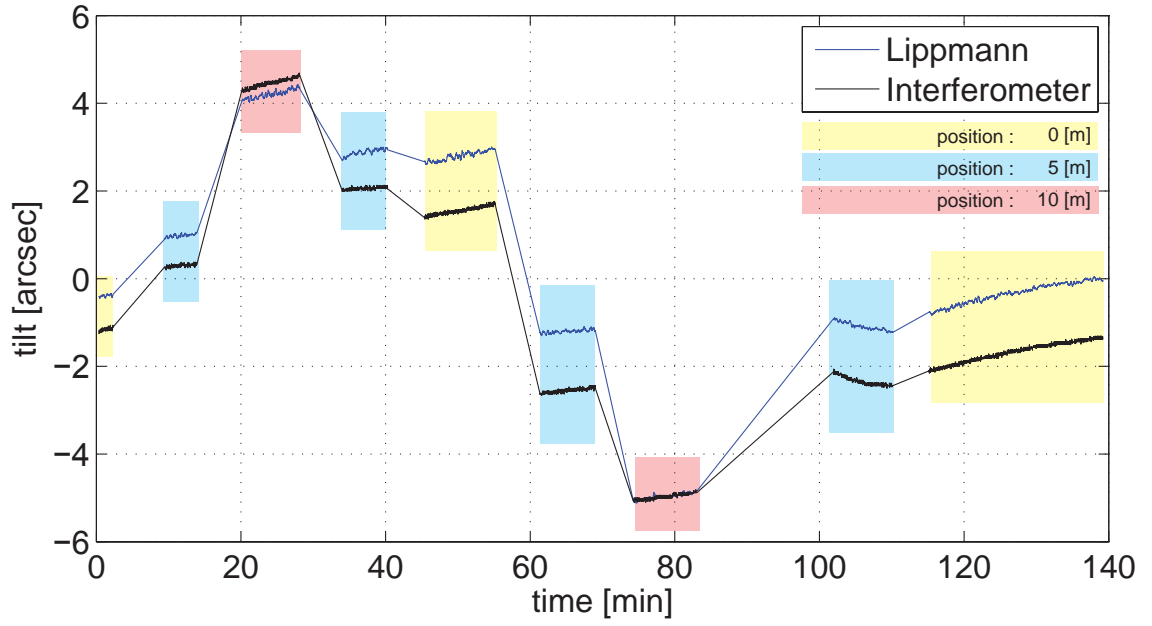


**Figure 9.5:** Raw time series of the Lippmann tiltmeter and the HP Agilent angular interferometer at 0, 5 and 10 m.

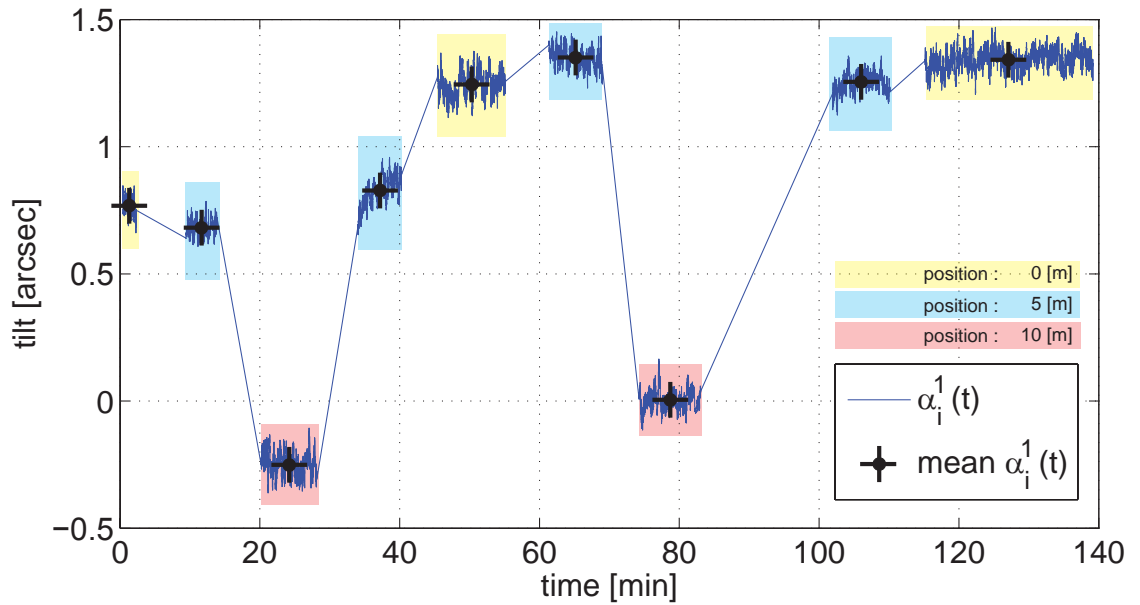


**Figure 9.6:** Time series of the difference between Lippmann tiltmeter and the HP Agilent angular interferometer at 0, 5 and 10 m.

Theoretically, after adjustment and according to Section 9.3.1, the deflections  $\epsilon_i^1$  should only contain the signal from the variation of the direction of the vertical, approximately 0.16 and 0.32 arcsec at  $s = 5$  and  $s = 10$  m distances, respectively. These values can be

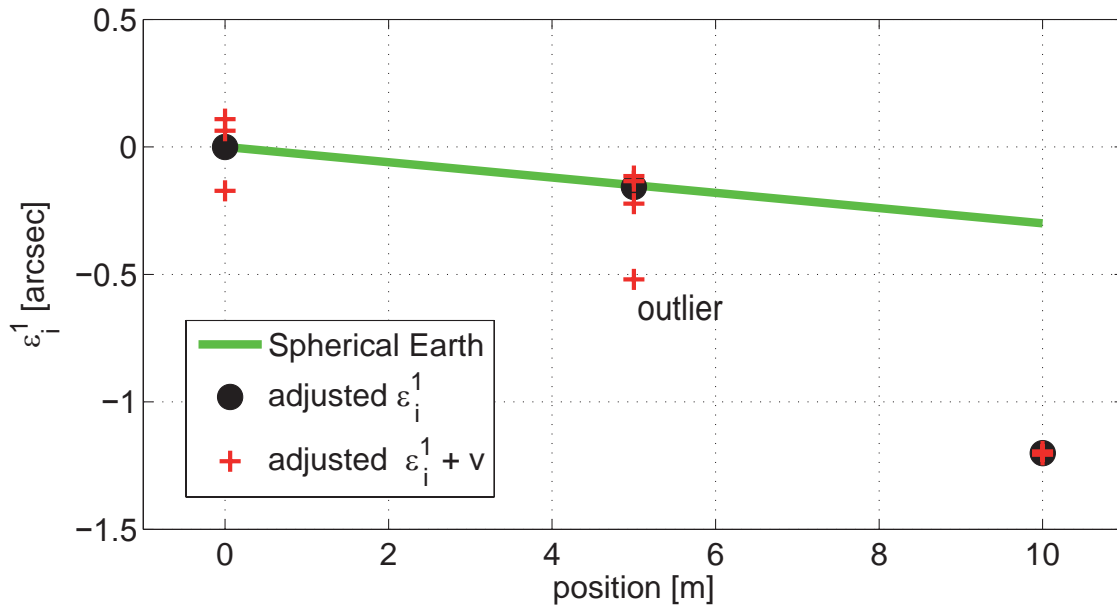


**Figure 9.7:** Adjusted deflections and residuals compared to deflections from a spherical model of the Earth.

**Table 9.5:** Adjustment of the Measurements along the Profile

parameter	value	unit
# observations	9	
# unknowns	5	
# conditions	1	
# outliers	1	
# redundancy	5	
duration	~ 140	[min]
$\epsilon_1^1, 0$ [m]	$0.000 \pm 0.1$	[arcsec]
$\epsilon_2^1, 5$ [m]	$-0.157 \pm 0.1$	[arcsec]
$\epsilon_3^1, 10$ [m]	$-1.201 \pm 0.1$	[arcsec]
$c^1$	$0.000 \pm 0.0$	[arcsec]
$m^1$	$0.005 \pm 0.001$	[arcsec]/[min]

derived from a simple spherical Earth model as:

$$\epsilon(s) [\text{arcsec}] = \frac{s [\text{m}]}{R [\text{m}]} \cdot \frac{180}{\pi} \cdot 3600 \cong 0.032 \frac{[\text{arcsec}]}{[\text{m}]} \cdot s [\text{m}] \quad (9.20)$$

where  $s$  represents the horizontal distance from the first position of the cart and  $R = 6'380'000$  m the radius of the Earth. Unfortunately, see Figure 9.7 and Table 9.5, only the deflections at 0 and 5 m seem to be governed by the deflections predicted by a spherical Earth model. At 10 m a systematic effect is most likely. In fact, both measurements carried out at this position are consistent.

## 9.5 Conclusion

We investigated the possibility of determining underground variation in the direction of the vertical by introducing a new measurement system called High Precision Interferometric Deflectometer. The simulations show that the system, in various configurations, is conceptually capable of determining underground equipotential profiles for wavelength of 200 m at a level of precision better than 10  $\mu\text{m}$ .

However, from the first experiments it is clear that the prototype instrument does not yet demonstrate the feasibility of the approach system, but does allow to identify the evident weak points which still have to be improved. The next step will be to install an alternative angular interferometer and to improve the automation of the deflectometer in order to identify systematic effects and their origin.



## Chapter 10

# Conclusions and Outlooks

The major aim of this thesis is to demonstrate the feasibility and propose a realistic practical strategy for the determination of underground equipotential profiles, with an accuracy of 10 microns over 200 meters, in the perspective of the alignment of the future linear collider CLIC based on hydrostatic levelling systems (HLS). The feasibility is demonstrated and a practical strategy for the determination is proposed. For this, several theoretical aspects have been revisited in order to quantify some physical and computational approximations which are often implicitly assumed in Geodesy. The feasibility studies rely on new alignment accuracy analyzes of astrogravimetric levelling, based on Monte-Carlo simulations. Furthermore, they are also based on the estimation of signals expected at short-wavelengths, generated by lateral varying anomalies, and on the new concept of observability which permits to predict if a certain part of a profile can be determined, with sufficient accuracy, by observations only. All numerical gravity field simulations have been performed with a new software developed as part of this thesis, called **QGravity**, which permits to generate mass models in various and flexible ways, to compute all gravitational functionals up the order 2 and to visualize the results in real-time. The methods and concepts developed in this thesis are successfully applied for the determination of an equipotential profile situated in an existing tunnel of 850 meters in length at CERN in Geneva. Finally, a new ambitious system for measuring underground variations of the vertical is presented.

### Theoretical Findings

**The Newtonian framework** is suitable considering the alignment objectives of CLIC. The maximal misalignment generated by the discrepancies between the classical and general relativity framework is equal to 1 microns for wavelengths larger than 4'000 kilometers.

**The fluid-air interface** in a HLS can be approximated with sufficient accuracy by the apparent equipotential surface of the gravity field. The non-irrotational Eulerian acceleration term can be neglected. Maximal amplitudes occur at daily periods with horizontal amplitudes of about  $10^{-9} \frac{\text{m}}{\text{s}^2}$  and produce, for an HLS of 200 meters, non-hydrostatic water level changes below 1 micrometer.

**The geometry of equipotential surfaces** formed by the geometry of the normal po-

tential and the geometric separation related to the disturbing potential can be computed with sufficient accuracy by the first order Brun's approximation. Furthermore, an alternative first order Brun's approximation, a function of gravity field quantities given at a fixed position in space, is presented.

**Geometric determinations of equipotential profiles** are revisited. Rigorous formulas are presented for the computation of deflections of the vertical and terrestrial gradiometric observations. The problem of the temporal and spatial reductions of observations and the gravity field is presented in a systematic and general way. In particular, the determination of the mean gravity along the plumbline is discussed. Existing and new formulas based on gravimetric observations on the topography and in the tunnel are analyzed from theoretical and practical points of view. Based on two symptomatic realistic examples, the limitations and artifacts of the various methods are exposed. They show that the presence of non-modeled masses between the surface of topography and the tunnel can generate completely wrong determinations, even if gravimetric measurements are carried out at both places.

### Alignment Accuracy of Astrogravimetric Levelling

With current technologies, the astrogravimetric levelling, is able to determine equipotential profiles with alignment accuracies better than 10 microns over 200 meters. The limiting precision factor of the astrogeodetic part is generated by the anomalous refraction. It is proven that the impact of anomalous refraction, if it acts like a random bias, can be reduced, when several cameras are deployed simultaneously on adjacent stations and when the different acquisition sets overlap. A complete mathematical model is presented, which allows to unbiased raw deflections of the vertical and permits to significantly increase the determination of short-wavelength equipotential profiles. Concerning the accuracy of the determination of the orthometric correction, the simulations demonstrate that the limiting factor is the mean gravity along the plumbline which should not be affected by white noise larger than  $30 \mu\text{gal}$  and correlated noise of 125 or  $5'000 \mu\text{gal}$  for correlation lengths of 1'000 and 16'000 meters, respectively.

### Expected Signals and Observability

The main general findings are that only lateral density contrasts ( $\leq 500 \frac{\text{kg}}{\text{m}^3}$ ) of wavelengths larger than 120 meters can generate misalignment signals in equipotential profiles larger than 10 microns over 200 meters. It follows that observations must be carried out with a spacing shorter than 60 meters. In addition, the observability is only limited by the precision of the determination of the mean gravity along the plumbline. All mass anomalies below the tunnel (and 50 meters below) generate signals which are observable by astrogravimetric levelling. The rest of the masses must be known with a precision better than  $100\text{--}200 \frac{\text{kg}}{\text{m}^3}$  with a resolution of approximately 100 meters.

**Significant signals along the CLIC profile** due to topography are expected for the first 17 kilometers only, which represent 17.8% of the whole profile. In addition, 60% of these significant signals are directly observables. The first 3 kilometers remain not observable even after reductions. In this part, the density field between the surface of

topography and the tunnel must be known with a precision better than  $100 \frac{\text{kg}}{\text{m}^3}$ . Concerning the time-varying phenomena, only the Earth's tide signals must be considered. The existing Earth's tide models are sufficient. The disturbing centrifugal potential and the variation of the surface of the Lake of Geneva can be neglected.

### Strategy for the Determination of Underground Equipotential Surfaces

The determination is based on the combination of modern astrogravimetric levelling and a forward modeling of the gravity field based on known density fields. The following recommendations are only valid for the projected emplacement of CLIC in the region of Geneva.

**The astrogravimetric levelling** part is based on the astrogeodetic determination of deflections of the vertical and gravimetric measurements along the profile. The astrogeodetic part needs 5 zenith cameras working in parallel during 2 hours on successive points separated by 50 meters. In addition, in order to reduce the impact of anomalous refraction, the different sets must have an overlap of 1 point. With this configuration, the whole 50 kilometers profile can be carried out in less than 1 year, and the misalignment over 200 meters, at 68% confidence level, is predicted at 5.4 microns. The gravimetric measurements must be carried out on the surface of the topography and in the tunnel, with a spacing of 10-20 meters. Based on a precise absolute gravimetric reference network, they can be observed with precise relative gravimeters with a precision better than  $10 \mu\text{gal}$ . The positioning of the gravimeters must be performed with an accuracy better than 1 centimeter. With this setting, the gravimetric measurements can be carried out by a single crew (1 gravimeter) in less than 1 year.

**The forward modeling** part is based on known density fields. This part is crucial for the reduction and the prediction of the gravity field generated by the density field between the surface of topography and the tunnel. It is mandatory to provide a density field model between the surface of topography and approximately 50 meters below the tunnel, with an accuracy of 100 to  $200 \frac{\text{kg}}{\text{m}^3}$ , for wavelengths between 200 meters and 3 kilometers along the profile. The density fields can be obtained from existing geological underground maps and soundings, new soundings and/or gravity inversions. Particular care must be taken for the precise determination of the density field of the first 3 kilometers of the CLIC profile.

**The computation of the equipotential profiles** is performed with the formulas of the astrogravimetric levelling based on the remove and restore technique. The astrogeodetic part is computed from adjusted deflections of the vertical observations. In order to reduce the impact of anomalous refraction, the raw astrogeodetic observations are adjusted according to the approach, which estimates biases between overlapping sets. For the orthometric correction, the mean gravity along the plumbline is obtained by the remove and restore technique. However, it is predicted differently along the profile, depending on the results of the observability analysis. For segments for which the observability is attested, the reduced mean gravity is computed by averaging superposed gravimetric observations. For the segments for which the observability is not attested, the mean gravity along the plumbline is computed by averaging superposed gravimetric observations which are pre-

viously low-pass filtered. The filter cutoff of approximately 5-6 kilometers can be derived from the observability analysis directly.

### **Validation of the Strategy by the Astrogravimetric Campaign at CERN (TZ32)**

The main findings resulting from the campaign are that astrogeodetic determinations of the deflections of the vertical on soft ground are possible with the same level of precision as in the case of standard measurements, at about 0.07-0.08 arcsec. The combination of an absolute and precise reference gravity network, the measurements of a modern CG-5 relative gravimeter and a precise geodetic network, for the positioning, provide an absolute accuracy better than 10  $\mu\text{gal}$  for underground and surface gravity observations. The predictions of the gravity field, performed by QGravity, based on a precise 3D density models are in very good agreement with the observations with an RMS of 0.07 arcsec and 80  $\mu\text{gal}$  for astrogeodetic and gravimetric measurements, respectively. The discrepancies between the equipotential profile determined on the one hand by astrogravimetric levelling and on the other hand by the mass models only, generate misalignments over 200 meters which are mainly below 20 microns. This demonstrates that the observations as well the whole simulation chain are correct and agree on a very precise level.

### **Differential Geodetic Interferometric Deflectometer**

The basic principle and the first analyses of the precision of the differential geodetic interferometric deflectometer demonstrates that this system is potentially very promising for direct underground determination of short-wavelength equipotential profiles. In addition, a first prototype of 12 m length was designed, constructed and first measurements have been performed. Unfortunately, the first results show that the expected accuracy is not yet obtained and that further investigations must be performed in order to reduce systematic effects of at least one order of magnitude.

### **Outlooks**

The main topics to be investigated in future are ranked in order of priority:

- Investigations with respect to anomalous refraction in astrogeodetic observations. Using at least two identical zenith camera systems, as for example the new system CODIAC, the anomalous refraction can be investigated in terms of correlations at short distances. The aim would be to prove that it is possible to model anomalous refraction as random bias for parallel observations separated by several hundred meters. In addition, the anomalous refraction can be investigated using ray tracing predictions in precise 3D meteo models. And if time series from a permanent zenith camera are available, it will be possible to see if corrections computed from numerical models are sufficiently accurate in order to be applied to the observations.
- investigations in the development of the differential interferometric deflectometer. Using different techniques for the measurement of the angle of the chariot with respect to a straight line and with a better automation of the measurement process, the systematic effects can be investigated.



- Investigations in the determination of the mean gravity along the plumbline from gravity observables. This subject is very difficult because it is directly related to the theories of gravimetric inversions. However, theoretical and computational developments which could determine the boundaries of the space of realistic density fields which generate a particular set of gravity observables would definitively help the understanding and the bounding of underground equipotential surface determination.
- Investigations in the determination and modeling of 3D underground density fields. In collaboration with geologist and geophysicist, it is necessary to investigate the most appropriate ways in order to determine near-field underground density fields by alternative methods.
- Investigations of alternative underground equipotential surface determination. Once a laser alignment system will be able to reach performances approaching 10 microns over 200 meters, it will be possible to determine underground equipotential profiles in combination with a HLS in a very straightforward way. And comparisons with astrogravimetric determinations could serve to validate both techniques in a very independent manner.



# Bibliography

Agnew, D. C. (2007), *Earth Tides*, vol. 3, pp. 163–195.

Aicheler, M., P. Burrows, M. Draper, T. Garvey, P. Lebrun, K. Peach, N. Phinney, H. Schmickler, D. Schulte, and N. Toge (2012), A Multi-TeV Linear Collider Based on CLIC Technology: CLIC Conceptual Design Report, *Tech. Rep. CERN-2012-007. SLAC-R-985. KEK-Report-2012-1. PSI-12-01. JAI-2012-001*, Geneva.

Aoki, S., B. Guinot, G. Kaplan, H. Kinoshita, D. McCarthy, and P. Seidelmann (1982), The new definition of universal time, *Astronomy and Astrophysics*, 105, 359–361.

Ardalan, A. A., and E. W. Grafarend (2001), Ellipsoidal geoidal undulations (ellipsoidal bruns formula): case studies, *Journal of Geodesy*, 75(9-10), 544–552, doi: 10.1007/s001900100212.

Arnet, F. (1992), POTENZ ein Programm zur exakten Berechnung der Gravitationsfeld-grossen Potential, Beschleunigung und Schweretensor von beliebigen Polyhedern, *Tech. rep.*, IGP-Bericht Nr.192, ETH Zurich.

Ashby, B. (2003), Integratortv. <http://www.unige.ch/hairer/prog/integratort.tgz>.

Bauer, S. W. (1979), Three-dimensional irregular-grid finite difference model of wind induced water level fluctuations and currents in a homogeneous lake with applications to the lake of Geneva, Ph.D. thesis, Lausanne, doi:10.5075/epfl-thesis-335.

Becker, F. (2003), Définition d’un réseau de référence métrologique pour le positionnement d’un grand accélérateur linéaire, Ph.D. thesis, Université Louis Pasteur, Strasbourg, France.

Becker, F., W. Coosemans, and M. Jones (2002), Consequences of perturbations of the gravity field on hls measurements, *Proceedings of the 7th International Workshop on Accelerator Alignment (IWAA 2002)*.

Birch, K. P., and M. J. Downs (1993), An updated edlén equation for the refractive index of air, *Metrologia*, 30(3), 155.

Blakely, R. J. (1996), *Potential Theory in Gravity and Magnetic Applications*, Cambridge University Press.

Boudin, F. (2004), Développement et validation d’un inclinomètre longue base de subsurface à silice et mercure: application à des mesures géophysiques de haute résolution sur

- le chantier pilote du Golfe de Corinthe, Ph.D. thesis, Institut de Physique du Globe de Paris.
- Braun, H., R. Corsini, J.-P. Delahaye, A. De Roeck, S. Doeber, G. Geschonke, A. Grudiev, C. Hauviller, B. Jeanneret, E. Jensen, T. Lefevre, Y. Papaphilippou, G. Riddone, L. Rinnolfi, W.-D. Schlatter, H. Schmickler, D. Schulte, I. Syratcev, M. Taborrelli, F. Tecker, R. Tomas, S. Weisz, and W. Wunsch (2008), Clic 2008 parameters, clic-note-764, *Tech. rep.*, European Organization for Nuclear Research (CERN).
- Britting, K. R. (1971), *Inertial Navigation Systems Analysis*, John Wiley & Sons.
- Bürki, B. (1989), Integrale Schwerefeldbestimmung in der Ivrea-Zone und deren geophysikalische Interpretation, Ph.D. thesis, Eidgenössische Technische Hochschule Zürich.
- Caboussat, A. (2005), Numerical simulation of two-phase free surface flows, *Archives of Computational Methods in Engineering*, 12(2), 165–224, doi:10.1007/BF03044518.
- Chambat, F., Y. Ricard, and B. Valette (2010), Flattening of the Earth: further from hydrostaticity than previously estimated, *Geophysical Journal International*, 183(2), 727–732, doi:10.1111/j.1365-246X.2010.04771.x.
- Chandrasekhar, S. (1967), Ellipsoidal figures of equilibrium—an historical account, *Communications on Pure and Applied Mathematics*, 20(2), 251–265, doi:10.1002/cpa.3160200203.
- Ciddor, P. E. (1996), Refractive index of air: new equations for the visible and near infrared, *Appl. Opt.*, 35(9), 1566–1573, doi:10.1364/AO.35.001566.
- Doms, G., and U. Schättler (2002), A Description of the Nonhydrostatic Regional Model LM. Part I: Dynamics and Numerics, COSMO.
- d’Oreye de Lantremange, N. (2003), Inclinomètre à niveaux hydrostatiques de haute résolution en géophysique / high resolution water-tube tiltmeter in geophysics, Ph.D. thesis, Université catholique de Louvain.
- D’Urso, M. (2013), On the evaluation of the gravity effects of polyhedral bodies and a consistent treatment of related singularities, *Journal of Geodesy*, 87(3), 239–252, doi:10.1007/s00190-012-0592-1.
- D’Urso, M. (2014), Analytical computation of gravity effects for polyhedral bodies, *Journal of Geodesy*, 88(1), 13–29, doi:10.1007/s00190-013-0664-x.
- Einstein, A. (1916), Die Grundlage der allgemeinen Relativitätstheorie, *Ann. Phys.*, 354, 769–822.
- Featherstone, W., and S. Claessens (2008), Closed-form transformation between geodetic and ellipsoidal coordinates, *Studia Geophysica et Geodaetica*, 52(1), 1–18, doi:10.1007/s11200-008-0002-6.
- Feynman, R., Leyhton, Sands, G. Delacote, and M. Bloch (1999), *Le cours de physique de Feynman: Mécanique*, v. 1, Dunod.

- Forel, F. (1895), *Le Léman, Monographie Limnologique*, Librairie de l'Université, Lausanne.
- Forsberg, R. (1984), A study of terrain reductions, density anomalies and geophysical inversion methods in gravity field modelling., *Tech. rep.*, Department of Geodetic Science and Surveying, Ohio State University, Columbus. Report 355.
- Gallavotti, G. (2002), *Foundations of Fluid Dynamics*, Physics and Astronomy Online Library, Springer.
- Geiger, A. (1988), Der Lichtstrahl in differentialgeometrischer Formulierung, *Bericht 140*, Institut für Geodäsie und Photogrammetrie, ETH Zürich.
- Gelb, A., J. F. Kasper, R. A. Nash, C. F. Price, and A. A. Sutherland (Eds.) (1974), *Applied Optimal Estimation*, MIT Press, Cambridge, MA.
- Ghatak, A. (2005), *Optics*, McGraw-Hill.
- Graf, W. H. (1983), Hydrodynamics of the Lake of Geneva, *Schweizerische Zeitschrift für Hydrologie*, 45(1), 62–100, doi:10.1007/BF02538152.
- Grafarend, E., T. Krarup, and R. Syffus (1996), An algorithm for the inverse of a multivariate homogeneous polynomial of degree n, *Journal of Geodesy*, 70(5), 276–286, doi:10.1007/BF00867348.
- Grafarend, E. W., A. Ardalan, and M. G. Sideris (1999), The spheroidal fixed-free two-boundary-value problem for geoid determination (the spheroidal bruns' transform), *Journal of Geodesy*, 73(10), 513–533, doi:10.1007/s001900050263.
- Gröger, G., and L. Plümer (2011), How to achieve consistency for 3d city models, *GeoInformatica*, 15(1), 137–165, doi:10.1007/s10707-009-0091-6.
- Griffith, L. V. (1989), The poisson line as a straight line reference, in *Proceedings of the 1st International Workshop on Accelerator Alignment, SLAC*.
- Guillaume, S., M. Jones, B. Bürki, and A. Geiger (2014a), Determination of High Precision Underground Equipotential Profiles for the Alignment of a Future Linear Collider, in *Earth on the Edge: Science for a Sustainable Planet*, edited by C. Rizos and P. Willis, International Association of Geodesy Symposia, Springer.
- Guillaume, S., M. Jones, B. Bürki, and A. Geiger (2014b), Measurement of Underground Variations in the Deflection of the Vertical with a High Precision Interferometric Deflectometer, in *Earth on the Edge: Science for a Sustainable Planet*, edited by C. Rizos and P. Willis, International Association of Geodesy Symposia, Springer.
- Hairer, E., and G. Wanner (1993), *Solving Ordinary Differential Equations. Nonstiff Problems. 2nd edition*, Springer series in computational mathematics.
- Hamayun, I. Prutkin, and R. Tenzer (2009), The optimum expression for the gravitational potential of polyhedral bodies having a linearly varying density distribution, *Journal of Geodesy*, 83(12), 1163–1170, doi:10.1007/s00190-009-0334-1.

- Hanson, A. J., and H. Ma (1995), Parallel transport approach to curve framing, *Indiana University, Techreports-TR425*, 11, 3–7.
- Hinkley, N., J. A. Sherman, N. B. Phillips, M. Schioppo, N. D. Lemke, K. Beloy, M. Pizzocaro, C. W. Oates, and A. D. Ludlow (2013), An atomic clock with 10-18 instability, *Science*, 341(6151), 1215–1218, doi:10.1126/science.1240420.
- Hirt, C. (2004), Entwicklung und Erprobung eines digitalen Zenitkamarasystems für die hochpräzise Lotabweichungsbestimmung, Ph.D. thesis, Universität Hannover.
- Hirt, C. (2006), Monitoring and analysis of anomalous refraction using a digital zenith camera system, *Astronomy & Astrophysics*, 459, 283–290.
- Hirt, C. (2008), Zur Berücksichtigung von Scherung und Umschlagwinkel bei der Neigungsmessung mit zweiachsigen Neigungssensoren, *Zeitschrift für Vermessungswesen (zfv)*, (133), 266–273.
- Hirt, C. (2009), Hochauflösende astrogeodätische Bestimmung von Geoid- und Aequipotentialprofilen mit Submillimetergenauigkeit für die Vermessung von Teilchenbeschleunigern, *AVN Allgemeine Vermessungs-Nachrichten*, 02/2009.
- Hirt, C. (2010), Modern determination of vertical deflections using digital zenith cameras, *Journal Surveying Engineering*, 136(1), 1–12.
- Hirt, C. (2013), Rtm gravity forward-modeling using topography/bathymetry data to improve high-degree global geopotential models in the coastal zone., *Marine Geodesy*, 36(2), 1–20, doi:DOI: 10.1080/01490419.2013.779334.
- Hirt, C., and G. Seeber (2008), Accuracy analysis of vertical deflection data observed with the Hannover Digital Zenith Camera System TZK2-D, *Journal of Geodesy*, 82(6), 347–356.
- Hirt, C., M. Kuhn, S. Claessens, R. Pail, K. Seitz, and T. Gruber (2014), Study of the earth’s short-scale gravity field using the ertm2160 gravity model, *Computers & Geosciences*, 73, 71–80, doi:doi: 10.1016/j.cageo.2014.09.00.
- Hoffmann, C. M. (1989), *Geometric and Solid Modeling: An Introduction*, Morgan Kaufmann Publishers Inc., San Francisco, CA, USA.
- Hofmann-Wellenhof, B., and H. Moritz (2005), *Physical Geodesy*, SpringerWienNewYork.
- ICAO (1976), ICAO Standard Atmosphere 1976.
- Jekeli, C. (1999), An analysis of vertical deflections derived from high-degree spherical harmonic models, *Journal of Geodesy*, 73(1), 10–22, doi:10.1007/s001900050213.
- Jekeli, C. (2001), *Inertial Navigation Systems with Geodetic Applications*, Walter de Gruyter.
- Jekeli, C. (2007), 100 Years of Gravity Gradiometry, in *lecture presented in Geological Science 781, Gravimetry, Division of Geodesy and Geospatial Science, School of Earth Sciences, Ohio State University*.

- Jekeli, C. (2011), *Encyclopedia of Solid Earth Geophysics*, chap. Gravity, Gradiometry, Springer-Verlag Berlin Heidelberg.
- Jones, M. (2000), Geodetic definition (datum parameters) of the CERN coordinate system, *Tech. rep.*, EST-SU Internal Note, EDMS Document No. 107906, CERN, Geneva, Switzerland.
- Kaplan, G., J. Bangert, J. Bartlett, W. Puatua, and A. Monet (2009), *User's Guide to NOVAS 3.0*, USNO Circular 180 (Washington, DC: USNO).
- Kaplan, G. H. (2005), *The IAU Resolutions on Astronomical Reference Systems, Time Scales, and Earth Rotation Models : Explanation and Implementation*, United States Naval Observatory Circular ; no 179., Washington : U.S. Naval Observatory, 2005.
- Kaplan, G. H., J. A. Hughes, P. K. Seidelmann, C. A. Smith, and B. D. Yallop (1989), Mean and apparent place computations in the new IAU system. III - Apparent, topocentric, and astrometric places of planets and stars, *The Astronomical Journal*, 97, 1197–1210, doi:10.1086/115063.
- Kazhdan, M., M. Bolitho, and H. Hoppe (2006), Poisson surface reconstruction, in *Proceedings of the Fourth Eurographics Symposium on Geometry Processing*, SGP '06, pp. 61–70, Eurographics Association, Aire-la-Ville, Switzerland, Switzerland.
- Klioner, S. A. (2002), Relativistic modelling of positional observations with microarcsecond accuracy, *EAS Publications Series*, 2, 93–106, doi:10.1051/eas:2002008.
- Klioner, S. A., and S. M. Kopeikin (1992), Microarcsecond astrometry in space: Relativistic effects and reduction of observations, *The Astronomical Journal*.
- Kopeikin, S. (1991), Relativistic manifestations of gravitational fields in gravimetry and geodesy., *Manuscr. Geod.*, 16, 301–312.
- Kopeikin, S., M. Efroimsky, and G. Kaplan (2011), *Relativistic Celestial Mechanics of the Solar System*, John Wiley & Sons, Hoboken.
- Lautrup, B. (2005), *Physics of Continuous Matter: Exotic and Everyday Phenomena in the Macroscopic World*, Institute of Physics.
- Ledoux, H. (2013), On the validation of solids represented with the international standards for geographic information, *Computer-Aided Civil and Infrastructure Engineering*, 28(9), 693–706, doi:10.1111/mice.12043.
- Limpach, P. (2009), Sea surface topography and marine geoid by airborne laser altimetry and shipborne ultrasound altimetry in the Aegean Sea, Ph.D. thesis, Diss., Eidgenössische Technische Hochschule ETH Zürich, Nr. 18225, 2009.
- Love, A. E. H. (1911), *Some problems of geodynamics: being an essay to which the Adams prize in the University of Cambridge was adjudged in 1911*, Cambridge Univ. Press, Cambridge.

- Mai, E. (2013), *Time, atomic clocks and relativistic geodesy*, Deutsche Geodätische Kommission bei der Bayerischen Akademie der Wissenschaften: Theoretische Geodäsie, Verlag der Bayerischen Akademie der Wissenschaften.
- Marti, U. (1997), Geoid der Schweiz 1997, in *Geodätisch-Geophysikalische Arbeiten in der Schweiz*, Schweizerischen Geodätischen Kommission.
- McCarthy, D. D. (Ed.) (1996), *IERS Conventions (1992)*, IERS Technical Note 21, Observatoire de Paris.
- Melchior, P. (1983), *The Tides of Planet Earth*, Pergamon Press, Oxford.
- Mirtich, B. (1996), Fast and accurate computation of polyhedral mass properties, *Journal of Graphics Tools*, 1, 31–50.
- Moritz, H. (1990), *The Figure of the Earth: Theoretical Geodesy and the Earth's Interior*, Wichmann.
- Moritz, H. (2000), Geodetic reference system 1980, *Journal of Geodesy*, 74(1), 128–133, doi:10.1007/s001900050278.
- Möser, M., W. Welsch, O. Heunecke, and H. Kuhlmann (2000), *Auswertung geodätischer Überwachungsmessungen*, Handbuch Ingenieurgeodäsie, Wichmann.
- Müller, J., M. Soffel, and S. Klioner (2008), Geodesy and relativity, *Journal of Geodesy*, 82, 133–145.
- Newton, I. (1687), *Philosophiæ Naturalis Principia Mathematica*, The Royal Society.
- Petit, G., and B. Luzum (2010), IERS conventions (2010), *Tech. rep.*, IERS Convention Centre.
- Petrovic, S. (1996), Determination of the potential of homogeneous polyhedral bodies using line integrals, *Journal of Geodesy*, 71, 44–52.
- Pohanka, V. (1988), Optimum expression for computation of the gravity field of a homogeneous polyhedral body, *Geophysical Prospecting*, 36(7), 733–751, doi:10.1111/j.1365-2478.1988.tb02190.x.
- Pohanka, V. (1998), Optimum expression for computation of the gravity field of a polyhedral body with linearly increasing density, *Geophysical Prospecting*, 46(4), 391–404, doi:10.1046/j.1365-2478.1998.960335.x.
- Qt Company (2014), Qt project, <http://qt-project.org/>.
- Rankine, W. (1853), Xviii. On the general law of the transformation of energy, *Philosophical Magazine Series 4*, 5(30), 106–117, doi:10.1080/14786445308647205.
- Rexer, C., M.; Hirt (2014), Comparison of free high-resolution digital elevation data sets (aster 1 gdem2, srtm v2.1/v4.1) and validation against accurate heights from the Australian national gravity database, *Australian Journal of Earth Sciences*, pp. 1–15, doi:10.1080/08120099.2014.884983.



- Roche, J. (2003), What is potential energy?, *European Journal of Physics*, 24(2), 185.
- Rothacher, M., and R. Rummel (2012), Physikalische Geodäsie und Geodynamik, Lecture Notes.
- Schlatter, A. (2007), Das neue Landes-/”ohennetz der Schweiz LHN95, Ph.D. thesis, Eidgenössische Technische Hochschule Zürich.
- Schulte, D. (2009), Pre-alignment needs for clic, in *CLIC Prealignment Workshop 2009*, CERN, Geneva, Switzerland.
- Shewchuk, J. R. (1996), Triangle: Engineering a 2D Quality Mesh Generator and Delaunay Triangulator, in *Applied Computational Geometry: Towards Geometric Engineering, Lecture Notes in Computer Science*, vol. 1148, edited by M. C. Lin and D. Manocha, pp. 203–222, Springer-Verlag, from the First ACM Workshop on Applied Computational Geometry.
- Shewchuk, J. R. (2002), Delaunay refinement algorithms for triangular mesh generation, *Computational Geometry*, 22(1-3), 21 – 74, doi:http://dx.doi.org/10.1016/S0925-7721(01)00047-5, 16th {ACM} Symposium on Computational Geometry.
- Smith, D. A., S. A. Holmes, X. Li, S. Guillaume, Y. M. Wang, B. Bürki, D. R. Roman, and T. M. Damiani (2013), Confirming regional 1 cm differential geoid accuracy from airborne gravimetry: the Geoid Slope Validation Survey of 2011, *Journal of Geodesy*, 87, 885–907, doi:10.1007/s00190-013-0653-0.
- Soffel, M. (1989), Relativity in Astrometry, Celestial Mechanics and Geodesy, in *Relativity in Astrometry, Celestial Mechanics and Geodesy*, Astronomy and Astrophysics Library, pp. 1–31, Springer Berlin Heidelberg.
- Soffel, M., H. Herold, H. Ruder, and M. Schneider (1988), Relativistic theory of gravimetric measurements and definition of the geoid., *Manuscr. Geod.*, 13, 143–146.
- Soffel, M., S. A. Klioner, G. Petit, P. Wolf, S. M. Kopeikin, P. Bretagnon, V. A. Brumberg, N. Capitaine, T. Damour, T. Fukushima, B. Guinot, T.-Y. Huang, L. Lindegren, C. Ma, K. Nordtvedt, J. C. Ries, P. K. Seidelmann, D. Vokrouhlicky, C. M. Will, and C. Xu (2003), The IAU 2000 Resolutions for Astrometry, Celestial Mechanics, and Metrology in the Relativistic Framework: Explanatory Supplement, *The Astronomical Journal*, 126(6), 2687.
- Somieski, A. E. (2008), Astrogeodetic geoid and isostatic considerations in the north aegean sea, greece, Ph.D. thesis, ETH Zurich.
- Stern, G., J. Kemppinen, F. Lackner, H. Mainaud-Durand, D. Piedigrossi, J. Sandomierski, M. Sosin, A. Geiger, and S. Guillaume (2013), Development and validation of a multipoint based laser alignment system for clic, *Proceedings of IPAC2013, Shanghai, China*.
- Stone, J. A. A., and J. H. Zimmerman (2011), Index of refraction of air.

- Talwani, M., and M. Ewing (1960), Rapid computation of gravitational attraction of three-dimensional bodies of arbitrary shape, *GEOPHYSICS*, 25(1), 203–225, doi:10.1190/1.1438687.
- Torge, W. (1989), *Gravimetry*, Walter de Gruyter.
- Torge, W., and J. Müller (2012), *Geodesy*, Walter de Gruyter.
- Touzé, T. (2011), Proposition d’une méthode d’alignement de l’accélérateur linéaire CLIC – des réseaux de géodésie au pré-alignement actif, Ph.D. thesis, Université de Paris-Est.
- Tsoulis, D. (2012), Analytical computation of the full gravity tensor of a homogeneous arbitrarily shaped polyhedral source using line integrals, *Geophysics*, 77(2), F1–F11, doi:10.1190/geo2010-0334.1.
- Tsoulis, D., and S. Petrovic (2001), On the singularities of the gravity field of a homogeneous polyhedral body, *Geophysics*, 66, 535–539.
- Tsoulis, D., O. Jamet, J. Verdun, and N. Gonindard (2009), Recursive algorithms for the computation of the potential harmonic coefficients of a constant density polyhedron.
- van Altena, W. (2012), *Astrometry for Astrophysics: Methods, Models, and Applications*, Astrometry for Astrophysics: Methods, Models, and Applications, Cambridge University Press.
- Vaníček, P., and E. Krakiwsky (1982), *Geodesy, the concepts*, North-Holland Pub. Co.
- Voigt, C. (2013), Astrogeodätische Lotabweichungen zur Validierung von Schwerefeldmodellen, Ph.D. thesis, Hannover : Fachrichtung Geodäsie und Geoinformatik der Leibniz-Univ.
- Völgyesi, L. (2001), Geodetic applications of torsion balance measurements in hungary, *Reports on Geodesy, Warsaw University of Technology, Vol. 57, Nr. 2*.
- Wenzel, H.-G. (1993), ETERNA, <http://www.upf.pf/icet/soft/index.html>.
- Wenzel, H.-G. (1997), Tide-generating potential for the earth, in *Tidal Phenomena, Lecture Notes in Earth Sciences*, vol. 66, edited by H. Wilhelm, W. Zürn, and H.-G. Wenzel, pp. 9–26, Springer Berlin Heidelberg, doi:10.1007/BFb0011455.
- Wirth, B. (1990), Höhensysteme, Schwerepotentiale und Niveauflächen, Ph.D. thesis, Eidgenössische Technische Hochschule Zürich.
- Wunderlin, N. (1979), ALGOL-Programm TGREFR Modellatmosphäre und Refraktion, *Mitteilungen 26*, Institut für Geodäsie und Photogrammetrie, ETH Zürich.
- Yang, B., and H. Friedsam (2006), Introduction to high-resolution accelerator alignment using x-ray optics, in *Proceedings of the 9th International Workshop on Accelerator Alignment, SLAC*.

## Appendix A

# Transformation between Celestial and Terrestrial Reference Systems

Nowadays, for practical applications, there are mainly two conventional procedures to transform a vector  $\boldsymbol{\rho}^{\text{GCRS}}$  given in the geocentric celestial reference system (GCRS)<sup>1</sup> into a vector  $\boldsymbol{\rho}^{\text{ITRS}}$  given in a terrestrial reference system (ITRS):

1. The transformation according to the IAU<sup>2</sup> 1980 resolutions.
2. The transformation according to the IAU 2006/2000 resolutions.

However, assuming that the Earth rotation parameters (EOP) provided by the IERS<sup>3</sup> are correctly implemented, the transformations according to IAU 1980 and IAU 2006/2000 resolutions are equivalent. The principal differences are only visible at intermediate steps of the transformation. In the modern version, IAU 2006/2000, polar motion and precession-nutation are properly separated (Voigt, 2013).

### A.1 Transformation according to the IAU 1980 resolutions

According to McCarthy (1996), a position vector  $\boldsymbol{\rho}^{\text{GCRS}}$ , given in the GCRS, can be transformed into the ITRS by:

$$\boldsymbol{\rho}^{\text{ITRS}}(t) = \mathbf{R}_2(-x_p) \cdot \mathbf{R}_1(-y_p) \cdot \mathbf{R}_3(\text{GAST}) \cdot \mathbf{N}(\delta\Delta\epsilon, \delta\Delta\psi, t) \cdot \mathbf{P}(t) \cdot \boldsymbol{\rho}^{\text{GCRS}}(t) \quad (\text{A.1})$$

where:

---

<sup>1</sup>Geocentric Celestial Reference System. A special case of a Celestial Reference System which has its origin at the center of mass of the Earth and not at the center of mass of the solar system as the ICRS.

<sup>2</sup>International Astronomical Union

<sup>3</sup>International Earth Rotation and Reference Systems Service

$\boldsymbol{\rho}^{\text{ITRS}}$	[m]	=	vector in terrestrial reference system.
$\boldsymbol{\rho}^{\text{GCRS}}$	[m]	=	vector in geocentric celestial reference system.
$\mathbf{R}_i$		=	rotation matrices around the axis $\mathbf{e}_i$ .
GAST	[s]	=	Greenwich apparent sidereal time. Function of $\Delta\text{UT1}$ and $\delta\Delta\psi$
$\mathbf{N}$		=	nututation rotation matrix.
$\mathbf{P}$		=	precession rotation matrix.
$x_p, y_p$	[arcsec]	=	polar motion provided by IERS, see A.1.1.
$\delta\Delta\epsilon, \delta\Delta\psi$	[arcsec]	=	correction terms for the nututation, in obliquity and longitude, provided by IERS.
$\Delta\text{UT1}$	[s]	=	UT1-UTC difference between UTC and UT1 provided by IERS, see A.1.2.

### A.1.1 Polar Motion including Diurnal and Sub-Diurnal Periods

According to *Petit and Luzum* (2010), the pole coordinates  $(x_p, y_p)$  appearing in Equation A.1 can be computed as follows:

$$(x_p, y_p) = (x, y)_{\text{IERS}} + (\Delta x, \Delta y)_{\text{ocean tides}} + (\Delta x, \Delta y)_{\text{libration}} \quad (\text{A.2})$$

where  $(x, y)_{\text{IERS}}$  represents the traditional pole coordinates provided by the IERS data center with a time interval of one day. The term  $(\Delta x, \Delta y)_{\text{ocean tides}}$  represents the diurnal and semi-diurnal variations of the pole caused by ocean tides. The last term  $(\Delta x, \Delta y)_{\text{libration}}$  corresponds to celestial motions with periods less than two days which are not modeled in the nututation model.

For numerical computations, the first term  $(x, y)_{\text{IERS}}$  is directly given in listings provided by the IERS data center (e.g. EOP 08 C04 (IAU1980)). The second  $(\Delta x, \Delta y)_{\text{ocean tides}}$  and third  $(\Delta x, \Delta y)_{\text{libration}}$  term can be computed by the routine `INTERP.f` of the IERS EOP Product Center.

### A.1.2 Earth Rotation Angle including Diurnal and Sub-Diurnal Periods

Concerning the Earth rotation angle, the procedure to obtain diurnal and sub-diurnal values for  $\Delta\text{UT1}$  or  $\text{LOD}^4$  is similar to for the pole coordinates  $(x_p, y_p)$ . The usual corrections  $\Delta\text{UT1}_{\text{IERS}}$  or  $\text{LOD}_{\text{IERS}}$  provided by the IERS data center are refined by the ocean tides and libration terms as follows:

$$\Delta\text{UT1} = \Delta\text{UT1}_{\text{IERS}} + \delta\Delta\text{UT1}_{\text{ocean tides}} + \delta\Delta\text{UT1}_{\text{libration}} \quad (\text{A.3})$$

or

$$\text{LOD} = \text{LOD}_{\text{IERS}} + \Delta\text{LOD}_{\text{ocean tides}} + \Delta\text{LOD}_{\text{libration}} \quad (\text{A.4})$$

<sup>4</sup>the LOD, or *length of day*, represents the difference between the astronomically determined duration of the day and 86400 SI seconds

## A.2 Transformation using Axis Vectors

There is an other possibility to write Equation A.1 in a purely kinematic way, without worrying about physical phenomena. This can be done, if we just consider that the product of the matrices:

$$\mathbf{S}_{\text{GCRS}}^{\text{ITRS}} = \mathbf{R}_2(-x_p) \cdot \mathbf{R}_1(-y_p) \cdot \mathbf{R}_3(\text{GAST}) \cdot \mathbf{N}(\delta\Delta\epsilon, \delta\Delta\psi, t) \cdot \mathbf{P}(t) \quad (\text{A.5})$$

can be resumed in a single orthogonal rotation matrix  $\mathbf{S}_{\text{GCRS}}^{\text{ITRS}}$  which contains the unit vectors of the ITRS axes  $\mathbf{e}_{\text{ITRS}i}^{\text{GCRS}}$  in the GCRS system.

$$\boldsymbol{\rho}^{\text{ITRS}}(t) = \mathbf{S}_{\text{GCRS}}^{\text{ITRS}}(t) \cdot \boldsymbol{\rho}^{\text{GCRS}}(t) \quad (\text{A.6})$$

with:

$$\mathbf{S}_{\text{GCRS}}^{\text{ITRS}}(t) = \begin{pmatrix} \mathbf{e}_{\text{ITRS}x}^{\text{GCRS}T}(t) \\ \mathbf{e}_{\text{ITRS}y}^{\text{GCRS}T}(t) \\ \mathbf{e}_{\text{ITRS}z}^{\text{GCRS}T}(t) \end{pmatrix} \quad (\text{A.7})$$

and for the inverse transformation, from ITRS to GCRS we simply have:

$$\boldsymbol{\rho}^{\text{GCRS}}(t) = \mathbf{S}_{\text{GCRS}}^{\text{ITRS}T}(t) \cdot \boldsymbol{\rho}^{\text{ITRS}}(t) = \mathbf{S}_{\text{ITRS}}^{\text{GCRS}}(t) \cdot \boldsymbol{\rho}^{\text{ITRS}}(t) \quad (\text{A.8})$$

with:

$$\mathbf{S}_{\text{ITRS}}^{\text{GCRS}}(t) = \begin{pmatrix} \mathbf{e}_{\text{ITRS}x}^{\text{GCRS}}(t) & \mathbf{e}_{\text{ITRS}y}^{\text{GCRS}}(t) & \mathbf{e}_{\text{ITRS}z}^{\text{GCRS}}(t) \end{pmatrix} \quad (\text{A.9})$$



## Appendix B

# Numerical Computation of the Earth's Rotation Vector

In the frame of this thesis, a precise time series of the Earth's rotation vector  $\omega_{\delta}$  and its time derivative  $\dot{\omega}_{\delta}$  are computed numerically using the IAU 1980 resolutions transformation together with the EOP provided by IERS. They are computed using the libraries **NOVAS-C** (*Kaplan et al.*, 2009) together with the long-term Earth orientation data **EOP 08 C04** (IAU1980) of IERS, between 1980 and 2013, with a time interval of one hour, in ITRS and GCRS. Moreover it is important to note that the sub-daily values of the EOP parameters are interpolated piecewise linearly, since they are only given at daily time interval.

### B.1 Earth's rotation vector in ITRS

In the terrestrial reference system, the Earth's rotation vector  $\omega_{\delta}^{\text{ITRS}}$  can be computed with polar motion and LOD by:

$$\omega_{\delta}^{\text{ITRS}}(t) = \omega_{\delta}(t) \cdot \begin{pmatrix} +x_p(t) \\ -y_p(t) \\ \sqrt{1 - x_p^2(t) - y_p^2(t)} \end{pmatrix} \quad (\text{B.1})$$

and, according to *Aoki et al.* (1982), the Earth's rotation velocity  $\omega_{\delta}$  can be computed from LOD by:

$$\omega_{\delta}(t) = [72921151.467064 - 0.843994809 \cdot \text{LOD}(t)] \cdot 10^{-12} \quad (\text{B.2})$$

where:

$\omega_{\delta}^{\text{ITRS}}$	$\left[\frac{\text{rad}}{\text{s}}\right]$	=	Earth's rotation vector in the terrestrial reference system.
$\omega_{\delta}$	$\left[\frac{\text{rad}}{\text{s}}\right]$	=	Earth's rotation velocity in the terrestrial reference system; which can be computed from the <i>Length of Day</i> (LOD) provided by IERS according to Equation B.2.
$x_p, y_p$	[rad]	=	polar motion provided by IERS.
LOD	[ms]	=	Length of day provided by IERS.

### B.1.1 Time Series and Spectral Analysis

The time series and the amplitude spectrum of  $\omega_{\delta}^{\text{ITRS}}(t)$  are shown in Figures B.1 and B.2. Concerning the spectral analyses, the components  $(\omega_{\delta x}^{\text{ITRS}}, \omega_{\delta y}^{\text{ITRS}})$  are decomposed into prograde and retrograde motions. The component  $\omega_{\delta z}^{\text{ITRS}}$  is decomposed with a standard FFT. Finally, the periods of the 10 largest amplitudes are listed in Table B.1.

**Table B.1:** List of the periods of the 10 largest amplitudes of the components of the Earth's rotation vector  $\omega_{\delta}^{\text{ITRS}}(t)$  computed numerically from a times series based on the dataset EOP 08 C04 (IAU1980) of IERS from 1980 to 2013.

Rank	$\omega_{\delta x}^{\text{ITRS}}, \omega_{\delta y}^{\text{ITRS}}$		$\omega_{\delta x}^{\text{ITRS}}, \omega_{\delta y}^{\text{ITRS}}$		$\omega_{\delta z}^{\text{ITRS}}$	
	Prograde		Retrograde			
	Period [day]	Amplitude $\left[\frac{\text{rad}}{\text{s}}\right]$	Period [day]	Amplitude $\left[\frac{\text{rad}}{\text{s}}\right]$	Period [day]	Amplitude $\left[\frac{\text{rad}}{\text{s}}\right]$
1	430.499	$4.907 \cdot 10^{-11}$	6026.979	$2.968 \cdot 10^{-12}$	12053.917	$5.962 \cdot 10^{-13}$
2	365.271	$2.943 \cdot 10^{-11}$	12053.958	$2.547 \cdot 10^{-12}$	6026.958	$3.763 \cdot 10^{-13}$
3	446.443	$2.323 \cdot 10^{-11}$	4017.986	$1.559 \cdot 10^{-12}$	365.270	$3.287 \cdot 10^{-13}$
4	482.158	$8.049 \cdot 10^{-12}$	3013.490	$1.510 \cdot 10^{-12}$	182.635	$2.793 \cdot 10^{-13}$
5	12053.958	$7.711 \cdot 10^{-12}$	365.271	$1.482 \cdot 10^{-12}$	4017.972	$2.643 \cdot 10^{-13}$
6	463.614	$7.449 \cdot 10^{-12}$	2410.792	$1.089 \cdot 10^{-12}$	13.667	$2.236 \cdot 10^{-13}$
7	401.799	$7.423 \cdot 10^{-12}$	1339.329	$1.061 \cdot 10^{-12}$	3013.479	$1.834 \cdot 10^{-13}$
8	415.654	$6.708 \cdot 10^{-12}$	1506.745	$7.603 \cdot 10^{-13}$	13.636	$1.668 \cdot 10^{-13}$
9	388.837	$5.499 \cdot 10^{-12}$	182.636	$5.777 \cdot 10^{-13}$	13.651	$1.551 \cdot 10^{-13}$
10	376.686	$3.660 \cdot 10^{-12}$	803.597	$5.496 \cdot 10^{-13}$	0.518	$1.429 \cdot 10^{-13}$

## B.2 Earth's rotation vector in GCRS

In the geocentric celestial reference system, the Earth's rotation vector  $\omega_{\delta}^{\text{GCRS}}$  can be computed by transforming the Earth's rotation vector  $\omega_{\delta}^{\text{ITRS}}$  given in ITRS with Equation A.8:

$$\omega_{\delta}^{\text{GCRS}}(t) = \mathbf{S}_{\text{ITRS}}^{\text{GCRS}}(t) \cdot \omega_{\delta}^{\text{ITRS}}(t) \quad (\text{B.3})$$

where:



- $\omega_{\delta}^{\text{GCRS}} \left[ \frac{\text{rad}}{\text{s}} \right]$  = Earth's rotation vector in the geocentric celestial reference system.  
 $\omega_{\delta}^{\text{ITRS}} \left[ \frac{\text{rad}}{\text{s}} \right]$  = Earth's rotation vector in the terrestrial reference system.  
 $\mathbf{S}_{\text{ITRS}}^{\text{GCRS}}$  = Transformation matrix from ITRS to GCRS.

### B.3 Time derivative of the Earth's rotation vector in GCRS

In the geocentric celestial reference system, at time  $t_i$ , the time derivative of the Earth's rotation vector  $\dot{\omega}_{\delta}^{\text{GCRS}}$  can be computed numerically from the Earth's rotation vector in GCRS  $\omega_{\delta}^{\text{GCRS}}$  by:

$$\dot{\omega}_{\delta}^{\text{GCRS}}(t_i) \cong \frac{\omega_{\delta}^{\text{GCRS}}(t_{i+1}) - \omega_{\delta}^{\text{GCRS}}(t_i)}{t_{i+1} - t_i} \quad (\text{B.4})$$

where:

- $\dot{\omega}_{\delta}^{\text{GCRS}} \left[ \frac{\text{rad}}{\text{s}^2} \right]$  = Time derivative of the Earth's rotation vector in the geocentric celestial reference system.  
 $\omega_{\delta}^{\text{GCRS}} \left[ \frac{\text{rad}}{\text{s}} \right]$  = Earth's rotation vector in the geocentric celestial reference system.

#### B.3.1 Time Series and Spectral Analysis

The time series and the amplitude spectrum of  $\dot{\omega}_{\delta}^{\text{GCRS}}(t)$  are shown in Figures B.4 and B.5. Concerning the spectral analyses, the components ( $\dot{\omega}_{\delta x}^{\text{ITRS}}, \dot{\omega}_{\delta y}^{\text{GCRS}}$ ) are decomposed into prograde and retrograde motions. The component  $\dot{\omega}_{\delta z}^{\text{GCRS}}$  is decomposed with a standard FFT. Finally, the periods of the 10 largest amplitudes are listed in Table B.2.

**Table B.2:** List of the periods of the 10 largest amplitudes of the components of the time derivative of the Earth's rotation vector  $\dot{\omega}_{\delta}^{\text{GCRS}}(t)$  computed numerically from a times series based on the dataset EOP 08 C04 (IAU1980) of IERS from 1980 to 2013.

Rank	$\dot{\omega}_{\delta x}^{\text{GCRS}}, \dot{\omega}_{\delta y}^{\text{GCRS}}$		$\dot{\omega}_{\delta x}^{\text{GCRS}}, \dot{\omega}_{\delta y}^{\text{GCRS}}$		$\dot{\omega}_{\delta z}^{\text{GCRS}}$	
	Prograde		Retrograde			
	Period	Amplitude	Period	Amplitude	Period	Amplitude
	[day]	$\left[ \frac{\text{rad}}{\text{s}^2} \right]$	[day]	$\left[ \frac{\text{rad}}{\text{s}^2} \right]$	[day]	$\left[ \frac{\text{rad}}{\text{s}^2} \right]$
1	13.666	$1.362 \cdot 10^{-16}$	6026.979	$2.808 \cdot 10^{-17}$	12053.916	$2.411 \cdot 10^{-19}$
2	13.651	$8.834 \cdot 10^{-17}$	27.583	$8.518 \cdot 10^{-18}$	13.651	$1.331 \cdot 10^{-19}$
3	182.636	$7.730 \cdot 10^{-17}$	27.520	$8.011 \cdot 10^{-18}$	6026.958	$1.267 \cdot 10^{-19}$
4	13.635	$6.407 \cdot 10^{-17}$	12053.958	$7.676 \cdot 10^{-18}$	13.666	$1.082 \cdot 10^{-19}$
5	13.682	$3.646 \cdot 10^{-17}$	13.636	$5.456 \cdot 10^{-18}$	4017.972	$6.933 \cdot 10^{-20}$
7	9.131	$3.468 \cdot 10^{-17}$	13.667	$5.029 \cdot 10^{-18}$	3013.479	$5.286 \cdot 10^{-20}$
6	13.697	$2.082 \cdot 10^{-17}$	4017.986	$5.015 \cdot 10^{-18}$	2410.783	$4.206 \cdot 10^{-20}$
8	13.713	$1.454 \cdot 10^{-17}$	27.458	$4.968 \cdot 10^{-18}$	179.909	$3.987 \cdot 10^{-20}$
9	13.620	$1.439 \cdot 10^{-17}$	13.651	$3.824 \cdot 10^{-18}$	2008.986	$3.507 \cdot 10^{-20}$
10	13.604	$1.284 \cdot 10^{-17}$	182.636	$3.516 \cdot 10^{-18}$	185.444	$3.461 \cdot 10^{-20}$

## B.4 Time derivative of the Earth's rotation vector in ITRS

The time derivative of the Earth's rotation vector in the terrestrial reference system  $\dot{\omega}_{\delta}^{\text{ITRS}}$  can be computed by transforming  $\dot{\omega}_{\delta}^{\text{GCRS}}$  into the ITRS according to Equation A.6:

$$\dot{\omega}_{\delta}^{\text{ITRS}}(t_i) \cong \mathbf{S}_{\text{GCRS}}^{\text{ITRS}}(t_i) \cdot \dot{\omega}_{\delta}^{\text{GCRS}}(t_i) \quad (\text{B.5})$$

where:

$\dot{\omega}_{\delta}^{\text{ITRS}} \left[ \frac{\text{rad}}{\text{s}^2} \right]$  = Time derivative of the Earth's rotation vector in the terrestrial reference system.

$\dot{\omega}_{\delta}^{\text{GCRS}} \left[ \frac{\text{rad}}{\text{s}^2} \right]$  = Time derivative of the Earth's rotation vector in the geocentric celestial reference system.

$\mathbf{S}_{\text{GCRS}}^{\text{ITRS}}$  = Transformation matrix from GCRS to ITRS.

### B.4.1 Time Series and Spectral Analysis

The time series and the amplitude spectrum of  $\dot{\omega}_{\delta}^{\text{ITRS}}(t)$  are shown in Figures B.6 and B.7. Concerning the spectral analyses, the components  $(\dot{\omega}_{\delta x}^{\text{ITRS}}, \dot{\omega}_{\delta y}^{\text{ITRS}})$  are decomposed into prograde and retrograde motions. The component  $\dot{\omega}_{\delta z}^{\text{ITRS}}$  is decomposed with a standard FFT. Finally, the periods of the 10 largest amplitudes are listed in table B.3.

**Table B.3:** List of the periods of the 10 largest amplitudes of the components of the time derivative Earth's rotation vector  $\dot{\omega}_{\delta}^{\text{ITRS}}(t)$  computed numerically from a times series based on the dataset EOP 08 C04 (IAU1980) of IERS from 1980 to 2013.

Rank	$\dot{\omega}_{\delta x}^{\text{ITRS}}, \dot{\omega}_{\delta y}^{\text{ITRS}}$ Prograde		$\dot{\omega}_{\delta x}^{\text{ITRS}}, \dot{\omega}_{\delta y}^{\text{ITRS}}$ Retrograde		$\dot{\omega}_{\delta z}^{\text{ITRS}}$	
	Period [day]	Amplitude $\left[ \frac{\text{rad}}{\text{s}^2} \right]$	Period [day]	Amplitude $\left[ \frac{\text{rad}}{\text{s}^2} \right]$	Period [day]	Amplitude $\left[ \frac{\text{rad}}{\text{s}^2} \right]$
1	430.500	$8.265 \cdot 10^{-18}$	0.99727	$2.275 \cdot 10^{-16}$	0.99726	$3.605 \cdot 10^{-22}$
2	365.273	$5.888 \cdot 10^{-18}$	1.07577	$1.366 \cdot 10^{-16}$	1.07576	$2.246 \cdot 10^{-22}$
3	446.444	$3.811 \cdot 10^{-18}$	1.07586	$8.792 \cdot 10^{-17}$	0.99496	$1.542 \cdot 10^{-22}$
4	401.800	$1.316 \cdot 10^{-18}$	1.00274	$7.730 \cdot 10^{-17}$	1.07586	$1.346 \cdot 10^{-22}$
5	482.160	$1.235 \cdot 10^{-18}$	1.07596	$6.400 \cdot 10^{-17}$	1.00274	$1.195 \cdot 10^{-22}$
6	463.615	$1.196 \cdot 10^{-18}$	1.07567	$3.645 \cdot 10^{-17}$	1.07318	$1.076 \cdot 10^{-22}$
7	415.655	$1.145 \cdot 10^{-18}$	1.11953	$3.465 \cdot 10^{-17}$	1.07595	$9.630 \cdot 10^{-23}$
8	388.839	$1.001 \cdot 10^{-18}$	0.99710	$2.830 \cdot 10^{-17}$	0.99455	$9.202 \cdot 10^{-23}$
9	376.687	$7.259 \cdot 10^{-19}$	1.07557	$2.081 \cdot 10^{-17}$	1.07308	$7.073 \cdot 10^{-23}$
10	182.636	$5.041 \cdot 10^{-19}$	1.07548	$1.453 \cdot 10^{-17}$	0.99504	$6.985 \cdot 10^{-23}$

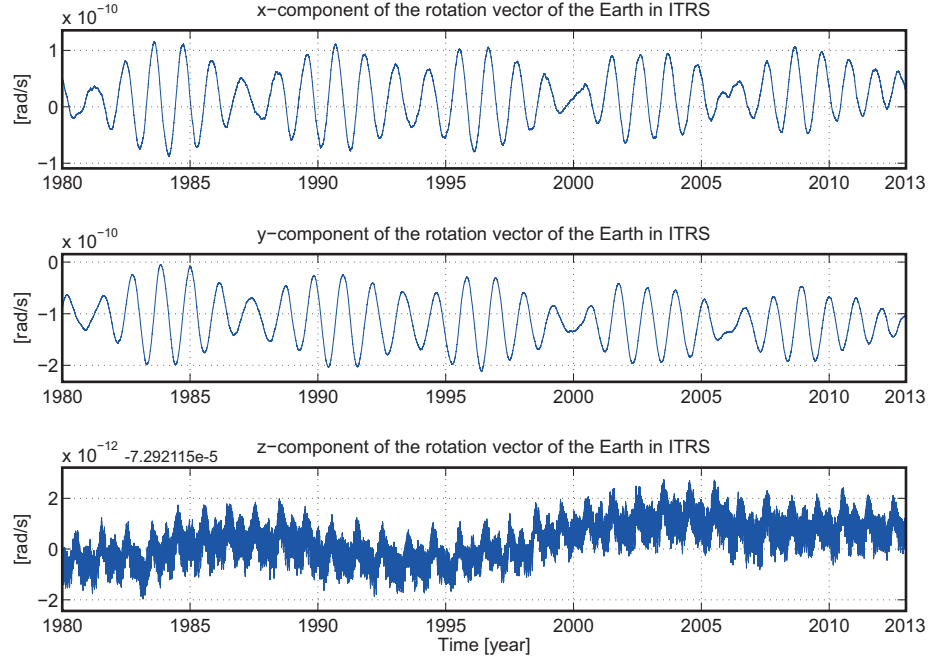


**Figure B.1:** Time series of the x-y-z components of the Earth's rotation vector  $\omega_{\delta}^{\text{ITRS}}$ .

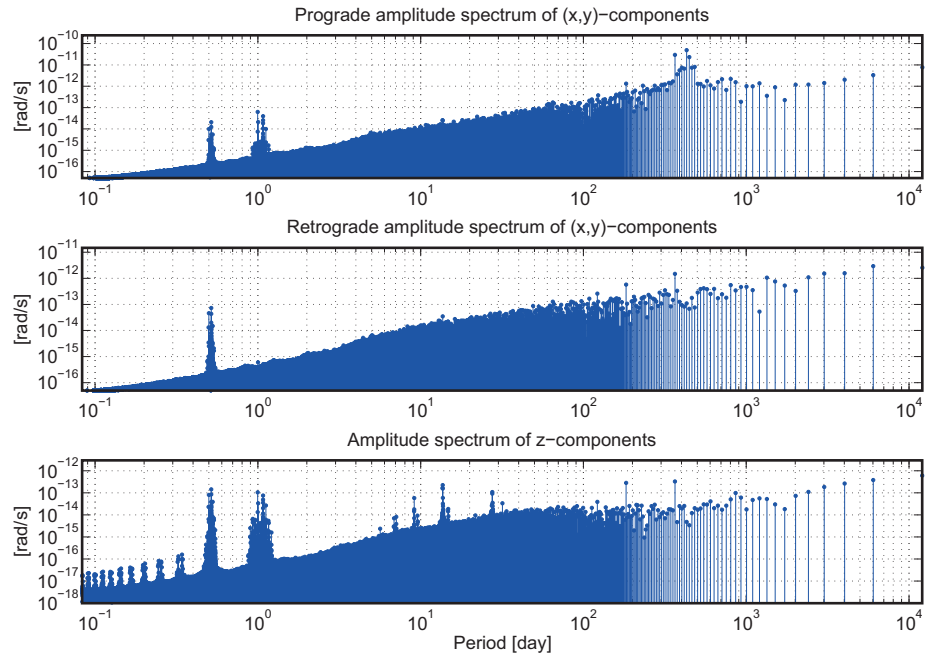


**Figure B.2:** Amplitude spectrum of the Earth's rotation vector  $\omega_{\delta}^{\text{ITRS}}$  shown in Figure B.1. The vectorial time series formed by the components  $(\omega_{\delta x}^{\text{ITRS}}, \omega_{\delta y}^{\text{ITRS}})$  is decomposed into prograde (upper) and retrograde (middle) periods. The time series of the component  $\omega_{\delta z}^{\text{ITRS}}$  is decomposed by a 1D FFT (lower).

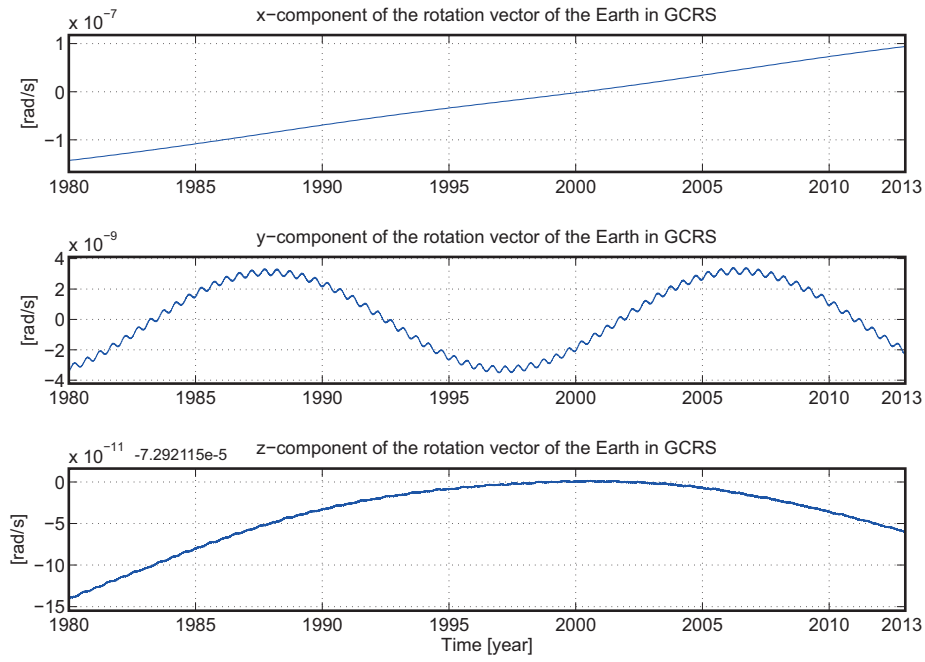


**Figure B.3:** Time series of the x-y-z components of the Earth's rotation vector  $\omega_{\delta}^{\text{GCRS}}$ .

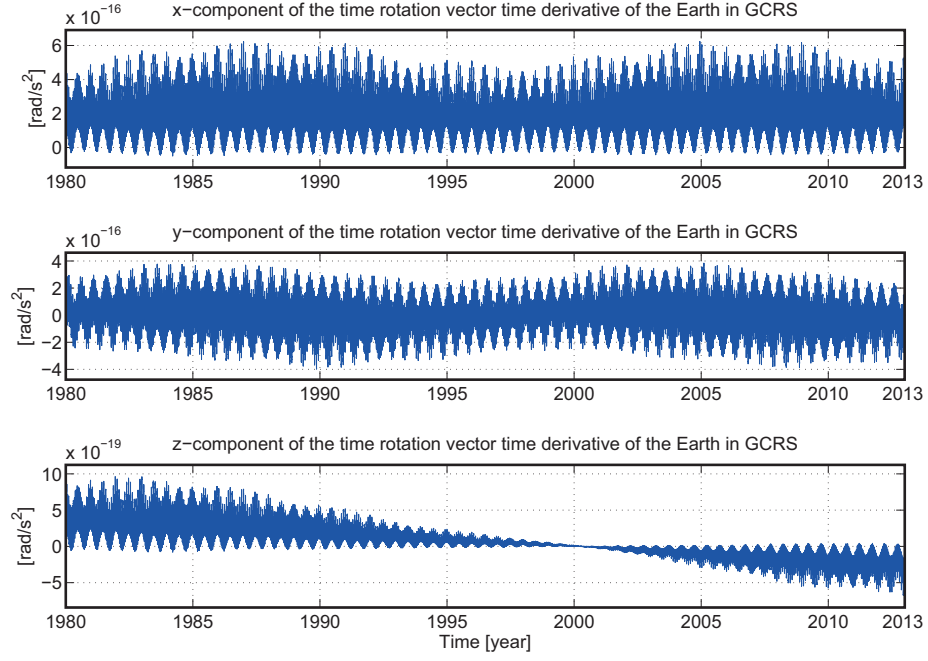


**Figure B.4:** Time series of the x-y components of the time derivative of the Earth's rotation vector  $\dot{\omega}_{\delta}^{\text{GCRS}}$ .

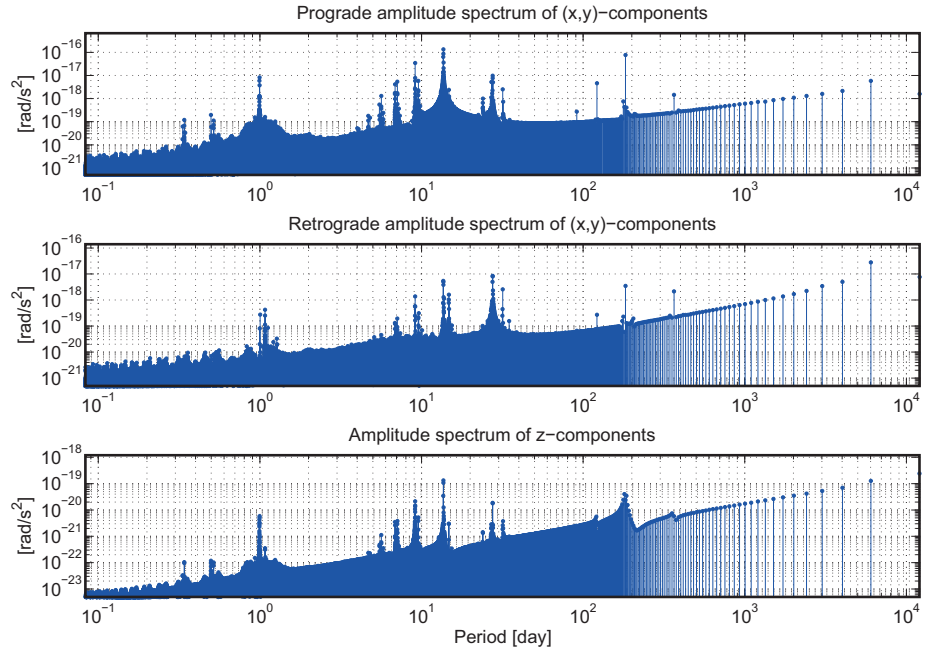


**Figure B.5:** Amplitude spectrum of the time derivative of the Earth's rotation vector  $\dot{\omega}_{\delta}^{\text{GCRS}}$  shown in Figure B.4. The vectorial time series formed by the components  $(\dot{\omega}_{\delta x}^{\text{GCRS}}, \dot{\omega}_{\delta y}^{\text{GCRS}})$  is decomposed into prograde (upper) and retrograde (lower) periods.

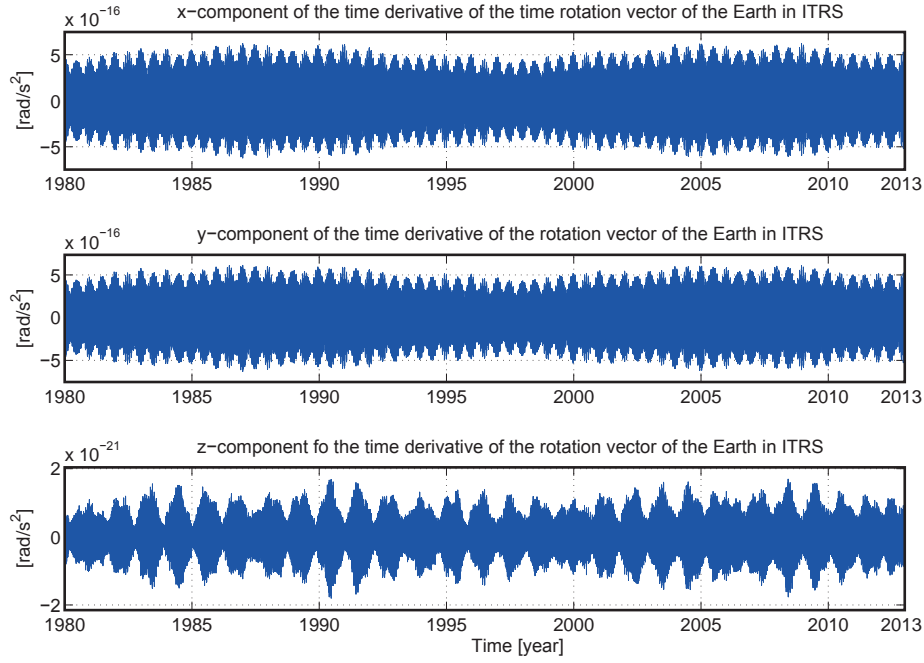


**Figure B.6:** Time series of the x-y components of the time derivative of the Earth's rotation vector  $\dot{\omega}_{\delta}^{\text{ITRS}}$ .

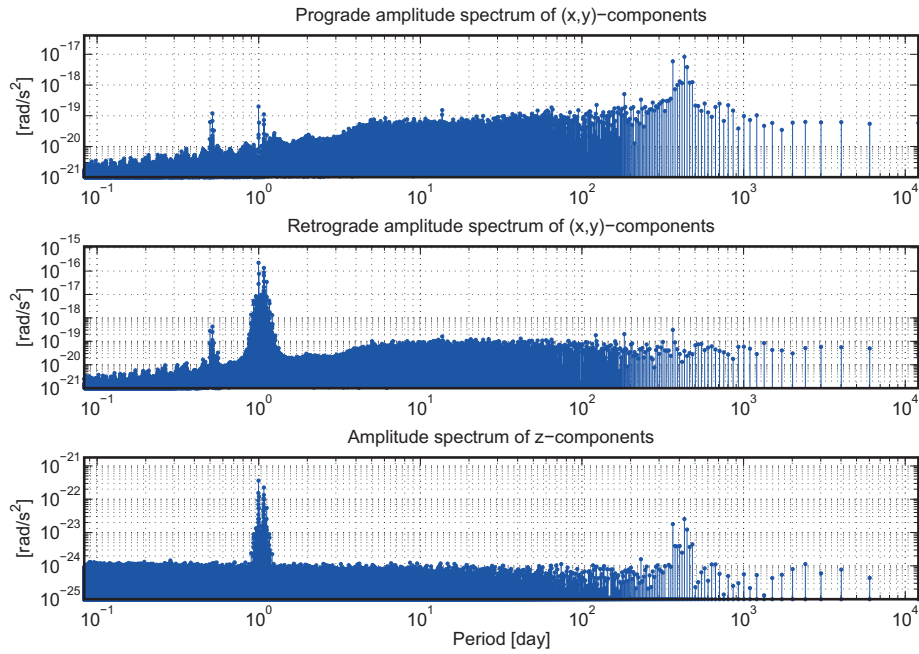


**Figure B.7:** Amplitude spectrum of the time derivative of the Earth's rotation vector  $\dot{\omega}_{\delta}^{\text{ITRS}}$  shown in Figure B.6. The vectorial time series formed by the components  $(\dot{\omega}_{\delta x}^{\text{ITRS}}, \dot{\omega}_{\delta y}^{\text{ITRS}})$  is decomposed into prograde (upper) and retrograde (lower) periods.

## Appendix C

# Conversion between Geodetic and Ellipsoidal Coordinates

Here closed formulas for the conversion between geodetic and ellipsoid coordinates are given. They are transcribed from *Featherstone and Claessens* (2008) with the difference that, in this thesis,  $\beta$  is defined as the ellipsoidal latitude and not as the ellipsoidal co-latitude. where:

- $\lambda, \varphi, h$  [deg], [m] = Geodetic longitude, latitude and height.
- $\lambda, \beta, u$  [deg], [m] = Ellipsoidal longitude, latitude and third parameter.
- $a, b$  [m] = Semi-major and semi-minor axis of the ellipsoid of revolution.

### C.1 Geodetic to Ellipsoidal Coordinates $(\lambda, \varphi, h) \rightarrow (\lambda, \beta, u)$

- Ellipsoidal longitude  $\lambda$ :

$$\lambda = \lambda \quad (\text{C.1})$$

- Ellipsoidal third parameter  $u$ :

$$\begin{aligned} u = & \left\{ \frac{1}{2} \left[ (R_n + h)^2 \cos^2 \varphi + [R_n(1 - e^2) + h]^2 \sin^2 \varphi - E^2 \right] \right. \\ & + \sqrt{\frac{1}{4} \left[ E^2 - (R_n + h)^2 \cos^2 \varphi - [R_n(1 - e^2) + h]^2 \sin^2 \varphi \right]^2} \\ & \left. + E^2 [R_n(1 - e^2) + h]^2 \sin^2 \varphi \right\}^{\frac{1}{2}} \end{aligned} \quad (\text{C.2})$$

- Ellipsoidal latitude  $\beta$ :

$$\begin{cases} \text{if } \varphi < 45 : & \beta = 90 - \arcsin \left[ \frac{(R_n + h) \cos \varphi}{\sqrt{u^2 + E^2}} \right] \\ \text{if } \varphi \geq 45 : & \beta = 90 - \arccos \left[ \frac{(R_n(1 - e^2) + h) \sin \varphi}{u} \right] \end{cases} \quad (\text{C.3})$$

with:

$$\begin{aligned}
 e &= \frac{\sqrt{a^2 - b^2}}{a} \\
 E &= \sqrt{a^2 - b^2} \\
 R_n &= \frac{a}{\sqrt{1 - e^2 \sin^2 \varphi}}
 \end{aligned} \tag{C.4}$$

## C.2 Ellipsoidal to Geodetic Coordinates $(\lambda, \beta, u) \rightarrow (\lambda, \varphi, h)$

- Geodetic longitude  $\lambda$ :

$$\lambda = \lambda \tag{C.5}$$

- Geodetic latitude  $\varphi$ :

$$\varphi = 2 \cdot \arctan \left( \frac{u \cos \beta}{F + \sqrt{F^2 + u^2 \cos^2 \beta}} \right) \tag{C.6}$$

- Geodetic height  $h$ :

$$h = \frac{u \cos \beta}{\sin \varphi - R_n(1 - e^2)} \tag{C.7}$$

with:

$$\begin{aligned}
 e &= \frac{\sqrt{a^2 - b^2}}{a} \\
 E &= \sqrt{a^2 - b^2} \\
 R_n &= \frac{a}{\sqrt{1 - e^2 \sin^2 \varphi}}
 \end{aligned} \tag{C.8}$$



and:

$$\begin{aligned}
 M &= \frac{(1 - e^2)u^2 \cos^2 \beta}{a^2} \\
 N &= \frac{(u^2 + E^2) \sin^2 \beta}{a^2} \\
 K &= \frac{M + N - e^4}{6} \\
 O &= \frac{e^4 \cdot M \cdot N}{4K^3} \\
 L &= \left(1 + O + \sqrt{2O + O^2}\right)^{\frac{1}{3}} \\
 H &= K \left(1 + L + \frac{1}{L}\right) \\
 I &= \sqrt{H^2 + e^4 M} \\
 J &= \frac{e^2}{2I(H + I - M)} \\
 G &= \sqrt{H + I + J^2} - J \\
 F &= \frac{G\sqrt{u^2 + E^2} \sin \beta}{G + e^2}
 \end{aligned} \tag{C.9}$$



## Appendix D

# Very Short Introduction to Stochastic Processes

### D.1 Stochastic Processes

The usual way to describe the behavior of noise is to consider that it is formed by a single or by the sum of *stochastic processes*, which associate random variables and deterministic parameters like a time or space coordinate (*Jekeli, 2001*). A stochastic process can be represented by a random vector  $\boldsymbol{\mathcal{X}}(s)$ , here as a function of the position  $s$ , where each single element is a random variable  $\mathcal{X}_{s_i}$  of a given probability density function (PDF)  $f_{\mathcal{X}_{s_i}}(x)$ :

$$\boldsymbol{\mathcal{X}}(s) = \begin{pmatrix} \mathcal{X}_{s_1} \\ \vdots \\ \mathcal{X}_{s_i} \\ \vdots \\ \mathcal{X}_{s_n} \end{pmatrix} \quad (\text{D.1})$$

The dependence in space  $s$  — or the statistical relation between two individual random variables  $\mathcal{X}_{s_i}$  and  $\mathcal{X}_{s_j}$  is given by the autocovariance function  $\mathcal{C}_{\boldsymbol{\mathcal{X}}}(s_i, s_j)$ . If the process is stationary, the covariances between two points do not depend on their absolute position but just on their separation  $\Delta s = |s_j - s_i|$ . In this case, we can define  $\mathcal{C}_{\boldsymbol{\mathcal{X}}}(\Delta s)$  as:

$$\begin{aligned} \mathcal{C}_{\boldsymbol{\mathcal{X}}}(\Delta s) &= E[(\boldsymbol{\mathcal{X}}(s) - \mu_{\boldsymbol{\mathcal{X}}}) \cdot (\boldsymbol{\mathcal{X}}(s + \Delta s) - \mu_{\boldsymbol{\mathcal{X}}})] \\ &= \int_{-\infty}^{+\infty} \int_{-\infty}^{+\infty} [x_s - \mu_{\boldsymbol{\mathcal{X}}}] \cdot [x_{s+\Delta s} - \mu_{\boldsymbol{\mathcal{X}}}] \cdot f_{\boldsymbol{\mathcal{X}}}(x_s, x_{s+\Delta s}) \cdot dx_s dx_{s+\Delta s} \quad \forall s \end{aligned} \quad (\text{D.2})$$

In addition, if we consider a finite and discrete representation of the stochastic process, where the individual elements  $i, j$  are separated by  $\Delta s_{ij}$ , the covariance function  $\mathcal{C}_{\boldsymbol{\mathcal{X}}}(\Delta s)$

can be represented by the covariance matrix:

$$\mathbf{C}_{\mathcal{X}} = \begin{pmatrix} \mathcal{C}_{\mathcal{X}}(\Delta s_{11}) & \dots & \mathcal{C}_{\mathcal{X}}(\Delta s_{1i}) & \dots & \mathcal{C}_{\mathcal{X}}(\Delta s_{1n}) \\ \vdots & \ddots & \vdots & \ddots & \vdots \\ \mathcal{C}_{\mathcal{X}}(\Delta s_{i1}) & \dots & \mathcal{C}_{\mathcal{X}}(\Delta s_{ii}) & \dots & \mathcal{C}_{\mathcal{X}}(\Delta s_{in}) \\ \vdots & \ddots & \vdots & \ddots & \vdots \\ \mathcal{C}_{\mathcal{X}}(\Delta s_{n1}) & \dots & \mathcal{C}_{\mathcal{X}}(\Delta s_{ni}) & \dots & \mathcal{C}_{\mathcal{X}}(\Delta s_{nn}) \end{pmatrix} \quad (\text{D.3})$$

The derivation of  $\mathcal{C}_{\mathcal{X}}(\Delta s)$  can be done in various ways: by empirical estimation or based on some theoretical assumptions. A famous theoretical way is given by solving a stochastic differential equation. If we restrict ourselves to the class of linear stochastic differential equations, we can find different well-known processes that are of first importance in this thesis.

## D.2 Gaussian Random Bias Process

According to *Jekeli* (2001), a Gaussian random bias process is described by the following first-order stochastic differential equation:

$$\frac{d\mathcal{X}_{\text{Rnd Bias}}(s)}{ds} = 0 \quad (\text{D.4})$$

associated with the initial condition:

$$\mathcal{X}_{\text{Rnd Bias}}(0) = \mathcal{N}(0, \sigma_{\text{Rnd Bias}}^2) \quad (\text{D.5})$$

where  $\mathcal{N}$  is a Gaussian random variable. The autocovariance function is given by:

$$\mathcal{C}_{\mathcal{X}_{\text{Rnd Bias}}}(\Delta s) = \sigma_{\text{Rnd Bias}}^2 \quad (\text{D.6})$$

## D.3 Gaussian Random Drift Process

A Gaussian random drift process is described by the following first-order stochastic differential equation:

$$\frac{d\mathcal{X}_{\text{Rnd Drift}}(s)}{ds} = \alpha \quad (\text{D.7})$$

associated with the initial condition:

$$\mathcal{X}_{\text{Rnd Drift}}(0) = 0 \quad \text{and} \quad \alpha = \mathcal{N}(0, \sigma_{\text{Rnd Drift}}^2) \quad (\text{D.8})$$

where  $\mathcal{N}$  is a Gaussian random variable.

## D.4 White Noise Process

According to *Jekeli* (2001), a white noise process is described as follows:

$$\mathcal{X}_{\text{White}}(s) = \mathcal{N}(0, \sigma_{\text{White}}^2) \quad (\text{D.9})$$

The autocovariance function is given by:

$$\mathcal{C}_{\mathcal{X}_{\text{White}}}(\Delta s) = \sigma_{\text{White}}^2 \delta(\Delta s) \quad (\text{D.10})$$

where  $\delta(\Delta s)$  is the *Dirac delta distribution* centered at the origin.

## D.5 First-Order Gauss-Markov Processes

A Gauss-Markov process of order  $n$  is associated with the a linear stochastic differential equation of order  $n$ . It has the advantage to be completely described statistically ,by its autocovariance function which is given by a closed formula. If we look at the first order ( $n=1$ ), according to *Gelb et al.* (1974), the process is modeled by a first-order stochastic differential equation as follows:

$$\frac{d\mathcal{X}_{\text{Corr}}(s)}{ds} = -\beta \cdot \mathcal{X}_{\text{Corr}}(s) + \mathcal{X}_{\text{White}}(s) \quad (\text{D.11})$$

where  $\mathcal{X}_{\text{White}}(s)$  is a white noise process and  $\beta \geq 0$  represents the inverse of the correlation length  $d_{\text{Corr}} = \frac{1}{\beta}$ . In opposition to the random walk process, the initial condition is chosen in a way so that the stochastic process becomes stationary which ensures a time-invariant expectation and allows for a possible covariance function depending on  $\Delta s_{ij}$  (*Jekeli*, 2001):

$$\mathcal{C}_{\mathcal{X}_{\text{Corr}}}(\Delta s) = \sigma_{\text{Corr}}^2 \cdot e^{-\beta|\Delta s|} \quad (\text{D.12})$$

Here, it is important to understand that, if we set  $\beta = 0$ , we do not obtain a random walk process as might be suggest Equation D.11. In fact, we obtain a white noise process  $\mathcal{X}_{\text{White}}$ . In the case, where  $\beta \rightarrow \infty$ , the Gaussian-Markov process converges to a Gaussian random bias process  $\mathcal{X}_{\text{Rnd Bias}}$ .

## D.6 Gaussian Random Walk Process

The Gaussian random walk process is not directly used in order to generate noisy observations. However, it is generated indirectly with the computation of the equipotential profiles from astrogeodetic white noise observations. From this point of view, it is interesting to look at its formulation in terms of stochastic processes. According to *Jekeli* (2001), a Gaussian random walk process — also called Brownian motion process — is described by the following first-order stochastic differential equation:

$$\frac{d\mathcal{X}_{\text{Rnd Walk}}(s)}{ds} = \mathcal{X}_{\text{White}}(s) \quad (\text{D.13})$$

associated with the initial condition:

$$\mathcal{X}_{\text{Rnd Walk}}(0) = 0 \quad (\text{D.14})$$

This equation can be solved by integrating D.13:

$$\mathcal{X}_{\text{Rnd Walk}}(s) = \int_0^s \mathcal{X}_{\text{White}}(s') \cdot ds' \quad (\text{D.15})$$

but does not results in a stationary process. Thus, the autocovariance function cannot be given as a function of the relative distance  $\Delta s$  but as a function of the absolute positions  $s_i$  and  $s_j$  as follows:

$$\mathcal{C}_{\mathcal{X}_{\text{Rnd Walk}}}(s_i, s_j) = \begin{cases} \sigma_{\text{Rnd Walk}}^2 \cdot (s_i - s_0), & \text{if } s_j \geq s_i > t_0 \\ \sigma_{\text{Rnd Walk}}^2 \cdot (s_j - s_0), & \text{if } s_i \geq s_j > t_0 \end{cases} \quad (\text{D.16})$$

## Appendix E

# Very Short Introduction to Monte-Carlo Simulations

The basic principle of Monte Carlo simulations is inspired by the relative frequency definition of probabilities. In this definition, probabilities are computed empirically by reproducing many times an experiment and then count the number of occurrences which fulfill a certain event.

In this section, we will focus on the application of Monte Carlo simulations applied to random variables. The objectives are:

- to generate *uniform random numbers*.
- to generate, empirically, realizations of arbitrary random PDF or CDF from a *uniform random generator*.
- to empirically compute functions of arbitrary PDF or CDF.

### E.1 Uniform Random Generator

A uniform random number generator generates a sequence of *uncorrelated uniformly distributed* numbers  $[RN_1^U, RN_2^U, \dots, RN_n^U]$  in the interval  $[0, 1]$ . There are two principal methods to do this: *physical* and *computational* methods.

#### E.1.1 Physical Methods

Physical random generators can generate real random numbers. They are based on quantum physical phenomena which are conceptually unpredictable. Radioactive decay, thermal noise, shot noise, clock drifts can be used as sources of randomness. Nevertheless, additional processing must usually be applied to get a really uniform distribution.

#### E.1.2 Computational Methods

Computational methods are based on algorithms which generate a sequence of *pseudo-random numbers*. Usually, the algorithms are recurrent and use the previous number to

generate the next one. This implies that two sequences are identical when the algorithm starts with the same initial value. One of the most common algorithm is the *linear congruential generator*:

$$RN_{n+1}^U = (a \cdot RN_n^U + b) \mod m \quad (\text{E.1})$$

An example of 1000 uniformly distributed random numbers generated with Equation E.1 can be seen in Figure E.1. An important property of pseudo-random number generators is the period. It gives the length of the sequence which can be generated before repeating itself. For example, in MATLAB, the function `rand` has a period of  $2^{1492}$ .

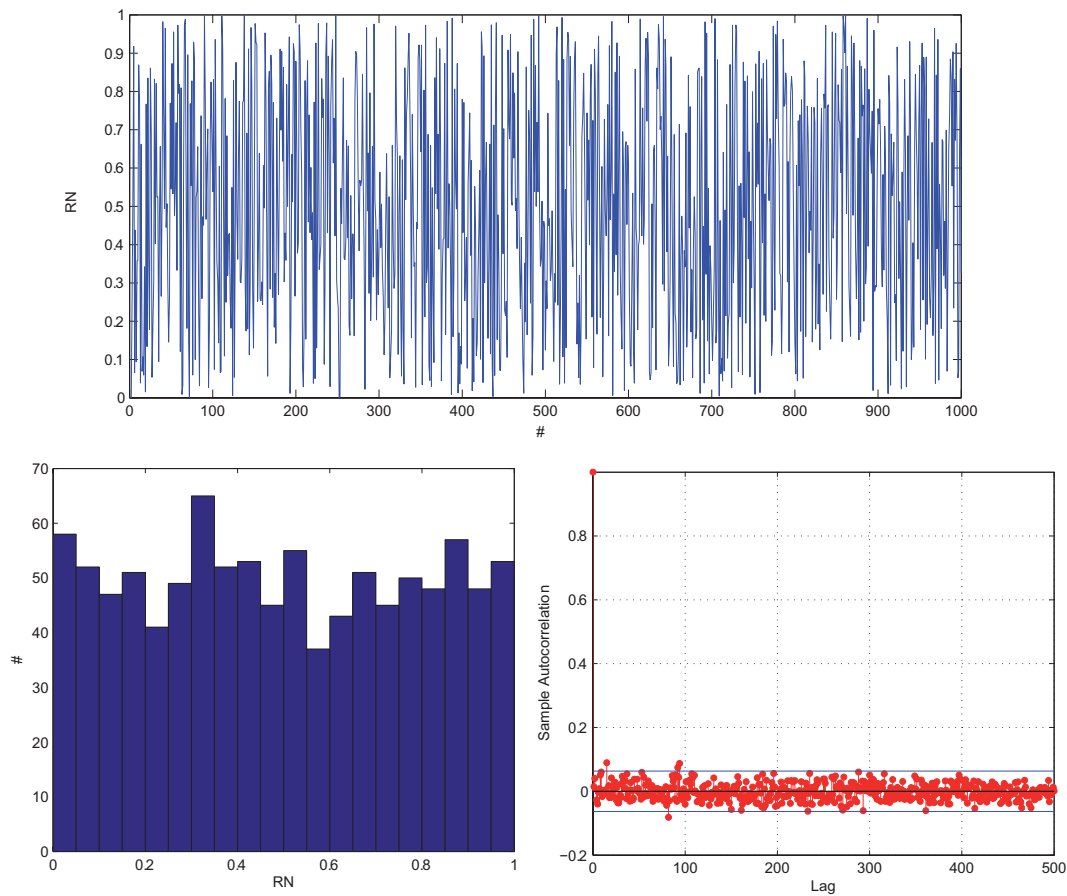


**Figure E.1:** Time series of 1000 uniformly distributed random numbers generated with the linear congruential generator,  $a = 7^5$ ,  $b = 0$ ,  $m = 2^{31} - 1$  (top). Histogram of the time series (bottom left). Sample autocorrelation function of the time series (bottom right).

## E.2 Generation of Uncorrelated Random Variables

A sequence of random numbers  $[RN_1^U, RN_2^U, \dots, RN_i^U, \dots, RN_n^U]$  generated from a uniform random number generator can be transformed into a sequence of random numbers which has the properties of an arbitrary random variable  $X$ . In the literature, we can find several methods for generating random variables, for example the inverse-transform method, the



alias method, the composition method and the acceptance-rejection method. In this script, only the inverse-transform method is explained. This method has the advantage to be general, very intuitive and easy to implement.

### E.2.1 The Inverse-Transform Method

The goal is to transform a uniform random variable  $U$  into an other arbitrary random variable  $X$  with a known CDF  $F_X$ . Basically, thanks to the fact that  $F_X(x)$  is non-decreasing and  $F_U(u)$  a uniform CDF in the interval  $[0, 1]$ , it is possible to prove that:

$$u = F_X(x) \quad (\text{E.2})$$

or

$$x = F_X^{-1}(u) \quad (\text{E.3})$$

Applied to realizations generated by a uniform random generator we have:

$$RN_i^X = F_X^{-1}(RN_i^U) \quad (\text{E.4})$$

where  $RN_i^U$  is a uniform random number, and  $RN_i^X$  is a random number which follows the distribution of  $X$ , see Figure E.2. If  $u = F_X(x)$  is known analytically and  $F_X^{-1}(u)$  can be found explicitly, we can directly apply Equation E.4 to get  $RN_i^X$ .

In the case, where  $F_X(x)$  is not known analytically or  $F_X^{-1}(x)$  cannot be given by an analytic function but numerically by two monotonic non-decreasing series of  $m$  real values:

$$x \cong [x_1, x_2, \dots, x_k, \dots, x_m] \quad (\text{E.5})$$

$$F_X(x) \cong [F_X(x_1), F_X(x_2), \dots, F_X(x_k), \dots, F_X(x_m)], \quad (\text{E.6})$$

$RN_i^X$  corresponds to the  $x_k$  such that:

$$F(x_{k-1}) < RN_i^U \leq F(x_k) \quad (\text{E.7})$$

which can simply be found by a linear search on  $[F_X(x_1), F_X(x_2), \dots, F_X(x_k), \dots, F_X(x_m)]$ .

**Example** We want to generate a sequence of 10000 uncorrelated realizations of a random variable  $X$  which has a PDF given by:

$$f_X(x) = \begin{cases} 0 & \text{if } x < 0 \\ \frac{\sin^2(x) \cdot e^{-0.2 \cdot x}}{\int_0^{2\pi} \sin^2(t) \cdot e^{-0.2 \cdot t} \cdot dt} & \text{if } 0 \leq x \leq 2\pi \\ 0 & \text{if } x > 2\pi \end{cases} \quad (\text{E.8})$$

To do this, we proceed using the following steps:

1. Discretize  $x$  in the sequence  $x \cong [0, 0.05, 0.1, \dots, 2\pi]$ .
2. Compute the discrete PDF  $f_X(x)$ .

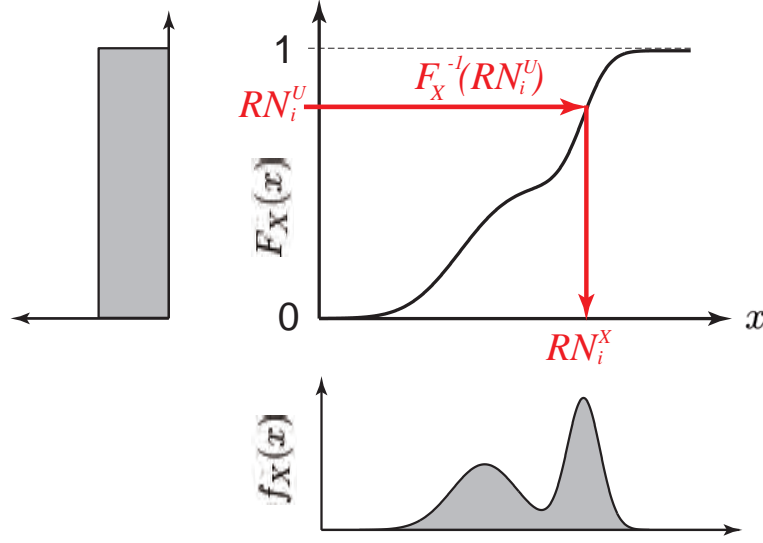


**Figure E.2:** Principle of the inverse-transform method for the generation of realizations of arbitrary random variables.

3. Compute the discrete CDF  $F_X(x)$ .
4. Compute a sequence of  $n = 10000$  uniform random numbers  $RN_i^U$  with Equation E.1.
5. Generate the sequence of  $n = 10000$  random numbers  $RN_i^X$  with Equation E.7.

The result of the generation of the sequence  $RN_i^X$  can be seen in Figure E.3.

### E.3 Generation of Correlated Random Variables

In the previous section, we have seen how to generate uncorrelated realizations of random variables of arbitrary distributions. Here, we want to see how to generate realizations of a correlated random vector when we know the distributions of every single variable, the expectation and the variance-covariance matrix of the random vector.

The generation of realizations of a random vector  $\mathbf{X} = (X_1, X_2, \dots, X_n)^T$  is possible if we know:

- its expectation  $E[\mathbf{X}] = \boldsymbol{\mu}_X$ .
- its variance-covariance matrix  $E[(\mathbf{X} - \boldsymbol{\mu}_X) \cdot (\mathbf{X} - \boldsymbol{\mu}_X)^T] = \mathbf{K}_{\mathbf{xx}}$ .
- the distribution of each single random variable  $X_1, X_2, \dots, X_n$ .

The principle is to generate a realization of a random vector  $\mathbf{Y}$  based on the distribution of uncorrelated single random variables  $X_1, X_2, \dots, X_n$ , which are centered and normalized.

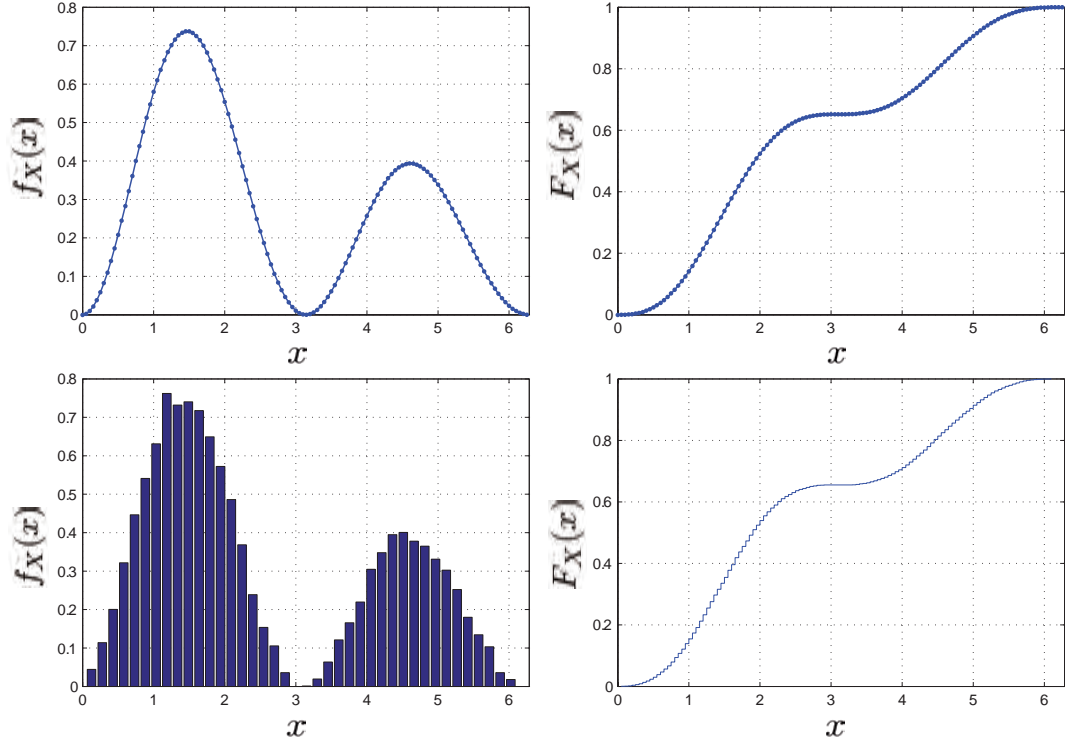


**Figure E.3:** Theoretical PDF and CDF computed from Equation E.8 (top). Empirical PDF and CDF computed from the sequence of random numbers generated by the inverse-transform method (bottom).

This implies that  $\mathbf{K}_{yy} = \mathbf{I}$ :

$$\mathbf{RN}^Y = \begin{pmatrix} \frac{RN_1^{X_1} - \mu_{X_1}}{\sigma_{X_1}} \\ \frac{RN_1^{X_2} - \mu_{X_2}}{\sigma_{X_2}} \\ \vdots \\ \frac{RN_1^{X_n} - \mu_{X_n}}{\sigma_{X_n}} \end{pmatrix} \quad (\text{E.9})$$

which can be transformed into the vector  $\mathbf{RN}^X$  with

$$\mathbf{RN}^X = \mathbf{L} \cdot \mathbf{RN}^Y + \boldsymbol{\mu}_X \quad (\text{E.10})$$

$\mathbf{L}$  can be computed with the *eigendecomposition* of  $\mathbf{K}_{xx}$

$$\mathbf{L} = \mathbf{U} \cdot \sqrt{\boldsymbol{\Lambda}} \quad (\text{E.11})$$

where  $\mathbf{U}$  represents the matrix of the normalized eigenvectors, and  $\boldsymbol{\Lambda}$  the diagonal matrix containing the eigenvalues of  $\mathbf{K}_{xx}$ . This can be proven when we apply the law of variance-

covariance propagation to Equation E.10:

$$\begin{aligned}
 \mathbf{K}_{\mathbf{xx}} &= \mathbf{L} \cdot \mathbf{K}_{\mathbf{yy}} \cdot \mathbf{L}^T \\
 &= \mathbf{L} \cdot \mathbf{I} \cdot \mathbf{L}^T \\
 &= \mathbf{L} \cdot \mathbf{L}^T
 \end{aligned} \tag{E.12}$$

If we are able to find a matrix  $\mathbf{L}$  which fulfills Equation E.12,  $\mathbf{RN}^{\mathbf{X}}$  will have its variance-covariance matrix like  $\mathbf{K}_{\mathbf{xx}}$ . This can be done with the eigendecomposition of  $\mathbf{K}_{\mathbf{xx}}$ . In fact, we know that  $\mathbf{K}_{\mathbf{xx}}$  is a positive definite symmetric matrix which can be decomposed as follows:

$$\begin{aligned}
 \mathbf{K}_{\mathbf{xx}} &= \mathbf{U} \cdot \mathbf{\Lambda} \cdot \mathbf{U}^T \\
 &= \mathbf{U} \cdot \sqrt{\mathbf{\Lambda}} \cdot \sqrt{\mathbf{\Lambda}} \cdot \mathbf{U}^T \\
 &= \mathbf{U} \cdot \sqrt{\mathbf{\Lambda}} \cdot \sqrt{\mathbf{\Lambda}}^T \cdot \mathbf{U}^T \\
 &= \underbrace{(\mathbf{U} \cdot \sqrt{\mathbf{\Lambda}})}_{\mathbf{L}} \cdot \underbrace{(\mathbf{U} \cdot \sqrt{\mathbf{\Lambda}})^T}_{\mathbf{L}^T}
 \end{aligned} \tag{E.13}$$

Another possibility to compute  $\mathbf{L}$  is the *Cholesky decomposition* of  $\mathbf{K}_{\mathbf{xx}}$ .

### E.3.1 Example

In this example (see Figures E.4, E.5 and E.6) we want to generate  $n = 1000$  realizations of a colored Gaussian noise which can be modeled as random vector  $\mathbf{X} = (X_1, X_2, \dots, X_n)^T$  with the following properties:

- all random variables  $X_1, X_2, \dots, X_n$  are Gaussian  $\sim \mathcal{N}(0, 1)$ .
- the correlation  $\rho_{ij}$  between two random variables  $i, j$  can be computed with:  $\rho_{ij} = \frac{\sin(d)}{d}$ ,  $d = 0.5 \cdot |i - j|$ .

## E.4 Monte Carlo Simulations

The computation of PDF and CDF with the Monte Carlo method is trivial and powerful. It gives the possibility to simulate PDF and CDF of systems excited by random variables. This is very useful for non-linear systems or when the stochastic behavior of the input is not Gaussian. Usually, a simulation can be divided into the following steps:

1. Create a deterministic model  $\mathbf{y} = \mathbf{f}(\mathbf{x})$  which relates an input vector  $\mathbf{x} = (x_1, x_2, \dots, x_n)^T$  to an output vector  $\mathbf{y} = (y_1, y_2, \dots, y_m)^T$ .
2. Assign a random vector  $\mathbf{X}$  to  $\mathbf{x}$ , with its PDF or CDF.
3. Generate a realization of  $\mathbf{X}$ ,  $\mathbf{RN}_i^{\mathbf{X}}$ .

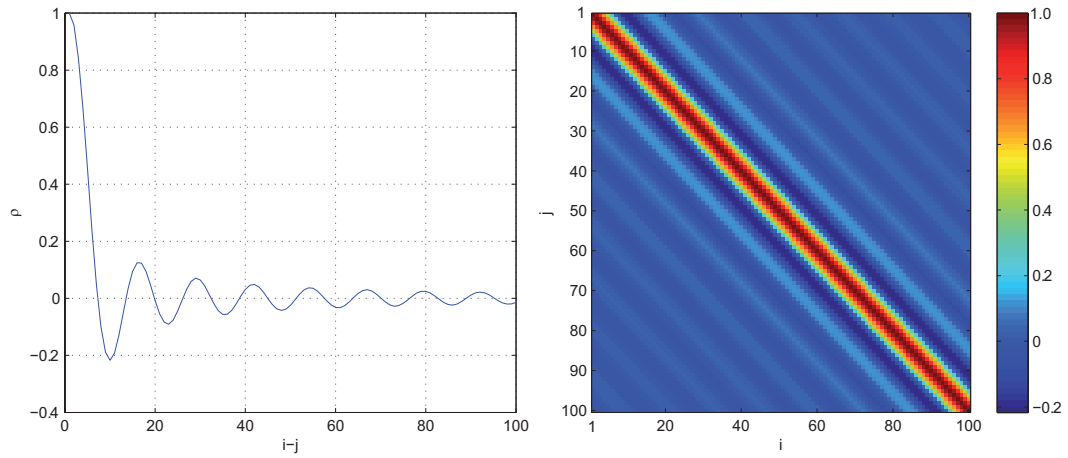


**Figure E.4:** Correlation function (left) and covariance matrix (right) of the first 100 elements of  $\mathbf{K}_{xx}$ .

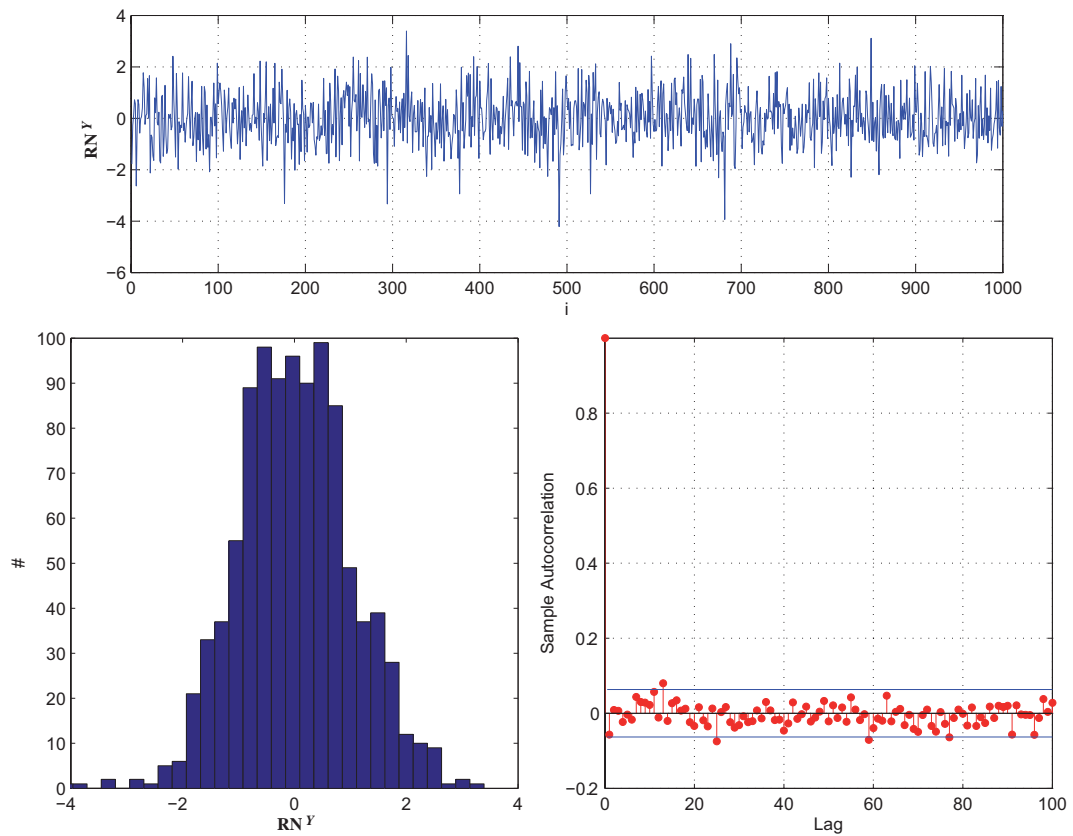


**Figure E.5:**  $RN^Y$  plotted as time series (top), as empirical PDF (bottom left) and its autocorrelation function (bottom right).

4. Evaluate the model  $RN_i^Y = f(RN_i^X)$  and store the results as  $RN_i^Y$ .
5. Repeat steps 3 and 4 for  $i = 1 \dots k$ .

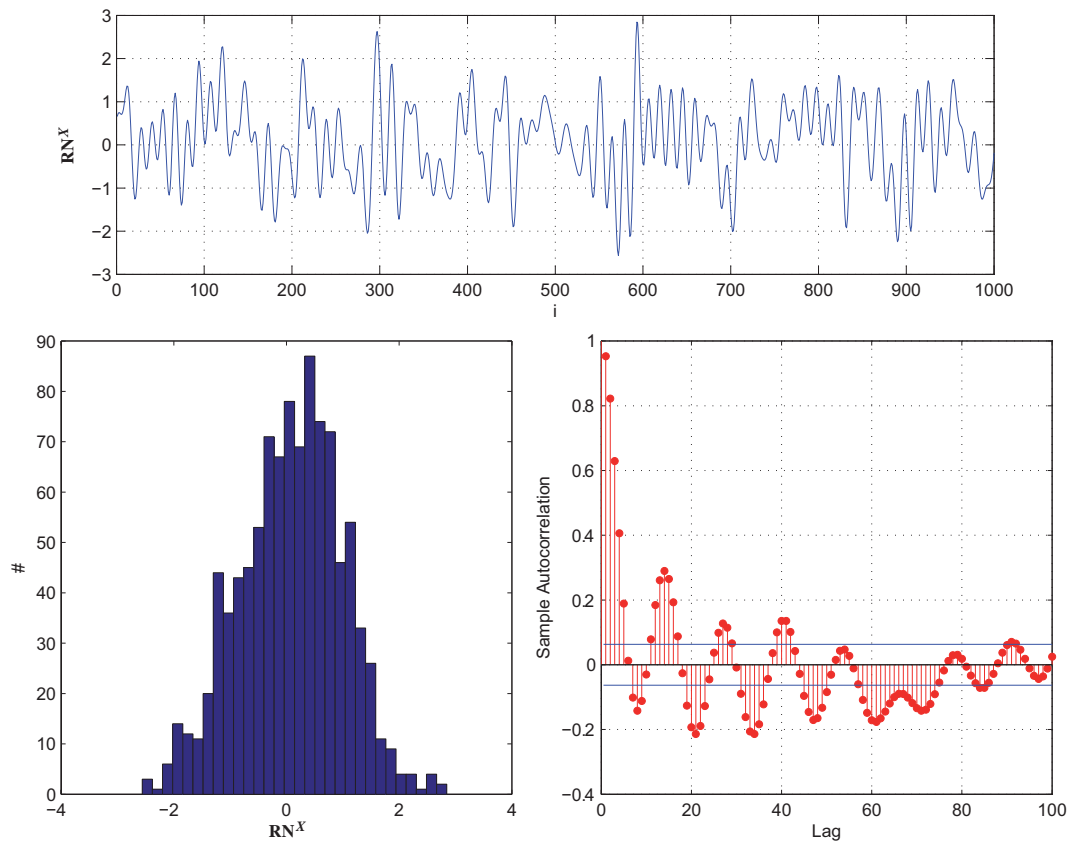


**Figure E.6:**  $RN^X$  plotted as time series (top), as empirical PDF (bottom left) and its autocorrelation function (bottom right).

6. Analyze the results using empirical PDF and CDF, summary statistics, confidence intervals, etc.

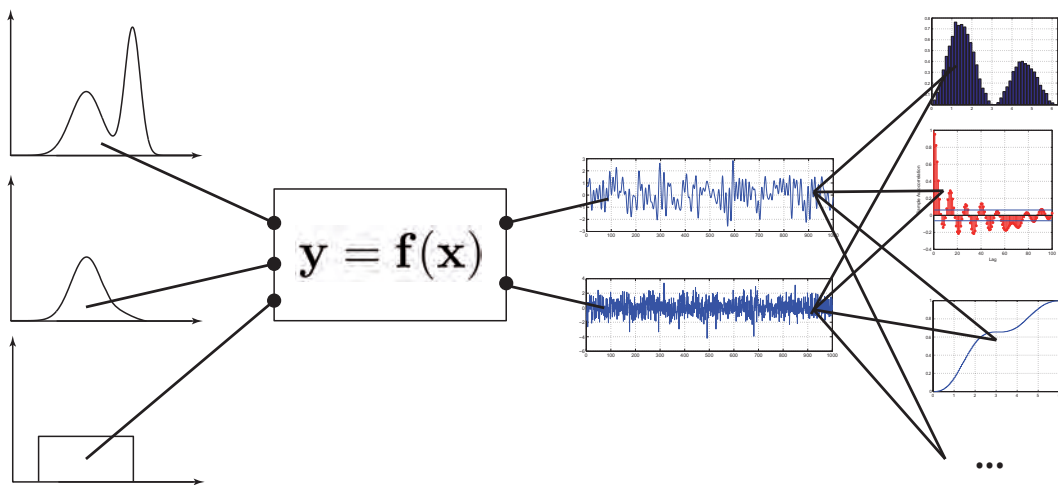


**Figure E.7:** Overview of a Monte Carlo simulation.

## Appendix F

# Results of the Simulations: Alignment Accuracy of Geometric Determinations

### F.1 Astrogeodetic Levelling

#### F.1.1 Misalignment due to Drift Noise

Here, the misalignment due to a deterministic drift noise is analysed by estimating:

$$\sigma_{\mathcal{M}(\Sigma_{\text{Drift}})}^{1-\alpha} \quad \text{with: } \Sigma_{\text{Drift}} = (\delta\epsilon_{\text{Drift}}, \Delta s_{\text{obs}}) \quad (\text{F.1})$$

for various  $\delta\epsilon_{\text{Drift}}$  and  $\Delta s_{\text{obs}}$ . As can be seen in Figure F.1, the misalignments are independent of the number of observations carried out along the profile and independent of the confidence level  $1 - \alpha$ . In the prospect of a misalignment accuracy of 10 microns over 200 meters, the maximally systematic drift  $\delta\epsilon_{\text{Drift}}$  allowed is of about  $6.5 \cdot 10^{-4} \frac{\text{arcsec}}{\text{m}}$  which represents equivalently 0.065 arcsec over 100 meters.

#### F.1.2 Misalignment due to Random Drift Noise

Here, the misalignment due to a random drift noise is analysed by estimating:

$$\sigma_{\mathcal{M}(\Sigma_{\text{Rnd Drift}})}^{1-\alpha} \quad \text{with: } \Sigma_{\text{Rnd Drift}} = (\delta\epsilon_{\text{Rnd Drift}}, \Delta s_{\text{obs}}) \quad (\text{F.2})$$

for various  $\sigma_{\text{Drift}}$  and  $\Delta s_{\text{obs}}$  as it can be seen in Figure F.2. Here the misalignments are also independent from the number of observations along the profile but not from the confidence level  $1 - \alpha$ . In the prospect of a misalignment accuracy of 10 microns over 200 meters at 68% confidence level, the maximally allowed random drift noise is about  $6.5 \cdot 10^{-4} \frac{\text{arcsec}}{\text{m}}$  which represents equivalently 0.065 arcsec over 100 meters.

#### F.1.3 Misalignment due to White Noise

Here, the misalignment due to a white noise is analysed by estimating:

$$\sigma_{\mathcal{M}(\Sigma_{\text{White}})}^{1-\alpha} \quad \text{with: } \Sigma_{\text{White}} = (\delta\epsilon_{\text{White}}, \Delta s_{\text{obs}}) \quad (\text{F.3})$$

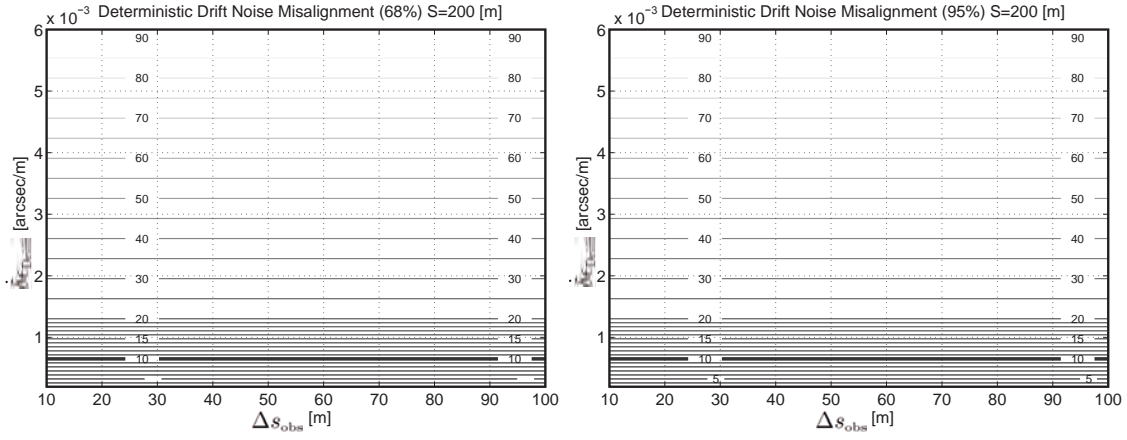


**Figure F.1:** Misalignment  $\sigma_{\mathcal{M}(\Sigma_{\text{Drift}})}^{0.68}$  (left) and  $\sigma_{\mathcal{M}(\Sigma_{\text{Drift}})}^{0.95}$  (right), in microns, as a function of the drift  $\delta\epsilon_{\text{Drift}}$  and the distance between stations  $\Delta s_{\text{obs}}$ .

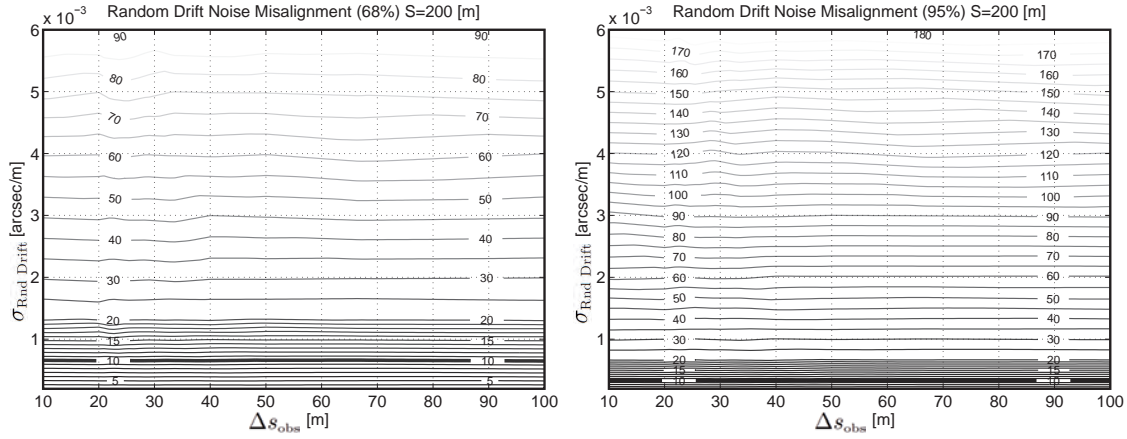


**Figure F.2:** Misalignment  $\sigma_{\mathcal{M}(\Sigma_{\text{Rnd Drift}})}^{0.68}$  (left) and  $\sigma_{\mathcal{M}(\Sigma_{\text{Rnd Drift}})}^{0.95}$  (right), in microns, as a function of  $\sigma_{\text{Rnd Drift}}$  and the distance between stations  $\Delta s_{\text{obs}}$ .

for various  $\sigma_{\text{White}}$  and  $\Delta s_{\text{obs}}$  as shown in Figure F.3. In the prospect of a misalignment accuracy of 10 microns over 200 meters at 68% confidence level, the maximally allowed white noise is about 0.09 arcsec. Regardless of the reduction of the observations, this kind of accuracy is accessible to modern zenith cameras. In this case, it is supposed that an observation is carried out every 10 meters. In addition, it is interesting to note that the incidence of increasing the distance between the observations  $\Delta s_{\text{obs}}$  is significant up to  $\Delta s_{\text{obs}} = 40$  meters only. For larger spacings  $40 \leq \Delta s_{\text{obs}} \leq 100$  meters, the white noise must not exceed 0.06 arcsec. Concerning the transition to the confidence level  $1 - \alpha = 95\%$ , we would expect to have a proportionality factor of  $\approx 2$  compared to the results for  $1 - \alpha = 68\%$ . Actually we find a factor approaching 1.5 which comes from the fact that the PDF of the misalignment random variable decreases faster than the Gaussian PDF.



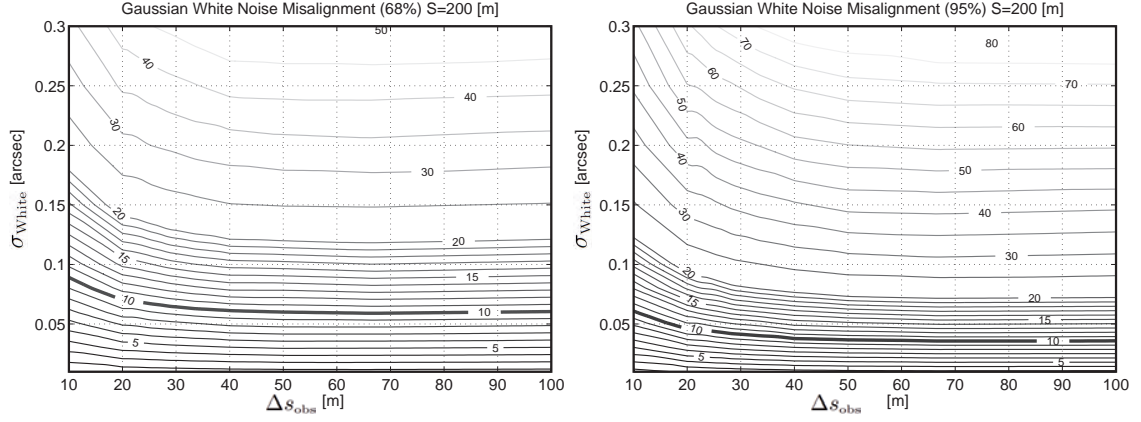


**Figure F.3:** Misalignment  $\sigma_{\mathcal{M}(\Sigma_{\text{White}})}^{0.68}$  (left) and  $\sigma_{\mathcal{M}(\Sigma_{\text{White}})}^{0.95}$  (right), in microns, as a function of  $\sigma_{\text{White}}$  and the distance between stations  $\Delta s_{\text{obs}}$ .

#### F.1.4 Misalignment due to Correlated Noise

Here, the misalignment due to a correlated noise is analysed by estimating:

$$\sigma_{\mathcal{M}(\Sigma_{\text{Corr}})}^{1-\alpha} \quad \text{with: } \Sigma_{\text{Corr}} = (\delta\epsilon_{\text{Corr}}, \Delta s_{\text{obs}}) \quad (\text{F.4})$$

for various  $\sigma_{\text{Corr}}$ ,  $d_{\text{Corr}}$  and  $\Delta s_{\text{obs}}$  as shown in Figures F.4, F.5, F.6 and F.7. In Figures F.4 and F.5, the spacing between the observations is fixed to  $\Delta s_{\text{obs}} = 10$  meters. The data are identical. Only the horizontal scale is different to better show the behavior at short and large correlation lengths  $d_{\text{Corr}}$ , respectively. As regards Figures F.6 and F.7, the spacing between the observations is fixed to  $\Delta s_{\text{obs}} = 20$  and  $\Delta s_{\text{obs}} = 40$  meters.

Concerning the dependency on the correlation length, we find an identical misalignment to that generated by white noise for  $d_{\text{Corr}} = 0$ , see Figure F.4. On the other side, when  $d_{\text{Corr}} \rightarrow \infty$ , the correlated noise behaves like a random bias which has less and less impact on the misalignment, see Figure F.5. In between, we can clamp that there are two different regions, the first  $\mathcal{R}_-$  where the correlations act negatively on the accuracy of the alignment, the second one  $\mathcal{R}_+$  where the correlation acts positively, see Table F.1. In addition, the worst case happens for  $d_{\text{Corr}} = 40$  meters regardless of the separation  $\Delta s_{\text{obs}}$ .

**Table F.1:** Regions where the correlations act negatively  $\mathcal{R}_-$  and positively  $\mathcal{R}_+$  on the accuracy of the alignment.

$\Delta s_{\text{obs}}$ [m]	$\sigma_{\text{Corr}} : \sigma_{\mathcal{M}(\Sigma_{\text{Corr}})}^{0.68} = 10 \text{ } \mu\text{m}$ [arcsec]	$\mathcal{R}_-$ [m]	$\min \{\mathcal{R}_-\}$ [m]	$\mathcal{R}_+$ [m]
10	0.09	[0, 300]	40	[300, $\infty$ [
20	0.07	[0, 150]	40	[150, $\infty$ [
40	0.06	[0, 75]	40	[75, $\infty$ [

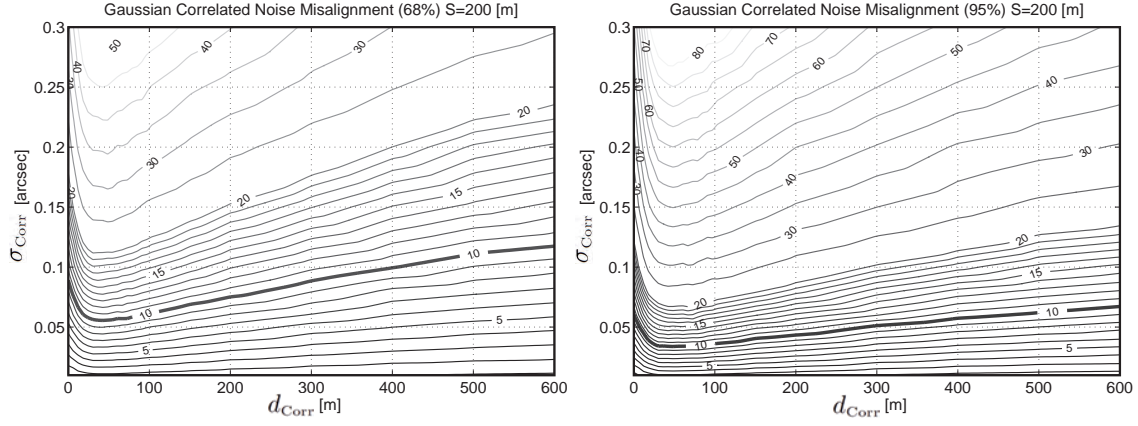


**Figure F.4:** Misalignment  $\sigma_{\mathcal{M}(\Sigma_{\text{Corr}})}^{0.68}$  (left) and  $\sigma_{\mathcal{M}(\Sigma_{\text{Corr}})}^{0.95}$  (right), in microns, as a function of  $\sigma_{\text{Corr}}$  and the correlation length  $d_{\text{Corr}}$ . The spacing between the observations is fixed to  $\Delta s_{\text{obs}} = 10$  meters.

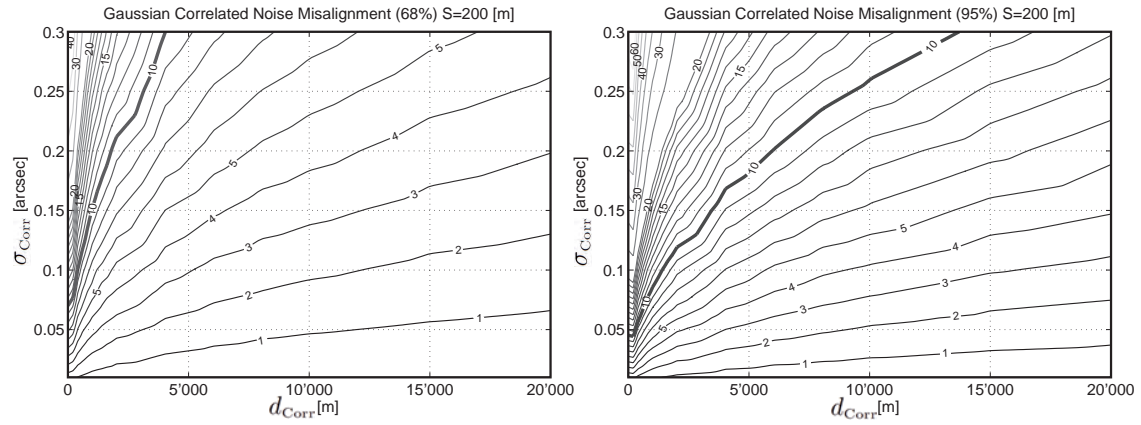


**Figure F.5:** Misalignment  $\sigma_{\mathcal{M}(\Sigma_{\text{Corr}})}^{0.68}$  (left) and  $\sigma_{\mathcal{M}(\Sigma_{\text{Corr}})}^{0.95}$  (right), in microns, as a function of  $\sigma_{\text{Corr}}$  and the correlation length  $d_{\text{Corr}}$ . The spacing between the observations is fixed to  $\Delta s_{\text{obs}} = 10$  meters.

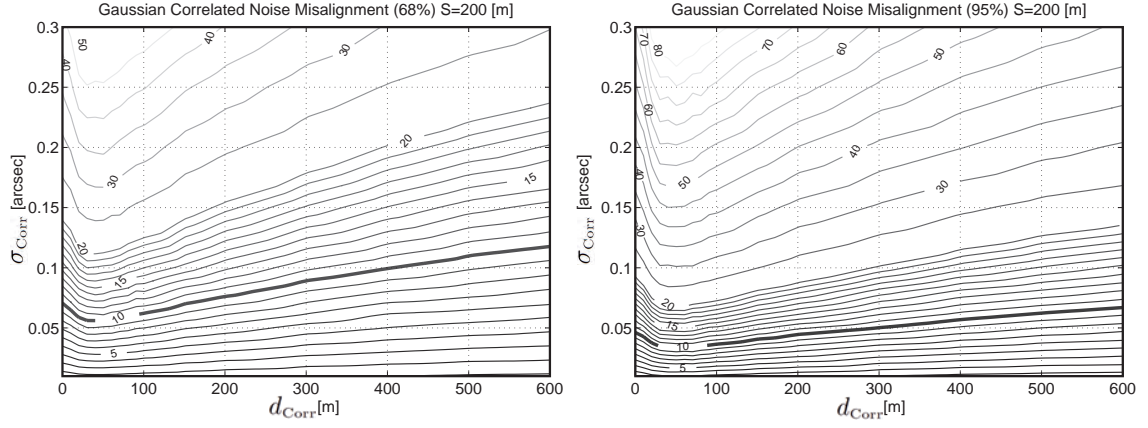


**Figure F.6:** Misalignment  $\sigma_{\mathcal{M}(\Sigma_{\text{Corr}})}^{0.68}$  (left) and  $\sigma_{\mathcal{M}(\Sigma_{\text{Corr}})}^{0.95}$  (right), in microns, as a function of  $\sigma_{\text{Corr}}$  and the correlation length  $d_{\text{Corr}}$ . The spacing between the observations is fixed to  $\Delta s_{\text{obs}} = 20$  meters.

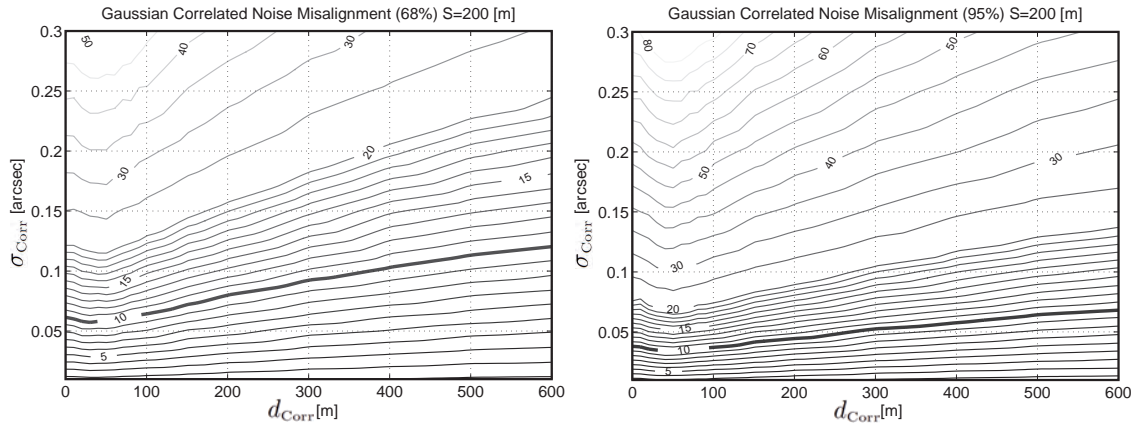


**Figure F.7:** Misalignment  $\sigma_{\mathcal{M}(\Sigma_{\text{Corr}})}^{0.68}$  (left) and  $\sigma_{\mathcal{M}(\Sigma_{\text{Corr}})}^{0.95}$  (right), in microns, as a function of  $\sigma_{\text{Corr}}$  and the correlation length  $d_{\text{Corr}}$ . The spacing between the observations is fixed to  $\Delta s_{\text{obs}} = 40$  meters.

## F.2 Alignment Accuracy of the Orthometric Corrections

### F.2.1 Misalignment due to Drift Noise ( $E1$ )

Here, the misalignment due to a deterministic drift noise is analysed by estimating:

$$\sigma_{\mathcal{M}(\Sigma_{\text{Drift}})}^{1-\alpha} \quad \text{with: } \Sigma_{\text{Drift}} = (\delta g_{\text{Drift}}, \Delta s_{\text{obs}}) \quad (\text{F.5})$$

for various  $\delta g_{\text{Drift}}$  and  $\Delta s_{\text{obs}}$ . As shown in Figure F.8, the misalignments are independent from the number observations carried out along the profile and independent of the confidence level  $1 - \alpha$ . In the prospect of a misalignment accuracy of 10 microns over 200 meters, the maximally systematic drift  $\delta g_{\text{Drift}}$  allowed is about  $30.0 \frac{\mu\text{gal}}{\text{m}}$  which represents equivalently 3.0 mgal over 100 meters.

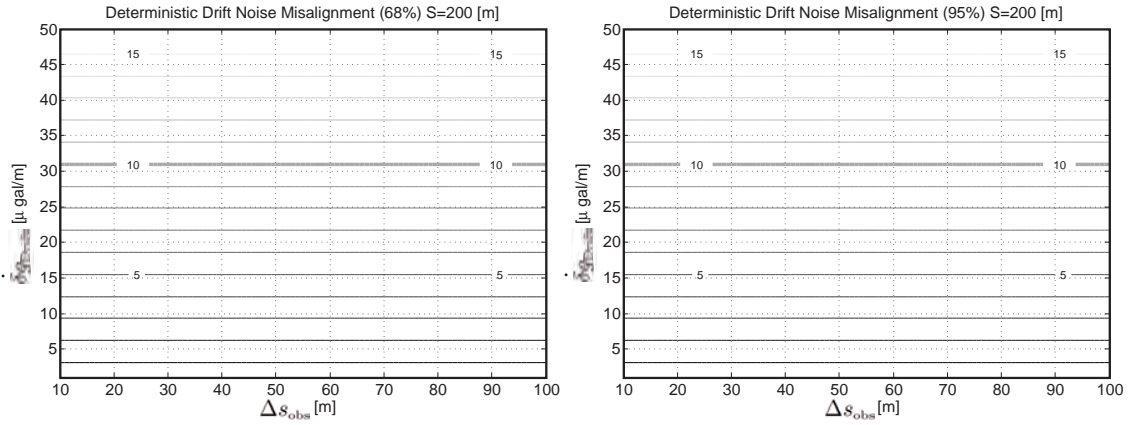


**Figure F.8:** Misalignment  $\sigma_{\mathcal{M}(\Sigma_{\text{Drift}})}^{0.68}$  (left) and  $\sigma_{\mathcal{M}(\Sigma_{\text{Drift}})}^{0.95}$  (right), in microns, as a function of the drift  $\delta g_{\text{Drift}}$  and the distance between stations  $\Delta s_{\text{obs}}$ .

### F.2.2 Misalignment due to Random Drift Noise ( $E1$ )

Here, the misalignment due to a random drift noise is analysed by estimating:

$$\sigma_{\mathcal{M}(\Sigma_{\text{Rnd Drift}})}^{1-\alpha} \quad \text{with: } \Sigma_{\text{Rnd Drift}} = (\delta g_{\text{Rnd Drift}}, \Delta s_{\text{obs}}) \quad (\text{F.6})$$

for various  $\sigma_{\text{Drift}}$  and  $\Delta s_{\text{obs}}$ . This can be seen in Figure F.9. Here the misalignments are also independent from the number of observations along the profile but not from the confidence level  $1 - \alpha$ . In the prospect of a misalignment accuracy of 10 microns over 200 meters, the maximally allowed drift noise is about  $30.0 \frac{\mu\text{gal}}{\text{m}}$  which represents equivalently 3.0 mgal over 100 meters.

### F.2.3 Misalignment due to White Noise ( $E1$ )

Here, the misalignment due to a white noise is analysed by estimating:

$$\sigma_{\mathcal{M}(\Sigma_{\text{White}})}^{1-\alpha} \quad \text{with: } \Sigma_{\text{White}} = (\delta g_{\text{White}}, \Delta s_{\text{obs}}) \quad (\text{F.7})$$

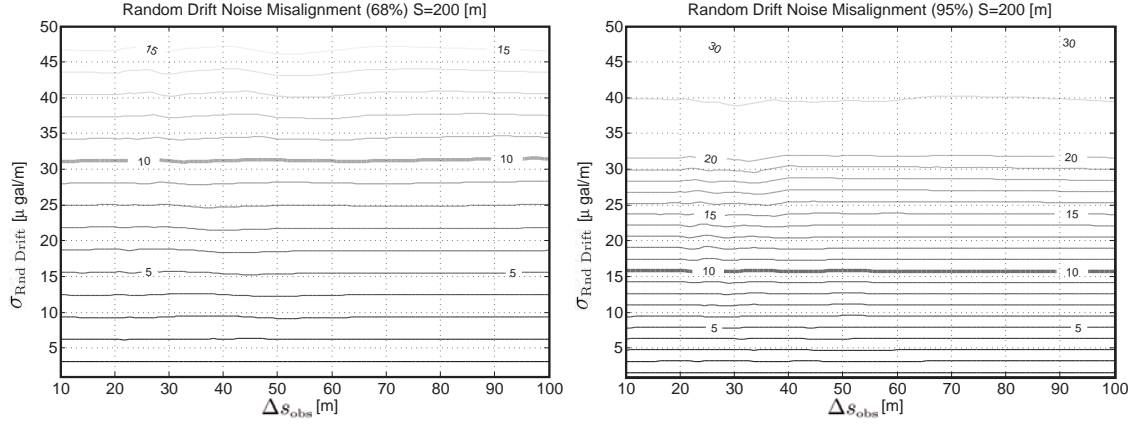


**Figure F.9:** Misalignment  $\sigma_{\mathcal{M}(\Sigma_{\text{Rnd Drift}})}^{0.68}$  (left) and  $\sigma_{\mathcal{M}(\Sigma_{\text{Rnd Drift}})}^{0.95}$  (right), in microns, as a function of  $\sigma_{\text{Rnd Drift}}$  and the distance between stations  $\Delta s_{\text{obs}}$ .

for various  $\sigma_{\text{White}}$  and  $\Delta s_{\text{obs}}$  as depicted in Figure F.10. In the prospect of a misalignment accuracy of 10 microns over 200 meters at 68% confidence level, the maximally allowed white noise is about 3.0 – 4.0 mgal. Regarding the white noise level, of about 5  $\mu\text{gal}$ , expected in gravimetric measurements, we can consider that the effects due to white noise can be completely neglected for the determination of  $E1$ .

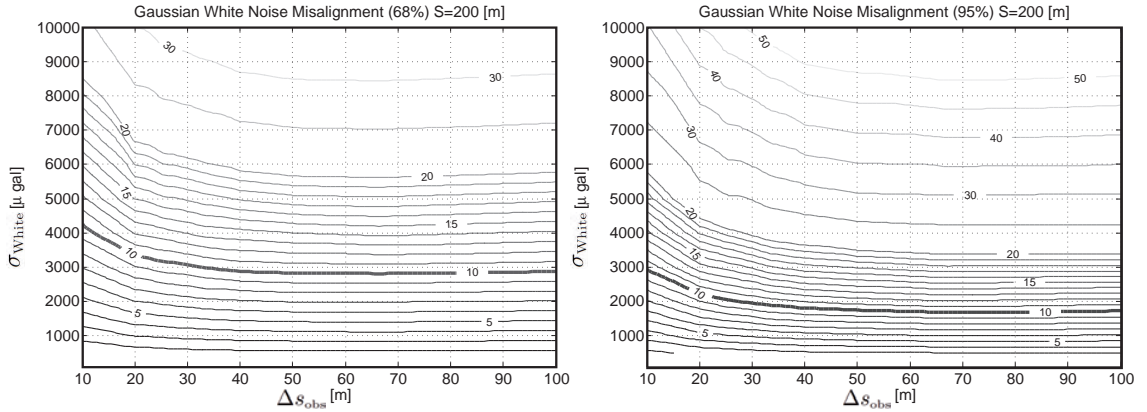


**Figure F.10:** Misalignment  $\sigma_{\mathcal{M}(\Sigma_{\text{White}})}^{0.68}$  (left) and  $\sigma_{\mathcal{M}(\Sigma_{\text{White}})}^{0.95}$  (right), in microns, as a function of  $\sigma_{\text{White}}$  and the distance between stations  $\Delta s_{\text{obs}}$ .

### F.2.4 Misalignment due to Correlated Noise ( $E1$ )

Here, the misalignment due to a correlated noise is analysed by estimating:

$$\sigma_{\mathcal{M}(\Sigma_{\text{Corr}})}^{1-\alpha} \quad \text{with: } \Sigma_{\text{Corr}} = (\delta g_{\text{Corr}}, \Delta s_{\text{obs}}) \quad (\text{F.8})$$

for various  $\sigma_{\text{Corr}}$  and  $d_{\text{Corr}}$ . The spacing between the observations is fixed at  $\Delta s_{\text{obs}} = 10$  meters as shown in Figure F.11. Concerning the dependency on the correlation length, we find an misalignment identical to that generated by white noise for  $d_{\text{Corr}} = 0$ . On the

other side, when  $d_{\text{Corr}} \rightarrow \infty$ , the correlated noise behaves like a random bias which has less and less impact on the misalignment. Regarding the correlated noise level  $< 20 \mu\text{gal}$ , expected in gravimetric measurements, we can consider that the effects due to correlated noise can also be completely neglected for the determination of  $E1$ .

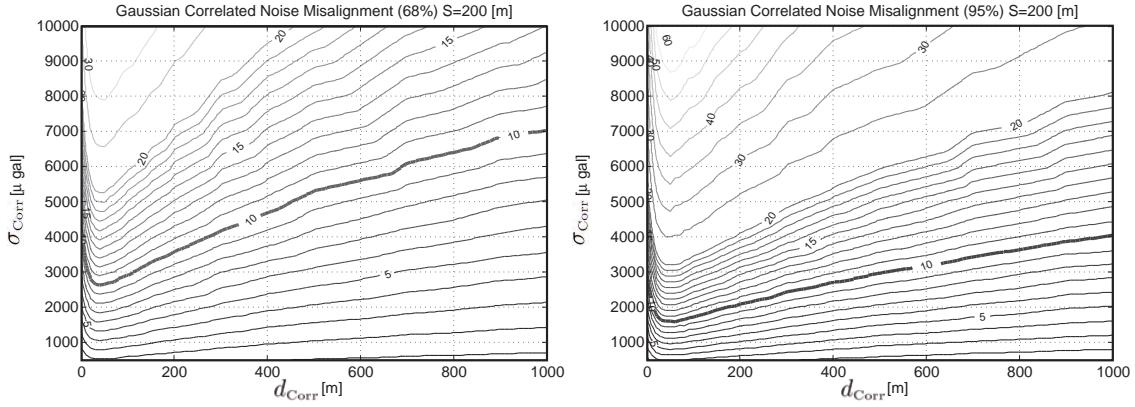


**Figure F.11:** Misalignment  $\sigma_{\mathcal{M}(\Sigma_{\text{Corr}})}^{0.68}$  (left) and  $\sigma_{\mathcal{M}(\Sigma_{\text{Corr}})}^{0.95}$  (right), in microns, as a function of  $\sigma_{\text{Corr}}$  and the correlation length  $d_{\text{Corr}}$ . The spacing between the observations is fixed to  $\Delta s_{\text{obs}} = 10$  meters.

### F.2.5 Misalignment due to White Noise ( $E2$ )

Here, the misalignment due to a white noise is analysed by estimating:

$$\sigma_{\mathcal{M}(\Sigma_{\text{White}})}^{1-\alpha} \quad \text{with: } \Sigma_{\text{White}} = (\delta \bar{g}_{\text{White}}, \Delta s_{\text{obs}}) \quad (\text{F.9})$$

for various  $\sigma_{\text{White}}$  and  $\Delta s_{\text{obs}}$ . The results can be seen in Figure F.12. In the prospect of a misalignment accuracy of 10 microns over 200 meters at 68% confidence level, the maximally allowed white noise is about  $30.0 \mu\text{gal}$  for a spacing  $\Delta s = 10$  meters. For larger spacings, it could be surprising that the maximal allowed white noise level increase. This is just due to the fact that, for a flat topography, the determination of  $E2$ , at a given position, depends only on the local  $\bar{g}_{\text{tot}}$ . Increasing the number of  $\bar{g}_{\text{tot}}$  along a profile reduce the omission errors but not the accuracy of the determination of  $E2$ .

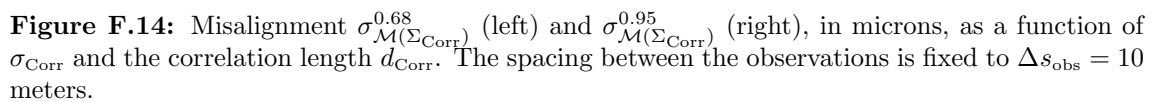
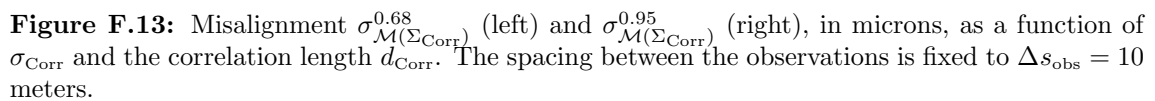
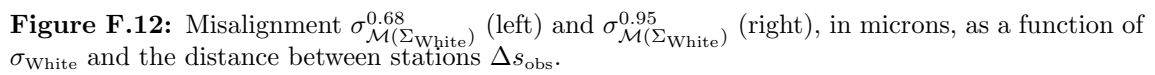
### F.2.6 Misalignment due to Correlated Noise ( $E2$ )

Here, the misalignment due to a correlated noise is analysed by estimating:

$$\sigma_{\mathcal{M}(\Sigma_{\text{Corr}})}^{1-\alpha} \quad \text{with: } \Sigma_{\text{Corr}} = (\delta \bar{g}_{\text{Corr}}, \Delta s_{\text{obs}}) \quad (\text{F.10})$$

for various  $\sigma_{\text{Corr}}$  and  $d_{\text{Corr}}$ . The spacing between the observations is fixed at  $\Delta s_{\text{obs}} = 10$  meters. The results can be seen in Figures F.13 and F.14 (the figures differ in horizontal and vertical scales). Concerning the dependency on the correlation length, we find a misalignment identical to that the one generated by white noise for  $d_{\text{Corr}} = 0$ . On the other side, when  $d_{\text{Corr}} \rightarrow \infty$ , the correlated noise behaves like a random bias which has less and less impact on the misalignment. Moreover, we can see that the maximally allowed correlated errors in  $\bar{g}_{\text{tot}}$  increase with  $d_{\text{Corr}}$ . For  $d_{\text{Corr}} = 1000$  meters the maximally correlated error is about  $125 \mu\text{gal}$  and reaches about  $500 \mu\text{gal}$  for  $d_{\text{Corr}} = 16'000$  meters.





### F.3 Alignment Accuracy of Gradiometric Levelling

#### F.3.1 Misalignment due to Bias Noise

Here, the misalignment due to a deterministic bias noise is analysed by estimating:

$$\sigma_{\mathcal{M}(\Sigma_{\text{Bias}})}^{1-\alpha} \quad \text{with: } \Sigma_{\text{Bias}} = (\delta\Delta\Gamma_{\text{Bias}}, \Delta s_{\text{obs}}) \quad (\text{F.11})$$

for various  $\delta\Delta\Gamma_{\text{Bias}}$  and  $\Delta s_{\text{obs}}$ . As shown in Figure F.15, the misalignments are independent from the number observations carried out along the profile and independent of the confidence level  $1 - \alpha$ . In the prospect of a misalignment accuracy of 10 microns over 200 meters, the maximally allowed systematic bias  $\delta\Delta\Gamma_{\text{Bias}}$  is about 31 E.

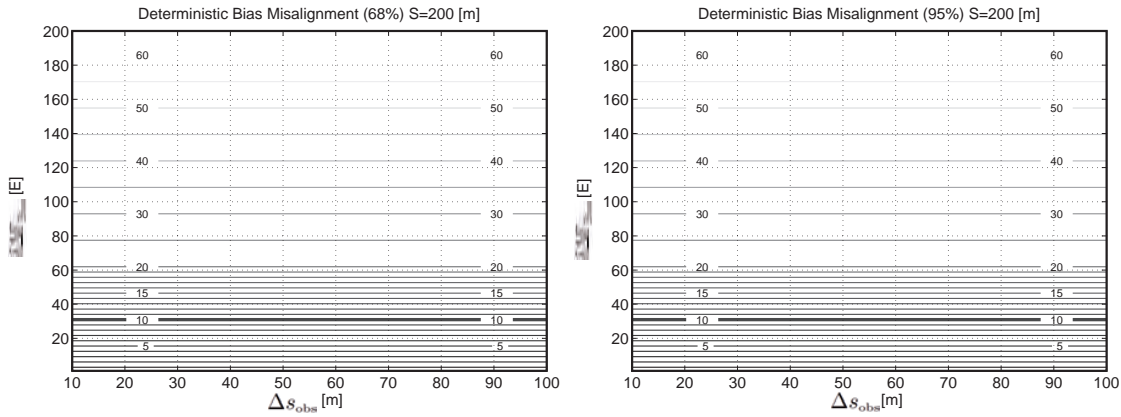


**Figure F.15:** Misalignment  $\sigma_{\mathcal{M}(\Sigma_{\text{Bias}})}^{0.68}$  (left) and  $\sigma_{\mathcal{M}(\Sigma_{\text{Bias}})}^{0.95}$  (right), in microns, in function of the bias  $\delta\Delta\Gamma_{\text{Bias}}$  and the distance between stations  $\Delta s_{\text{obs}}$ .

#### F.3.2 Misalignment due to Random Bias Noise

Here, the misalignment due to a random bias noise is analysed by estimating:

$$\sigma_{\mathcal{M}(\Sigma_{\text{Rnd Bias}})}^{1-\alpha} \quad \text{with: } \Sigma_{\text{Rnd Bias}} = (\delta\Delta\Gamma_{\text{Rnd Bias}}, \Delta s_{\text{obs}}) \quad (\text{F.12})$$

for various  $\sigma_{\text{Rnd Bias}}$  and  $\Delta s_{\text{obs}}$ . As shown in Figure F.16, the misalignments are also independent from the number of observations along the profile but not from the confidence level  $1 - \alpha$ . In the prospect of a misalignment accuracy of 10 microns over 200 meters, the maximally allowed standard deviation of a random bias  $\sigma_{\text{Bias}}$  is about 31 E.

#### F.3.3 Misalignment due to Deterministic Drift Noise

Here, the misalignment due to a deterministic drift noise is analysed by estimating:

$$\sigma_{\mathcal{M}(\Sigma_{\text{Drift}})}^{1-\alpha} \quad \text{with: } \Sigma_{\text{Drift}} = (\delta\Delta\Gamma_{\text{Drift}}, \Delta s_{\text{obs}}) \quad (\text{F.13})$$

for various  $\delta\Delta\Gamma_{\text{Drift}}$  and  $\Delta s_{\text{obs}}$ . As Figure F.17 shows, the misalignments are independent from the number observations carried out along the profile and independent of the confidence level  $1 - \alpha$ . In the prospect of a misalignment accuracy of 10 microns over 200 meters, the maximally allowed drift  $\delta\Delta\Gamma_{\text{Drift}}$  is about  $0.26 \frac{\text{E}}{\text{m}}$ .



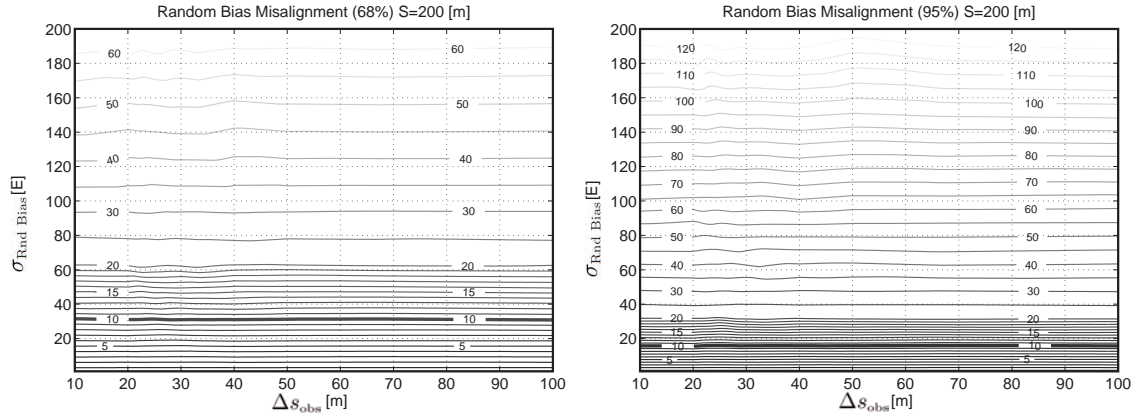


**Figure F.16:** Misalignment  $\sigma_{\mathcal{M}(\Sigma_{\text{Bias}})}^{0.68}$  (left) and  $\sigma_{\mathcal{M}(\Sigma_{\text{Bias}})}^{0.95}$  (right), in microns, as a function of  $\sigma_{\text{Bias}}$  and the distance between stations  $\Delta s_{\text{obs}}$ .

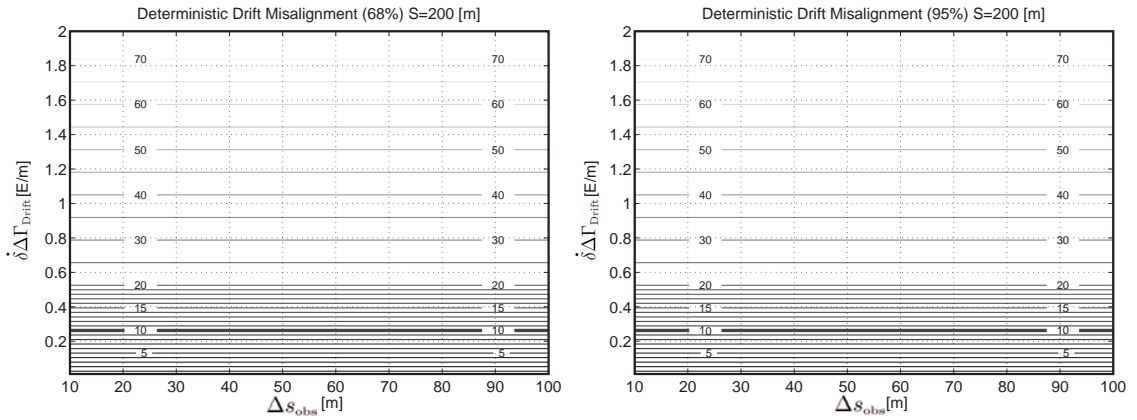


**Figure F.17:** Misalignment  $\sigma_{\mathcal{M}(\Sigma_{\text{Drift}})}^{0.68}$  (left) and  $\sigma_{\mathcal{M}(\Sigma_{\text{Drift}})}^{0.95}$  (right), in microns, as a function of  $\delta\Delta\Gamma_{\text{Drift}}$  and the distance between stations  $\Delta s_{\text{obs}}$ .

### F.3.4 Misalignment due to Random Drift Noise

Here, the misalignment due to a random drift noise is analysed by estimating:

$$\sigma_{\mathcal{M}(\Sigma_{\text{Rnd Drift}})}^{1-\alpha} \quad \text{with: } \Sigma_{\text{Rnd Drift}} = (\delta\Delta\Gamma_{\text{Rnd Drift}}, \Delta s_{\text{obs}}) \quad (\text{F.14})$$

for various  $\sigma_{\text{Rnd Drift}}$  and  $\Delta s_{\text{obs}}$ . As Figure F.18 shows, the misalignments are also independent from the number of observations along the profile but not from the confidence level  $1 - \alpha$ . In the prospect of a misalignment accuracy of 10 microns over 200 meters, the maximally allowed drift  $\sigma_{\text{Rnd Drift}}$  is about  $0.26 \frac{\text{E}}{\text{m}}$ .

### F.3.5 Misalignment due to White Noise

Here, the misalignment due to a white noise is analysed by estimating:

$$\sigma_{\mathcal{M}(\Sigma_{\text{White}})}^{1-\alpha} \quad \text{with: } \Sigma_{\text{White}} = (\delta\Delta\Gamma_{\text{White}}, \Delta s_{\text{obs}}) \quad (\text{F.15})$$

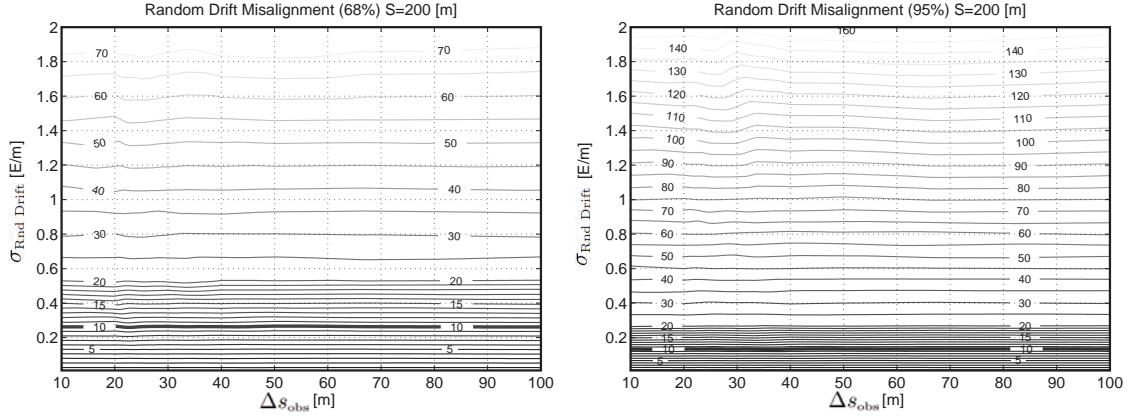


**Figure F.18:** Misalignment  $\sigma_{\mathcal{M}(\Sigma_{\text{Rnd Drift}})}^{0.68}$  (left) and  $\sigma_{\mathcal{M}(\Sigma_{\text{Rnd Drift}})}^{0.95}$  (right), in microns, as a function of  $\sigma_{\text{Rnd Drift}}$  and the distance between stations  $\Delta s_{\text{obs}}$ .

for various  $\sigma_{\text{White}}$  and  $\Delta s_{\text{obs}}$  (see Figure F.19). In the prospect of a misalignment accuracy of 10 microns over 200 meters at 68% confidence level, the maximally allowed white noise is about 100 E for  $\Delta s_{\text{obs}} = 10$  meters and of about 40 E for  $\Delta s_{\text{obs}} = 100$  meters.

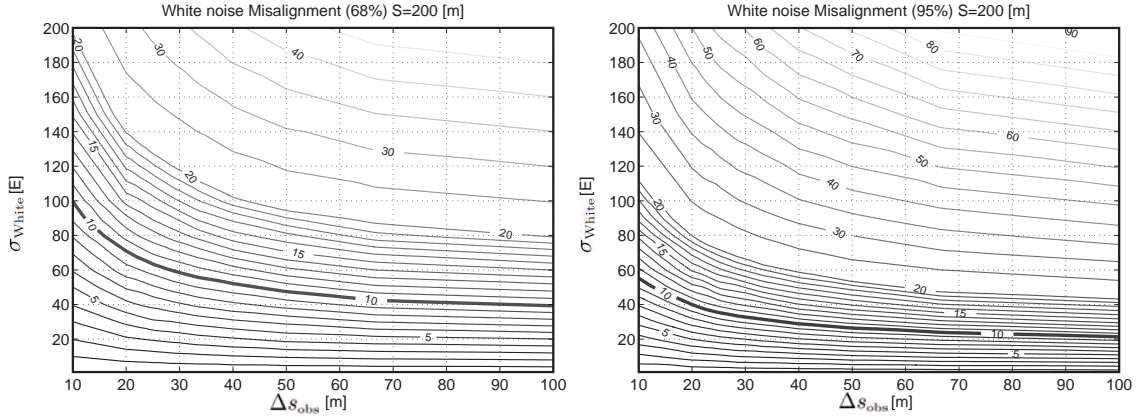


**Figure F.19:** Misalignment  $\sigma_{\mathcal{M}(\Sigma_{\text{White}})}^{0.68}$  (left) and  $\sigma_{\mathcal{M}(\Sigma_{\text{White}})}^{0.95}$  (right), in microns, as a function of  $\sigma_{\text{White}}$  and the distance between stations  $\Delta s_{\text{obs}}$ .

### F.3.6 Misalignment due to Correlated Noise

Here, the misalignment due to a correlated noise is analysed by estimating:

$$\sigma_{\mathcal{M}(\Sigma_{\text{Corr}})}^{1-\alpha} \quad \text{with:} \quad \Sigma_{\text{Corr}} = (\delta \Delta \Gamma_{\text{Corr}}, \Delta s_{\text{obs}}) \quad (\text{F.16})$$

for various  $\sigma_{\text{Corr}}$ ,  $d_{\text{Corr}}$  and  $\Delta s_{\text{obs}}$  (see Figure F.20).

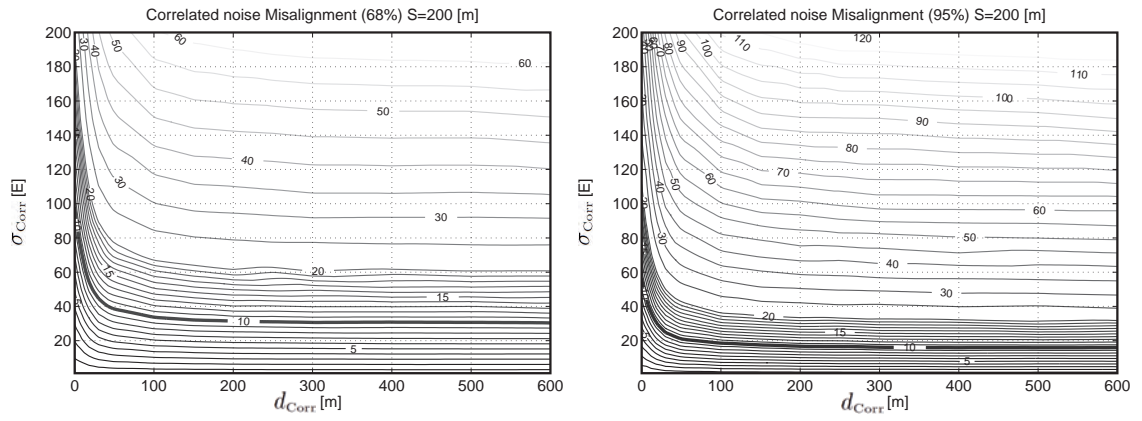


**Figure F.20:** Misalignment  $\sigma_{\mathcal{M}(\Sigma_{\text{Corr}})}^{0.68}$  (left) and  $\sigma_{\mathcal{M}(\Sigma_{\text{Corr}})}^{0.95}$  (right), in microns, as a function of  $\sigma_{\text{Corr}}$  and the distance between stations  $\Delta s_{\text{obs}}$ .



## **Appendix G**

# **Batch Functionalities in QGravity**

**Table G.1:** List of available batch functionalities implemented in QGravity.

FUNCTION	Description
AGR2BIN	Import an AGR file and export the corresponding 3D points in a binary *.bin file. This function is useful for the generation of multi-resolution digital terrain models.
IMPORT_EXPORT	Import points and export the same points passing through the coordinate transformation pipelines. This function is useful for transforming points from one reference system to another.
MULTI_RESOLUTION_POINTS	Given a set of points, select and export the points of this set which are inside a region defined by a rectangular band. This function is useful for the creation of multi-resolution point clouds.
MULTI_RESOLUTION_MASS	Create a polyhedron from 2 tessellations. The points of the upper surface are given by link to a MULTI_RESOLUTION_POINTS input file. The points of the lower surface are given by a link to a binary point file *.bin.
MASS_FROM_2_TESSELATIONS	Create a polyhedron from 2 tessellations. The points of the common boundary, the upper and the lower surface are given by link to binary point files *.bin.
MASS_FROM_PRIMITIVE_TUBE	Create a polyhedron using the functionality: 3D tube of arbitrary section and path. The path and the section are given by a link to *.xyz files.
MASS_FROM_OFF	Create a polyhedron from a *.off file.
REPLACE_DATA	Given two sets of points and a closed boundary, this function replace the points of the first set which are inside the boundary by the points of the second set which are also inside the boundary. This functionality is useful when it is necessary to update DTM (lake and sea are usually given by their water surface) with bathymetric data.
MASSMODELS_PROPERTIES	Compute the volume, the mass and the center of mass of a polyhedron create by one of the function MULTI_RESOLUTION_MASS, MASS_FROM_2_TESSELATIONS, MASS_FROM_PRIMITIVE_TUBE and MASS_FROM_OFF, or by the importation of a *.qgr mass model file.
MASSMODEL_TO_GRAVITY	Compute the gravitational field at points given by a *.xyz file, generated by one or several mass models generated by one of the function MULTI_RESOLUTION_MASS, MASS_FROM_2_TESSELATIONS, MASS_FROM_PRIMITIVE_TUBE and MASS_FROM_OFF, or by the import of *.qgr or *.xyz mass model files. This is the most important and useful function which permit to compute gravitational fields with a high level of automation.

## Appendix H

# Validation of the Polyhedron Algorithm in QGravity

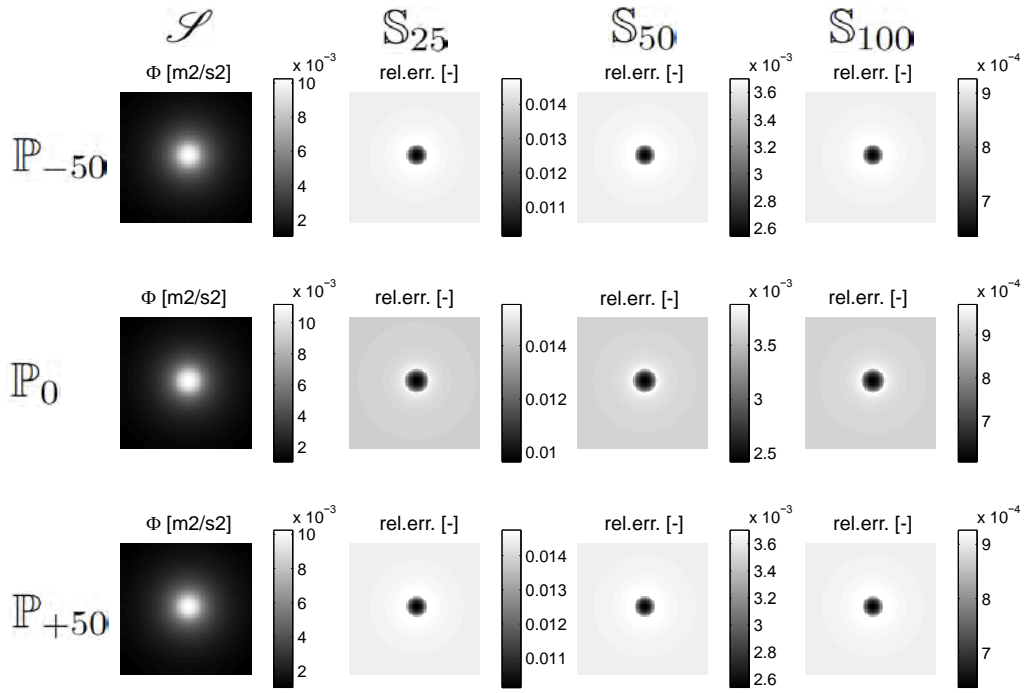


**Figure H.1:** Gravitational potential  $\Phi_{\text{grav}}$  of  $\mathcal{S}$  and the respective relative errors of the fields  $\mathbb{S}_{25}$ ,  $\mathbb{S}_{50}$  and  $\mathbb{S}_{100}$  computed with QGravity.

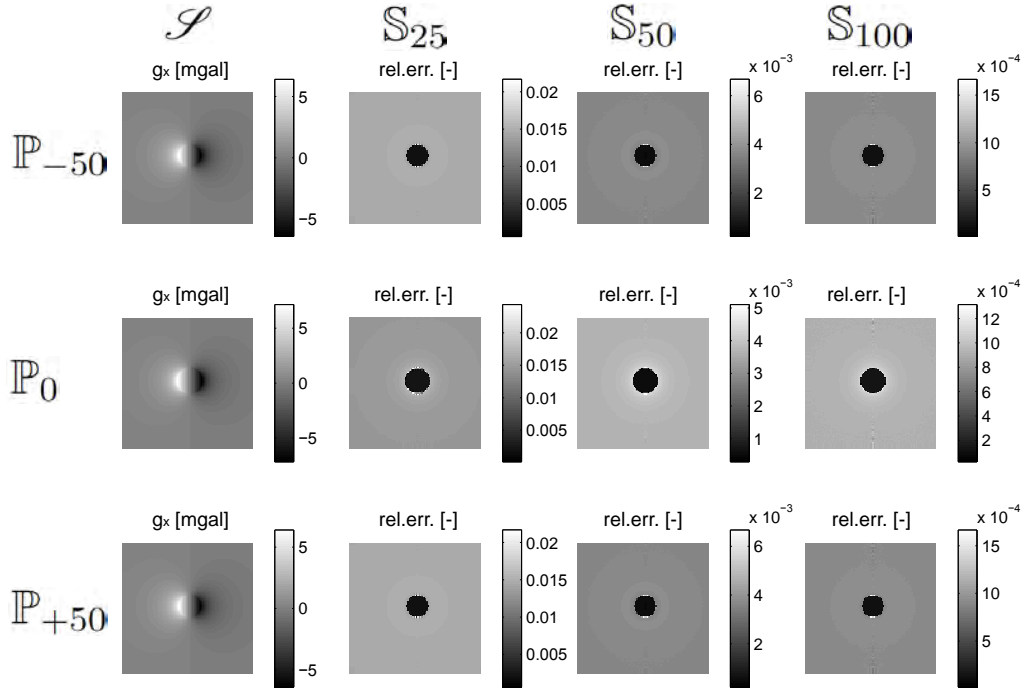


**Figure H.2:** Gravitational acceleration  $g_{x,\text{grav}}$  of  $\mathcal{S}$  and the respective relative errors of the fields  $S_{25}$ ,  $S_{50}$  and  $S_{100}$  computed with QGravity.

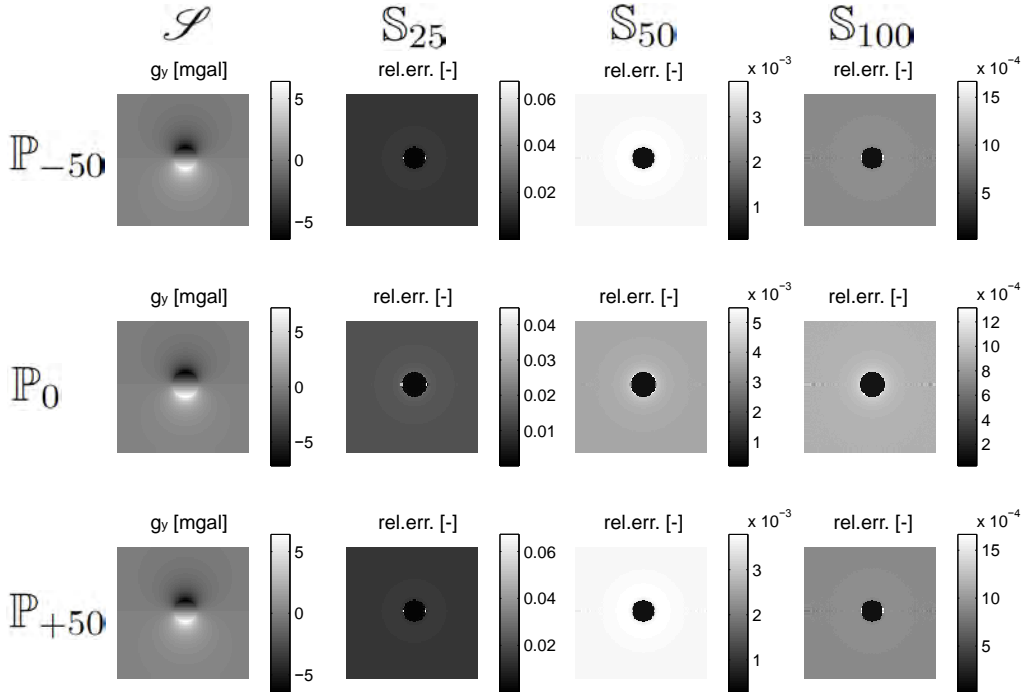


**Figure H.3:** Gravitational acceleration  $g_{y,\text{grav}}$  of  $\mathcal{S}$  and the respective relative errors of the fields  $S_{25}$ ,  $S_{50}$  and  $S_{100}$  computed with QGravity.



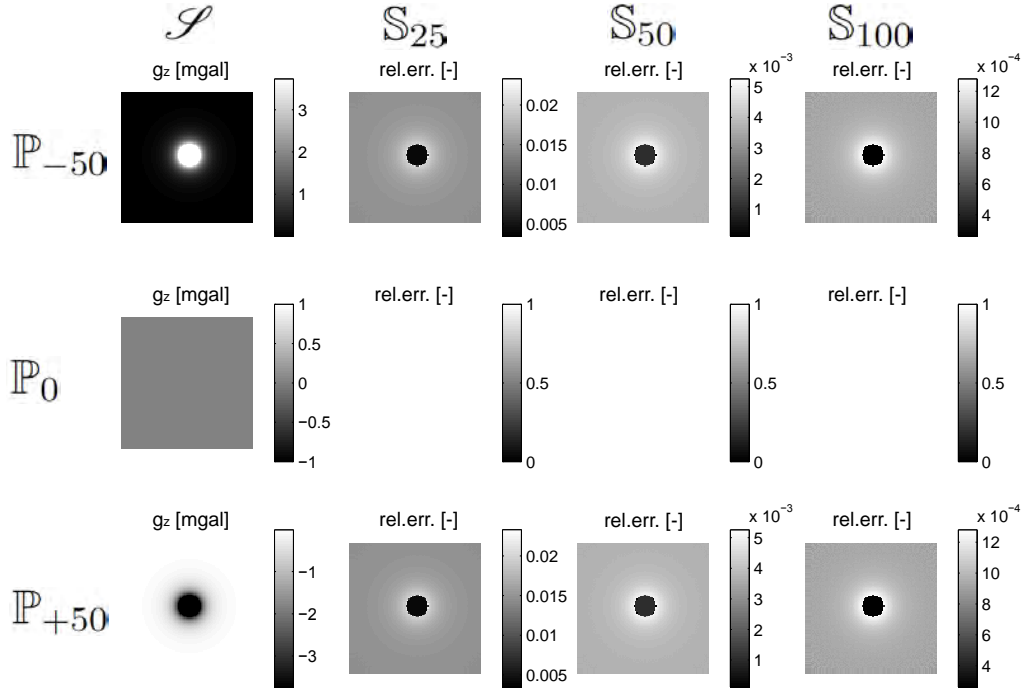


**Figure H.4:** Gravitational acceleration  $g_{z,\text{grav}}$  of  $\mathcal{S}$  and the respective relative errors of the fields  $\mathcal{S}_{25}$ ,  $\mathcal{S}_{50}$  and  $\mathcal{S}_{100}$  computed with QGravity.

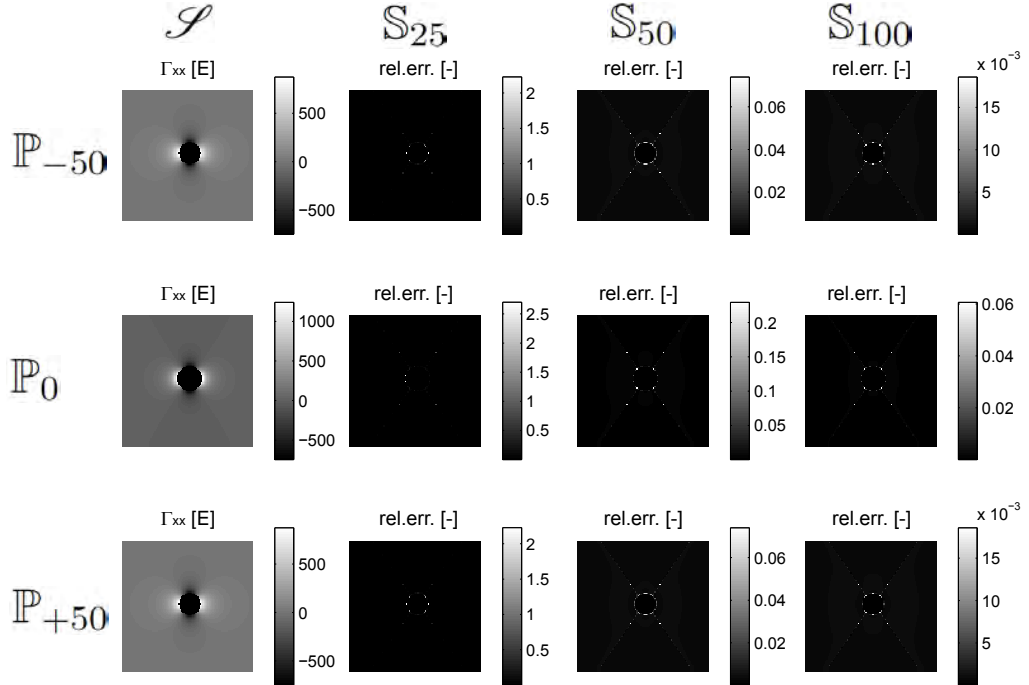


**Figure H.5:** Gravitational tensor  $\Gamma_{xx,\text{grav}}$  of  $\mathcal{S}$  and the respective relative errors of the fields  $\mathcal{S}_{25}$ ,  $\mathcal{S}_{50}$  and  $\mathcal{S}_{100}$  computed with QGravity.

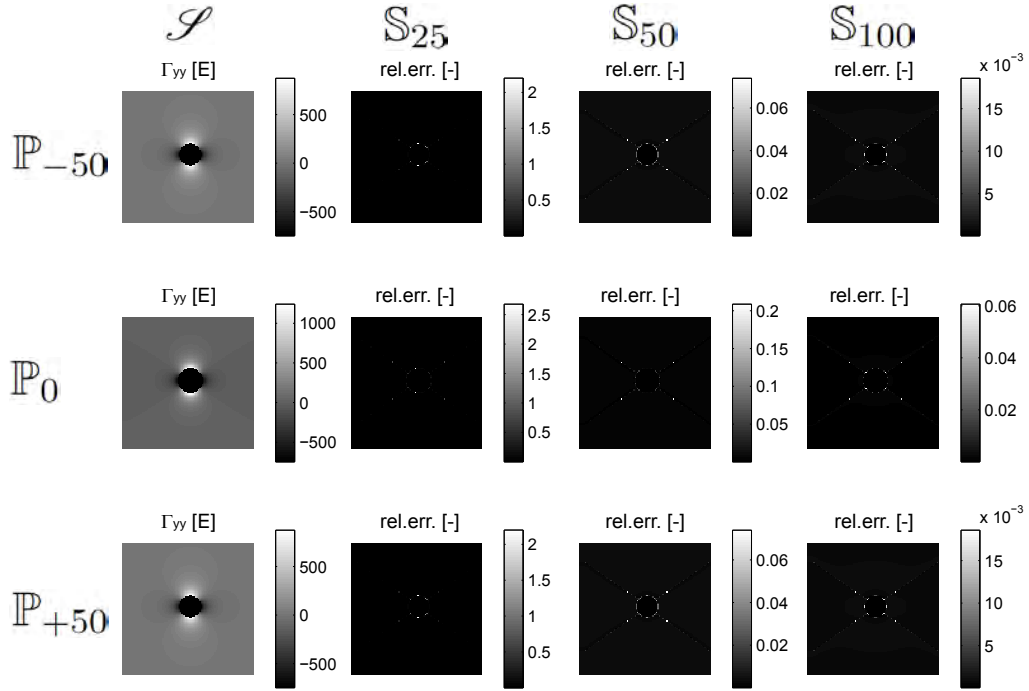


**Figure H.6:** Gravitational tensor  $\Gamma_{yy, \text{grav}}$  of  $\mathcal{S}$  and the respective relative errors of the fields  $S_{25}$ ,  $S_{50}$  and  $S_{100}$  computed with QGravity.

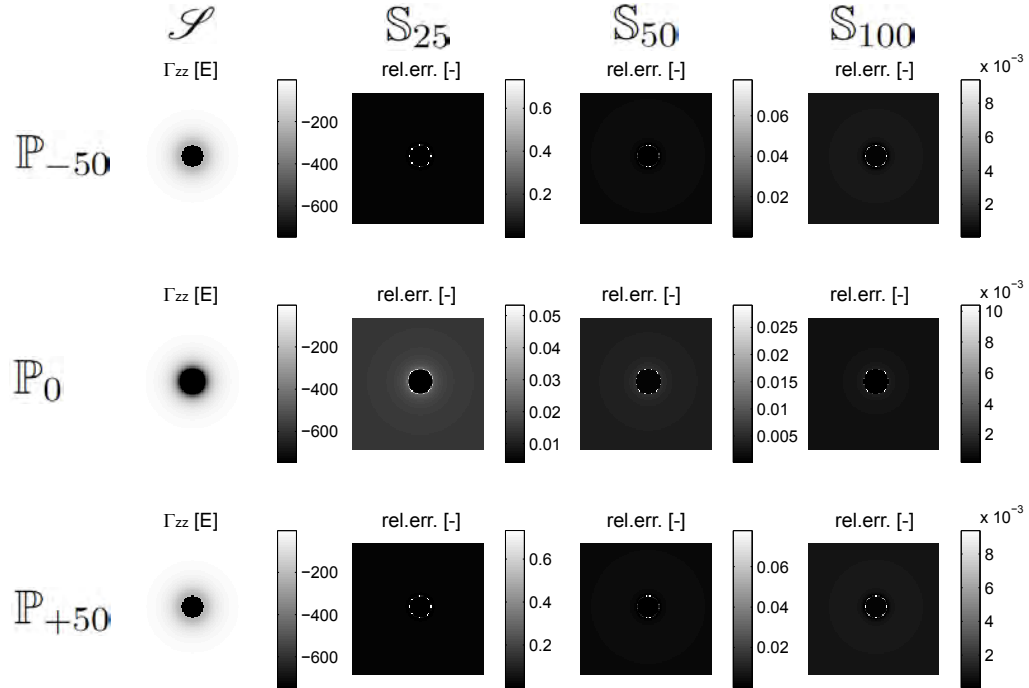


**Figure H.7:** Gravitational tensor  $\Gamma_{zz, \text{grav}}$  of  $\mathcal{S}$  and the respective relative errors of the fields  $S_{25}$ ,  $S_{50}$  and  $S_{100}$  computed with QGravity.

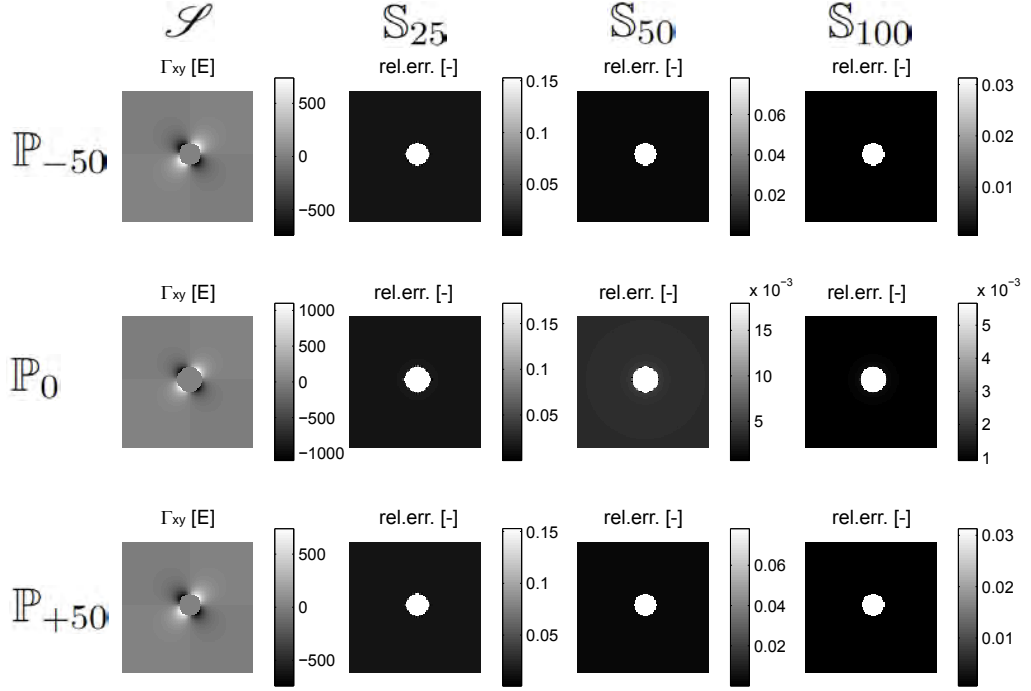


**Figure H.8:** Gravitational tensor  $\Gamma_{xy, \text{grav}}$  of  $\mathcal{S}$  and the respective relative errors of the fields  $\mathbb{S}_{25}$ ,  $\mathbb{S}_{50}$  and  $\mathbb{S}_{100}$  computed with QGravity.

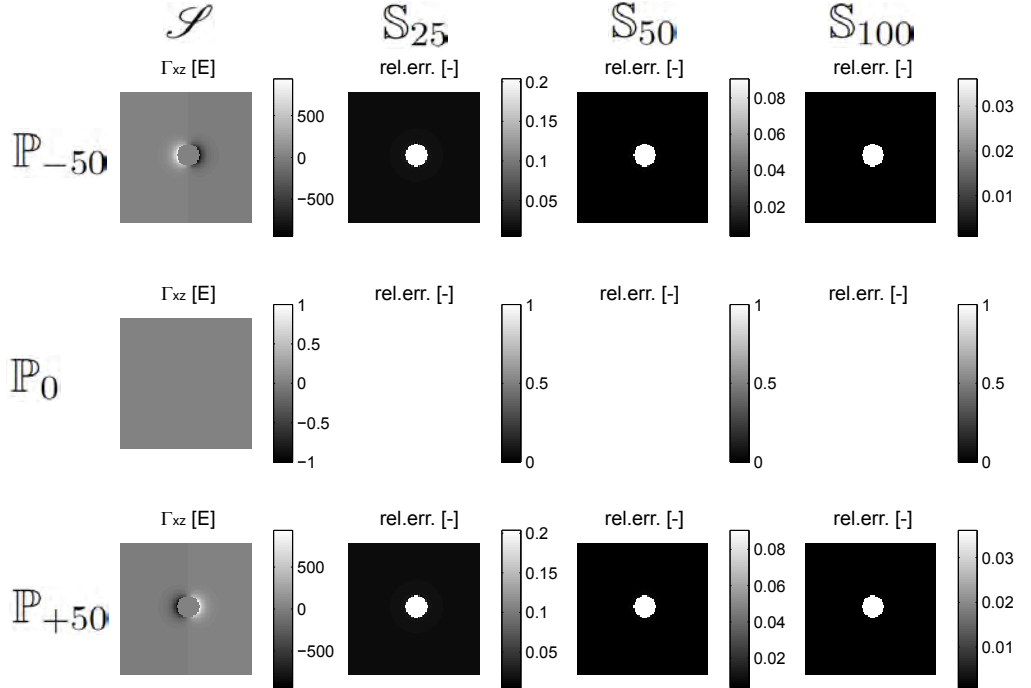


**Figure H.9:** Gravitational tensor  $\Gamma_{xz, \text{grav}}$  of  $\mathcal{S}$  and the respective relative errors of the fields  $\mathbb{S}_{25}$ ,  $\mathbb{S}_{50}$  and  $\mathbb{S}_{100}$  computed with QGravity.

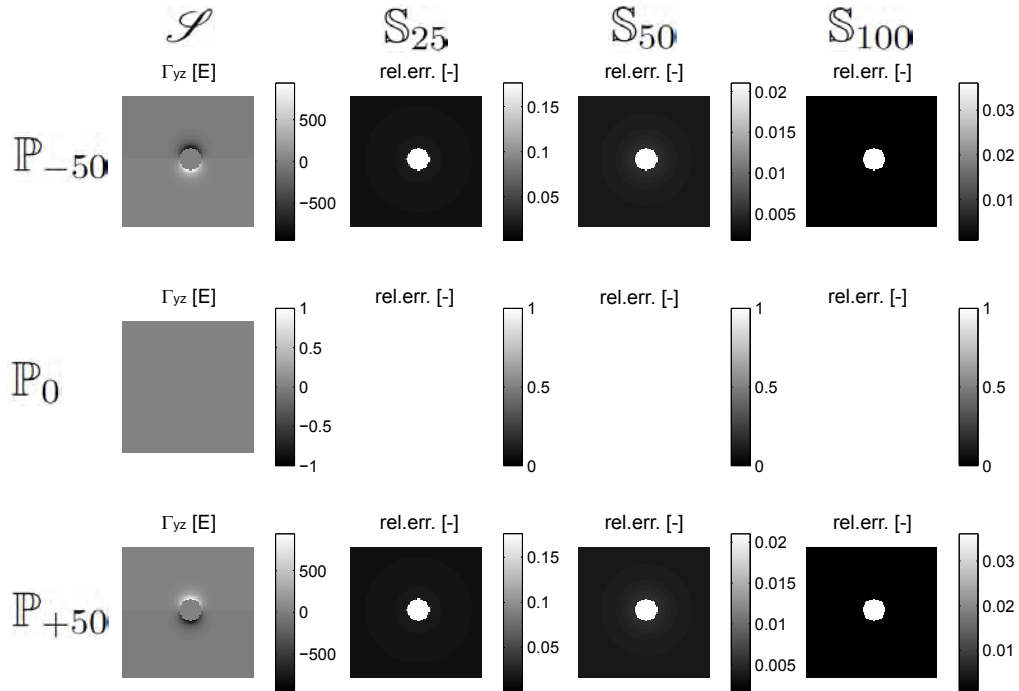


**Figure H.10:** Gravitational tensor  $\Gamma_{yz,\text{grav}}$  of  $\mathcal{S}$  and the respective relative errors of the fields  $S_{25}$ ,  $S_{50}$  and  $S_{100}$  computed with QGravity.

## **Appendix I**

# **Summary of the Observations of the TZ32 Campaign**

Table I.1: Gravimetric measurements in the tunnel along the TZ32.

No	Topo TZ32			LV03		WGS84				
	$y$ [m]	$x$ [m]	$z$ [m]	East [m]	North [m]	$H$ [m]	$\lambda$ [deg]	$\phi$ [deg]	$h$ [m]	$g_{\text{obs}}$ [mgal]
1	0.061	67.278	0.318	490'498.416	125'063.357	421.268	6.0182097	46.2680553	473.69	980578.497
2	0.045	77.394	0.347	490'491.506	125'070.745	421.297	6.0181183	46.2681206	473.72	980578.454
3	-0.017	87.441	0.386	490'484.609	125'078.052	421.337	6.0180272	46.2681852	473.76	980578.419
4	0.020	97.419	0.521	490'477.832	125'085.374	421.472	6.0179375	46.2682499	473.89	980578.384
5	0.035	107.437	0.672	490'471.011	125'092.712	421.623	6.0178474	46.2683148	474.04	980578.349
6	0.063	117.359	0.834	490'464.266	125'099.989	421.785	6.0177582	46.2683792	474.20	980578.304
7	0.095	127.348	0.996	490'457.478	125'107.317	421.947	6.0176684	46.2684440	474.37	980578.263
8	0.120	137.358	1.162	490'450.670	125'114.656	422.113	6.0175784	46.2685089	474.53	980578.218
9	0.160	147.359	1.317	490'443.879	125'121.998	422.269	6.0174886	46.2685738	474.69	980578.155
10	0.142	157.363	1.471	490'437.045	125'129.303	422.423	6.0173982	46.2686384	474.84	980578.114
11	0.096	167.364	1.641	490'430.190	125'136.586	422.593	6.0173076	46.2687028	475.01	980578.044
12	0.115	177.356	1.802	490'423.390	125'143.907	422.754	6.0172177	46.2687675	475.17	980577.990
13	0.098	187.359	1.968	490'416.557	125'151.212	422.921	6.0171274	46.2688321	475.34	980577.926
14	0.101	197.372	2.117	490'409.730	125'158.538	423.070	6.0170371	46.2688969	475.49	980577.863
15	0.078	207.376	2.279	490'402.892	125'165.840	423.232	6.0169467	46.2689614	475.65	980577.823
16	0.120	217.283	2.426	490'396.168	125'173.114	423.380	6.0168578	46.2690258	475.80	980577.784
17	0.159	227.314	2.596	490'389.355	125'180.478	423.550	6.0167677	46.2690909	475.97	980577.755
18	0.087	237.285	2.755	490'382.503	125'187.721	423.709	6.0166771	46.2691549	476.13	980577.712
19	0.095	247.212	2.916	490'375.739	125'194.988	423.871	6.0165877	46.2692192	476.29	980577.673
20	0.100	257.222	3.060	490'368.917	125'202.314	424.015	6.0164975	46.2692839	476.43	980577.614
21	0.114	267.128	3.220	490'362.172	125'209.568	424.176	6.0164083	46.2693481	476.59	980577.558
22	0.116	277.154	3.376	490'355.337	125'216.903	424.332	6.0163179	46.2694129	476.75	980577.500
23	0.098	287.195	3.534	490'348.476	125'224.235	424.490	6.0162272	46.2694778	476.91	980577.447
24	0.094	297.205	3.693	490'341.647	125'231.554	424.650	6.0161369	46.2695425	477.07	980577.378
25	0.067	307.146	3.842	490'334.849	125'238.806	424.799	6.0160471	46.2696066	477.22	980577.348
26	0.055	317.139	4.008	490'328.025	125'246.108	424.966	6.0159568	46.2696712	477.38	980577.295
27	0.064	327.167	4.168	490'321.194	125'253.448	425.126	6.0158665	46.2697361	477.54	980577.258
28	0.095	337.150	4.327	490'314.409	125'260.771	425.286	6.0157768	46.2698008	477.70	980577.215
29	0.066	347.148	4.486	490'307.569	125'268.064	425.445	6.0156864	46.2698653	477.86	980577.138
30	0.068	357.150	4.641	490'300.751	125'275.381	425.601	6.0155962	46.2699300	478.02	980577.087
31	0.097	366.965	4.811	490'294.079	125'282.580	425.772	6.0155080	46.2699936	478.19	980577.029
32	0.055	397.178	5.276	490'273.445	125'304.650	426.238	6.0152352	46.2701888	478.65	980576.886
33	0.075	407.241	5.464	490'266.597	125'312.024	426.427	6.0151446	46.2702540	478.84	980576.828
34	0.034	417.128	5.619	490'259.825	125'319.227	426.583	6.0150551	46.2703177	479.00	980576.765
35	0.010	427.200	5.774	490'252.939	125'326.578	426.738	6.0149640	46.2703826	479.15	980576.705
36	0.039	437.190	5.939	490'246.148	125'333.905	426.904	6.0148742	46.2704474	479.32	980576.636
37	0.015	447.155	6.096	490'239.335	125'341.177	427.062	6.0147842	46.2705117	479.48	980576.551
38	0.039	457.137	6.251	490'232.546	125'348.494	427.217	6.0146944	46.2705764	479.63	980576.475
39	0.024	467.049	6.389	490'225.776	125'355.734	427.356	6.0146049	46.2706404	479.77	980576.399
40	0.008	477.062	6.560	490'218.936	125'363.047	427.528	6.0145144	46.2707051	479.94	980576.338
41	0.010	487.090	6.724	490'212.099	125'370.383	427.693	6.0144240	46.2707700	480.11	980576.278
42	0.017	497.022	6.880	490'205.332	125'377.652	427.849	6.0143346	46.2708342	480.26	980576.207
43	0.010	507.026	7.019	490'198.504	125'384.965	427.989	6.0142443	46.2708989	480.40	980576.150
44	0.031	517.050	7.198	490'191.684	125'392.311	428.169	6.0141541	46.2709638	480.58	980576.058
45	0.036	527.039	7.363	490'184.875	125'399.620	428.335	6.0140641	46.2710285	480.75	980576.000
46	0.070	537.053	7.514	490'178.072	125'406.968	428.487	6.0139741	46.2710935	480.90	980575.929
47	0.080	547.038	7.677	490'171.270	125'414.278	428.650	6.0138842	46.2711581	481.06	980575.862
48	0.078	557.055	7.835	490'164.438	125'421.604	428.809	6.0137938	46.2712229	481.22	980575.787
49	0.055	567.038	7.995	490'157.613	125'428.890	428.970	6.0137036	46.2712873	481.38	980575.706
50	-0.002	577.032	8.163	490'150.757	125'436.161	429.139	6.0136129	46.2713515	481.55	980575.649
51	0.045	587.031	8.319	490'143.973	125'443.506	429.296	6.0135232	46.2714165	481.71	980575.595
52	-0.012	597.018	8.486	490'137.121	125'450.772	429.464	6.0134326	46.2714807	481.88	980575.529
53	0.063	607.007	8.643	490'130.363	125'458.129	429.622	6.0133433	46.2715458	482.04	980575.470
54	0.077	617.154	8.802	490'123.454	125'465.561	429.782	6.0132519	46.2716115	482.20	980575.409
55	0.111	627.145	8.975	490'116.666	125'472.891	429.956	6.0131621	46.2716763	482.37	980575.355
56	0.071	637.158	9.136	490'109.809	125'480.188	430.118	6.0130715	46.2717408	482.53	980575.298
57	0.078	647.153	9.316	490'102.998	125'487.503	430.299	6.0129814	46.2718055	482.71	980575.232
58	0.047	657.137	9.440	490'096.168	125'494.785	430.424	6.0128911	46.2718699	482.84	980575.179
59	0.077	667.421	9.599	490'089.176	125'502.327	430.584	6.0127986	46.2719366	483.00	980575.118
60	0.044	677.402	9.750	490'082.346	125'509.604	430.736	6.0127083	46.2720009	483.15	980575.096
61	0.101	687.351	9.906	490'075.603	125'516.921	430.893	6.0126191	46.2720656	483.31	980575.049
62	0.070	697.384	10.071	490'068.738	125'524.237	431.059	6.0125284	46.2721303	483.47	980575.001
63	0.039	707.417	10.236	490'061.874	125'531.555	431.225	6.0124376	46.2721950	483.64	980574.963
64	0.025	717.798	10.391	490'054.785	125'539.139	431.381	6.0123439	46.2722620	483.79	980574.882
65	0.051	727.782	10.562	490'047.995	125'546.459	431.554	6.0122541	46.2723268	483.97	980574.848
66	0.037	737.782	10.713	490'041.167	125'553.763	431.706	6.0121638	46.2723913	484.12	980574.794
67	0.092	747.769	10.881	490'034.396	125'561.105	431.875	6.0120743	46.2724563	484.29	980574.724
68	0.153	757.723	11.042	490'027.653	125'568.428	432.037	6.0119851	46.2725210	484.45	980574.656
69	0.112	767.750	11.204	490'020.785	125'575.734	432.200	6.0118943	46.2725856	484.61	980574.588
70	0.151	777.775	11.363	490'013.977	125'583.093	432.360	6.0118042	46.2726507	484.77	980574.520
71	0.087	787.708	11.528	490'007.157	125'590.315	432.527	6.0117141	46.2727145	484.94	980574.443
72	0.089	797.739	11.687	490'000.318	125'597.653	432.687	6.0116236	46.2727794	485.10	980574.362
73	0.109	807.718	11.851	489'993.528	125'604.966	432.852	6.0115338	46.2728441	485.26	980574.279
74	0.082	817.610	12.016	489'986.762	125'612.182	433.018	6.0114444	46.2729079	485.43	980574.188
75	0.084	827.581	12.189	489'979.964	125'619.476	433.193	6.0113545	46.2729723	485.60	980574.075
76	0.104	837.577	12.342	489'973.163	125'626.801	433.347	6.0112645	46.2730371	485.76	980573.992
77	0.068	847.566	12.479	489'966.324	125'634.083	433.485	6.0111741	46.2731015	485.90	980573.903

Table I.2: Gravimetric measurements on topography along the TZ32.

No	Topo TZ32			LV03			WGS84			
	$y$ [m]	$x$ [m]	$z$ [m]	East [m]	North [m]	$H$ [m]	$\lambda$ [deg]	$\phi$ [deg]	$h$ [m]	$g_{\text{obs}}$ [mgal]
1	-0.005	67.239	68.588	490'498.395	125'063.282	489.538	6.0182094	46.2680546	541.96	980572.357
2	0.004	77.348	68.807	490'491.508	125'070.683	489.757	6.0181184	46.2681201	542.18	980572.310
3	0.011	87.386	69.083	490'484.668	125'078.029	490.034	6.0180279	46.2681850	542.45	980572.273
4	-0.060	97.414	69.336	490'477.778	125'085.316	490.287	6.0179369	46.2682494	542.71	980572.220
5	-0.075	107.392	69.533	490'470.962	125'092.604	490.484	6.0178468	46.2683139	542.90	980572.173
6	-0.141	117.298	69.779	490'464.160	125'099.804	490.730	6.0177568	46.2683775	543.15	980572.120
7	-0.051	127.218	70.058	490'457.460	125'107.122	491.009	6.0176682	46.2684422	543.43	980572.043
8	0.232	137.276	70.364	490'450.809	125'114.671	491.315	6.0175802	46.2685091	543.73	980571.992
9	0.039	147.232	70.881	490'443.878	125'121.821	491.833	6.0174886	46.2685722	544.25	980571.866
10	0.181	157.257	71.194	490'437.146	125'129.251	492.146	6.0173996	46.2686380	544.56	980571.826
11	-0.093	167.310	71.501	490'430.090	125'136.417	492.453	6.0173064	46.2687013	544.87	980571.804
12	-0.034	177.329	71.939	490'423.302	125'143.785	492.891	6.0172166	46.2687664	545.31	980571.705
13	0.035	187.249	72.373	490'416.587	125'151.087	493.326	6.0171278	46.2688310	545.74	980571.626
14	-0.004	197.314	72.821	490'409.695	125'158.423	493.774	6.0170367	46.2688959	546.19	980571.551
15	0.031	207.302	73.408	490'402.910	125'165.752	494.361	6.0169470	46.2689607	546.78	980571.433
16	0.012	217.157	73.962	490'396.176	125'172.947	494.916	6.0168579	46.2690243	547.33	980571.347
17	0.068	227.303	74.574	490'389.298	125'180.406	495.528	6.0167670	46.2690902	547.95	980571.224
18	0.056	237.268	75.180	490'382.494	125'187.687	496.134	6.0166770	46.2691546	548.55	980571.129
19	0.222	247.182	75.574	490'375.854	125'195.051	496.529	6.0165892	46.2692198	548.95	980571.040
20	0.107	257.201	76.112	490'368.938	125'202.301	497.067	6.0164978	46.2692838	549.48	980570.938
21	-0.077	267.092	76.527	490'362.059	125'209.409	497.483	6.0164069	46.2693467	549.90	980570.867
22	0.151	277.252	76.935	490'355.298	125'216.997	497.891	6.0163174	46.2694138	550.31	980570.787
23	0.172	287.164	77.429	490'348.554	125'224.260	498.385	6.0162282	46.2694780	550.80	980570.697
24	0.070	297.143	77.944	490'341.674	125'231.489	498.901	6.0161373	46.2695419	551.32	980570.608
25	0.063	307.057	78.315	490'334.909	125'238.736	499.272	6.0160479	46.2696060	551.69	980570.533
26	0.256	317.051	78.535	490'328.235	125'246.178	499.493	6.0159595	46.2696718	551.91	980570.487
27	0.012	327.108	78.652	490'321.199	125'253.367	499.610	6.0158666	46.2697353	552.03	980570.459
28	0.061	337.124	78.764	490'314.404	125'260.727	499.723	6.0157767	46.2698004	552.14	980570.418
29	0.066	347.070	78.820	490'307.626	125'268.005	499.779	6.0156871	46.2698648	552.20	980570.407
30	0.060	357.107	78.860	490'300.777	125'275.342	499.820	6.0155966	46.2699297	552.24	980570.415
31	0.098	366.650	79.086	490'294.517	125'282.552	500.047	6.0155137	46.2699935	552.46	980570.349
32	0.087	397.057	79.616	490'273.554	125'304.580	500.578	6.0152366	46.2701882	552.99	980570.252
33	0.007	407.160	79.906	490'266.606	125'311.915	500.869	6.0151448	46.2702530	553.28	980570.198
34	-0.344	416.926	80.467	490'259.690	125'318.818	501.431	6.0150534	46.2703140	553.85	980570.078
35	-0.023	427.077	80.760	490'253.003	125'326.462	501.724	6.0149649	46.2703816	554.14	980570.023
36	-0.128	434.329	81.578	490'247.980	125'331.695	502.543	6.0148985	46.2704279	554.96	980569.811
37	0.014	447.133	81.890	490'239.353	125'341.157	502.856	6.0147844	46.2705116	555.27	980569.808
38	0.137	457.283	82.604	490'232.521	125'348.665	503.570	6.0146940	46.2705780	555.99	980569.696
39	-0.141	467.054	83.338	490'225.655	125'355.622	504.305	6.0146034	46.2706394	556.72	980569.584
40	-0.210	476.997	84.250	490'218.825	125'362.847	505.218	6.0145131	46.2707033	557.63	980569.412
41	-0.241	487.030	84.900	490'211.960	125'370.164	505.869	6.0144223	46.2707680	558.28	980569.295
42	0.231	496.914	85.817	490'205.565	125'377.715	506.786	6.0143376	46.2708349	559.20	980569.114
43	-0.134	507.056	86.573	490'198.383	125'384.884	507.543	6.0142427	46.2708982	559.96	980568.973
44	-0.154	517.059	87.217	490'191.547	125'392.186	508.188	6.0141524	46.2709627	560.60	980568.849
45	-0.101	527.016	87.739	490'184.796	125'399.505	508.711	6.0140631	46.2710274	561.13	980568.753
46	0.092	536.676	88.278	490'178.350	125'406.703	509.251	6.0139778	46.2710911	561.67	980568.654
47	-0.389	547.096	88.524	490'170.892	125'413.996	509.497	6.0138793	46.2711555	561.91	980568.602
48	-0.221	557.011	88.849	490'164.254	125'421.363	509.823	6.0137915	46.2712207	562.24	980568.550
49	-0.039	567.022	89.106	490'157.560	125'428.808	510.081	6.0137029	46.2712865	562.50	980568.511
50	0.016	577.019	89.340	490'150.783	125'436.158	510.316	6.0136133	46.2713515	562.73	980568.469
51	0.074	587.006	89.598	490'144.016	125'443.502	510.575	6.0135238	46.2714165	562.99	980568.415
52	0.101	596.953	89.832	490'137.253	125'450.796	510.810	6.0134344	46.2714810	563.22	980568.382
53	-0.221	607.026	90.063	490'130.148	125'457.944	511.042	6.0133405	46.2715441	563.46	980568.347
54	-0.199	617.070	90.389	490'123.315	125'465.305	511.369	6.0132502	46.2716092	563.78	980568.298
55	0.028	627.088	90.698	490'116.649	125'472.787	511.679	6.0131619	46.2716754	564.09	980568.235
56	-0.130	637.114	91.112	490'109.697	125'480.012	512.094	6.0130701	46.2717392	564.51	980568.151
57	-0.010	647.061	91.576	490'103.002	125'487.370	512.559	6.0129815	46.2718043	564.97	980568.061
58	-0.229	657.121	92.031	490'095.982	125'494.579	513.015	6.0128887	46.2718680	565.43	980567.978
59	-0.373	667.397	92.467	490'088.869	125'501.996	513.452	6.0127947	46.2719336	565.87	980567.885
60	0.019	677.311	92.839	490'082.395	125'509.515	513.825	6.0127090	46.2720001	566.24	980567.802
61	0.146	687.577	93.499	490'075.488	125'517.110	514.486	6.0126176	46.2720673	566.90	980567.668
62	0.075	697.709	94.277	490'068.527	125'524.472	515.265	6.0125256	46.2721324	567.68	980567.509
63	0.353	707.532	94.581	490'062.032	125'531.846	515.570	6.0124396	46.2721976	567.98	980567.443
64	-0.189	717.708	94.899	490'054.696	125'538.920	515.889	6.0123428	46.2722601	568.30	980567.377
65	0.101	726.983	95.249	490'048.583	125'545.901	516.240	6.0122619	46.2723219	568.65	980567.304
66	0.035	737.765	95.587	490'041.182	125'553.742	516.580	6.0121640	46.2723912	568.99	980567.232
67	0.456	747.745	95.953	490'034.685	125'561.329	516.947	6.0120780	46.2724583	569.36	980567.156
68	-0.068	757.731	96.348	490'027.492	125'568.275	517.343	6.0119830	46.2725196	569.76	980567.069
69	-0.102	767.637	96.756	490'020.713	125'575.498	517.752	6.0118934	46.2725835	570.16	980566.982
70	0.351	777.703	97.174	490'014.180	125'583.169	518.171	6.0118069	46.2726514	570.58	980566.887
71	0.057	787.694	97.676	490'007.152	125'590.276	518.675	6.0117140	46.2727142	571.09	980566.788
72	0.059	797.658	98.124	490'000.359	125'597.566	519.124	6.0116242	46.2727786	571.54	980566.702
73	0.094	807.692	98.608	489'993.542	125'604.928	519.609	6.0115340	46.2728437	572.02	980566.607
74	0.008	817.767	99.125	489'986.609	125'612.239	520.127	6.0114424	46.2729084	572.54	980566.516
75	0.053	827.543	99.644	489'979.976	125'619.419	520.648	6.0113547	46.2729719	573.06	980566.422
76	0.175	837.537	100.201	489'973.249	125'626.812	521.206	6.0112657	46.2730372	573.62	980566.317
77	-0.037	847.433	100.655	489'966.347	125'633.906	521.661	6.0111745	46.2730999	574.07	980566.245

Table I.3: Surface deflections of the vertical measurements along the TZ32.

No	Topo TZ32			LV03			WGS84		UTC	
	<i>y</i>	<i>x</i>	<i>z</i>	East	North	<i>H</i>	$\epsilon_x$	$\epsilon_y$	[dd.mm.yyyy	
	[m]	[m]	[m]	[m]	[m]	[m]	[arcsec]	[arcsec]	HH:MM]	
1	1.565	67.489	69.873	490'499.373	125'064.536	490.823	-12.959	-0.117	18.08.2009 21:27	
2	-0.210	77.091	70.062	490'491.527	125'070.349	491.012	-12.975	-0.119	18.08.2009 22:25	
3	-0.288	86.092	70.342	490'485.332	125'076.879	491.293	-12.972	-0.181	18.08.2009 23:18	
4	-0.064	97.364	70.635	490'477.809	125'085.277	491.586	-13.019	-0.128	19.08.2009 00:08	
5	-0.068	107.421	70.827	490'470.948	125'092.629	491.778	-13.123	-0.099	19.08.2009 22:12	
6	-0.034	117.381	71.046	490'464.181	125'099.937	491.997	-13.079	-0.149	19.08.2009 23:00	
7	-0.053	127.329	71.401	490'457.383	125'107.201	492.352	-13.249	-0.172	19.08.2009 23:47	
8	0.107	137.518	71.707	490'450.552	125'114.762	492.658	-13.097	-0.119	20.08.2009 00:42	
9	0.212	147.302	72.140	490'443.957	125'121.990	493.092	-13.133	0.013	20.08.2009 01:46	
10	0.273	157.384	72.503	490'437.127	125'129.406	493.455	-13.319	0.010	26.08.2009 20:58	
11	0.210	167.643	72.829	490'430.085	125'136.866	493.781	-13.241	0.016	27.08.2009 22:40	
12	0.230	177.411	73.280	490'423.439	125'144.025	494.232	-13.279	0.081	27.08.2009 23:37	
13	0.060	187.412	73.691	490'416.494	125'151.224	494.644	-13.320	0.047	28.08.2009 00:21	
14	0.080	197.667	74.186	490'409.516	125'158.738	495.139	-13.396	0.009	28.08.2009 01:12	
15	0.044	207.380	74.700	490'402.866	125'165.817	495.653	-13.457	-0.016	28.08.2009 01:52	
16	0.087	217.625	75.316	490'395.912	125'173.340	496.270	-13.326	0.009	28.08.2009 02:40	
17	0.026	227.283	75.879	490'389.281	125'180.363	496.833	-13.381	0.027	28.08.2009 03:26	
18	0.162	237.128	76.473	490'382.667	125'187.657	497.427	-13.360	-0.031	30.08.2009 20:34	
19	0.178	247.071	76.921	490'375.899	125'194.940	497.876	-13.437	-0.065	30.08.2009 21:18	
20	0.071	257.110	77.369	490'368.974	125'202.210	498.324	-13.385	-0.017	30.08.2009 21:55	
21	0.141	267.103	77.798	490'362.211	125'209.566	498.754	-13.440	0.051	30.08.2009 22:38	
22	0.017	276.973	78.215	490'355.390	125'216.701	499.171	-13.590	0.105	30.08.2009 23:49	
23	0.023	287.155	78.745	490'348.451	125'224.152	499.701	-13.444	0.008	31.08.2009 00:29	
24	0.099	297.206	79.282	490'341.652	125'231.555	500.239	-13.553	0.043	31.08.2009 01:07	
25	-0.031	307.192	79.607	490'334.748	125'238.770	500.564	-13.567	0.100	31.08.2009 01:44	
26	-0.189	317.151	79.820	490'327.841	125'245.947	500.778	-13.677	0.110	31.08.2009 02:22	
27	-0.796	327.102	79.925	490'320.612	125'252.811	500.883	-13.620	0.206	31.08.2009 03:00	
28	-1.569	337.111	79.951	490'313.221	125'259.605	500.910	-13.685	0.104	31.08.2009 03:59	
29	-1.556	347.257	80.042	490'306.312	125'267.035	501.001	-13.684	0.171	31.08.2009 20:48	
30	-0.004	356.373	80.193	490'301.231	125'274.761	501.153	-13.593	0.182	31.08.2009 21:34	
31	0.127	363.831	80.297	490'296.241	125'280.305	501.257	-13.706	0.075	31.08.2009 22:16	
32	0.196	400.185	80.983	490'271.500	125'306.942	501.946	-14.066	0.366	01.09.2009 00:14	
33	-0.069	407.155	81.242	490'266.554	125'311.859	502.205	-14.002	0.189	01.09.2009 01:13	
34	-0.108	419.614	81.945	490'258.029	125'320.945	502.909	-14.013	0.201	01.09.2009 01:55	
35	-0.139	432.027	82.913	490'249.542	125'330.003	503.878	-14.063	0.092	01.09.2009 02:37	
36	0.141	442.131	82.980	490'242.856	125'337.584	503.945	-14.040	0.161	01.09.2009 03:21	
37	-0.083	452.071	83.528	490'235.914	125'344.702	504.494	-14.062	0.109	07.09.2009 20:15	
38	0.058	462.164	84.270	490'229.135	125'352.181	505.237	-14.099	0.100	07.09.2009 21:05	
39	-0.081	472.183	85.175	490'222.201	125'359.414	506.142	-14.064	0.070	07.09.2009 21:41	
40	-0.015	481.968	85.881	490'215.577	125'366.615	506.849	-14.045	0.112	07.09.2009 22:27	
41	-0.054	491.894	86.670	490'208.780	125'373.848	507.639	-13.987	0.144	07.09.2009 23:15	
42	-0.111	502.016	87.544	490'201.836	125'381.214	508.514	-14.058	0.183	07.09.2009 23:56	
43	0.056	511.901	88.227	490'195.217	125'388.557	509.198	-14.142	0.143	08.09.2009 00:47	
44	0.031	521.902	88.791	490'188.380	125'395.854	509.762	-14.111	0.217	08.09.2009 20:12	
45	-0.088	531.973	89.419	490'181.425	125'403.140	510.391	-14.332	0.262	08.09.2009 20:58	
46	-0.278	541.974	89.643	490'174.467	125'410.325	510.616	-14.109	0.055	08.09.2009 21:50	
47	-0.120	552.143	90.008	490'167.647	125'417.871	510.982	-14.140	0.124	08.09.2009 22:37	
48	-0.208	562.504	90.311	490'160.518	125'425.389	511.286	-14.290	0.223	08.09.2009 23:26	
49	-0.299	572.096	90.552	490'153.910	125'432.342	511.528	-14.360	0.267	09.09.2009 00:06	
50	-0.290	582.168	90.814	490'147.049	125'439.716	511.791	-14.344	0.234	09.09.2009 00:58	
51	-0.283	591.906	91.003	490'140.413	125'446.842	511.980	-14.459	0.133	09.09.2009 01:46	
52	-0.152	601.897	91.256	490'133.696	125'454.240	512.234	-14.443	0.233	09.09.2009 02:26	
53	-0.090	611.994	91.551	490'126.856	125'461.667	512.530	-14.412	0.213	09.09.2009 03:08	
54	0.035	621.995	91.871	490'120.128	125'469.067	512.851	-14.495	0.367	27.10.2009 18:46	
55	-0.155	632.165	92.312	490'113.054	125'476.375	513.293	-14.554	0.394	27.10.2009 19:28	
56	-0.087	641.974	92.680	490'106.415	125'483.596	513.662	-14.540	0.320	27.10.2009 20:29	
57	0.026	652.198	93.098	490'099.526	125'491.152	514.081	-14.618	0.301	27.10.2009 21:20	
58	0.045	662.051	93.585	490'092.820	125'498.371	514.569	-14.642	0.361	27.10.2009 21:57	
59	-0.032	672.427	94.003	490'085.688	125'505.908	514.988	-14.609	0.234	27.10.2009 22:33	
60	0.112	683.064	94.443	490'078.541	125'513.786	515.430	-14.510	0.249	29.10.2009 18:35	
61	0.015	692.296	95.246	490'072.174	125'520.472	516.234	-14.613	0.287	29.10.2009 19:18	
62	-0.146	702.435	95.892	490'065.143	125'527.778	516.881	-14.674	0.308	29.10.2009 19:56	
63	-0.017	712.341	96.057	490'058.482	125'535.112	517.047	-14.696	0.297	29.10.2009 20:35	
64	0.022	722.776	96.434	490'051.394	125'542.770	517.425	-14.693	0.381	29.10.2009 21:18	
65	-0.022	732.812	96.761	490'044.519	125'550.081	517.753	-14.811	0.331	29.10.2009 22:15	
66	0.001	742.640	97.066	490'037.834	125'557.284	518.059	-14.827	0.310	06.10.2010 23:13	
67	0.100	752.622	97.464	490'031.100	125'564.653	518.458	-14.851	0.282	06.10.2010 22:38	
68	0.103	762.665	97.890	490'024.253	125'572.001	518.886	-14.882	0.297	06.10.2010 22:01	
69	0.128	772.685	98.285	490'017.439	125'579.347	519.282	-14.854	0.216	06.10.2010 21:27	
70	0.258	782.580	98.742	490'010.787	125'586.673	519.740	-14.814	0.320	06.10.2010 20:51	
71	0.292	791.646	99.099	490'004.629	125'593.327	520.098	-14.970	0.314	06.10.2010 20:09	
72	0.155	802.715	98.162	489'996.980	125'601.330	519.163	-15.030	0.163	06.10.2010 19:36	
73	0.850	812.822	98.748	489'990.597	125'609.195	519.750	-15.133	0.344	28.09.2010 22:56	
74	0.882	822.430	99.315	489'984.069	125'616.245	520.318	-15.196	0.373	28.09.2010 22:20	
75	0.418	831.690	99.802	489'977.415	125'622.701	520.806	-15.218	0.330	28.09.2010 21:37	
76	-0.341	841.803	100.310	489'969.963	125'629.581	521.316	-15.228	0.399	28.09.2010 20:37	
77	-0.581	857.606	102.569	489'959.012	125'640.975	523.577	-15.271	0.333	28.09.2010 19:56	



Table I.4: Surface deflections of the vertical measurements along the TZ32.

No	WGS84			ITRS		WGS84		UTC
	$\lambda$ [m]	$\phi$ [m]	$h$ [m]	$\Lambda$ [m]	$\Phi$ [m]	$\eta$ [arcsec]	$\xi$ [arcsec]	[dd.mm.yyyy HH:MM]
1	6.0182297	46.2680755	541.381	6.0218231	46.2654678	8.942	-9.388	18.08.2009 21:27
2	6.0181266	46.2681265	541.570	6.0217209	46.2655152	8.945	-9.401	18.08.2009 22:25
3	6.0180447	46.2681842	541.851	6.0216362	46.2655615	8.938	-9.442	18.08.2009 23:18
4	6.0179583	46.2682449	542.086	6.0215607	46.2656237	8.965	-9.436	19.08.2009 00:08
5	6.0178545	46.2683235	542.337	6.0214761	46.2656863	9.013	-9.494	19.08.2009 22:12
6	6.0177651	46.2683881	542.555	6.0213840	46.2657501	9.006	-9.497	19.08.2009 23:00
7	6.0176752	46.2684524	542.910	6.0213417	46.2657759	9.124	-9.635	19.08.2009 23:47
8	6.0175848	46.2685192	543.216	6.0212060	46.2658834	9.012	-9.489	20.08.2009 00:42
9	6.0174980	46.2685830	543.687	6.0211790	46.2659639	9.161	-9.429	20.08.2009 01:46
10	6.0174044	46.2686525	544.005	6.0211339	46.2659948	9.281	-9.568	26.08.2009 20:58
11	6.0173142	46.2687147	544.339	6.0210243	46.2660761	9.233	-9.499	27.08.2009 22:40
12	6.0172264	46.2687780	544.790	6.0209629	46.2661444	9.299	-9.481	27.08.2009 23:37
13	6.0171346	46.2688416	545.202	6.0208725	46.2661935	9.302	-9.533	28.08.2009 00:21
14	6.0170424	46.2689080	545.697	6.0207876	46.2662371	9.320	-9.615	28.08.2009 01:12
15	6.0169545	46.2689706	546.211	6.0207126	46.2662830	9.352	-9.675	28.08.2009 01:52
16	6.0168625	46.2690371	546.828	6.0205908	46.2663805	9.278	-9.564	28.08.2009 02:40
17	6.0167749	46.2690992	547.391	6.0205234	46.2664350	9.329	-9.591	28.08.2009 03:26
18	6.0166874	46.2691637	547.985	6.0204150	46.2664924	9.276	-9.617	30.08.2009 20:34
19	6.0165979	46.2692281	548.434	6.0203267	46.2665350	9.280	-9.695	30.08.2009 21:18
20	6.0165064	46.2692923	548.882	6.0202376	46.2666189	9.285	-9.624	30.08.2009 21:55
21	6.0164169	46.2693574	549.312	6.0201891	46.2666861	9.387	-9.617	30.08.2009 22:38
22	6.0163268	46.2694204	549.729	6.0201610	46.2667295	9.542	-9.687	30.08.2009 23:49
23	6.0162351	46.2694863	550.259	6.0199967	46.2668059	9.361	-9.650	31.08.2009 00:29
24	6.0161452	46.2695518	550.797	6.0199643	46.2668561	9.504	-9.704	31.08.2009 01:07
25	6.0160539	46.2696155	551.122	6.0198825	46.2669283	9.528	-9.674	31.08.2009 01:44
26	6.0159627	46.2696790	551.336	6.0198303	46.2669718	9.625	-9.746	31.08.2009 02:22
27	6.0158673	46.2697395	551.441	6.0197126	46.2670622	9.569	-9.638	31.08.2009 03:00
28	6.0157699	46.2697994	551.468	6.0196310	46.2670892	9.609	-9.757	31.08.2009 03:59
29	6.0156785	46.2698651	551.559	6.0195531	46.2671684	9.642	-9.708	31.08.2009 20:48
30	6.0156108	46.2699337	551.711	6.0194603	46.2672572	9.580	-9.635	31.08.2009 21:34
31	6.0155448	46.2699828	551.815	6.0194059	46.2672630	9.609	-9.791	31.08.2009 22:16
32	6.0152177	46.2702183	552.504	6.0192603	46.2674829	10.060	-9.847	01.09.2009 00:14
33	6.0151524	46.2702617	552.763	6.0190888	46.2675051	9.796	-9.924	01.09.2009 01:13
34	6.0150397	46.2703420	553.467	6.0190199	46.2675853	9.905	-9.924	01.09.2009 01:55
35	6.0149275	46.2704221	554.436	6.0188755	46.2676408	9.825	-10.013	01.09.2009 02:37
36	6.0148390	46.2704892	554.503	6.0188171	46.2677194	9.900	-9.971	01.09.2009 03:21
37	6.0147473	46.2705520	555.052	6.0187133	46.2677679	9.869	-10.023	07.09.2009 20:15
38	6.0146577	46.2706182	555.795	6.0186084	46.2678250	9.831	-10.056	07.09.2009 21:05
39	6.0145660	46.2706821	556.700	6.0185194	46.2678899	9.838	-10.052	07.09.2009 21:41
40	6.0144784	46.2707458	557.407	6.0184270	46.2679658	9.826	-10.008	07.09.2009 22:27
41	6.0143886	46.2708097	558.197	6.0183459	46.2680472	9.848	-9.945	07.09.2009 23:15
42	6.0142968	46.2708748	559.072	6.0182764	46.2681059	9.903	-9.968	07.09.2009 23:56
43	6.0142092	46.2709398	559.756	6.0182051	46.2681461	9.944	-10.057	08.09.2009 00:47
44	6.0141188	46.2710043	560.320	6.0181347	46.2682312	9.993	-9.983	08.09.2009 20:12
45	6.0140269	46.2710687	560.949	6.0181108	46.2682602	10.163	-10.110	08.09.2009 20:58
46	6.0139350	46.2711321	561.174	6.0179009	46.2683282	9.869	-10.094	08.09.2009 21:50
47	6.0138448	46.2711989	561.541	6.0178307	46.2684021	9.919	-10.069	08.09.2009 22:37
48	6.0137506	46.2712653	561.844	6.0178074	46.2684577	10.095	-10.108	08.09.2009 23:26
49	6.0136632	46.2713268	562.086	6.0177523	46.2685133	10.176	-10.129	09.09.2009 00:06
50	6.0135725	46.2713920	562.349	6.0176511	46.2685756	10.150	-10.139	09.09.2009 00:58
51	6.0134848	46.2714550	562.538	6.0175484	46.2685961	10.112	-10.292	09.09.2009 01:46
52	6.0133959	46.2715204	562.792	6.0175233	46.2686843	10.271	-10.210	09.09.2009 02:26
53	6.0133055	46.2715861	563.088	6.0173939	46.2687524	10.174	-10.201	09.09.2009 03:08
54	6.0132165	46.2716515	563.409	6.0173720	46.2688323	10.341	-10.149	27.10.2009 18:46
55	6.0131230	46.2717161	563.851	6.0173091	46.2688911	10.417	-10.170	27.10.2009 19:28
56	6.0130352	46.2717799	564.220	6.0171803	46.2689440	10.315	-10.209	27.10.2009 20:29
57	6.0129441	46.2718468	564.639	6.0171186	46.2689886	10.388	-10.289	27.10.2009 21:20
58	6.0128554	46.2719106	565.127	6.0170538	46.2690596	10.447	-10.264	27.10.2009 21:57
59	6.0127611	46.2719772	565.546	6.0169175	46.2691081	10.343	-10.329	27.10.2009 22:33
60	6.0126666	46.2720469	565.988	6.0167927	46.2692003	10.268	-10.248	29.10.2009 18:35
61	6.0125825	46.2721060	566.792	6.0167545	46.2692464	10.382	-10.294	29.10.2009 19:18
62	6.0124895	46.2721705	567.439	6.0166818	46.2693030	10.432	-10.323	29.10.2009 19:56
63	6.0124014	46.2722354	567.605	6.0166005	46.2693611	10.449	-10.347	29.10.2009 20:35
64	6.0123077	46.2723031	567.983	6.0165265	46.2694454	10.498	-10.288	29.10.2009 21:18
65	6.0122168	46.2723677	568.311	6.0164585	46.2694771	10.555	-10.406	29.10.2009 22:15
66	6.0121284	46.2724314	568.617	6.0163642	46.2695335	10.541	-10.433	06.10.2010 23:13
67	6.0120393	46.2724966	569.016	6.0162736	46.2695885	10.537	-10.469	06.10.2010 22:38
68	6.0119488	46.2725615	569.444	6.0161932	46.2696500	10.562	-10.481	06.10.2010 22:01
69	6.0118587	46.2726265	569.840	6.01610748	46.2697048	10.491	-10.518	06.10.2010 21:27
70	6.0117707	46.2726913	570.298	6.0160089	46.2697979	10.546	-10.416	06.10.2010 20:51
71	6.0116893	46.2727501	570.656	6.0159657	46.2698242	10.641	-10.533	06.10.2010 20:09
72	6.0115882	46.2728208	569.721	6.0158419	46.2698542	10.585	-10.680	06.10.2010 19:36
73	6.0115036	46.2728905	570.308	6.0158348	46.2699382	10.778	-10.628	28.09.2010 22:56
74	6.0114172	46.2729528	570.876	6.0157742	46.2699935	10.842	-10.654	28.09.2010 22:20
75	6.0113294	46.2730098	571.364	6.0156774	46.2700376	10.820	-10.700	28.09.2010 21:37
76	6.0112312	46.2730704	571.874	6.0156160	46.2701098	10.911	-10.658	28.09.2010 20:37
77	6.0110864	46.2731711	574.135	6.0154603	46.2701890	10.884	-10.736	28.09.2010 19:56



# Curriculum Vitae

## Personal Details

Name: Guillaume  
First Name: Sébastien  
Date of Birth: 22 September 1979  
Citizen: Diesse (BE)  
Nationality: Swiss

## Education and Professional Positions

2012 to 2015: Lecturer at ETH Zurich for the Lectures  
Geodetic Networks and Parameter Estimation & Astro and Gravity Lab  
2009 to 2015: Research Assistant at ETH Zurich in the Geodesy and Geodynamic Lab  
2009 to 2011: Doctoral Student at CERN in Geneva  
2007 to 2009: Scientific collaborator at ETH Zurich in the Geodesy and Geodynamic Lab  
2003 to 2007: Studies of Geomatics Engineering at ETH Zurich  
Degree as Dipl. Ing. Geomatik-Ing. ETH Zurich  
1999 to 2003 University of Applied Sciences in Yverdon-les-Bains  
Degree as Dipl. Ing. HES in Geomatics  
1995 to 1999 Professional in Geomatics, Geometerbüro Bättig in Murten